



Journal of Turbomachinery

Published Quarterly by ASME

VOLUME 130 • NUMBER 4 • OCTOBER 2008

RESEARCH PAPERS

- 041001 **The Influence of Shroud and Cavity Geometry on Turbine Performance: An Experimental and Computational Study—Part I: Shroud Geometry**
Budimir Rosic, John D. Denton, and Eric M. Curtis
- 041002 **The Influence of Shroud and Cavity Geometry on Turbine Performance: An Experimental and Computational Study—Part II: Exit Cavity Geometry**
Budimir Rosic, John D. Denton, Eric M. Curtis, and Ashley T. Peterson
- 041003 **Effects of Hole Arrangements on Local Heat/Mass Transfer for Impingement/Effusion Cooling With Small Hole Spacing**
Hyung Hee Cho, Dong Ho Rhee, and R. J. Goldstein
- 041004 **Periodical Unsteady Flow Within a Rotor Blade Row of an Axial Compressor—Part I: Flow Field at Midspan**
Ronald Mailach, Ingolf Lehmann, and Konrad Vogeler
- 041005 **Periodical Unsteady Flow Within a Rotor Blade Row of an Axial Compressor—Part II: Wake-Tip Clearance Vortex Interaction**
Ronald Mailach, Ingolf Lehmann, and Konrad Vogeler
- 041006 **Effects of Deposits on Film Cooling of a Vane Endwall Along the Pressure Side**
N. Sundaram, M. D. Barringer, and K. A. Thole
- 041007 **The Augmentation of Internal Blade Tip-Cap Cooling by Arrays of Shaped Pins**
Ronald S. Bunker
- 041008 **Measurements in Film Cooling Flows With Periodic Wakes**
Kristofer M. Womack, Ralph J. Volino, and Michael P. Schultz
- 041009 **The Effects of Blade Passing on the Heat Transfer Coefficient of the Overtip Casing in a Transonic Turbine Stage**
Steven J. Thorpe and Roger W. Ainsworth
- 041010 **Combined Effects of Wakes and Jet Pulsing on Film Cooling**
Kristofer M. Womack, Ralph J. Volino, and Michael P. Schultz
- 041011 **The Influence of Sweep on Axial Flow Turbine Aerodynamics in the Endwall Region**
Graham Pullan and Neil W. Harvey
- 041012 **Effects of Regular and Random Roughness on the Heat Transfer and Skin Friction Coefficient on the Suction Side of a Gas Turbine Vane**
Jason E. Dees and David G. Bogard
- 041013 **Bump and Trench Modifications to Film-Cooling Holes at the Vane-Endwall Junction**
N. Sundaram and K. A. Thole
- 041014 **Prestall Behavior of a Transonic Axial Compressor Stage via Time-Accurate Numerical Simulation**
Jen-Ping Chen, Michael D. Hathaway, and Gregory P. Herrick
- 041015 **Large Eddy Simulation of Leading Edge Film Cooling—Part II: Heat Transfer and Effect of Blowing Ratio**
Ali Rozati and Danesh K. Tafti
- 041016 **Large Eddy Simulation Investigation of Flow and Heat Transfer in a Channel With Dimples and Protrusions**
Mohammad A. Elyyan and Danesh K. Tafti

(Contents continued on inside back cover)

This journal is printed on acid-free paper, which exceeds the ANSI Z39.48-1992 specification for permanence of paper and library materials. ©™

♻️ 85% recycled content, including 10% post-consumer fibers.

Editor, **DAVID C. WISLER (2008)**
Assistant to the Editor: **ELIZABETH WISLER**
Associate Editors
Gas Turbine (Review Chair)
KLAUS BRUN (2008)
Aeromechanics
M. MONTGOMERY (2008)
A. SINHA (2008)
Boundary Layers and Turbulence
G. WALKER (2008)
Compressor Aero
ZOLTAN S. SPAKOVSKY (2011)
Computational Fluid Dynamics
J. ADAMCZYK (2008)
M. CASEY (2008)
Experimental Methods
W.-F. NG (2008)
Heat Transfer
R. BUNKER (2009)
J.-C. HAN (2008)
Radial Turbomachinery
R. VAN DEN BRAEMBUSSCHE (2008)
Turbomachinery Aero
S. GALLIMORE (2008)
D. PRASAD (2008)
A. R. WADIA (2009)

PUBLICATIONS COMMITTEE
Chair, **BAHRAM RAVANI**

OFFICERS OF THE ASME
President, **THOMAS M. BARLOW**
Executive Director, **THOMAS G. LOUGHLIN**
Treasurer, **T. PESTORIUS**

PUBLISHING STAFF
Managing Director, Publishing
PHILIP DI VIETRO
Manager, Journals
COLIN MCATEER
Production Coordinator
JUDITH SIERANT

Transactions of the ASME, Journal of Turbomachinery (ISSN 0889-504X) is published quarterly (Jan., Apr., July, Oct.) by The American Society of Mechanical Engineers, Three Park Avenue, New York, NY 10016. Periodicals postage paid at New York, NY and additional mailing offices.
POSTMASTER: Send address changes to Transactions of the ASME, Journal of Turbomachinery, c/o THE AMERICAN SOCIETY OF MECHANICAL ENGINEERS, 22 Law Drive, Box 2300, Fairfield, NJ 07007-2300.
CHANGES OF ADDRESS must be received at Society headquarters seven weeks before they are to be effective. Please send old label and new address.

STATEMENT from By-Laws. The Society shall not be responsible for statements or opinions advanced in papers or ... printed in its publications (B7.1, Par. 3).
COPYRIGHT © 2008 by the American Society of Mechanical Engineers. For authorization to photocopy material for internal or personal use under those circumstances not falling within the fair use provisions of the Copyright Act, contact the Copyright Clearance Center (CCC), 222 Rosewood Drive, Danvers, MA 01923, tel: 978-750-8400, www.copyright.com. Request for special permission or bulk copying should be addressed to Reprints/Permission Department. Canadian Goods & Services Tax Registration #126148048

- 041017 Transition on the T106 LP Turbine Blade in the Presence of Moving Upstream Wakes and Downstream Potential Fields
Maciej M. Opoka and Howard P. Hodson
- 041018 Numerical Study of Turbulent-Spot Development in a Separated Shear Layer
Brian R. McAuliffe and Metin I. Yaras
- 041019 The Effect of Combustor-Turbine Interface Gap Leakage on the Endwall Heat Transfer for a Nozzle Guide Vane
S. P. Lynch and K. A. Thole
- 041020 A Comparative Investigation of Round and Fan-Shaped Cooling Hole Near Flow Fields
James S. Porter, Jane E. Sargison, Gregory J. Walker, and Alan D. Henderson

TECHNOLOGY REVIEWS

- 044001 Mixed Flow Turbine Research: A Review
Srithar Rajoo and Ricardo Martinez-Botas

ERRATA

- 047001 Erratum: "Curtis Stage Nozzle/Rotor Aerodynamic Interaction and the Effect on Stage Performance" [Journal of Turbomachinery, 2007, 129(3), pp. 551–562]
Stephen Rashid, Matthew Tremmel, John Waggott, and Randall Moll

i Author Index

The ASME Journal of Turbomachinery is abstracted and indexed in the following:

Aluminum Industry Abstracts, Aquatic Science and Fisheries Abstracts, Ceramics Abstracts, Chemical Abstracts, Civil Engineering Abstracts, Compendex (The electronic equivalent of Engineering Index), Corrosion Abstracts, Current Contents, Ei EncompassLit, Electronics & Communications Abstracts, Energy Information Abstracts, Engineered Materials Abstracts, Engineering Index, Environmental Science and Pollution Management, Excerpta Medica, Fluidex, Fuel and Energy Abstracts, INSPEC, Index to Scientific Reviews, Materials Science Citation Index, Mechanical & Transportation Engineering Abstracts, Mechanical Engineering Abstracts, METADEX (The electronic equivalent of Metals Abstracts and Alloys Index), Metals Abstracts, Oceanic Abstracts, Pollution Abstracts, Referativnyi Zhurnal, Shock & Vibration Digest, Steels Alert

The Influence of Shroud and Cavity Geometry on Turbine Performance: An Experimental and Computational Study—Part I: Shroud Geometry

Budimir Rosic
e-mail: br241@cam.ac.uk

John D. Denton

Eric M. Curtis

Whittle Laboratory,
Cambridge University,
Cambridge CB30DY, UK

Imperfections in the turbine annulus geometry, caused by the presence of the shroud and associated cavity, have a significant influence on the aerodynamics of the main passage flow path. In this paper, the datum shroud geometry, representative of steam turbine industrial practice, was systematically varied and numerically tested. The study was carried out using a three-dimensional multiblock solver, which modeled the flow in a 1.5 stage turbine. The following geometry parameters were varied: inlet and exit cavity length, shroud overhang upstream of the rotor leading edge and downstream of the trailing edge, shroud thickness for fixed casing geometry and shroud cavity depth, and shroud cavity depth for the fixed shroud thickness. The aim of this study was to investigate the influence of the above geometric modifications on mainstream aerodynamics and to obtain a map of the possible turbine efficiency changes caused by different shroud geometries. The paper then focuses on the influence of different leakage flow fractions on the mainstream aerodynamics. This work highlighted the main mechanisms through which leakage flow affects the mainstream flow and how the two interact for different geometrical variations and leakage flow mass fractions. [DOI: 10.1115/1.2777201]

Introduction

In high pressure (HP) steam turbines, shrouded blades are commonly used in order to minimize and control the leakage flow.

Traditionally, all methods of predicting the influence of the leakage flow on turbine performance were empirical, based on experimental tests for a particular shroud geometry. These empirical correlations specify that changes in efficiency are proportional to leakage mass fraction, with the constant of proportionality specific to the particular stage geometry. Denton and Johnson [1] presented a comprehensive survey of, at that time, available methods for predicting the loss of efficiency caused by the shroud leakage. Most of them estimate the stage efficiency debit to be proportional to the leakage flow, i.e., $\Delta \eta = K \gamma$, where γ is the ratio of clearance to blade height or leakage area to annulus area and K is a constant dependent on turbine and shroud geometry and varies significantly for different shroud and stage geometries. Traupel [2] and Hubert [3] found that the change of efficiency with clearance is slightly nonlinear, but the change in the slope was also dependent on the turbine geometry. The strong dependence of the empirical correlations on particular shroud geometry makes them impractical for use in the turbine design process.

In order to accommodate rotor to casing relative movement during turbine operation, circumferential inlet and exit shroud cavities must be formed. These necessary alterations in the overall flow path geometry significantly modify the main blade flow field. All reported works (i.e., Wallis [4], Pfau et al. [5], Rushton [6], and Giboni et al. [7]) show the highly three-dimensional nature of the flow in the cavities and the complex interaction between the leakage flow and the main passage flow. The cavities are fed by

mainstream fluid and the flow inside the cavities is influenced by the blade-to-blade pressure field from the upstream and the downstream blade row and secondary flow structures from the upstream blade row (passage vortex, wakes, etc.). The presence of the shroud cavities, the mixing process when the leakage flow reenters the mainstream, and the influence of leakage flow on the downstream blade row flow field all cause additional losses.

Shroud leakage loss mechanisms have been investigated by many authors. Traupel [2], Denton and Johnson [1], Denton [8], Gier et al. [9], Rosic and Denton [10] all tried to quantify these losses. However, the loss-generating mechanisms are highly dependent on the particular shroud and stage geometry; therefore, it is difficult to develop universal design rules and to correlate different geometrical and operational turbine parameters to generic shroud design. Turbine manufacturers develop correlations (based on limited experimental data) that are usually of limited accuracy and only valid for a certain range of stage geometries.

In this paper, a datum shroud geometry, representative of steam turbine industrial practice, was systematically varied and numerically tested. The aim of this numerical study was to investigate the influence of each geometric parameter on the mainstream aerodynamics. As a result, a map of the possible turbine efficiency changes caused by different shroud modifications was obtained. The intention was to summarize these effects and to highlight efficiency trends that can be used by turbine designers as guidelines for their particular shroud geometry rather than to create universal design rules.

In the second part of this paper, the influence of different leakage flow fractions on the mainstream aerodynamics, using the same datum shroud configuration, was analyzed. This study confirmed the dominant effect of leakage flow on the aerodynamics of low aspect ratio turbines. It also showed how the interaction between the leakage and mainstream flow is modified by the leakage fraction.

Contributed by the International Gas Turbine Institute of ASME for publication in the JOURNAL OF TURBOMACHINERY. Manuscript received June 18, 2007; final manuscript received June 19, 2007; published online June 17, 2008. Review conducted by David Wisler. Paper presented at the ASME Turbo Expo 2007: Land, Sea and Air (GT2007), Montreal, Quebec, Canada, May 14–17, Paper No. GT2007-27769.

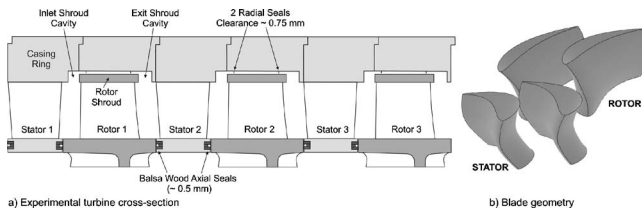


Fig. 1 Representation of the experimental turbine

Numerical Code and Flow Domain

The numerical study presented in this paper was completed using a 3D multiblock Reynolds averaged Navier–Stokes solver TBLOCK, written by Denton. TBLOCK is a finite volume solver using the explicit “Scree” scheme (Denton [11]). Turbulence is modeled using a mixing length approach with wall functions for surface skin friction. The solver was run in steady mode using the mixing plane approach. TBLOCK was run in parallel with domain decomposition done on a block basis. Both stator and rotor blades used $75 \times 49 \times 49$ grid points in axial pitchwise and spanwise directions, respectively. The grid is a structured, sheared H -type mesh.

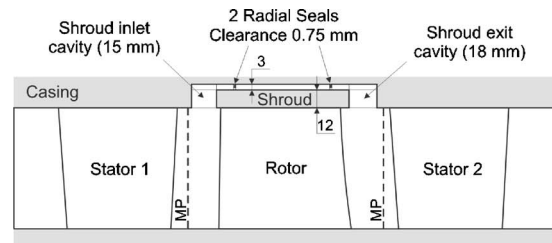
Due to significant influence of the shroud leakage flow on the downstream stator flow field, the computational fluid dynamics (CFD) geometry modeled a 1.5 stage turbine (embedded second rotor of the model turbine). The stage and shroud geometries are the same as the experimental multistage air turbine, described in Rosic et al. [12]. The low speed, three-stage air turbine was designed to represent the first few stages of a HP steam turbine. The cross section of the model turbine with three identical stages and the blade geometry are shown in Fig. 1. The rotor shroud leakage flow is controlled by two approximately 0.75 mm clearance radial seals (resulting in approximately 1.8% leakage flow). Inlet and exit shroud cavities are representative of a real industrial turbine. In order to isolate the influence of the rotor shroud geometry on the mainstream aerodynamics, the stator hub cavities are sealed with minimized leakage flow. The key rig geometrical and operational parameters are presented in Table 1. More details about the turbine operational parameters can be found in Rosic et al. [12].

The 1.5 stage turbine used for the numerical flow domain is shown in Fig. 2. The rotor shroud cavity was modeled completely. This geometry is denoted as the “datum shroud geometry” and has a 15 mm inlet cavity, 18 mm exit cavity, and 12 mm thick shroud. The number of seals and clearance were kept constant in the study, and all changes in the shroud leakage mass fraction resulted

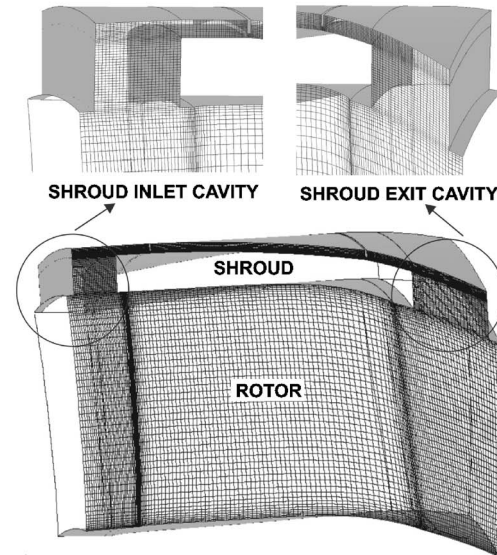
Table 1 Turbine geometrical and operational parameters

| Design operating point data | | |
|---|--------------------|--------------------|
| Flow coefficient ϕ | 0.384 | |
| Stage loading $\Psi = \Delta h_0 / U^2$ | 1.0 | |
| Design speed (rpm) | 830 | |
| Inlet Mach number | 0.045 | |
| Number of stages | 3 | |
| Interblade row spacing (mm) | 25 | |
| Blade height h (mm) | 75 | |
| Hub to tip ratio | 0.85 | |
| Blade parameters (at midheight) | | |
| | Stator | Rotor |
| Blade number | 40 | 38 |
| True chord l (mm) | 89.73 | 105 |
| Aspect ratio h/l | 0.836 | 0.714 |
| Pitch to chord ratio | 0.81 | 0.728 |
| Reynolds number ^a | 2.53×10^5 | 2.97×10^5 |

^aBased on true chord and exit velocity.



a) Computational flow domain - 1.5 stage turbine



b) Grid details

Fig. 2 TBLOCK computational flow domain and grid details

from changes in the shroud and cavity geometry. The stator hub cavity was not modeled. The mixing planes (MPs) were located just upstream of the shroud inlet cavity and downstream of the shroud exit cavity (Fig. 2(a)) and hence both cavities were modeled in the relative frame of reference together with the rotor. In this way, the influence of the rotor pressure field was taken into account, but the circumferential variation of the upstream and downstream stator blade pressure fields was neglected. Its inability to transfer the circumferential variation of some flow properties from one frame of reference to another is one of the main limitations of the mixing plane approach. For the model turbine, it was found that the rotor blade pressure field dominates the flow field in the exit cavity, while the downstream stator potential field causes the circumferential variation of the reentry leakage jet. Therefore, it was decided to model the shroud cavity in the same frame of reference as the rotor blade row. The detailed grid and block structure used to model rotor blade and shroud is presented in Fig. 2(b).

The code was calibrated against experiments, and the capabilities of the solver in predicting the flow in the multistage turbine with shrouded blades were demonstrated in the work of Rosic et al. [12]. Figure 3 shows the comparison of experimental and numerical results of pitchwise mass averaged axial velocity (a) and relative yaw angle (b) for the rotor shroud configuration shown in Fig. 1.

In spite of the inherent limitations of a mixing plane approach, good agreement between measured and predicted flow fields and overall turbine efficiencies can still be realized. The measured difference in overall turbine efficiency between the configurations with minimized and open shroud cavities was 1.16%. TBLOCK predicted a reduction in efficiency of 1.00% for the same configurations (Rosic et al. [12]).

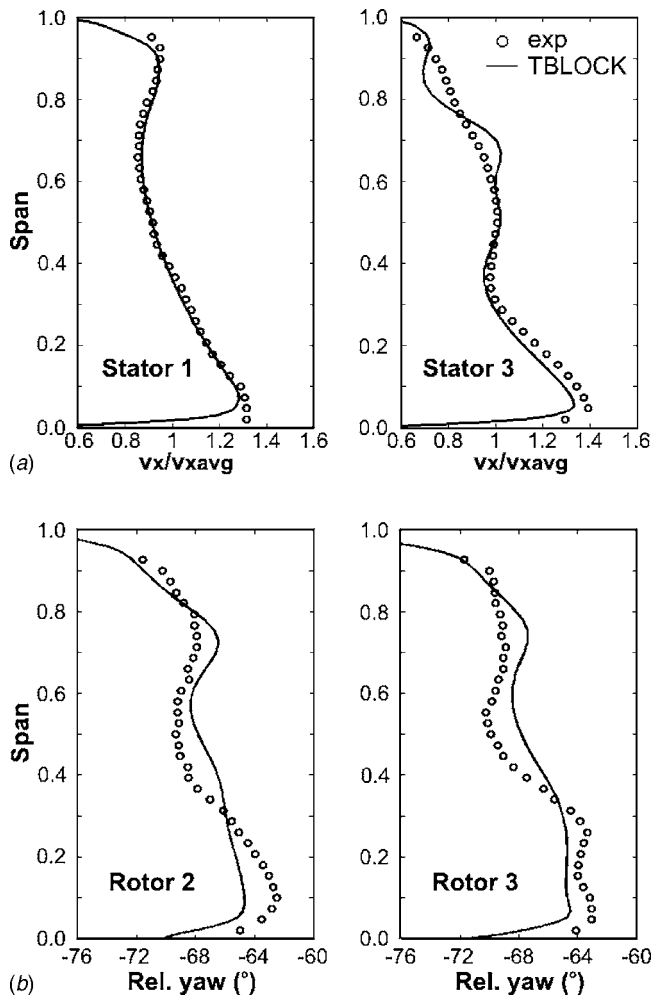


Fig. 3 Comparison of experiment and CFD: (a) axial velocity and (b) relative yaw angle

Evaluation of Different Shroud Geometry Modifications

The following geometry parameters were varied and investigated numerically:

- inlet and exit cavity length
- shroud overhang upstream of the rotor leading edge and downstream of the trailing edge
- shroud thickness for fixed casing geometry and shroud cavity depth, and
- shroud cavity depth for the fixed shroud thickness

The flow field in the shroud cavity for each geometrical modification is presented in the form of radial velocity contours at the circumferential position close to the pressure side of the rotor blade. The effects of the geometry modifications on the mainstream flow were quantified using the change in turbine efficiency and leakage mass flow fraction.

Variation of Exit Shroud Cavity Length. The length of the exit shroud cavity c was varied systematically from 3 mm to 18 mm (Fig. 4) in a way that the shroud length was kept constant and the downstream cavity end wall was moved upstream from the datum location. The length of the cavity directly influenced the flow field in the cavity and therefore the interaction between the leakage flow and main passage flow. The radial velocity contours in the exit shroud cavity for two different cavity lengths (3 mm and 12 mm) are presented in Fig. 4. It can be seen that the leakage jet stayed attached to the cavity downstream end

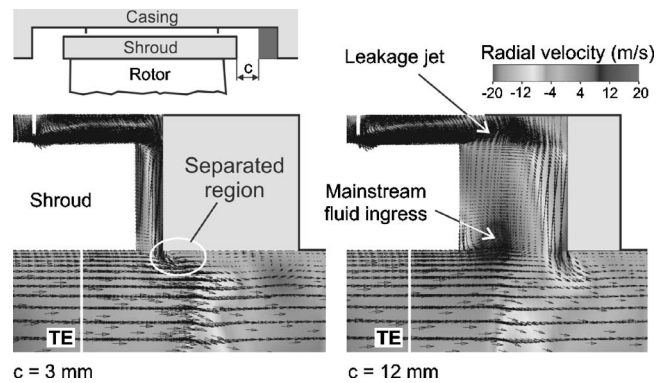


Fig. 4 Radial velocity distribution in the exit cavity for different cavity lengths c

wall. This caused a strong separation downstream of the cavity when the leakage jet reenters the mainstream and intensified the secondary flows in the downstream stator. By reducing the cavity length, the position where the leakage flow reenters the mainstream was shifted further upstream from Stator 2. This allowed the mixing process between the leakage flow and mainstream flow to occur at a more upstream location and minimized the negative influence of the almost radial reentry of the leakage jet. The leakage jet acted as a “curtain” forcing the mainstream fluid into the cavity. The mainstream fluid ingress was almost completely eliminated in the case of the 3 mm cavity and consequently the loss associated with mixing in the exit cavity was reduced. Figure 5(a) gives the change in predicted turbine efficiency with the exit cavity length. The efficiency monotonically increased with the reduction in cavity length. Much of the increase in efficiency can be explained by the reduction in leakage flow (Fig. 5(b)) and reduced mixing in the cavity.

Steam turbine manufacturers usually tend to maximize the length of the shroud cavity, opening almost the whole available interblade row space, in order to accommodate the potential rotor axial movement. This analysis illustrated that the reduction in the cavity length, by moving the downstream cavity end wall to an upstream location, is beneficial and indicates that the shroud cavity should be reduced as much as the turbine operational conditions allow.

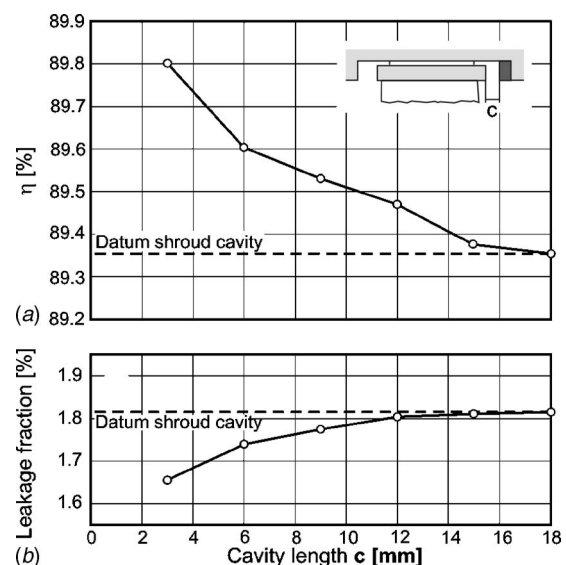


Fig. 5 Influence of the exit cavity length on (a) turbine performance and (b) leakage fraction

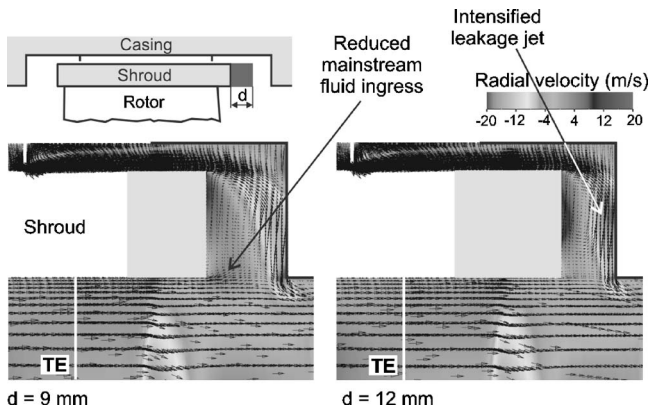


Fig. 6 Radial velocity distribution in the exit cavity for different shroud overhangs d

Variation of Shroud Overhang in Exit Cavity. The length of the exit shroud cavity can be changed also by extending the shroud overhang through the cavity, d (Fig. 6). The shroud overhang extension modifies the flow field in the exit cavity, as illustrated in Fig. 6, using radial velocity contours. It is evident that in the case of the 9 mm shroud overhang, the ingress of the main passage fluid into the cavity is almost stopped. The extended shroud overhang reduced the influence of the pressure gradient downstream on the rotor trailing edge, which is responsible for the formation of the cavity flow.

On the other side, extending the shroud caused a strengthening of the leakage jet, which was pushed even closer to the cavity downstream end wall, causing an almost radial reentry of the leakage jet with a strong separation downstream. It also increased windage loss on the increased shroud surface. The effect of reduced mainstream fluid ingress into the cavity counteracts the effects of leakage jet strengthening and increased windage loss. This is illustrated in Fig. 7(a) with the efficiency plotted against the shroud overhang.

The change in shroud overhang did not significantly change the leakage mass fraction, as shown in Fig. 7(b). For the small shroud overhangs, the efficiency dropped even below the value of the datum cavity. The shroud overhang was further extended and from 6 mm the influence of the reduction of mainstream fluid ingress

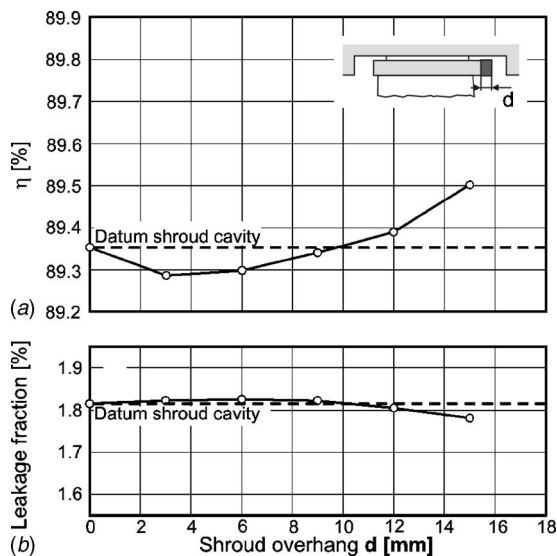


Fig. 7 Influence of the shroud overhang in the exit cavity on (a) turbine performance and (b) leakage fraction

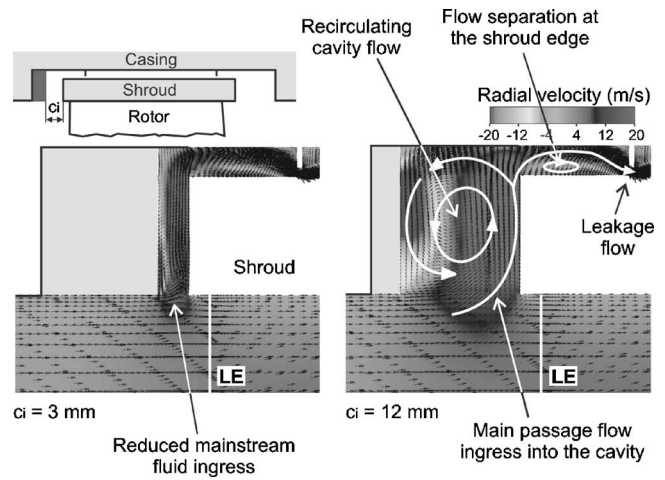


Fig. 8 Radial velocity distribution in the inlet cavity for different cavity lengths c_i

into the cavity became dominant and the efficiency started to increase. In the case of 15 mm shroud extension (the cavity size was 3 mm), the losses associated with the mixing inside the cavity were eliminated. Besides the fact that the extended shroud limits the axial movement of the rotor and increases overall weight of the shroud and stress on the blade root, this analysis indicated that the shroud overhang extension in the exit cavity is not beneficial from the aerodynamic point of view until extremely high values.

Variation of Inlet Shroud Cavity Length. A similar parametric study was completed for the inlet shroud cavity, and the length of the cavity was varied by moving the casing wall upstream (Fig. 8). The radial velocity contours indicate that the ingress of the main passage fluid into the cavity was reduced as the inlet cavity length was reduced. In the case of the 3 mm inlet cavity, only leakage flow leaves the main passage. This resulted in an increase in turbine efficiency as the cavity length was reduced (Fig. 9(a)). The reduction in cavity size reduces the mixing losses in the cavity and the influence of the cavity on the main passage. This is illustrated by the variation of the relative yaw angle downstream of the rotor (Fig. 10). It is evident that the reduction of the cavity size improved the flow field in the rotor, reducing the flow under-

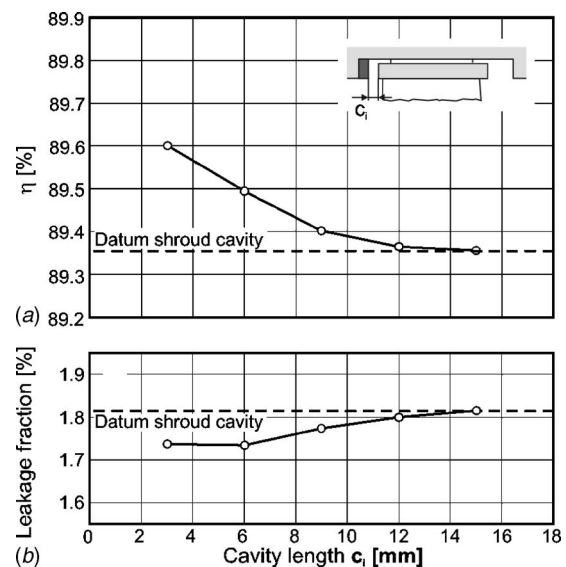


Fig. 9 Influence of the inlet cavity length on (a) turbine performance and (b) leakage fraction

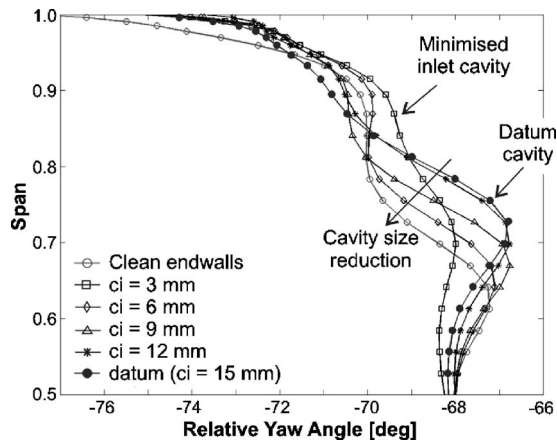


Fig. 10 Pitchwise mass averaged relative yaw angle downstream of the rotor for different inlet cavity lengths c_i

turning at 70% of the span and causing the relative yaw angle distribution to be closer to the ideal case with clean end walls. There was also a small drop in the leakage mass flow fraction with reduced cavity size, as is indicated in Fig. 9(b).

Variation of Shroud Overhang in Inlet Cavity. The shroud overhang was also varied in the inlet cavity, d_i . Again, the reduction in cavity size reduced the main passage fluid ingress and hence the mixing process in the cavity. The efficiency monotonically increased with the shroud overhang extension (i.e., the cavity reduction), and a maximum increase in efficiency of approximately 0.3% was achieved for the maximum shroud overhang (12 mm), as shown in Fig. 11(a). The variation of the shroud overhang did not have a significant effect on the leakage mass fraction, as shown in Fig. 11(b). Hence, it is likely that most of the improvement in the efficiency comes from the reduced mixing in the inlet cavity and minimized influence on the rotor casing secondary flows, the same as in the case with reduced cavity length (c_i). By extending the shroud, the region of interaction between

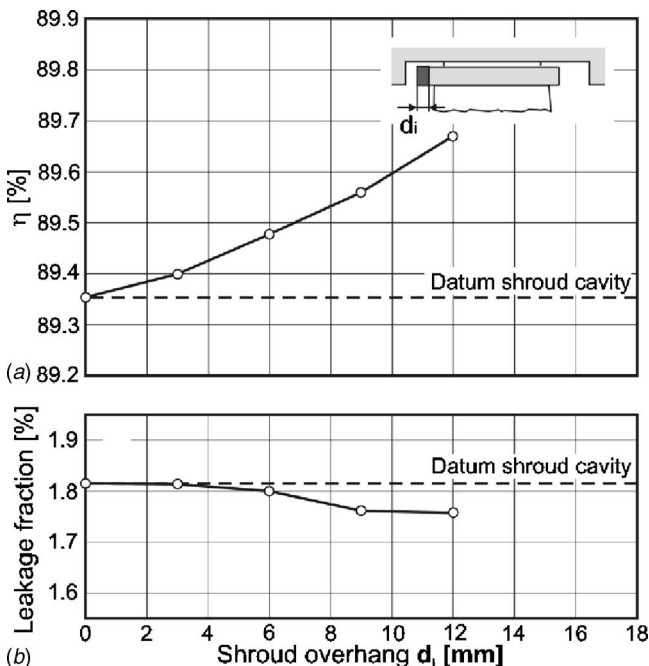


Fig. 11 Influence of the shroud overhang in the inlet cavity on (a) turbine performance and (b) leakage fraction

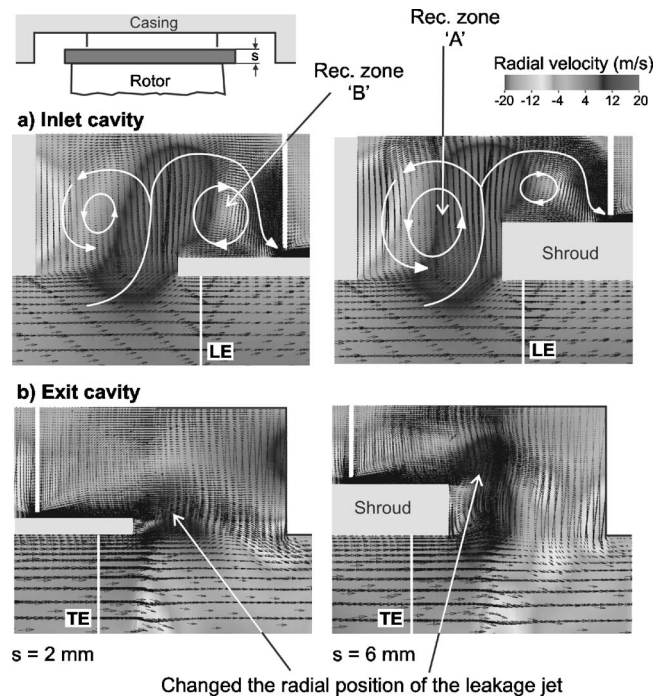


Fig. 12 Radial velocity distribution in the inlet and exit cavity for different shroud thicknesses s

the cavity and mainstream fluid was shifted more upstream from the rotor leading edge, allowing the mainstream fluid to mix out the flow disturbances in the casing region caused by the presence of the cavity.

For a given shroud geometry, the leakage mass flow is driven by the difference between the stagnation pressure upstream and the static pressure downstream of the shroud. The leakage flow can be reduced if the inlet cavity is designed so that the leakage fluid comes from the end wall boundary layer, with low stagnation pressure, rather than from the higher stagnation pressure mainstream fluid. The shroud extension in the inlet cavity reduces the influence of the potential field upstream of the rotor leading edge, reducing the high stagnation pressure mainstream fluid ingress into the cavity.

Variation of Shroud Thickness. In this section, the shroud thickness s was varied and the cavity length and depth were kept constant, as illustrated in Fig. 12. The change in the shroud thickness modified the flow field in the whole leakage flow path. Figure 12(a) shows the flow field in the inlet cavity and Fig. 12(b) the flow field in the exit cavity for two different shroud thickness values. It is clear in Fig. 12(a) that the variation in shroud thickness did not significantly modify the flow structure in the inlet cavity. As the shroud thickness was reduced, the recirculation zone "A" and main passage fluid ingress were reduced, and the recirculation zone "B" above the shroud upstream of the seal increased at the same time. The structure of the flow field at the interface plane between the cavity and the mainstream was not considerably altered by the shroud thickness, and consequently the flow field through the rotor blade row stayed almost unchanged (see more details in Rosic [13]).

Downstream of the rotor, the flow field in the exit shroud cavity was highly affected by the change in the shroud thickness (see Fig. 12(b)). The main reason is that the variation of shroud thickness changed the radial position at which the leakage jet penetrated the cavity. The position of the leakage jet also influences the main passage fluid ingress into the cavity (Fig. 12(b)). In the case of the 2 mm thin shroud, the leakage jet acts as a curtain minimizing the ingress into the cavity. At the same time, the un-

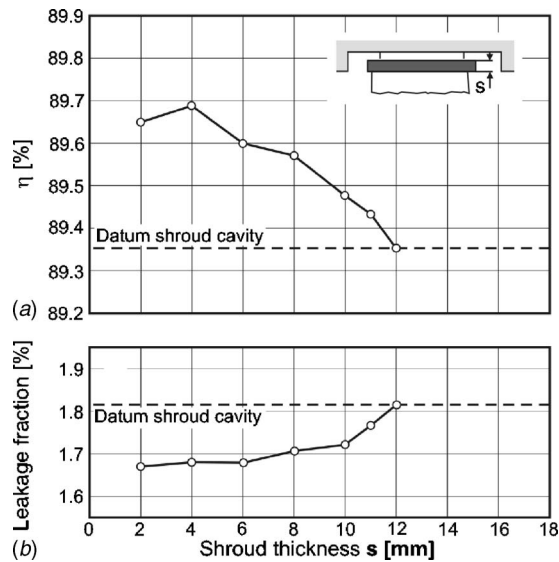


Fig. 13 Influence of the shroud thickness s on (a) turbine performance and (b) leakage fraction

mixed leakage fluid enters the downstream stator directly. Significant difference in the tangential velocity between the leakage and the mainstream flow causes negative incidence and intensifies the secondary flows at the casing of the downstream stator. Wallis [4] claimed that the local mainstream flow ingress and mixing in the exit shroud cavity can even be beneficial in reducing the difference in the tangential velocity between these two flows.

The turbine efficiency increased with reduction of shroud thickness, as seen in Fig. 13(a). This was mainly due to reduction of the leakage fraction (Fig. 13(b)). In the case of the thin shroud, the leakage fluid approaches the upstream seal almost radially, which reduces the discharge coefficient of the seal and hence the leakage fraction. The cavity between two seals is also increased in the case of thin shroud. This caused an increased dissipation of the leakage jet's kinetic energy downstream of the first seal and the reduced carryover effect and finally the leakage fraction. The change in the shroud thickness affected the flow field in the whole shroud leakage flow path and the flow in the main passage. Therefore, it is difficult to reconstruct all processes that contributed to the predicted change in efficiency. As was mentioned, the shroud thickness did not affect the flow field in the inlet cavity and the rotor. On the other side, due to complexity of the mixing, the flow interactions between the leakage and the mainstream flow in the exit cavity are highly dependent on the shroud and cavity geometry. Hence, it is difficult to draw a conclusion about an optimum shroud thickness in the exit cavity. Turbine designers should be particularly careful in designing this part of the shroud geometry.

Variation of Shroud Cavity Depth. In the final geometrical modification of this study, the shroud cavity depth g was analyzed. This time, a 2 mm shroud thickness was kept constant and the cavity depth was simultaneously changed in the inlet and exit cavity (Fig. 14). The practical advantage of this modification and the previous one, compared to varying the inlet and the exit cavity length and the shroud overhang, is that in this case the axial movement of the rotor was not limited.

The reduction in the cavity depth in both cases for the inlet and the exit cavity caused a reduction in the amount of mainstream fluid that entered the cavity, as seen in Figs. 14(a) and 14(b). This reduced cavity associated losses and led to an increase in the turbine efficiency of 0.3% in the case with the 5 mm cavity depth (Fig. 15(a)). In this case of the 5 mm cavity depth, the dissipation of the leakage jet's kinetic energy in the interseal cavity was reduced and the carryover effect was intensified, resulting in in-

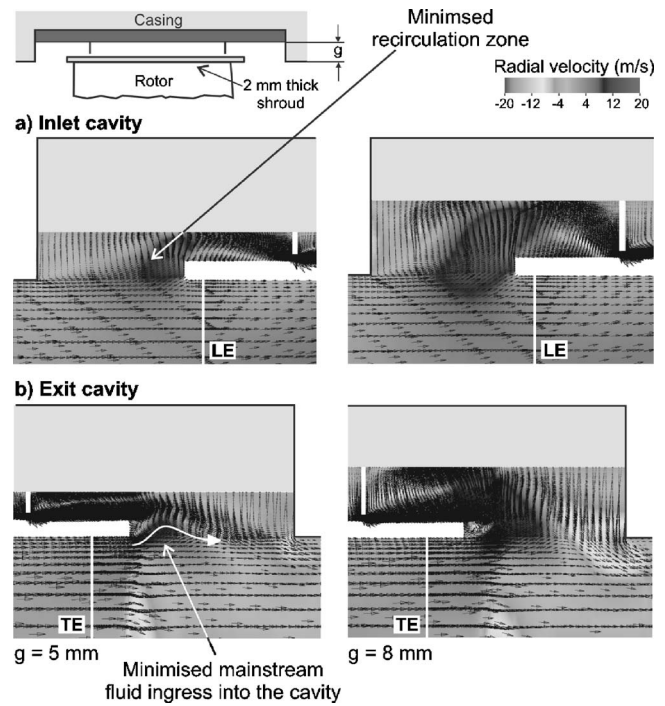


Fig. 14 Radial velocity distribution in the inlet and exit cavity for different shroud cavity depths g

creased leakage flow (Fig. 15(b)). The increase in cavity depth caused an expected drop in the leakage flow fraction. This beneficial effect was not followed by an expected rise in efficiency. By increasing the cavity depth, more of the main passage fluid was driven into both cavities, resulting in an increased mixing loss in both cavities and intensifying the interaction between the cavity and the main annulus flow.

The increased cavity depth also enhanced secondary flows in the rotor. In the exit cavity, the influence of the cavity depth on the flow field in the downstream stator is opposite. Although the extremely small cavity depth (i.e., 5 mm) reduced the amount of ingested fluid, and therefore the mixing in the cavity, the leakage jet propagates directly to the downstream stator, causing enhanced

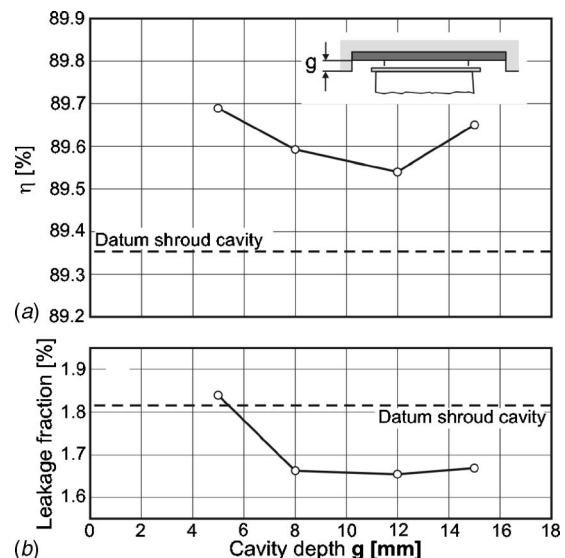


Fig. 15 Influence of the shroud cavity depth g on (a) turbine performance and (b) leakage fraction

secondary flows in the downstream stator by the mechanism described earlier. Similar conclusions can be found in the experimental study of Schlienger et al. [14]. They investigated two different exit shroud cavity geometries using a two-stage model turbine. The exit shroud cavity geometry with a contoured end wall and reduced height altered the reentry angle of the leakage flow but increased the secondary flows at the downstream stator compared to the datum case with a large rectangular cavity. The work analyzed in this section highlighted once more that the geometry of the exit shroud cavity should be carefully chosen in order to minimize the losses associated with the shroud leakage flow. A simple reduction in the rotor exit shroud cavity size does not necessarily mean improvement in the turbine efficiency.

Different Leakage Mass Flow Fraction

According to steam turbine industrial practice, leakage fractions for shrouded blades vary from 1% to 4% within HP turbines. During long-term turbine operation, the sealing effectiveness deteriorates due to rubbing and worn sealing elements. Therefore, it is important to investigate the influence of the different leakage fractions on the same blading geometry. This was done in a numerical study using the same numerical flow domain as in the first part of this paper (Fig. 2). The leakage mass fraction was controlled by varying the seal clearance over both radial fins simultaneously, while the datum shroud geometry was kept unchanged.

The flow field in the exit shroud cavity, where the leakage flow reenters the main passage, is greatly affected by the leakage jet generated in the downstream seal gap. Figure 16 shows the radial velocity contours in the meridional plane at two different circumferential positions, close to the pressure and suction side of the rotor blade row for different leakage fractions. The mainstream fluid periodically moves into and out of the exit cavity driven by the rotor blade potential field. Close to the blade pressure side, fluid enters the cavity and leaves it in the low pressure region close to the suction side. In the case of small leakage fraction (0.25%), the cavity fluid formed a strong cavity vortex with the main passage fluid entering the cavity close to the cavity downstream end wall. For this leakage fraction, the axial momentum of the leakage jet was not high enough to allow the leakage flow to penetrate through the whole cavity, but rather loses its energy in an intensive mixing process with the cavity fluid. As the leakage flow increased (Fig. 16(b)), it reached the cavity downstream wall and shifted the location where the mainstream fluid enters the cavity upstream, and reduced the size of the cavity vortex. The leakage jet propagated through the cavity and bent toward the casing wall under the influence of the cavity vortex. The leakage jet then stayed attached to the downstream cavity end wall, as is illustrated in Fig. 16(c). The majority of the leakage fluid therefore reenters the mainstream almost radially at this location close to the cavity end wall. This also caused a strong separation at the cavity downstream corner and a thickening of the inlet boundary layer of the downstream stator. A similar flow structure remained in the cavity even for larger leakage fractions (Fig. 16(d)). In the case with even higher leakage fraction, the leakage jet dominated the cavity flow. The leakage jet had enough momentum to suppress further the cavity vortex and hence reduces its strength and size.

The high swirl velocity component of the leakage jet is responsible for the development of negative skew in the casing boundary layer upstream of Stator 2. Figure 17 shows the variation of absolute yaw angle downstream of the shroud cavity with leakage fraction. In the case of small leakage fractions (<0.6%), the leakage flow is not enough to overcome the cavity dynamics, the cavity fluid mixes out the leakage flow, and therefore the yaw angle did not change significantly. As the leakage flow fraction increases, the leakage jet leaves the cavity almost unmixed, forming a region of high yaw angle in the near casing region of the main annulus.

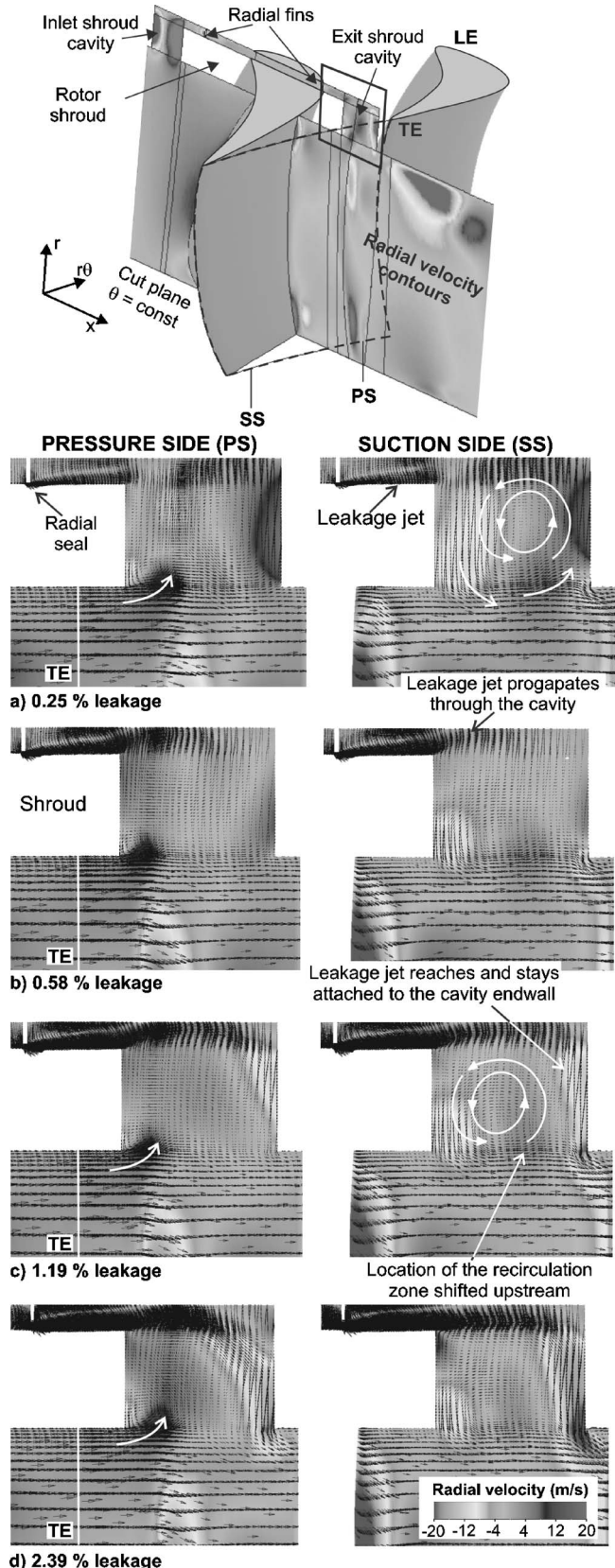


Fig. 16 Radial velocity distribution in the exit cavity for different leakage fractions

This caused a significant change in the flow field of the downstream stator. Figure 18 compares the entropy function contours in a quasiorthogonal plane at the exit of the downstream stator for

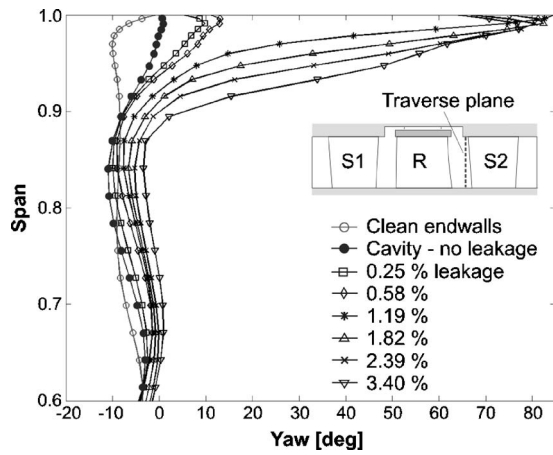


Fig. 17 Pitchwise mass averaged yaw angle upstream of Stator 2 for different leakage fractions

different leakage fractions. In the case with shroud cavities but without leakage flow (Fig. 18(a)), the region of low entropy and high loss is located close to the wake region on the suction side of the blade with two loss cores close to the end walls associated with the secondary flows. The flow in the exit shroud cavity causes a thickening of the inlet boundary layer and therefore stronger secondary flows in the casing region. In the case of small leakage fractions ($<0.6\%$), there is no significant difference in entropy contours (Fig. 18(b)) because the cavity fluid mixes out the majority of leakage flow (as illustrated in Fig. 17). In the case of higher leakage fractions, the leakage jet propagates through the cavity, reentering the mainstream almost unmixed (Fig. 17), thereby enhancing further the secondary flows. This causes a strong radial migration of the low momentum casing fluid toward the midspan (Fig. 18(c)). This process continues with further increased leakage fraction (Fig. 18(d)). The radial migration of the low momentum fluid is so strong that these two loss cores almost merged together and the region of the low entropy fluid occupies a considerable portion of the blade passage.

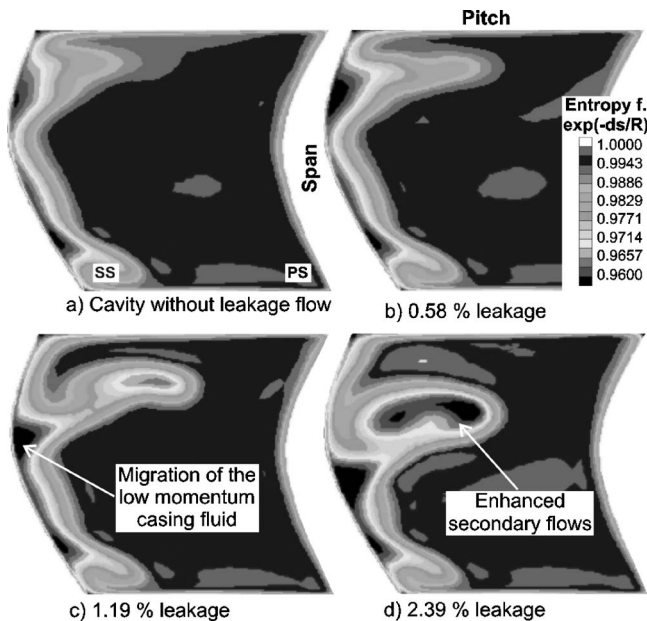


Fig. 18 Entropy function contours downstream of Stator 2 for different leakage fractions

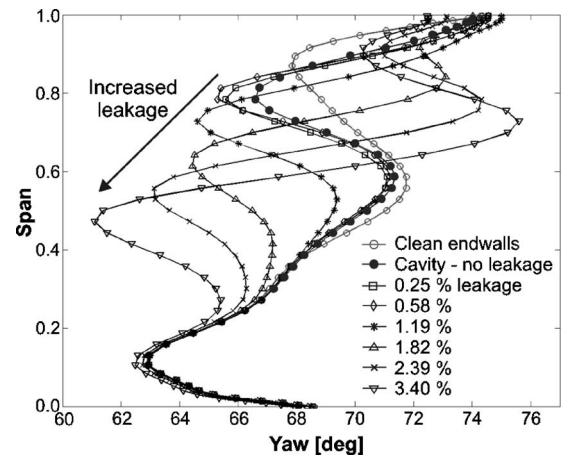


Fig. 19 Pitchwise mass averaged yaw angle downstream of Stator 2 for different leakage fractions

The negative influence of the leakage flow on the flow field in the downstream blade row can also be seen by analyzing the yaw angle distribution at the downstream stator exit (Fig. 19). Compared to the ideal case with clean end walls, the leakage flow caused a strong underturning of the flow at the midspan, and also the "S" shape angle distribution close to the casing, associated with the casing secondary flows, was enhanced. As was observed earlier, the small leakage fractions (0.25% and 0.58%) did not affect the yaw angle distribution, which remained close to that of the case without leakage flow. The severity of the leakage influence on the flow mainstream field is illustrated by the fact that more than 70% of the blade flow field was affected for leakage flows larger than 2%.

The nature of the interaction is different in the inlet cavity. The leakage flow effectively removes the cavity fluid and the boundary layer upstream of the rotor, reducing the casing secondary flows. Figure 20 shows the entropy function contours downstream of the rotor for different leakage fractions. The presence of the inlet cavity without leakage flow (Fig. 20(a)) thickens the inlet boundary layer, which results in enhancing the casing passage vortex and thickening of the low momentum fluid close to the casing

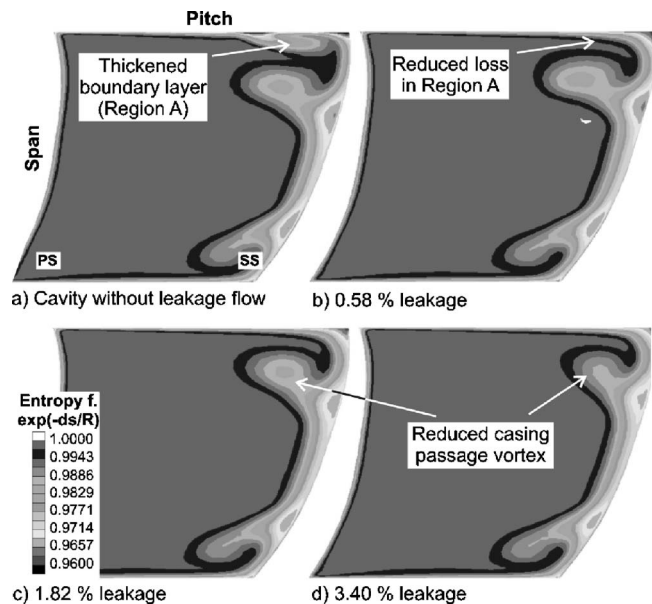


Fig. 20 Entropy function contours downstream of the rotor for different leakage fractions

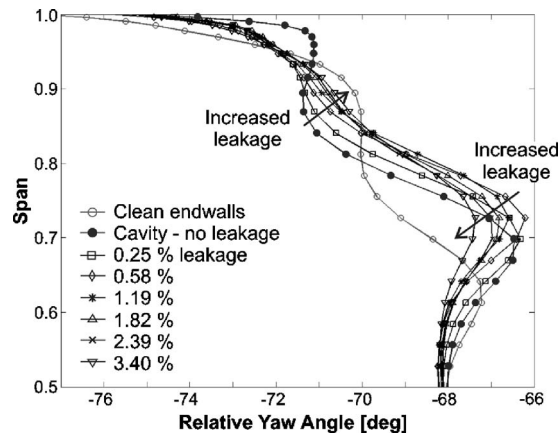


Fig. 21 Pitchwise mass averaged relative yaw angle downstream of the rotor for different leakage fractions

(region A). The introduction of small leakage flow fractions (Fig. 20(b)) reduced loss in the near casing region A, but did not affect the strength of the casing passage vortex. With further increasing of the leakage flow, the strength of the casing passage vortex started to reduce (Fig. 20(c)). In the case of 3.4% leakage fraction, most of the inlet boundary layer and low momentum fluid upstream off the rotor casing end wall was removed. This resulted in a significant reduction of the rotor secondary flows and the casing passage vortex. Another confirmation of the positive leakage flow influence on the flow field in the rotor can be found in the flow angle distribution downstream of the rotor, as shown in Fig. 21. It is evident that with the increased leakage the flow angle distribution was improved and became similar to the ideal case of clean end walls.

One should not forget that although the leakage flow locally reduces secondary flows in the rotor, increasing the leakage fraction has an overwhelmingly detrimental effect on turbine performance for reasons already discussed such as less possible extracted work, reentry mixing, negative incidence on the downstream stator, etc.

All aforementioned aspects of the influence of the leakage flow on the mainstream flow in the 1.5 stage turbine analyzed in this paper can be summarized with the diagram shown in Fig. 22. The diagram shows the change in turbine efficiency with leakage fraction for the datum shroud configuration. In the case without leakage flow, there is an offset loss caused by the presence of the shroud cavity in the main annulus.

The origin and structure of the offset loss was analyzed by Rosic and Denton [10]. Classical shroud leakage theory assumes that the loss of efficiency associated with the leakage flow is directly proportional to the leakage flow rate.

The dotted line on the plot represents the simple shroud leakage theory and has a slope $\Delta\eta/\Delta(\dot{m}_L/\dot{m}_m)=1$. In the cases with a leakage fraction less than approximately 0.7%, the exit shroud cavity flow mixes out the leakage flow and it does not have a significant effect on the flow field in the downstream stator. At the same time, the introduction of the leakage flow in the inlet cavity removes the inlet boundary layer upstream of the rotor and reduces its secondary flows. This is likely to be the explanation for the slope less than 1 in the region of small leakage fractions. As the leakage fraction is high enough to penetrate the cavity, and directly enhance the secondary flows in the downstream stator, the slope of the line changed to value of $\Delta\eta/\Delta(\dot{m}_L/\dot{m}_m)=1.5$. For this range of leakage fractions (0.7–1.6%), this effect is dominant and the positive effect of the leakage flow on the rotor flow field is not able to counterbalance it. The positive effect of the leakage flow on the reduction of the rotor casing secondary flows seems to grow constantly for all leakage fractions. In the case of leakage

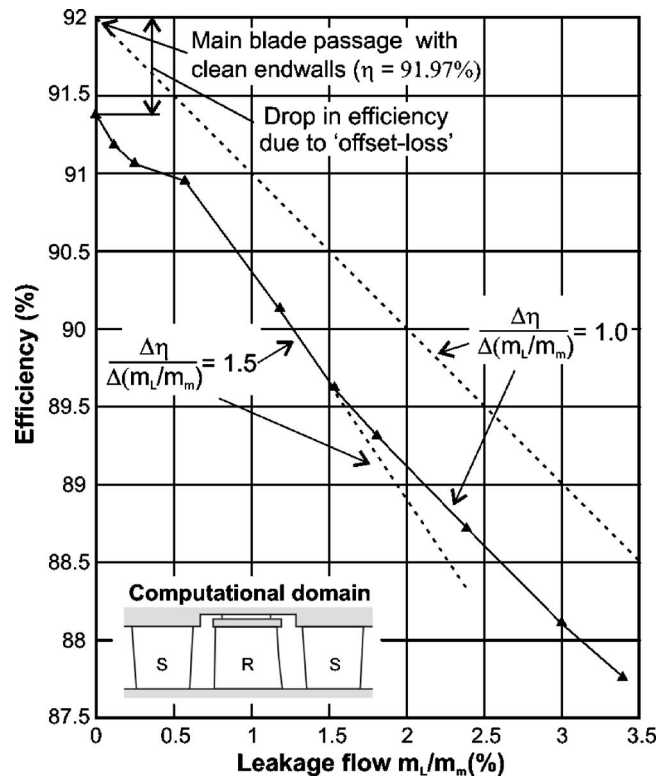


Fig. 22 Change in turbine efficiency with leakage fraction

fractions larger than 1.6%, these two effects, negative of growth of secondary flows in the downstream stator and positive of reduction of the rotor secondary flows, cancel each other and the change of efficiency approaches an equilibrium with the slope of the curve close to 1.

Conclusions

The aerodynamics of low aspect ratio turbines is highly influenced by the geometry of the whole shroud leakage flow path and leakage fraction.

Effects of rotor shroud cavity geometry on the mainstream aerodynamics were investigated in the first part of this paper. It was found that the reduction of the length of both the inlet and the exit shroud cavities is beneficial, and the cavities should be reduced as much as turbine operational conditions allow. This is mainly due to reduction of the main passage fluid ingress and mixing losses in the cavity. The shroud extension in the inlet cavity has a total positive effect. The shroud overhang extension in the exit cavity intensified the leakage jet and increased the windage loss. Only very long shrouds reduced the mixing losses in the cavity, and hence for the analyzed turbine, this modification did not show practical benefit.

The shroud thickness variation for a fixed cavity size highlighted that this modification did not significantly affect the flow field in the inlet cavity and the rotor. The minimized shroud thickness resulted in reduced leakage fraction. The change in shroud thickness altered the radial position of the leakage jet in the exit cavity, which modified the flow field in the cavity and the downstream stator.

It was highlighted that reduced cavity depth minimized the mixing loss in the inlet cavity and improved the flow field in the rotor. In the exit cavity, the mixing losses were also reduced but the unmixed leakage jet caused an enhancement of the secondary flows in the downstream stator. The depth reduction in the exit cavity increased the leakage flow fraction.

In the second part of this paper, the influence of different leakage fractions on the mainstream flow was discussed. In the inlet cavity, the leakage flow removes the low momentum fluid and improves the flow field in the rotor. In the exit shroud cavity, the mixing process reduces the influence of the leakage flow in the case of small leakage fractions. Further increase in the leakage flow intensifies significantly the casing secondary flows in the downstream stator. Above a certain leakage fraction, these two effects cancel each other and the change of efficiency with leakage fraction approaches equilibrium.

The results presented in this paper are obtained for a particular low aspect ratio blading and particular shroud geometry. It is unlikely that they can be applied directly to general turbine design. However, this work highlighted the main mechanisms through which the leakage flow affects the mainstream flow field and how they interact for different geometrical variations and different leakage fractions. Most of these mechanisms are going to be present for the majority of shroud designs and different aspect ratio blading.

Acknowledgment

The authors would like to thank Siemens Power Generation for funding this work.

Nomenclature

| | | |
|------------|---|---|
| c | = | shroud cavity length |
| d | = | shroud overhang length |
| g | = | shroud cavity depth |
| m_L, m_m | = | leakage and mainstream flow mass fraction |
| p_0 | = | total pressure |
| s | = | shroud thickness |
| η | = | efficiency |

| | | |
|--------|---|--------------------------------------|
| HP, IP | = | high pressure, intermediate pressure |
| MP | = | mixing plane |
| LE, TE | = | leading edge, trailing edge |
| PS, SS | = | pressure side, suction side |

References

- [1] Denton, J. D., and Johnson, C. G., 1972, "The Tip Leakage Loss of Turbine Blades—A Review and a Theory for Shrouded Blades," Marchwood Engineering Laboratories, CEGB Report No. R/M/N627.
- [2] Traupel, W., 1970, "Ergebnisse von Turbinenversuchen," *Flow Research on Blading*, Elsevier, New York.
- [3] Hubert, G., 1963, "Untersuchungen ueber die Sekundarverluste in Axialem Turbomaschinen," VDI Forschungsheft.
- [4] Wallis, A. M., 1997, "Secondary and Leakage Flows in a Multistage Turbine," Ph.D. thesis, Cambridge University, Cambridge.
- [5] Pfau, A., Treiber, M., Sell, M., and Gyarmathy, G., 2001, "Flow Interaction From the Exit Cavity of an Axial Turbine Blade Row Labyrinth Seal," *ASME J. Turbomach.*, **123**, pp. 342–352.
- [6] Rushton, G. J., 2003, "High-Pressure Turbine Shroud Leakage," Ph.D. thesis, Cambridge University, Cambridge.
- [7] Giboni, A., Menter, J. R., Peters, P., Wolter, K., Pfof, H., and Breisig, V., 2003, "Interaction of Labyrinth Seal Leakage Flow and Main Flow in an Axial Turbine," *ASME Paper No. GT2003-38722*.
- [8] Denton, J. D., 1993, "Loss Mechanisms in Turbomachines," *ASME Paper No. 93-GT-435*.
- [9] Gier, J., Stubert, B., Brouillet, B., and de Vito, L., 2003, "Interaction of Shroud Leakage Flow and Main Flow in a Three-Stage LP Turbine," *ASME Paper No. GT2003-38025*.
- [10] Rosic, B., and Denton, J. D., 2006, "The Control of Shroud Leakage Loss by Reducing Circumferential Mixing," *ASME Paper No. GT2006-90946*.
- [11] Denton, J. D., 1990, "The Calculation of Three Dimensional Viscous Flow Through Multistage Turbomachines," *ASME Paper No. 90-GT-19*.
- [12] Rosic, B., Denton, J. D., and Pullan, G., 2005, "The Importance of Shroud Leakage Modelling in Multistage Turbine Flow Calculations," *ASME Paper No. GT2005-68459*.
- [13] Rosic, B., 2006, "The Control of Shroud Leakage Flows in Low Aspect Ratio Multistage Turbines," Ph.D. thesis, Cambridge University, Cambridge.
- [14] Schlienger, J., Pfau, A., Kalfas, A. I., and Abhari, R. S., 2003, "Effects of Labyrinth Seal Variation on Multistage Axial Turbine Flow," *ASME Paper No. GT2003-38270*.

The Influence of Shroud and Cavity Geometry on Turbine Performance: An Experimental and Computational Study— Part II: Exit Cavity Geometry

Budimir Rosic

e-mail: br241@cam.ac.uk

John D. Denton

Eric M. Curtis

Ashley T. Peterson

Whittle Laboratory,
Cambridge University,
Cambridge CB30DY, UK

The geometry of the exit shroud cavity where the rotor shroud leakage flow reenters the main passage flow is very important due to the dominant influence of the leakage flow on the aerodynamics of low aspect ratio turbines. The work presented in this paper investigates, both experimentally and numerically, possibilities for the control of shroud leakage flow by modifications to the exit shroud cavity. The processes through which the leakage flow affects the mainstream aerodynamics identified in the first part of this study were used to develop promising strategies for reducing the influence of shroud leakage flow. The experimental program of this study was conducted on a three-stage model air turbine, which was extensively supported by CFD analysis. Three different concepts for shroud leakage flow control in the exit cavity were analyzed and tested: (a) profiled exit cavity downstream end wall, (b) axial deflector, and (c) radial deflector concepts. Reductions in aerodynamic losses associated with shroud leakage were achieved by controlling the position and direction at which the leakage jet reenters the mainstream when it leaves the exit shroud cavity. Suggestions are made for an optimum shroud and cavity geometry. [DOI: 10.1115/1.2777202]

Introduction

The shroud leakage flow mainly affects the turbine performance by reducing extracted work in the rotor blades. This work reduction is an inviscid process and does not necessarily create loss (Denton [1]). However, considerable losses are created due to various viscous mixing processes (mixing through the labyrinth seal, mixing in the shroud cavities, and mixing when the leakage flow reenters the main annulus) due to difference in velocity from the mainstream flow. Some aspects of the loss can be changed by altering the shroud and cavity geometry and some are fixed for a fixed seal geometry and blade geometry.

The leakage flow undergoes a throttling process from upstream stagnation pressure to the stagnation pressure at the exit from the last seal. If the leakage flow does no work, its change in specific entropy is fixed by its change in stagnation pressure. The stagnation pressure at the exit from the last seal is determined by the static pressure in the downstream cavity and the velocity of the leakage jet. The jet velocity is fixed by the leakage mass flow and seal clearance and the static pressure in the cavity is close to that of the mainstream flow at the exit from the blade row. Hence, for a fixed seal geometry and blade geometry, the increase in specific entropy between these points is almost fixed and cannot be greatly influenced by changes in the cavity geometry. Small changes in the exit static pressure from the last seal can be made by changing the geometry of the exit (downstream) cavity and this should be designed to increase the static pressure as much as possible.

For a given number of seals and seal geometry, the leakage mass flow can be changed by introducing loss upstream of the seals, i.e., in the inlet (upstream) cavity. The inlet cavity should

also be designed so that the leakage fluid comes from the end-wall boundary layer (with low stagnation pressure) rather than from the mainstream (higher stagnation pressure). This not only reduces the leakage flow rate but also, by bleeding off the entering boundary layer, reduces the secondary loss within the blade row. This is described in Part 1 of this study. However, the leakage mass flow is mainly determined by the number of seals, seal clearance, and seal geometry; these should be chosen to reduce the leakage flow as much as possible within mechanical constraints. Denton and Johnson [2], Sasada et al. [3], Pfau et al. [4], and Reid [5] investigated the influence of different geometry modifications in the inlet shroud cavity region on turbine performance.

The mixing loss between the jet leaving the last seal and the mainstream flow is not fixed and depends on where the mixing takes place (Denton [1]); hence, it can be reduced by careful design of the exit cavity. A major contribution to this mixing loss is the difference in tangential velocity and this can only be reduced by applying a tangential force to the leakage flow either by friction on the casing or by vanes in the cavity, as described in Rosic and Denton [6].

Another major source of loss due to seal leakage is the increase in secondary loss in the downstream blade row. This is determined by the casing boundary layer entering the blade row, which in turn is greatly influenced by how the leakage flow reenters the mainstream. In particular, the difference in tangential velocity introduces streamwise vorticity in a direction to amplify the secondary flow. Also the reentry of the leakage flow may cause a separation on the casing, which will greatly thicken the boundary layer and increase the secondary losses. These losses in the downstream blade row can be substantial and can be potentially controlled by design of the exit cavity.

This indicates that the geometry of the exit shroud cavity plays a significant role in the loss generating process associated with the leakage flow. The physics of the cavity flow and its interaction with the main passage flow were analyzed by many authors, among others Wallis [7], Pfau et al. [4,8], Rushton [9], Gier et al.

Contributed by the International Gas Turbine Institute of ASME for publication in the JOURNAL OF TURBOMACHINERY. Manuscript received June 18, 2007; final manuscript received June 19, 2007; published online June 17, 2008. Review conducted by David Wisler. Paper presented at the ASME Turbo Expo 2007: Land, Sea and Air (GT2007), Montreal, Quebec, Canada, May 14–17, 2007, Paper No. GT2007-27770.

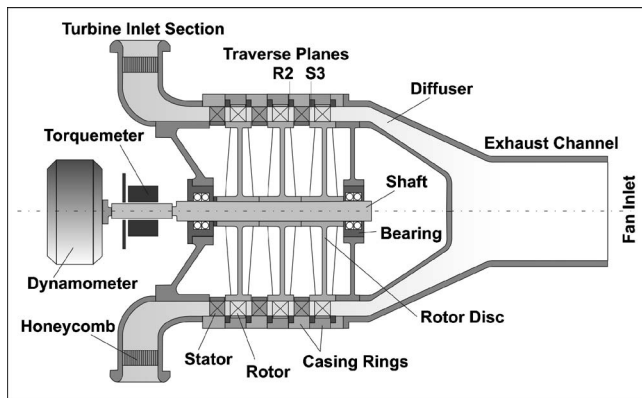


Fig. 1 Schematic of model turbine

[10], Giboni et al. [11,12], Peters et al. [13], etc. Few studies have investigated possibilities of controlling the shroud leakage flow by modifying the exit shroud cavity geometry and reducing its influence on the main annulus aerodynamics.

Schlienger et al. [14] modified a datum rectangular cavity by contouring the cavity end wall in order to improve the reentry angle of the cavity flow by avoiding the sharp corner edge. Pfau et al. [4] proposed nonaxisymmetric shroud and casing end-wall contouring, to reduce circumferential nonuniform leakage reentry and reduce main passage fluid ingress into the cavity.

The work presented in this paper investigated further, both experimentally and numerically, possibilities for the control of shroud leakage flow by modifying the exit shroud cavity geometry. As a result, three different concepts for shroud leakage flow control, based on the identified cavity flow dynamics, were investigated. This paper summarizes the main results of this study and highlights dominant phenomena of the complex leakage flow and main passage flow interaction.

Model Turbine and Experimental Methods

The experimental results were obtained from a low speed three-stage air turbine that was designed to represent the first few stages of a high pressure (HP) steam turbine (Fig. 1). The facility was successfully used in the past and there are several publications describing results obtained using this model turbine, i.e., Lewis [15] and Wallis [7]. Details about the turbine geometrical and operational parameters and key blade parameters can be found in Part 1 of this study [16] and Rosic et al. [17].

All three stages of the model turbine are identical, with 50% reaction blading, and a detailed diagram of the stage geometry used in this study is presented in Fig. 2. Both stator and rotor blades were shrouded. The 15 mm inlet and the 18 mm exit shroud cavity are representative of a real industrial turbine and this geometry is denoted as the “datum shroud geometry” in the following text. The rotor shroud leakage flow is controlled by two approximately 0.75 mm clearance radial seals (resulting in approximately 1.8% leakage flow). In order to isolate the influence of the rotor shroud geometry on the mainstream aerodynamics, the stator hub cavities are sealed with minimized leakage flow.

The time mean flow properties of the main passage were obtained using a five hole pneumatic probe. The properties were measured by performing full-span area traverses over one blade pitch downstream of each blade row. In the model turbine, a repeating stage condition develops downstream of the second stage (Lewis [15]) and, therefore, the experimental results downstream of Rotor 2 and Stator 3 are given (the traverse plane positions are shown in Fig. 1). The results are presented in the form of spanwise distribution of the pitchwise mass averaged yaw angle and

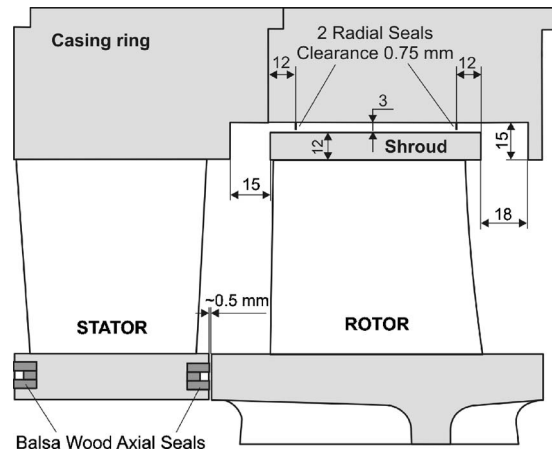


Fig. 2 The stage geometry with open shroud cavities

total pressure coefficient contours C_{p0} . The brake turbine efficiency η_b was also measured for each geometrical modification tested.

Numerical Code and Flow Domain

Numerical predictions were used in this study to help resolve and understand the flow details in the exit shroud cavity and to analyze additional cavity geometries, which were not experimentally tested. The computations were completed using 3D multi-block Reynolds averaged Navier–Stokes solver TBLOCK, written by Denton. TBLOCK is a finite volume solver using the explicit “Scree” scheme (Denton [18]). Turbulence is modeled using a mixing length approach with wall functions for surface skin friction. The solver was run in parallel and steady mode using the mixing plane approach.

The CFD geometry modeled 1.5 stages of the model turbine (embedded second rotor of the model turbine). The rotor shroud cavity (see Fig. 2) was modeled completely. The number of seals and clearance were kept constant in the study. The stator hub cavity was not modeled. The computational domain and grid are the same as in Part 1 of this study (Fig. 3).

The code was calibrated against experiments, and the capabilities of the solver in predicting the flow in the multistage turbine with shrouded blades were demonstrated in the work of Rosic et al. [17]. Several previous works have used TBLOCK to model leakage flows and complex stage geometries and showed very good agreement with experimental results, see Reid et al. [19].

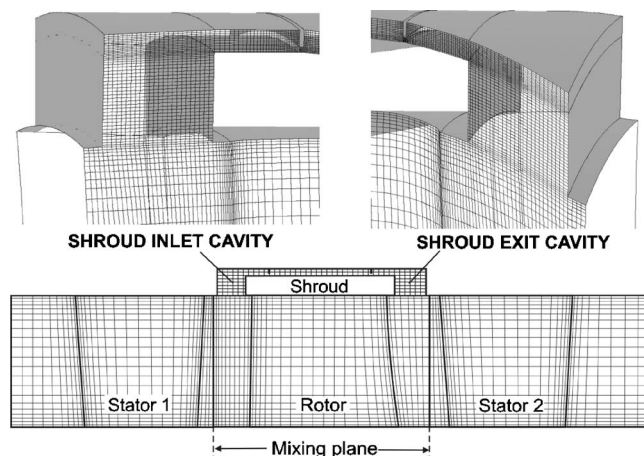


Fig. 3 Computational domain (1.5 stage turbine) and grid details (every three nodes in span- and streamwise directions)

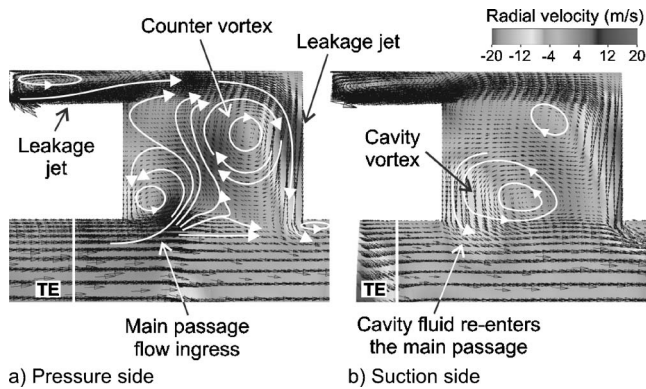


Fig. 4 Radial velocity distribution in the exit cavity for two different circumferential positions, close to (a) pressure side and (b) suction side (CFD)

Flow Field in the Datum Exit Shroud Cavity

This section explains the topology of the flow field in the datum exit shroud cavity (Fig. 2). This will help in understanding the influence that different modifications of the cavity geometry has on the main annulus aerodynamics.

The flow field in the exit cavity is illustrated using the predicted radial velocity contours for two different circumferential positions of the rotor pitch (Fig. 4). The flow structure in the cavity agrees with the findings of Wallis [7] and Pfau et al. [8]. The rotor blade potential field extended downstream of the trailing edge allowing the mainstream fluid to enter the cavity downstream of the shroud in the region of higher pressure close to the blade pressure side (Fig. 4(a)). The ingested mainstream fluid splits into two streams. One bends forward and mixes with the leakage jet forming a countervortex, and the other bends backwards and rolls up feeding the cavity vortex. The cavity vortex traveled along the cavity toward the blade suction side and the net inflow slowly diminished until close to the suction side the cavity fluid started to reenter the main passage (Fig. 4(b)). The cavity vortex filled the cavity space and acted as a blockage, deflecting the leakage flow in the cavity toward the low pressure region close to the suction side, and so causing the nonuniform leakage flow reentry. Leaving the gap of the second radial fin, the leakage jet widens and propagates through the cavity, remaining almost attached to the casing wall and reentering the main passage with a strong radial velocity component close to the cavity downstream wall causing a strong separation at the inlet of the downstream stator.

In the case of the datum cavity geometry, there are two flow features that dominate the cavity flow—the ingress of the main passage fluid into the cavity and the radial reentry of the leakage jet. In an attempt to minimize the influence of the cavity flow dynamics on the mainstream, three different concepts for shroud leakage flow control were analyzed: profiled exit cavity downstream end wall, axial deflector, and radial deflector concepts.

Profiled Exit Cavity Downstream End Wall. This concept investigated the potential of shroud leakage control by reducing the leakage jet radial velocity component and the separation at the downstream cavity edge. This was achieved by profiling the exit cavity downstream end wall.

Chamfered Corner of the Cavity Downstream Edge. Tested first was a geometry with a 5 mm wide foam insert with a chamfered (5 mm radius) exit cavity downstream corner, as detailed in Fig. 5(a). The contours of the predicted radial velocity for the two different circumferential positions indicate that the chamfered corner reduces the radial angle of the reentry leakage jet (Fig. 5(b)). However, the general flow structure inside the cavity remained similar to that of the datum rectangular cavity presented in Fig. 2. A drop of 0.08% in turbine efficiency was measured. This value

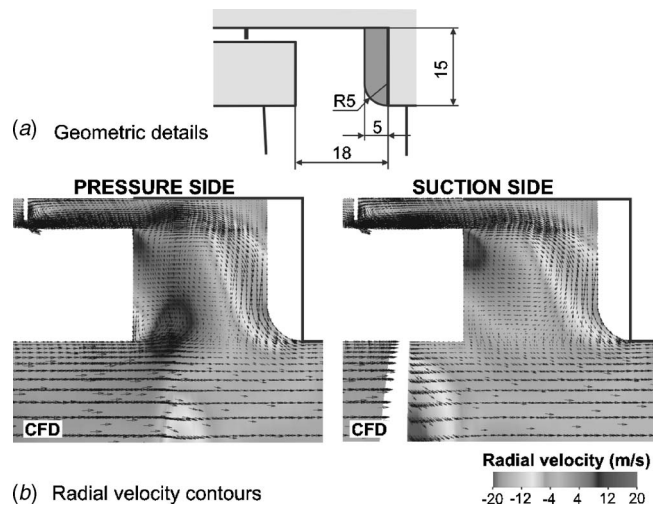


Fig. 5 (a) Geometric details and (b) the radial velocity distribution in the case with the chamfered cavity downstream edge

indicates that the change in turbine efficiency was less than the repeatability error of the efficiency measurement (estimated to 0.2%). Modeling the same cavity geometry, CFD predicted an increase in efficiency of 0.03%. The small influence of the chamfered cavity downstream corner on the turbine performance was also confirmed by analyzing the total pressure and yaw angle distribution downstream of Stator 3. The total pressure distribution appeared very similar to the datum cavity (see Fig. 6), but with the central loss core strength slightly reduced in the case with the chamfered corner. A small improvement in the flow angle distribution was also measured (Fig. 7) in the case with the chamfered corner.

Contoured Cavity Downstream End Wall. In order to reduce further the radial velocity component of the leakage jet, the exit cavity end wall was profiled, as it is illustrated in Fig. 8(a). The curvature of the end wall consisted of two 90 deg circular arcs, with 7.5 mm radii. By filling in the exit cavity, the size of the cavity was almost halved, and the allowable axial movement of the rotor relative to the casing was considerably reduced, and this is the main limitation of this approach. Figure 8(b) shows the predicted radial velocity contours in the exit cavity. The leakage jet followed the end-wall curvature and reentered the main passage with a reduced radial velocity component. The region of separated flow at the downstream edge of the datum cavity, which is responsible for thickening of the boundary layer upstream of the stator blade row, was also eliminated. The main passage fluid

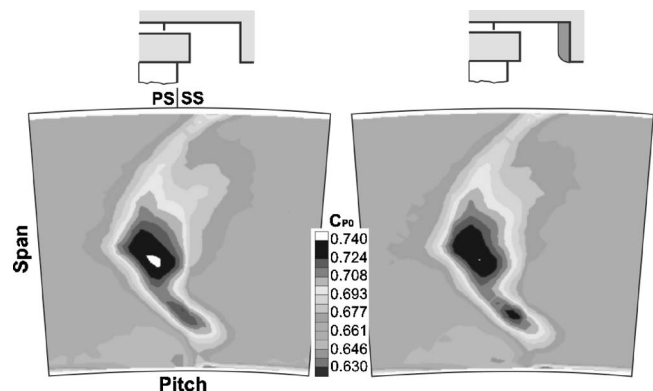


Fig. 6 C_{p0} contours downstream of Stator 3 in the case with chamfered cavity downstream edge (expt.)

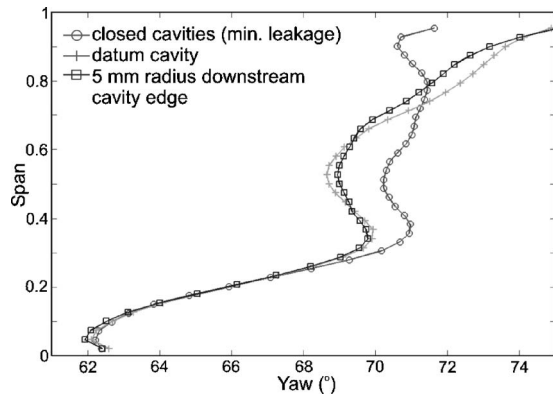


Fig. 7 Yaw angle distribution downstream of Stator 3 in the case with chamfered cavity downstream edge (expt.)

enters the cavity close to the pressure side, and part of it joins the leakage jet and the other part forms the cavity vortex and reenters the main passage close to the rotor blade suction side. It can be also noticed that the curvature of the wall reduced the amount of ingested main passage fluid, compared to the datum configuration. Figure 9 shows the radial velocity on the interface plane between the cavity and the main blade passage for the datum cavity and two cavities with profiled end walls. In the case with contoured cavity end wall (Fig. 9(c)), the leakage jet's radial velocity is significantly reduced and the area of the leakage flow reentry was wider than in the case of the datum cavity.

The measured efficiency improvement was +0.19%, and the CFD prediction was +0.16%. Further evidence of the improved performance can be found in analyzing the flow field in the downstream stator. Figure 10 shows the C_{p0} contours downstream of Stator 3. Again, the central loss core is reduced in strength and stretched out compared to the datum cavity. The reduction of the secondary flows in the stator is indicated in the yaw angle distribution (Fig. 11). The flow underturning at the midspan and overturning in the casing region that characterizes increased secondary flows were also reduced.

The mixing process between the leakage and the ingested mainstream fluid in the cavity creates loss by itself, but in this case it is likely that this process reduced the high swirl in the flow in the casing region upstream of the stator blade row. This is shown in Fig. 12 using the CFD predicted absolute yaw angle downstream of

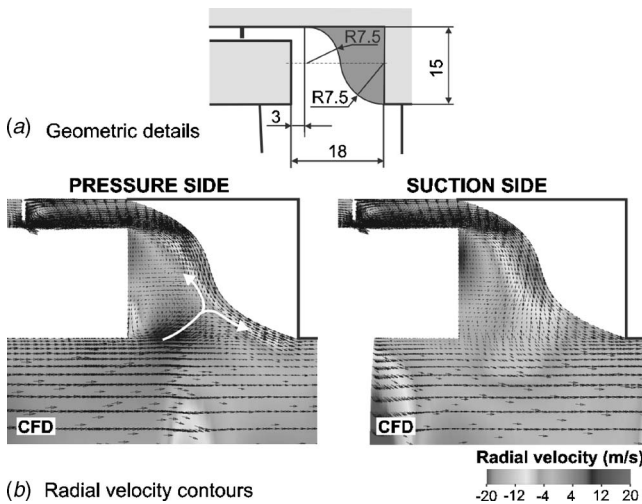


Fig. 8 (a) Geometric details and (b) the radial velocity distribution in the case with the contoured cavity downstream end wall

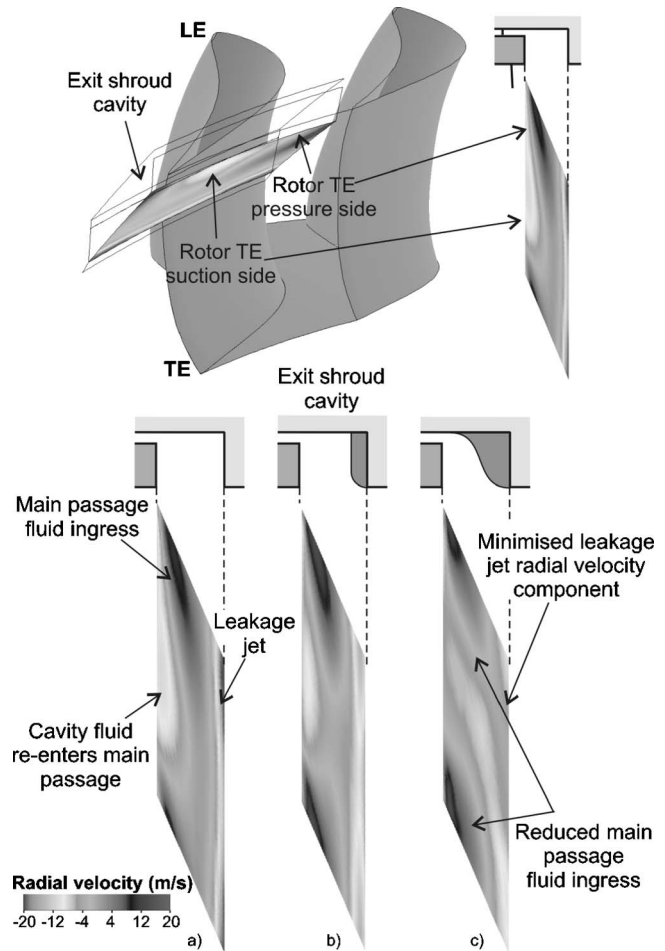


Fig. 9 Radial velocity distribution at the interface between the exit cavity and the main passage in the case with profiled cavity downstream end wall (CFD)

the exit shroud cavity. A summary of the turbine performance changes and resulting leakage flow fractions for this shroud leakage control concept is given in Table 1.

Axial Deflector. The results of the aforementioned tests indicated that the reduction of aerodynamic loss associated with the shroud leakage flow could result from shifting the position where the leakage jet rejoins the mainstream and reducing the amount of

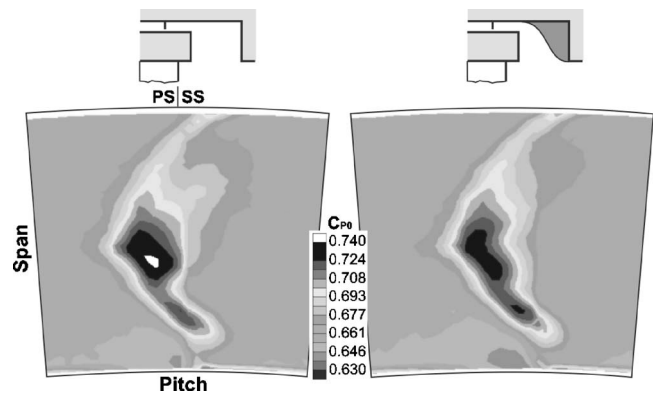


Fig. 10 C_{p0} contours downstream of Stator 3 in the case with contoured cavity downstream end wall (expt.)

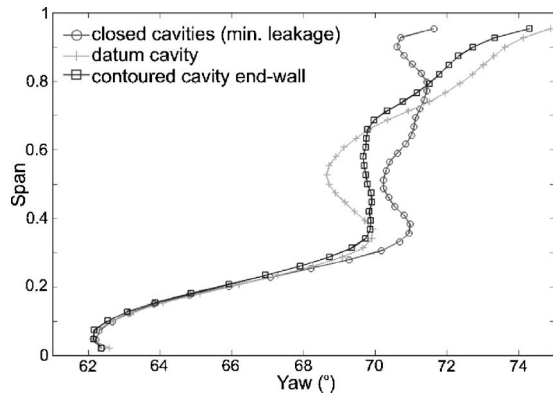


Fig. 11 Yaw angle distribution downstream of Stator 3 in the case with contoured cavity downstream end wall (expt.)

mainstream fluid entering the cavity. Hence, the concept of an axial deflector was tested and is presented in this section.

Straight Axial Deflector. An axial deflector, consisting of a 0.5 mm thick and 7 mm long aluminum plate, was mounted on the cavity end wall (Fig. 13(a)). The idea was to deflect the leakage jet from the cavity end wall. Figure 13(b) illustrates the flow structure in the exit cavity. The presence of the deflector modified the leakage jet compared to the datum case by redirecting the jet back into the cavity. At the plane that connects the cavity and the main blade annulus, the leakage jet undergoes a strong turning to rejoin the mainstream under the influence of the main passage pressure field. This extreme streamline curvature at the deflector's tip modifies the pressure field at the cavity-mainstream interface, and hence reduces the available area for mainstream fluid ingress into the cavity. Therefore, the mainstream fluid is deflected by the leakage jet and enters the cavity close to the shroud edge. This reduces the interaction and mixing between these two streams and, consequently, the leakage fluid approaches the downstream stator with an almost unchanged yaw angle compared to the datum case. This can be seen in Fig. 18, which compares the numerically predicted absolute yaw angle distribution in the casing

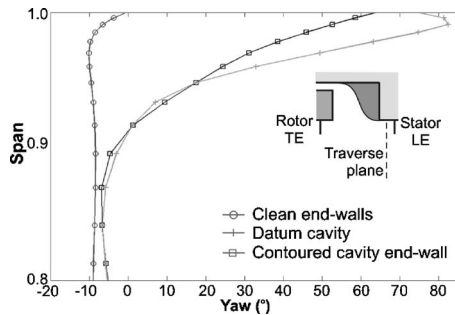


Fig. 12 Absolute yaw angle downstream of the exit cavity in the case with contoured cavity downstream end wall (CFD)

Table 1 Summary of profiled cavity end-wall concept

| | | Minimised cavity | Chamfered cavity | Contoured cavity |
|----------------------------|-----|------------------|------------------|------------------|
| $\Delta\eta$ [%] | EXP | + 0.36 | - 0.08 | + 0.19 |
| | CFD | + 0.45 | + 0.03 | + 0.16 |
| Leakage fraction [%] (CFD) | | 1.66 | 1.82 | 1.80 |

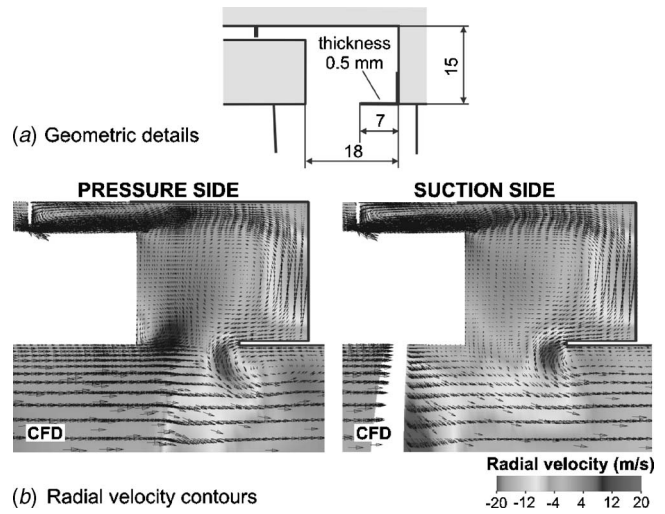


Fig. 13 (a) Geometric details and (b) the radial velocity distribution in the case with straight axial deflector

region downstream of the cavity.

The axial deflector also modified the flow field in Stator 3, compared to the datum cavity. Measured C_{p0} contours (Fig. 14) show that the loss core strength was slightly reduced. Figure 15 shows the yaw angle distribution downstream of Stator 3, and it can be seen that the flow angle distribution was slightly improved compared to the datum cavity. The straight, 7 mm long axial deflector caused a measured change in efficiency of +0.11% com-

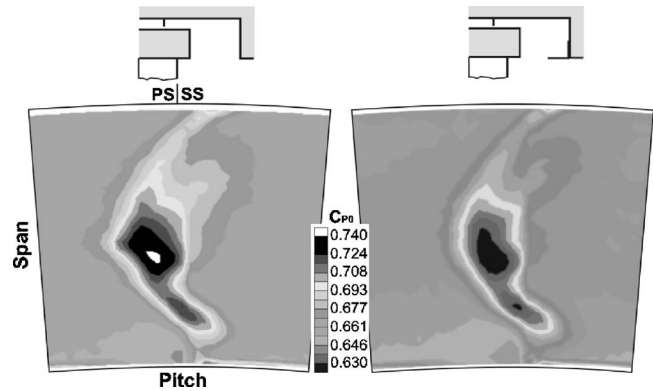


Fig. 14 C_{p0} contours downstream of Stator 3 in the case with straight axial deflector (expt.)

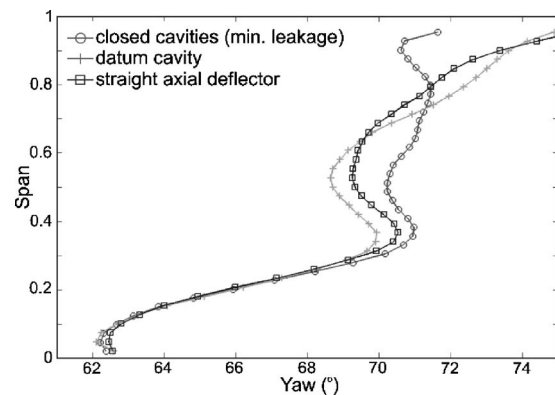


Fig. 15 Yaw angle distribution downstream of Stator 3 in the case with straight axial deflector (expt.)

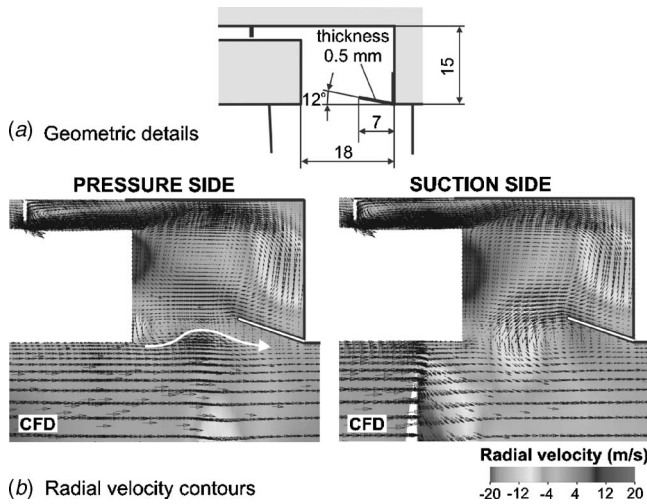


Fig. 16 (a) Geometric details and (b) the radial velocity distribution in the case with inclined axial deflector

pared to the datum open cavity. For the same axial deflector, CFD predicted a +0.27% change in the efficiency.

Inclined Axial Deflector. In the next test, the straight axial deflector was modified in order to minimize the main passage fluid ingress into the exit cavity. The length of the deflector was kept the same as in the previous experiment, but the deflector was inclined 12 deg inside the cavity. Geometric details of the inclined axial deflector in the exit cavity are presented in Fig. 16(a).

Figure 16(b) indicates that the ingress of the main passage fluid was significantly reduced in the region close to the rotor pressure side. The inclined axial deflector also reduced the region of separated flow downstream of the cavity. Figure 17 gives the radial velocity distribution at the interface plane between the exit cavity and main passage for the datum cavity and the three different axial deflectors analyzed in this study. The inclined axial deflector (Fig. 17(c)) minimized the main passage fluid ingress into the cavity (positive radial velocity). The area of negative radial velocity where the leakage flow and cavity flow reenter the main passage flow is spread over a larger area compared with the datum con-

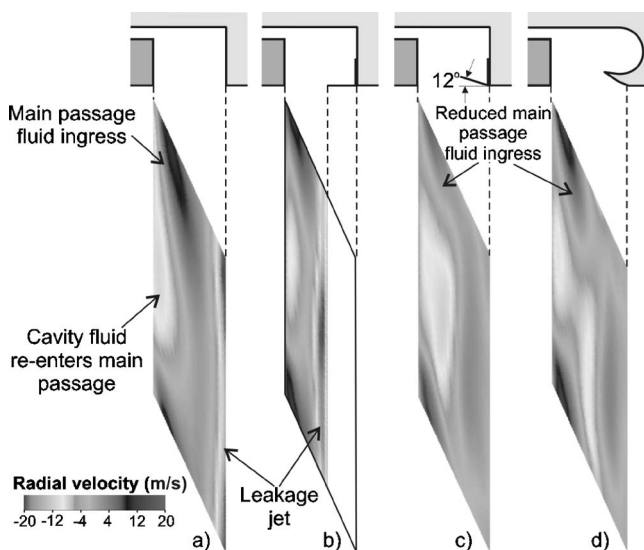


Fig. 17 Radial velocity distribution at the interface between the exit cavity and the main passage in the case with different axial deflector geometries (CFD)

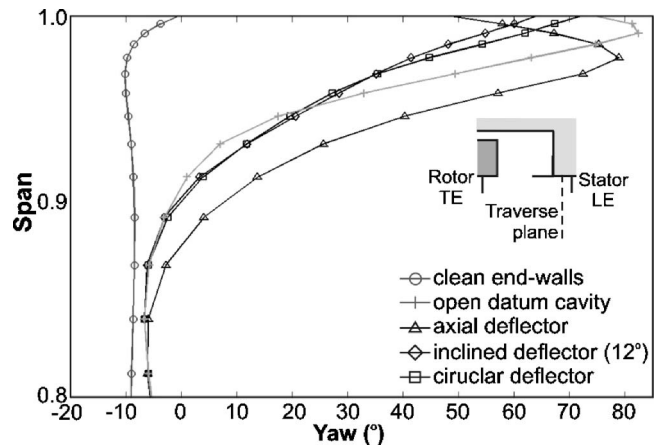


Fig. 18 Absolute yaw angle downstream of the exit cavity in the case with different axial deflector geometries (CFD)

figuration. This demonstrated how the cavity flow could be sensitive to small geometry changes. It is also likely that the mixing process between the leakage fluid and cavity fluid was more intensive, compared to the case with the straight deflector. A confirmation of this can be seen in the reduced absolute yaw angle downstream of the cavity in the casing region in the case with the inclined axial deflector (Fig. 18).

Figure 19 is a contour plot of the measured C_{p0} downstream of Stator 3, from which it is obvious that the deflector reduced the influence of leakage flow. The central loss core is reduced in size and stretched toward the casing. Similarly, the leakage flow influence on flow angle was also reduced, as it is seen in Fig. 20. The yaw angle distribution over the whole span shifted toward the yaw angle distribution of the case with closed cavities and minimized influence of the leakage flow. These changes in the cavity and the downstream stator flow field caused an increase in measured efficiency of 0.36%, while numerical predictions indicated a change in efficiency of +0.43%. The presence of the 7 mm long deflector in the exit cavity limited the available axial movement of the rotor. In the following section, the influence of a reduced deflector length on turbine aerodynamics and performance is analyzed.

Circular Deflector. Figure 21(a) shows geometric details of the cavity with a 4 mm long deflector. To improve the leakage jet deflection back into the cavity space, a circular cavity end-wall profiling was applied. Also, the underside of the deflector was shaped to eliminate possible flow separation at the cavity downstream edge. The circular deflector geometry was only tested numerically in order to compare changes in the cavity flow field and

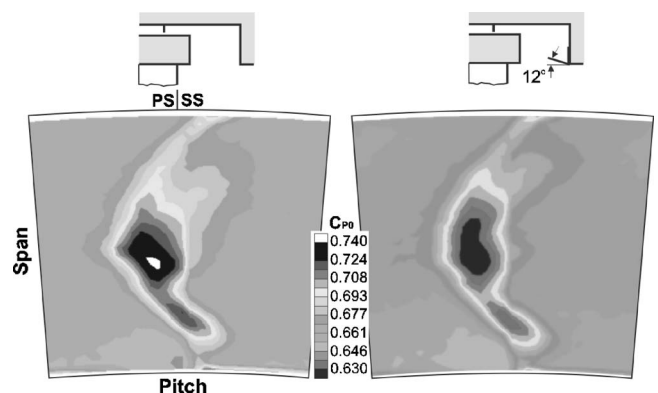


Fig. 19 C_{p0} contours downstream of Stator 3 in the case with inclined axial deflector (expt.)

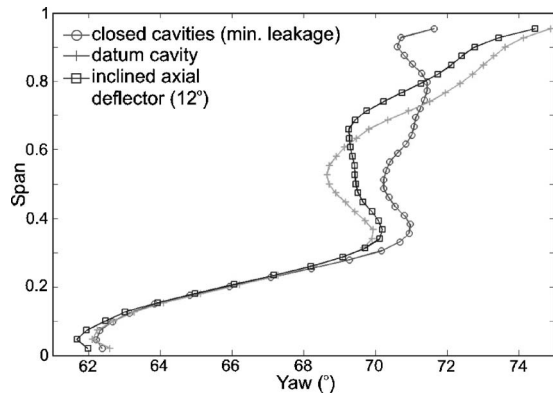


Fig. 20 Yaw angle distribution downstream of Stator 3 in the case with inclined axial deflector (expt.)

mainstream with the two axial deflectors already discussed.

From Fig. 21(b), it is evident that the leakage jet was deflected away from the cavity end wall and reentered the main passage at the middle of the cavity. The contours of radial velocity in the connecting plane between the cavity and main passage for the circular cavity are presented in Fig. 17(d). The area with positive radial velocity (fluid ingress) was reduced and reentry of the leakage flow (negative radial velocity) was also shifted further upstream from the cavity downstream edge. The effectiveness of the deflector was reduced compared to the 7 mm long inclined deflector (Fig. 16(a)). The circular deflector caused an increase in the predicted overall turbine efficiency of 0.25%.

A summary of the turbine performance improvement and resulting leakage flow fractions for the different axial deflector geometries is given in Table 2. For all three types of the axial deflectors, the leakage mass fraction did not change significantly compared with the datum configuration.

Radial Deflector. The last concept for shroud leakage flow control in the exit cavity presented in this paper, the radial deflector (Fig. 22(a)), combines the positive effects of the two previously presented concepts. Compared to the datum geometry, the depth of the space between the shroud and the casing downstream of the second radial fin was increased to 6 mm and closed downstream by *Radial deflector A*. The tip of the radial deflector was located 2 mm axially from the shroud edge. The chamber between the radial fin and the deflector was enlarged in order to dissipate

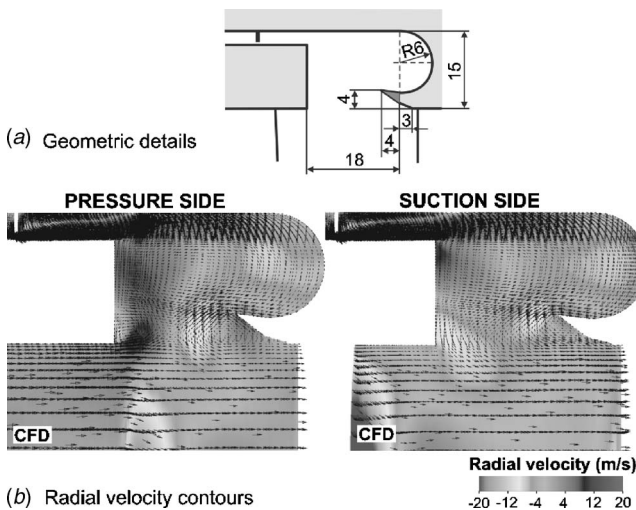


Fig. 21 (a) Geometric details and (b) the radial velocity distribution in the case with circular deflector

Table 2 Summary of axial deflector concept

| | | Straight deflector | Inclined deflector | Circular deflector |
|----------------------------|-----|--------------------|--------------------|--------------------|
| $\Delta\eta$ [%] | EXP | + 0.11 | + 0.36 | - |
| | CFD | + 0.27 | + 0.43 | + 0.25 |
| Leakage fraction [%] (CFD) | | 1.79 | 1.79 | 1.80 |

the kinetic energy of the leakage jet and reduce the leakage flow. For the same reason, the deflector was inclined toward the upstream direction. The radial clearance between the deflector and the shroud outer surface was the same as the radial clearance under the fin, 0.75 mm, allowing unrestricted axial movement of the rotor relative to the casing. This is the main advantage of this flow control concept compared to the previously analyzed concepts (profiled cavity end wall and axial deflector), which limit the rotor axial movement to a certain extent. The concept of the radial deflector was analyzed only numerically.

Figure 22(b) shows that the leakage jet was redirected toward the cavity interior and the angle of propagation through the cavity was similar to that of the cavity with the contoured downstream end wall (Fig. 8). The reentry region of the leakage flow was spread out more upstream compared with the datum cavity case, and the flow separation at the cavity downstream corner was also minimized. The predicted improvement in turbine efficiency was 0.35%.

The leakage fraction was reduced from 1.82% for the datum cavity to 1.61% with the radial deflector (0.21%). This by itself is beneficial in terms of turbine efficiency and leads to the conclusion that the radial deflector controls effectively the cavity flow field and acts as an additional seal at the same time. In a real turbine, the axial position of the rotor in the shroud cavity is not known with high accuracy. Therefore, different radial deflector positions relative to the shroud were numerically tested to illustrate the effectiveness of the concept.

In the next step the position of the radial deflector was shifted axially upstream, as is shown in Fig. 23(a). In this case, *Radial deflector B* was fully engaged with the shroud creating an additional seal. All other geometrical parameters were kept the same

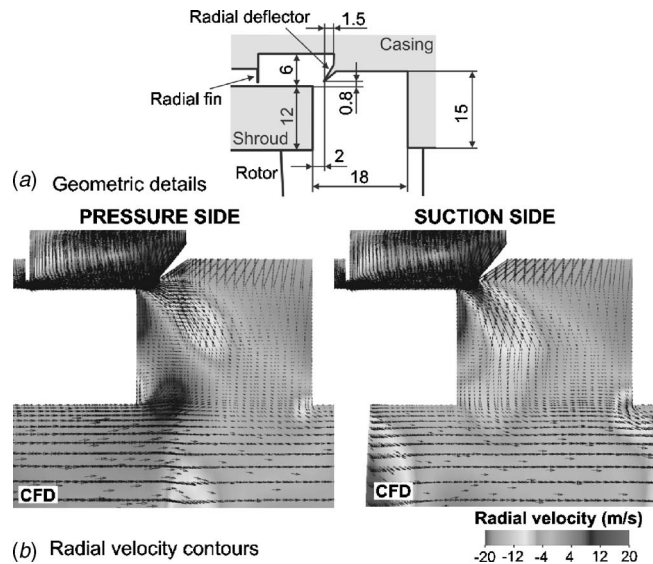


Fig. 22 (a) Geometric details, and (b) the radial velocity distribution in the case with Radial deflector A

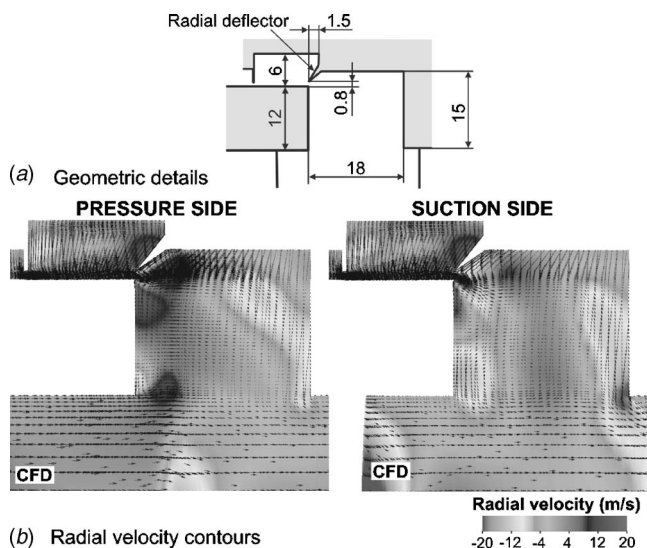


Fig. 23 (a) Geometric details and (b) the radial velocity distribution in the case with Radial deflector B

as in the previous case (Deflector A). Figure 23(b) shows the flow field in the cavity with Deflector B. It is evident that the cavity flow structure was very similar to that of the datum cavity, with the leakage jet staying attached to the cavity downstream end wall and the region of the separated flow downstream of the cavity corner. The radial deflector acted as an extra sealing element causing a further drop in leakage mass flow fraction to 1.44%. However, the predicted +0.29% change in efficiency was not as high as expected. The reason for this is that the reduction in leakage flow fraction was not followed by favorable flow modifications in the exit cavity, as was the case of the original deflector (A), and, consequently, the flow field in the downstream stator was not modified.

The geometry of *Radial deflector C* is presented in Fig. 24(a). The tip of the radial deflector edge was 5 mm from the shroud edge and all other parameters were kept as in the previous case. The leakage jet was deflected toward the cavity interior, in a similar way to the case of Radial deflector A (Fig. 24(b)). Although the deflector in this case was farther from the shroud edge than De-

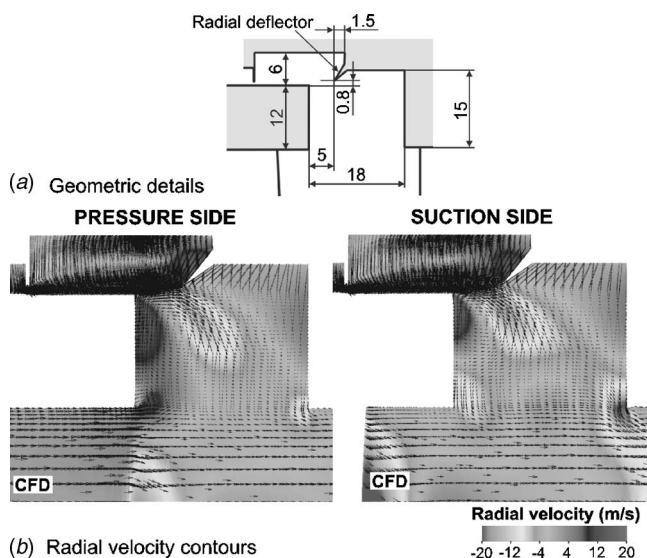


Fig. 24 (a) Geometric details and (b) the radial velocity distribution in the case with Radial deflector C

Table 3 Summary of radial deflector concept

| | Deflector A | Deflector B | Deflector C |
|----------------------------|-------------|-------------|-------------|
| $\Delta\eta$ [%] (CFD) | + 0.35 | + 0.29 | + 0.24 |
| Leakage fraction [%] (CFD) | 1.61 | 1.44 | 1.63 |

flector A, it was still effective in reducing the leakage flow fraction to 1.63%. This is because the curvature of the leakage jet increases the pressure in the cavity behind the second seal. The separation at the cavity downstream edge was stronger than in the case with Deflector A and, hence, the effectiveness of this geometry was reduced. The predicted efficiency improvement was +0.24%.

The study demonstrated the effectiveness of the radial deflector concept for a range of different axial positions. Therefore, this concept is a promising strategy for shroud leakage flow control and can be easily implemented in the current turbine design process. A summary of the turbine performance improvement and resulting leakage fractions is given in Table 3.

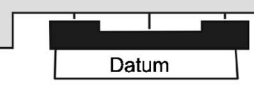

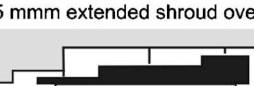
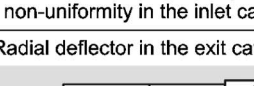
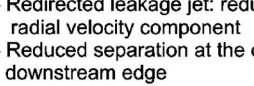
Optimized Shroud Geometry

The understanding about the interaction between the shroud leakage and the mainstream flow gained during this study and presented in Parts 1 and 2 was applied to optimize the shroud leakage flow path of a typical low aspect ratio industrial turbine. In a comprehensive numerical study, a datum shroud configuration was systematically modified in order to estimate the possible improvements in turbine performance if the previously discussed concepts of shroud leakage flow control were applied.

The datum rotor shroud configuration (Geometry A in Table 4) consisted of a stepped shroud and three radial fins (different to the previous datum given in Fig. 2). The inlet and exit shroud cavities are the same as in Fig. 2. In the first step, the shroud thickness was reduced to 2 mm above the rotor leading edge, together with a 10 mm reduction in inlet shroud cavity depth (Geometry B). For that reason the first radial fin was moved further upstream. The downstream part of the shroud was kept unchanged. The study was continued by analyzing the influence of a 5 mm shroud overhang extension in the inlet cavity (Geometry C). A radial deflector (Deflector A) 2 mm downstream of the shroud edge was introduced in the exit shroud cavity (Geometry D). Finally, the downstream corner of the exit shroud cavity was chamfered to form Geometry E. During this numerical study, the number of seals, seal clearance, and the distance between rotating and stationary surfaces were kept constant (so the axial movements were unrestricted).

Table 4 summarizes the efficiency improvement for all analyzed shroud geometries compared with the datum configuration. The study was completed in parallel for two different seal clearance values. In the case with the 0.75 mm clearance and 1.47% of leakage, the final shroud geometry modification (Geometry E) resulted in a 0.60% improvement in turbine efficiency. It can be also noticed that the largest contribution to the efficiency improvement (of +0.28%) came from the reduction in the inlet cavity depth and shroud thickness (Geometry B). The radial deflector, mounted in the exit cavity, caused the second largest efficiency improvement of 0.18%. The increased clearance to 1.0 mm generated a leakage flow of 1.78%. The most important conclusion is that the effectiveness of the applied geometrical modifications increased with the leakage fraction. The final Geometry (E) caused a positive change in turbine efficiency of 0.75%. This is very important, bearing in mind that the effectiveness of the sealing elements deteriorates with time. Opening the seal clearance from 0.75 mm to 1 mm caused a drop in efficiency of 0.42% (89.84%–

Table 4 Optimized shroud geometry. Performance change (CFD predictions)

| Geometry | $\eta / (\Delta\eta)$ [%] | |
|---|---------------------------|------------------|
| | Leakage 1.48 % | Leakage 1.78 % |
| A  Datum | 89.84 | 89.42 |
| B Minimised inlet cavity  - Reduced mixing losses in the cavity, - Improved flow field in the rotor, - Reduced leakage fraction | 90.12 (+0.28) | 89.77 (+0.35) |
| C 5 mm extended shroud overhang  - Reduced main passage fluid ingress - Reduced circumferential pressure non-uniformity in the inlet cavity | 90.20 (+0.36) | 89.86 (+0.44) |
| D Radial deflector in the exit cavity  - Redirected leakage jet: reduced jet radial velocity component - Reduced separation at the cavity downstream edge - Improved downstream stator secondary flows - Reduced leakage fraction | 90.38 (+0.54) | 90.09 (+0.67) |
| E Chamfered downstream cavity corner  - Further reduction in corner separation - Improved downstream stator secondary flows | 90.44 (+0.60) | 90.17 (+0.75) |

89.42%) for the datum configuration (Geometry A). However, the same change in the radial clearance from 0.75 mm to 1.0 mm only caused a drop in efficiency of 0.27% (90.44–90.17%) for the optimized shroud geometry (Geometry E).

This section analyzes the influence of the final shroud geometrical modification (Geometry E) on the main annulus aerodynamics in the case with a 1.0 mm seal clearance. Figure 25 compares

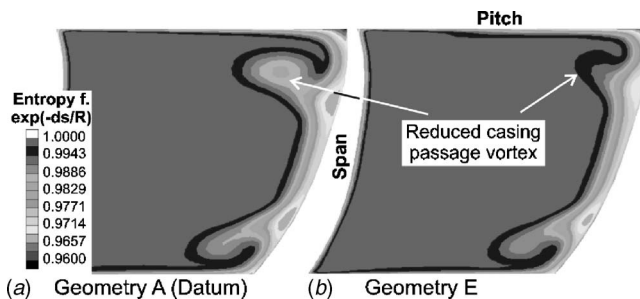


Fig. 25 Entropy function downstream of the rotor for the (a) datum and (b) optimized shroud geometry (CFD)

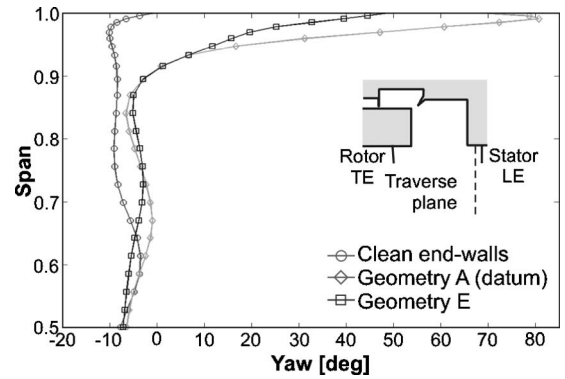


Fig. 26 Absolute yaw angle downstream of the exit cavity in the case with (a) datum and (b) optimized cavity (CFD)

entropy function contours downstream of the rotor for the datum and optimised shroud geometry (E). It is evident that the minimized inlet cavity (Geometry E) reduced the casing loss core significantly. This demonstrates that in the case of the properly designed inlet cavity geometry, together with the inlet boundary layer removal by the action of the leakage flow, the flow field in the rotor blade row can be significantly improved. Figure 26 shows the spanwise distribution of the absolute yaw angle downstream of the exit cavity. The mixing process in the cavity and reduced leakage fraction reduced the difference in swirl velocity between the leakage and the mainstream flow in the case of the optimized geometry (E) compared with the datum shroud configuration. This effect, together with eliminating the region of separated flow by introducing the radial deflector and the cavity end-wall chamfering, favorably influenced the development of casing secondary flows in the downstream stator. This is shown using entropy function contours downstream of the stator (Fig. 27). The optimized shroud geometry (E) reduced the strength of the loss core close to the casing compared with the datum geometry.

Although each shroud geometrical modification separately does not necessarily have a substantial effect on the main flow field, when all are combined, it is possible to achieve a significant improvement in turbine performance.

The limitations in the rig design did not allow this configuration to be tested experimentally without significant reconstruction of the model turbine. However, the achieved agreement between the experimental and numerical results demonstrated in both parts of this study, indicates that the numerical results presented in this study can be treated with a high level of confidence.

Conclusions

The geometrical modifications investigated demonstrated that it is possible to reduce aerodynamic losses associated with shroud

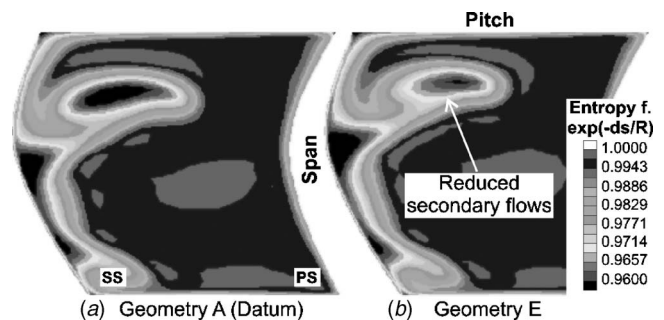


Fig. 27 Entropy function downstream of the stator for the (a) datum and (b) optimised shroud geometry (CFD)

leakage flow by controlling the interaction between the leakage and the mainstream flow in the exit shroud cavity.

In the case of the profiled cavity downstream end wall, it was shown that reducing the leakage jet radial velocity reduced flow separation at the cavity downstream corner and associated mixing losses, and consequently reduced the secondary flows in the downstream stator. The main limitation of the approach is that it limits the allowable rotor axial movement relative to the casing.

The main idea of the axial deflector concept was to deflect the leakage jet from the downstream end wall and to shift the position of leakage flow reentry region further upstream. This improved the flow in the downstream stator. The inclined axial deflector was also shown to be effective in minimizing the main passage fluid ingress into the cavity. The effectiveness of this concept was directly proportional with the axial deflector length. Although the axial deflector minimizes the available rotor axial movement, this concept could be considered for application in industrial practice. The axial deflector can be mounted using the same technology developed for radial fins above the shroud. In the case of rubbing, they can be easily replaced if they are damaged or removed, and the overall turbine reliability would not be affected.

The radial deflector concept combined the positive effects of the profiled end wall and axial deflector concepts and demonstrated to be a very effective flow control device. It reduced the leakage fraction and also redirected the leakage jet towards the cavity center and reduced the jet's radial velocity at the reentry plane. The position of the leakage reentry was also shifted more upstream. The results highlighted that the concept was effective for a wide range of radial deflector positions relative to the shroud edge. This concept also does not restrict the rotor axial movement and can be easily incorporated into the current turbine design process and therefore represents a promising strategy for shroud leakage flow control.

Using the understanding gained during this project about the interaction between the main passage flow and both the leakage and cavity flows, the datum shroud geometry of an industrial HP steam turbine was optimized resulting in a performance improvement of 0.75%. The effectiveness of the optimized shroud geometry increased with increasing leakage fraction. This is important in the sense of long-term seal deterioration that is likely to occur in turbines during operation.

Acknowledgment

The authors would like to thank Siemens Power Generation for funding this work.

Nomenclature

| | | |
|------------------------------------|---|--|
| c_p | = | specific heat at $p = \text{const}$ |
| \dot{m} | = | mass flow rate |
| p_0 | = | total pressure |
| $p_{0,\text{in}}, p_{0,\text{ex}}$ | = | turbine inlet pressure and exit total pressure |
| $T_{0,\text{in}}$ | = | turbine inlet total temperature |

T_{qb} = torque

γ = specific heat ratio

η_b = turbine brake efficiency

3D = three dimensional

HP = high pressure

LE, TE = leading edge and trailing edge

PS, SS = pressure side and suction side

$C_{p0} = p_{0,\text{in}} - p_0 / p_{0,\text{in}} - p_{0,\text{ex}}$ = total pressure coefficient

$\eta_b = \frac{\omega T_{\text{qb}}}{\dot{m} c_p T_{0,\text{in}}} \left[1 - \left(\frac{p_{0,\text{ex}}}{p_{0,\text{in}}} \right)^{(\gamma-1)/\gamma} \right]$

References

- [1] Denton, J. D., 1993, "Loss Mechanisms in Turbomachines," ASME Paper No. 93-GT-435.
- [2] Denton, J. D., and Johnson, C. G., 1976, "An Experimental Study of the Tip Leakage Flow Around Shrouded Turbine Blades," Marchwood Engineering Laboratories, CEGB Report No. R/M/N848.
- [3] Sasada, T., Sato, T., Urushidani, H., Hisano, K., Kaneko, R., Ikeuchi, K., and Tsuji, K., 1987, U.S. Patent No. 4,662,820.
- [4] Pfau, A., Kalfas, A. I., and Abhari, R. S., 2004, "Making Use of Labyrinth Interaction Flow," ASME Paper No. GT2004-53797.
- [5] Reid, K., 2005, "Effect of Leakage Flows on Turbine Performance," Ph.D. thesis, Cambridge University, Cambridge, UK.
- [6] Rosic, B., and Denton, J. D., 2006, "The Control of Shroud Leakage Loss by Reducing Circumferential Mixing," ASME Paper No. GT2006-90946.
- [7] Wallis, A. M., 1997, "Secondary and Leakage Flows in a Multistage Turbine," Ph.D. thesis, Cambridge University, Cambridge, UK.
- [8] Pfau, A., Treiber, M., Sell, M., and Gyarmathy, G., 2001, "Flow Interaction From the Exit Cavity of an Axial Turbine Blade Row Labyrinth Seal," ASME J. Turbomach., **123**, pp. 342-352.
- [9] Rushton, G. J., 2003, "High-Pressure Turbine Shroud Leakage," Ph.D. thesis, Cambridge University, Cambridge, UK.
- [10] Gier, J., Stubert, B., Brouillet, B., and de Vito, L., 2003, "Interaction of Shroud Leakage Flow and Main Flow in a Three-Stage LP Turbine," ASME Paper No. GT2003-38025.
- [11] Giboni, A., Menter, J. R., Peters, P., Wolter, K., Pfost, H., and Breisig, V., 2003, "Interaction of Labyrinth Seal Leakage Flow and Main Flow in an Axial Turbine," ASME Paper No. GT2003-38722.
- [12] Giboni, A., Wolter, K., Menter, J. R. P., and Pfost, H., 2004, "Experimental and Numerical Investigation Into the Unsteady Interaction of Labyrinth Seal Leakage Flow and Main Flow in a 1.5 Stage Axial Turbine," ASME Paper No. GT2004-53024.
- [13] Peters, P., Menter, J. R., Pfost, H., Giboni, A., and Wolter, K., 2005, "Unsteady Interaction of Labyrinth Seal Leakage Flow and Downstream Stator Flow in a Shrouded 1.5 Stage Axial Turbine," ASME Paper No. GT2005-68065.
- [14] Schlienger, J., Pfau, A., Kalfas, A. I., and Abhari, R. S., 2003, "Effects of Labyrinth Seal Variation on Multistage Axial Turbine Flow," ASME Paper No. GT2003-38270.
- [15] Lewis, K. L., 1993, "Spanwise Transport in Axial-Flow Turbines: Part I—The Multistage Environment," ASME Paper No. 93-GT-289.
- [16] Rosic, B., Denton, J. D., and Curtis, E. M., 2008, "The Influence of Shroud and Cavity Geometry on Turbine Performance: An Experimental and Computational Study—Part I: Shroud Geometry," ASME J. Turbomach., **130**, p. 041001.
- [17] Rosic, B., Denton, J. D., and Pullan, G., 2005, "The Importance of Shroud Leakage Modelling in Multistage Turbine Flow Calculations," ASME Paper No. GT2005-68459.
- [18] Denton, J. D., 1990, "The Calculation of Three Dimensional Viscous Flow Through Multistage Turbomachines," ASME Paper No. 90-GT-19.
- [19] Reid, K., Denton, J. D., Pullan, G., Curtis, E. M., and Longley, J. P., 2006, "The Effects of Stator-Rotor Hub Sealing Flow on the Mainstream Aerodynamics of a Turbine," ASME Paper No. GT2006-90838.

Effects of Hole Arrangements on Local Heat/Mass Transfer for Impingement/Effusion Cooling With Small Hole Spacing

Hyung Hee Cho

Department of Mechanical Engineering,
Yonsei University,
Seoul 120-749, Korea

Dong Ho Rhee

Korea Aerospace Research Institute,
Daejeon 305-333, Korea

R. J. Goldstein

Department of Mechanical Engineering,
University of Minnesota,
Minneapolis, MN 55455

The present study investigates the local heat (mass) transfer characteristics of flow through perforated plates. Two parallel perforated plates were placed, relative to each other, in either staggered, in line, or shifted in one direction. Hole length to diameter ratio of 1.5, hole pitch to diameter ratio of 3.0, and distance between the perforated plates of 1–3 hole diameters are used at hole Reynolds numbers of 3000 to 14,000. For flows through the staggered layers and the layers shifted in one direction, the mass transfer rates on the surface of the effusion plate increase approximately 50% from impingement cooling alone and are about three to four times that with effusion cooling alone (single layer). The high transfer rate is induced by strong secondary vortices formed between two adjacent impinging jets and flow transition so that heat/mass transfer coefficient in the midway region is as high as stagnation heat/mass transfer coefficient. The mass transfer coefficient for the in-line arrangement is approximately 100% higher on the target surface than that of the single layer case. In overall, the staggered hole arrangement shows better performance than other cases.

[DOI: 10.1115/1.2812325]

1 Introduction

The thermal efficiency and the specific power of the gas turbine systems depend strongly on turbine inlet temperature. The inlet temperature is limited by the potential structural failure of the engine components mainly attributable to high temperature. Wall temperature can be reduced by various cooling techniques including transpiration and film cooling and internal jet impingement cooling.

The transpiration (porous) wall materials can produce near-uniform heat/mass transfer rates on their surface with flow through the plate. These characteristics are desirable to protect the surface in components of high-performance gas turbine engines. However, transpiration materials are prone to be partially or totally clogged by internal oxidation and particles, and are structurally weak. To alleviate clogging and improve the strength of the transpiration material in combustor walls, laminated plates with perforations have been developed.

Impingement/effusion cooling technique is one of the cooling methods using two perforated plates, that is, injection and effusion plates. With impingement/effusion cooling, the jet flow after impingement is discharged through the vent (effusion) hole on the effusion plate and makes a cooling film on the outer surface of the effusion plate. In addition, accelerating flow (sink flow) on the inner surface of the effusion plate creates a thin boundary layer and helps prevent the reentrainment of the spent air. The higher heat transfer rate is attributed to both effects.

Although the research on single/array jet impingement has been performed for the past few decades and reviewed extensively by many researchers [1–4], most studies on the impingement/effusion cooling have been conducted since the 1990s.

Hollwarth and Dagan [5] measured average heat transfer rates for flow through two perforated plates in staggered and in-line

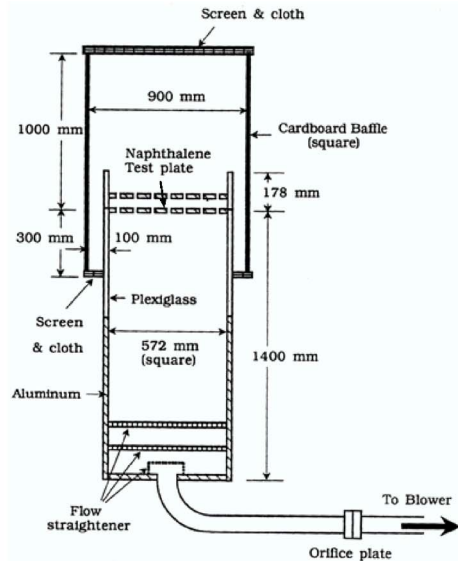
arrangements. Jet Reynolds numbers ranged from $Re_d=3000$ to 35,000, the jet hole spacing was 5–20 times hole diameter, and the gap distance was equal to the hole diameter or the hole spacing. The two layers with staggered arrangement yielded 20–35% higher heat transfer rates than that of impingement cooling alone. In-line arrays had significantly lower heat transfer rates, especially at small gap distances. Hollwarth et al. [6] continued their work measuring local heat transfer along two symmetry lines and providing flow visualization using helium bubbles. They showed a strong recirculation of spent fluid between neighboring jets for impingement alone, but the recirculation is greatly suppressed with the staggered arrays of impingement/effusion flow due to a suction effect.

Andrews et al. [7] and Al Dabagh et al. [8] measured average heat transfer rates with impingement/effusion cooling of two plates with a staggered arrangement. The hole spacing was the same in the two plates, but different hole sizes were used. Jet Reynolds numbers ranged from 2000 to 20,000, the jet hole spacing was 1.8–11 times hole diameter, and the gap distance was 0.5–6.1 times hole diameter. The heat transfer rates for the impingement/effusion cooling were 45% and 30% higher on the second plate than that for impingement cooling alone. However, they did not measure local distributions of heat transfer rates, which are important to design and analysis of heat transfer for flow through laminates.

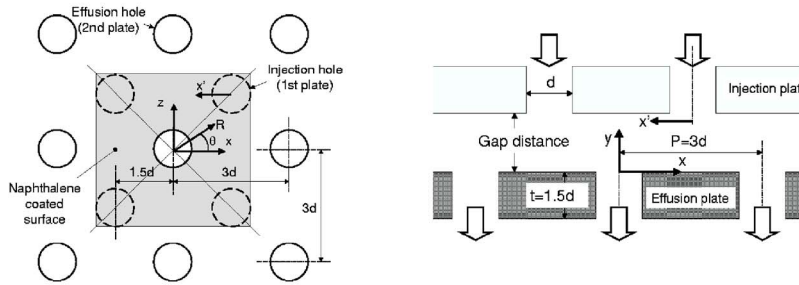
In recent years, a few studies focusing on both local and average heat transfer characteristics for impingement/effusion cooling have been performed. Funazaki et al. [9] studied the heat transfer characteristics for the impingement/effusion cooling with pin fins of staggered arrangement using Thermochromic Liquid Crystal (TLC) technique, and reported that high heat transfer is generated not only on the target plate but also on the surfaces of the pins, and high cooling performance can be obtained with less cooling air consumption.

Cho and Rhee [10] and Rhee et al. [11] investigated the local heat/mass transfer characteristics on the inner surface of effusion plate for the impingement/effusion cooling with a large hole spacing of $P/d=6.0$. They conducted experiments for two different

Contributed by the Turbomachinery Division of ASME for publication in the JOURNAL OF TURBOMACHINERY. Manuscript received July 26, 2004; final manuscript received May 9, 2007; published online June 24, 2008. Review conducted by Je-Chin Han.



(a) experimental apparatus



(b) test section for the staggered hole arrangement

Fig. 1 Schematic view of experimental apparatus and test section: (a) experimental apparatus and (b) test section for the staggered hole arrangement

hole arrangements with various gap distances and reported that the cooling performance is enhanced with the small gap distance, and the hole arrangement between injection and effusion plates is very important to obtain a high and uniform transfer on the effusion plate. However, the region between two adjacent impinging jets has low heat/mass transfer coefficient due to weak interaction of the wall jets with larger hole spacing.

In general, for smaller gap spacing, there is a transition region to turbulent flow of the wall jet radially $1.5d$ from the stagnation point on the target plate and this flow transition causes heat transfer enhancement. Therefore, different heat transfer patterns are expected in the region between the adjacent impinging jets (midway region) with smaller hole spacing because the wall jet interaction and the flow transition affect heat transfer on the target plate at the same time.

However, when the spacing is small, the heat transfer characteristics are thought to be different from those for impingement with relatively large hole spacing because the effects of jet interaction will increase. The present study, therefore, focused on the effects of hole arrangements, gap distance, and Reynolds number on local heat/mass transfer characteristics on the effusion plate with a small hole spacing of $P/d=3.0$. The comparisons with the case of large hole spacing ($P/d=6.0$) were also presented. A naphthalene sublimation technique is used to measure detailed mass transfer coefficients on the effusion plate because not only the overall heat transfer coefficient is required but also the local variation to improve efficiency and prevent hot spots [12].

The numerical calculations using a commercial code (FLUENT

6.1) are also performed to analyze flow and heat/mass transfer characteristics in detail.

2 Experimental Apparatus and Procedure

2.1 Experimental Apparatus. The experimental apparatus is shown schematically in Fig. 1(a). To simulate impingement/effusion cooling, two parallel perforated plates are used. Room air drawn into a settling baffle passes through the perforated plates (injection and effusion plates) into the plenum chamber, through an orifice flow meter and a blower, and then is discharged outside the building. To ensure the uniform flow condition in the chamber, the settling baffle is installed in the plenum chamber.

Figure 1(b) shows the schematic view of effusion plate with staggered hole arrangement. Each plate has a square array of holes of which diameter is 25.4 mm. The hole-to-hole spacing is three times of hole diameter ($P/d=3.0$), and the thickness of each plate (i.e., hole length) is $1.5d$ ($t/d=1.5$). Three different gaps between the two plates are used: 25.4 mm ($1d$), 50.8 mm ($2d$), and 76.2 mm ($3d$) in height.

The center of effusion hole is set to be the origin of coordinate, and R and θ mean the radial direction and angle with respect to the origin, as shown in Fig. 2. To measure the local heat/mass transfer coefficients, a naphthalene coated test plate is installed at the center of the effusion plate. The measurement domain covers the area of $-2.0 \leq x/d \leq 2.0$ and $-2.0 \leq z/d \leq 2.0$ (indicated as a gray square box in Fig. 1(b)).

To investigate the effects of hole arrangement, three different

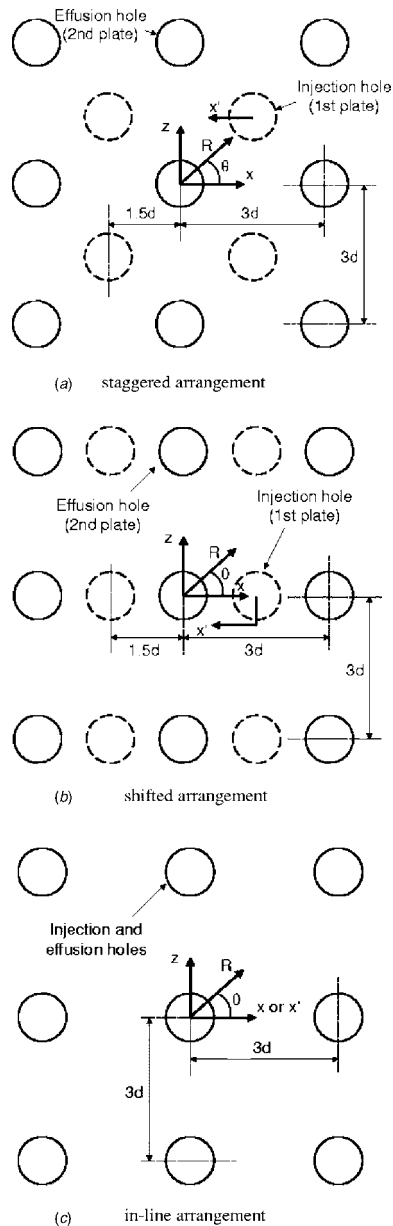


Fig. 2 Three different hole arrangements: (a) staggered arrangement, (b) shifted arrangement, and (c) in-line array

arrangements are investigated with the two perforated plates; (1) staggered, (2) shifted in one direction, and (3) in-line hole patterns, and each hole arrangement is presented in Fig. 2. For the staggered arrangement, the impinging jets from the first plate are centered between effusion holes on the second plate. For the shifted hole arrangement, the first plate is offset a half pitch ($1.5d$) in one direction. In the in-line arrangement, the projected position of the injection hole is identical to the effusion hole position. To enable to obtain various hole arrangements, effusion plate has 49 (7×7) holes and injection plate has 64 (8×8) holes to change the hole arrangement by shifting injection plate.

2.2 Data Reduction. In order to obtain local mass transfer coefficients, the profile of the naphthalene surface is measured on the measurement tables before and after each test run. The measurement systems consist of a depth gauge, a linear signal conditioner, a digital multimeter, stepping motor driven positioners, a motor controller, and a microcomputer. The details of measure-

ment system and procedure are described in Ref. [12].

The local mass transfer coefficient is defined as

$$h_m = \frac{\dot{m}}{\rho_{v,w} - \rho_{v,\infty}} = \frac{\rho_s \Delta y / \Delta t}{\rho_{v,w}} \quad (1)$$

since $\rho_{v,\infty} = 0$ in the present study. The Sherwood number can be expressed as

$$Sh = h_m d / D_{\text{naph}} \quad (2)$$

D_{naph} is determined from a correlation recommended by Goldstein and Cho [13]. During the experiment, extraneous sublimation losses by natural convection are corrected from the total sublimation rate based on a natural convection rate and the measurement duration.

Uncertainty of the Sherwood numbers using the method of Kline and McClintock [14] is within $\pm 7.1\%$ for the entire operating range of the measurement based on a 95% confidence interval.

3 Numerical Simulation

In the present study, the numerical simulations have been performed to understand the flow patterns for the impingement/effusion cooling with three hole arrangements at $Re_d = 13,500$ and $H/d = 1.0$. To calculate flow fields, FLUENT 6.1 is used and computation domain grids are created using GAMBIT solid modeling.

The computation domain has an inlet region with plenum chamber on injection plate, injection and effusion plates with holes, gap between plates, and outflow chamber, which model the test section of experiments. The symmetry boundary conditions are imposed on sidewalls to reduce grid size and calculation time. Uniform flow condition is imposed on the inlet plane. The velocity at the inlet plane is set to be 0.71 m/s, which corresponds to Re_d of $13,500$. The turbulence intensity and static temperature are 10% and 300 K, respectively. To solve the heat transfer, the temperature of effusion surface is set to be 350 K while other wall boundaries are set to be adiabatic for all the tested cases.

Different grids with $300,000$ to 1.5×10^6 cells are tested to verify the grid independence of the solution, and the results for the grid with about 1×10^6 cells are presented in the present study. The steady solutions for turbulent flow field in the impingement/effusion cooling are calculated using a RNG $k-\varepsilon$ model with enhanced wall treatment (two layer model), which is served in FLUENT 6.1, for the near wall region [15]. As suggested, the mesh near the wall is resolved to y^+ values less than 4 . The convergence of residuals for continuity, momentum, k , and ε is resolved to levels of 10^{-5} for all entities and energy equation is set to be a level of 10^{-7} .

4 Results and Discussion

4.1 Flow Characteristics. Figure 3 shows the velocity vector plots on the injection and effusion planes for the staggered hole arrangement at $H/d = 1.0$ and $Re_d = 13,500$. On the injection plane (Fig. 3(a)), a strong upward flow is generated in the midway ($z/d = 0.0$) due to the interaction between the adjacent wall jets, and then a large-scale vortex (primary vortex) is formed. At the effusion plane (Fig. 3(b)), the upward flow is dominant because of the interaction of wall jets. Near the effusion holes, the flow is accelerated and drawn into the effusion holes.

When the flow patterns on the injection planes are compared with flow field for the case with a large hole spacing of $P/d = 6.0$ [10], the difference caused by changing hole spacing is clearly shown. The upward flow is stronger and the center of the primary vortex is more lifted from the effusion surface and closer to the impinging jet for the smaller hole spacing. For example, the center of primary vortex is at $z/d = 0.6 - 0.7$ and $y/d \cong 0.7$ while its center is at $y/d \cong 0.5$ with the large hole spacing. This is due to the difference of strength of wall jets in the midway region. At the

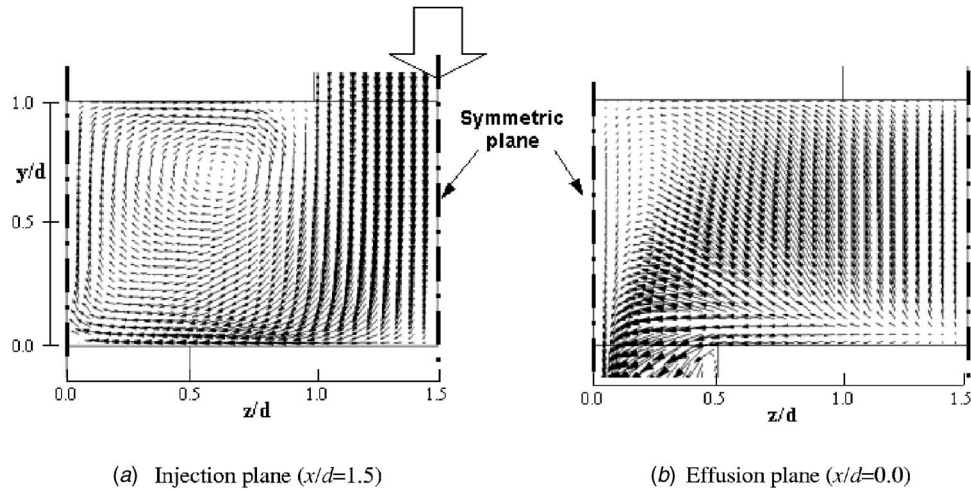


Fig. 3 Vector plots on the injection and effusion planes for staggered arrangement at $H/d=1.0$ and $Re_d=13,500$; (a) injection plane ($x/d=1.5$) and (b) effusion plane ($x/d=0.0$)

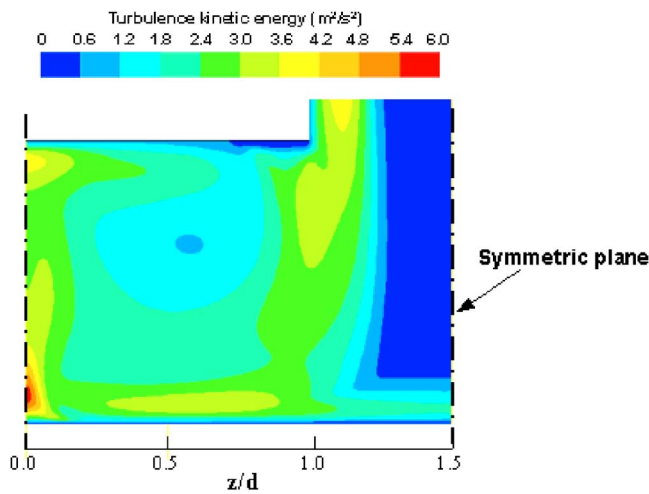


Fig. 4 Contour plot of turbulent kinetic energy on the injection plane ($x/d=1.5$) for staggered arrangement at $H/d=1.0$ and $Re_d=13,500$

effusion plane, the overall flow patterns are similar.

Figure 4 shows the contour plot of turbulence kinetic energy on the injection plane for the staggered arrangement at $H/d=1.0$ and $Re_d=13,500$. The value is very low at the center of the impinging jet with its undeveloped uniform flow velocity, and relatively high turbulent kinetic energy is observed at the shear layer and wall jet region as expected.

Remarkable increase of turbulent kinetic energy is found in the midway region ($z/d=0.0$) because of the interaction of the wall jets inducing secondary vortices in the midway. Another possible reason is the flow transition to turbulence and/or rolling vortices with the small gap distance, which are typical patterns in single jet impingement with the small gap. Highly disturbed flow moves upward and then high values of turbulent kinetic energy are observed on the upper plate (injection plate) due to the flow impingement effect as shown in the vector plot. The region of low turbulent kinetic energy is coincident with the center position of primary vortex.

Figure 5 shows the velocity vector plots for the shifted hole arrangement at $H/d=1.0$ and $Re_d=13,500$. At the injection plane, like the staggered arrangement, the wall jets collide in the midway region generating the upward flow and large flow recirculation. However, the center of large recirculation is more shifted toward the midway region than the staggered case. The reason is that a certain amount of wall jet flowing toward the z direction is dis-

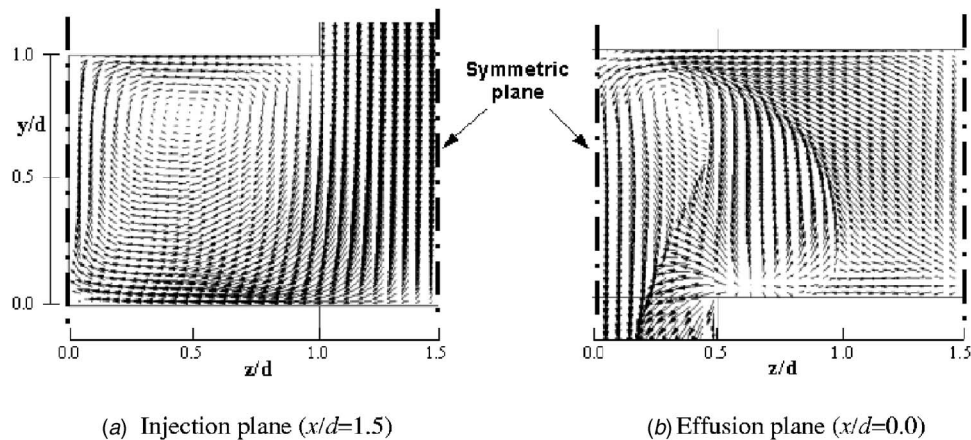


Fig. 5 Vector plots on the injection and effusion planes for shifted arrangement at $H/d=1.0$ and $Re_d=13,500$: (a) injection plane ($x/d=1.5$) and (b) effusion plane ($x/d=0.0$)

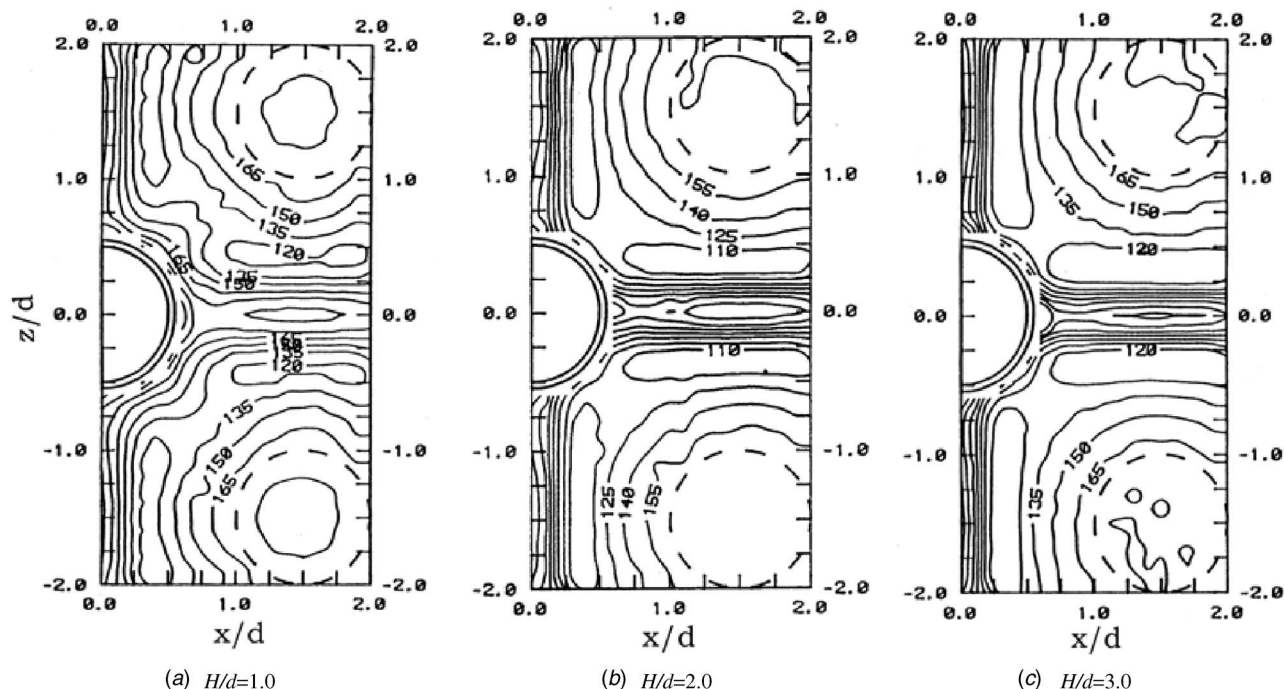


Fig. 6 Contour plots of Sh on the effusion surface for staggered layers with various gap distances at $Re_d=13,500$: (a) $H/d=1.0$, (b) $H/d=2.0$, and (c) $H/d=3.0$.

charged and consequently the amount of flow on this plane is reduced. This results in weaker interaction of flow and lower heat/mass transfer rate in the midway region. At the effusion plane, a very complex flow pattern is shown since the upward flow due to the interaction of wall jets and a sink flow through the effusion hole are generated simultaneously. From the flow patterns at the effusion plane, it is expected that heat transfer around the effusion hole will increase due to the interaction of wall jets and flow acceleration.

For the in-line hole arrangement, which is not presented in the manuscript, since most of the impinging jet is discharged through the effusion hole directly, a weak flow recirculation is generated between two plates. The jet flow through the injection hole becomes diffused as the flow moves; hence, the flow disturbance around the edge of the effusion hole is observed. This flow disturbance causes high turbulence intensity and consequently high heat transfer at that region.

4.2 Local Heat/Mass Transfer Characteristics

4.2.1 Staggered Hole Arrangement. Effects of Gap Distance.

Figure 6 shows the contour plots of Sh for the staggered arrangement with various gap distances at $Re_d=13,500$. The dotted circles represent the position of the injection holes projected on the effusion plate and the half circle is the effusion hole with the aluminum rim between two circles. Since each case shows good symmetry, Sh values on a half of measurement domain are presented.

The distributions of Sh are similar in the overall region for all the tested gap distances. Sh distributions at the stagnation regions are uniform and then Sh decreases with developing boundary layer of the wall jets as the wall jet spreads. In the midway regions, the local peaks exist at the midline of two adjacent jets ($z/d=0.0$ or along $x/d=0.0$ line) due to the interaction of the wall jets and elevated turbulence intensity.

Since the flow in the midway region is drawn to the effusion hole and accelerated, high heat/mass transfer regions are formed along the midway line ($z/d=0.0$ and $x/d=0.0$). In addition, high heat/mass transfer coefficients are formed around the effusion

hole due to the flow acceleration with sink flow. This trend is observed for all the examined gap distances, while the heat/mass transfer enhanced region for $H/d=1.0$ is slightly larger than those for other cases.

Local Sh distributions for the staggered arrangement at $Re_d=13,500$ and $H/d=2.0$ are represented in Fig. 7. In the graph, the value of "0" means the position of effusion hole. Sh for the single layer with an array of holes is also plotted. The single layer means the situation that only the effusion plate is installed without the injection plate and this represents the conventional film cooling. As easily expected, Sh on the target surface for the staggered arrangement is much higher than that for the single layer (effusion only).

Along the stagnation line ($x/d=1.5$), the uniform distributions of Sh are formed at the stagnation regions ($z/d=\pm 1.5$) and the values decrease as flow moves toward the midway ($z/d=0.0$). The

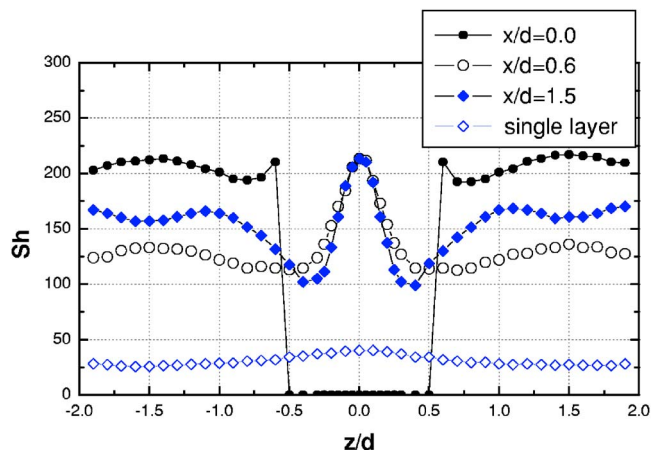


Fig. 7 Local Sh for staggered arrangement on the effusion surface at $Re_d=13,500$ and $H/d=2.0$

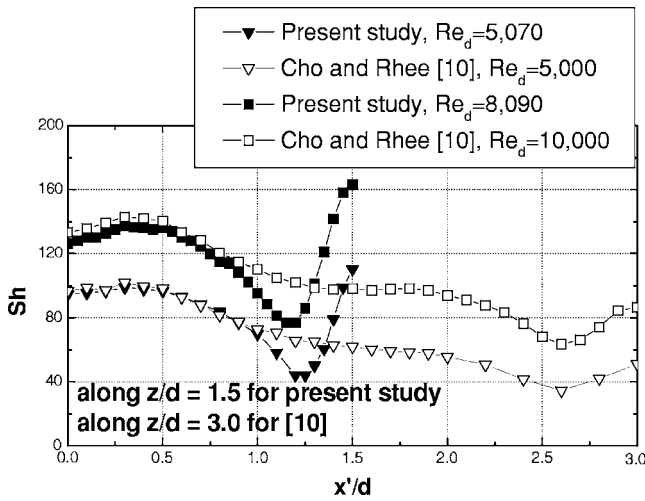


Fig. 8 Comparison of Sh with other results ($P/d=6.0$, [10]) for staggered hole arrangement with $H/d=2.0$ at different Reynolds numbers

minimum Sh values are formed at $z/d \cong \pm 0.4$ and the highest Sh values are formed along the midway region. The magnitude of the peaks in the midway region is almost constant along the midway line (maintained within 10% difference) because of the flow acceleration as mentioned above.

It is noted that these peak values are about 30% higher than those at the stagnation points. There are two possible reasons for these high values along the midway. One reason is the strong interaction of wall jets with small hole spacing. This induces strong secondary vortices and increases local turbulence intensity in the midway region. The other reason is related to the heat transfer characteristics of the jet impingement with small gap between the nozzle and the target plates. For the jet impingement with small gaps, the additional peak values formed at $r/d \cong 1.5$ are due to flow transition to turbulent flow of wall jets and/or the vortex near the target surface related to a main rolling vortex [16,17]. In the present study, the midway region ($1.5d$ apart from the stagnation points; along $z/d=0.0$ or $x/d=0.0$) is coincident with the position of additional peaks for the jet impingement with small gaps ($r/d \cong 1.5$). Therefore, these two flow characteristics (i.e., strong interaction of the wall jets and flow transition) interact each other and cause higher heat/mass transfer in the midway region.

When the local distributions of Sh along the stagnation lines are compared with those for larger hole spacing ($P/d=6.0$), the heat transfer for the small hole spacing is much higher in the midway region. Figure 8 shows the local Sh distributions for the case with different hole spacings at $H/d=2.0$. The distributions of Sh in the stagnation regions are consistent for both cases at each Reynolds number. As to be expected, the heat/mass transfer at the stagnation region is hardly affected by the injection hole spacing. As the wall jet spreads on the target surface (effusion plate), the difference in the local distributions arises. For the cases with large hole spacing, the flat distributions are formed around $x'/d=1.5$ due to flow transition [10] and then the peak values are observed in the midway. However, the level of the peak values in the midway is only 50–60% of that at the stagnation point for the cases of large hole spacing while the Sh values are even 30% higher than those at the stagnation points for the cases of small hole spacing. This is mainly due to the difference of the flow interaction of the wall jets between the cases of different hole spacings.

Figure 9 shows the local distributions of Sh along $x/d=1.5$ and 0.6 for the staggered hole arrangement with various gap distances at $Re_d=13,500$. Along $x/d=1.5$, as shown in Fig. 8, the overall distributions and levels are similar for all cases. However, a close

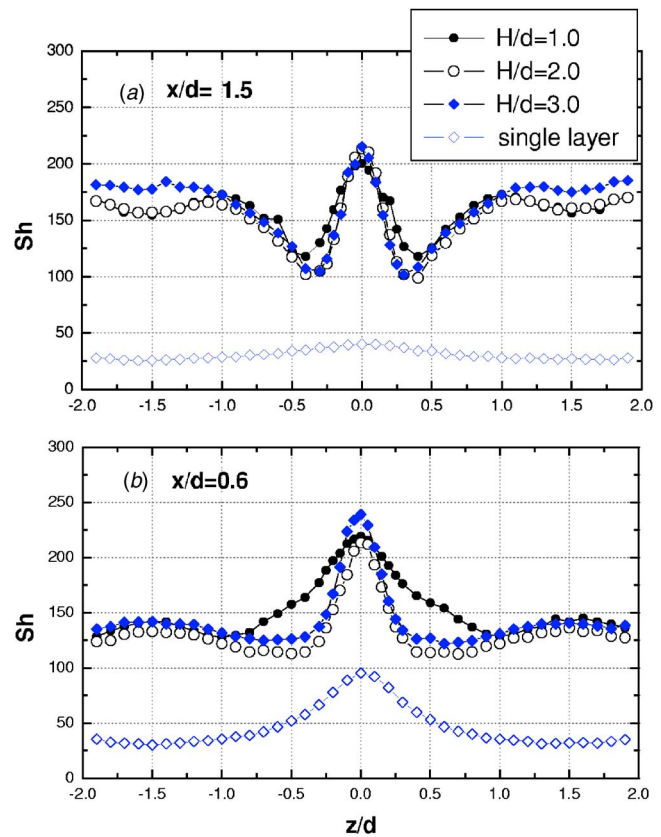


Fig. 9 Comparison of Sh on the effusion surface for different gap distances at $Re_d=13,500$

examination reveals that the Sh values for $H/d=1.0$ and 2.0 are the same with an indent at the center ($z/d = \pm 1.5$) of the stagnation regions while Sh for $H/d=3.0$ is slightly higher than those for other cases. This is because the turbulence intensity of impinging flow increases with larger gap distance. In the midway region, on the contrary, the cases of $H/d=2.0$ and 3.0 have almost the same Sh distributions while the level of Sh values for $H/d=1.0$ is slightly lower, and high heat/mass transfer region is somewhat wider than those for other cases. These patterns are also shown along $x/d=0.6$ (Fig. 9(b)). Especially, in the midway region, high heat/mass transfer region is expanded up to $z/d = \pm 0.8$ for $H/d=1.0$. However, the enhanced regions are confined to $-0.4 \leq z/d \leq 0.4$ for $H/d=2.0$ and 3.0.

Effects of Reynolds number. In Fig. 10, local Sh distributions along $x/d=1.5$ are presented for the staggered hole arrangement with various Reynolds numbers at $H/d=2.0$. Since the stagnation Nusselt number is proportional to $Re^{0.52}$ for simple nozzle geometry at the gap distance of $2d$ as reported by Lee and Lee [16], the results normalized by $Re^{0.52}$ are also presented. The left graph represents Sh distributions and the right one shows normalized Sh distributions. As clearly shown in the left graph of Fig. 13, the levels of Sh increase continuously with Reynolds numbers and the patterns are similar for all Re_d .

When the normalized values are compared, some interesting features with the Reynolds number are found in the midway region. The values around the stagnation point are fairly identical as suggested by Ref. [16]; however, some discrepancies between the normalized values around the midway region are observed, that is to say, the values at the lower Reynolds numbers ($Re_d \leq 5070$) are about 20% lower than the values at the higher Reynolds numbers ($Re_d \geq 8090$). In addition, the position of the lowest values is $x/d \cong 0.25$ for lower Reynolds numbers, while it is $x/d \cong 0.35$ for the higher Reynolds numbers. This means that the Reynolds num-

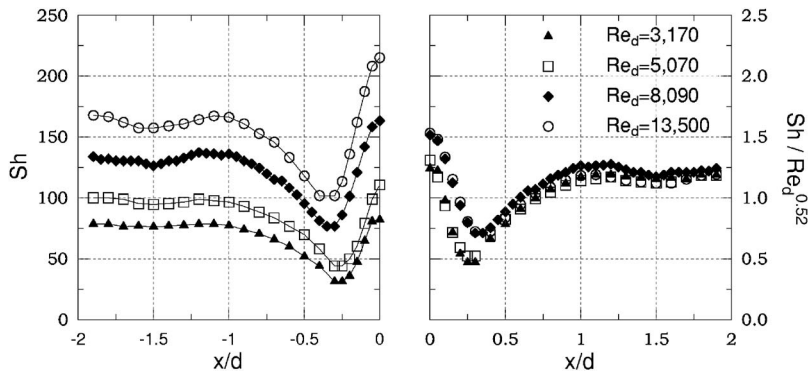


Fig. 10 Comparison of Sh along $x/d=1.5$ on the effusion surface for staggered hole arrangement at $H/d=2.0$.

ber affects the heat/mass transfer in the midway region in a different way from the stagnation region, and these are possibly due to the difference in the strength and the interaction of the wall jets.

4.2.2 Shifted Hole Arrangement. Figure 11 presents the contour plots of the Sherwood numbers for the shifted hole arrangement with various gap distances at $Re_d=13,500$. For the small gap distances of $H/d \leq 2.0$, the distributions of Sh on the effusion surface are very complex and asymmetric unlike the staggered arrangement. The major reason is as follows: The wall jets interact in the midway region, and vortices are generated by a similar mechanism as with the staggered hole arrangement. Since the lines of symmetry ($z/d = \pm 1.5$) separate rows of holes, one could expect that two merged vortices are split along these midlines of the rows. The vortex pair would divide and then move into the two adjacent effusion holes. However, the vortex pair chooses one effluent escape between adjacent effusion holes by means of a small perturbation, due to the difficulty of separating the merged vortices. Therefore, in the contour plots, the shifted enhanced region is caused by the merged vortices flow direction. Consequently, the next region from the neighboring rows shifts in the same direction due to pressure difference of neighboring wall jets. The shift does not influence shifts along the row, only from row to row. Note that the shift direction of vortices is arbitrary upward or downward and the information of the shift vortices is transferred only to the next row (in the vertical direction). At the next column of impinging the jet, the shift direction of secondary vortices will be arbitrary but not affected by neighboring columns. Therefore, there are two possible vortex patterns.

Cho and Rhee [10] reported that low transfer regions are formed in the region between the effusion holes for the shifted hole arrangement with large hole spacing due to the low flow momentum and the weak effects of the wall jets. This trend is also observed although the hole spacing in the present study is half of that. However, the low transfer regions are shifted in one direction due to these asymmetric flow patterns (for example, for $H/d=1.0$, low transfer regions are formed at $z/d \cong 1.0$ in the right side of the effusion hole ($x/d > 0$) but formed at $z/d \cong -1.0$ in the other side). For the higher gap distance of $H/d=3.0$, the distribution of Sh is fairly symmetric and the low heat/mass transfer coefficients upward and downward regions of effusion hole are observed clearly.

Local distributions of Sh at $H/d=2.0$ and $Re_d=13,500$ are presented in Fig. 12. As mentioned above, the distributions are somewhat asymmetric. For example, at $x/d=1.5$, the positions of additional peaks are about $0.2d$ shifted toward the $+z$ direction while Sh in the stagnation region shows symmetric distribution. Also, the valleys which represent low heat/mass transfer are shifted in one direction, i.e., these are found around $z/d \cong -1.0$ and 1.25 . Note that the highest Sh values are formed near the effusion holes at $x/d=0.0$ due to the combined effects of wall jet interaction and

flow acceleration as mentioned before.

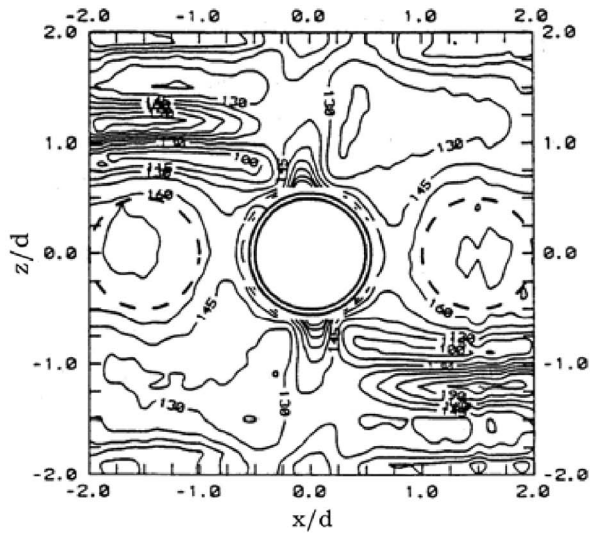
For the case with large hole spacing [10], the overall heat/mass transfer characteristics are similar to the case with small hole spacing although the pattern is symmetric. In addition, the secondary peaks in the midway regions are much lower, and the regions of low heat/mass transfer coefficients formed between the effusion holes in the z direction are larger than those for the cases with the small hole spacing. As mentioned, this is mainly due to the reduced effect of wall jet on those regions with the large hole spacing.

4.2.3 In-Line Hole Arrangement. Figure 13 shows the contour plot and local distribution of Sh for the in-line arrangement at $Re_d=13,500$. The injection holes projected on the effusion plate are coincident with the effusion hole with the aluminum rim between two circles.

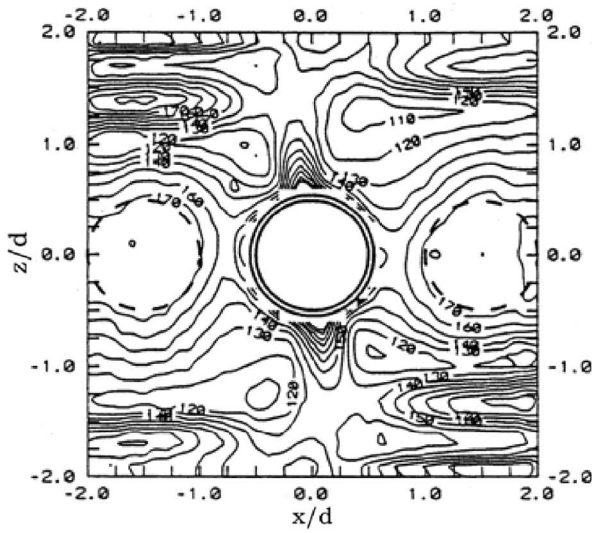
The level of Sh is much lower than that for the staggered or the shifted hole arrangements. Most of the impinging jet is discharged directly through the effusion holes due to its geometric feature. Therefore, the highest values are formed around the effusion hole because of the flow disturbance and then Sh decreases monotonously as R/d increases. Weak enhancement of heat/mass transfer is observed in the midway regions (along $x/d=1.5$ or $z/d = \pm 1.5$). However, the level of these peaks is less than 50% of that for other hole arrangements because the amount of wall jet flow is small.

In the left figure of Fig. 13, the local distributions of Sh at $z/d=0.0$ for the in-line hole arrangement with various gap distances at $Re=13,500$ are presented. As the gap distance increases, the jet flow become diffused more in the radial direction and then the amount of wall jet affecting heat/mass transfer on the effusion plate increases. Therefore, the Sh values increase with the gap distance, especially in the middle region ($R/d=1.5$).

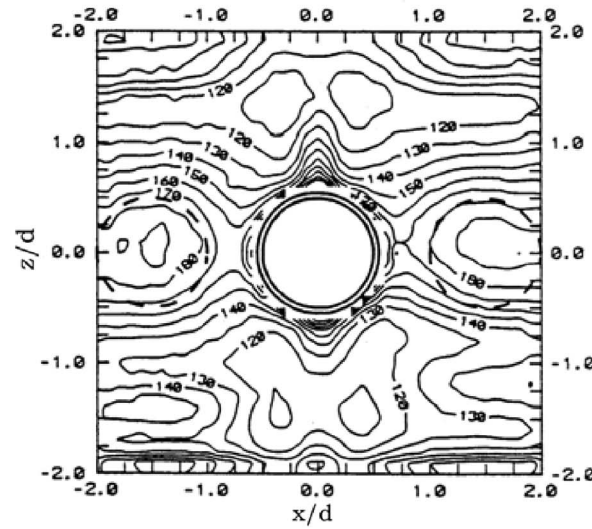
4.3 Comparison of Local Heat/Mass Transfer. Figure 14 presents the comparison of local Sh at $x/d=1.5$ and 0.6 for the three hole arrangements at $H/d=2.0$ and $Re_d=13,500$. At $x/d=1.5$, the levels of Sh for the staggered and the shifted cases are much higher than the other two cases, and the distributions match quite well if the data of one case (staggered or shifted case) are shifted by $1.5d$ in the z direction, e.g., the stagnation region of uniform Sh distributions, valleys, and additional peaks in the midway region. However, some differences are found. When Sh values at the stagnation points are compared, the value for the staggered arrangement is about 6% lower than that for the shifted arrangement possibly because of the increased effects of flow re-entrainment with a larger amount of the wall jets between the plates, although the difference is within experimental uncertainty. In addition, the peak values in the midway for the staggered arrangement are about 12% higher than those for the shifted while the shifted arrangement has higher Sh at the valleys (z/d



(a) $H/d=1.0$



(b) $H/d=2.0$



(c) $H/d=3.0$

Fig. 11 Contour plots of Sh on the effusion surface for shifted arrangement at $Re_d=13,500$: (a) $H/d=1.0$, (b) $H/d=2.0$, and (c) $H/d=3.0$

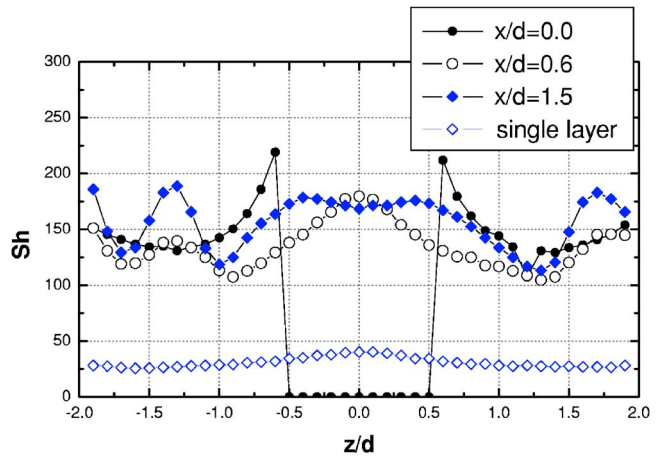
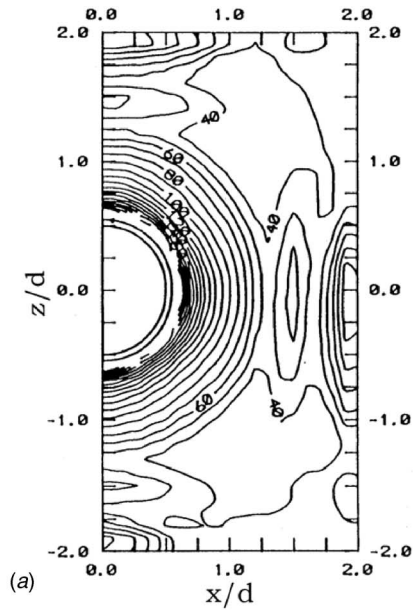


Fig. 12 Local Sh on the effusion surface for shifted arrangement at $H/d=2.0$ and $Re_d=13,500$

$\cong \pm 1.25$). The reason is that, for the shifted arrangement, a larger amount of the wall jets is discharged before spreading toward the radial direction and then the effects of wall jet on heat/mass trans-



(a)

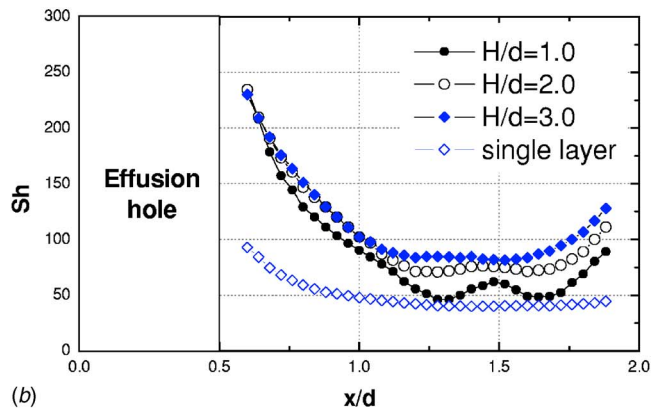


Fig. 13 Contour and local plots of Sh on the effusion surface for in-line arrangement at $Re_d=13,500$ ($H/d=1.0$ for contour plot)

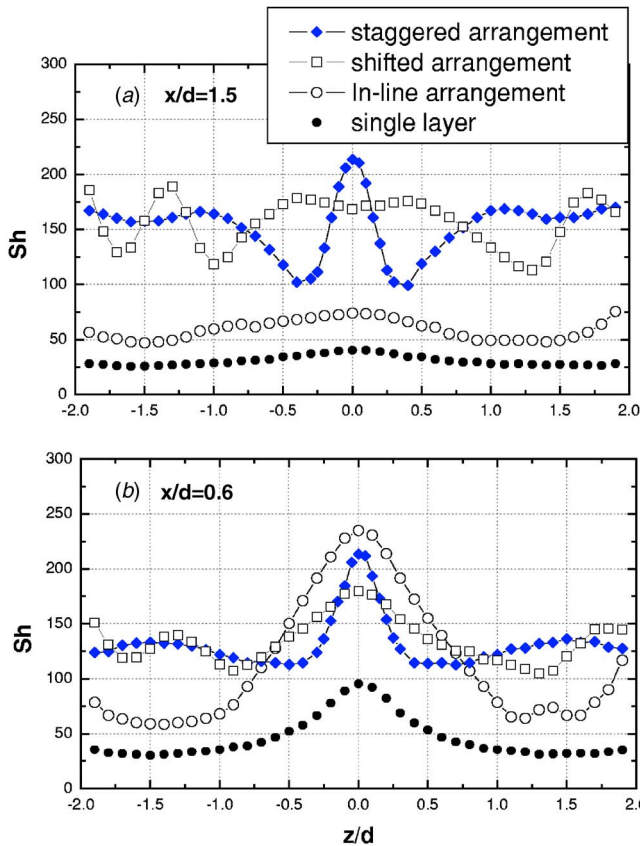


Fig. 14 Comparison of Sh on the effusion surface for various hole arrangements at $H/d=2.0$ and $Re_d=13,500$: (a) $x/d=1.5$ and (b) $x/d=0.6$

fer in the midway region are weakened as shown in numerical results.

At $x/d=0.6$ (Fig. 14(b)), the in-line arrangement has the highest Sh at $z/d=0.0$ because the impinging jet flow affects heat/mass transfer at this region directly. However, the staggered and the shifted arrangements have uniform distributions in the overall region.

4.4 Average Heat/Mass Transfer. Overall averaged Sh values for three hole arrangements at $H/d=2.0$ are presented in Fig. 15. The staggered and the shifted hole arrangements have about 70% higher average heat/mass transfer coefficients than the in-line hole arrangement. This is mainly due to direct impingement on the effusion surface and the secondary peaks in the midway region as shown in the local Sh distributions. Between two arrangements, the shifted arrangement has slightly lower values in the tested range of Reynolds number mainly due to the larger regions of low heat/mass transfer between the effusion holes although the difference of averaged value between two arrangements is within the experimental uncertainty (about 2–3%). On the contrary, for the case with large hole-to-hole spacing, the shifted array has 10% lower value than the staggered array as reported by Cho and Rhee [10]. The reason is that great enhancement of heat/mass transfer in the midway region compensates the reduction of heat/mass transfer between the effusion holes for the shifted array at the small hole spacing. Also, it means that the effects of hole arrangement on average heat/mass transfer become weaker as the hole spacing decreases.

For Re_d ranged between 3000 and 13,500, the overall averaged Sh value on the effusion plate for each hole arrangement is fitted as follows.

For the staggered hole arrangement,

$$\overline{Sh} = 0.253 Re_d^{0.67} \quad (3)$$

For the shifted hole arrangement,

$$\overline{Sh} = 0.213 Re_d^{0.68} \quad (4)$$

For the in-line hole arrangement,

$$\overline{Sh} = 0.254 Re_d^{0.61} \quad (5)$$

For the staggered and the shifted arrangements, the overall averaged values are proportional to $Re_d^{0.67}$ or $Re_d^{0.68}$ although heat/mass transfer coefficients at the stagnation region are proportional to $Re_d^{0.52}$.

4.5 Comparison With Numerical Simulation. Figures 16 and 17 show the contour plots and the comparison of the area-averaged Sh values of the calculated Nusselt number for each hole arrangement at $H/d=1.0$ and $Re_d=13,500$. In Fig. 17, the experimental data are converted to the Nusselt numbers using the heat and mass transfer analogy. On the whole, the calculated results are in quite good agreement qualitatively with the experimental results as shown in contour plots. However, some discrepancies re-

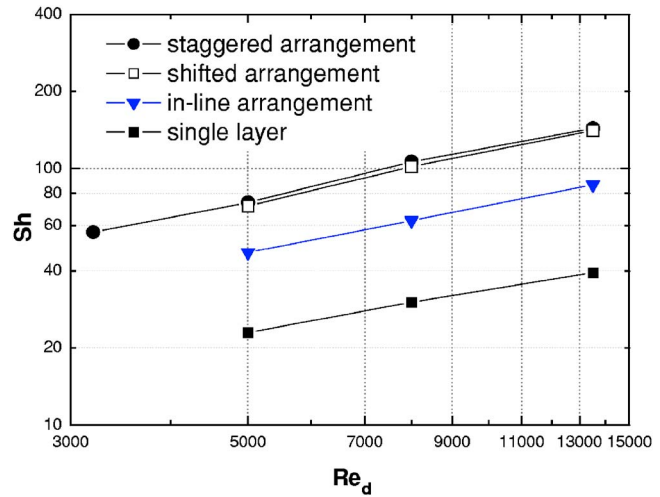


Fig. 15 Area-averaged Sh for impingement/effusion cooling with various hole arrangements at $H/d=2.0$

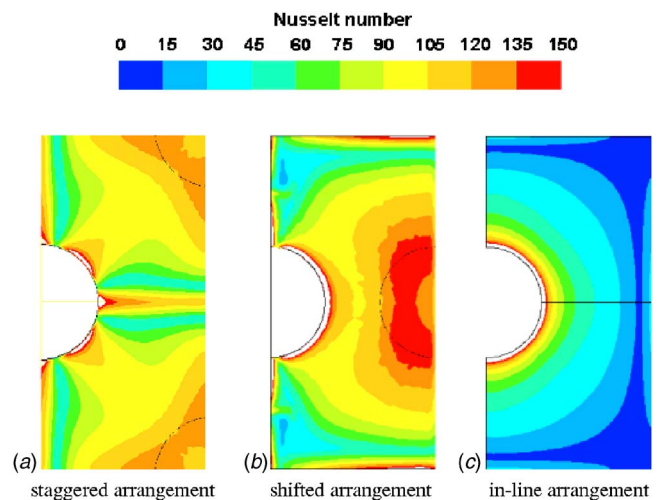


Fig. 16 Contour plots of calculated Nusselt number for various hole arrangements at $H/d=1.0$ and $Re_d=13,500$: (a) staggered arrangement, (b) shifted arrangement, and (c) in-line arrangement

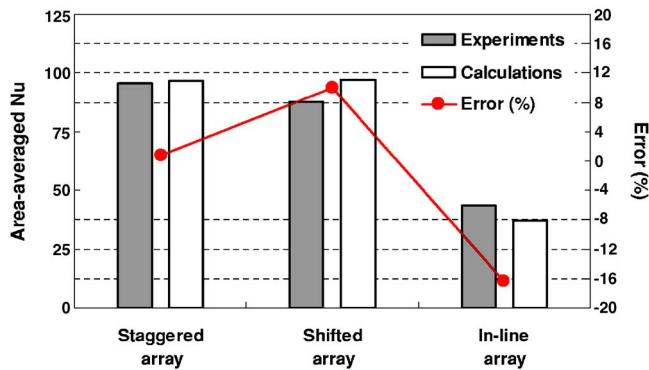


Fig. 17 Comparison of area-averaged Nusselt number with experimental data for various hole arrangements at $H/d=1.0$ and $Re_d=13,500$

lated to complex flow patterns arise. In area-averaged value, the difference between experimental and calculated results is less than 1% for staggered arrangement. For the shifted arrangement, the numerical simulation overpredicted Nusselt number (about 10% higher than experimental result) while it underpredicted (more than 15%) for in-line arrangement.

5 Summary

Flow patterns. For the staggered hole arrangement, a large-scale primary vortex is generated due to strong interaction of the wall jets in the midway region, and counter-rotating secondary vortices are also generated between the primary vortices. Therefore, local flow turbulence in the midway region is enhanced significantly and consequently the heat/mass transfer at this region increases greatly. For the shifted arrangement, the primary vortex flow pattern is also dominant, but the strength of these flows and secondary vortices is weaker.

Local Heat/Mass Transfer Characteristics. For the staggered arrangement, great enhancement of heat/mass transfer is achieved by jet impingement, flow acceleration into effusion hole, and interaction of wall jets in the midway regions. Especially, the peak values in the midway region are even higher than those at the stagnation points mainly due to the small hole spacing with increased effects of the wall jets. As a result, the overall transfer rate is enhanced greatly. For the shifted arrangement, low transfer regions are formed around the effusion holes and the additional peaks in the midway region are lower than those for the staggered arrangement due to its geometry. Also, the asymmetric distributions are formed due to instability of vortex movement with small gap distance while there are no asymmetric patterns with the larger gap distance or larger hole spacing. For the in-line arrangement, the level of Sh is much lower than those of other hole arrangements since most of the impinging flow is discharged directly. The calculated results are in quite good agreement qualitatively with the experimental results. However, some discrepancies of values are observed mainly due to the complex flow patterns related to jet impingement and sink flow.

Average heat/mass transfer. The overall averaged Sh for the staggered arrangement and the shifted arrangement are approximately 70–75% higher than that for the in-line arrangement and 3–3.5 times higher than that for the single layer flow (effusion only). Between the staggered and shifted arrangements, the staggered pattern would give better performance from a viewpoint of uniformity. For the small hole spacing, unlike the case with the large hole spacing, the staggered and the shifted hole arrangements have almost the same average values although the shifted

case has slightly lower values due to the formation of low transfer regions.

Acknowledgment

The authors wish to acknowledge support for this study by Korean Ministry of Science and Technology through National Research Laboratory program.

Nomenclature

- d = hole diameter; $d=25.4$ mm in the present study
- D_{naph} = mass diffusion coefficient of naphthalene vapor in air
- H = gap distance between two parallel perforated plates
- h_m = local mass transfer coefficient
- \dot{m} = local naphthalene mass transfer per unit area and time
- P = pitch of array holes
- R = radius, distance from hole center
- Re_d = Reynolds number based on the hole diameter and the average velocity in the hole
- Sc = Schmidt number for naphthalene in air, v/D_{naph}
- Sh = Sherwood number based on the hole diameter
- t = thickness of perforated plates ($t/D_h=1.5$)
- T_w = local wall temperature
- x, y, z = distance from the center of an effusion hole (Fig. 1)
- x' = distance from the stagnation point (Fig. 1), $(0.5P-X)/d$

Greek Symbols

- Δt = test duration
- Δy = naphthalene sublimation depth per unit area during the experiment
- ρ_s = density of solid naphthalene
- $\rho_{v,w}$ = naphthalene vapor density at the surface
- $\rho_{v,\infty}$ = naphthalene vapor density of the approaching flow
- θ = angle around hole (Fig. 1)

References

- [1] Martin, H., 1977, "Heat and Mass Transfer Between Impinging Gas Jets and Solid Surfaces," *Adv. Heat Transfer*, **13**, pp. 1–60.
- [2] Metzger, D. E., Florschuetz, L. W., Takeuchi, D. I., Behee, R. D., and Berry, R. A., 1979, "Heat Transfer Characteristics for In-line and Staggered Arrays of Circular Jets With Crossflow of Spent Air," *ASME J. Heat Transfer*, **101**, pp. 526–531.
- [3] Florschuetz, L. W., Metzger, D. E., Su, C. C., Isoda, Y., and Tseng, H. H., 1982, "Jet Array Impingement Flow Distributions and Heat Transfer Characteristics," NASA Report No. CR-3630.
- [4] Behnabani, A. I., and Goldstein, R. J., 1983, "Local Heat Transfer to Staggered Arrays of Impinging Circular Air Jets," *ASME J. Eng. Power*, **105**, pp. 354–360.
- [5] Hollwarth, B. R., and Dagan, L., 1980, "Arrays of Impinging Jets With Spent Fluid Removal Through Vent Holes on the Target Surface Part 1: Average Heat Transfer," *ASME J. Eng. Power*, **102**, pp. 994–999.
- [6] Hollwarth, B. R., Lehmann, G., and Rosiczkowski, J., 1981, "Arrays of Impinging Jets With Spent Fluid Removal Through Vent Holes on the Target Surface Part 2: Local Heat Transfer," *ASME J. Eng. Power*, **105**, pp. 393–402.
- [7] Andrews, G. E., Asere, A. A., Hussain, C. I., Mkpadi, M. C., and Nazari, A., 1988, "Impingement/Effusion Cooling: Overall Wall Heat Transfer," ASME Paper No. 88-GT-290.
- [8] Al Dabagh, A. M., Andrews, G. E., Abdul Hussain, R. A. A., Hussain, C. I., Nazari, A., and Wu, J., 1989, "Impingement/Effusion Cooling: The Influence of the Number of Impingement Holes and Pressure Loss on the Heat Transfer Coefficient," ASME Paper No. 89-GT-188.
- [9] Funazaki, K., Imamatsu, N., and Yamawaki, S., 1999, "Heat Transfer

Measurements of an Integrated Cooling Configuration Designed for Ultra-High Temperature Turbine Blades," *Proceedings of Seventh IGTC*, Vol. 2, pp. 833–840.

- [10] Cho, H. H., and Rhee, D. H., 2001, "Local Heat/Mass Transfer Measurement on the Effusion Plate in Impingement/Effusion Cooling System," *ASME J. Turbomach.*, **123**, pp. 601–608.
- [11] Rhee, D. H., Choi, J. H., and Cho, H. H., 2003, "Heat (Mass) Transfer on Effusion Plate in Impingement/Effusion Cooling Systems," *J. Thermophys. Heat Transfer*, **17**(1), pp. 95–102.
- [12] Cho, H. H., and Goldstein, R. J., 1997, "Total Coverage Discrete Hole Wall Cooling," *ASME J. Turbomach.*, **119**(2), pp. 320–329.
- [13] Goldstein, R. J., and Cho, H. H., 1995, "A Review of Mass Transfer Measurement Using Naphthalene Sublimation," *Exp. Therm. Fluid Sci.*, **10**, pp. 416–434.
- [14] Kline, S. J., and McClintock, F., 1953, "Describing Uncertainty in Single Sample Experiments," *Mech. Eng. (Am. Soc. Mech. Eng.)*, **75**, pp. 3–8.
- [15] *Fluent 6.1 User's Guide Volume 2*, Chaps. 8–19, 2003.
- [16] Lee, J. H., and Lee, S. J., 2000, "The Effect of Nozzle Configuration on Stagnation Region Heat Transfer Enhancement of Axisymmetric Jet Impingement," *Int. J. Heat Mass Transfer*, **43**, pp. 3497–3509.
- [17] Cho, H. H., Lee, C. H., and Kim, Y. S., 1997, "Characteristics of Heat Transfer in Impinging Jets by Control of Vortex Pairing," *ASME Paper No. 97-GT-276*.

Periodical Unsteady Flow Within a Rotor Blade Row of an Axial Compressor—Part I: Flow Field at Midspan

Ronald Mailach
Technische Universität Dresden,
Institut für Strömungsmechanik,
01062 Dresden, Germany
e-mail: ronald.mailach@tu-dresden.de

Ingolf Lehmann
Kompressorenbau Bannewitz GmbH,
Windbergstrasse 45,
01728 Bannewitz, Germany
e-mail: ingolf.lehmann@kbb-turbo.de

Konrad Vogeler
Technische Universität Dresden,
Institut für Strömungsmechanik,
01062 Dresden, Germany
e-mail: konrad.vogeler@tu-dresden.de

In this two-part paper, results of the periodical unsteady flow field within the third rotor blade row of the four-stage Dresden low-speed research compressor are presented. The main part of the experimental investigations was performed using laser Doppler anemometry. Results of the flow field at several spanwise positions between midspan and rotor blade tip will be discussed. In addition, time-resolving pressure sensors at midspan of the rotor blades provide information about the unsteady profile pressure distribution. In Part I of the paper, the flow field at midspan of the rotor blade row will be discussed. Different aspects of the blade row interaction process are considered for the design point and an operating point near the stability limit. The periodical unsteady blade-to-blade velocity field is dominated by the incoming stator wakes, while the potential effect of the stator blades is of minor influence. The inherent vortex structures and the negative jet effect, which is coupled to the wake appearance, are clearly resolved. Furthermore the time-resolved profile pressure distribution of the rotor blades is discussed. Although the negative jet effect within the rotor blade passage is very pronounced, the rotor blade pressure distribution is nearly independent of the convectively propagating chopped stator wakes. [DOI: 10.1115/1.2812329]

Keywords: axial compressor, laser Doppler anemometer, periodical unsteady flow field, unsteady profile pressure, rotor-stator interaction, tip clearance vortex, wake, negative jet effect, wake-tip clearance vortex interaction

1 Introduction

A primary goal of the current compressor design is to increase the pressure ratio and the efficiency while reducing the number of blades and stages. This can be achieved by the use of fewer but more highly loaded compressor blades. One of the challenges of the present and future compressor designs is to include beneficial unsteady effects to improve the engine parameters. This requires a detailed physical understanding of the unsteady flow field and the resulting effects on the performance and flow stability.

The rotor and stator blades, moving relative to each other, aerodynamically interact because of the viscous wakes and the potential effects of the blades. In addition, the wakes and potential effects of the blades superimpose with other flow patterns, for instance, the tip clearance vortices and other secondary flow phenomena. Furthermore, in transonic compressors, the interaction of shocks and wakes plays an important role. As a result, the flow field in compressors is highly periodically unsteady and very complex.

The topic blade row interaction has been addressed in a variety of publications within the past decades. Early analytical studies into the propagation of wakes through blade rows were performed by Kemp and Sears [1], Meyer [2], and Lefcort [3]. Further detailed investigations on the wake chopping and the intrablade passage transport of the chopped wake segments in turbomachines were done by Kerrebrock and Mikolajczak [4] and Hodson [5].

A simplified schematic of the fundamental wake characteristics during the propagation of the wakes through a subsequent blade

row is shown in Fig. 1. If a wake impinges the leading edge of the downstream blades, it is chopped into two segments (Fig. 1(a)). During the downstream transport of the wake segments through the blade passages, they reorient, deform, and decay. The fundamental mechanisms determining the wake structure and decay are the viscous mixing, the inviscid wake stretching, and the negative jet effect. These effects superimpose to each other in the real flow field.

The viscous wake mixing tends to a broadening of the wake segments. Simultaneously, the velocity deficit of the wake decreases due to the mixing of the wake with the surrounding free stream. The inviscid straining of the wake segment (“wake stretching”) during its transport through the blade channels appears due to the widening of the compressor blade channels in the downstream direction. So the wake stretching in compressor blade rows leads to a faster wake decay in the presence of a downstream blade row and therefore reduces the viscous mixing losses. This effect was first described by Smith, Jr. [6] and is commonly denoted as “wake recovery.” The investigations of Smith, Jr. [7], Deregél and Tan [8], and Van Zante et al. [9] pointed out the beneficial effect of the wake recovery on axial compressor performance.

Another flow effect, commonly denoted as “negative jet effect,” comes into being due to the lower momentum of the wake fluid. This is illustrated in Fig. 1(a) for stator wakes entering the subsequent rotor blade passages. Within the stator wakes, the absolute velocity c , as well as its axial component c_{ax} , is reduced compared to the free stream velocity. This leads to a reduced relative velocity w within the wakes and an increased blade incidence if the stator wakes impinge the rotor blade leading edges.

Due to the different lengths and orientations of the relative velocity vectors of the wake and the free stream, a slip velocity appears, which is responsible for the “negative jet” (Fig. 1(a)).

Contributed by the International Gas Turbine Institute of ASME for publication in the JOURNAL OF TURBOMACHINERY. Manuscript received June 5, 2007; final manuscript received September 10, 2007; published online July 31, 2008. Review conducted by David Wisler. Paper presented at the ASME Turbo Expo 2007: Land, Sea and Air (GT2007), Montreal, Quebec, Canada, May 14–17, 2007.

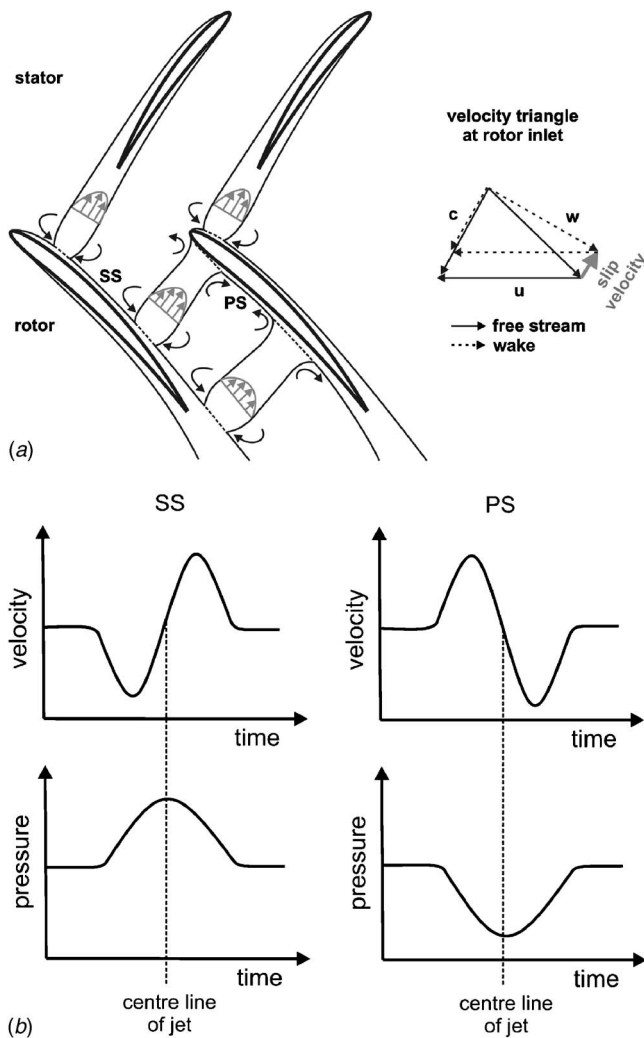


Fig. 1 (a) Negative jet effect within a compressor blade row; (b) effect of negative jet on velocity and pressure at a fixed position near the blade surface

This slip velocity stimulates the low-momentum wake fluid to move along the wake segment path from the suction side (SS) through the blade passage toward the pressure side (PS) of the adjacent rotor blade. Near the SS, high-momentum fluid enters the chopped wake segment to replace the fluid that has moved across the passage.

As discussed by Meyer [2], the negative jet effect has an influence on the unsteady profile velocity and pressure distributions. Near the PS surface, at the upstream boundary of a wake segment, a reduction of velocity appears, while the velocity increases just downstream the wake segment (Fig. 1(a) and 1(b)). Near the SS surface, the opposite behavior is found. Therefore, at the position of the wake segment, a local pressure decrease at the PS and an increase at the SS appear. The time-resolved velocity and pressure development at a position on the PS and the SS during the passing of a wake segment is schematically shown in Fig. 1(b). Depending on the wake properties, the unsteady profile pressure distribution can strongly be affected by the negative jet effect (Sanders and Fleeter [10]). This topic will also be addressed in the present paper. More investigations discussing the negative jet effect are from Sanders et al. [11], Lehmann [12], and Valkov and Tan [13], for instance.

The main part of the present paper deals with the results of the investigation of the periodical unsteady flow field within a rotor blade row using laser Doppler anemometry. Experiments concern-

ing the convection of wakes through blade rows and within the axial gaps using laser measurement techniques can already be found from Hathaway et al. [14], Stauter et al. [15], and Lehmann et al. [16], for instance. Recently, Michon et al. [17] investigated the phase-averaged flow field within the blade rows of a single-stage axial compressor using a three-component laser Doppler anemometer (LDA). These authors provide a detailed database of the 3D flow field of the entire compressor stage for off-design conditions.

Within recent years, the particle-image velocimetry (PIV) has been demonstrated to be a useful tool for flow field investigations in turbomachinery. Tisserant and Breugelmann [18] investigated the rotor blade-to-blade flow field at 85% blade height using a 2D-PIV system in a single-stage compressor. The PIV measurements in this compressor are continued for several other measurement planes by Balzani et al. [19]. Sanders et al. [11] investigated the flow field of a $1\frac{1}{2}$ -stage transonic axial compressor using PIV. Results of the time-resolved flow field at midspan for both subsonic and transonic flow conditions are discussed by these authors. Wernet et al. [20] performed flow field measurements in the rotor tip region of the first stage rotor of a four-stage low-speed compressor. Using a 3D-PIV system, they provided results of the rotor-phase-locked flow field.

The aim of this two-part paper is to complete the picture of the different features of blade row interaction in the Dresden low-speed research compressor (LSRC). Recently, several aspects of blade row interaction were already discussed for this compressor. This comprises the investigation of the periodical unsteady boundary layer on the blades, the unsteady profile pressure distributions, as well as the excited aerodynamic blade forces in several blade rows (Mailach et al. [21–24]). With the present two-part paper, the periodical unsteady flow field inside an embedded rotor blade row will be discussed in detail. The unsteady flow field measurements were carried out at several spanwise positions between midspan and near the blade tip of Rotor 3 using a 2D-LDA system. In Part I, the details of the periodical unsteady flow field at midspan are discussed. A comparison to the unsteady profile pressure distribution is drawn. In Part II [25], the flow field near the blade tip is discussed with special emphasis on the unsteady stator wake–rotor tip clearance vortex interaction.

2 Experimental Setup

The experiments discussed in this paper were performed in the Dresden LSRC, which was put into operation in 1995. The compressor consists of four identical stages, which are preceded by an inlet guide vane row, Fig. 2.

Several bladings were tested within the past years. The results discussed in this paper are for the reference blading of this compressor with cantilevered stator blades. This blading was developed on the basis of the profiles of a middle stage of a high-pressure compressor of a jet engine. More detailed descriptions of the compressor and selected results of standard measurements for this reference blading are given by Sauer et al. [26], Müller et al. [27], and Boos et al. [28]. Table 1 gives a summary of the main design parameters.

The flow field measurements discussed in this paper were performed within the third rotor blade row. The rotor tip clearance ratio amounts to 1.3% of the rotor tip chord length. Results will be presented for two operating points: the design point ($\xi=1.00$) and an operating point near stability limit with 85% of reduced mass flow ($\xi=0.85$) at design speed ($\zeta=1.0$). For design speed, the stability limit is reached at about $\xi=0.81$.

2.1 Flow Field Investigations With Laser Doppler Anemometer. The flow field measurements inside the blade passages of Rotor 3 of the Dresden LSRC were carried out using a fiber-optic 2D-LDA system. The maximum power of this argon-ion laser is 10 W. The measurement volume size is $0.06 \times 0.06 \times 0.63 \text{ mm}^3$. As tracer fluid, a 50% mixture of water and glycer-

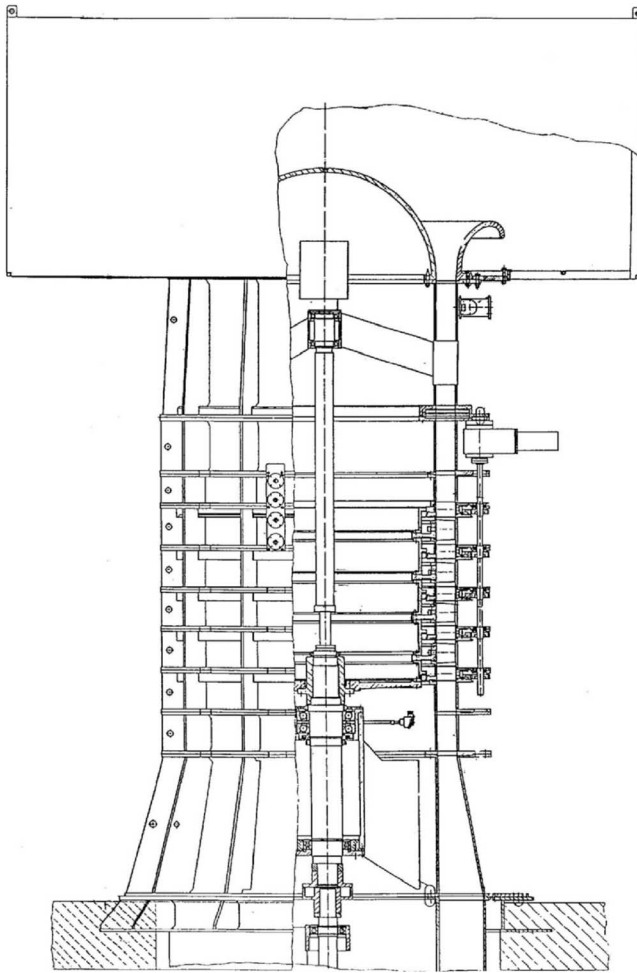


Fig. 2 Sectional drawing of the Dresden LSRC

ine was used. It was atomized using a commercial particle generator. The mean geometric particle diameter is $0.36 \mu\text{m}$. The tracer fluid is locally introduced via probes located in the upstream stage. Preliminary tests proved that the interferences caused by the probes can be neglected.

Table 1 Design parameters of Dresden LSRC (MS, midspan; DP, design point)

| | | | |
|--|-------|-------|-------------------|
| IGV+four identical stages | | | |
| Reynolds number, rotor inlet, MS, DP (related to rotor chord length) | | | 5.7×10^5 |
| Mach number, rotor inlet, MS, DP | | | 0.22 |
| Design speed | | | 1000 rpm |
| Mass flow, DP | | | 25.35 kg/s |
| Mean flow coefficient, DP | | | 0.553 |
| Enthalpy coefficient Ψ_{is} , DP | | | 0.794 |
| Hub diameter | | | 1260 mm |
| Hub to tip ratio | | | 0.84 |
| Axial gaps between all blade rows, MS | | | 32 mm |
| | IGV | Rotor | Stator |
| Blade number | 51 | 63 | 83 |
| Chord length, MS (mm) | 80 | 110 | 89 |
| Stagger angle, MS (versus circumference) (deg) | 82.8 | 49.3 | 64.0 |
| Solidity, MS | 0.941 | 1.597 | 1.709 |

A straight quartz glass window of 20 mm width was inserted into the casing to provide an optimum optical access. The deviations from the casing contour line remain within the tolerance of the tip clearance width.

Using the LDA system, the axial and the circumferential components of the absolute flow velocity c_{ax} and c_u were measured simultaneously. With the known rotor speed, the circumferential component of the relative velocity w_u , the relative velocity w , and the relative flow angle β are calculated.

The position of the rotor blades relative to the measurement volume of the LDA was determined using a once-per-revolution signal. The investigations were performed for 14 radial positions between midspan (MS) and near the rotor blade tip. The radial positions r^* are 50.0%, 58.3%, 66.7%, 75.0%, 79.2%, 81.3%, 83.3%, 85.4%, 87.5%, 89.6%, 91.7%, 93.8%, 95.6%, and 97.9% of the channel height.

The measurement volume was shifted in 18 steps into the axial direction from the leading edge toward the trailing edge of the rotor blades for a given radial position. At each axial position, altogether 40,000 measurement values were acquired. In the post-processing, the spatial resolution in the circumferential direction was defined with 25 steps per rotor blade pitch. A minimum of 250 measurement values for each step was accepted for calculating the mean value; otherwise, the mean value is neglected in the final results. The uncertainty of these velocity measurements is below 1% (Lehmann [12]). In Fig. 3, the resulting spatial resolution of the LDA measurements is shown for midspan.

To realize the unsteady effects of the stator blades on the flow field within the considered rotor blade row, in different measurement campaigns, the stator blade rows of all stages were synchronously traversed into the circumferential direction (Fig. 4). This shift was done with 20 steps over one stator blade pitch for each fixed position of the LDA measurement volume. This way, the wake and potential effects of the stator blades are moved over the measurement position. (Note that the stator blade numbers in all stages are equal.)

Using a special sorting algorithm, quasi-time-dependent results of the flow structure inside the rotor blade passages are generated. Assuming a periodical flow field in the circumferential direction, the data are resorted taking the relative position of the rotor and stator blades concerning the LDA measurement volume as well as the different pitches of the rotor and stator blade rows into account. In this way, snapshots of the flow field in adjacent passages of the rotor blade row for fixed rotor-stator positions are obtained. When considering the consecutive rotor-stator positions in an animation, the time-resolved development of the flow field within the rotor blade row becomes obvious. These movies are included in the work of Lehmann [12]. A more detailed description of the measurement setup, the measurement uncertainties, and the data sorting algorithm is also given there.

At each measurement position, further parameters are calculated from the measured axial and circumferential absolute velocity components. With the known rotor speed, the other velocity components and the flow angles in the absolute and relative frames are obtained. To resolve furthermore the vortical structures of the periodical unsteady flow field, two additional parameters are calculated from the measurement data. The vorticity Γ_x within the relative frame of reference can be determined with the following equation:

$$\Gamma_x = \left(\frac{\partial w_{ax}}{\partial y} - \frac{\partial w_u}{\partial z} \right) \frac{l_c}{\bar{w}_1} \quad (1)$$

while y and z are the coordinates in the circumferential and axial directions, respectively. The chord length l_c and the mean relative velocity of the incoming flow \bar{w}_1 are used to make this parameter dimensionless. A positive sign of the vorticity indicates a clockwise turning of the vortices, a negative sign indicates the opposite turning direction. Certainly, discrete vortices that appear stochastically or with frequencies that are not related to the passing stator

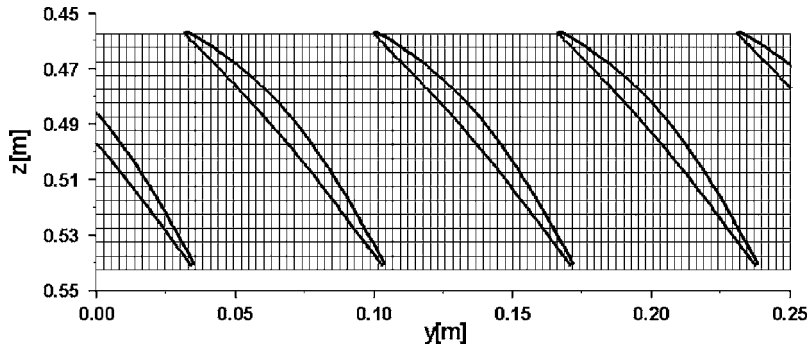


Fig. 3 LDA measurement grid at midspan ($r^* = 50\%$)

blades are not resolvable due to the pointwise measuring LDA and the data averaging.

Another method to analyze the secondary flow field within the rotor passages is to calculate the perturbation velocity. In the wake region, this perturbation velocity is qualitatively comparable to the slip velocity, which is coupled to the negative jet effect (see Fig. 1(a)). The slip velocity itself cannot be determined for the real flow field within a blade row. This is due to the fact that the free stream velocity is not exactly known, since the flow field is affected anyway by the periodically appearing influence of the passing blades at each point of time, even outside the region of the direct wake and potential effect of the blades. As a compromise, a perturbation velocity w_p will be used, which is defined as the vector between the time-averaged velocity and the ensemble-averaged velocity at a given point of the flow field (Fig. 5),

$$\vec{w}_p = \vec{w} - \vec{\bar{w}} \quad (2)$$

The ensemble-averaged velocity vector in the relative frame of reference is mainly influenced by the periodically passing wakes and the potential effects of the stator blades. In the time-averaged

results, these effects are averaged out. Hence, the perturbation velocity is a qualitative measure for the secondary flow field in the considered measurement plane (here, in the relative frame of reference).

2.2 Measurement of Unsteady Profile Pressures. As already discussed in the Introduction, the convectively propagating chopped stator wake segments can have an influence on the unsteady profile pressures of the considered rotor blades. This will be verified with the measured unsteady profile pressure distribution. A single rotor blade of the third stage was equipped with time-resolving piezoresistive miniature pressure transducers (Kulite LQ47) to acquire the unsteady profile pressure distribution at midspan. The sensors are equally distributed along the midspan as well on the PS and the SS of this blade (Fig. 6). They are positioned from 10% to 90% chord with steps of 10% chord. To minimize the influence on the flow, the sensors and the wires were fitted into the blade surfaces. The positions near the leading edge and the trailing edge could not be equipped with pressure transducers without disturbing the flow noticeably. In this paper, only the fluctuating part of the profile pressures will be discussed. A more detailed description of this pressure measurement setup and further results for different blade rows are given by Mailach et al. [23].

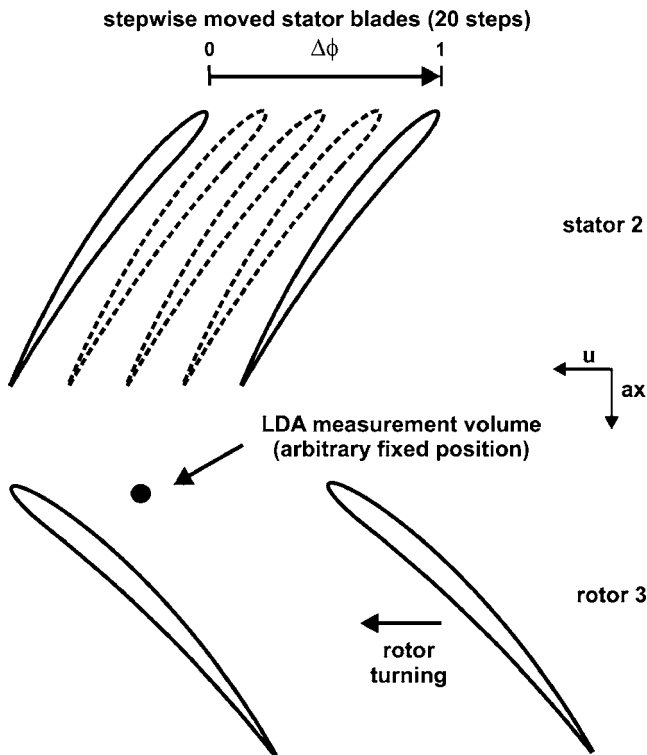


Fig. 4 Stepwise moved stator blade rows during LDA measurements (reference rotor-stator position: $\Delta\phi=0$)

3 Flow Field Within the Rotor Blade Row at Midspan

3.1 Periodical Unsteady Flow Field: Reference Rotor-Stator Position ($\Delta\phi=0$), Design Point ($\xi=1.00, \zeta=1.0$). In the following section, the results of the flow field measurements at midspan for the design point will be discussed. Selected results of the periodical unsteady flow field are shown in Fig. 7. (For the time-averaged results, please refer to Lehmann [12] and Mailach and Vogeler [24].) The selected parameters are the relative flow velocity, the relative flow angle, the axial velocity component, and

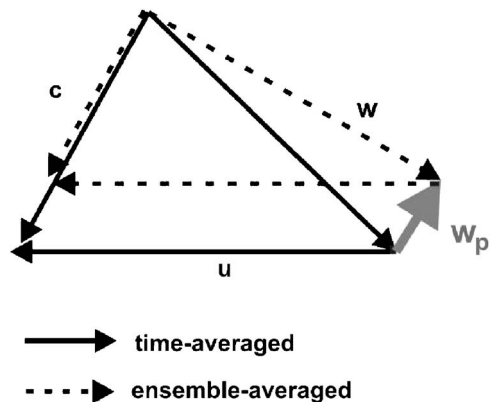


Fig. 5 Definition of perturbation velocity w_p

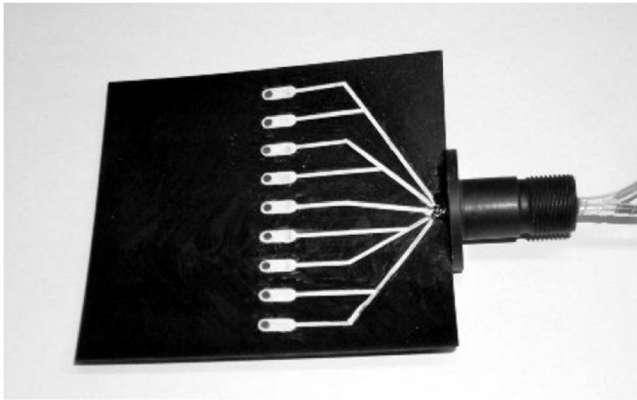


Fig. 6 Rotor blade equipped with piezoresistive pressure transducers on PS and SS (view on PS)

its rms value (Figs. 7(a)–7(d)). Furthermore, the vorticity and the perturbation velocity distributions are shown in Figs. 7(e) and 7(f).

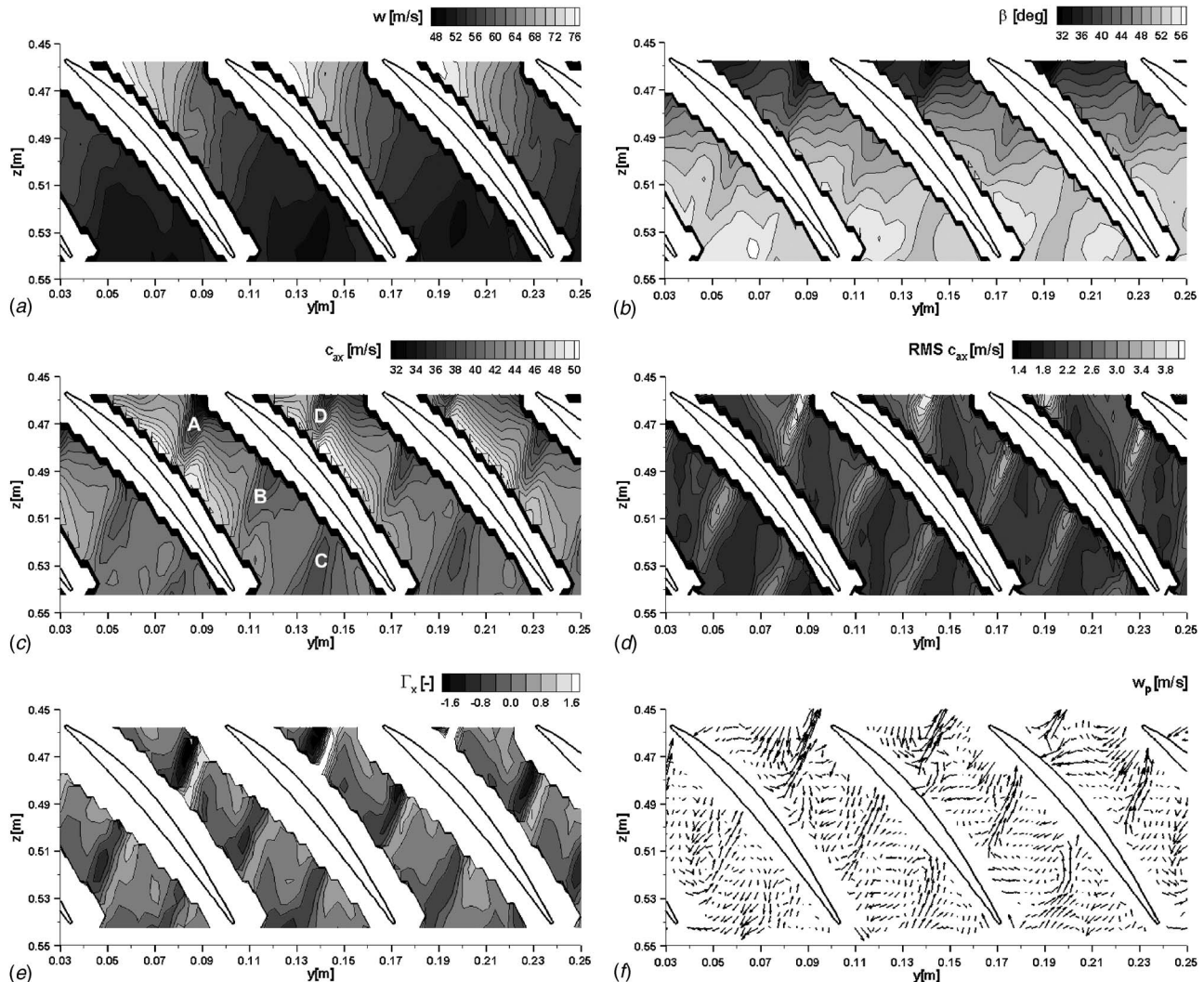


Fig. 7 Periodical unsteady flow field inside the blade passages of Rotor 3, reference rotor-stator position ($\Delta\phi=0$), midspan, design point ($\xi=1.0$, $\zeta=1.0$)

Results for the flow field are available for 20 different relative positions of the stator blades concerning the considered rotor blade row. A single rotor blade and a stator blade were selected as reference blades. At the arbitrarily defined reference position, the trailing edge of this stator blade and the leading edge of this rotor blade are at the same circumferential position (compare to Fig. 4). The results in Figs. 7 and 8 refer to this reference rotor-stator position $\Delta\phi=0$. These pictures can be understood as a view on the periodical unsteady flow field at an arbitrary fixed point of time. An exemplary result for a further rotor-stator position, showing the wake propagation and development during the rotor turning, will be discussed later in this section.

The stator-rotor blade count ratio is 83:63, this is about 4:3. Therefore, within every third rotor passage, a nearly identical periodical unsteady flow field is found. Because of the intersection of the two laser beams, shadow regions appear near the blade surfaces, where no measurement could be performed. This effect becomes more dominant for positions toward the hub.

Compared to the time-averaged flow field (not shown), clear changes due to the stator influence can be observed for all flow parameters shown in Fig. 7. The dominant influence on the flow field within the blade passages are the wakes stemming from the upstream stator blades. The potential effect of Stator 3 is of minor influence. (This is consistent with the results of the hot-wire mea-

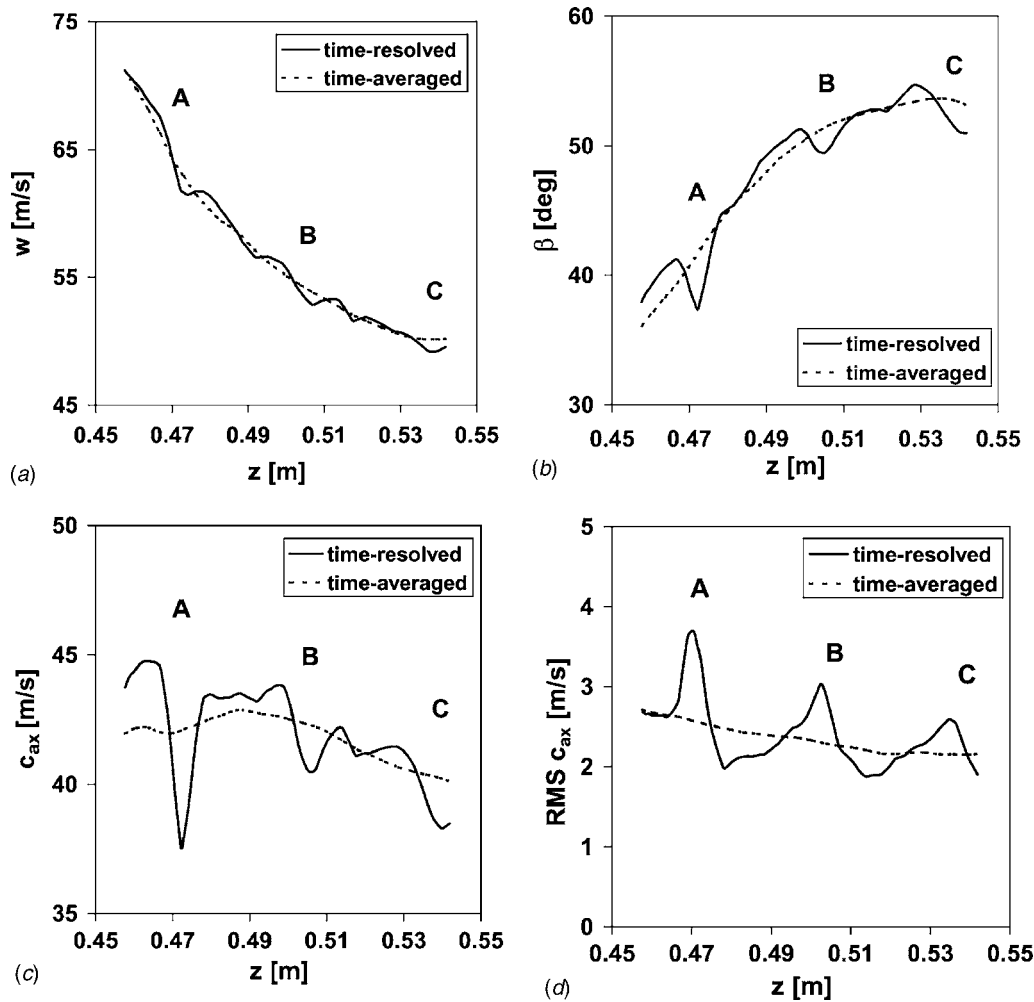


Fig. 8 Flow field inside a blade passage of Rotor 3, parameters along midpassage, comparison of time-resolved result ($\Delta\phi=0$) and time-averaged values, midspan, design point (extracted from Fig. 7)

measurements up- and downstream a rotor blade row from Mailach and Vogeler [24].) Clear signs of the potential effect of the downstream blade rows on the unsteady flow field are not detectable. This is due to the fact that the blade numbers of the up- and downstream stator blade rows are identical. Therefore, the phase shift of the superimposed stator wakes and potential effects remains constant around the circumference.

As expected, the highest value of the relative flow velocity appears near the blade leading edge and the SS (Fig. 7(a)). A nearly continuous decrease of the relative velocity can be observed toward the PS of the adjacent blade at constant axial positions. Following the flow path through the blade passage, a clear reduction of the relative velocity is reflected by the measurement results.

The periodical influence of the stator blades on the relative flow velocity distribution is recognizable (Fig. 7(a)). Due to the different rotor and stator blade numbers, differences of the flow field in the adjacent rotor blade channels can be found. However, the wake segment positions themselves are not obvious at first view using this form of representation. They can be identified by local reductions of the relative flow velocity compared to the mean value (compare to Fig. 8(a)).

Using other flow parameters, the positions of the wake segments become evident. In Fig. 7(b), the relative flow angle distribution is shown. The mean relative flow angle (defined versus circumference) at the rotor blade inlet is about 35 deg. The flow turning of the rotor blades amounts to about 18 deg. The wakes

can be identified by a local reduction of the flow angle. Also, the reduction of the axial velocity component and the increase of the rms values clearly indicate the positions of the wake segments (Figs. 7(c) and 7(d)).

The wakes from Stator 2 are chopped at the rotor blade leading edge and divided into two segments. The chopped wake segments propagate independently of each other within the adjacent rotor blade channels with the free stream velocity. Depending on the blade geometry and the solidity, several chopped stator wakes can be found within a single rotor blade passage. For the stator-rotor blade count of the Dresden LSRC, three to four stator wake segments (or parts of it) appear within a single rotor blade passage, depending on the point of time. As an example, the wake segments in a selected rotor blade passage, stemming from the wakes of three subsequent passing stator blades, are denoted as A, B, and C in Fig. 7(c).

The wake segments extend across the whole rotor passage from the PS toward the SS. Although the flow field close to the blade surface cannot be resolved, a local effect of the wake segments on the velocity and pressure distribution on the blade profile can be expected from these measurement results.

At the given point of time, Wake A is just chopped at the rotor blade leading edge into two segments. The corresponding segment does not yet appear in the adjacent rotor blade passage, since it is still upstream of the measurement region. The corresponding wake segments of the previous passing stator blade are denoted as B and D (Fig. 7(c)).

A reorientation of the wake segment appears since it follows the flow path inside the rotor passage. However, due to the relatively low flow turning of the compressor blades, this effect is not as dominant as in turbine blade rows. The propagation velocity of the wake segments is determined by the velocity distribution within the blade passages. For this reason, in the front part of the blades, the wake segments propagate faster near the SS than near the PS surface. This is visible for the positions of Wake segments B and D in Fig. 7(c).

The different aspects of the wake segment development in the passages—the inviscid wake stretching coupled with the wake recovery effect and the viscous wake mixing—were discussed in Sec. 1. These effects cannot be separated in the real flow field, shown in Fig. 7.

Figure 8 shows the development of selected flow field parameters along the midpassage as a part of the data of Fig. 7 (cut through Wake segments A, B, and C). One can see a clear reduction of the relative flow velocity w along this flow path (Fig. 8(a)). The positions of the three wake segments can be identified by a local decrease of the velocity. As previously discussed, they become more obvious by a local decrease of the axial velocity component (Fig. 8(c)). In the downstream direction, the wake decay can be recognized by the decrease of the wake velocity deficit, while the width of the consecutive wake segments increases.

Also, the development of the relative flow angle β confirms this trend (Fig. 8(b)). Near the leading edge, the amount of the relative flow angle within the wake is about 4 deg below the mean relative flow angle (Wake segment A). Please note that the difference of the mean relative flow angles between the design point and near stability limit are in the same order of magnitude. This reveals the remarkable change of the rotor blade loading if the stator wake impinges. For the downstream Wake segment B, the difference between the time-resolved flow angle and the mean flow angle is reduced to about 2 deg. A local overturning of the flow (larger β) appears just upstream the wake segments, while an underturning is observed downstream of it. This is due to the induced velocities at the wake segment boundaries because of the negative jet effect.

The rms value of the axial velocity component also clearly indicates the wake segment positions and their reducing turbulence when moving through the rotor passage (Fig. 8(d)). The maximum fluctuations appear upstream of the wake center, which means in the wake portion stemming from the SS boundary layer of the passing stator blade.

The results of the vorticity distribution clearly show the positions of the vortex street, which is attributed to the wake (Fig. 7(e)). The discrete vortices of the von Kármán vortex street are not resolvable with the pointwise measuring LDA. However, the existence of the counter-rotating vortices within the wake segments can be verified by calculating the vorticity (Eq. (1)). A positive sign of the vorticity indicates a clockwise turning of the vortices, a negative sign indicates the opposite turning direction. The results clearly reflect the existence of the counter-rotating vortices in the PS and SS branches of the wake as well as within the chopped wake segments. Due to the wake mixing, the vorticity is reduced when the wake segments are transported through the rotor blade passage. Also, with these data the weakening and broadening of the wake segments during their downstream propagation can be observed.

The calculated perturbation velocity distribution (Eq. (2), Fig. 5) will be used to analyze the secondary flows within the rotor passage, Fig. 7(f). This parameter is a qualitative measure to the “slip velocity,” which appears due to the low-momentum fluid within the wake segments. The latter term is typically used to describe the velocity deficit of the wake and its effects (compare to Fig. 1). Figure 7(f) points out that the wake segments are not orthogonal but inclined to the rotor blade surfaces. Their fundamental orientation is determined by the wake orientation in the absolute frame of reference. This figure shows a very clear picture of the negative jet effect within the chopped wake segments.

Within these regions, the perturbation velocity vectors are directed from SS toward the PS of the adjacent blade exactly along the wake segment direction. The maximum amount of the perturbation velocity can be found there. The broadening of the wake segments, coupled with a reduction of the slip velocity during its downstream transport, is obvious.

Due to the negative jet, the free stream flow is sucked into the wake segment near the SS surface of the blade. Therefore, near the SS, an increase of the velocity just upstream of the wake segment appears, while it decreases downstream the wake compared to the flow field without the wake. The induced velocities near the PS are directed opposite those near the SS. These induced velocities, appearing near the blade surfaces due to the negative jet effect, can also be identified in most cases in our results. However, no measurements could be performed in the regions very close to the blade surfaces, where the induced velocities are assumed to be more dominant. Large amounts of the induced velocity can be found if the wake segments are located in the front part of the rotor blade passage, especially near the SS just upstream the wake segment.

After the propagation along the wake segment path, the fluid accumulates near the PS of the adjacent blade. This can lead to a thickening of the PS boundary layer in blade rows compared to isolated blades. As a result, the wake segment width is reduced near the SS and increased near the PS. This can also be observed in the results in Figs. 7(b)–7(d), most clearly around the midchord position.

However, only part of the fluid, which is transported along the wake segment path across the passage, accumulates within the PS boundary layer. The perturbation velocity distribution indicates that another part is released and moves back toward the SS in the area between the wake sections (Fig. 7(f)). This effect can also be observed in the results of the computational fluid dynamics (CFD) calculations of Valkov and Tan [13]. In our results, this secondary flow toward the SS is especially evident just upstream of the wake segments. Following this, fluid reenters the negative jet near the SS. This way, a counterclockwise vortex is formed.

Another part of the fluid, which leaves the negative jet at the PS, has a relative velocity deficit compared to the free stream. Therefore, it tends to move upstream toward the wake segment stemming from the next stator blade. Following this, it interacts with the negative jet due to this subsequent wake segment. As a result, an additional vortex is formed between the subsequent wake segments near the PS of the blade. This is visible in Fig. 7(f) for this rotor-stator position depicted most clearly in the right blade passage. The existence of this vortex is also evident from the vorticity distribution, shown in Fig. 7(e). In this figure, a region of positive vorticity indicates this clockwise turning vortex. (Since the vorticity adherent to this additional vortex is weaker than that of the wake segments, it is not clearly visible between all wake segments.) The influence of these vortices is also reflected in the contours of the flow field, especially in the axial velocity distribution (Fig. 7(c)). Thus, the effect of the chopped wakes is not only the negative jet, appearing in the wake segments itself, but also the forming of additional vortices that transport fluid in the opposite direction and between subsequent wake segments. The interaction between the subsequent wake segments is assumed to depend on the wake characteristics and the stator pitch, which influences the distance between the subsequent wake segments.

3.2 Time-Resolved Development of the Periodical Unsteady Flow Field, Design Point ($\xi=1.0, \zeta=1.0$). The flow field is resolved for 20 equidistant steps of the stator in the circumferential direction covering one stator pitch (compare to Fig. 4). These figures can be understood as snapshots of the periodical unsteady flow field when the rotor blades move along the stator. A selected result of the axial velocity component for a further time step, where the stator is shifted 25% of the blade pitch to the right, is shown in Fig. 9. This is in reality equivalent to the rotor turning

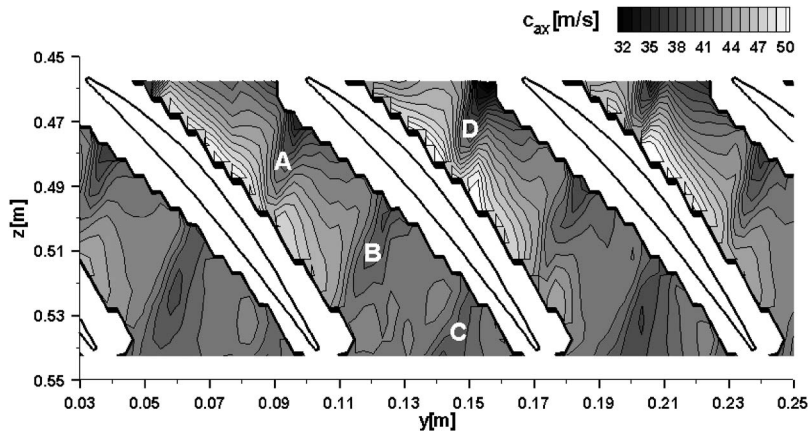


Fig. 9 Periodical unsteady flow field inside the blade passages of Rotor 3, rotor-stator position $\Delta\phi=0.25$, midspan, design point ($\xi=1.0$, $\zeta=1.0$)

into the opposite direction with the same distance. In this figure, the shape and the propagation of the chopped stator wake segments inside the different rotor passages can be realized in comparison to Fig. 7(c). In this figure, Wake segments A–D are labeled. The development of the stator wake segments within the rotor passages is already discussed for the reference rotor-stator position (Fig. 7). The sequence of the subsequent 20 rotor-stator positions, showing the time-resolved periodical unsteady flow field in this rotor blade row, is integrated into an animation by Lehmann [12]. The movies for the different flow parameters are available on request from the lead author of the present paper.

3.3 Periodical Unsteady Flow Field: Reference Rotor-Stator Position ($\Delta\phi=0$), Operating Point Near Stability Limit at Design Speed ($\xi=0.85$, $\zeta=1.0$). In Figs. 10(a)–10(f), the flow field for the reference rotor-stator position for an operating point near the stability limit is shown (85% of design mass flow at design speed).

As for the design point, the wake positions become more apparent in the axial velocity component than in the relative velocity distribution (Figs. 10(a) and 10(c)). Due to the higher loading of the preceding stator blade row, the SS boundary layer thickness of the stator blades grows. This leads to an increase of the stator wake width. Furthermore, the velocity deficit within the wake increases compared to the design point. As a result, a stronger wake effect at the inlet of the rotor blade row can be found. The reduction of the minimum relative flow angle in the wake center amounts to about 3 deg compared to the design point (estimated for the wake position at the rotor inlet, midpassage), Fig. 10(b). This nearly corresponds to the reduction of the mean relative flow angle of the incoming flow of Rotor 3 for the considered operating point compared to design conditions.

If a stator wake impinges the leading edge of the rotor blade, the relative flow angle is reduced further to about 25 deg, while the mean relative flow angle at the rotor inlet is 32.5 deg. Thus, the periodical unsteady changes of β are larger than the change of the mean value of β between the design point and stability limit. This clearly points out the remarkable unsteady changes of the loading due to the passing wakes.

Furthermore, the incoming wakes are characterized by higher turbulence levels compared to the design point (Fig. 10(d)). Therefore, a faster mixing of the wake segments with the main flow can be observed if they propagate downstream. At the rotor outlet plane, the wake segments are nearly mixed out.

This faster wake mixing becomes also apparent in the vorticity and the perturbation velocity distribution (Figs. 10(e) and 10(f)). Again, in the front part of the rotor blade, the counter-rotating vorticities of the wake segments are obvious in the vorticity distribution. The perturbation velocity distribution gives evidence of

the negative jet effect. In the rear half-part of the rotor blade, this picture becomes more diffuse due to the broadened and flattened wakes. Here, the vorticity distribution does not provide explicit information about the wake positions, since the vorticity between the wake segments is of the same order of magnitude like in the wake segments themselves. The perturbation velocity, however, reflects the transport of fluid coupled with the negative jet effect in this region of the flow field.

4 Unsteady Pressure Distribution of the Rotor Blades at Midspan

Although the flow field close to the blade surfaces is not resolved, an effect of the negative jet on the unsteady profile pressures can be expected from the data discussed in the previous section. To prove this hypothesis, the unsteady profile pressures of Rotor 3 at midspan will be discussed in Figs. 11 and 12 for the two operating points considered so far. (Further results for several rotor and stator blade rows of the Dresden LSRC are provided by Mailach et al. [23].)

In general, there are different mechanisms affecting the periodical unsteady pressure distribution of a considered compressor blade. These are

- the wakes/chopped wake segments (coupled with the negative jet effect), propagating convectively along the blade surfaces
- the change of blade circulation appearing during the wake impingement
- the effect of the potential flow field of the passing blades

There exists no general rule or correlation on which of these effects is the dominant one in a particular machine. Anyway, there are only a few data on time-resolved profile pressure distributions on compressor blades available in open literature (see literature survey by Mailach et al. [23]).

Durali and Kerrebrock [29] investigated the unsteady profile pressures in a single-stage transonic compressor. These authors conclude that the pressure distribution is substantially determined by the blade circulation, which is affected by the passing blades. As a result, the unsteady profile pressure changes nearly instantaneously along the blade chord during wake impingement. Sanders and Fleeter [10] investigated the unsteady stator profile pressure distribution in a $1\frac{1}{2}$ -stage compressor for both subsonic and transonic flow conditions. In their case, at subsonic speed, the unsteady profile pressures mainly respond to the circulation changes. At transonic speed, the rotor wakes were much broader with a higher slip velocity. In this case, the chopped rotor wake segments had a clear local influence on the unsteady profile pressures of the

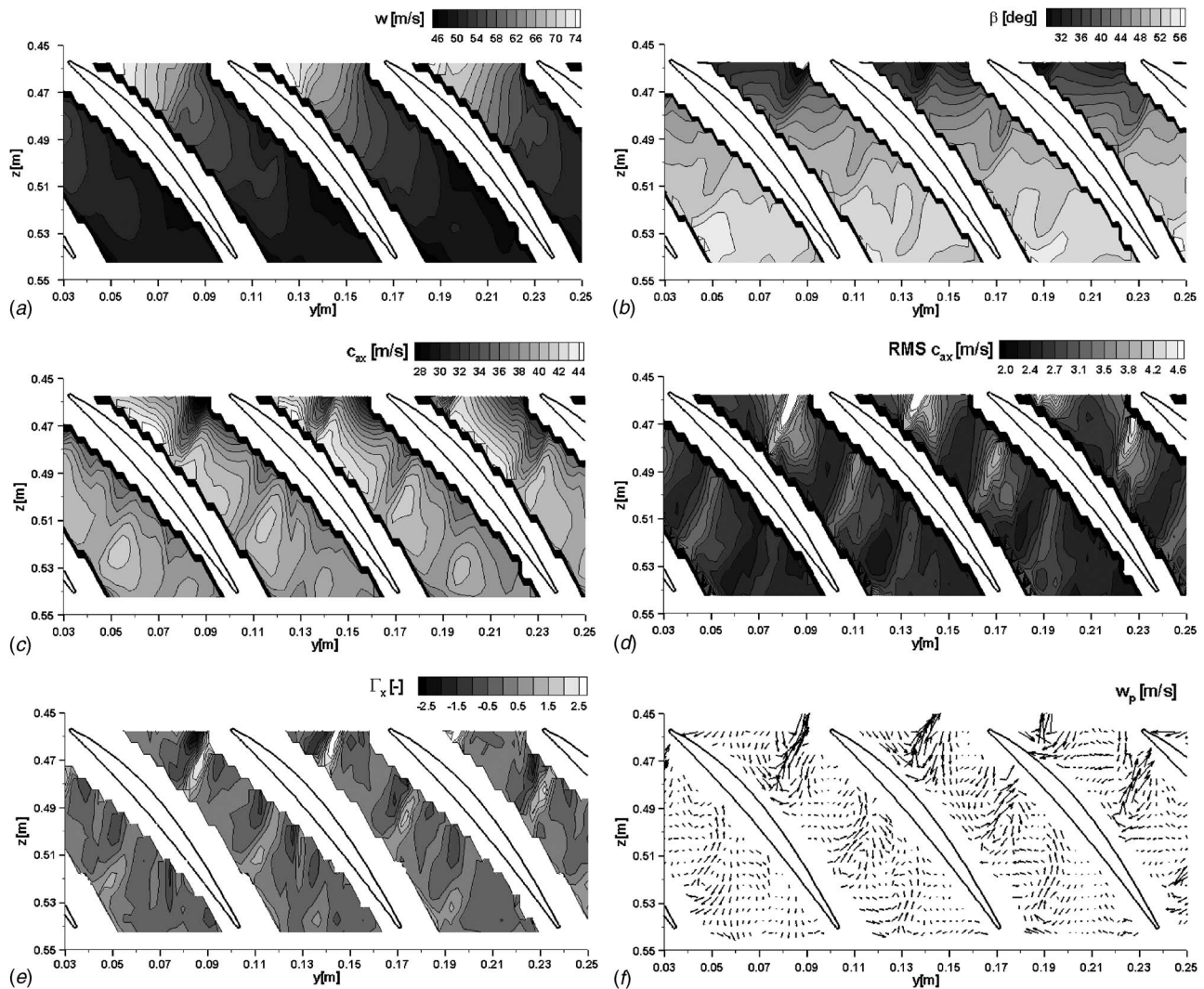


Fig. 10 Periodical unsteady flow field inside the blade passages of Rotor 3, reference rotor-stator position ($\Delta\phi=0$), midspan, operating point near stability limit at design speed ($\xi=0.85$, $\zeta=1.0$)

stator blades. Hence, it can be supposed that the particular wake characteristics determine in which way the profile pressure responds to a wake.

The results for the unsteady profile pressure distributions of Rotor 3 of the Dresden LSRC for the design point are shown in Fig. 11. This figure shows the ensemble-averaged pressure distributions at midspan on the PS and the SS in s - t diagrams. Since the unsteady effects are of interest, the fluctuating part of the pressure is shown.

The profile pressures are periodically influenced by the incoming wakes and the potential effect of the upstream Stator 2 as well as the upstream acting potential effect of Stator 3. If a stator wake impinges the leading edge of the considered rotor blade, the circulation of this blade changes due to the altered incidence angle and incoming flow velocity. Because of this, the wake influence propagates along the blade surface toward the trailing edge as a pressure wave with the velocity of sound, which is well above the convective speed of flow in this low-speed machine. As a result, a nearly instantaneous change of the pressure along the PS and the SS blade surface appears (Fig. 11). Pressure changes due to the convectively propagating wake segments within the rotor blade passages would appear along inclined lines (positive slope) in the depicted s - t diagrams. This is obviously not the dominant effect in this case. Thus, the profile pressures are nearly independent of the wake propagation within the rotor blade passages.

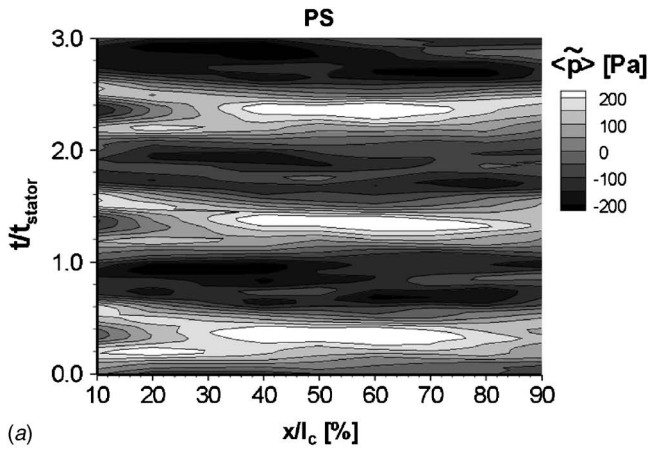
The potential effects of the downstream stator blades propagate upstream with the velocity of sound. Therefore, the pressure along the blade surface responds to this stator-periodic influence again nearly instantaneously in time. On Rotor 3, the influence of the wakes and the potential effect of the downstream blade row cannot clearly be distinguished. This is because of the identical blade numbers of the up- and downstream stator blade rows and the fast propagation of the pressure fluctuations along the blade surface.

Thus, the negative jet effect, which is coupled to the convectively propagating stator wake segments, has no recognizable effect on the unsteady profile pressure distribution of Rotor 3. However, the flow field within the rotor blade passages is clearly influenced by this secondary flow effect, as discussed in the previous section.

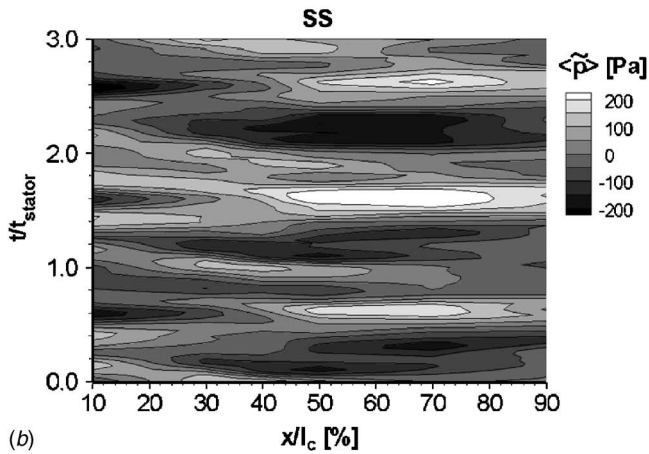
For the considered operating point near the stability limit, the qualitative picture is the same (Fig. 12). Also, in this case, the convectively propagating chopped stator wakes are only of secondary importance for the unsteady pressure distribution of the rotor blades.

5 Conclusions

Using a two-component LDA, the flow field within the third rotor blade row of the four-stage Dresden LSRC was investigated. Applying a special sorting algorithm, time-resolved results of the



(a)



(b)

Fig. 11 Unsteady pressure distribution on PS and SS of Rotor 3, midspan, design point ($\xi=1.00$, $\zeta=1.0$)

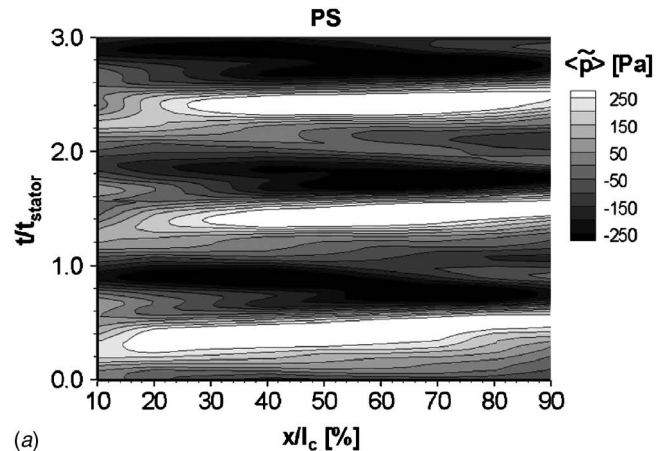
periodical unsteady flow field within a rotor blade row are derived from the pointwise measurements. Movies of the time-resolved flow field are available on request from the lead author.

In Part I of this two-part paper, the results for midspan are presented. The results of the flow field measurements are discussed in detail and compared to the unsteady pressure distribution of the rotor blades. Besides the results for the design point, selected results for an operating point near the stability limit are shown. In Part II, the flow field in the rotor blade tip region is discussed.

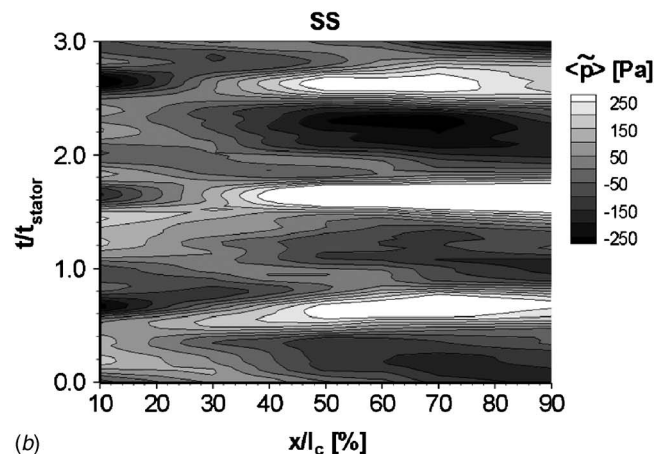
The incoming stator wakes are the dominant influence on the periodical unsteadiness of the flow field at midspan of the rotor blade row. The stator wakes are chopped at the rotor blade leading edges and propagate through the rotor blade passages with the same velocity as the surrounding free stream. The wake segments are not completely mixed out during their transport through the subsequent rotor blade passages.

The potential effects of the stator blades are of minor influence on the unsteady flow field within the rotor blade row. Probably due to the identical blade numbers of Stators 2 and 3, no clear signs of the potential effect from the downstream stator blade row on the unsteady flow field within Rotor 3 could be noticed.

The time-resolved development of different flow field parameters is discussed. Besides the velocity components and the flow angles, the vorticity and the perturbation velocity are used to investigate the secondary flow motion. Using these parameters, the counter-rotating vortex streets within the two branches of the wake become apparent. The negative jet effect, which appears due to the velocity deficit of the wake, is also clearly resolved. Due to this effect, the fluid is transported across the rotor blade passage



(a)



(b)

Fig. 12 Unsteady pressure distribution on PS and SS of Rotor 3, midspan, operating point near stability at design speed ($\xi=0.85$, $\zeta=1.0$)

along the wake segment path from the suction side toward the pressure side of the adjacent blade. Further secondary flow motions between the subsequent negative jets are identified.

Owing to the negative jet effect, the local velocity distribution near the blade surfaces is also affected. Although the flow field close to the rotor blades could not be resolved, a local influence of the negative jet effect on the unsteady profile pressure distribution could be expected. Indeed, the unsteady pressure distribution of the rotor blades does not reveal the effect of the convectively propagating stator wake segments. The dominant periodical influences on the time-resolved profile pressure distribution are the wake impingement as well as the potential effect of the stator blades.

Acknowledgment

Part of the work reported in this two-part paper was supported by the Bundesministerium für Bildung und Forschung (German ministry) and the Deutsche Forschungsgemeinschaft (DFG, German Research Society). The permission to publish this work is gratefully acknowledged.

Nomenclature

- $\langle \rangle$ = ensemble-averaged value
- $-$ = mean value
- c = absolute velocity (m/s)
- h = enthalpy (J/kg)
- l_c = chord length (m)
- \dot{m} = mass flow (kg/s)

n = number of revolutions (s^{-1})
 p = pressure (Pa)
 \tilde{p} = fluctuating part of pressure (Pa)
 r^* = relative channel height (%)
 T = temperature (K)
 t = time (s)
 u = rotor speed (m/s)
 w = relative velocity (m/s)
 w_p = perturbation velocity, relative frame of reference (m/s)
 x = chordwise position (m)
 y = circumferential coordinate (LDA measurements) (m)
 z = axial coordinate (LDA measurements) (m)
 β = relative flow angle (deg)
 Γ_x = vorticity
 $\Delta\varphi$ = relative position between stator and rotor (see Fig. 4)
 ζ = reduced speed/reduced design speed,
 $\zeta = (n/\sqrt{T_t}) / (n_{DP}/\sqrt{T_{t,DP}})$
 ξ = reduced mass flow/reduced design mass flow
 $\xi = (\dot{m}\sqrt{T_t/p_t}) / (\dot{m}_{DP}\sqrt{T_{t,DP}/p_{t,DP}})$
 Ψ_{is} = enthalpy coefficient, $\Psi_{is} = \Delta h_{is}/u_{MS}^2$

Abbreviations and Subscripts

l = inlet plane of considered rotor blade row
 ax = axial component
 is = isentropic
 t = total
 u = circumferential component
 DP = design point
 IGV = inlet guide vane
 LDA = laser Doppler anemometer
 $LSRC$ = low-speed research compressor
 MS = midspan
 PIV = particle-image velocimetry
 PS = pressure side
 rms = root mean square value
 SS = suction side

References

- [1] Kemp, N. H., and Sears, W. R., 1955, "The Unsteady Forces Due to Viscous Wakes in Turbomachines," *J. Aeronaut. Sci.*, **22**(7), pp. 478–483.
- [2] Meyer, R. X., 1958, "The Effect of Wakes on the Transient Pressure and Velocity Distributions in Turbomachines," *Trans. ASME*, **80**, pp. 1544–1552.
- [3] Lefcort, M. D., 1965, "An Investigation Into Unsteady Blade Forces in Turbomachines," *ASME J. Eng. Power*, **87**, pp. 345–354.
- [4] Kerrebrock, J. L., and Mikolajczak, A. A., 1970, "Intra-Stator Transport of Rotor Wakes and its Effect on Compressor Performance," *ASME J. Eng. Power*, **92**, pp. 359–368.
- [5] Hodson, H. P., 1985, "Measurements of Wake-Generated Unsteadiness in the Rotor Passages of Axial Flow Turbines," *ASME J. Eng. Gas Turbines Power*, **107**, pp. 467–476.
- [6] Smith, L. H., Jr., 1966, "Wake Dispersion in Turbomachines," *ASME J. Basic Eng.*, **88**, pp. 688–690.
- [7] Smith, L. H., Jr., 1970, "Casing Boundary Layers in Multistage Axial Compressors," *Flow Research on Blading*, L. S. Dzung, ed., Elsevier, Amsterdam.
- [8] Dereguel, P., and Tan, C. S., 1996, "Impact of Rotor Wakes on Steady-State Axial Compressor Performance," *ASME Paper No. 96-GT-253*.
- [9] Van Zante, D. E., Adamczyk, J. J., Strazisar, A. J., and Okiishi, T. H., 2002, "Wake Recovery Performance Benefit in a High-Speed Axial Compressor," *ASME J. Turbomach.*, **124**, pp. 275–284.
- [10] Sanders, A. J., and Fleeter, S., 2001, "Multi-Blade Row Interactions in a Transonic Axial Compressor, Part II: Rotor Wake Forcing Function and Stator Unsteady Aerodynamic Response," *ASME Paper No. 2001-GT-0269*.
- [11] Sanders, A. J., Papalia, J., and Fleeter, S., 2001, "Multi-Blade Row Interactions in a Transonic Axial Compressor, Part I: Stator Particle Image Velocimetry (PIV) Investigations," *ASME Paper No. 2001-GT-0268*.
- [12] Lehmann, I., 2003, "Strömungsuntersuchungen in stehenden und rotierenden Schaufelkanälen mittels Laser-Doppler-Anemometrie," Ph.D. thesis, TU Dresden, Düsseldorf, Germany.
- [13] Valkov, T., and Tan, C. S., 1995, "Control of the Unsteady Flow in a Stator Blade Row Interacting With Upstream Moving Wakes," *ASME J. Turbomach.*, **117**, pp. 97–105.
- [14] Hathaway, M. D., Suder, K. L., Okiishi, T. H., Strazisar, A. J., and Adamczyk, J. J., 1987, "Measurement of the Unsteady Flow Field Within the Stator Row of a Transonic Axial-Flow Fan: Part II—Results and Discussion," *ASME Paper No. 87-GT-227*.
- [15] Stauter, R. C., Dring, R. P., and Carta, F. O., 1991, "Temporally and Spatially Resolved Flow in a Two-Stage Axial Compressor: Part 1—Experiment," *ASME J. Turbomach.*, **113**, pp. 212–226.
- [16] Lehmann, I., Wolf, E., and Vogeler, K., 2001, "Stator Wake Propagation Inside Rotating Blade Passages," *Proceedings of the Fourth European Conference on Turbomachinery*, Florence, Italy, ImechE Paper No. C557/006/99
- [17] Michon, G.-J., Miton, H., and Ouayahya, N., 2005, "Unsteady Off-Design Velocity and Reynolds Stresses in an Axial Compressor," *J. Propul. Power*, **21**(6), pp. 961–972.
- [18] Tisserant, D., and Breugelmans, F. A. E., 1997, "Rotor Blade-to-Blade Measurements Using Particle Image Velocimetry," *ASME J. Turbomach.*, **119**, pp. 176–181.
- [19] Balzani, N., Scarano, F., Riethmuller, M. L., and Breugelmans, F. A. E., 2000, "Experimental Investigation of the Blade-to-Blade Flow in a Compressor Rotor by Digital Particle Image Velocimetry," *ASME J. Turbomach.*, **122**, pp. 743–750.
- [20] Wernet, M. P., Van Zante, D., Strazisar, T. J., John, W. T., and Prahst, P. S., 2002, "3-D Digital PIV Measurements of the Tip Clearance Flow in an Axial Compressor," *ASME Paper No. GT-2002-30643*.
- [21] Mailach, R., and Vogeler, K., 2002, "Wake-Induced Boundary Layer Transition in a Low-Speed Axial Compressor," *Flow, Turbul. Combust.*, Special Issue of Unsteady Flow in Turbomachinery, **69**(3–4), pp. 271–294.
- [22] Mailach, R., and Vogeler, K., 2004, "Aerodynamic Blade Row Interactions in an Axial Compressor, Part I: Unsteady Boundary Layer Development," *ASME J. Turbomach.*, **126**, pp. 35–44; "Part II: Unsteady Profile Pressure Distribution and Blade Forces," *ASME J. Turbomach.*, **126**, pp. 45–51.
- [23] Mailach, R., Müller, L., and Vogeler, K., 2004, "Rotor-Stator Interactions in a Four-Stage Low-Speed Axial Compressor, Part I: Unsteady Profile Pressures and the Effect of Clocking," *ASME J. Turbomach.*, **126**, pp. 507–518; "Part II: Unsteady Aerodynamic Forces of Rotor and Stator Blades," *ASME J. Turbomach.*, **126**, pp. 519–528.
- [24] Mailach, R., and Vogeler, K., 2006, "Blade Row Interaction in Axial Compressors, Part I: Periodical Unsteady Flow Field," *Lecture Series 2006-06 on Advances in Axial Compressor Aerodynamics*, Rhode-Saint-Genève, Belgium, May 15–18; "Part II: Unsteady Behaviour of Boundary Layer, Pressure Distribution and Excited Pressure Force of Compressor Blades," *Lecture Series 2006-06 on Advances in Axial Compressor Aerodynamics*, Rhode-Saint-Genève, Belgium, May 15–18.
- [25] Mailach, R., Lehmann, I., and Vogeler, K., 2008, "Periodical Unsteady Flow Within a Rotor Blade Row of an Axial Compressor—Part II: Wake-Tip Clearance Vortex Interaction," *ASME J. Turbomach.*, **130**(4), p. 041005.
- [26] Sauer, H., Bernstein, W., Bernhard, H., Biesinger, T., Boos, P., and Möckel, H., 1996, "Konstruktion, Fertigung und Aufbau eines Verdichter-prüfstandes und Aufnahme des Versuchsbetriebes an einem Nieder-geschwindigkeits-Axialverdichter in Dresden," Abschlussbericht zum BMBF-Vorhaben 0326758A, Dresden, Germany.
- [27] Müller, R., Mailach, R., and Lehmann, I., 1997, "The Design and Construction of a Four-Stage Low-Speed Research Compressor," *Proceedings of the IMP '97 Conference on Modelling and Design in Fluid-Flow Machinery*, J. Badur, Z. Bilicki, J. Mikielewicz, and E. Sliwicki, eds., Nov. 18–21, Gdansk, Poland, pp. 523–530.
- [28] Boos, P., Möckel, H., Henne, J. M., and Selmeier, R., 1998, "Flow Measurement in a Multistage Large Scale Low Speed Axial Flow Research Compressor," *ASME Paper No. 98-GT-432*.
- [29] Durali, M., and Kerrebrock, J. L., 1998, "Stator Performance and Unsteady Loading in Transonic Compressor Stages," *ASME J. Turbomach.*, **120**, pp. 224–232.

Periodical Unsteady Flow Within a Rotor Blade Row of an Axial Compressor—Part II: Wake-Tip Clearance Vortex Interaction

Ronald Mailach

Technische Universität Dresden,
Institut für Strömungsmechanik,
01062 Dresden, Germany
e-mail: ronald.mailach@tu-dresden.de

Ingolf Lehmann

Kompressorenbau Bannewitz GmbH,
Windbergstrasse 45,
01728 Bannewitz, Germany
e-mail: ingolf.lehmann@kbb-turbo.de

Konrad Vogeler

Technische Universität Dresden,
Institut für Strömungsmechanik,
01062 Dresden, Germany
e-mail: konrad.vogeler@tu-dresden.de

In this two-part paper, results of the periodical unsteady flow field within the third rotor blade row of the four-stage Dresden low-speed research compressor are presented. The main part of the experimental investigations was performed using laser Doppler anemometry. Results of the flow field at several spanwise positions between midspan and rotor blade tip will be discussed. In addition, time-resolving pressure sensors at midspan of the rotor blades provide information about the unsteady profile pressure distribution. In Part II of the paper, the flow field in the rotor blade tip region will be discussed. The experimental results reveal a strong periodical interaction of the incoming stator wakes and the rotor blade tip clearance vortices. Consequently, in the rotor frame of reference, the tip clearance vortices are periodical with the stator blade passing frequency. Due to the wakes, the tip clearance vortices are separated into different segments. Along the mean vortex trajectory, these parts can be characterized by alternating patches of higher and lower velocities and flow turning or subsequent counter-rotating vortex pairs. These flow patterns move downstream along the tip clearance vortex path in time. As a result of the wake influence, the orientation and extension of the tip clearance vortices as well as the flow blockage periodically vary in time. [DOI: 10.1115/1.2812330]

Keywords: axial compressor, laser Doppler anemometer, periodical unsteady flow field, unsteady profile pressure, rotor-stator-interaction, tip clearance vortex, wake, negative jet effect, wake-tip clearance vortex interaction

1 Introduction

The tip leakage flow is of crucial importance for the compressor design and operation because of its detrimental impact on the efficiency and the pressure rise due to the blockage effect in the endwall region (Wisler [1], Khalid et al. [2], Hoeger et al. [3]). Furthermore, the tip leakage flow plays an important role on the flow stability and the rotating stall inception process (Hoying et al. [4], Mailach et al. [5], Vo et al. [6]).

The flow field in the rotor blade tip region is dominated by the tip clearance vortex (TCV). Early models describing the time-averaged behavior of the TCV are from Rains [7] and Vavra [8]. The TCV comes into being because of the construction-conditioned tip gap of the rotor blades. The pressure difference between the two sides of the blade drives the fluid to move through this gap from the pressure side (PS) toward the suction side (SS). When the jetlike tip leakage flow enters the next blade passage, it interacts with the main flow and other secondary flow phenomena such as the passage vortex and rolls up into a spiral vortex (Fig. 1). The maximum leakage flow over the blade tip can be expected at the position of the maximum profile pressure difference between PS and SS (Inoue and Kuroumaru [9]). This position can be considered as the point of origin of the TCV. From there, the spiral vortex moves through the rotor blade passage. Depending on its orientation, it impacts the PS of the adjacent blade or leaves the blade passage at the outlet of the blade row without directly interacting with the flow around the adjacent blade.

Contributed by the International Gas Turbine Institute of ASME for publication in the JOURNAL OF TURBOMACHINERY. Manuscript received June 5, 2007; final manuscript received September 10, 2007; published online July 31, 2008. Review conducted by David Wisler. Paper presented at the ASME Turbo Expo 2007: Land, Sea and Air (GT2007), Montreal, Quebec, Canada, May 14–17, 2007.

At the upstream boundary of the TCV, the tip leakage flow interacts with the incoming main flow (Fig. 1). As a result, a blockage zone is formed near the casing and the incoming main flow is partly diverted toward the hub.

Chen et al. [10] and Storer and Cumpsty [11] considered the leakage flow and the main flow as separate mass flows. The orientation of the vortex trajectory is therefore determined by the momentum ratio of the tip leakage flow and the main passage flow. Mainly depending on this parameter and the solidity of the blades, the TCV can interact with the flow at the PS of the adjacent blade.

The characteristics of the TCV depend on various geometrical and aerodynamical parameters. As discussed by Lakshminarayana et al. [12] beside parameters such as the tip clearance height, Reynolds and Mach numbers, blade thickness, and loading also the machine configuration (rotor alone, single or multistage compressor, etc.), the inlet flow turbulence, the casing wall boundary layer and others play an important role on the formation of the TCV. A comprehensive overview on three-dimensional and tip clearance flows in compressors is given by Tan [13].

Topic of the present part of the paper is the investigation of the unsteady flow field in the tip region of a rotor blade row using a laser Doppler anemometer (LDA) system. Several investigations of the flow field in axial compressors were carried out within recent years using optical measurement methods (literature survey in Part I of the paper [14]). Amongst them, a number of studies are focused on the rotor tip region flow. Murthy and Lakshminarayana [15] and Stauter [16] provide information on the characteristics of the time-averaged rotor blade tip clearance vortex on the basis of LDA measurements in axial compressors.

Suder and Celestina [17] experimentally and numerically investigated the tip region flow field in a transonic axial compressor rotor. These authors discussed the passage shock-tip clearance

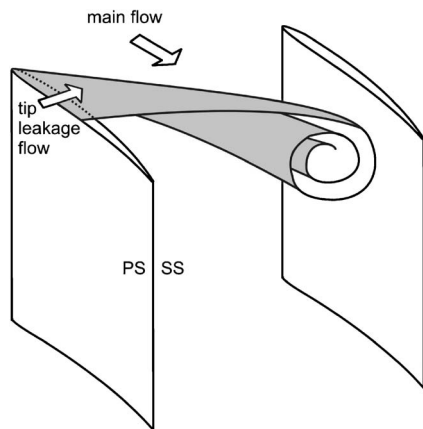


Fig. 1 Schematic of the rotor blade tip clearance flow for steady flow conditions

vortex interaction at design speed as well as the tip clearance vortex features at part speed in the absence of shocks.

Further experiments in a $1\frac{1}{2}$ -stage large scale compressor using stereoscopic particle image velocimetry (PIV) were performed by Liu et al. [18]. These authors showed instantaneous pictures in several cross sections of the rotor blade passage flow field. The time-resolved results indicate the inherent unsteadiness of the TCV, which finally breaks down.

The rotor tip flow field of the first stage rotor of a four-stage low-speed compressor was investigated by Wernet et al. [19]. They provide results of the phase-locked blade-to-blade flow field in the rotor tip region using a PIV system.

Another important aspect of the tip flow behavior is the periodical unsteadiness of the rotor TCV, which can appear due to blade row interactions, especially because of the passing wakes. There are only few attempts to address this problem. Ma et al. [20] examined the 3D flow field in the rotor blade tip region of a single-stage axial compressor with inlet guide vane (IGV) using a LDA system. However, these authors could not detect a clear influence of the IGV wake on the time-resolved rotor TCV.

Sirakov and Tan [21] numerically investigated the influence of the interaction of stator wakes and the rotor tip clearance flow on the time-averaged compressor performance. They observed a “double leakage”; in this case, the tip clearance fluid moves through the tip gap of the adjacent blade. Double leakage was found to be detrimental for compressor performance. Sirakov and

Tan [21] concluded that the double leakage is reduced due to the periodical incoming stator wakes. Thus, the time-averaged performance is improved for stronger stator-rotor interaction.

A lack of information exists concerning the structure of the unsteady blade tip flow field, which is affected by the passing wakes. To the best knowledge of the present authors, the periodical wake influence on the tip clearance vortex is not yet experimentally investigated in an axial compressor in detail. The motivation of this work is to contribute to the physical understanding of the wake-tip clearance vortex interaction process, which is a special aspect of rotor-stator interaction. The relevance of these investigations is obvious because of the influence of the periodical unsteadiness of the tip clearance vortices on the performance [21] as well as on the time-resolved blockage, the blade excitation, and the flow stability.

The setup of the experiments, which were performed in the Dresden LSRC, is described in Part I of this paper [14]. In the present paper, Part II, selected results of the flow field near rotor blade tip will be discussed ($r^*=97.9\%$ and 91.7%) and compared to the midspan results, which were presented in Part I.

2 Flow Field Within the Rotor Blade Row Near Blade Tip (97.9% Channel Height)

2.1 Time-Averaged Results. Figure 2 shows the time-averaged results of the LDA measurements close to the blade tip at a channel height of $r^*=97.9\%$. The blade tip position is $r^*=98.8\%$. The tip clearance amounts to 1.3% of the blade tip chord length. The exemplary result in Fig. 2 shows the relative velocity distribution for the design point of the compressor.

The maximum local loading in the tip region occurs near the leading edge of the considered rotor blade (no figure). Therefore, the maximum leakage jet flow appears there. Starting near the leading edge, the tip leakage vortex transverses the rotor blade passage and interacts with the flow on the PS in the rear part of the adjacent blade. The estimated mean vortex trajectory is highlighted by a dashed line in Fig. 2. A double leakage, as reported by Sirakov and Tan [21], is not obvious in the present results.

A dividing line can be found between the incoming flow and the upstream boundary of the TCV. This inclined line spans from the SS toward the PS in the front part of the blade passage. The incoming undisturbed flow upstream of this line has a noticeably higher relative flow velocity than the fluid within the TCV itself (Fig. 2). Due to the blockage of the TCV, the incoming flow is partly diverted toward the hub (later visible in Fig. 12).

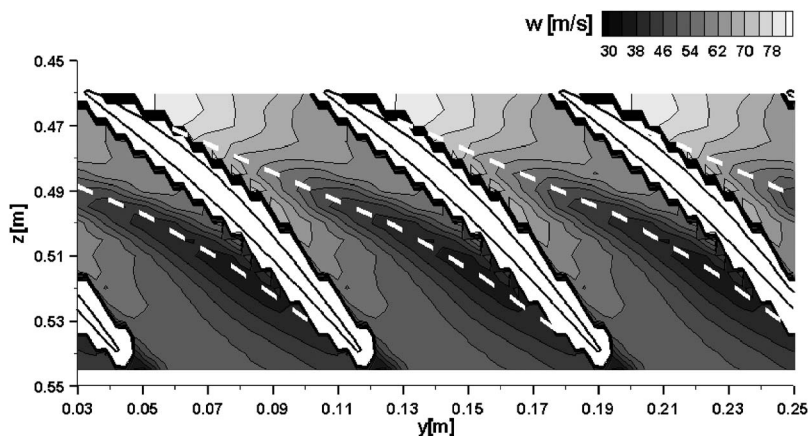


Fig. 2 Time-averaged flow field inside the blade passages of Rotor 3, near blade tip ($r^*=97.9\%$), design point ($\xi=1.0$, $\zeta=1.0$), dashed line: estimated trajectory of TCV

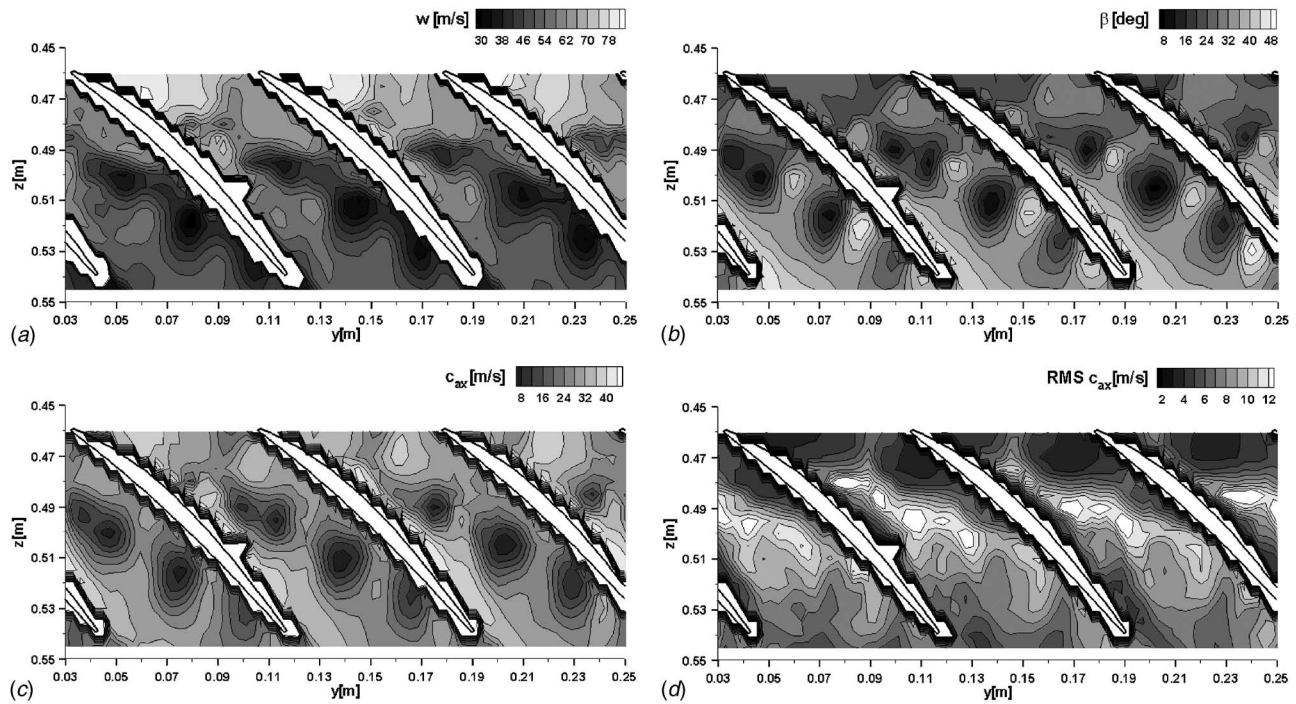


Fig. 3 Periodical unsteady flow field inside the blade passages of Rotor 3, reference rotor-stator position ($\Delta\phi=0$), near blade tip ($r^*=97.9\%$), design point ($\xi=1.0, \zeta=1.0$)

Since the TCV dominates the flow field at the rotor blade tip, also the other flow parameters clearly indicate its position and extension. The TCV can be identified by a decrease of the velocity, its axial component and the relative flow angle as well as an increase of the velocity fluctuations (no figures).

The mean radial extension of the TCV at the exit plane of the considered rotor blade row is about 15% of the channel height for the design point (later discussed with Fig. 12).

2.2 Periodical Unsteady Flow Field: Reference Rotor-Stator Position ($\Delta\phi=0$), Design Point ($\xi=1.0, \zeta=1.0$). In Figs. 3(a)–3(d), selected parameters of the periodical unsteady flow field at a radial position close to the rotor blade tip are depicted for the design point. In contrast to the time-averaged results, the TCV is divided into different segments. These patches appear because of the periodical interaction of the TCV with the incoming wakes. There are two main reasons for this wake-tip clearance vortex interaction:

- Firstly, the incoming wakes periodically change the rotor blade loading distribution. Thus, the amount and the chord-wise position of the maximum local loading change with the passing wakes. Therefore, the vortex intensity, the position of maximum tip clearance mass flow, and consequently the orientation of the TCV are periodically affected.
- Secondly, a periodical interaction of the chopped wake segments and the tip clearance flow occurs within the rotor blade passage.

Also in these time-dependent results, the interaction zone of the incoming flow and the upstream boundary of the TCV can clearly be defined. As in the time-averaged results (Fig. 2), the incoming undisturbed flow upstream of it has a noticeably higher relative flow velocity than the fluid within the TCV (Fig. 3(a)). Due to the blockage of the TCV, the wakes do not extend across the rotor blade passage from SS toward PS (contrary to the midspan results, compare to Part I, Fig. 7). In the rotor blade tip region, the direct wake influence only appears upstream of the TCV.

The wakes entering the blade passage interact with the TCV

near the leading edge and SS of the blade. The propagation of the wake influence within the TCV and in front of it seems to be nearly independent. Because of the lower flow velocity inside the TCV region, the wake influence propagates slower than in the region upstream of the TCV.

Due to the periodically incoming wakes, the TCV is divided into different segments. This can clearly be seen in Figs. 3(a)–3(d). There are several patches along the vortex trajectory, which are characterized by a clearly lower relative flow velocity, troughflow component, and relative flow angle, respectively. Their number within a considered rotor blade passage mainly depends on the rotor-stator blade count ratio as well as on the flow angle and velocity distributions.

The segments of the periodically disturbed TCV propagate downstream along the vortex trajectory in time. A sequence of the time-resolved development of the tip clearance flow is later discussed with Fig. 8. Due to the interaction with the passing stator wakes, the TCV is strongly periodic with the blade passing frequency of the upstream stator blades.

As a result of this wake-tip clearance flow interaction, the flow near the rotor blade tip moves along a wiggly line around the mean trajectory of the TCV with an alternating under- and overturning of the flow. This can be seen in Fig. 4 by means of the relative flow vectors. The flow path within the TCV in a selected blade passage is qualitatively marked with a gray arrow. This propagation direction in the considered axial-circumferential plane is superimposed to the spiral movement of the tip clearance flow including remarkable radial velocity components.

Furthermore, fluctuations with the inherent vortex shedding frequency of the TCV as well as stochastic fluctuations appear. These fluctuations of the flow parameters are reflected by the rms values, which are clearly higher in the region of the TCV compared to the passage flow near the rotor inlet (Fig. 3(d)). Maximum fluctuations of the flow field parameters appear at the interaction zone between the tip clearance flow and the incoming flow. Furthermore, larger values can be found between the different patches

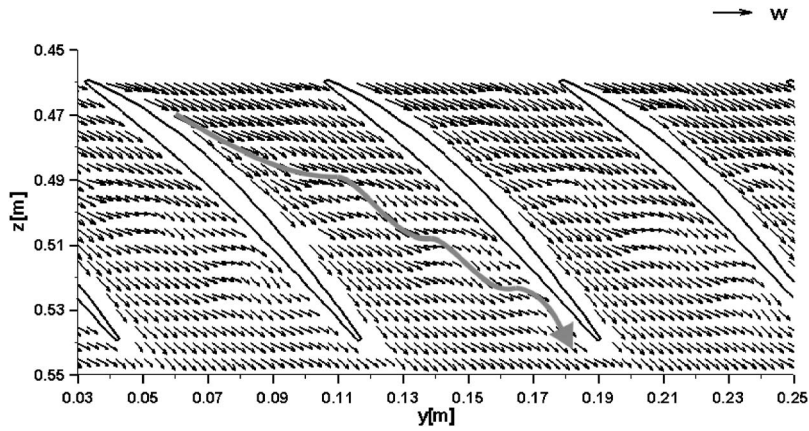


Fig. 4 Periodical unsteady flow field inside the blade passages of Rotor 3 ($\Delta\phi=0$), near blade tip ($r^*=97.9\%$), design point

along the vortex path. In Fig. 3(d), one can also clearly see that the extension of the basically cone-shaped TCV changes along the blade passage because of the recurring influence of the stator wakes.

At a given point of time, large fluctuations of the velocity, the velocity components, and the flow angle along the path of the tip clearance vortex across the passage appear (Fig. 3). These fluctuations

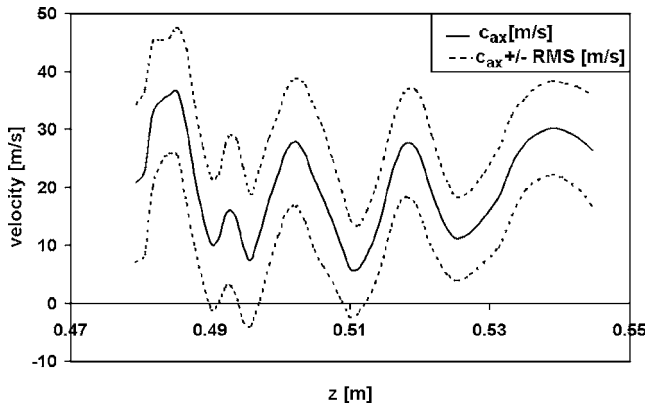


Fig. 5 Axial velocity and fluctuations along the tip clearance vortex path of Rotor 3 ($\Delta\phi=0$), near blade tip ($r^*=97.9\%$), design point

due to the wake influence on the tip clearance flow are much larger than those between the wakes and the freestream outside the blade tip region. This is the case for all flow parameters discussed with Fig. 3. This becomes obvious, when the results in Fig. 3 are compared to the midspan results, discussed with Fig. 7 in Part I, for instance.

As an example, the flow angle β fluctuates along the vortex path between about 10 deg and 40 deg at the considered point of time (Fig. 3(b)). In Fig. 5, the axial velocity distribution along the vortex trajectory for the reference rotor-stator position is shown at a fixed point of time (extracted from the results in Fig. 3). The dashed lines indicate the fluctuations of this parameter. These fluctuations include stochastic portions as well as fluctuations with all frequencies beside the stator blade passing frequency and its harmonics. The wavelike distribution of the velocity with remarkable peak-to-peak amplitudes appears due to the periodical stator wake influence. Due to the strong fluctuations of the flow parameters, the real peak-to-peak amplitudes (dashed lines) along the vortex trajectory are clearly larger than those of the ensemble-averaged distribution (solid line). Actually, this can lead to axial reversed flow within small zones of the TCV already at the design point (at the considered point of time at about $z=0.495$ m and $z=0.510$ m, Fig. 5). These positions correspond to the patches of the local axial velocity minima along the vortex trajectory in Fig. 3(c).

The vortex distribution of the flow field near rotor blade tip will

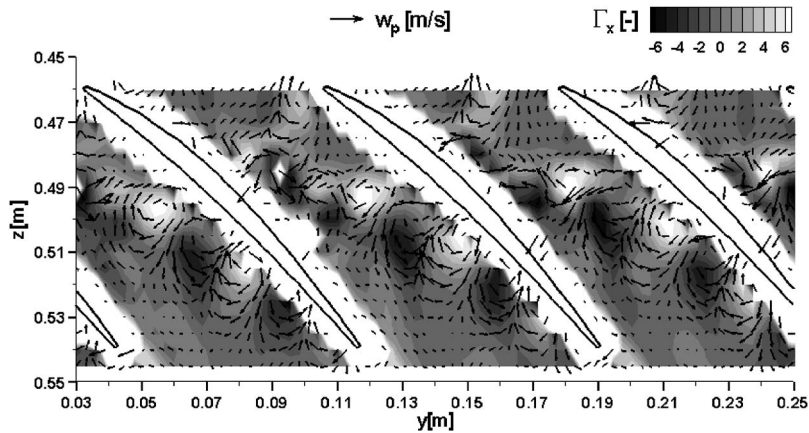


Fig. 6 Periodical unsteady flow field inside the blade passages of Rotor 3 ($\Delta\phi=0$): vorticity contours and perturbation velocity vectors, near blade tip ($r^*=97.9\%$), design point

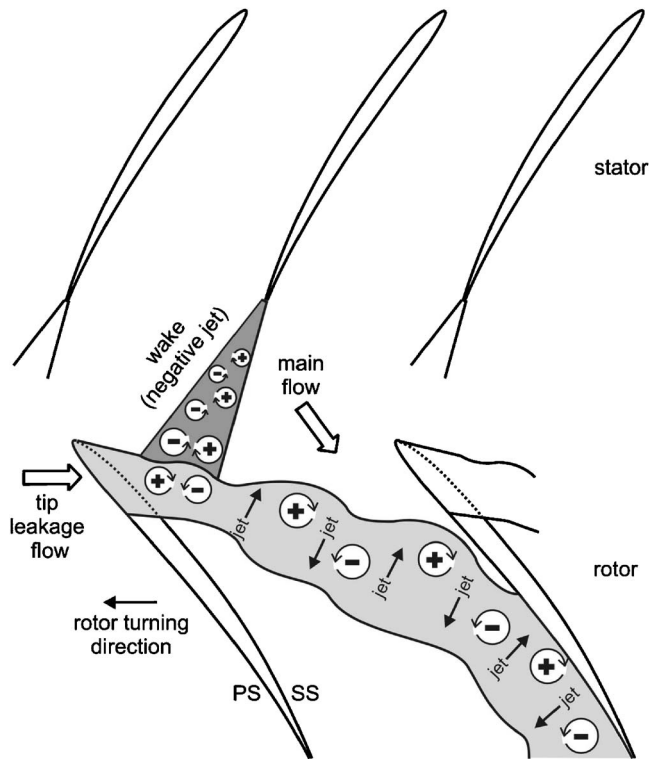


Fig. 7 Schematic of tip clearance vortex influenced by the passing wakes, 2D view, near rotor blade tip ($r=\text{const}$, $t=\text{const}$)

be discussed with Fig. 6; the main features of it are summarized in the schematic in Fig. 7. In Fig. 6, the vorticity distribution for the reference stator-rotor position is depicted as contour. The vectors are the perturbation velocity, which is determined as described in Part I of the paper (Part I: Fig. 5, Eqs. (1) and (2)). A good accordance of the information from these two parameters concerning the vortex distribution is evident in Fig. 6. In the front of the blade passages (upstream of the TCV), the wakes can be identified as stripes of counter-rotating vortices, which are responsible for the negative jet effect, Figs. 6 and 7. A positive sign of the vorticity indicates a clockwise turning, a negative sign an anticlockwise turning of the vortices. (Due to the scaling the counter-rotating vortices belonging to the wake are not clearly to be seen in Fig. 6.) The perturbation velocity vectors confirm the turning direction and indicate the amplitudes of the induced velocities. Very large secondary flow velocities can be found due to the periodical wake influence on the TCV.

Within the TCV, subsequent counter-rotating vortex pairs can be found at fixed points of time (fixed stator-rotor position). These vortex pairs are excited due to the periodical influence of the wakes, which divide the TCV into several parts. The results reveal that the dominant interaction takes place in the region of the origination of the TCV, i.e., near rotor blade leading edge and SS. As depicted in the model in Fig. 7, the presumably dominant interaction takes place at the shear layer between the incoming wake and the tip clearance flow. There the pairs of counter-rotating vortices, inherent in the wake, induce a vortex pair within the tip clearance flow, turning into opposite direction.

Following this pair of counter-rotating vortices moves along the path of the tip clearance flow. The next arriving wake again induces a vortex pair within the tip clearance flow. As a result, at a given point of time in average four vortex pairs can be found in the TCV within a rotor blade passage in our case. Between the subsequent counter-rotating vortices successive jets appear, which are alternately directed toward the SS and the PS within a consid-

ered blade passage (Figs. 6 and 7). Presumably, this has an influence on the aerodynamic blade excitation and the time-resolved blade boundary layer development.

The vortex pairs move along the path of the tip clearance flow and are still existent at the outlet plane of the rotor blade row. Thus, the tip clearance vortex is strongly periodic with the blade passing frequency of the upstream stator blade row, moving relatively to the considered rotor blades. As a result of the wake influence, the orientation and extension of the tip clearance vortices as well as the flow blockage periodically vary in time.

2.3 Sequence of Periodical Unsteady Flow Field, Design Point ($\xi=1.0$, $\zeta=1.0$). Figure 8 shows a sequence of the time-resolved development of the periodical unsteady flow field. As stated in Part I, the flow field within Rotor 3 is resolved with 20 equidistant steps for a single stator blade passing. In Fig. 8, the flow field at four selected points of time during one stator blade passing period is shown. Starting with the reference rotor-stator position, in the subsequent figures the stator blades move 25% of its pitch to the right (see definition in Part I, Fig. 4). As an example, the axial velocity distribution is shown.

The downstream transport of the low-velocity patches within the TCV can be tracked in the subsequent figures. This way the low-velocity patches transverse the passage and hit the PS of the adjacent rotor blade. Due to the strong velocity fluctuations, a local periodical influence of these patches on the profile pressure distribution in this region of the rotor blade can be hypothesized. Finally, the rotor exit flow field is periodically disturbed by the TCV's (later discussed with Fig. 12).

In the same way, the wake-induced alternating vortices within the tip clearance flow move downstream along the vortex trajectory in time (no figure). Since the stator blade passing is responsible for this TCV unsteadiness, the changes of the flow field parameters at a fixed position appear with the blade passing frequency of the upstream stator blades.

2.4 Periodical Unsteady Flow Field: Reference Rotor-Stator Position ($\Delta\phi=0$), Operating Point Near Stability Limit at Design Speed ($\xi=0.85$, $\zeta=1.0$). Exemplary results for an operating point near stability limit with 85% of design mass flow at design speed ($\xi=0.85$, $\zeta=1.0$) are shown in Fig. 9. (The stability limit of the compressor at design speed is at $\xi=0.81$). Again, the reference rotor-stator position is considered.

Due to the throttling of the compressor, the rotor blade loading in the leading edge region increases while the mean incoming flow velocity is reduced. Therefore, the momentum ratio of the tip clearance flow to the incoming flow increases. As a result, the TCV is shifted upstream and more aligned into circumferential direction (Fig. 9). This way the interaction zone of the TCV of a rotor blade with the flow around the adjacent blade also moves upstream.

The fundamental unsteady influence of the passing stator wakes is the same as discussed for the design point. Again strong variations of the flow properties along the tip clearance flow path can be found as a result of the impact of the stator wakes, Fig. 9(a). The pairs of counter-rotating vortices and the strong secondary flow vectors are clearly visible in Fig. 9(b).

As already discussed for the design point, low-velocity patches periodically appear within the TCV. Qualitatively, the same effect is observed for the considered operating point near the stability limit (Fig. 9(a)). Since stochastic influences superimpose to the periodical flow pattern, axial reversed flow can appear in the low-velocity patterns of the TCV (discussed with Fig. 5). However, for the operating point near the stability limit the TCV is shifted upstream and interacts with the adjacent rotor blade already in the front part of it. For operating conditions more close to the stability limit, a further upstream shifting of the TCV will appear. Thus, the axial reversed flow can probably lead to a spillover of the tip clearance flow within these wake-affected low velocity patches. As shown in the investigations of Hoying et al. [4] and Mailach et

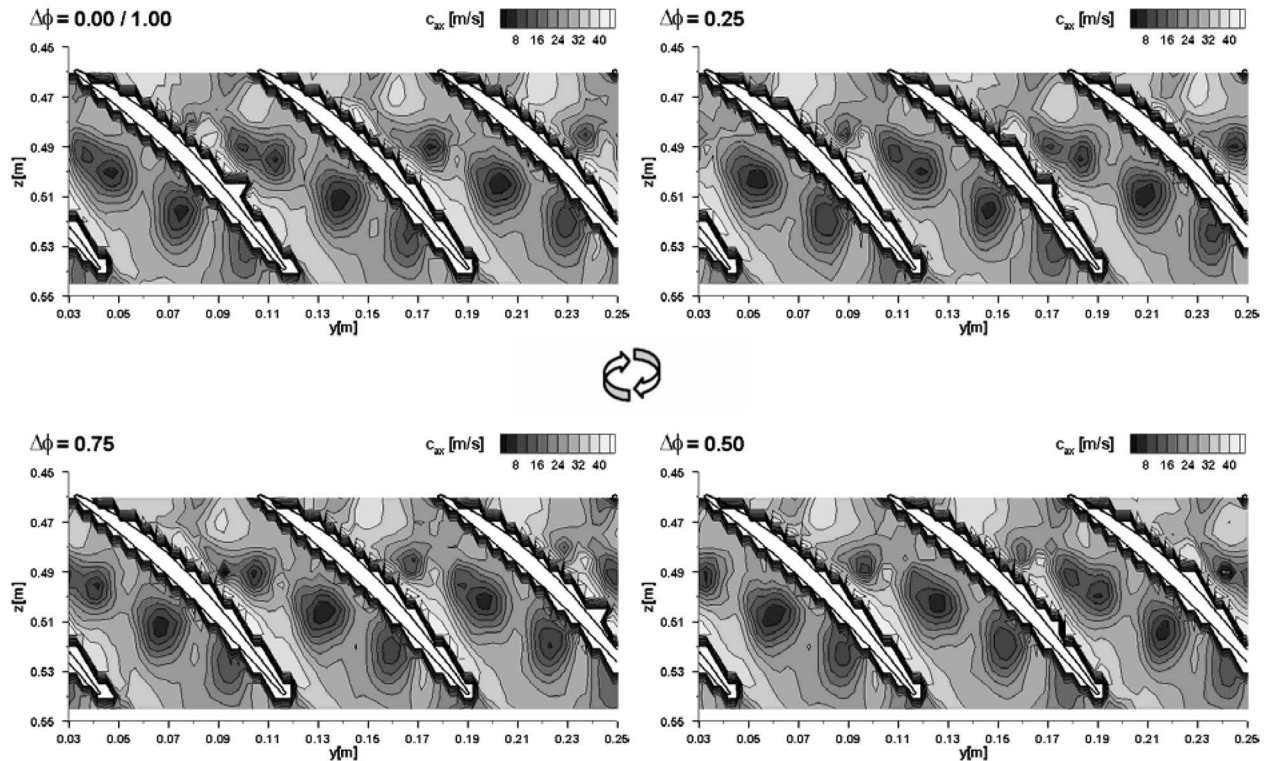


Fig. 8 Sequence of periodical unsteady flow field, Rotor 3, near blade tip ($r^* = 97.9\%$), design point

al. [5], for instance, this spillover of the tip clearance flow can lead to a strong tip clearance flow interaction within the rotor blade row. This process can trigger the rotating stall inception if it appears in the stage, which is most likely to stall. With the current results, it can be hypothesized that the periodical passing wakes can have an influence on the spillover of the tip clearance flow for operating conditions near the stability limit and therefore for the rotating stall inception process. (In the Dresden LSRC, the rotating stall inception starts in the first stage and is triggered by modal waves; see Mailach and Vogeler [22]. So for this individual compressor, the spill-over of the tip clearance flow is not relevant for stall inception.)

3 Flow Field Within the Rotor Blade Row at 91.7% Channel Height

3.1 Time-Averaged Results, Design Point. At the exit of the considered rotor blade row, the TCV radially extends from about $r^* = 85\%$ to the casing in average. Following the results for a further blade-to-blade measurement plane, cutting the TCV, will be discussed. At the chosen radial position $r^* = 91.7\%$ at first the time-averaged result will be discussed for the design point (Fig. 10).

The maximum tip leakage flow appears in the leading edge region. From there, the leakage flow rolls up into a basically cone-shaped TCV (compare to Fig. 1). The mean vortex trajectory is directed toward the rear part of the adjacent rotor blade. Along the fluid path across the passage, the radial extension of the TCV increases.

As a result of this, the flow field in the front part of the blade passages is not recognizably affected by the tip clearance flow at the considered radial position (Fig. 10). However, because of the increase of the radial extension of the TCV, it can clearly be seen as a region of reduced velocity in the rear part of the passage near the PS of the blades.

3.2 Periodical Unsteady Flow Field: Reference Rotor-Stator Position ($\Delta\phi=0$), Design Point. The time-resolved results confirm that the flow field in the front part of the blade passages is not affected by the TCV (Fig. 11). In the front part of the blade passages, the periodical unsteady flow field is dominated by the stator wakes. As discussed in detail for the midspan flow field in Part I, the chopped wake segments can be recognized as low velocity regions extending the rotor blade passage from the SS toward the PS of the adjacent blade (Fig. 11(a)). Furthermore, they can be identified as a counter-rotating vortex street in the vorticity distribution (Fig. 11(b)). The perturbation velocity vectors clearly show the negative jet effect associated with the wakes. Due to the nearly cylindrical stator blades, the wake position is practically identical for all radial positions (compare to the mid-span results, Fig. 7 in Part I, for instance).

At about the midchord position, the measurement plane cuts the TCV. Downstream of this point, one can clearly see the subsequent vortex pairs of the periodically disturbed TCV. As a result of their interaction with the TCV, the chopped wakes do not affect the flow around the SS in the rear part of the rotor blades. The fundamental features of the time-resolved TCV are comparable to that discussed for the near blade tip position and is summarized in the model in Fig. 7.

For the radial positions more away from the blade tip (listed in Part I), the influence zone of the TCV is shifted further toward the rotor blade trailing edges (no figure). Below $r^* = 85\%$, the flow field is not directly influenced by the TCV anymore.

4 Flow Field in the Outlet Plane of the Rotor Blade Row

In Fig. 12, a sequence of the periodical unsteady flow field in radial-circumferential direction just behind the rotor is shown. The axial position is $z=0.544$ (compare to Fig. 3, for instance). As an example, the axial velocity component for design point will be

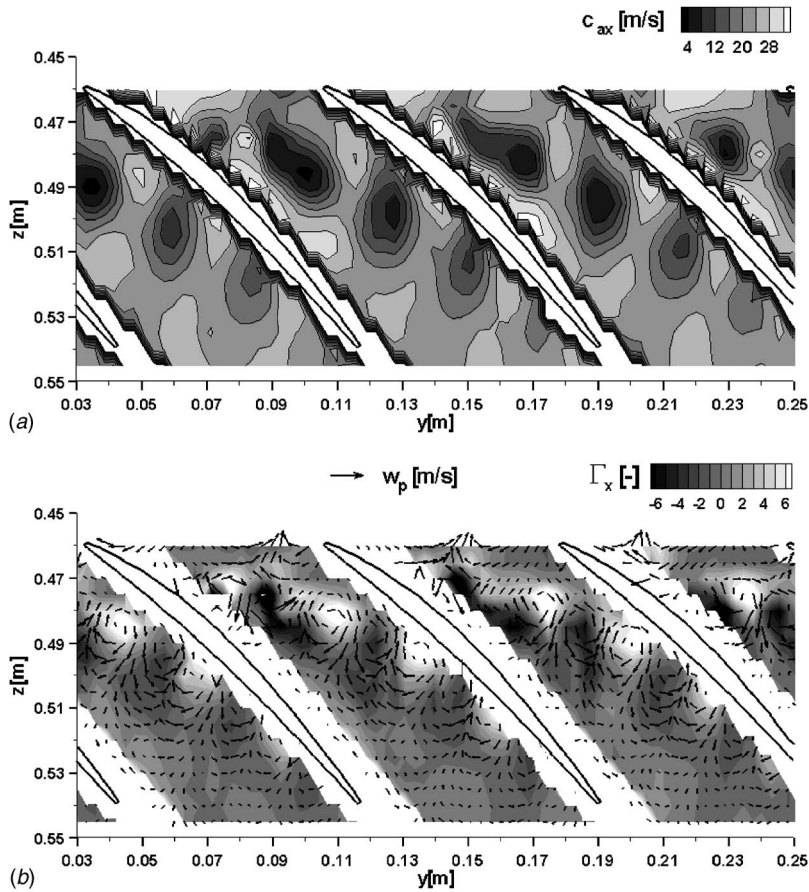


Fig. 9 Periodical unsteady flow field inside the blade passages of Rotor 3 ($\Delta\phi=0$), near blade tip ($r^*=97.9\%$), operating point near stability limit at design speed ($\xi=0.85, \zeta=1.0$)

discussed. The selected rotor-stator positions are the same like in Fig. 8. For the subsequent figures, the stator wake segments move 25% of the stator pitch to the right. This is in reality equivalent to the rotor turning in the opposite direction with the same distance. Since Fig. 12 shows results in the rotor frame of reference, the positions of the rotor wakes are nearly unchanged.

The rotor wakes can be identified by a strong reduction of the velocity (Fig. 12). As discussed before, the stator wakes are not yet mixed out after their propagation through the rotor blade pas-

sages. However, the velocity deficit of the stator wakes is moderate. Selected positions of the rotor and stator wakes and the TCV's are marked in the result for the reference position $\Delta\phi=0$.

It can be seen that the TCV's dominate the rotor flow field between about 85% of the channel height and the casing. Due to the interaction with the casing boundary layer the top of the basically cone-shaped TCV is flattened. As discussed previously, the rotor tip clearance flow periodically interacts with the incoming

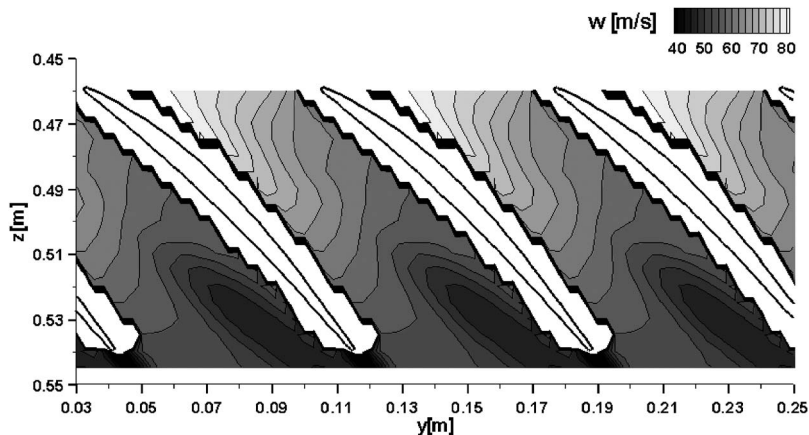


Fig. 10 Time-averaged flow field inside the blade passages of Rotor 3, $r^*=91.7\%$, design point

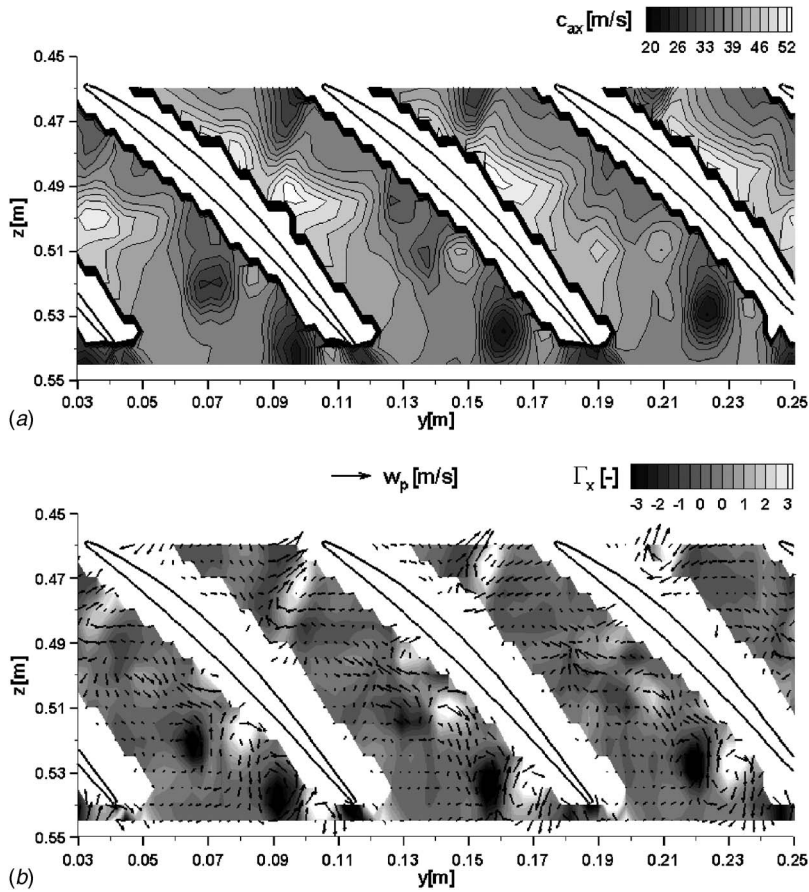


Fig. 11 Periodical unsteady flow field inside the blade passages of Rotor 3 ($\Delta\phi=0$, $r^*=91.7\%$, design point)

stator wakes. As a result of this, in the considered rotor exit plane, the low velocity regions of the TCV's move in circumferential direction for the subsequent rotor-stator positions. This means that the distance between the vortex core and the rotor wake at blade

tip periodically fluctuates in time and is different for the adjacent rotor blades. Moreover, the radial extension of the TCV's periodically varies. As a result of this, the blockage in the rotor blade tip region periodically varies in time (for the subsequent rotor-stator

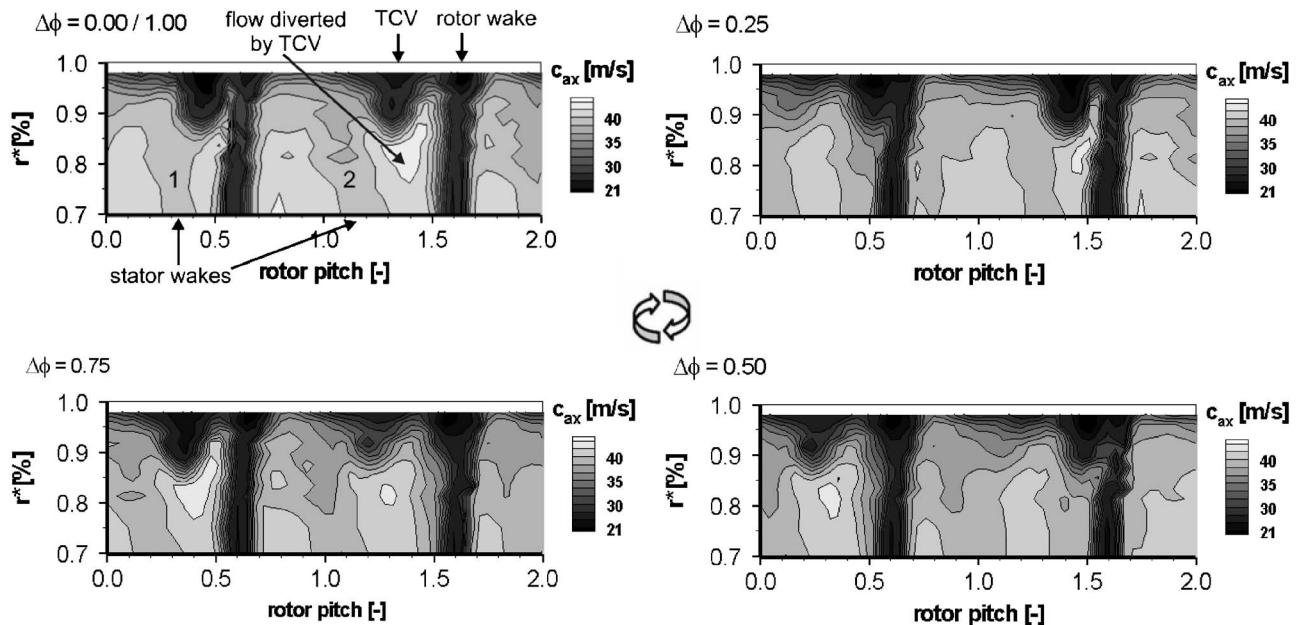


Fig. 12 Sequence of periodical unsteady flow field just behind Rotor 3 ($z=0.544$), design point ($\xi=1.0$, $\zeta=1.0$)

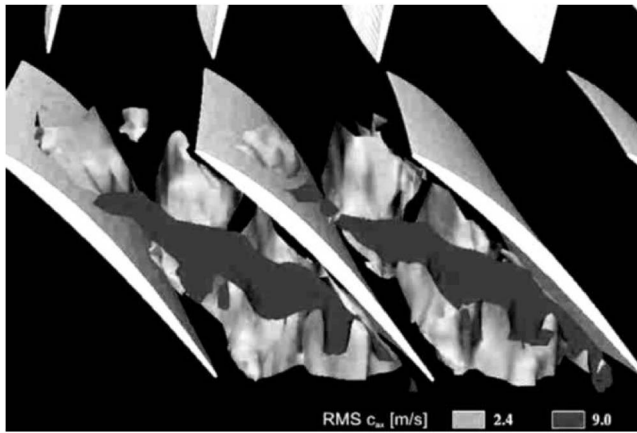


Fig. 13 Three-dimensional view of the flow field within the rotor blade row ($t=\text{const}$), design point

positions, Fig. 12) in a considered rotor blade channel. Due to the blockage of the TCV the flow, incoming to the considered rotor blade row, is diverted toward the hub. At the rotor exit plane, therefore, regions of increased velocity can be found radially below the TCV. For the first time step $\Delta\phi=0$ of the sequence in Fig. 12, this effect can clearly be seen around $r^*=0.8$ and the rotor pitch value of 1.4, for instance.

The circumferential positions of the stator wake influence in the rotor blade tip region and below 85% of channel height are different (Fig. 12). This circumferential shift appears due to the lower flow velocity in the blade tip region and the stator wake-rotor TCV interaction.

For the subsequent time steps, the stator wake pattern (radially below the TCV) changes with this circumferential shift, especially near the rotor blade wake positions (Fig. 12). Moreover, it can be seen that the circumferential distance of the adjacent stator wakes varies. This effect appears because of the interaction of the chopped stator wake segments with the flow around the rotor blade surface. For the time step $\Delta\phi=0.0$, the distance between the marked stator Wake Nos. 1 and 2 is clearly larger than that between the same stator wakes, which has moved to the right for $\Delta\phi=0.5$, for instance.

Furthermore, it can be seen that the chopped stator wakes split up into two parts if they are close to the rotor wake positions. This effect appears for instance for $\Delta\phi=0.25$ with stator Wake No. 1, which can now be found around the left rotor wake position, for instance (rotor pitch=0.6 at $r^*=0.7$). Part of this stator wake has already passed this rotor wake (is right from it), while another part of the low-momentum stator wake fluid is accumulated at the PS branch of this rotor wake (left boundary of rotor wake). The wake width of this stator wake is therefore clearly larger than in the previous time step $\Delta\phi=0$. These effects will also influence the stator-stator interaction process.

5 Three-Dimensional View of the Flow Field

Finally, a 3D view of the periodically disturbed flow structures within the rotor blade row will be provided. As an attempt to visualize these flow structures, selected isosurfaces of the flow parameters are used. Figure 13 shows an exemplary 3D view of the unsteady flow field within the rotor blade row between midspan and blade tip at a fixed point of time. To summarize the measurement results, a schematic of the periodically unsteady flow field is given in Fig. 14.

In Fig. 13 as an example, two selected isosurfaces of the velocity fluctuations ($\text{RMS } c_{ax}$) are shown. The largest velocity fluctuations appear due to the TCV. The isosurface $\text{RMS } c_{ax}=9 \text{ m/s}$ represents therefore the approximate extension of the TCV (dark gray surfaces in Fig. 13). A strong influence of the passing stator

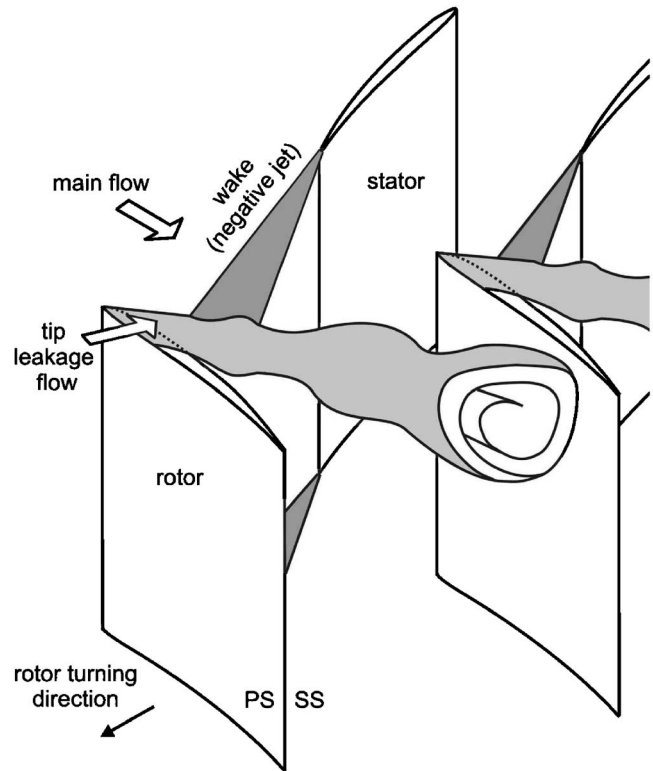


Fig. 14 Schematic of tip clearance vortex influenced by the passing wakes, 3D view ($t=\text{const}$)

wakes on the extension and local orientation of the basically cone-shaped TCV's is clearly visible in the 3D view of these measurement results. This is also schematically shown in Fig. 14 for a fixed point of time. The details of this wake-TCV interaction are already discussed with Fig. 7 for a selected axial-circumferential plane near the blade tip.

Figure 13 furthermore reveals the different shapes of TCV's of the adjacent rotor blades, which appear due to the different numbers of rotor and stator blades. For subsequent time steps (no figures), the shape and extension of the TCV's change due to the propagating wakes. Therefore, the blockage due to the TCV periodically varies in a considered rotor blade channel (clearly to be seen in the sequence in Fig. 12).

Regions of "undisturbed" flow, e.g., between the wakes and outside the influence of the TCV are represented by the isosurface $\text{RMS } c_{ax}=2.4 \text{ m/s}$ (light gray surfaces in Fig. 13). These regions are separated by the chopped wakes.

6 Conclusions

Using a two-component laser Doppler anemometer, the flow field within the third rotor blade row of the four-stage Dresden low-speed research compressor was investigated. Applying a special sorting algorithm time-resolved results of the periodical unsteady flow field within a rotor blade row are derived from the pointwise measurements. Movies of the time-resolved flow field are available on request from the lead author.

In Part I of the paper, the results for midspan are presented. In Part II, the flow field in the rotor blade tip region is discussed. Besides the results for the design point, selected results for an operating point near the stability limit are shown.

Similar to the midspan, the incoming unsteady flow field in the tip region of the rotor blade row is dominated by the passing stator wakes. Also in the tip region, the secondary flow characteristics of

the wakes could clearly be resolved. The main features of interest are the negative jet effect as well as the counter-rotating vortices inherent to the wake.

The time-dependent tip clearance vortices are strongly affected by the passing wakes. Due to the wake impact, the position of the maximum tip clearance mass flow, the vortex intensity, and consequently the orientation and extension of the tip clearance vortices change in time. Therefore, the tip clearance vortices periodically pulsate. In the rotor frame of reference, these fluctuations appear with the stator blade passing frequency. The blockage in the blade tip region, therefore, also varies with this frequency.

At a fixed point of time, the basically cone-shaped tip clearance vortex changes its extension and orientation along the vortex path. Due to the recurring stator wakes, the tip clearance vortices are divided into different segments with strongly varying flow properties. The transport of these patches along the tip clearance flow path can be tracked in the sequences of the periodical unsteady flow field.

At the shear layer between the stator wake and the rotor tip leakage flow, the pairs of counter-rotating vortices inherent to the wake induce pairs of counter-rotating vortices within the tip leakage flow. These vortex pairs move along the path of the tip clearance vortex in time. Between these vortices, fluid jets are generated. These jets are directed toward or away from the pressure side of the adjacent rotor blade, respectively. Therefore, an influence of the periodically unsteady tip clearance vortex on the time-resolved profile pressure distribution at the tip of this adjacent rotor blade can be expected.

For the operating point near the stability limit, the tip clearance vortices are shifted upstream and more aligned into circumferential direction. It is hypothesized that the periodical passing wakes can have an influence on the spillover of the tip clearance flow for operating conditions near the stability limit and therefore for the rotating stall inception process.

The results of the investigations are summarized in schematics describing the periodical unsteady behavior of the tip clearance vortex. To the best knowledge of the authors, these are the first experimental investigations in an axial compressor describing this wake-tip clearance vortex interaction process in detail.

Acknowledgment

Part of the work reported in this two-part paper was supported by the Bundesministerium für Bildung und Forschung (German Ministry) and the Deutsche Forschungsgemeinschaft (DFG, German Research Society). The permission to publish this work is gratefully acknowledged.

Nomenclature

| | |
|-----------------|---|
| c | = absolute velocity (m/s) |
| \dot{m} | = mass flow (kg/s) |
| n | = number of revolutions (s^{-1}) |
| r^* | = relative channel height (%) |
| T | = temperature (K) |
| w | = relative velocity (m/s) |
| w_p | = perturbation velocity, relative frame of reference (m/s) |
| y | = circumferential coordinate (m) |
| z | = axial coordinate (m) |
| β | = relative flow angle (deg) |
| Γ_x | = vorticity |
| $\Delta\varphi$ | = relative position between stator and rotor (see Fig. 4 in Part I) |
| ζ | = reduced speed/reduced design speed, $\zeta = (n/\sqrt{T_t}) / (n_{DP}/\sqrt{T_{t,DP}})$ |

$$\xi = \text{reduced mass flow/reduced design mass flow,} \\ \xi = (\dot{m}\sqrt{T_t/p_t}) / (\dot{m}_{DP}\sqrt{T_{t,DP}/P_{t,DP}})$$

Abbreviations and Subscripts

| | |
|------|---------------------------------|
| ax | = axial component |
| t | = total |
| TCV | = tip clearance vortex |
| IGV | = inlet guide vane |
| LDA | = laser Doppler anemometer |
| LSRC | = low-speed research compressor |
| PIV | = particle image velocimetry |
| PS | = pressure side |
| RMS | = root mean square value |
| SS | = suction side |

References

- [1] Wisler, D. C., 1985, "Loss Reduction in Axial Flow Compressors Through Low-Speed Model Testing," *ASME J. Turbomach.*, **107**, pp. 354–363.
- [2] Khalid, S. A., Khalsa, A. S., Waitz, I. A., Tan, C. S., Greitzer, E. M., Cumpsty, N. A., Adamczyk, J. J., and Marble, F. E., 1999, "Endwall Blockage in Axial Compressors," *ASME J. Turbomach.*, **121**, pp. 499–509.
- [3] Hoeger, M., Lahmer, M., Dupslaff, M., and Fritsch, G., 2000, "A Correlation for Tip Leakage Blockage in Compressor Blade Passages," *ASME J. Turbomach.*, **122**, pp. 426–432.
- [4] Hoying, D. A., Tan, C. S., Vo, H. D., and Greitzer, E. M., 1998, "Role of Blade Passage Flow Structures in Axial Compressor Rotating Stall Inception," *ASME Paper No. 98-GT-588*.
- [5] Mailach, R., Lehmann, I., and Vogeler, K., 2001, "Rotating Instabilities in an Axial Compressor Originating From the Fluctuating Blade Tip Vortex," *ASME J. Turbomach.*, **123**, pp. 453–463.
- [6] Vo, H. D., Tan, C. S., and Greitzer, E. M., 2005, "Criteria for Spike Initiated Rotating Stall," *ASME Paper No. GT-2005-68374*.
- [7] Rains, D. A., 1954, "Tip Clearance Flow in Axial Flow Compressors and Pumps," California Institute of Technology, Hydrodynamics and Mechanical Engineering Laboratories Report No. 5.
- [8] Vavra, M. H., 1960, *Aero-Thermodynamics and Flow in Turbomachines*, Wiley, New York.
- [9] Inoue, M., and Kuroumaru, M., 1989, "Structure of Tip Clearance Flow in an Isolated Axial Compressor Rotor," *ASME J. Turbomach.*, **111**, pp. 250–256.
- [10] Chen, G. T., Greitzer, E. M., Tan, C. S., and Marble, F. E., 1991, "Similarity Analysis of Compressor Tip Clearance Flow Structure," *ASME J. Turbomach.*, **113**, pp. 260–271.
- [11] Storer, J. A., and Cumpsty, N. A., 1991, "Tip Leakage Flow in Axial Compressors," *ASME J. Turbomach.*, **113**, pp. 252–259.
- [12] Lakshminarayana, B., Zaccaria, M., and Marathe, B., 1995, "The Structure of Tip Clearance Flow in Axial Flow Compressors," *ASME J. Turbomach.*, **117**, pp. 336–347.
- [13] Tan, C. S., 2006, "Three-Dimensional and Tip Clearance Flows in Compressors," *Von Kármán Institute for Fluid Dynamics (VKI), Lecture Series 2006-06 Advances in Axial Compressor Aerodynamics*, Rhode-Saint-Genève, Belgium, May 15–18.
- [14] Mailach, R., Lehmann, I., and Vogeler, K., 2008, "Periodical Unsteady Flow Within a Rotor Blade Row of an Axial Compressor—Part I: Flow Field at Midspan," *ASME J. Turbomach.*, **130**(4), p. 041004.
- [15] Murthy, K. N. S., and Lakshminarayana, B., 1986, "Laser Doppler Velocimeter Measurements in the Tip Region of a Compressor Rotor," *AIAA J.*, **24**, pp. 807–814.
- [16] Stauter, R. C., 1993, "Measurement of Three-Dimensional Tip Region Flow Field in an Axial Compressor," *ASME J. Turbomach.*, **115**, pp. 468–476.
- [17] Suder, K. L., and Celestina, M. L., 1994, "Experimental and Computational Investigation of the Tip Clearance Flow in a Transonic Axial Compressor Rotor," *ASME Paper No. 94-GT-365*.
- [18] Liu, B., Wang, H., Liu, H., Yu, H., Jiang, H., and Chen, M., 2004, "Experimental Investigation of Unsteady Flow Field in the Tip Region of an Axial Compressor Rotor Passage at Near Stall Condition With Stereoscopic Particle Image Velocimetry," *ASME J. Turbomach.*, **126**, pp. 360–374.
- [19] Wernet, M. P., Van Zante, D., Strazisar, T. J., John, W. T., and Praht, P. S., 2002, "3-D Digital PIV Measurements of the Tip Clearance Flow in an Axial Compressor," *ASME Paper No. GT-2002-30643*.
- [20] Ma, H., Jiang, H., and Zhang, Q., 2001, "Three-Dimensional Unsteady Flow Field due to IGV-Rotor Interaction in the Tip Region of an Axial Compressor Rotor Passage," *ASME Paper No. 2001-GT-0296*.
- [21] Sirakov, B. T., and Tan, C. S., 2003, "Effect of Unsteady Stator Wake—Rotor Double-Leakage Tip Clearance Flow Interaction on Time-Average Compressor Performance," *ASME J. Turbomach.*, **125**, pp. 465–474.
- [22] Mailach, R., and Vogeler, K., 2007, "Unsteady Aerodynamic Blade Excitation at the Stability Limit and During Rotating Stall in an Axial Compressor," *ASME J. Turbomach.*, **129**, pp. 503–511.

Effects of Deposits on Film Cooling of a Vane Endwall Along the Pressure Side

N. Sundaram

Mechanical Engineering Department,
Virginia Polytechnic Institute and
State University,
Blacksburg, VA 24061
e-mail: nasundar@vt.edu

M. D. Barringer

K. A. Thole

Mechanical and Nuclear Engineering Department,
The Pennsylvania University,
University Park, PA 16802

Film cooling is influenced by surface roughness and depositions that occur from contaminants present in the hot gas path, whether that film cooling occurs on the vane itself or on the endwalls associated with the vanes. Secondary flows in the endwall region also affect the film-cooling performance along the endwall. An experimental investigation was conducted to study the effect of surface deposition on film cooling along the pressure side of a first-stage turbine vane endwall. A large-scale wind tunnel with a turbine vane cascade was used to perform the experiments. The vane endwall was cooled by an array of film-cooling holes along the pressure side of the airfoil. Deposits having a semielliptical shape were placed along the pressure side to simulate individual row and multiple row depositions. Results indicated that the deposits lowered the average adiabatic effectiveness levels downstream of the film-cooling rows by deflecting the coolant jets toward the vane endwall junction on the pressure side. Results also indicated that there was a steady decrease in adiabatic effectiveness levels with a sequential increase in the number of rows with the deposits. [DOI: 10.1115/1.2812332]

Introduction

The flow along the endwall in a first-stage turbine vane is influenced by both roughness levels present on the surface and vortices that extend from the airfoil leading edge region to the trailing edge region. These secondary flows impact the endwall film-cooling effectiveness levels by lifting coolant jets from the endwall surface and directing them toward the vane suction side. This jet lift-off results in low adiabatic effectiveness levels along the pressure side of the vane endwall, which ultimately results in a weak layer of coolant shielding the metal hardware from the hot mainstream gases. Continuous exposure of the endwall to these extreme conditions reduces the operability and life of the hardware. The adiabatic effectiveness is a measure of the film-cooling potential along a surface downstream of the coolant injection location.

Film-cooling performance is also affected by surface deposits formed by small particles and unburned combustion products adhering to the turbine hardware. Modern gas turbines are being developed to have the capability of operating with fuels other than natural gas. Coal derived synthetic gas is one such alternative fuel, which is comparable to natural gas in terms of performance; however, it can have contaminants. The size of the contaminant particles can vary greatly from 5 μm to 60 μm [1]. While the smaller particles tend to follow the mainstream flow path, the larger particles may not due to their larger momentum and can deposit on the pressure side of the vane and endwall surfaces [2]. These larger particles when in molten form tend to quench near cooled regions on turbine component surfaces, for example, near a film-cooling hole or slot, thus leading to film-cooling depositions.

This study is aimed at understanding the effects of surface deposition and deposit location on the adiabatic effectiveness levels along the pressure side of a vane endwall. In particular, the work presented in this paper is aimed at understanding the row-

by-row interaction due to depositions on the endwall surface. The effects of placing deposits upstream and downstream of single and multiple cooling hole rows were investigated.

Relevant Past Studies

A number of studies in the literature have documented the effects of using alternative fuels on the surface contamination of turbine engine components. Studies have also specifically focused on determining the effects of surface roughness and surface depositions on film-cooling performance. The current literature includes studies that have investigated the effects of using coal and other solid fuels on ash and other contaminant levels on deposition, corrosion, and erosion.

A study by Wenglarz et al. [3] showed that high levels of ash up to 40 tons/y can enter a turbine. DeCorso et al. [4] found that most coal derived fuels, even after conversion and purification, had higher levels of impurities than natural gas. They found that sulfur levels in natural gas are about 10 ppm, while for coal derived fuels the sulfur levels are approximately 1000 ppm. Moses and Bernstein [5] found that a fuel burning with 0.5% ash results in about 1.5 tons of ash per day flowing through the turbine engine. In a separate study by Wenglarz [6], it was reported that the mass fraction of the ash particles that adhere to the engine surface and contribute to deposit buildup was 0.06 with an average particle diameter of 10 μm . A recent study by Bons et al. [7] investigated the effect of ash deposits present in coal fuels using an accelerated deposition test facility. Their tests were conducted with ash particles slightly higher in mean mass diameter (13.3 μm) than those found in coal fuels. For a test duration of 3 h, they found the net particle loading to be 165 ppmw/h (parts per million by weight per hour), which resulted in an average deposit thickness of 1.3 mm.

Deposition of contaminants and other particulate matter present in the mainstream gas takes place through an impingement process in which the particles make contact with and adhere to the surface. The first row of vanes is directly subjected to the combustion products that exit the combustion chamber. This direct exposure results in an elevated level of particulate deposition via impingement [8]. The mechanism for this can be attributed to particle breakup and redistribution upon impacting the component wall surface [9]. More specifically, the leading edge film-cooling

Contributed by the International Gas Turbine Institute of ASME for publication in the JOURNAL OF TURBOMACHINERY. Manuscript received June 5, 2007; final manuscript received June 25, 2007; published online July 31, 2008. Review conducted by David Wisler. Paper presented at the ASME Turbo Expo 2007: Land, Sea and Air (GT2007), Montreal, Quebec, Canada, May 14–17, 2007.

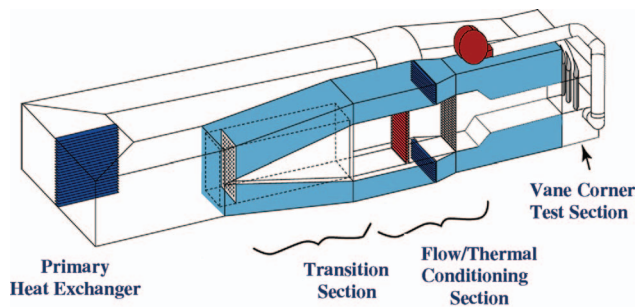


Fig. 1 Illustration of the wind tunnel facility

regions on a turbine vane endwall are most prone to this deposition phenomenon since this is the first relatively cold surface the hot mainstream flow encounters as it enters the turbine. Bons et al. [10] showed through their turbine surface measurements that the leading edge region will have the greatest degradation. Other turbine component measurements by Taylor [11] and Tarada and Suzuki [12] revealed that all regions of a turbine blade and vane are prone to deposition and surface roughening at varying levels.

Bonding of ash and other contaminants to turbine component surfaces is also dependent on the properties of the hardware. Some studies have been performed that specifically report the effects of surface roughness on film cooling. Goldstein et al. [13] placed cylindrical roughness elements at the upstream and downstream location of film-cooling holes on a flat plate. They observed that at low blowing rates, there is a decrease in adiabatic wall effectiveness by 10–20% over a smooth surface. However, at higher blowing rates, they observed an enhancement of 40–50% in cooling performance. Schmidt et al. [14] did a similar study using conical roughness elements. They found a higher degradation of film-cooling effectiveness at lower momentum flux ratios than at higher momentum flux ratios. Barlow and Kim [15] studied the effect of a staggered row of roughness elements on adiabatic effectiveness. They found that roughness degraded cooling effectiveness compared to a smooth surface and that smaller elements caused a greater reduction than larger elements.

In addition to these studies, Cardwell et al. [16] showed that an endwall surface with uniform roughness decreased cooling effectiveness at higher blowing ratios but at lower blowing ratios there was no significant change. More recently, Sundaram and Thole [17] conducted a study to investigate the effect of localized deposition at the leading edge of a vane endwall. Their results indicated that deposits of smaller heights placed in the leading edge region enhanced the adiabatic effectiveness levels. They also found that the adiabatic effectiveness levels degraded with the increase in deposit height.

In summary, the current literature contains few studies that have focused on understanding how surface deposition affects the film-cooling performance along an endwall in a turbine. The results from this study shed some new light onto the flow physics associated with film cooling along the pressure side of turbine vane endwall and thus allow improvements to be made in endwall designs.

Experimental Methodology

The cascade test section was placed in the closed loop wind tunnel facility shown in Fig. 1. The flow encounters an elbow downstream of the fan and passes through a primary heat exchanger used to cool the bulk flow. The flow is then divided into three channels including the center passage and two cooled secondary passages located above and below the test section. Note that only the top secondary passage was used for this study. The primary core flow, located in the center passage, passes through a heater bank where the air temperature is increased to about 60°C. The secondary flow, in the outer passage, was cooled to 20°C,

Table 1 Geometric and flow conditions

| | |
|--------------------------------|-------------------|
| Scaling factor | 9 |
| Scaled up chord length (C) | 59.4 cm |
| Pitch/Chord (P/C) | 0.77 |
| Span/Chord | 0.93 |
| Hole L/D | 8.3 |
| Re_{in} | 2.1×10^5 |
| Inlet and exit angles | 0 deg and 72 deg |
| Inlet, exit Mach number | 0.017 0.085 |
| Inlet mainstream velocity | 6.3 m/s |
| Upstream slot width | 0.024 C |

thereby maintaining a temperature difference of 40°C between the primary and secondary flows. The secondary flow provided the coolant through the film-cooling holes located on the endwall within the test section. For all of the tests carried out in this study, a density ratio of 1.1 was maintained between the coolant and mainstream flows. Since the density ratios were not matched to that of the engine, the velocity ratios for the cooling holes were significantly higher than those found in an engine for the same mass flux or momentum flux ratios. In this study, momentum flux ratios were set relevant to engine conditions as previous studies have shown that momentum flux ratios scale the jet lift-off well for flat plate cooling.

Downstream of the flow and thermal conditioning section is the test section that consists of two full vane passages with one center vane and two half vanes. Table 1 provides a description of the turbine vane geometry and operating conditions. The vane geometry used in the current study is a commercial first-stage vane previously described by Radomsky and Thole [18]. A detailed description of the endwall construction has been previously described by Knost and Thole [19] and Sundaram and Thole [17], who used the exact same film-cooling geometries that were used for this study. The endwall of the vane was constructed of 1.9 cm thick, low-density foam having a low thermal conductivity of 0.033 W/m K, which was mounted on a 1.2 cm thick Lexan plate. The cooling hole pattern on the endwall was cut with a five-axis water jet to ensure precision and integrity. The endwall surface was covered with 36 grit sandpaper to simulate a uniform surface roughness. The sandpaper corresponded to an equivalent sand grain roughness of 420 μm at the engine scale. In addition to the surface roughness, the endwall also simulated a combustor-turbine interface gap upstream of the vane and a vane-to-vane interface gap between the vanes. In all, the endwall used in this study simulated the geometries and surface conditions of an actual engine.

The inlet turbulence intensity and length scales were measured to be 1.3% and 4 cm, respectively. These tests were carried out at a low turbulence intensity of 1.3% to isolate the effects of deposits on endwall adiabatic effectiveness levels. For every test condition, the dimensionless pressure coefficient distribution was verified to ensure periodic flow through the passages. To set the coolant mass flow rate through the film-cooling holes, a global blowing ratio was calculated using an inviscid blowing ratio along with a global discharge coefficient C_D that was obtained from CFD studies reported by Knost and Thole [20].

Instrumentation and Temperature Measurements. A FLIR P20 infrared camera was used to spatially resolve adiabatic wall temperatures along the vane cascade endwall. Measurements were taken at six different viewing locations to ensure that the entire endwall surface was thermally mapped. The camera was placed perpendicular to the endwall surface at a distance of 55 cm from the endwall. Each picture covered an area of $24 \times 18 \text{ cm}^2$, with the area being divided into 320×240 pixel locations. The spatial integration circle of the camera had a diameter equal to 0.715 mm (0.16 hole diameters). Thermocouples were also placed on the

endwall surface at different locations to directly measure the temperature and to postcalibrate the infrared images. The postcalibration process involved setting the surface emissivity at a constant value of 0.92 and the background temperature ($\sim 45^\circ\text{C}$) was then adjusted until the temperatures from the infrared images were within 0.05°C of the corresponding thermocouple data. Six camera images were taken at each of the viewing locations and an in-house MATLAB program was used to obtain a single averaged picture. The same program was also used to assemble the averaged pictures at all locations to give a complete temperature distribution along the passage endwall.

Freestream temperatures were measured at multiple locations along the vane pitch and the average was determined by using a thermocouple rake consisting of three thermocouples along the span. It was found that the variations along the pitch were less than 0.2°C and along the span they were less than 1.5°C . Voltage outputs from the thermocouples were acquired using a 32 channel National Instruments data acquisition module and a 12 bit digitizing card. All temperature data were acquired and compiled after the system reached a steady state operating condition.

The one-dimensional conduction correction method described by Ethridge et al. [21] was applied in a point-by-point manner to all adiabatic effectiveness measurements made on the endwall surface. This correction involved measuring the endwall surface effectiveness without flow passing through the film-cooling holes. This required the film-cooling holes to be blocked on the endwall in the passage under study; however, similar film-cooling flow rates were maintained through the adjacent passage to ensure the correct boundary condition was established under the endwall. The resulting correction in adiabatic effectiveness η_o was found to be 0.16 at the entrance of the vane passage for a η_{meas} value of 0.9, and 0.02 at the exit of the vane passage for a η_{meas} value of 0.2.

Experimental Uncertainty. An uncertainty analysis was performed on the adiabatic effectiveness measurements using the partial derivative method described by Moffat [22]. The precision uncertainty was determined by taking the standard deviation of six measurement sets of IR camera images with each set consisting of six images. The precision uncertainty of the measurements was found to be $\pm 0.014^\circ\text{C}$. The bias uncertainty was $\pm 1.0^\circ\text{C}$ based on the camera specifications supplied by the manufacturer. The bias uncertainty of the thermocouples was $\pm 0.5^\circ\text{C}$. The total uncertainty was then calculated to be $\pm 1.02^\circ\text{C}$ for the infrared images and $\pm 0.51^\circ\text{C}$ for the thermocouples. The uncertainties in the measured adiabatic effectiveness η_{meas} and the correction adiabatic effectiveness η_o were determined based on its partial derivative with respect to each temperature in the definition and the total uncertainty in the temperature measurements. The uncertainty in the measured adiabatic effectiveness was then calculated to be $\partial\eta_{\text{meas}} = \pm 0.03$ for all values of η_{meas} . Similarly, there is an uncertainty associated with the correction adiabatic effectiveness, which was estimated to be $\partial\eta_o = \pm 0.03$ at all values of η_o . Hence the total uncertainty in the adiabatic effectiveness η was calculated to be $\partial\eta = \pm 0.04$ over the entire measured range.

Test Design. The primary aim of this study was to investigate the effects of surface deposition on the adiabatic effectiveness levels along the pressure side of the vane endwall. This study was designed to examine deposition on (1) the upstream and downstream sides of the cooling hole rows, (2) a single cooling hole row, and (3) multiple cooling hole rows. The tests were conducted for three different film-cooling mass flow rates corresponding to 0.5% ($M_{\text{in}}=1.6$), 0.75% ($M_{\text{in}}=2.3$), and 0.9% ($M_{\text{in}}=2.7$) of the total passage mass flow rate for one vane pitch. Note that for all cases there was a 0.75% coolant flow from the upstream slot, which simulated the combustor-turbine interface gap.

Figure 2 shows a schematic of a row of film-cooling holes and the location of the upstream and downstream deposition with respect to the cooling row. Figure 2 also illustrates the cross-

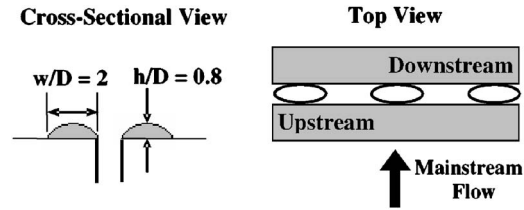


Fig. 2 Illustration of the deposit shape and geometry tested along the pressure side of the vane endwall

sectional shape of the semielliptical deposits used in this study. A detailed description of the shape and construction of the deposit was previously described by Sundaram and Thole [17]. For this study, a constant deposit height was used such that $h/D=0.8$ and $w/D=2$, where D is the film-cooling hole diameter. The deposit height was not varied in this study since Sundaram and Thole [17] showed that $h/D=0.8$ is representative of most results achieved for surface depositions.

Figure 3 shows the film-cooling hole arrangement on the pressure side of the vane endwall. Note that these holes are aligned in the axial direction such that they inject flow directly toward the vane. Studies were conducted with single row and multiple row deposits on the first four rows of cooling holes along the vane pressure side, where each row contains three holes. The first row is located nearest to the leading edge of the vane and the fourth row is located closer to the trailing edge. The deposit on the first row will be referred to as 1R1 where the first numeral designates the number of rows that have deposits, and the second numeral designates the row in which the deposit was placed. Similarly, the single row deposit on the second film-cooling row will be referred to as 1R2, the third row as 1R3, and the fourth row as 1R4. These studies were carried out for a low film-cooling flow rate of 0.5% and a high flow rate of 0.9% through the cooling holes.

Figure 4 shows a schematic of the configuration for multiple row deposition study. This study was carried out by sequentially increasing the number of row deposits from Rows 1–4 along the

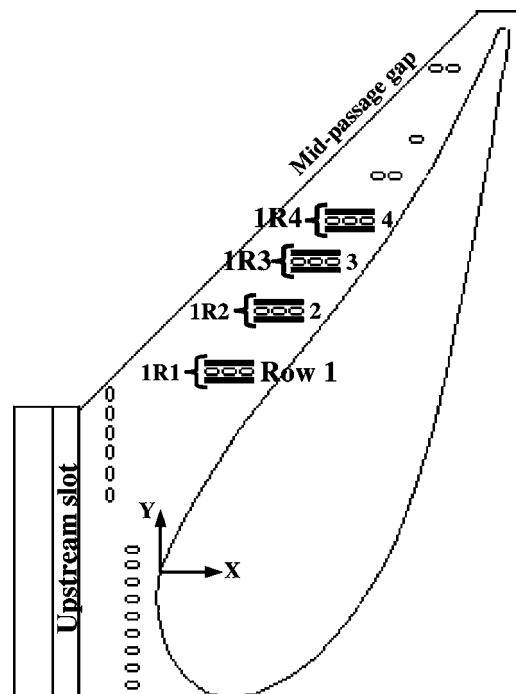


Fig. 3 Illustration of the single row deposition on the pressure side along four film cooling rows

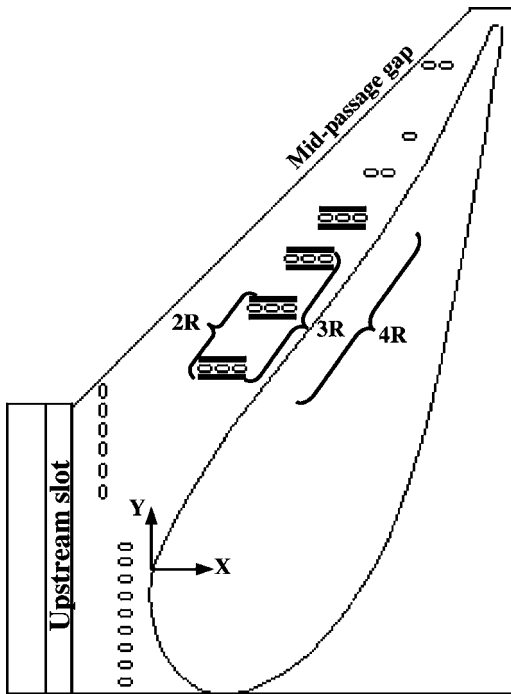


Fig. 4 Illustration of the multiple row deposition on the end-wall along the pressure side

pressure side. Deposits placed along Row 1 will be referred to as 1R, which is similar to the single row 1R1 configuration. When the deposits are placed simultaneously along Rows 1 and 2, it will be referred to as 2R. Similarly, the configuration where deposits are placed simultaneously along three and four film-cooling rows will be referred to as 3R and 4R, respectively.

Discussion of Results

Base line tests were conducted without any deposits on the pressure side of the rough endwall surface. Figures 5(a)–5(c) compare the contours of adiabatic effectiveness for the base line study with varying film-cooling flow rates. It was found that with an increase in flow rate, the adiabatic effectiveness levels increased on the pressure side. From Fig. 5(a), it can be seen that at a coolant flow rate of 0.5%, the coolant spreads in the direction of the mainstream passage flow. At this coolant level, the coolant exiting the film-cooling holes follows the mainstream flow path toward the suction side in spite of the coolant injection direction being toward the pressure side. As a result, there is a formation of a thin hot band along the endwall junction. With the increase in coolant flow rate to 0.75%, there is an improved streamwise spreading of the coolant resulting in an increase in the adiabatic effectiveness levels. For the 0.75% flow rate, the width of the hot band decreases in size as the coolant extends further along the endwall toward the vane-endwall junction. Further increasing the cooling flow rate to 0.9% resulted in a very small increase in adiabatic effectiveness levels with the coolant behavior being similar to the 0.75% case.

The overall effect of the cooling mass flow rate was quantified by examining the laterally averaged adiabatic effectiveness, $\bar{\eta}$. The lateral averaging was performed across the pitch in the streamwise direction within the boxed region shown in Fig. 5(a). Figure 6 shows the laterally averaged effectiveness for the 0.5% base line study along the pressure side. It can be seen that the effectiveness levels increase into the passage with the addition of coolant from each successive cooling row. However, downstream of Row 4 there is a decrease in $\bar{\eta}$ as the number of cooling holes in each row decreases.

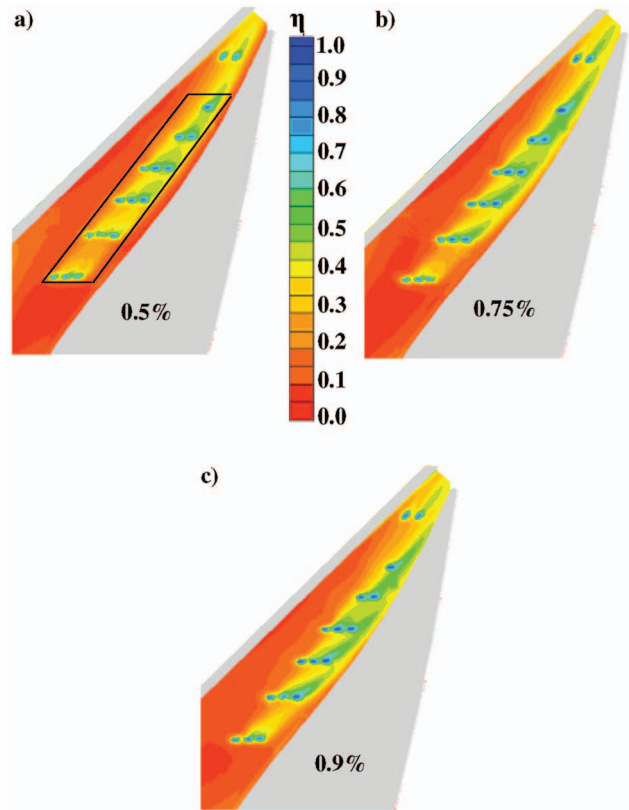


Fig. 5 Contours of adiabatic effectiveness showing the effect of increasing the film cooling mass flow rate on the pressure side for the base line study

Also shown in Fig. 6 is the augmentation in $\bar{\eta}$ as a result of increasing the coolant mass flow rate from 0.5% to 0.75% and 0.9%. Note that the values less than one are reductions in effectiveness levels and values greater than one are enhancements in effectiveness levels. An overall enhancement was achieved by increasing the coolant flow rate to 0.75% and a further increase to 0.9% resulted in minimal change in the enhancement levels. A flow rate of 0.9% showed higher effectiveness enhancement than 0.75% downstream of Rows 1 and 2; however, downstream of Row 3 the cooling flow rate of 0.75% showed higher effectiveness enhancement than 0.9%. This reduction in effectiveness levels

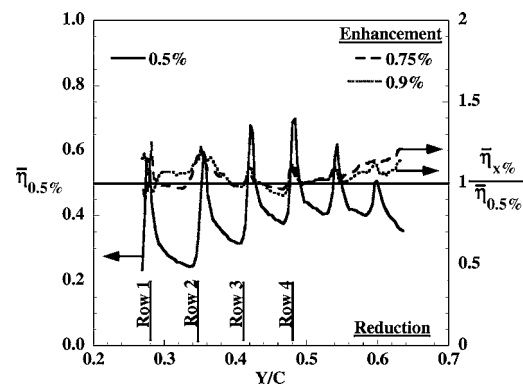


Fig. 6 Laterally averaged effectiveness for the base line study with 0.5% cooling flow rate, and enhancements in laterally averaged effectiveness for the 0.75% and 0.9% mass flow rates

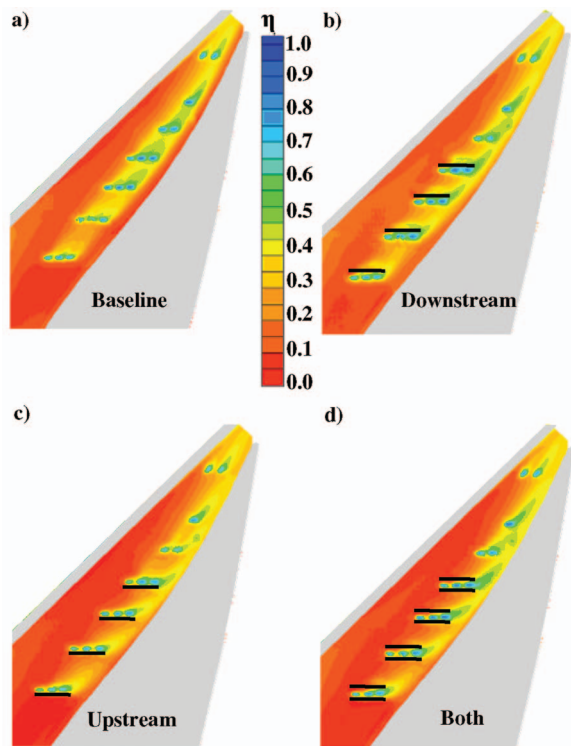


Fig. 7 Contours of adiabatic effectiveness comparing the effect of deposition at a film cooling flow rate of 0.5%

downstream of Row 3 at 0.9% coolant flow rate is because the jets are injected at a higher trajectory leading to more mixing with the mainstream flow.

Effect of Simultaneous Multiple Row Deposits. Surface measurements made on a vane endwall by Bons et al. [10] revealed that deposition could occur at any location around the film-cooling hole. To study these effects, the base line study results were compared to cases in which the deposits were placed at the upstream side, downstream side, and both upstream and downstream sides of the cooling rows.

Figures 7(a)–7(d) compare the contours of adiabatic effectiveness levels for the three deposit configurations with the base line study. Note that deposits were simulated for the first four rows of cooling holes with a constant coolant flow rate of 0.5% through the film-cooling holes. Comparisons were made at a constant coolant flow rate of 0.5% as it is more representative of actual engine conditions. Comparing the downstream deposition shown in Fig. 7(b) to the base line study in Fig. 7(a), it is seen that this deposit configuration causes an overall reduction in adiabatic effectiveness levels. The deposit deflects the coolant jets toward the vane-endwall junction on the pressure side, which is the designed direction of the jets. The deposit acts to locally reduce the endwall cross-passage pressure gradient near the holes that would otherwise pull the coolant toward the suction surface of the adjacent vane. As the coolant flows toward the junction, there is an overall reduction in effectiveness downstream of the cooling rows.

Upstream deposition shown in Fig. 7(c) resulted in more coolant flowing toward the endwall junction and caused a higher reduction in effectiveness levels downstream of the cooling rows, relative to downstream deposition. Similar to these results, placing deposits on both upstream and downstream sides of the cooling rows (Fig. 7(d)) resulted in the bulk of the coolant becoming more confined and streamlined toward the vane-endwall junction.

From Fig. 7(a), it can be seen that for the base line case, the coolant from the pressure side flowed more toward the suction side resulting in higher effectiveness downstream of the holes as

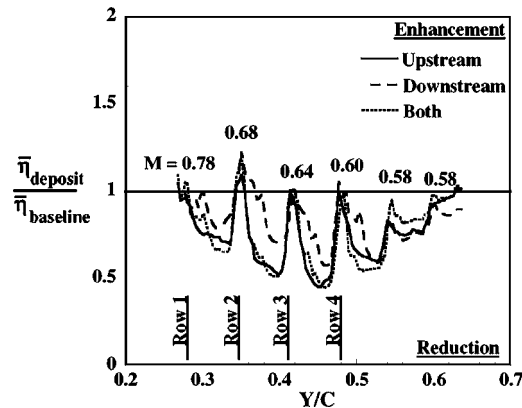


Fig. 8 Reduction in laterally averaged adiabatic effectiveness as a result of deposition located upstream, downstream, and on both sides of the cooling rows

compared to Figs. 7(b)–7(d). Placing deposits along the pressure side cooling holes redirected the coolant toward the vane-endwall junction on the pressure side causing an overall reduction in the effectiveness levels downstream of the cooling rows.

The above effects can be further quantified by comparing the laterally averaged effectiveness. Figure 8 shows the reduction in $\bar{\eta}$ as a result of deposits located upstream, downstream, and on both upstream and downstream sides of the cooling rows. Also shown in Fig. 8 are the average local blowing ratios for each row of holes along the pressure side for a coolant mass flow rate of 0.5%. Computational predictions of the local static pressure (and local external velocity at each hole location) were used to quantify the local coolant blowing ratios from each cooling hole. It was seen that deposits upstream of the cooling rows and on both upstream and downstream sides of the cooling rows caused similar and higher degradation than deposits placed downstream of the cooling rows. As such, it can be concluded that the upstream deposits have a more dominating effect than the downstream deposits on degrading the effectiveness when the deposits are placed on both upstream and downstream sides of the cooling rows. Note that the deposits were placed on the first four cooling hole rows, but the effects are present on all the six rows. This is because in the absence of the deposits the coolant from the upstream rows adds to the effectiveness of the downstream rows, but with deposits, the coolant gets deflected toward the vane-endwall junction. This causes a reduction in effectiveness levels downstream of the coolant rows and the effect cascades to all the six rows.

An overall effect of deposits on the adiabatic effectiveness levels can be compared by using the area averaged effectiveness. Note that the area used was that shown in the box in Fig. 5(a). Figure 9 compares the area averaged adiabatic effectiveness levels for the different deposit configurations with the base line study for each of the three film-cooling flow rates. At a film-cooling flow rate of 0.5%, the overall effectiveness levels are the lowest for deposition on the upstream and on both sides of the cooling rows. Reduction in adiabatic effectiveness levels were seen at all the three coolant flows for the three deposit configurations, relative to the base line study. As shown earlier, the adiabatic effectiveness levels improved with an increase in coolant flow for the base line study. A similar trend in increased effectiveness levels with increased coolant flow was seen for the downstream deposition, but the overall levels were still lower than the base line study. For deposition on the upstream location and on both upstream and downstream sides of the cooling row, an increase in effectiveness levels were seen from 0.5% to 0.75%, but a further increase to 0.9% reduced the effectiveness levels. The reduction in effectiveness levels for deposits on both sides was higher than the upstream deposition at a coolant flow rate of 0.9%. Deposits on both sides showed the highest reduction in effectiveness levels and

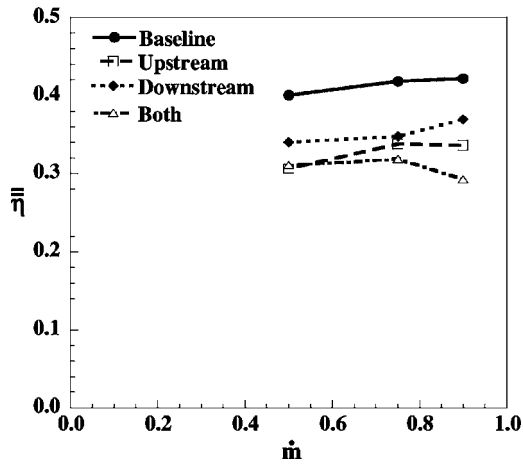


Fig. 9 Area averaged effectiveness comparing the base line study to the deposition located upstream, downstream, and both upstream and downstream

showed the combined effect of upstream and downstream depositions. As such, the configuration of placing deposits on both sides of the cooling rows was used to investigate the effects of single row and multiple row depositions.

Effect of Single Row Deposits. Tests were also performed by placing individual row deposits from Row 1 to Row 4 for film-cooling flow rates of 0.5% and 0.9%. The aim of these studies was to determine the row-to-row deposit interaction. Figure 10 compares the degradation in laterally averaged effectiveness as a result of single row deposition at a coolant mass flow rate of 0.5%. The smallest reduction in adiabatic effectiveness occurred at Row 1 for configuration 1R1. When the deposits were placed at Row 2, there was a 40% reduction caused by deposit 1R2 at that location and its effect is carried further downstream. Similarly, the local reduction in adiabatic effectiveness because of deposits 1R3 and 1R4 at location Row 3 and Row 4 was also found to be near 40%. It can be seen that at the location of the deposit there is a maximum reduction in adiabatic effectiveness levels.

The overall effect of single row deposits on the pressure side can be compared with the area averaged adiabatic effectiveness, as shown in Fig. 11. Adiabatic effectiveness values were averaged over the pressure side film-cooling rows for the area shown in Fig. 5(a) (boxed region). Figure 11 compares the effect of deposits with the base line study at a low coolant flow rate of 0.5% and a high coolant flow rate of 0.9%. Deposits placed in Row 1 resulted

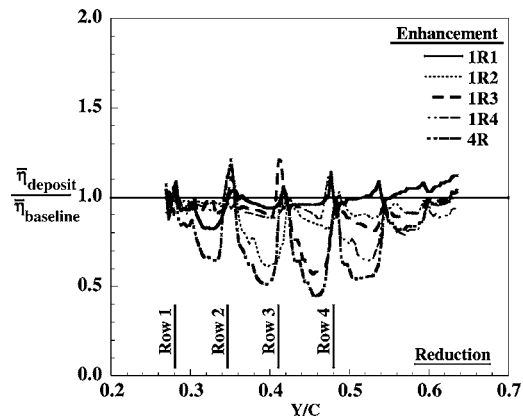


Fig. 10 Reduction in laterally averaged effectiveness as a result of single row deposits located along the pressure side at a coolant flow rate of 0.5%

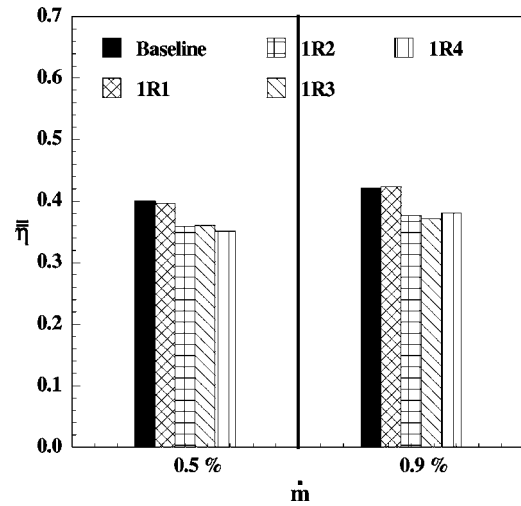


Fig. 11 Area averaged effectiveness comparing the effect of single row deposition with the base line for a low and a high film cooling flow rate

in very little effect on the overall effectiveness at both the coolant flow rates. This is explained by the fact that at Row 1 the local blowing ratio is higher than the succeeding cooling row within the passage, which results in coolant jet lift-off. As a result, the deposit at Row 1 does not deflect the coolant jets and hence there is no degradation in adiabatic effectiveness levels. Whereas the deposit configurations 1R2, 1R3, and 1R4, placed at Rows 2, 3, and 4, respectively, resulted in a similar overall degradation in effectiveness. It can be concluded that the individual effect of a single row deposit on the overall adiabatic effectiveness levels on the pressure side is independent of its location since it results in a similar overall reduction in effectiveness levels.

Effect of Sequentially Added Multiple Row Deposits. In addition to single row deposits, a study was conducted on the effects of multiple cooling row depositions along the pressure side. This was done by sequentially increasing the number of row deposits from one row (1R) to four rows (4R) along the pressure side. Figure 12 compares the degradation in laterally averaged adiabatic effectiveness with deposits placed on a single film-cooling row to those with deposits placed on two, three, and four rows at a coolant mass flow rate of 0.5%. It can be seen that the deposit at location 1R (same as deposit 1R1) has very little effect on the pressure side effectiveness levels, whereas deposit configurations 2R, 3R, and 4R have a substantial effect on lowering the effec-

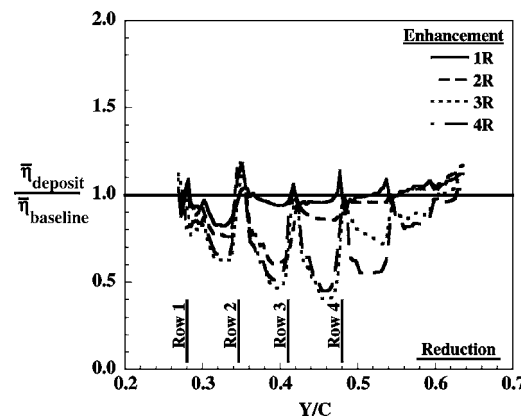


Fig. 12 Reduction in laterally averaged effectiveness as a result of sequentially added multiple row deposits on the pressure side at a coolant flow rate of 0.5%

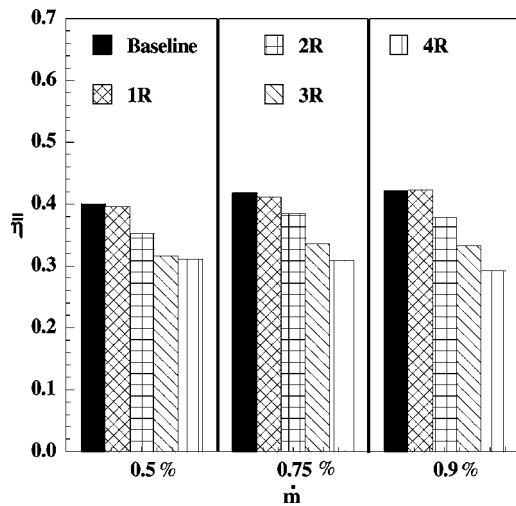


Fig. 13 Area averaged effectiveness comparing the effect of multiple row deposition with the base line for a low and a high film cooling flow rate

tiveness levels downstream of the film-cooling holes. Sequentially increasing the number of deposits rows had a cascading effect on lowering the effectiveness levels.

The overall result of multiple row deposits was further quantified by comparing the area averaged effectiveness levels along the pressure side. Figure 13 compares the effect of increasing the number of deposit rows with the base line study at coolant mass flow rates of 0.5%, 0.75%, and 0.9%. At the low mass flow rate of 0.5%, there is a reduction of 10% in effectiveness levels with the successive increase in the number of deposit rows from 1R to 3R. There was only a slight continued reduction in effectiveness levels from changing the deposit configuration from 3R to 4R. At the high flow rate of 0.9%, there was a near linear reduction of 10% in the area averaged effectiveness levels with a sequential increase in the number of row deposits. Note that the trends shown at the coolant flow rate of 0.75% were consistent with the high coolant flow rate of 0.9%. Multiple row deposits on the endwall were found to have a detrimental effect on the effectiveness levels along the pressure side. This multiple row deposition is most likely what occurs in an actual engine.

Superposition of Deposits. An overall comparison of the laterally averaged adiabatic effectiveness between the base line study, single row deposition study (1R1), and the multiple row deposition (4R) study is shown in Fig. 14 at a film-cooling flow rate of 0.5%. The question of whether or not the results from the four row deposit study (4R) can be accurately predicted by superimposing the results from single rows of deposits is an important one. Two superposition approaches were considered to determine if the results from a single hole row were cumulative.

The first method involved using the superposition method developed by Sellers [23] to predict the overall reduction in $\bar{\eta}$ due to multiple row deposition. The reduction in $\bar{\eta}$ at the first film-cooling row due to a single row deposit was calculated to be $\Delta \bar{\eta}_{1R1} = \bar{\eta}_{\text{baseline}} - \bar{\eta}_{1R1}$. Similarly, reductions along Rows 2, 3, and 4 were calculated to be $\Delta \bar{\eta}_{1R2}$, $\Delta \bar{\eta}_{1R3}$, and $\Delta \bar{\eta}_{1R4}$, respectively. Using the above single row reductions in adiabatic effectiveness, the overall reduction in adiabatic effectiveness $\Delta \bar{\eta}_{\text{overall}}$ was calculated by applying the method developed by the Sellers [23]. Then the predicted result was simply $\Delta \bar{\eta}_{4R} = \bar{\eta}_{\text{baseline}} - \Delta \bar{\eta}_{\text{overall}}$ and the result is shown in Fig. 15. It can be seen that this method resulted in overpredicting the degradation in $\bar{\eta}$ at each film-cooling hole row by about 40%.

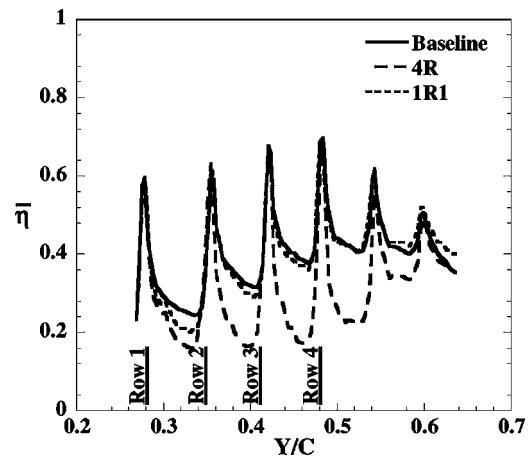


Fig. 14 Comparison of $\bar{\eta}$ between the base line and cases 1R1 and 4R (film cooling at 0.5%)

The second superposition method involved using the reduction in $\bar{\eta}$ from the base line due to adding a single row of deposits at each individual corresponding row of film-cooling holes. This resulted in a prediction of the form $\Delta \bar{\eta}_{4R} = \bar{\eta}_{\text{baseline}} - \Delta \bar{\eta}_{1R1} - \Delta \bar{\eta}_{1R2} - \Delta \bar{\eta}_{1R3} - \Delta \bar{\eta}_{1R4}$ and the results are also shown in Fig. 15. It can be seen that this second method also resulted in overestimating the reduction in $\bar{\eta}$ and the error at each film-cooling row was about 40% similar to Method 1.

This study indicates that there is not a linear cumulative effect in adding the reduction in resulting from the single row of deposits in order to predict the results when multiple rows of deposits are present. This is due to the fact that there is a varied effect that the deposits at the downstream hole row have on adiabatic effectiveness levels at the upstream hole rows. The degrading effect on the adiabatic effectiveness levels at the upstream hole row due to deposits on the downstream hole row is contingent upon the simultaneous presence of a deposit at the upstream location. This effect violates most superposition methods and hence there is a discrepancy between the predicted and measured adiabatic effectiveness levels. Another important result is that from viewing Figs. 10, 12, and 14, it can be seen that the third row was the row that was most affected by the presence of the deposits in both the single row configurations and the multiple row configurations.

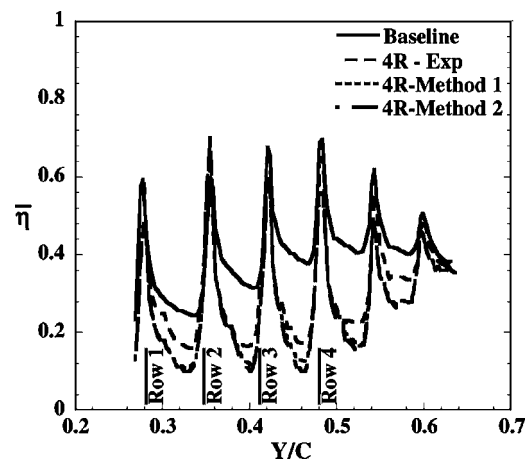


Fig. 15 Comparison of two superposition methods in predicting the results for the four row deposition study (film cooling at 0.5%)

Conclusions

Measurements of adiabatic effectiveness levels were presented on a turbine vane endwall with simulated surface depositions. The depositions were studied along the pressure side of the endwall, and were placed upstream, downstream, and on both sides of four rows of film-cooling holes. The focus of this paper was on evaluating the effect of single row, multiple row, and sequentially added deposits to the overall reductions that would occur for endwall film cooling. The effect of the deposits on endwall adiabatic effectiveness levels was compared with a base line study having no surface deposition.

It was found that deposition upstream and on both the upstream and downstream of the cooling holes resulted in similar and higher degradation in effectiveness levels than deposition located just downstream of the cooling holes. When using deposits on both the upstream and downstream regions of the cooling holes, the effect of a single row deposition was investigated. The single row deposits resulted in similar degradation of the total area averaged effectiveness that was independent of row location, with the exception of the first row, which showed little degradation.

Sequentially increasing the number of deposition rows resulted in a significant decrease in the overall adiabatic effectiveness levels. The results indicate that there is a linear reduction in adiabatic effectiveness levels with the sequential increase in the number of row deposits. This effect is more prominent at the higher coolant flow rate of 0.9% than at the lower flow rate of 0.5%.

Finally, the work presented in this paper indicates that by applying superposition methods the degradation in adiabatic effectiveness can be predicted within a 40% error. The overprediction using superposition occurs because of the large effect that the downstream deposits can have on upstream rows when deposits are placed along multiple rows.

Acknowledgment

This publication was prepared with the support of the US Department of Energy, Office of Fossil Fuel, and National Energy Technology Laboratory. Any opinions, findings, conclusions, or recommendations expressed herein are solely those of the authors and do not necessarily reflect the views of the DOE. The authors thank Mike Blair (Pratt & Whitney), Ron Bunker (General Electric), and John Weaver (Rolls-Royce) for their input on the modeling of realistic turbine features.

Nomenclature

| | |
|-----------|---|
| C | = true chord of stator vane |
| D | = diameter of film-cooling hole |
| h | = height of the deposit |
| L | = film-cooling hole length |
| M_{in} | = blowing ratio based on inlet mainstream velocity $M_{in} = \rho_j U_j / \rho_{in} U_{in}$ |
| \dot{m} | = coolant mass flow rate |
| P | = vane pitch, hole pitch |
| PS | = pressure side |
| Re_{in} | = Reynolds number defined as $Re_{in} = CU_{in} / \nu$ |
| S | = span of stator vane |
| T | = temperature |
| U | = velocity |
| w | = width of the deposit |
| X, Y, Z | = local coordinates |

Greek

| | |
|--------------------|--|
| η_{meas} | = measured adiabatic effectiveness, $\eta_{meas} = (T_{\infty} - T_{meas}) / (T_{\infty} - T_j)$ |
| η_o | = correction adiabatic effectiveness |
| η | = adiabatic wall effectiveness, $\eta = (\eta_{meas} - \eta_o) / (1 - \eta_o)$ |
| $\bar{\eta}$ | = laterally averaged effectiveness |
| $\bar{\bar{\eta}}$ | = area-averaged effectiveness |
| ν | = kinematic viscosity |

Subscripts

| | |
|----------|---|
| aw | = adiabatic wall |
| in | = inlet conditions |
| j | = coolant flow through film-cooling holes |
| ∞ | = local freestream conditions |

References

- [1] Bons, J. P., Crosby, J., Wammack, J. E., Bentley, B. I., and Fletcher, T. H., 2005, "High Pressure Turbine Deposition in Land Based Gas Turbines From Various Synfuels," ASME Paper No. GT2005-68479.
- [2] Wenglarz, R. A., 1985, "Deposition, Erosion, and Corrosion Protection for Coal-Fired Gas Turbines," ASME Paper No. 85-IGT-61.
- [3] Wenglarz, R. A., Nirmalan, N. V., and Daehler, T. G., 1995, "Rugged ATS Turbines for Alternate Fuels," ASME Paper No. 95-GT-73.
- [4] Decorso, S. M., Newby, R. A., Anson, D., Wenglarz, R. A., and Wright, I. G., 1996, "Coal/Biomass Fuels and the Gas Turbine: Utilization of Solid Fuels and Their Derivatives," ASME Paper No. 96-GT-76.
- [5] Moses, C. A., and Bernstein, H. L., 1996, "Fuel-Specification Considerations for Biomass Pyrolysis Liquids to be Used in Stationary Gas Turbines," ASME Paper No. 96-GT-406.
- [6] Wenglarz, R. A., 1992, "An Approach for Evaluation of Gas Turbine Deposition," ASME J. Eng. Gas Turbines Power, **114**, pp. 230–234.
- [7] Bons, J. P., Crosby, J., Wammack, J. E., Bentley, B. I., and Fletcher, T. H., 2005, "High Pressure Turbine Deposition in Land Based Gas Turbines From Various Synfuels," ASME Paper No. GT2005-68479.
- [8] Bornstein, N. S., 1996, "Reviewing Sulfidation Corrosion—Yesterday and Today," J. Minerals, Metals, and Materials Society, **48**(11), pp. 37–39.
- [9] Wright, I. G., Leyens, C., and Pint, B. A., 2000, "An Analysis of the Potential for Deposition, Erosion, or Corrosion in Gas Turbines Fueled by the Products of Biomass Gasification or Combustion," ASME Paper No. 2000-GT-0019.
- [10] Bons, J. P., Taylor, R. P., McClain, S. T., and Rivir, R. B., 2001, "The Many Faces of Turbine Surface Roughness," ASME J. Turbomach., **123**, pp. 739–748.
- [11] Taylor, R. P., 1990, "Surface Roughness Measurements on Gas Turbine Blades," ASME J. Turbomach., **112**, pp. 175–180.
- [12] Tarada, F., and Suzuki, M., 1993, "External Heat Transfer Enhancement to Turbine Blading Due to Surface Roughness," ASME Paper No. 93-GT-74.
- [13] Goldstein, R. J., Eckert, E. R. G., and Chiang, H. D., 1985, "Effect of Surface Roughness on Film Cooling Performance," ASME J. Eng. Gas Turbines Power, **107**, pp. 111–116.
- [14] Schmidt, D. L., Sen, B., and Bogard, D. G., 1996, "Effects of Surface Roughness on Film-Cooling," ASME Paper No. 96-GT-299.
- [15] Barlow, D. N., and Kim, Y. W., 1995, "Effect of Surface Roughness on Local Heat Transfer and Film Cooling Effectiveness," ASME Paper No. 95-GT-14.
- [16] Cardwell, N. D., Sundaram, N., and Thole, K. A., 2005, "Effects of Mid-Passage Gap, Endwall Misalignment, and Roughness on Endwall Film-Cooling," ASME J. Turbomach., **128**, pp. 62–70.
- [17] Sundaram, N., and Thole, K. A., 2006, "Effects of Surface Deposition, Hole Blockage, and Thermal Barrier Coating Spallation on Vane Endwall Film-Cooling," ASME J. Turbomach., **129**, pp. 599–607.
- [18] Radomsky, R., and Thole, K. A., 2000, "Flowfield Measurements for a Highly Turbulent Flow in a Stator Vane Passage," ASME J. Turbomach., **122**, pp. 255–262.
- [19] Knost, D. G., and Thole, K. A., 2004, "Adiabatic Effectiveness Measurements of Endwall Film Cooling for a First Stage Vane," ASME J. Turbomach., **127**, pp. 297–305.
- [20] Knost, D. G., and Thole, K. A., 2003, "Computational Predictions of Endwall Film Cooling for a First Stage Vane," ASME Paper No. GT2003-38252.
- [21] Ethridge, M. I., Cutbirth, J. M., and Bogard, D. G., 2000, "Scaling of Performance for Varying Density Ratio Coolants on an Airfoil With Strong Curvature and Pressure Gradient Effects," ASME J. Turbomach., **123**, pp. 231–237.
- [22] Moffat, R. J., 1988, "Describing the Uncertainties in Experimental Results," Exp. Therm. Fluid Sci., **1**, pp. 3–17.
- [23] Sellers, J. P., 1963, "Gaseous Film Cooling With Multiple Injection Stations," AIAA J., **1**, pp. 2154–2156.

The Augmentation of Internal Blade Tip-Cap Cooling by Arrays of Shaped Pins

Ronald S. Bunker
GE Global Research Center,
Niskayuna, NY 12309

The objective of the present study is to demonstrate a method to provide substantially increased convective heat flux on the internal cooled tip cap of a turbine blade. The new tip-cap augmentation consists of several variations involving the fabrication or placement of arrays of discrete shaped pins on the internal tip-cap surface. Due to the nature of flow in a 180 deg turn, the augmentation mechanism and geometry have been designed to accommodate a mixture of impingementlike flow, channel flow, and strong secondary flows. A large-scale model of a sharp 180 deg tip turn is used with the liquid crystal thermography method to obtain detailed heat transfer distributions over the internal tip-cap surface. Inlet channel Reynolds numbers range from 200,000 to 450,000 in this study. The inlet and exit passages have aspect ratios of 2:1, while the tip turn divider-to-cap distance maintains nearly the same hydraulic diameter as the passages. Five tip-cap surfaces were tested including a smooth surface, two different heights of aluminum pin arrays, one more closely spaced pin array, and one pin array made of insulating material. Effective heat transfer coefficients based on the original smooth surface area were increased by up to a factor of 2.5. Most of this increase is due to the added surface area of the pin array. However, factoring this surface area effect out shows that the heat transfer coefficient has also been increased by about 20–30%, primarily over the base region of the tip cap itself. This augmentation method resulted in negligible increase in tip turn pressure drop over that of a smooth surface. [DOI: 10.1115/1.2812333]

Introduction

The cooling of high temperature turbine blades must include all regions exposed to the hot gas flows. Blade tip turn regions are conventionally cooled using a combination of internal convection regions and external film and/or tip bleed cooling holes. One very common form of internal cooling is that of serpentine passages creating in essence a 180 deg turn region under the blade tip cap. In the case of closed-circuit cooled blades, whether by air or steam cooling, no film or tip bleed holes are present, so cooling is only by internal means. Such nonfilm cooled designs result in higher heat loads and potentially higher thermal stresses in the blade tip material, and therefore present greater cooling challenges. This is true of blade tips formed by integral investment casting, or by the joining of tip caps into blade castings. Methods of increasing the internal convective cooling in these tip-cap regions, both for open-circuit and closed-circuit cooling designs, are therefore required to increase blade life and reliability.

The present state of the art for cooling of blade internal tip turn regions, and the tip-cap surface of the 180 deg turn specifically, consists of the use of smooth (cast or machined) internal surfaces that are naturally augmented by the enhanced heat transfer coefficients due to the three-dimensional flow turning and pseudoimpingement present. The use of film cooling and tip bleed holes can increase the overall cooling effectiveness of these regions but are restricted to open-circuit, air-cooled designs and have only limited benefit due to the very complex nature of the tip region hot gas flow. Internal convective cooling is the primary means of assuring tip-cap integrity in all designs. The effect of

turning flow-induced secondary flows in the tip turn regions serves to somewhat lessen the natural cooling augmentation noted due to the radial inflow motion of the secondary flow. These secondary flows were detailed through particle imaging velocimetry measurements in the study of Schabacker et al. [1]. Their measurements at Reynolds number of 50,000 in a sharp 180 deg turn showed weak recirculating flows in the upstream corners of the turn, strong impingement flows over the initial and midturn regions, followed by a very dominant dual vortex pair generated in the downstream portion of the turn. The tip-cap heat transfer can be expected to follow these flow features in its distribution. For example, the corner regions of the turn should develop lower heat transfer coefficients due to flow recirculation. It is generally felt that such zones are minor and more than offset by the unsteadiness in the flow and the thermal averaging effects of the surrounding material.

In serpentine blades, the 180 deg turns under the blade tip are typically treated in design as surfaces of constant heat transfer coefficient of the order of two to three times that of fully developed turbulent duct flow at the same Reynolds number. In the study of Han et al. [2], mass transfer data were obtained for smooth surface tip turn surfaces with both smooth and turbulated inlet/exit channels. Their inlet and exit channels had aspect ratio of 1:1 with a rib divider gap equal to the hydraulic diameter. They found the all-smooth case with Re number of 30,000 to have an average tip heat transfer augmentation factor of 1.8 compared to the fully developed heat transfer in the inlet channel. A factor of 2.5 was found when the inlet/exit channels were turbulated to provide a far higher level of fluid turbulence; in essence, the inlet channel turbulence raised the entire level of augmentation for the tip surface internal heat transfer.

Strong centrifugal forces, in addition to the generally high passage Reynolds number, overcome the secondary flow effects and lead to heat transfer coefficients well above those of fully developed, stationary smooth duct flow. As such, rotational effects are

Contributed by the International Gas Turbine Institute of ASME for publication in the JOURNAL OF TURBOMACHINERY. Manuscript received June 6, 2007; final manuscript received June 23, 2007; published online July 31, 2008. Review conducted by David Wisler. Paper presented at the ASME Turbo Expo 2007: Land, Sea and Air (GT2007), Montreal, Quebec, Canada, May 14–17, 2007.

expected to have little or no detrimental influence on the tip-cap surface heat transfer. Mochizuki et al. [3] showed that rotational effects do not diminish the heat transfer coefficient enhancements on the internal tip-cap surface. Wagner et al. [4] tested a multipass serpentine channel with entirely smooth walls at both nonrotating and rotational number 0.24 conditions with Reynolds number of 25,000. The tip turn surface average heat transfer coefficient of the radially outflow channel was augmented by about 50%. However, Wagner et al. [5] performed a similar study in the same serpentine with repeated normal turbulators using the same overall flow conditions and found the average tip turn surface heat transfer coefficient augmentation to be about 10%. The turbulators of this latter study did not extend into the turn region. Both studies used channel aspect ratio of unity. From such prior evidence of averaged tip turn heat transfer, one may conclude that rotational effects will not degrade the tip surface heat transfer compared to stationary data and, in fact, might further augment cooling.

Heat transfer coefficient augmentation for tip turn internal surfaces depends on other factors as well, including the channel aspect ratio, transition of channel shape through the turn, Reynolds number, internal divider spacing to the tip surface, specific turbulence form of the inlet/exit channels, and also any other surface augmentation used through the turn region. A review of the tip turn geometries used in several previous studies is presented by Liou et al. [6], along with their own study of the effect of divider rib thickness. Virtually all past studies used either fully rounded, corner-rounded, or sharp 180 deg turns and generally confined the geometry to a 1:1 aspect ratio in the channel with the same aspect ratio between the divider and tip cap. This latter spacing has a definite effect on the turn flow field and heat transfer. One can visualize that a very large spacing would weaken the heat transfer on the tip-cap surface by allowing the flow to bypass through a large turn area. The general rule of thumb for this divider spacing is that it should be between one and two passage hydraulic diameters. This design rule is not substantiated in the literature relative to internal heat transfer effects but is actually imposed primarily for the control of turning pressure losses within the cooling circuits.

Several studies exist, such as that of Metzger et al. [7], in which turbulators are placed on the major adjacent walls through turning regions to provide uninterrupted heat transfer augmentation on all surfaces. Abuaf and Kercher [8] provided the detailed heat transfer coefficient distribution for a three-pass serpentine cooling circuit, in which the 180 deg tip turn major adjacent walls through turn regions (inside of the airfoil pressure and suction surfaces, not on the tip-cap surface) were turbulated to obtain continuous augmentation. In addition, other design features have been proposed and used, for example, by Metzger et al. [9] and also Rathjen et al. [10], in which a turning vane is placed in the turn path to further direct cooling flow at the tip-cap surface or to avoid low velocity flows in corners and around dividers. These turning vanes are positioned as connecting elements between the pressure and suction side internal surfaces, again not on the tip-cap surfaces.

A fairly large literature base exists concerning the augmentation of heat transfer coefficients through the use of pin or pedestal arrays of various shapes and spacing. This literature generally deals with either developed channel flows or jet impingement flow. The effect of pin-fin arrays on channel heat transfer is documented in the research of VanFossen [11] and also Metzger et al. [12], showing the substantial increase of heat transfer enhancement levels with successive pin rows. The effects of pin fillets, typically required for any cast features in cooled airfoils, are shown in the study of Wang et al. [13]. Pin arrays in the form of discrete shaped bumps have recently received increased attention as augmentation means for impingement cooling. The study of Son et al. [14] examined the use of cylindrical surface pins under

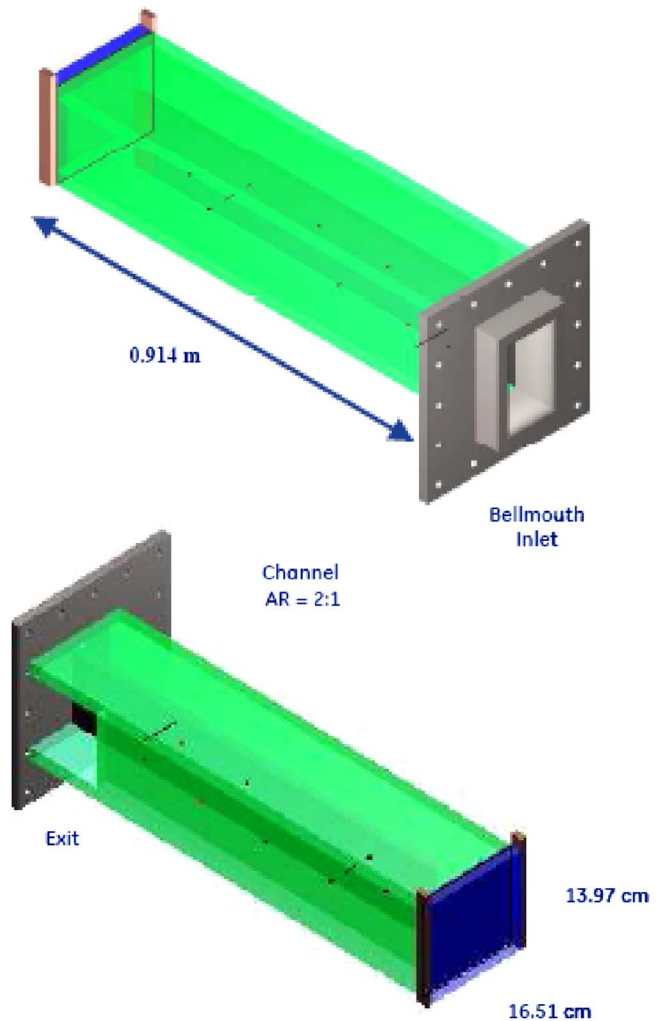


Fig. 1 General layout of test model

impingement jets for a flat surface, while that of Taslim et al. [15] investigated conical bumps to augment airfoil leading edge impingement cooling. Both studies found heat transfer to be augmented by at least the increased surface area ratio factor. Also of great significance was the finding that pressure losses were negligibly affected by the use of such surface methods with impingement flows.

The object of the present study is to develop a method to provide as much as twice the current smooth surface convective heat flux on the internal cooled tip-cap surface. This new tip-cap augmentation consists of several variations involving the fabrication or placement of arrays of discrete shaped pins on the internal tip-cap surface. Due to the nature of flow in a 180 deg turn, the augmentation mechanism and geometry must accommodate a mixture of impingementlike flow, channel flow, and strong secondary flows.

Experimental Approach

The overall test model is composed of a two-pass serpentine with sharp 180 deg tip turn as depicted in Fig. 1. As an average representative tip turn region, the inlet and exit flow passages were provided with an aspect ratio of 2:1, where the shorter walls are the airfoil pressure and suction sides. The two-pass tip turn model was scaled up to achieve a range of test Reynolds numbers from 200,000 to 450,000 with atmospheric pressure discharge

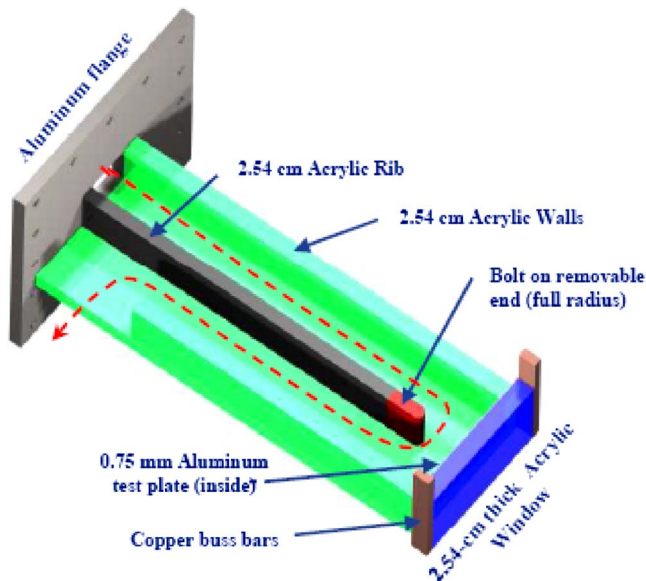


Fig. 2 Assembly view of test model

while maintaining a large enough size for full-surface data, as well as a small enough flow rate for in-house air supply. Each channel is 13.97 cm by 6.99 cm in size, with hydraulic diameter of 9.32 cm. Corresponding channel Mach numbers are from 0.091 to 0.192. A bellmouth inlet was used for the test model to reduce any inlet distortions. The inlet channel length is about ten hydraulic diameters. Both inlet and exit channels are smooth, without turbulators. Only the tip internal surface is heated in this model, which ignores any effect due to an upstream thermal flow development. This simplification is considered justified by the highly disrupted and three-dimensional nature of the tip turn flow, especially when tip surface augmentation is added. Figure 2 shows the assembly view of the test model. The internal separation rib is 2.54 cm thick, making the full tip-cap section 3.97 cm by 16.51 cm. A distance of 8.89 cm was used for the flow gap between the rib end and the tip cap, about the same as the channel hydraulic diameter as a rule of thumb. Figure 3 displays the monitoring pressures (P) and temperatures (T_c) for the model. The tip surface heat transfer coefficients are all based on the average of temperatures T_{c1} and T_{c2} , which differ by only a few degrees due to the large flow rate and limited heated surface area. The test method is that of thermochromic liquid crystals placed over an Inconel thin foil heater. The tip and other walls are made of 2.54 cm thick acrylic. Each test surface is formed of a 0.762 mm thick base aluminum plate with the desired features machined integrally. The liquid crystals and heater are trapped between the acrylic and the test surface. The color response of the liquid crystals is viewed from the outside of the model tip turn surface.

Surface temperatures are measured utilizing the liquid crystal video thermography method of Farina et al. [16]. A wide band

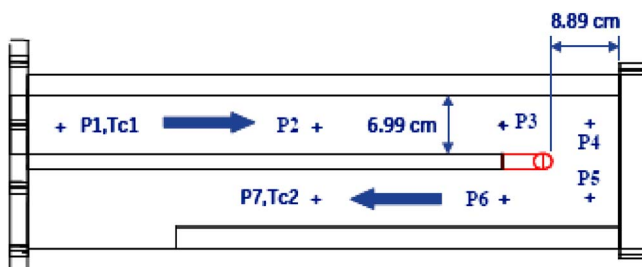


Fig. 3 Instrumentation locations



Fig. 4 Aluminum pin array test surface

liquid crystal (Hallcrest 40C5W) preapplied to a Mylar sheet was calibrated over its entire color band. A curve fit of liquid crystal hue versus calibration temperature was then used to calculate wall temperatures. The wall heater system was a stack up consisting of 2.54 cm of acrylic insulation, liquid crystal sheet, adhesive, foil heater, adhesive, and a 0.762 mm nominal aluminum plate. A thin aluminum plate was used to allow for machining of thermal enhancement features while minimizing thermal resistance. Though very thin, this plate will still result in some thermal spreading of the local heat transfer data; the main effects and even many details will still be apparent. A uniform heat flux boundary condition is created by applying high-current, low-voltage dc power to the foil heater. Liquid crystal images were taken with a red-green-blue (RGB) charge coupled device (CCD) camera. Each data set is comprised of four to six images taken at different heat flux settings. Heat losses were measured to be less than 2% of the total power input, as determined by nonflowing and internally insulated powered tests over the range of heater settings and also monitored by outside surface thermocouples. Radiation heat transfer is negligible in this test section relative to the total power and convective heat transfer. The definition of local heat transfer coefficient used in this study is

$$h = (Q_{\text{wall}}/A_{\text{wall}})/(T_{\text{surface}} - T_{\text{air average}})$$

where Q_{wall} is the power input to the heater divided by the heater area A_{wall} . The wall surface temperature is calculated using a one-dimensional temperature drop from the liquid crystal surface to the flow path surface. Experimental uncertainty in h , as calculated using the methods of Kline and McClintock [17], is between 8% and 15%. Higher uncertainty is associated with higher heat transfer coefficients. The flow rate uncertainty is $\pm 1\%$.

Five test surfaces were employed for this study, each with staggered pin arrays, described as follows:

1. smooth surface.
2. long aluminum pin array integrally machined on the 0.762 mm thick aluminum plate base as shown in Fig. 4. The pins have height Z of 8.13 mm, diameter of 4.06 mm,



Fig. 5 Aluminum base fillets with insulator pins

center spacing of 12.19 mm, pin tip radius of 1.524 mm, and pin base fillet radius of 3.05 mm. Each pin on this plate has a surface area enhancement of 4.07 relative to the smooth surface, but due to the array spacing, the total surface area enhancement is only 2.1.

3. long insulating pins on aluminum base fillets with the same dimensions as the long aluminum pins as shown in Fig. 5. The insulating material of the pins is Renshape, which has a very low thermal conductivity (1 W/m K). The insulating pins have attachment posts that extend inside the aluminum bases. The total surface thermal active area enhancement in this case is just 1.09.
4. short aluminum pin array of the same definition as above, in which the pin height is half, or 4.06 mm. An angled view of this pin array is shown in Fig. 6. Here, the surface area enhancement is 1.43.
5. short aluminum pin array with pin height of 4.06 mm and an increased density of pins achieved by decreased pin-to-pin spacing of 7.11 mm. As shown in Fig. 7, this spacing results in adjacent fillets that are almost touching. The surface area enhancement is 1.8.

In all of the aluminum pin geometries, the estimated fin conduction efficiencies are essentially 1.0. Tip turn gap distance is measured to the base of the pin array surface. It should be noted that the size and density of any pin array in the tip-cap region of a blade must be weighed against the possible added weight and resulting stress for the airfoil.

Results and Discussion

Smooth Surface. Figure 8 provides the smooth surface heat transfer coefficient distributions in the form of Nusselt numbers for Re numbers of 200,000, 310,000, and 440,000. The double vortex flow pattern typical of such turn regions in 2:1 aspect ratio channels is clearly evident, as is the impingementlike region at the inlet side of the tip turn. Figure 9 provides the local and averaged Nu numbers as normalized by the corresponding values for fully



Fig. 6 Short aluminum pin array

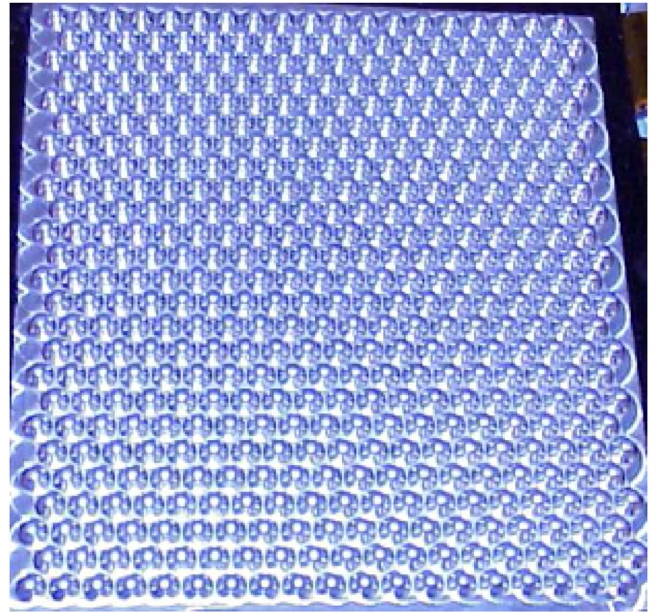


Fig. 7 Dense pin array

developed, turbulent flow heat transfer based on the inlet channel conditions. The fully developed channel Nu number was determined using the Dittus–Boelter correlation [18], as shown in Ref. [19], of $Nu=0.023 Re^{0.8}Pr^{0.3}$. The present data indicate an average tip turn surface heat transfer augmentation of only about 1.37–1.15, decreasing as Re is increased. This augmentation magnitude is much less than the 1.8 factor noted earlier from Ref. [2]. One possible reason for this lower augmentation is the much higher Re

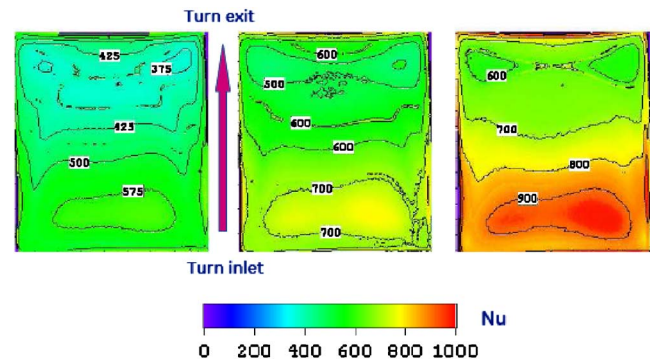


Fig. 8 Smooth tip turn Nu distributions for Re of 200,000, 310,000, and 440,000

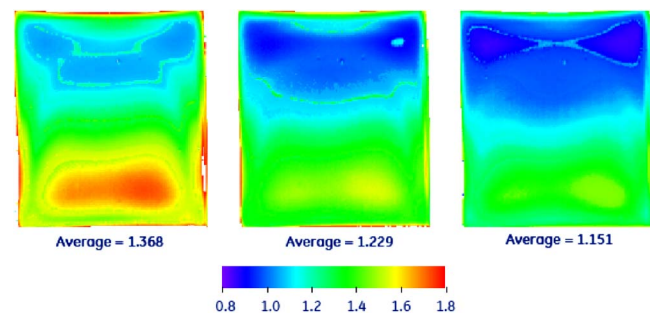


Fig. 9 Smooth surface tip heat transfer augmentation relative to fully developed, turbulent duct flow for Re of 200,000, 310,000, and 440,000

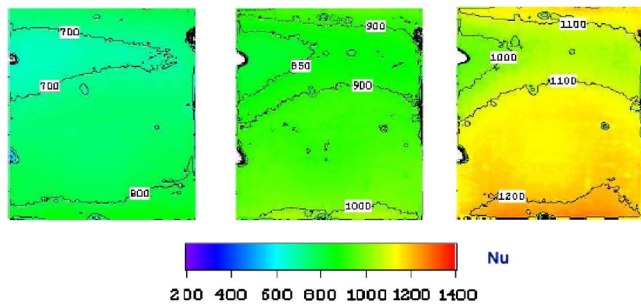


Fig. 10 Nu distributions for insulating pin array for Re of 200,000, 310,000, and 440,000

number of the present turn geometry, a full order of magnitude higher. As previously shown in the study of Bunker and Osgood [20], heat transfer coefficient enhancement magnitude can decrease as the Re increases at these higher Re levels, though the heat transfer coefficient itself continues to increase. In that study, a square channel was used with various turbulators at Re numbers from 50,000 to 400,000. The average enhancement decreased from about 2.25 to 1.75 over this range, a 22% decline. Applying the same factor to the data of Ref. [2] would result in a 1.4 factor of enhancement (treating the turn as a means for increased heat transfer, like turbulators). At the lowest Re of 200,000, local heat transfer enhancement factors are as high as 1.8. Another factor that may influence the comparison is the channel aspect ratio. The present study has aspect ratio of 2:1, while that of Ref. [2] used 1:1. This will most certainly affect the nature and strength of the secondary flows with the expectation that lower heat transfer regions of recirculating flows will be more significant in the present test geometry.

Pin Array With Fin Efficiency of Zero. Figure 10 shows the Nu distributions for the long pin array that has insulating material forming the cylindrical pin sections. Figure 11 provides the distributions of heat transfer coefficient enhancement factors relative to the smooth surface data of Fig. 8. The double vortex flow structure pattern seen in the smooth surface results is highly washed out to a more uniform distribution by the pin array. This is a result of the flow turbulence and secondary flow disruption produced locally by each pin and in ensemble by the array. Over the tip turn surface, heat transfer is highest in the inlet region. The heat flux augmentation factor is on average about 1.4, with the greatest augmentation of about 1.7 seen in the exit region of the tip-cap surface. This is a reversal of the augmentation behavior observed for the smooth surface. Recall that the surface area augmentation for this plate is only 1.09. Thus, the actual average enhancement to heat transfer coefficients that may be attributed to pin array turbulence effects is about 30% (the difference between 1.4 and

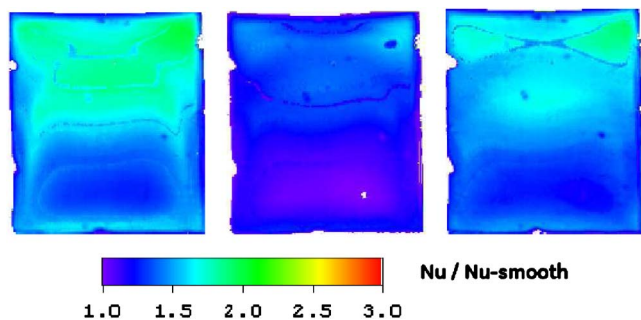


Fig. 11 Tall insulating pin array surface tip heat transfer augmentation relative to smooth surface for Re of 200,000, 310,000, and 440,000

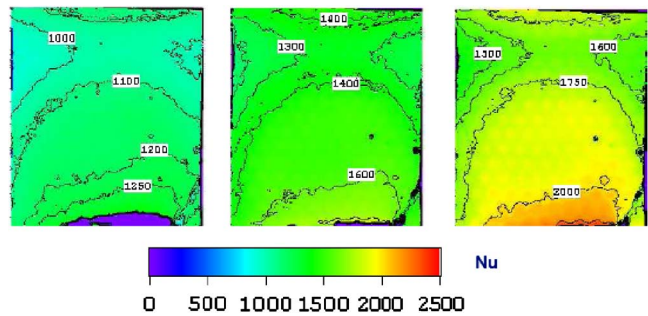


Fig. 12 Tall aluminum pin array Nu distributions for Re of 200,000, 310,000, and 440,000

1.09 factors). In the exit region, this enhancement increases to about 55%, probably due to the accumulated buildup of flow turbulence. These are significant enhancements realized over the entire surface, given that the pins are essentially thermally inactive here.

Pin Array With Fin Efficiency of Unity. The Nu distributions for the aluminum long pin array are shown in Fig. 12 (a small missing data region is apparent in one plot), while Fig. 13 provides the distributions of heat transfer enhancement factors (again relative to Fig. 8). Use of the high thermal conductivity pins now activates the full-surface area. The distributions show the local footprint of each and every pin. The effect of the double flow vortex is again washed out to a great degree. The overall average heat flux augmentation factor is now about 2.5. Here, too, the exit region displays the greater augmentation levels compared to the smooth surface. Recall that this surface has area augmentation of 2.1, resulting in a heat transfer coefficient average enhancement of about 20% over the entire surface. Combining this result with that of the insulated pins indicates that there is significant heat transfer coefficient enhancement on the base surface and fillets and little on the upper pin surfaces. The added pin surface area is, however, a definite benefit to increasing the total heat flux.

Increased Density Pin Array. Figure 14 shows the Nu distributions with a full-coverage array of essentially twice the number of pins, decreasing pin-to-pin spacing, and, at the same time, shorter pins of half the height. The overall heat flux enhancement is about 1.67 despite the surface area augmentation factor of 1.8. This result shows no added benefit to the much greater number of pins and associated surface area. It is speculated that, in this instance, the closer spacing of the pins is actually reducing the formation and intensity of individual wake regions and the consequent benefit to heat transfer. This shows that a definite minimum pin array spacing is present, below which heat transfer will actually decline. The apparent secondary flow structure indicated by

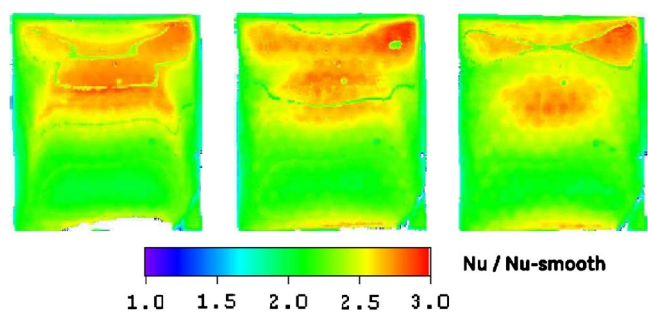


Fig. 13 Tall aluminum pin array surface tip heat transfer augmentation relative to smooth surface for Re of 200,000, 310,000, and 440,000

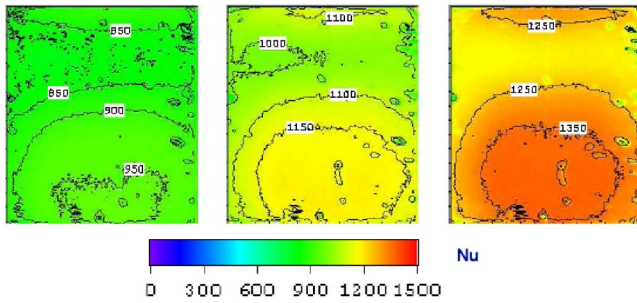


Fig. 14 Nu distributions for dense, shorter aluminum pin array for Re of 200,000, 310,000, and 440,000

the Nu contours shows a change in the inlet region to a more centralized impingement, possibly with lessened flow into the corners due to the denser pin array spacing.

Pin Array With Short Aluminum Pins. A final test was performed with the original pin array spacing but half-height pins. The shortened pin array surface area augmentation is only 1.43, reduced from the 2.1 factor of the longer pins. Figure 15 shows the Nu distribution for the highest Re number tested (Re = 387,000 for this case), compared with the corresponding highest Re data from each of the other test configurations (all on a common color scale). The average heat flux augmentation is actually increased in this case to 1.7. This provides a heat transfer coefficient augmentation of about 20%, which is the same as that of the longer pins.

Average Heat Transfer and Pressure Losses. The surface averaged values of Nu for all Reynolds numbers tested are summarized in Fig. 16. These Nu values have been corrected for a more typical engine material conductivity. An assessment of the fin efficiency change for a lower conductivity material such as steel or a nickel-based alloy rather than aluminum shows a reduction in individual fin efficiency to 89.8% of the aluminum level for the short pins and a reduction to 71.2% for the tall pins. These reductions, however, only apply to the portions of the surfaces occupied by the pins. In the wider spacing of pins, the pin occupied area is only 10% of the total, and in the denser array, is 26%. Furthermore, the fillet regions present negligible detriment in fin efficiency when a lower conductivity material is used, so only the cylindrical portions of the fins are of concern. Taking these factors

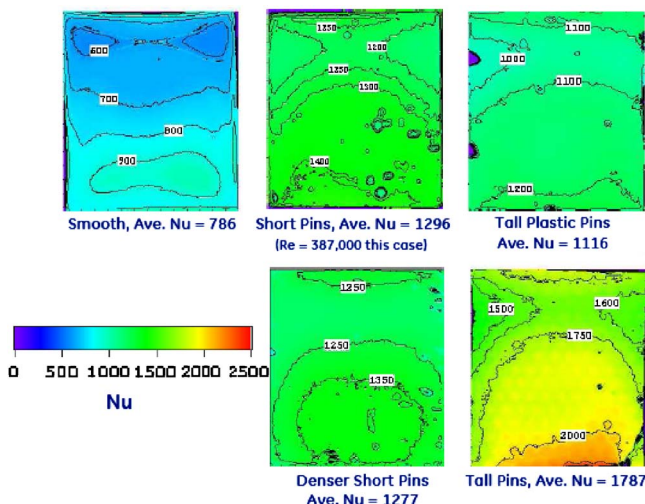


Fig. 15 Comparison of five tip turn surfaces at Re of 440,000

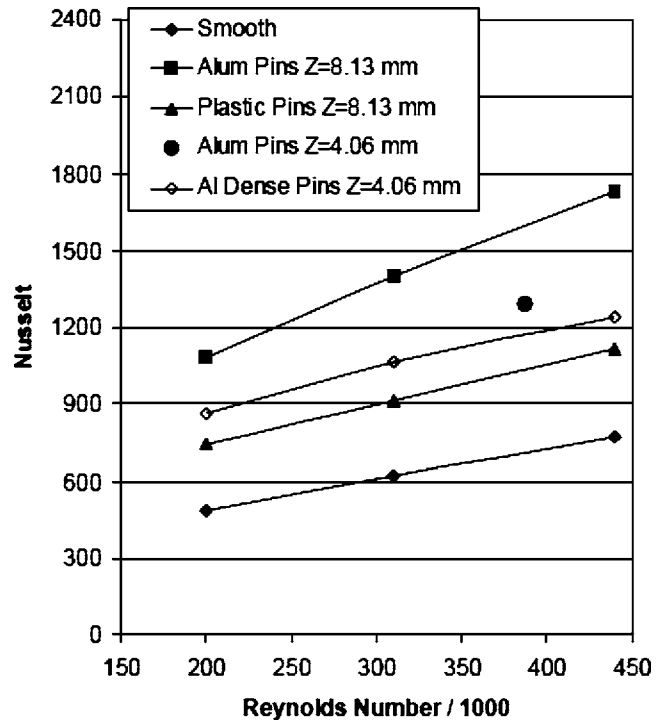


Fig. 16 Tip surface average Nu for all tests

into account, the correction in augmentation is at most -3% .

The standout heat transfer performance in this comparison is that of the tall pin array. This surface treatment provides both increased active surface area and augmentation of the heat transfer coefficients through flow turbulence and disruption. The benefits of this configuration also increase with Re to a greater degree, overcoming the tendency seen in the other results to lose enhancement magnitude. The surprising comparison is that the insulating pins perform nearly as well as the dense/shorter pin array. This is due to the benefits of flow turbulence when spacing allows such interactions over a larger surface area that has restricted flow access to the pins. The comparison shown in Fig. 16 is on the basis of what the engine component will experience, namely, the combined effect of increased surface area and augmented heat transfer coefficients. An alternate view of these data is presented in Fig. 17, in which the surface area factor has been removed from each data point and the resulting reduced Nu normalized by that of the corresponding fully developed turbulent duct flow value. The importance of the pin array's ability to turbulate the flow over the primary surface is emphasized here. It is also seen that this portion of the overall effect is substantially diminished as the Re number is increased.

Figure 18 provides the channel static gauge pressures measured at the designated locations (see Fig. 3) for three configurations, that of the smooth tip, the short pin array with higher spacing, and the tall pin array. At each nominal channel Re number condition, the treatment of the tip surface has an insignificant effect on pressure losses. Being an otherwise smooth channel, the tip turn pressure loss dominates under all tested conditions, with no additional loss due to the tip surface pin arrays.

Conclusions

The present study has demonstrated a method to provide substantially increased convective heat flux on the internal cooled tip-cap of a turbine blade. The new tip-cap augmentation consists of several variations involving the fabrication or placement of arrays of discrete shaped pins on the internal tip-cap surface. Due to the nature of flow in a 180 deg turn, the augmentation mecha-

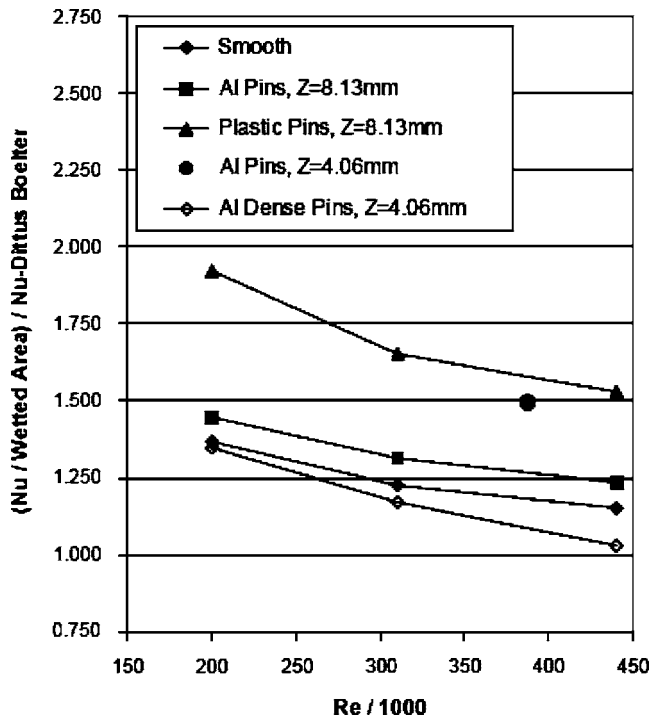


Fig. 17 Effect of pin array turbulence ability on heat transfer augmentation

nism and geometry have been designed to accommodate a mixture of impingementlike flow, channel flow, and strong secondary flows. The physics of the augmentation method combine two mechanisms. First, the short pin height-to-diameter ratio of 2 or less assures that the majority of the pin and fillet surface areas are effective as heat transfer wetted area. Second, the placement of such pins on the turning surface represented by the tip cap allows a combination of impingement and cross flow convection over the pins, which generates flow mixing and turbulence on the local level and as interactions in the array format. This specific flow-

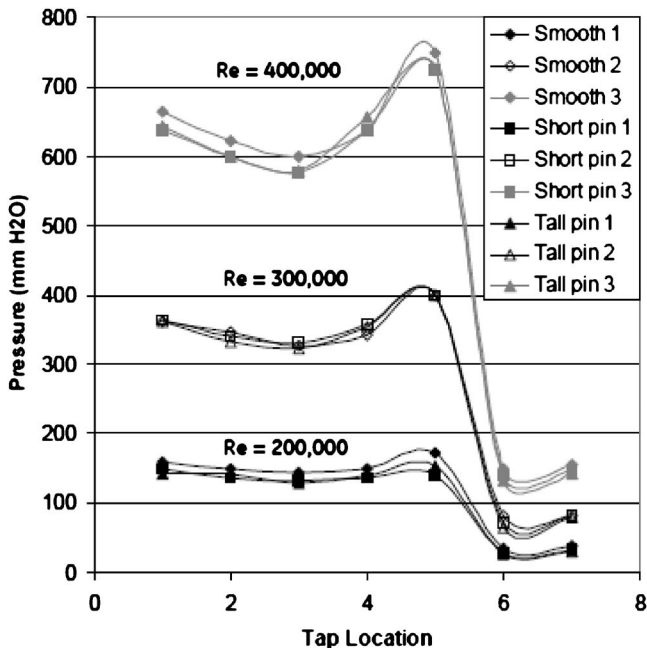


Fig. 18 Test model pressure distribution comparisons

surface interaction serves to at least partially disrupt the secondary flows that otherwise might decrease heat transfer on this surface. Effective heat transfer coefficients based on the original smooth surface area were increased by up to a factor of 2.5. Most of this increase is due to the added surface area of the pin array. However, factoring this surface area effect out shows that the heat transfer coefficient has also been increased by about 20–30%, primarily over the base region of the tip cap itself. This augmentation method resulted in negligible increase in tip turn pressure drop over that of a smooth surface. One additional point is worth noting for this application. While pin height plays an important role in overall heat flux enhancement through the addition of wetted area, pin spacing can severely affect the outcome. Pin spacing that is too close has been shown to lead to heat flux enhancement that is actually less than the area increase, a result that is counter to the intent.

Nomenclature

- A = wall heated surface area
- D = channel hydraulic diameter
- h = heat transfer coefficient
- k = thermal conductivity of air
- Nu = Nusselt number, hD/k
- Q = wall heat flux
- Re = channel Reynolds number, $\rho V D / \mu$
- T_c = cooling fluid temperature
- V = mean fluid velocity
- Z = pin height
- ρ = fluid density
- μ = fluid dynamic viscosity

References

- [1] Schabacker, J., Boelcs, A., and Johnson, B. V., 1998, "PIV Investigation of the Flow Characteristics in an Internal Coolant Passage With Two Ducts Connected by a Sharp 180-deg Bend," ASME Paper No. 98-GT-544.
- [2] Han, J. C., Chandra, P. R., and Lau, S. C., 1988, "Local Heat/Mass Transfer Distributions Around Sharp 180-deg Turns in Two-Pass Smooth and Rib-Roughened Channels," ASME J. Heat Transfer, **110**, pp. 91–98.
- [3] Mochizuki, S., Takamura, J., Yamawaki, S., and Yang, W. J., 1994, "Heat Transfer in Serpentine Flow Passages With Rotation," ASME J. Turbomach., **116**, pp. 133–140.
- [4] Wagner, J. H., Johnson, B. V., and Kopper, F. C., 1991, "Heat Transfer in Rotating Serpentine Passages With Smooth Walls," ASME J. Turbomach., **113**, pp. 321–330.
- [5] Wagner, J. H., Johnson, B. V., Graziani, R. A., and Yeh, F. C., 1992, "Heat Transfer in Rotating Serpentine Passages With Trips Normal to the Flow," ASME J. Turbomach., **114**, pp. 847–857.
- [6] Liou, T. M., Tzeng, Y. Y., and Chen, C. C., 1998, "Fluid Flow in a 180-deg Sharp Turning Duct With Different Divider Thicknesses," ASME Paper No. 98-GT-189.
- [7] Metzger, D. E., Bunker, R. S., and Fan, C., 1984, "Acquisition of Detailed Heat Transfer Behavior in Complex Internal Flow Passages," Advances in Aerospace Propulsion, Report No. SAE SP-594, pp. 47–54.
- [8] Abuaf, N., and Kercher, D. M., 1992, "Heat Transfer and Turbulence in a Turbulated Blade Cooling Circuit," ASME Paper No. 92-GT-187.
- [9] Metzger, D. E., Plevich, C. W., and Fan, C. S., 1984, "Pressure Loss Through Sharp 180-deg Turns in Smooth Rectangular Channels," ASME J. Eng. Gas Turbines Power, **106**, pp. 677–681.
- [10] Rathjen, L., Hennecke, D. K., Bock, S., and Kleinstueck, R., 2001, "Detailed Heat/Mass Transfer Distributions in a Rotating Two Pass Coolant Channel With Engine-Near Cross Section and Smooth Walls," *Heat Transfer in Gas Turbine Systems*, R. Goldstein, ed., New York Academy of Sciences, New York; 2001, Ann. N.Y. Acad. Sci., **934**, pp. 432–439.
- [11] VanFossen, G. J., 1982, "Heat Transfer Coefficients for Staggered Arrays of Short Pin Fins," ASME J. Eng. Power, **104**, pp. 268–274.
- [12] Metzger, D. E., Berry, R. A., and Bronson, J. P., 1982, "Developing Heat Transfer in Rectangular Ducts With Staggered Arrays of Short Pin Fins," ASME J. Heat Transfer, **104**, pp. 700–706.
- [13] Wang, Z., Ireland, P., Jones, T. V., and Kohler, S. T., 1994, "Measurements of Local Heat Transfer Coefficient Over the Full Surface of a Bank of Pedestals With Fillet Radii," ASME Paper No. 94-GT-307.
- [14] Son, C., Gillespie, D., Ireland, P., and Dailey, G. M., 2000, "Heat Transfer Enhancement Strategy for an Impingement Cooling System," *Proceedings of the Eighth International Symposium on Transport Phenomena and Dynamics of Rotating Machinery*, Pacific Center of Thermal-Fluids Engineering, Maui, Hawaii, Vol. 2, pp. 721–729.
- [15] Taslim, M. E., Setayeshgar, L., and Spring, S. D., 2002, "An Experimental

- Evaluation of Advanced Leading Edge Impingement Cooling Concepts," ASME J. Turbomach., **123**, pp. 147–153.
- [16] Farina, D. J., Hacker, J. M., Moffat, R. J., and Eaton, J. K., 1994, "Illuminant Invariant Calibration of Thermochromic Liquid Crystals," *Exp. Therm. Fluid Sci.*, **9**, pp. 1–9.
- [17] Kline, S. J., and McClintock, F. A., 1953, "Describing Uncertainties in Single-Sample Experiments," *Mech. Eng. (Am. Soc. Mech. Eng.)*, Jan., pp. 3–8.
- [18] Dittus, F. W., and Boelter, L. M. K., 1930, *Bandaoti Xuebao*, **2** (Berkeley Publications, University of California).
- [19] Holman, J. P., 1976, *Heat Transfer*, 4th ed., McGraw-Hill, New York, p. 204.
- [20] Bunker, R. S., and Osgood, S. J., 2003, "The Effect of Turbulator Lean on Heat Transfer and Friction in a Square Channel," ASME Paper No. GT2003-38137.

Measurements in Film Cooling Flows With Periodic Wakes

Kristofer M. Womack

Ralph J. Volino
e-mail: volino@usna.edu

Mechanical Engineering Department,
United States Naval Academy,
Annapolis, MD 21402

Michael P. Schultz
Naval Architecture and Ocean
Engineering Department,
United States Naval Academy,
Annapolis, MD 21402

Film cooling flows subject to periodic wakes were studied experimentally. The wakes were generated with a spoked wheel upstream of a flat plate. Cases with a single row of cylindrical film cooling holes inclined at 35 deg to the surface were considered at blowing ratios of 0.25, 0.50, and 1.0 with a steady freestream and with wake Strouhal numbers of 0.15, 0.30, and 0.60. Temperature measurements were made using an infrared camera, thermocouples, and constant current (cold-wire) anemometry. Hot-wire anemometry was used for velocity measurements. The local film cooling effectiveness and heat transfer coefficient were determined from the measured temperatures. Phase locked flow temperature fields were determined from cold-wire surveys. Wakes decreased the film cooling effectiveness for blowing ratios of 0.25 and 0.50 when compared to steady freestream cases. In contrast, effectiveness increased with Strouhal number for the 1.0 blowing ratio cases, as the wakes helped mitigate the effects of jet lift-off. Heat transfer coefficients increased with wake passing frequency, with nearly the same percentage increase in cases with and without film cooling. The time resolved flow measurements show the interaction of the wakes with the film cooling jets. Near-wall flow measurements are used to infer the instantaneous film cooling effectiveness as it changes during the wake passing cycle. [DOI: 10.1115/1.2812334]

Introduction

Film cooling has been studied extensively for over four decades, but most investigations have focused on flows with steady inflow conditions. The flow in a gas turbine engine, however, is inherently unsteady. Some unsteadiness results from nonuniformity in the flow exiting the combustor, which has been considered in some recent studies (e.g., Varadarajan and Bogard [1]). Turbine flows also have high freestream turbulence, which increases mixing between the main and cooling flows. This tends to cause faster dispersion of the coolant away from the surface, leading to lower film cooling effectiveness η and higher heat transfer coefficients, both of which reduce the benefits of film cooling. High freestream turbulence can also increase η in some cases, however, by increasing lateral spreading of the coolant from discrete holes. If film cooling jets lift off a surface, as is possible at high blowing ratios, high freestream turbulence can also help bring coolant back toward the surface. Several studies have examined high freestream turbulence effects, including Bons et al. [2], Kohli and Bogard [3], Ekkad et al. [4], and Burd et al. [5].

Another source of unsteadiness is the interaction between vane and blade rows in the turbine. Upstream airfoils shed wakes, which periodically impinge on the airfoils downstream. The wakes include a mean velocity deficit and increased turbulence, with effects similar to those of the increased freestream turbulence noted above. Wakes can disrupt film cooling jets, reducing the film cooling effectiveness in some areas and possibly enhancing it in others. Wake induced turbulence may also increase heat transfer coefficients, thereby reducing the overall benefit of film cooling. Airfoils passing both upstream and downstream of a turbine passage also cause periodic flow blockage, inducing pressure fluctuations which may cause film cooling jets to pulsate. None of these potentially important effects are captured in steady flow experiments. The incomplete knowledge of unsteady cooling flow behavior is typically overcome by supplying enough cooling air to prevent damage to all components in the turbine. This can lead to

overcooling in some areas, reducing engine efficiency. While steady flow studies have resulted in great advances in engine cooling, unsteady flow studies, particularly those which capture transient behavior, may lead to more efficient use of cooling air and increased engine efficiency.

A few studies have investigated the effect of wakes on film cooling. Funazaki et al. [6,7] considered flow around the leading edge of a blunt body subject to wakes produced by an upstream spoked wheel. They provide time averaged film cooling effectiveness results and note that the wakes tended to reduce η particularly at low blowing rates. When the cooling jet momentum was high, particularly if the jets lifted off the surface, the wake effect was reduced. Ou et al. [8] and Mehendale et al. [9] used a linear cascade with a spoked wheel to generate wakes. They note that heat transfer coefficients increased and film cooling effectiveness decreased with increased wake strength. Jiang and Han [10] similarly used a linear cascade with a spoked wheel, and present time averaged effectiveness results. They studied the effect of coolant injection from multiple hole locations in the showerhead region and on both sides of their airfoil. Results varied, depending on jet location, blowing ratio, the tendency of the coolant jets to lift off at each location, and jet density. High freestream turbulence resulted in lower effectiveness in all cases. Ekkad et al. [4] conducted a similar study and present film cooling effectiveness and local time averaged Nusselt numbers. They note that in the presence of very high freestream turbulence, the additional effect of periodic wakes is relatively small. Du et al. [11,12] also utilized a cascade and spoked wheel. They used a transient liquid crystal technique to obtain detailed time averaged film cooling effectiveness and Nusselt number distributions from an airfoil surface. They note that the wake effect on Nusselt numbers is small, but that wakes have a significant effect on film cooling effectiveness. Teng et al. [13–15] used a similar facility and also documented film cooling effectiveness and Nusselt numbers. They also used a traversing cold-wire probe to measure the flow temperature in planes downstream of the film cooling holes. They present time averaged mean and fluctuating temperature results. The unsteady wakes caused a faster dilution of the coolant jet. Higher blowing rates also result in more rapid mixing. The effects of wakes and blowing ratio on boundary layer transition were also reported. Heidmann et al. [16] used a rotating facility to investigate the

Contributed by the International Gas Turbine Institute of ASME for publication in the JOURNAL OF TURBOMACHINERY. Manuscript received June 6, 2007; final manuscript received June 22, 2007; published online July 31, 2008. Review conducted by David Wisler. Paper presented at the ASME Turbo Expo 2007: Land, Sea and Air (GT2007), Montreal, Quebec, Canada, May 14–17, 2007.

effect of wakes on showerhead film cooling. They report time averaged film effectiveness. The geometry tended to prevent jet lift-off, so η increased with blowing ratio. Higher wake passing rates skewed the coolant distribution, producing higher effectiveness on the pressure side of the airfoil and lower effectiveness on the suction side. Wolff et al. [17] utilized a three blade linear cascade in a high speed facility with one row of cooling holes on the suction side and one row on the pressure side of their center blade. Wakes were generated with rods fastened to belts which traveled around the cascade and two pulleys. Phase averaged velocity and turbulence levels were documented in multiple planes on both sides of the airfoil. The locations of the coolant jets were surmised from the mean velocity deficit and the turbulence level in the boundary layer. The effect of the pressure side coolant jets was reinforced by the passing wakes. On the suction side, the coolant jets were disrupted and nearly disappeared when the wake passed, but then recovered between wake passings. Adami et al. [18] did numerical simulations of the flow through this cascade.

While the above studies provide valuable information concerning the time averaged effects of wakes on film cooling, and a few provide time averaged flow field documentation, there is little information about the transient flow behavior during wake passing events. Such information could be valuable. If it is learned that film cooling jets provide effective coverage of the surface during part of the wake passing cycle but are dispersed as the wake passes, a change in design might be warranted to provide better coverage over the full cycle. Alternatively, the jets might be turned off during part of the cycle to only provide coolant when it is effective. Since film cooling jets pulse naturally in response to pressure fluctuations in the engine, it might be possible through clocking to time the jet pulses favorably with respect to wake passing events.

In the present study, film cooling jets were subject to wakes generated with upstream rods. The geometry consisted of a flat plate with a single row of five streamwise oriented round holes inclined at 35 deg to the surface. The holes were spaced $3D$ apart, center to center, with a length to diameter ratio $L/D=4$. The geometry has been used in many studies including Bons et al. [2], Burd and Simon [19], Schmidt et al. [20], Pedersen et al. [21], Kohli and Bogard [22], Sinha et al. [23], and Pietrzyk et al. [24]. Blowing ratios of 0.25, 0.5, and 1.0 were investigated with various wake passing frequencies. Phase averaged flow temperature distributions, and time averaged film cooling effectiveness and heat transfer results are presented below.

Experimental Facility and Measurements

Experiments were conducted in the facility used by Coulthard et al. [25–27]. It consists of an open loop subsonic wind tunnel with a test plate at the exit of the contraction, and a plenum to supply the film cooling jets. The wind tunnel, shown in Fig. 1, was comprised of a blower, a diffuser with three screens, a heat exchanger to maintain air nominally at 20°C, a honeycomb, a settling chamber with three screens, and a nozzle with an 8.8 area reduction. The nozzle exit area was $0.38 \times 0.10 \text{ m}^2$. The exiting mainstream air was uniform in temperature and velocity to within 0.1°C and 1%, respectively. The freestream turbulence intensity at the nozzle exit was 1%. This value is lower than typical intensity levels in engines. Air exiting the nozzle forms a wall jet at $U_\infty=8 \text{ m/s}$ along the flat plate test wall. The mainstream velocity remained at 8 m/s $18D$ downstream of the film cooling holes. At this downstream location, the velocity outside the boundary layer was uniform up to the edge of the free shear layer, which was located $3D$ from the wall. The freestream unsteadiness level gradually increased in the streamwise direction to 6%. This increase is due to the growth of the shear layer at the edge of the wall jet. Spectral measurements indicate that the freestream fluctuations are nearly all at frequencies between 5 Hz and 50 Hz, with a peak at 22 Hz. These low frequencies are associated with large scale structures formed in the shear layer, which buffet the

boundary layer but do not promote significant turbulent mixing. The boundary layer is therefore expected to behave as if subject to low freestream turbulence, and the heat transfer coefficient results by Coulthard et al. [27] are typical of low freestream turbulence conditions. The wall jet configuration is based on the facility of Burd and Simon [19].

The film cooling supply plenum was a box with $0.38 \times 0.18 \times 0.36 \text{ m}^3$ inside dimensions. It was supplied by a manifold connected to a high pressure air source. The supply pressure was adjusted to vary the blowing ratio from $B=0.25$ to 1.0. The air passed through small diameter valves which choked the flow between the manifold and the plenum. For a given supply pressure, the film cooling mass flow remains constant, independent of downstream conditions. Nine valves operating in parallel provided the desired coolant mass flow. The plenum contained a finned tube heat exchanger, midway between the valves and the film cooling holes. Warm water at 30°C circulated through the tubes and the air from the valves passed over the tubes, maintaining the temperature of the coolant jets at approximately 27°C.

The test wall was constructed of polyurethane foam with a thermal conductivity of 0.03 W/mK. The dimensions were 0.38 m wide, 44 mm thick, and 1.17 m long, with a starting length of $13.3D$ upstream of the row of film cooling holes. A wall opposite the starting length and sidewalls along the length of the test wall, as shown in Fig. 1(b), helped limit interaction between the wind tunnel flow and the still air in the room. Foil heating elements were placed on the foam surface to provide a uniform heat flux condition, and are described in more detail by Coulthard et al. [25,27]. Heaters were located both upstream and downstream of the film cooling holes. The heaters were covered with a 0.79 mm thick sheet of black Formica® laminate to provide a smooth test surface. The film cooling geometry consisted of a single row of five round holes inclined at 35 deg to the surface. The sharp edged holes had a diameter of $D=19.05 \text{ mm}$, were spaced $3D$ apart, center to center, and had a length to diameter ratio $L/D=4$. A 1.6 mm thick trip was installed $11D$ upstream of the leading edge of the film cooling holes, and a velocity profile acquired $0.8D$ upstream of the holes confirmed that the boundary layer was fully turbulent.

A wake generator, consisting of a spoked wheel, was installed for the present study between the contraction and the test plate. The test wall was moved 6.4 cm downstream of the contraction exit, and a 30 cm diameter, 2.5 cm thick aluminum hub was installed on an electric motor, just below the gap between the contraction and test plate. The axis of the rotation was parallel to the main flow direction. The hub had 24 threaded holes around its circumference, into which 38 cm long, 1.905 cm diameter hollow aluminum rods could be installed. When the hub was rotated, the rods cut through the main flow, generating wakes. The rods were intended to simulate the effect of the wakes shed from the trailing edges of upstream airfoils. In an engine, the diameter of an airfoil trailing edge is of the same order as the diameter of typical film cooling holes. The rods in the present study, therefore, were chosen to have the same diameter as the film cooling holes in the test plate. The wake passing velocity in a turbine is of the same order as the main flow velocity, so the rotation speed of the spoked wheel was set at 200 rpm, which produced rod velocities of 8 m/s at the spanwise centerline of the test section. Combinations of 3, 6, and 12 rods were used to produce wake passing frequencies of 10 Hz, 20 Hz, and 40 Hz. When nondimensionalized using the rod diameter and main flow velocity, these frequencies correspond to Strouhal numbers, $Sr=2\pi fD/U_\infty$, of 0.15, 0.30, and 0.60. These Sr are typical of engine conditions and match the range considered by Heidmann et al. [16]. The direction of rotation was set so that the rods moved toward the test plate (clockwise when looking upstream in Figs. 1(b) and 1(c)), to simulate wakes impacting the suction side of an airfoil.

For safety, the wake generator was enclosed in a plywood box, as shown in Fig. 1(b), with a rectangular hole of the contraction

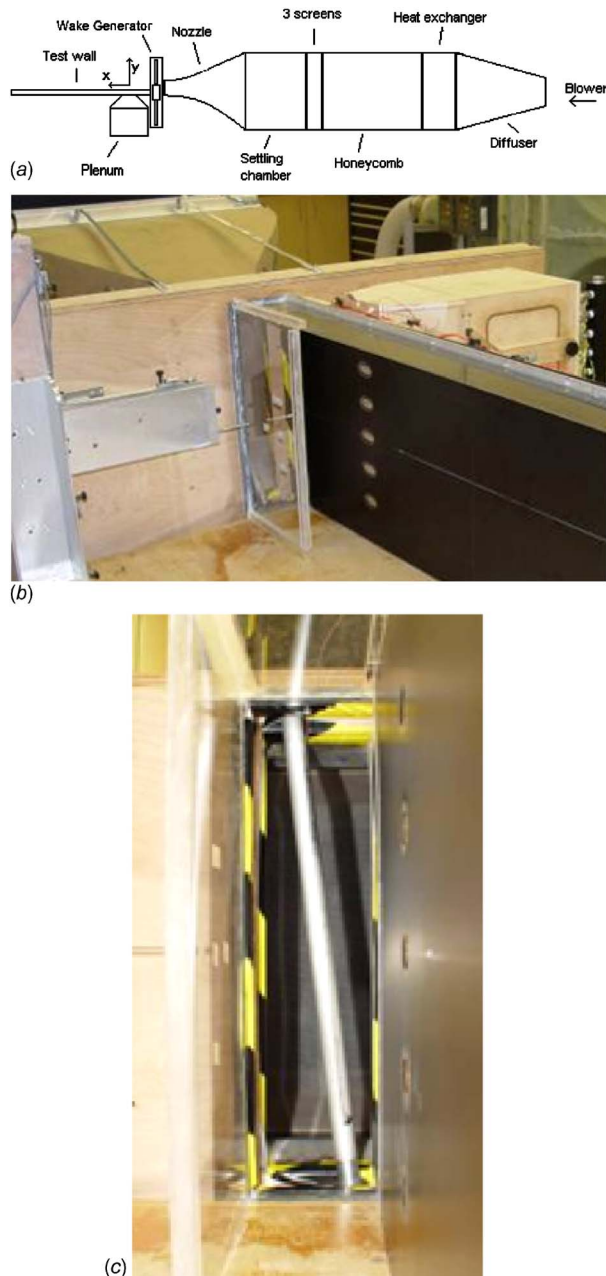


Fig. 1 Wind tunnel configuration: (a) schematic, (b) photograph of test wall with sidewalls, and (c) photograph looking upstream at rod moving across main flow

exit dimension to allow the main flow to pass through. The moving rods entrained air, producing a rotating flow within the box. To prevent this secondary flow from influencing the main flow, a set of rubber flaps were installed on the inside of the box, perpendicular to the direction of rod rotation and covering the plane where the rods entered the main flow. The rods pushed through the flaps, but between rods, the flaps closed, blocking the secondary flow.

Measurements. Thermocouples were placed in the film cooling plenum, at the plenum-side end of the outermost film cooling hole, at the wind tunnel exit, on the back of the test plate, in the ambient air, on the wall of the room to measure the surrounding temperature for radiation corrections, and in ice water as a reference. Constant current (cold-wire) and constant temperature (hot-wire) anemometry were used to measure flow temperature and velocity, respectively. Boundary layer probes with $1.27 \mu\text{m}$ diam-

eter platinum sensors (TSI model 1261A-P.5) were used for temperature measurements, and boundary layer probes with $3.81 \mu\text{m}$ diameter tungsten sensors (TSI model 1218-T1.5) were used for the velocity. An infrared (IR) camera (FLIR Systems Merlin model) with a Stirling cooled detector was used to measure the surface temperature field of the test wall. The temperature resolution of the camera was 0.05°C . The camera had a 255×318 pixel detector and was positioned such that each pixel corresponded to a $1 \times 1 \text{ mm}^2$ area on the test wall. The field of view on the test wall corresponded to $13.4D \times 16.7D$. The emissivity of the test wall was measured to be 0.95 and used in radiation corrections.

The film cooling effectiveness and Stanton number were defined, respectively, as follows.

$$\eta = \frac{T_{\text{aw}} - T_\infty}{T_{\text{jet}} - T_\infty} \quad (1)$$

$$\text{St} = \frac{q''_{\text{conv}}}{\rho C_p U_\infty (T_w - T_{\text{aw}})} \quad (2)$$

The jet, freestream, and wall (T_w) temperatures were measured. The convective heat flux, q''_{conv} , was determined based on the power input to the heaters, with corrections for conduction and radiation losses. Measurements were made for each flow condition with the wall heaters on and off, to determine local T_{aw} , η , and St. The procedure is described in more detail by Coulthard et al. [27]. Stanton numbers were determined for cases with film cooling (St_f), and in cases without film cooling (St_o) but otherwise similar main flow, wake, and surface heating conditions. Stanton number ratios (St_f/St_o) were then computed to determine the effect of film cooling on heat transfer coefficients.

The thermocouples and IR camera were calibrated against a precision blackbody source, and the cold-wire probe was calibrated against the thermocouples. The uncertainty in the measured temperature was 0.2°C , and the uncertainty in the measured velocity was 3%. The uncertainty in the film cooling effectiveness was determined to be 6% and the uncertainty in the Stanton number is 8%. The uncertainty in the ratio of two Stanton numbers is 11%, based on a standard propagation of error with a 95% confidence interval.

Velocity profiles were measured along the centerline of the test wall at three streamwise locations, $x=0D$, $7D$, and $14D$, where the origin for the coordinate system is the wall surface at the downstream edge of the center film cooling hole. The film cooling jets were off and the holes covered with thin tape during these measurements. Profiles were acquired for all three wake passing frequencies. Three-dimensional surveys of the flow temperature were measured using the cold-wire probe. Each survey consisted of a $29 \times 11 \times 5$ grid with 1595 measurement locations. In the streamwise direction, 29 evenly spaced locations extended from $x = -1.74D$ (the leading edge of the film cooling holes) to $12.2D$. In the wall normal direction, there were 11 evenly spaced locations extending from $y=0D$ to $2.55D$. Coulthard et al. [26] confirmed that the flow was symmetric about the spanwise centerline in this facility, so spanwise locations were all on one side of the centerline, with five evenly spaced points extending from $z=0$ to the midpoint between adjacent holes at $z=1.5D$. An infrared sensor was located in the wake generator box to detect the passing of the wake generator rods. The pulse train from this sensor was digitized along with the instantaneous anemometer voltages (13 s long traces at 10 kHz sampling rate) to allow phase averaging of the flow velocities and temperatures relative to the wake passing events. Phase averaged results were computed at 24 increments during the wake passing cycle.

Flow Conditions. As documented by Coulthard et al. [27] before installation of the wake generator, the boundary layer $0.8D$ upstream of the film cooling hole leading edge had a momentum

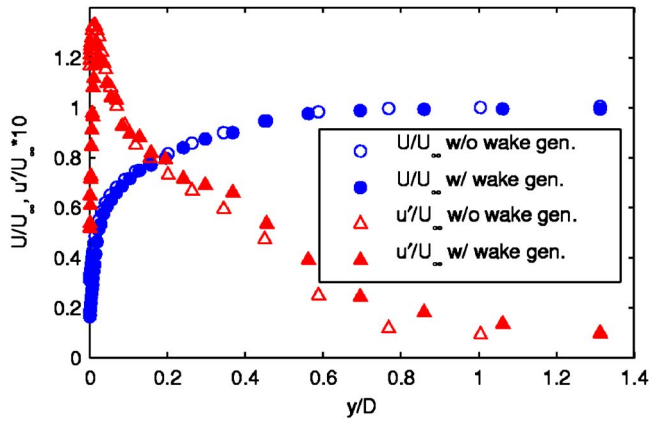


Fig. 2 Mean and fluctuating streamwise velocity upstream of film cooling holes, before installation of wake generator and during undisturbed phase of cycle with $Sr=0.15$

thickness Reynolds number of 550 and a shape factor of 1.48. The local skin friction coefficient at this location was 5.4×10^{-3} and the enthalpy thickness Reynolds number was 470. The Reynolds number based on hole diameter and mainstream velocity was 10,000. Data for cases without wakes shown below were acquired without the wake generator present. With the wake generator added, the gap between the contraction exit and the leading edge of the test plate created a disturbance, which increased the thickness of the boundary layer on the test wall in cases without wakes. With the wake generator spinning, however, the rods entrained a flow into the gap, sucking off the boundary layer upstream of the test plate. The result, as shown in Fig. 2, was a boundary layer, which at the phases between wake disturbances matched the boundary layer measured by Coulthard et al. [26]. To separate the turbulence from the wake passing unsteadiness, the turbulence values shown in Fig. 2 and in the figures below are based on fluctuations from the phase averaged mean as opposed to the time averaged mean of the full data trace.

Figure 3 shows the phase averaged mean velocity at $x=0$ for the lowest Strouhal number, $Sr=0.15$, case. The horizontal axis indicates the phase, t/T , where T is the wake passing period. The time $t/T=0$ in this figure is set by the rod passing the infrared sensor in the wake generator box. The vertical axis indicates distance from the wall. The freestream velocity is set to $U_\infty=8$ m/s, and this value is used to normalize all mean and fluctuating velocities. Far from the wall, there is a velocity deficit associated with the wake. Close to the wall, the wake causes a rise in velocity to about $1.2U_\infty$. The effect of the wake on the phase averaged turbulence level for this case is shown in Fig. 4. Very near the wall, for most of the cycle, the turbulence level is low due to damping in the viscous sublayer. Just above the sublayer, the fluctuation level is higher across the full cycle in the turbulent bound-

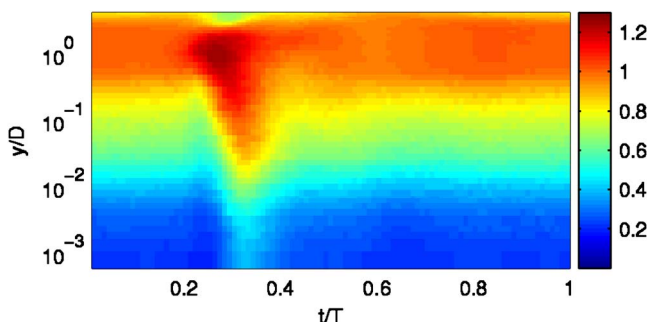


Fig. 3 Phase averaged U/U_∞ at $x/D=0$, $Sr=0.15$

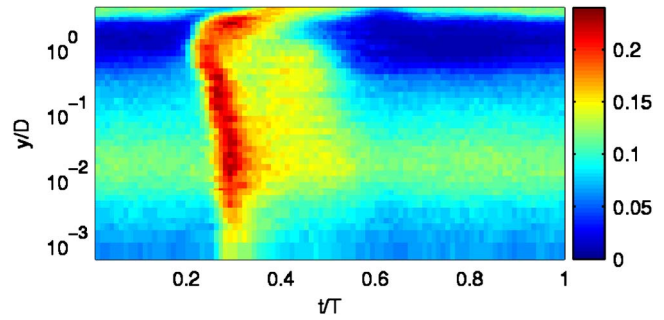


Fig. 4 Phase averaged u'/U_∞ at $x/D=0$, $Sr=0.15$

ary layer. Still farther from the wall, the freestream flow is calm for most of the cycle with 1% turbulence intensity. At the farthest locations from the wall, there are high fluctuation levels in the shear layer between the wall jet and the still air in the room. The location of the wake between $t/T=0.2$ and 0.6 is clear. The effect of the wake extends all the way to the wall, indicating that it may have an important effect on film cooling. A wavelet spectral analysis indicated that the frequency of peak fluctuation energy within the wake was 125 Hz in the freestream and was 63 Hz in the sublayer. The corresponding integral length scales at these two locations were 9 mm and 5 mm, respectively.

Slices through the contour plot of Fig. 4 at $y/D=0.01$ and $y/D=1.5$ are shown in Fig. 5 along with corresponding data from the higher Sr cases. For the $Sr=0.15$ case, the arrival of the wake induces a sudden rise in turbulence level both in the freestream and near the wall. This is followed by a more gradual decline to the undisturbed level between wakes. The peak freestream turbulence intensity within the wake is about 19%. Between wakes, the value drops to the 1% background level of the wind tunnel. The wake appears to occupy about 40% of the cycle, extending from about $t/T=0.2$ to 0.6 . The arrival of the wake near the wall is somewhat delayed relative to the freestream, as might be expected given the lower convective velocity near the surface. The region of strong wake influence near the wall extends from about $t/T=0.25$ to 0.40 . At the higher Strouhal numbers, the wake still occupies about the same amount of time in seconds, since the wake generator turns at the same speed in all cases, but it occupies a larger fraction of the wake passing period. For the $Sr=0.3$ case, there is still a sudden rise in turbulence when the wake arrives and a short period of calm flow between wakes. For the $Sr=0.6$ case, the wakes occupy the full cycle, so there is no clear calm period

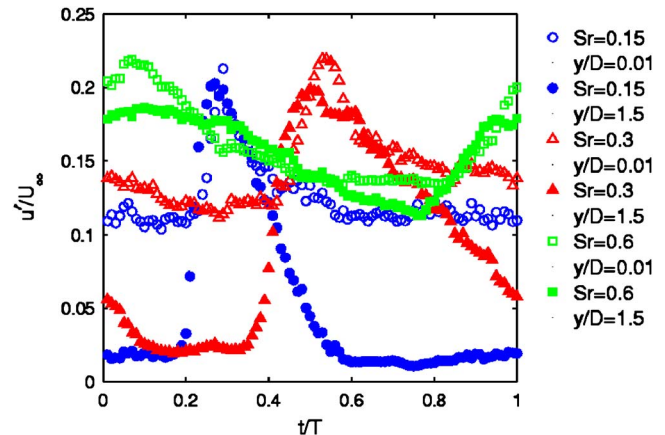


Fig. 5 Phase averaged u'/U_∞ at $x/D=0$, $y/D=0.01$ and 1.5 for $Sr=0.15, 0.30$, and 0.60

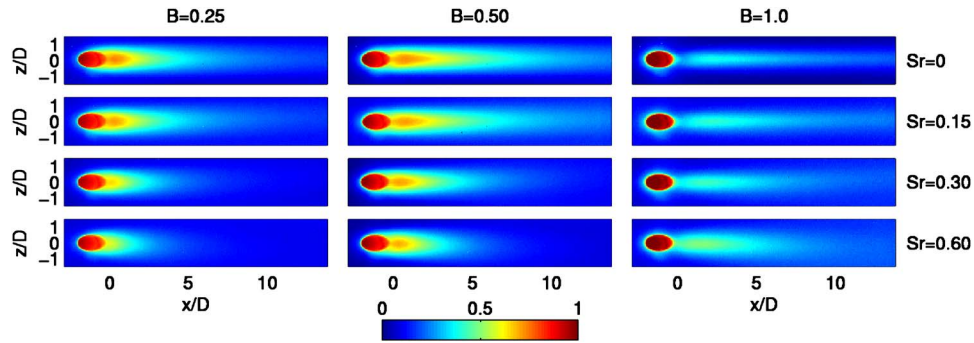


Fig. 6 Film cooling effectiveness contours around center hole at various B (columns) and Sr (rows)

and the freestream turbulence level is always above 10%.

Data similar to that in Figs. 3 and 4 were acquired at $x=7D$ and $14D$, and from these data, the propagation speed of the wake along the test wall was estimated. The leading edge of the wake moves at about the undisturbed freestream velocity, $U_\infty=8$ m/s. The trailing edge of the wake is somewhat slower, at about $0.8U_\infty$. Near the wall, the leading and trailing edges of the disturbed flow travel at about $0.9U_\infty$. Using the arrival time of the wake in Fig. 5 and the propagation speed of the wake, the data in all figures shown below are shifted along the time axis so that $t/T=0$ corresponds to the arrival of the wake at the trailing edge of the film cooling hole.

The film cooling jet velocity and temperature were documented by Coulthard et al. [26] by traversing the constant current and hot-wire probes over the hole exit plane with the main flow in the wind tunnel off. The jet temperature was very uniform and matched the plenum temperature to within 0.2°C . The velocity was highest in the upstream section of the hole, and agreed with the results of Burd and Simon [19], who considered the same geometry. Since the jets were only heated to approximately 7°C above the mainstream temperature, the density ratio of jets to mainstream was 0.98. Hence, the blowing and velocity ratios were essentially equal. Temperature and velocity measurements were compared between the five film cooling holes. The hole to hole variation in temperature was 2% of the jet to mainstream temperature difference, and velocity variation was 8% of the mainstream velocity.

For the $Sr=0$ (no-wake) cases, the main flow and coolant flow resulted in good periodicity downstream of all five coolant holes, as shown by Coulthard et al. [26]. Similar uniformity was observed for the $Sr=0.15$ cases. At the higher Sr , however, vortices generated at the hub and tip ends of the wake generator rods disturbed the flow around the outermost holes. To avoid these disturbances, spanwise averages were taken only about the center hole, between $z = \pm 1.5D$.

Results and Discussion

Time Averaged Film Cooling and Heat Transfer. The effects of the wakes on film cooling effectiveness are shown in Figs. 6–9. Coulthard et al. [26] showed that the $Sr=0$ (no-wake) cases agreed well with data from the literature. Effectiveness contours downstream of the center hole are shown for all cases in Fig. 6. Centerline and spanwise average effectiveness are shown in Figs. 7–9 for the $B=0.25$, 0.50, and 1.0 cases, respectively. Without wakes, the $B=0.50$ case has the highest effectiveness. The $B=0.25$ case has lower effectiveness because there is less coolant available to protect the surface. The effectiveness is low in the $B=1.0$ case due to jet lift-off, as shown by Coulthard et al. [26]. The effect of the wakes is similar for the $B=0.25$ and 0.50 cases. The wakes have little effect at $Sr=0.15$, but the streamwise extent of the region of effective cooling is noticeably reduced at the

higher Strouhal numbers. The wakes reduce the effectiveness by as much as 60%, with the strongest effect along the centerline. In contrast to the lower blowing ratio results, the results with $B=1.0$ show higher effectiveness with better lateral spreading at the higher Strouhal numbers. As will be shown below, the jets exhibit considerable lift-off at this blowing ratio, and the wakes help to force the coolant back toward the wall. At the centerline, the wakes raise the effectiveness immediately downstream of the holes in the $B=1.0$ cases by as much as 30%. There is little effect downstream of $x/D=4$. The spanwise average results show about a doubling of the effectiveness between the $Sr=0$ and $Sr=0.6$ cases at all streamwise locations. Comparing the results at the three blowing ratios, when $Sr=0$ or 0.15, the $B=0.5$ cases have the highest effectiveness. When $Sr=0.6$, the $B=1.0$ case has the best results downstream of $x=2D$. For $x>9D$, the effectiveness in the $B=1.0$ case is about double that in the $B=0.5$ case. The wakes mitigate the effects of jet lift-off, and the higher total coolant volume with $B=1.0$ produces higher effectiveness. It is noteworthy that a blowing ratio chosen based on the $Sr=0$ results will not necessarily be most effective when wakes are present.

The effects of wakes on Stanton number are shown in Figs. 10–12. Figure 10 shows Stanton numbers for cases without film cooling. Increasing Strouhal number raises the Stanton numbers above the no-wake case by about 7%, 18%, and 36% for the Sr

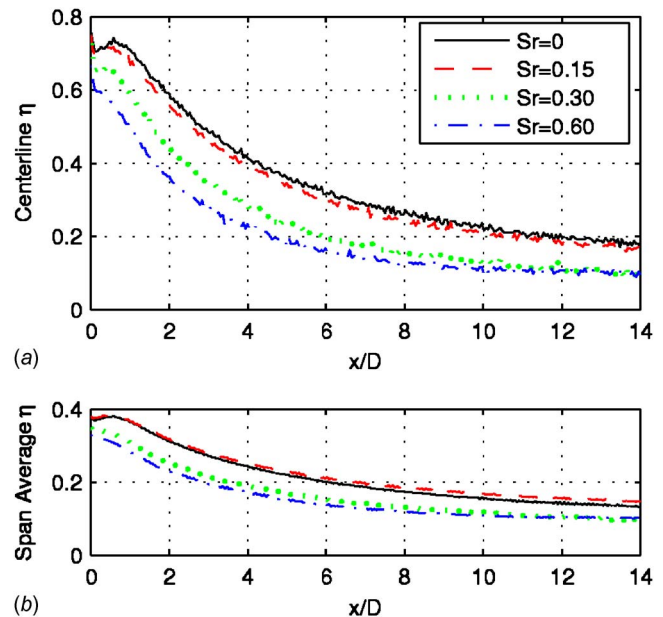


Fig. 7 Film cooling effectiveness for $B=0.25$ cases at various Sr ; (a) centerline and (b) spanwise averaged

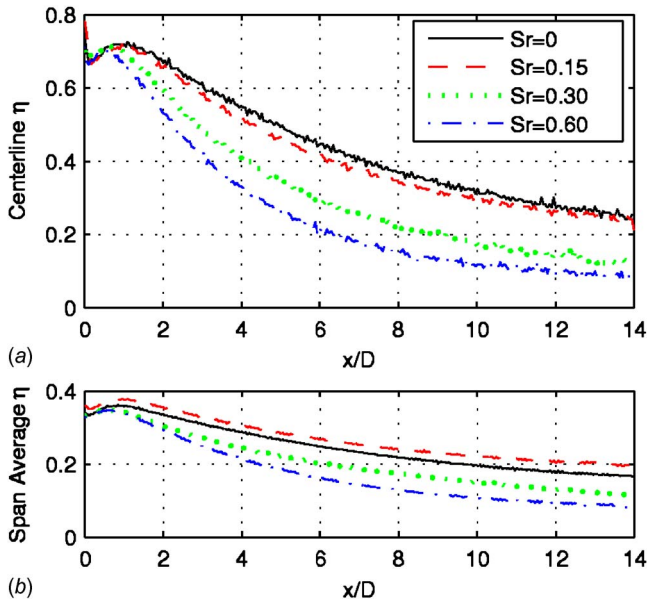


Fig. 8 Film cooling effectiveness for $B=0.5$ cases at various Sr ; (a) centerline and (b) spanwise averaged

$=0.15, 0.30,$ and 0.60 cases, respectively. The increases are consistent with the effective rise in the near-wall velocity and turbulence level caused by the wakes and shown in Figs. 3–5. Stanton number ratio contours are shown in Fig. 11. Two lines of high St_f/St_o , symmetric about the spanwise centerline and extending downstream of the hole, are visible in all cases. These are believed to result from the kidney shaped vortices which form in the film cooling jets, and are discussed in more detail by Coulthard et al. [25]. Also visible are regions of high St_f/St_o extending a short distance downstream from the lateral edges of the hole. These are believed to result from the horseshoe vortex which forms when the main flow boundary layer wraps around the film cooling jet. The centerline and spanwise average St_f/St_o are shown in Figs. 12–14 for the $B=0.25, 0.5,$ and 1.0 cases, respectively. In all cases, the ratio is high near the hole, but drops to near 1 by x

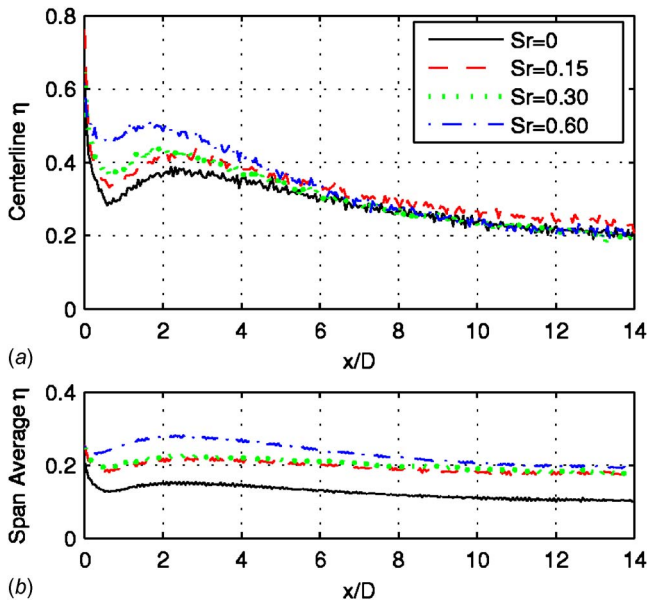


Fig. 9 Film cooling effectiveness for $B=1.0$ cases at various Sr ; (a) centerline and (b) spanwise averaged

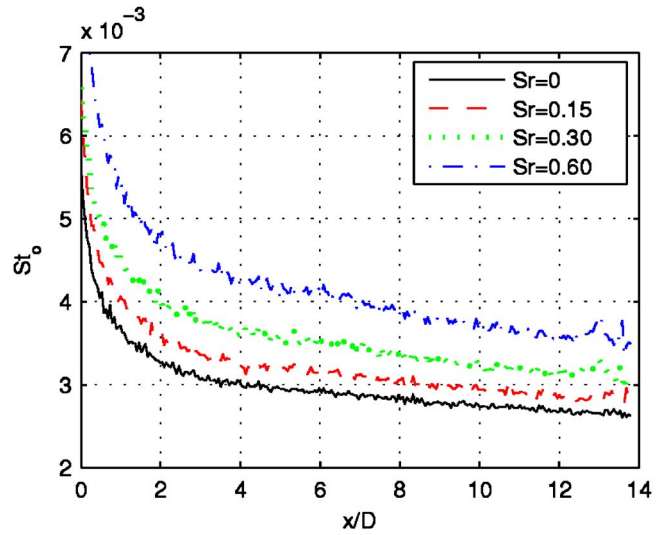


Fig. 10 Stanton numbers for cases without film cooling at various Sr

$=6D$. There appears to be a weak trend of the ratio decreasing with increasing Strouhal number, but the differences are small and within the uncertainty. The St_o values increase significantly with increasing wake frequency as shown in Fig. 10, and the wakes cause about the same percentage increase in Stanton numbers for the cases with film cooling. Hence, the Stanton number ratios do not depend strongly on Strouhal number.

The heat transfer to a surface depends on both the film cooling effectiveness and the heat transfer coefficient. The combined effect can be expressed as a heat flux ratio,

$$\frac{q''_f}{q''_o} = \frac{St_f}{St_o} \left(1 - \frac{\eta}{\psi} \right) \quad \psi = \frac{T_w - T_\infty}{T_{jet} - T_\infty} = 0.6 \quad (3)$$

The numerical value of $\psi=0.6$ is taken from Sen et al. [28] and others, and is a typical value for this temperature ratio under engine conditions. More discussion of the heat flux ratio for the $Sr=0$ cases is available in Ref. [27]. Contours of q''_f/q''_o for all cases are shown in Fig. 15. Because the Stanton number ratio is near unity at most locations, the heat flux ratios of Fig. 15 reflect the effectiveness values of Fig. 6. At low Strouhal numbers, q''_f/q''_o is lowest for the $B=0.5$ case. For the higher Strouhal numbers, q''_f/q''_o is lower for the $B=1.0$ cases, particularly at downstream locations.

Phase Averaged Flow Temperature. The time averaged surface results presented above can be better explained using flow temperature data. Figure 16 shows the time averaged temperature field for the $B=0.25, 0.5,$ and $1.0, Sr=0$ cases. The top image in each figure shows dimensionless temperature contours, $\phi=(T - T_\infty)/(T_{jet} - T_\infty)$, in multiple planes arranged to provide a three-dimensional image of the temperature field. The lower image in each figure shows an isothermal surface with $\phi=0.3$. This value of ϕ was found to give a good visual representation of the jet position. The jet clearly remains near the surface at the lower blowing ratios, and extends further downstream in the $B=0.5$ case before being dissipated. In the $B=1.0$ case, the jet clearly has lifted away from the surface, and although it extends farther downstream than in the other cases, it does not provide effective cooling. These results agree with the effectiveness results of Figs. 6–9.

Phase averaged flow temperature results for the $B=0.5, Sr=0.15$ case are shown in Fig. 17. Six phases from the cycle are shown. The format and color range of the plots are the same as in Fig. 16, so some of the axis labels have been removed for clarity.

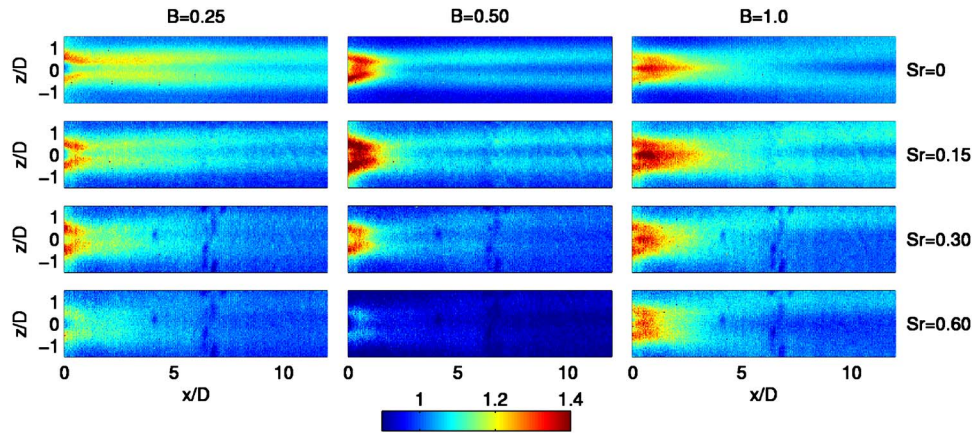


Fig. 11 Stanton number ratio, St_f/St_o , contours around center hole at various B (columns) and Sr (rows)

The start of the cycle, $t/T=0$, in Fig. 17(a), is set to correspond to the arrival of the leading edge of the wake at the hole location. The temperature field appears very similar to the $Sr=0$ case of Fig. 16(b). By $t/T=0.17$, there appears to be a slight reduction in the effective jet diameter at about $x=2D$, and a slight bulge at $x=4D$. These locations correspond to the location of strongest near-wall wake turbulence, as indicated by the timing shown in Fig. 5. By $t/T=0.33$, the strong wake turbulence is located between about $x=5$ and $10D$, and the jet has clearly been dispersed in this region. At $t/T=0.5$, the wake is beginning to move out of the field of view, and the jet has been dispersed in the downstream part of the measurement region. Also, new undisturbed jet fluid is following behind the wake. The undisturbed jet continues to extend farther downstream at $t/T=0.67$, and by $t/T=0.83$, the jet appears to have recovered to its steady state, between-wake, condition. It is

interesting that the wake is not able to disperse the jet when it first emerges from the hole, and the jet appears to remain intact between $x=0$ and $4D$ at all phases. It must take some small but finite time for the wake turbulence to mix the jet fluid with the main flow and begin to disperse it, and during this time, the fluid moves about $4D$ downstream.

The behavior in the $B=0.25$, $Sr=0.15$ case is very similar to that of the $B=0.5$ case of Fig. 17. With half the coolant volume, the lower momentum jet at $B=0.25$ does not extend as far from the wall as in the $B=0.5$ case, and the jet does not extend as far downstream before it is diluted by the main flow. The effect of the wake, however, appears to be the same for the two cases.

The temperature fields for the $B=1.0$, $Sr=0.15$ case are shown in Fig. 18. At $t/T=0$, the jet is clearly lifted off the wall, and

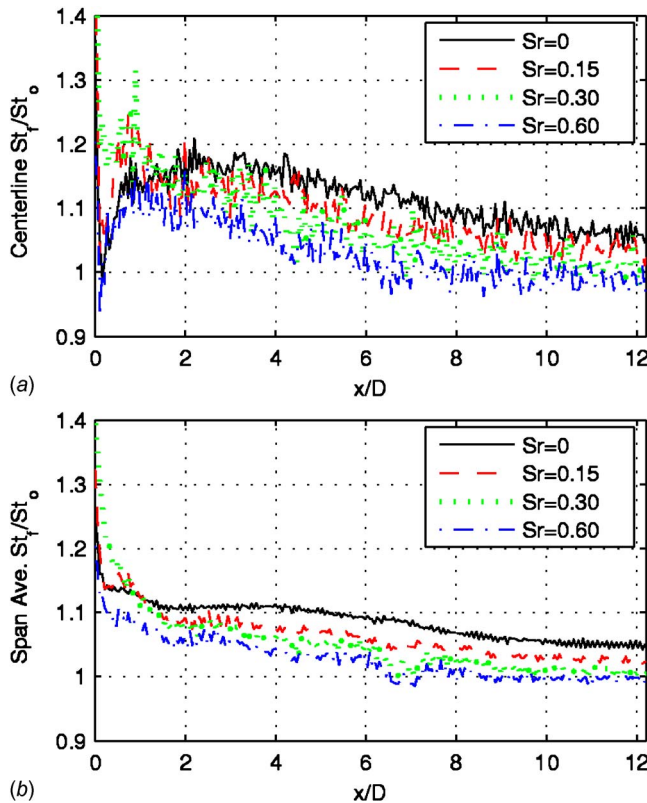


Fig. 12 Stanton number ratio, St_f/St_o , for $B=0.25$ cases at various Sr ; (a) centerline and (b) spanwise averaged

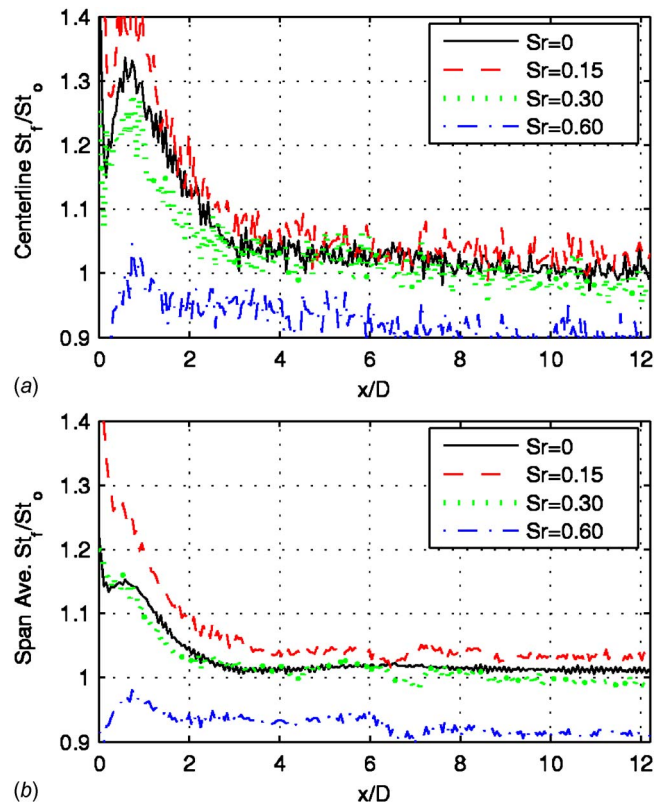


Fig. 13 Stanton number ratio, St_f/St_o , for $B=0.5$ cases at various Sr ; (a) centerline and (b) spanwise averaged

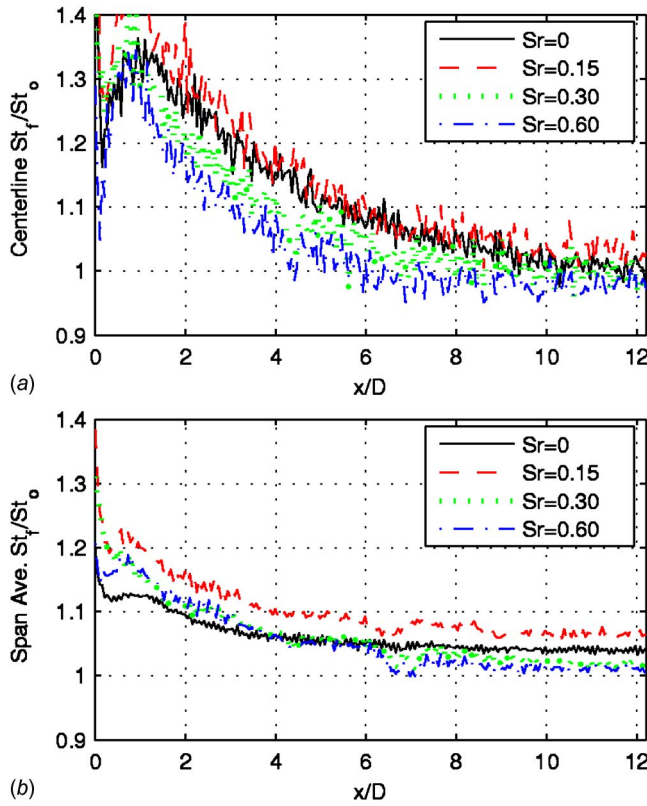


Fig. 14 Stanton number ratio, St_t/St_o , for $B=1.0$ cases at various Sr ; (a) centerline and (b) spanwise averaged

appears essentially the same as in the $Sr=0$ case of Fig. 16(c). At $t/T=0.17$, there is a bulge in the jet at $x=4D$ as the wake passes, similar to the $B=0.5$ case of Fig. 17(b). The upstream part of the jet also appears to be pushed closer to the wall by the wake at this phase, which would tend to momentarily increase the film cooling effectiveness. This agrees with the rise in effectiveness shown in Fig. 9, particularly for the spanwise average. At $t/T=0.33$, the wake has dispersed the jet between $x=5$ and $10D$, as in the $B=0.5$ case at this phase. For the remainder of the cycle, the jet recovers, as in the lower B cases, and the lift-off from the wall remains clear.

The $B=0.5$, $Sr=0.3$ case is shown in Fig. 19. The flow is moving at the same velocity as in the $Sr=0.15$ case, but the wakes are arriving twice as frequently, so there is less time for the jet to

recover between wakes. At $t/T=0$, the jet is against the surface, as in Fig. 17, but does not extend as far downstream before being dispersed. It has not, at this phase, fully recovered from the previous wake. The recovery continues to $t/T=0.17$, even as the next wake arrives. By $t/T=0.33$, the jet extends even farther downstream, but it is beginning to be disturbed between $x=2$ and $4D$, corresponding to the same behavior observed in Fig. 17(b) (Figs. 17(b) and 19(c) correspond to the same dimensional time after the arrival of the wake). The wake disperses the jet downstream of $x=2D$ over the next two phases shown, and is nearly out of the measurement region by $t/T=0.83$, as the jet begins to recover. The jet never fully recovers, however, to the steady flow condition of Figs. 16(b), 17(a), and 17(f). In agreement with the $Sr=0.15$ case, the jet appears to remain intact in the region immediately downstream of the hole. The film cooling effectiveness in Fig. 8 reflects this, with the effectiveness dropping only slightly between the $Sr=0$ and 0.30 cases upstream of $x=2D$, but more significantly farther downstream.

Figure 20 shows the $B=1.0$, $Sr=0.30$ case. As in the $B=0.50$ case at this Strouhal number, the jet is still recovering from the previous wake at $t/T=0$, the jet continues to extend farther downstream until $t/T=0.50$, and the disturbance of the next wake is visible between $x=2$ and $4D$ at $t/T=0.33$. The dispersal of the jet by the wake is clear between $x=4$ and $7D$ at $t/T=0.5$, and the affected region continues to move downstream at the next two phases shown, in agreement with the behavior at $B=0.5$ in Fig. 19. Figure 20 shows that the jet has lifted off the wall, but in agreement with the observation in Fig. 18(b) for the $B=1.0$, $Sr=0.15$ case, the wake appears to push the jet back closer to the wall than in the steady flow case of Fig. 16(c). This helps to explain the increase in film cooling effectiveness at higher Sr in Fig. 9.

The $Sr=0.6$ cases with $B=0.5$ and 1.0 are shown in Figs. 21 and 22, respectively. As shown by the turbulence traces in Fig. 5, there is no recovery period between wakes at this Strouhal number. There are two wakes present in the measurement region at all phases. At $t/T=0$ in both Figs. 21 and 22, the preceding wake is centered near $x=6D$ as the next wake arrives at the hole. The preceding wake moves downstream at the subsequent phases and moves out of the measurement region at about $t/T=0.67$. The streamwise extent of the jet increases slightly during this time, as the jet begins to recover. At $t/T=0.67$, however, the center of the next wake has arrived at about $x=2D$, and it is clearly affecting the jet by $t/T=0.83$. Hence, there is essentially no time for the jet to recover, and there is much less variation during the cycle than at the lower Strouhal numbers. The streamwise extent of the jet before dispersal is reduced for both blowing ratios compared to the lower Sr cases. In the $B=0.5$ case, this results in much lower

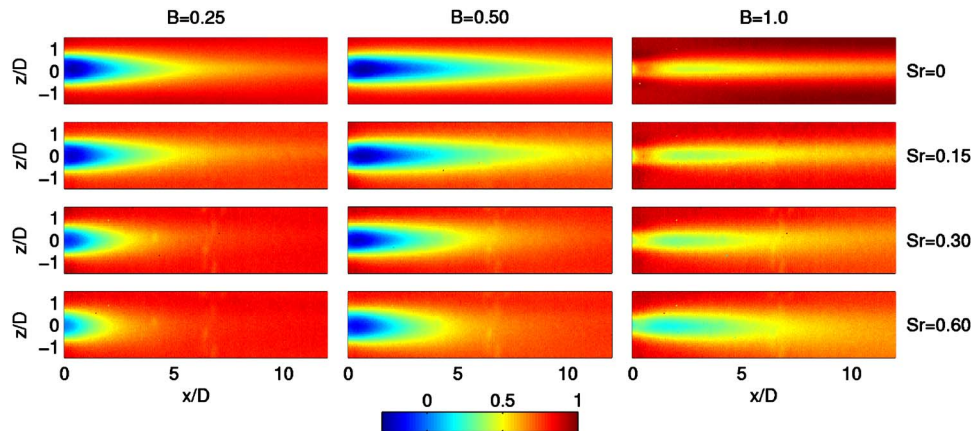


Fig. 15 Heat flux ratio, q''/q''_o , contours around center hole at various B (columns) and Sr (rows)

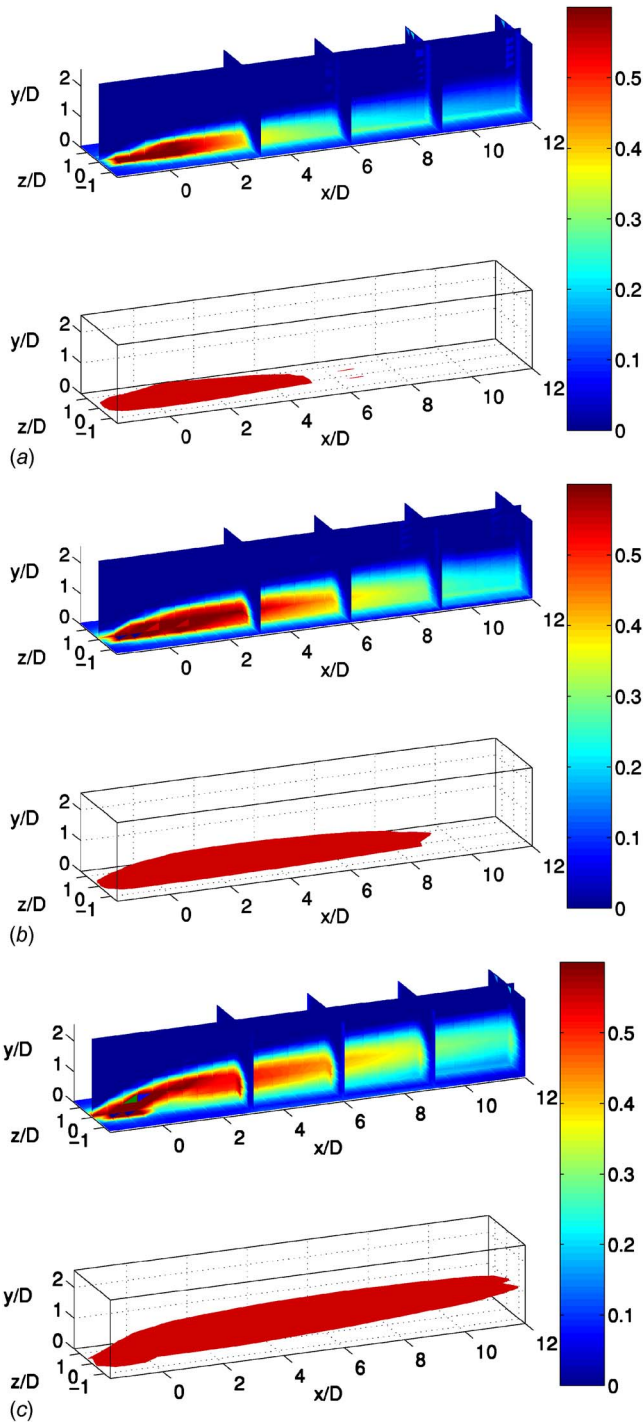


Fig. 16 Dimensionless temperature field, ϕ , for steady $Sr=0$ cases; upper image shows temperature contours in various planes, lower image shows isothermal surface with $\phi=0.3$; (a) $B=0.25$, (b) $B=0.5$, and (c) $B=1.0$

film cooling effectiveness, as shown in Fig. 8. In Fig. 22, it is clear that in addition to reducing the streamwise extent of the jet, the wake forces the jet back toward the wall during the full cycle. This raises the effectiveness, as shown in Fig. 9. The wake turbulence may cause more spreading of the jet in all directions, including laterally and toward the wall. The wake's acceleration of the near-wall flow, shown in Fig. 3, may also reduce lift-off.

Instantaneous Film Cooling Effectiveness. The changing flow temperature during the cycle indicates that the instantaneous film

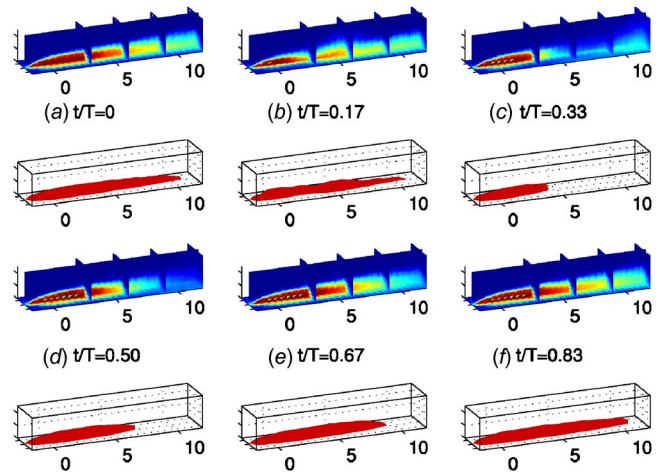


Fig. 17 Dimensionless temperature field at various phases for $B=0.5$, $Sr=0.15$ case

cooling effectiveness must also change. This cannot be measured directly with a real experimental surface, since the real surface is not perfectly adiabatic and has a nonzero heat capacity. The surface temperature cannot respond quickly enough to capture the instantaneous effects of the passing wakes. The flow temperature

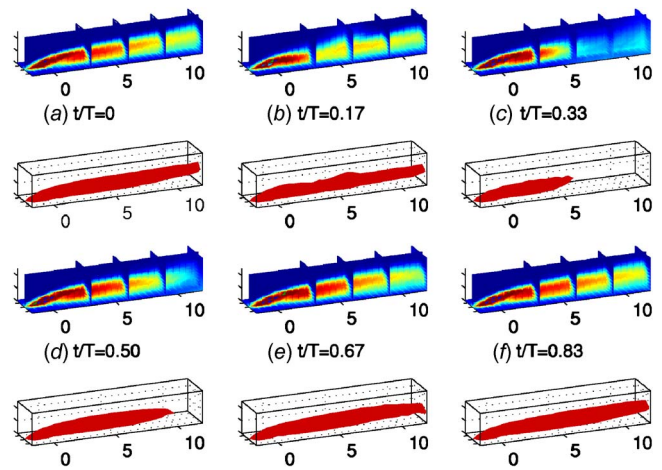


Fig. 18 Dimensionless temperature field at various phases for $B=1.0$, $Sr=0.15$ case

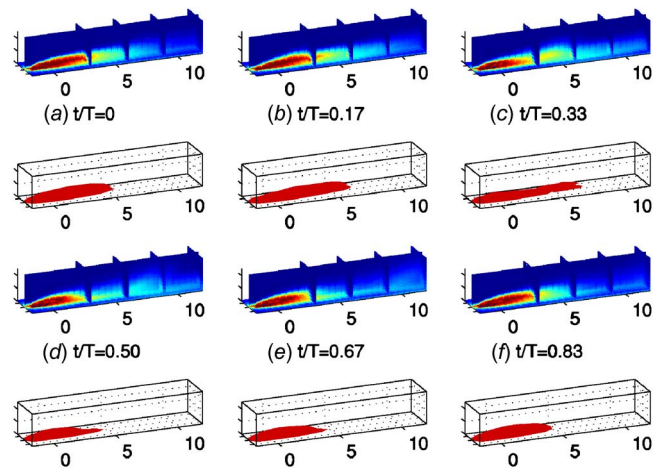


Fig. 19 Dimensionless temperature field at various phases for $B=0.5$, $Sr=0.30$ case

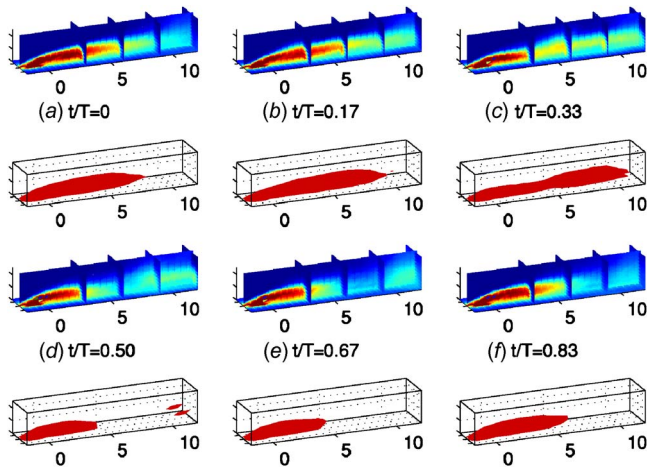


Fig. 20 Dimensionless temperature field at various phases for $B=1.0$, $Sr=0.30$ case

does respond quickly, however, as shown above, and the instantaneous flow temperature near the surface may approximate the temperature a perfectly responding surface would achieve. The approximation will not be perfect. The flow immediately adjacent to the wall will be influenced by the actual steady wall temperature. The temperature far from the wall will not be representative of the surface. Still, the instantaneous flow temperature close to the wall should give a reasonable approximation of the temperature a perfectly adiabatic wall would achieve, and it will provide insight into the unsteady film cooling effectiveness. Kohli and Bogard [22] used measured flow temperatures to extrapolate to the wall temperature and noted that the extrapolated value differed from the measured temperature at $y/D=0.1$ by only 0.02 in ϕ . In the present study, the instantaneous temperatures measured in a plane at $y=0.08D$ are phase averaged and used to define the approximate unsteady film cooling effectiveness as

$$\eta^* = \phi(y = 0.08D) = \frac{T(y = 0.08D) - T_\infty}{T_{\text{jet}} - T_\infty} \quad (4)$$

Figure 23 shows contours of the effectiveness, η (lower half of plot), and the time average of the approximation, η^* (upper half of plot), for the $B=0.5$, $Sr=0.30$ case. The agreement between η and η^* is good. The same good agreement was generally observed at the other blowing ratios and Strouhal numbers. More comparisons are presented below. The good time averaged agreement provides

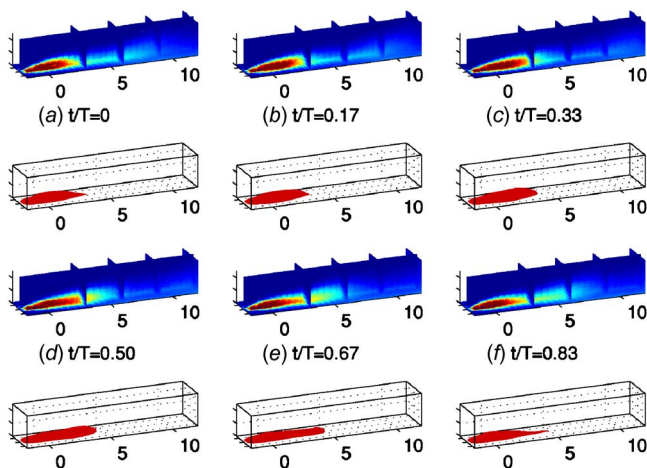


Fig. 21 Dimensionless temperature field at various phases for $B=0.5$, $Sr=0.60$ case

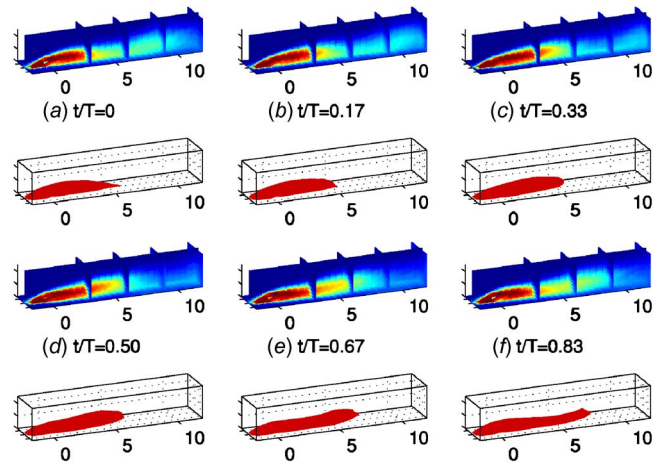


Fig. 22 Dimensionless temperature field at various phases for $B=1.0$, $Sr=0.60$ case

confidence to proceed with study of the phase averaged η^* results.

Figure 24 shows a time-space plot of the phase averaged η^* results for the $B=0.5$, $Sr=0.15$ case. The vertical axis indicates the phase, with the data repeated to show two cycles. A horizontal line in the figure shows the centerline (Fig. 24(a)) or spanwise average (Fig. 24(b)) value of η^* at a particular phase. The white lines show the location of the wake, as determined from the velocity data of Fig. 4. The thicker solid line corresponds to the leading edge of the wake in the freestream, and the thinner solid line indicates the trailing edge in the freestream. The dashed lines indicate the leading and trailing edges of the period of strong wake turbulence near the wall. The value of η^* drops quickly after the arrival of the wake near the wall, and continues to drop until the end of the strong wake turbulence near the wall. The value then rises between wakes.

Figure 25 shows η^* for the $B=1.0$, $Sr=0.15$ case. At the centerline (Fig. 25(a)), for $x > 3D$, the effect of the wake on η^* is similar to that in the $B=0.5$ case of Fig. 24. In the upstream region, however, low η^* indicates lift-off of the jet between wakes at $x < 2D$. The wakes raise η^* in this region by reducing lift-off, as shown in Fig. 18.

Results for the $Sr=0.6$, $B=0.5$ cases are shown in Fig. 26. As above, the thick solid line indicates the arrival of the wake in the freestream, and the dashed lines indicate the period of strong wake turbulence near the wall. The trailing edge line is not shown, however, because the effects of the preceding wake are still present in the freestream when the next wake arrives. As in the $Sr=0.15$ case, η^* changes during the cycle, but the variation is not as large at the higher Sr , and timing with respect to the wake is more complicated, because the recovery from the previous wake overlaps the response to the subsequent wake. The same behavior can be seen at $x > 3D$ in Fig. 27 for the $Sr=0.6$, $B=1.0$ case. Upstream of $x=3D$ in the $B=1.0$ case, the wake increases η^* , as

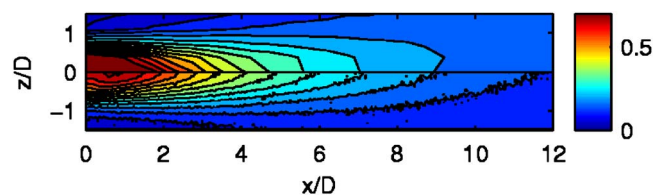


Fig. 23 Film cooling effectiveness, η (lower half of plot), and time averaged approximate effectiveness, η^* (upper half of plot), for $B=0.5$, $Sr=0.30$ case

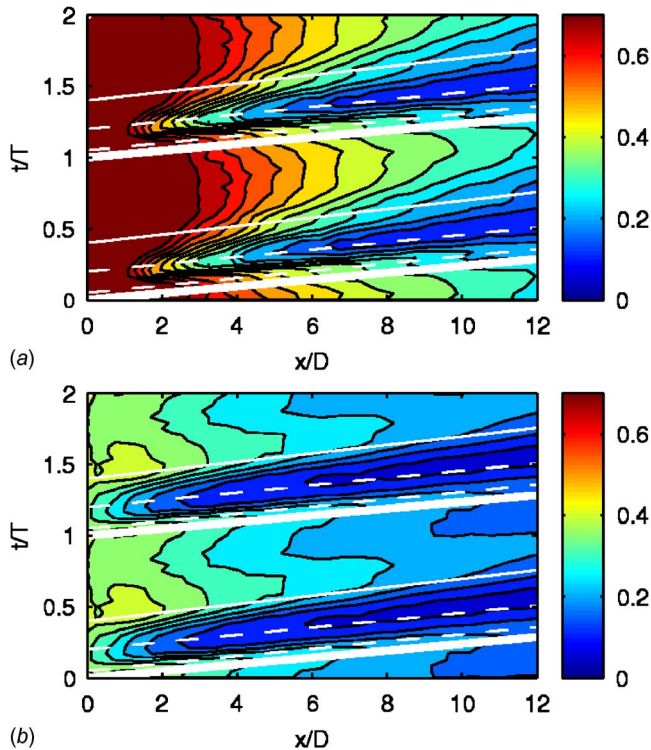


Fig. 24 Phase averaged η^* for $B=0.5$, $Sr=0.15$ case; (a) centerline and (b) spanwise average

in the $Sr=0.15$ case (Fig. 25), by reducing lift-off.

The effective in-wake and between-wake values of η^* are extracted from the data of Figs. 24 and 26 along lines sloped according to the convection velocity and passing through the data most disturbed and least disturbed by the wakes. These results, along

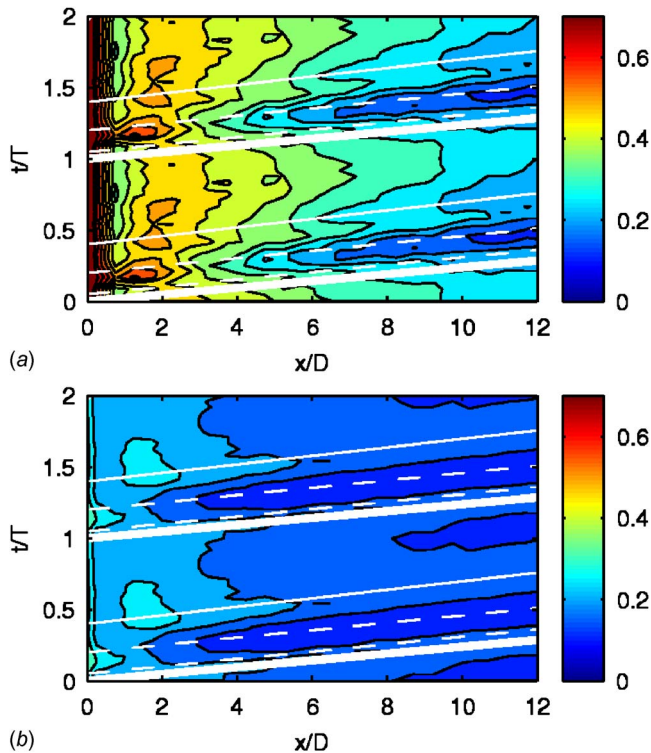


Fig. 25 Phase averaged η^* for $B=1.0$, $Sr=0.15$ case; (a) centerline and (b) spanwise average

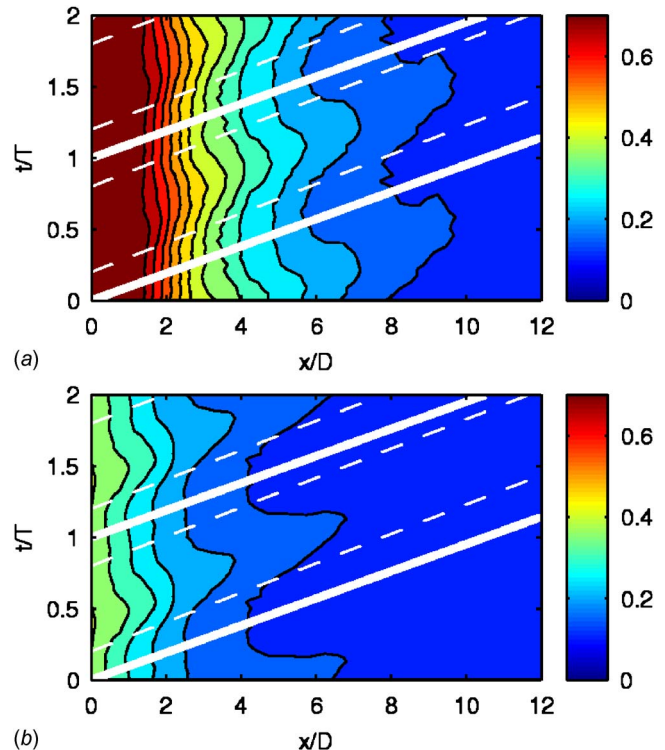


Fig. 26 Phase averaged η^* for $B=0.5$, $Sr=0.60$ case; (a) centerline and (b) spanwise average

with the time averaged η and η^* for all Strouhal numbers, are shown in Fig. 28 for the $B=0.5$ cases. At the centerline (Fig. 28(a)), the agreement between the time averaged η^* and η is good at all Sr . At $Sr=0.15$, the in-wake η^* is more than 50% lower than the between-wake value. The between-wake results agree well with the $Sr=0$ case values, indicating that the flow is able to recover to the undisturbed state between wakes. The in-wake values at $Sr=0.15$ agree well with the $Sr=0.30$ and 0.60 results, suggesting common behavior for the disturbed flow. The differences between the in-wake and between-wake η^* are smaller for the $Sr=0.30$ and 0.60 cases because the flow does not have time to recover to an undisturbed state between wakes. The spanwise average results (Fig. 28(b)) show the same trends as the centerline results, but the differences between cases and phases are smaller. Differences for the $B=1.0$ cases, as shown in Figs. 25 and 27, are of the order of the experimental uncertainty. The time averaged effectiveness is generally lower with $B=1.0$ than with $B=0.5$, which tends to make differences smaller as well. The wakes also increase mixing while reducing lift-off at $B=1.0$, and these competing effects tend to reduce differences in the effectiveness.

Conclusions

Unsteady wakes were shown to have a strong effect on the film cooling effectiveness and heat transfer for the cases considered. Stanton numbers increase significantly with wake Strouhal number. The increases were similar in cases with and without film cooling, however, so Stanton number ratios were not strongly dependent on Strouhal number. Phase averaged flow temperature measurements clearly showed how the wakes disturb the film cooling jets and the recovery between wakes. At low Strouhal numbers, the recovery was complete, and the time averaged film cooling effectiveness results differed only slightly from those in cases without wakes. At high Strouhal numbers, the time for recovery was insufficient, and the jets were disturbed throughout the cycle, resulting in 50% reductions in effectiveness with $B=0.5$. With $B=1.0$, the combined effects of reduced lift-off and in-

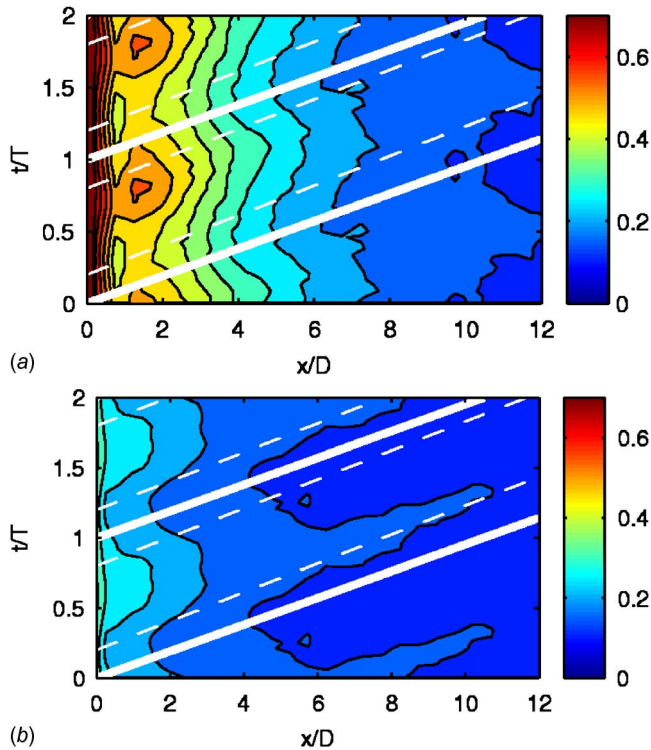


Fig. 27 Phase averaged η^* for $B=1.0$, $Sr=0.60$ case; (a) centerline and (b) spanwise average

creased mixing resulted in little variation of the centerline effectiveness with Strouhal number. Enhanced lateral spreading, however, resulted in noticeable increases with Sr in the spanwise average effectiveness for the $B=1.0$ cases. Unsteady near-wall flow temperature measurements were used to approximate the unsteady film cooling effectiveness during the wake passing cycle.

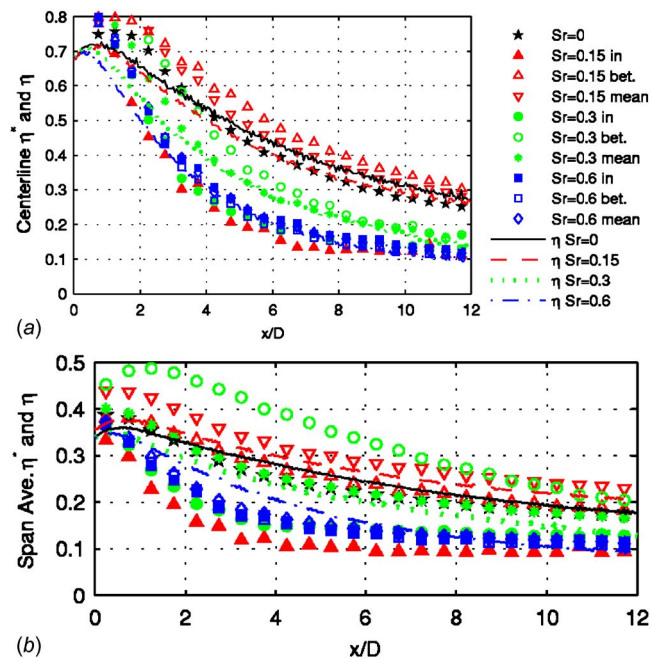


Fig. 28 Phase averaged η^* in wakes, between wakes, time mean of all phases, and corresponding η for $B=0.5$ cases; (a) centerline and (b) spanwise average

During the wake passing, the unsteady effectiveness was low and approximately equal for cases at all Strouhal numbers. Variation during the rest of the cycle depended on the time available for recovery between wakes.

Acknowledgment

The first author gratefully acknowledges the Office of Naval Research for partial support of this work, via the Naval Academy Trident Scholar Program, on funding Document No. N0001406WR20137. The second author gratefully acknowledges partial support by the Naval Air Systems Command.

Nomenclature

- $B = \rho_{jet} U_{jet} / \rho_{\infty} U_{\infty}$, blowing ratio
- c_p = specific heat at constant pressure
- D = film cooling hole and wake generator rod diameter
- f = frequency, Hz
- L = length of film cooling hole channel
- q'' = heat flux
- Sr = Strouhal number, $Sr = 2\pi f D / U_{\infty}$
- St = Stanton number, $q''_{conv} / [\rho c_p U_{\infty} (T_w - T_{aw})]$
- T = temperature or wake passing period
- t = time
- U = velocity
- u' = phase averaged rms streamwise velocity
- x = streamwise coordinate, distance from trailing edge of film cooling holes
- y = normal coordinate, distance from the wall
- z = spanwise coordinate, distance from the centerline of the center hole
- η = film cooling effectiveness, $(T_{aw} - T_{\infty}) / (T_{jet} - T_{\infty})$
- η^* = approximate unsteady film cooling effectiveness, Eq. (4)
- ρ = density
- ϕ = dimensionless temperature, $(T - T_{\infty}) / (T_{jet} - T_{\infty})$

Subscripts

- aw = adiabatic wall
- conv = convective
- f = with film cooling
- jet = film cooling jet
- o = without film cooling
- w = wall
- ∞ = mainstream

References

- [1] Varadarajan, K., and Bodard, D. G., 2004, "Effects of Hot Streaks on Adiabatic Effectiveness for a Film Cooled Turbine Vane," ASME Paper No. GT2004-54016.
- [2] Bons, J. P., MacArthur, C. D., and Rivir, R. B., 1994, "The Effect of High Freestream Turbulence on Film Cooling Effectiveness," ASME J. Turbomach., **118**, pp. 814-825.
- [3] Kohli, A., and Bogard, D. G., 1998, "Effects of Very High Free-Stream Turbulence on the Jet—Mainstream Interaction in a Film Cooling Flow," ASME J. Turbomach., **120**, pp. 785-790.
- [4] Ekkad, S. V., Mehendale, A. B., Han, J. C., and Lee, C. P., 1997, "Combined Effect of Grid Turbulence and Unsteady Wake on Film Effectiveness and Heat Transfer Coefficients of a Gas Turbine Blade With Air and CO₂ Film Injection," ASME J. Turbomach., **119**, pp. 594-600.
- [5] Burd, S. W., Kaszeta, R. W., and Simon, T. W., 1998, "Measurements in Film Cooling Flows: Hole L/D and Turbulence Intensity Effects," ASME J. Turbomach., **120**, pp. 791-798.
- [6] Funazaki, K., Yokota, M., and Yamawaki, S., 1997, "Effect of Periodic Wake Passing on Film Cooling Effectiveness of Discrete Cooling Holes Around the Leading Edge of a Blunt Body," ASME J. Turbomach., **119**, pp. 292-301.
- [7] Funazaki, K., Koyabu, E., and Yamawaki, S., 1998, "Effect of Periodic Wake Passing on Film Cooling Effectiveness of Inclined Discrete Cooling Holes Around the Leading Edge of a Blunt Body," ASME J. Turbomach., **120**, pp. 70-78.
- [8] Ou, S., Han, J. C., Mehendale, A. B., and Lee, C. P., 1994, "Unsteady Wake Over a Linear Turbine Blade Cascade With Air and CO₂ Film Injection: Part

- I—Effect on Heat Transfer Coefficients,” *ASME J. Turbomach.*, **116**, pp. 721–729.
- [9] Mehendale, A. B., Han, J. C., Ou, S., and Lee, C. P., 1994, “Unsteady Wake Over a Linear Turbine Blade Cascade With Air and CO₂ Film Injection: Part II—Effect on Film Effectiveness and Heat Transfer Distributions,” *ASME J. Turbomach.*, **116**, pp. 730–737.
- [10] Jiang, H. W., and Han, J. C., 1996, “Effect of Film Hole Row Location on Film Effectiveness on a Gas Turbine Blade,” *ASME J. Turbomach.*, **118**, pp. 327–333.
- [11] Du, H., Han, J. C., and Ekkad, S. V., 1998, “Effect of Unsteady Wake on Detailed Heat Transfer Coefficients and Film Effectiveness Distributions for a Gas Turbine Blade,” *ASME J. Turbomach.*, **120**, pp. 808–817.
- [12] Du, H., Ekkad, S. V., and Han, J. C., 1999, “Effect of Unsteady Wake With Trailing Edge Coolant Ejection on Film Cooling Performance for a Gas Turbine Blade,” *ASME J. Turbomach.*, **121**, pp. 448–455.
- [13] Teng, S., Sohn, D. K., and Han, J. C., 2000, “Unsteady Wake Effect on Film Temperature and Effectiveness Distributions for a Gas Turbine Blade,” *ASME J. Turbomach.*, **122**, pp. 340–347.
- [14] Teng, S., Han, J. C., and Poinsatte, P. E., 2001, “Effect of Film-Hole Shape on Turbine-Blade Heat-Transfer Coefficient Distribution,” *J. Thermophys. Heat Transfer*, **15**, pp. 249–256.
- [15] Teng, S., Han, J. C., and Poinsatte, P. E., 2001, “Effect of Film-Hole Shape on Turbine-Blade Film-Cooling Performance,” *J. Thermophys. Heat Transfer*, **15**, pp. 257–265.
- [16] Heidmann, J. D., Lucci, B. L., and Reshotko, E., 2001, “An Experimental Study of the Effect of Wake Passing on Turbine Blade Film Cooling,” *ASME J. Turbomach.*, **123**, pp. 214–221.
- [17] Wolff, S., Fottner, L., and Ardey, S., 2002, “An Experimental Investigation on the Influence of Periodic Unsteady Inflow Conditions on Leading Edge Film Cooling,” *ASME Paper No. GT-2002-30202*.
- [18] Adami, P., Belardini, E., Montomoli, F., and Martelli, F., 2004, “Interaction Between Wake and Film Cooling Jets: Numerical Analysis,” *ASME Paper No. GT2004-53178*.
- [19] Burd, S., and Simon, T. W., 2000, “Effects of Hole Length, Supply Plenum Geometry, and Freestream Turbulence on Film Cooling Performance,” *NASA, Report No. CR-2000-210336*.
- [20] Schmidt, D. L., Sen, B., and Bogard, D. G., 1996, “Effects of Surface Roughness on Film Cooling,” *ASME Paper No. 96-GT-299*.
- [21] Pedersen, D. R., Eckert, E. R. G., and Goldstien, R. J., 1977, “Film Cooling With Large Density Differences Between the Mainstream and the Secondary Fluid Measured by the Heat-Mass Transfer Analogy,” *ASME J. Heat Transfer*, **99**, pp. 620–627.
- [22] Kohli, A., and Bogard, D. G., 1998, “Fluctuating Thermal Field in the Near-Hole Region for Film Cooling Flows,” *ASME J. Turbomach.*, **120**, pp. 86–91.
- [23] Sinha, A. K., Bogard, D. G., and Crawford, M. E., 1991, “Film Cooling Effectiveness Downstream of a Single Row of Holes With Variable Ratio,” *ASME J. Turbomach.*, **113**, pp. 442–449.
- [24] Pietrzyk, J. R., Bogard, D. G., and Crawford, M. E., 1990, “Effect of Density Ratio on the Hydrodynamics of Film Cooling,” *ASME J. Turbomach.*, **112**, pp. 437–443.
- [25] Coulthard, S. M., Volino, R. J., and Flack, K. A., 2006, “Effect of Unheated Starting Lengths on Film Cooling Experiments,” *ASME J. Turbomach.*, **128**, pp. 579–588.
- [26] Coulthard, S. M., Volino, R. J., and Flack, K. A., 2007, “Effect of Jet Pulsing on Film Cooling, Part 1: Effectiveness and Flowfield Temperature Results,” *ASME J. Turbomach.*, **129**, pp. 232–246.
- [27] Coulthard, S. M., Volino, R. J., and Flack, K. A., 2007, “Effect of Jet Pulsing on Film Cooling, Part 2: Heat Transfer Results,” *ASME J. Turbomach.*, **129**, pp. 247–257.
- [28] Sen, B., Schmidt, D. L., and Bogard, D. G., 1996, “Film Cooling With Compound Angle Holes: Heat Transfer,” *ASME J. Turbomach.*, **118**, pp. 800–806.

The Effects of Blade Passing on the Heat Transfer Coefficient of the Overtip Casing in a Transonic Turbine Stage

Steven J. Thorpe

Department of Aeronautical and
Automotive Engineering,
Loughborough University,
Loughborough LE12 7TW, UK
e-mail: s.j.thorpe@lboro.ac.uk

Roger W. Ainsworth

Department of Engineering Science,
University of Oxford,
Oxford, UK

In a modern gas turbine engine, the outer casing (shroud) of the shroudless high-pressure turbine is exposed to a combination of high flow temperatures and heat transfer coefficients. The casing is consequently subjected to high levels of convective heat transfer, a situation that is complicated by flow unsteadiness caused by periodic blade-passing events. In order to arrive at an overtip casing design that has an acceptable service life, it is essential for manufacturers to have appropriate predictive methods and cooling system configurations. It is known that both the flow temperature and boundary layer conductance on the casing wall vary during the blade-passing cycle. The current article reports the measurement of spatially and temporally resolved heat transfer coefficient (h) on the overtip casing wall of a fully scaled transonic turbine stage experiment. The results indicate that h is a maximum when a blade tip is immediately above the point in question, while the lower values of h are observed when the point is exposed to the rotor passage flow. Time-resolved measurements of static pressure are used to reveal the unsteady aerodynamic situation adjacent to the overtip casing wall. The data obtained from this fully scaled transonic turbine stage experiment are compared to previously published heat transfer data obtained in low-Mach number cascade-style tests of similar high-pressure blade geometries. [DOI: 10.1115/1.2776950]

Introduction

In a gas turbine engine, the design of the blade tips and the control of the tip leakage flows are important factors in the design of shroudless axial turbines. Tip leakage has significant implications for stage efficiency, heat transfer, and durability in high-pressure turbines. An extensive summary of the current state of knowledge relating to the tip-leakage problem is provided by Arts [1]. The basic physical process by which the pressure difference across the blade tip drives a leakage of fluid through the tip gap is well characterized from cascade-style testing in low-speed facilities (see, for example, Yamamoto [2]). Investigations such as those of Heyes et al. [3] have revealed the effect of blade-tip treatments and tip-gap height on the tip-leakage physics in a low-speed cascade. Such testing has concentrated on the important issue of aerodynamic loss produced by the leakage flow. The reported investigations of heat transfer in the tip region of high-pressure turbines concentrate on the blade tip rather than the overtip casing (shroud). The work of Kim and Metzger [4], Papa et al. [5], and Srinivasan and Goldstein [6] are representative examples of low-speed cascade-style testing. Such work has considered the effects of tip-gap height, blade-tip geometry, and blade/casing relative motion on blade-tip heat transfer.

The issue of overtip casing heat transfer has received less attention in the literature than the related problem of blade-tip heat transfer. Low-Mach number studies of casing heat transfer include the work of Cho et al. [7] who used the mass transfer analogy technique to investigate casing heat transfer in a low-speed linear cascade with a tip clearance up to 2.85% of blade span. The effect of tip-gap height was considered and compared to the case with no tip gap. Large differences were observed between these cases,

which were subsequently related to the effects of tip leakage on the blade-row aerodynamics. In general, high levels of mass (heat) transfer were observed in the tip gap and adjacent to the axis of the tip-leakage vortex. Being a cascade based investigation, this work did not simulate the effects of varying flow temperature through the turbine rotor. The work of Guenette et al. [8] is the first to report measurements of the overtip casing heat transfer rate in a fully scaled high-pressure turbine stage. These workers measured the time-resolved casing heat transfer rate at various axial positions through the rotor using a short-duration facility. Measurements at a tip gap of 0.8% of blade span and at different operating conditions (Reynolds number and rotational speed) gave valuable insight into the highly unsteady nature of heat transfer to the overtip casing wall. Elevated heat transfer was seen within the blade-tip gap adjacent to the blade pressure surface corner. The work of Chana and Jones [9] also reported time-resolved casing heat transfer rate, with the axial variation of time-mean adiabatic wall temperature also being presented (showing the reduction in flow temperature through the rotor). Polanka et al. [10] measured time-mean heat flux to the blade tip and casing wall of a fully scaled turbine stage. Guenette et al. [8] and Polanka et al. [10] did not include the measurement of the adiabatic wall temperature at each measurement position and were not able to separate the individual effects of the stage aerodynamics (heat transfer coefficient) and driver temperature (adiabatic wall temperature). Computational studies of overtip casing heat transfer include the work of Ameri and Steinhilber [11] and Ameri et al. [12]. The results reported by these workers showed a generally falling trend of heat transfer coefficient (Stanton number) with increasing axial distance through the rotor. An instantaneous "snapshot" of Stanton number on the casing is given in Ref. [11], showing the high values and strong spatial variations in the tip gap. Most recently, the experimental investigations reported by Thorpe et al. [13] have provided more detail on the effects of blade passing on casing heat transfer rate and also the effect of vane-rotor interactions. This work does include the measurement of the local adiabatic

Contributed by the International Gas Turbine Institute of ASME for publication in the JOURNAL OF TURBOMACHINERY. Manuscript received August 18, 2006; final manuscript received January 10, 2007; published online July 31, 2008. Review conducted by David Wisler. Paper presented at the ASME Turbo Expo 2006: Land, Sea and Air (GT2006), Barcelona, Spain, May 8–11, 2006, Paper No. GT2006-90534

wall temperature distribution through the rotor (both steady and time resolved). Following on from this work, Thorpe et al. [14] considered the time-varying temperature field in more details and related this to the stage aerodynamics and work transfer. In a further step, the current article reports measurements of time-resolved heat transfer coefficient (h) obtained in the same test facility and seeks to explain how this is related to the turbine flow conditions. To the authors knowledge, this is the first time that such data have been presented for a fully scaled turbine stage experiment. It is hoped that this information will promote a deeper understanding of the influence of tip-leakage flow physics on casing heat load. Ultimately, this study aims to promote better predictive procedures that improve the turbine design cycle and offer physical understanding that will allow engineers to make better informed design choices.

Statement of the Problem

When considering the thermal aspects of the high-pressure turbine, a designer relies on heat transfer data that allows prediction of the wall heat load under various operating conditions. It is also desirable to understand how design features (e.g., blade-tip shape) influence the heat load, and therefore how a design might be improved. In a gas turbine engine, the tip-leakage region of the high-pressure turbine presents a complex fluid dynamic situation, involving the highly unsteady and compressible flow of combustor-exit gases. The current state of knowledge relating to overtip casing heat transfer is relatively poor compared to other parts of the turbine. The flow field in the blade-tip region is complicated by the leakage of fluid through the tip gap, which interacts with the rotor passage flow to give rise to the tip-leakage vortex. When considering heat transfer to the overtip casing, a further complication arises due to the fact that work is exchanged between the fluid and rotor, leading to spatial and temporal variations in fluid temperature adjacent to the casing wall. In fact, as shown by Thorpe et al. [13], the fluid temperature near the casing wall fluctuates significantly at the characteristic blade-passing frequency (with an amplitude of order the stage total temperature drop). The overtip casing wall is exposed to pulsating flow conditions, with the frequency of pulsation being the blade-passing frequency (see Refs. [8,13]). Each point on the overtip casing wall is alternately exposed to a blade passage and then to a blade-tip gap: The flow conditions during these two distinct phases of the blade passing cycle are dramatically different. The primary effect of blade passing is to impose fluctuations on the near wall flow, including changes in pressure, flow speed, flow direction, and flow temperature. At a particular instant in time, these effects manifest themselves as a spatial distribution of heat flux; this distribution moves around the annulus at blade speed. Conversely, at a fixed point on the casing wall, the effect of blade passing is to establish a temporal fluctuation in heat flux. These changes occur at the characteristic blade-passing frequency, which is of the order of tens of kilohertz (depending upon the particular design of the turbine).

In situations where both the heat transfer driver temperature ($T_{aw} - T_w$) and heat transfer coefficient (h) are fluctuating in space and time, the utility of measuring heat flux alone is limited (this is the physical situation on the overtip casing of a transonic turbine). In order to understand the complex flow and thermal environment in the blade-tip region, it is important to separate the individual effects of the local h and heat transfer driver temperature, that is, to separate the aerodynamic effects (h) from the temperature effects ($T_{aw} - T_w$). This study seeks to achieve this for the overtip casing in a fully scaled high-pressure turbine test facility.

Overtip Casing Cooling Systems. In order to keep the turbine endwalls below the limiting temperatures, gas turbine engine manufacturers employ several strategies. The first of these is to manipulate the combustor-exit temperature profile such that the flow temperature adjacent to the endwalls is reduced. However, in recent years, the trend in producing combustor-exit flow condi-

tions with flatter radial temperature profiles has tended to mean that hotter fluid is present near the turbine endwalls. Consequently, endwall cooling is an increasingly important part of the overall thermal design process (see, for example, Chyu [15] for a discussion of endwall cooling). Film cooling of the nozzle guide vane endwall is also utilized, which can result in a lowering of the flow temperature near the rotor endwalls. The utility of these techniques is hampered by the blade-passing events in which the high velocity tip-leakage flow effectively scrubs the casing wall every time a blade tip passes by and tends to introduce high temperature fluid close to the overtip casing. Secondary flow effects in the vane row and the radial migration of hotter fluid also promote the presence of the highest temperature fluid near the outer endwall. Studies of tip-leakage aerodynamics have shown that fluid entering the tip gap can be drawn from radial heights far removed from the blade-tip radial position. This has the tendency to draw hot fluid from rotor midpassage into close proximity with the endwall. Ultimately, the limiting metal temperatures are controlled by active cooling of the rear side of the casing wall using compressor bleed air. Thermal barrier coatings may also be applied to the hot-gas side. From a cooling system design point of view, it is essential to know the hot-side heat load at particular engine running conditions. This allows a thermal analysis of the casing wall to be conducted in association with the internal cooling characteristics to predict/optimize metal temperatures. Relevant design data and understanding for the hot-side gas path are particularly difficult to obtain, not least because of the time-varying aerothermal conditions, and changes in flow temperature that are present through the stage.

Definition of the Time-Resolved Heat Transfer Coefficient.

It is important to recognize the definition of heat transfer coefficient being employed in this study. On the casing wall, both T_{aw} and h fluctuate in space and time due to the effects of blade passing. In the experiments reported here, measurements of the local time-resolved heat flux, local time-resolved driver temperature, and local time-resolved heat transfer coefficient have been made. These are expressed as a function of the blade-passing cycle ϕ . The measurement parameters are defined and related by the following equation:

$$\dot{Q}(\phi) = h(\phi)[T_{aw}(\phi) - T_w] \quad (1)$$

where T_w has been assumed constant. The local time resolved h is therefore based on the local time resolved T_{aw} .

Experimental Approach

Turbine Test Facility. The experimental measurements described in this article were carried out in the Oxford Rotor Facility (Ainsworth et al. [16]). This facility has been used in various studies of high-pressure turbine aerodynamics and heat transfer, including blade-row interaction (Miller et al. [17]), blade-tip heat transfer (Thorpe et al. [18]), aerodynamic loss (Payne et al. [19]), and turbine stage performance (Atkins and Ainsworth [20]). This is a short-duration transonic turbine stage experiment that uses an isentropic light piston tube to generate the required flow conditions. The turbine operating parameters are typical of those found in modern high-pressure turbine stages. Before each test, the inlet air is isentropically compressed to raise its stagnation temperature (to 374 K). This ensures that an engine representative gas to wall temperature ratio of 1.18 is maintained during the 200 ms runtime of the facility, enabling the use of fast-response transient heat transfer instrumentation (described later).

The working section of the facility contains a 0.55 m diameter shroudless high-pressure turbine stage and allows the simulation of engine representative Mach and Reynolds numbers as well as the appropriate gas to wall temperature ratio. The turbine stage consists of 36 nozzle guide vanes with an exit Mach number of 0.95 and an exit Reynolds number of 2.7×10^6 based on axial chord. The rotor disk has 60 blades and a design rotational speed

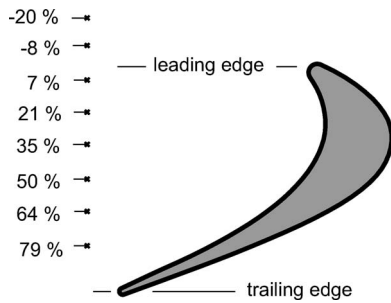


Fig. 1 A schematic diagram showing the axial positions of the casing heat transfer instrumentation (numbers refer to axial chord)

of 8910 rpm. The blade-exit Mach number is 0.98 and the blade axial chord is 24 mm. The tip clearance of the rotor was 2.25% of blade height. This tip gap is larger than might be seen in current engine service but is representative of a machine that has been in service and suffered some erosion of the tip surfaces. The axial gap between the upstream vanes and rotor was 36% of vane axial chord. The total flow-on time was 200 ms, which represents approximately 30 rotor disk revolutions.

Casing Heat Transfer Instrumentation. An array of fast-response thin-film gauges mounted on a contoured ceramic insert was used to measure the unsteady heat transfer rate to the overtip casing wall. In order to generate heat transfer data with high spatial fidelity, a new fabrication technique was devised that allows miniature thin-film sensors to be etched directly onto the turbine components at precisely known locations. Further details of the heat transfer instrumentation and laser etching technique are provided by Thorpe et al. [21]. The casing heat flux sensors are $1 \times 0.08 \text{ mm}^2$ in plan form and arranged in a regular 7×8 array across one nozzle guide vane pitch (7 in the circumferential direction and 8 in the axial direction). The frequency response of the heat transfer measurement system is from dc to 100 kHz. The axial positioning of the heat transfer gauges is shown in Fig. 1.

The unsteady heat transfer rate can be considered to consist of three components: the time-mean value, the deterministic unsteady fluctuation, and the random unsteady fluctuation. The deterministic unsteady component is related to the effects of blade passing. The data presented later are ensemble averaged at the blade-passing frequency so as to establish the effect of blade-passing and remove random fluctuations.

Measurement of Time-Resolved Heat Transfer Coefficient and Adiabatic Wall Temperature. As was noted previously, the fluctuating heat transfer rate to the casing wall is influenced by both aerodynamic and thermal unsteadiness, which cause the heat transfer coefficient and driver temperature to vary in space and time. The emphasis in the current work is to isolate the individual effects of these time-varying quantities on the wall heat flux. This has required the development of a new approach to heat transfer measurement in short-duration wind tunnels such as the Oxford Rotor Facility [21].

The method for measuring time-resolved heat transfer coefficient and adiabatic wall temperature is as follows. For each heat transfer gauge, the time-resolved wall heat flux is measured at a range of wall temperatures. This involves several repeat tests in the turbine facility, with the wall temperature being adjusted to a different value prior to each test. The time-resolved heat transfer data for each gauge are ensemble averaged at the blade-passing frequency to produce the deterministic unsteady component: That is, the heat transfer rate is expressed as a function of blade-passing phase. At each time point in the blade-passing cycle, the heat transfer rate is plotted as a function of wall temperature, using the data accumulated over typically ten turbine facility tests. A linear

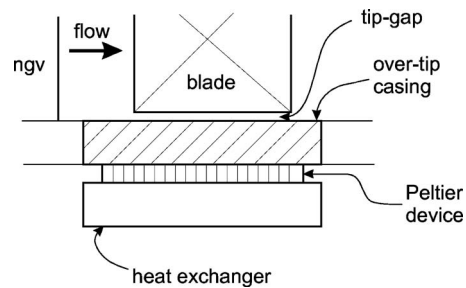


Fig. 2 Schematic diagram of the heat transfer instrumentation (showing Peltier installation)

relationship between \dot{Q} and T_w has been observed in both time-mean and time-resolved data. The values of h and T_{aw} at each phase in the blade-passing period are then determined from a straight line fit to the data. For each heat transfer gauge, this analysis produces the heat transfer coefficient and adiabatic wall temperature as a function of blade-passing phase.

To achieve this type of measurement, it is necessary to set the casing wall temperature to a particular value before each test in the short-duration turbine facility. The instrumented sector of the casing wall can therefore be heated or cooled prior to each test. In this way, the unsteady heat transfer rate can be measured as a function of the wall temperature. Heating or cooling of the wall has been achieved using a Peltier heat pump device. The wall temperature can be adjusted over a range of 35 K by varying the electrical power supplied to the heater/cooler. Figure 2 shows a schematic diagram of the instrumented casing wall sector.

Measurement Accuracy. The measurement of wall surface heat flux with thin-film gauges is a well characterized experimental technique that has been used for many years (Schultz and Jones [22]). The accuracy of this type of measurement system is generally around 5% in surface heat transfer rate (at 95% confidence); most of this uncertainty is associated with the thermal product of the substrate material. The measurement of adiabatic wall temperature and heat transfer coefficient as described in this article is a more complex experimental procedure that introduces additional uncertainties. The uncertainty in these measured parameters has been assessed and reported by Thorpe et al. [21]. The measurement performance depends upon several factors, including the calibration uncertainty of the thin-film gauge temperature response and the repeatability of the experimental facility flow conditions. In addition, the uncertainty is influenced by the range of wall temperatures employed in the procedure and the number of tests used to define the relationship between wall heat flux and wall temperature. Typical uncertainties are 3 K for T_{aw} and 12% for h . Spatial resolution is limited by the gauge size (1.0 mm).

Experimental Results

This section presents the experimental data obtained for the casing wall. The ensemble averaged heat flux, heat transfer coefficient, and adiabatic wall temperature are described at various axial positions and as a function of the blade-passing cycle. Note that the blade-passing period is $1.12 \times 10^{-4} \text{ s}$. The data from the seven heat transfer gauges at each axial location are phase shifted and averaged in order to remove vane-interaction effects. It should be noted that some vane-interaction effects have been observed in the data. However, the purpose of the current article is to present the overall effect of blade passing on the casing heat transfer coefficient rather than the details of vane-rotor interaction.

The graphs present data at positions that range from -20% to +79% rotor axial chord (the positions noted in Fig. 1). The graphs have lines that indicate the point in the blade-passing cycle when the suction surface (green) and pressure surface (red) arrive at the

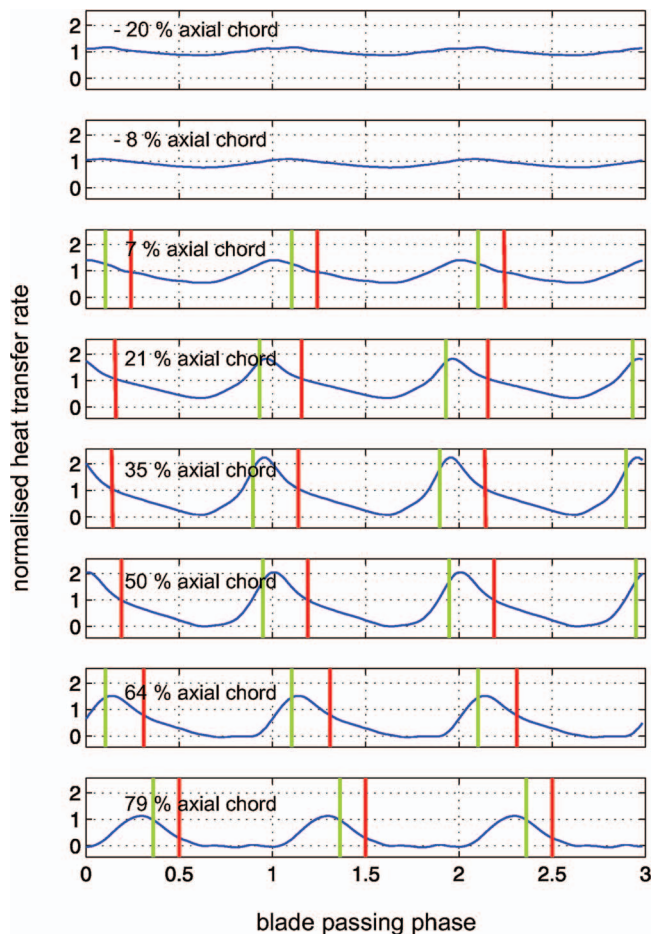


Fig. 3 The time-resolved heat transfer rate at various axial locations as a function of blade-passing phase (green line indicates blade suction surface, and red line the blade pressure surface)

particular measurement location. In addition to the graphs, the data are also plotted in contour format to illustrate the spatial effects of blade passing.

Heat Transfer Rate. Figure 3 shows a series of graphs of the time-resolved heat transfer rate at eight axial positions on the casing wall. Note that all the data have been normalized by the time-mean heat transfer rate at -20% axial chord. Upstream of the blade-row (in the vane-rotor axial gap) small amplitude fluctuations in the heat transfer rate can be observed. The peak is associated with the presence of a blade leading edge immediately downstream. This indicates that the presence of the moving blades propagates upstream of the blade leading edge and affects the heat transfer rate. These changes in heat flux may be due to a modification of h , T_{aw} , or both. Between 7% and 50% axial chords, the amplitude of the fluctuation in heat flux increases. Beyond 50% axial chord, the amplitude reduces slightly. In this region ($7\text{--}79\%$ axial chord), the blade tip passes directly over the measurement positions, giving characteristically large changes in heat transfer rate. At all axial locations, the highest heat transfer rates are associated with the tip-leakage flow. In general, the highest amplitude fluctuations are coincident with the regions of highest blade lift (around midaxial chord) where the tip-leakage flow is likely to be strongest. In the blade passage, the heat flux is high toward the blade pressure surface, with a minimum heat flux occurring in the midpassage region. However, a rapid increase in heat flux is observed as the blade suction surface approaches the measurement point. Toward the trailing edge of the rotor (79% axial chord), the

heat flux in the center of the passage becomes more uniform than is seen further forward, with a less pronounced minimum. This possibly reflects more uniform flow conditions in this region compared to further upstream where large cross-passage gradients exist in the flow conditions.

The casing heat flux data presented in Fig. 3 are also shown as a contour plot in Fig. 6(a). This figure graphically illustrates the relationship between the blade position and the spatial distribution of heat flux on the casing wall. It is clear that the heat flux falls as the flow transits the blade row, and that very high heat transfer to the casing occurs within the tip gap. The region of highest heat transfer occurs in the tip gap toward the blade suction surface and centered on midaxial chord (Label A). Lowest heat transfer rates occur in the blade passage towards blade exit (Label B). There appears to be little or no effect of the tip-leakage vortex on the casing heat transfer. This coincides with the observations of Guenette et al. [8] for a turbine with a smaller tip clearance (0.8% of blade span compared to 2.25% in the current work). The results given in Ref. [8] also show a region of highest heat transfer in the tip gap but adjacent to the pressure surface rather than the suction surface.

While the phase-resolved heat flux data are very useful for understanding the overall impact of blade passing on heat transfer, they do not immediately allow physical insight into why the heat flux is varying. A more useful understanding could be gained from knowing by how much h and T_{aw} are changing during the blade-passing cycle. It is the intention of the following sections to quantify the relative importance of these two factors.

Heat Transfer Coefficient. Figure 4 shows a series of graphs of the measured time-resolved heat transfer coefficient at eight axial positions on the casing wall as a function of blade-passing phase (note that all the data are normalized by the time mean h at -20% axial chord). The data are presented in the same format as the heat flux data shown in Fig. 3: the green and red vertical lines indicate the position of the blade suction surface and pressure surface (red), respectively. The data are generally characterized by large fluctuations in heat transfer coefficient as the blades pass over the casing wall. In the vane-blade axial gap (-20% and -8% axial chord), small blade-phase related changes in heat transfer coefficient are evident: An increase occurs when the blade leading edge is immediately downstream. It appears that the presence of the moving blades affects conditions upstream in the transonic exit conditions at vane exit, leading to a modification of the thermal conductance of the boundary layer.

At positions further downstream, a strong increase in heat transfer coefficient is clearly seen within the blade-tip gap, where the highest h values are measured at each axial location. The largest amplitude fluctuations in h are seen around the midaxial chord region (35% , 50% , and 64%). Comparing the data with that in Fig. 3, it is clear that the time-varying h is a significant factor in causing the related changes in heat flux.

In the overtip region, where the blade tips pass directly over the measurement positions, a sharp rise in h is evident as the blade suction surface approaches (green line), reaching a peak value within the tip gap. A fall in h is noted as the blade tip continues to pass over and the blade-pressure surface approaches. Within the blade passage h is generally higher near the blade pressure surface. However, h falls as the blade passage traverses the measurement point and reaches a minimum toward the blade suction surface.

The mean level of the heat transfer coefficient falls consistently with increasing axial distance. It is also clear that h can more than double during the blade-passing cycle (at 35% and 50% axial chord), and that a large fluctuation in h is seen throughout the overtip region of the casing.

The casing heat transfer coefficient data are also presented as a contour plot in Fig. 6(b), which clearly illustrates the spatial effects of blade passing. Comparing these data with the heat flux

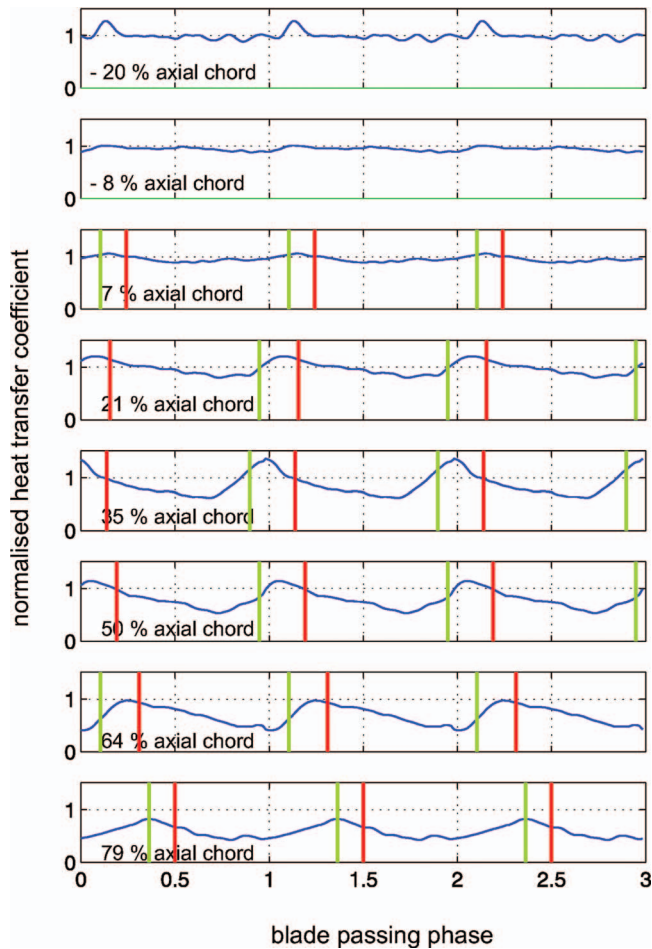


Fig. 4 The time-resolved heat transfer coefficient at various axial locations as a function of blade-passing phase (green line indicates blade suction surface, and the red line the blade pressure surface)

data presented in Fig. 6(a), it is clear that the time-varying heat flux distribution is associated with the changing level of the heat transfer coefficient (as might be anticipated). The highest values are seen in the tip gap (Label A). Likewise, the regions of low heat transfer rate in the blade passage (Label B) are regions of low h . However, the changes in h do not entirely explain the observed variation in heat flux. For example, along the forward part of the suction surface of the blade (Label “C”), a region of high heat flux extends axially upstream of the blade tip, but this is not reflected in a comparable area of high h in Fig. 6(b). Clearly, a second mechanism is also important in this region (this being the flow temperature and discussed in a later section). Interestingly, there is no evidence of an increase in h in the blade passage due to the tip-leakage vortex, in contrast to the results seen in low-Mach number cascade testing by Cho et al. [7]. In the results of Ref. [7], the tip-leakage vortex was seen to emerge from the tip gap at around 60% rotor axial chord for a similar tip-gap height to that used in the current work. It is of course difficult to draw conclusions since the blading in the two cases is not identical. The localized region of high h in the tip gap (Label A) is also not seen in the results of Ref. [7]. In fact, apart from the work of Cho et al. [7], no direct comparable data relating to h on the casing wall are known to the authors. A more detailed discussion of the factors affecting the heat transfer coefficient is presented in a later section.

Adiabatic Wall Temperature. Figure 5 shows a series of graphs of the measured time-resolved adiabatic wall temperature

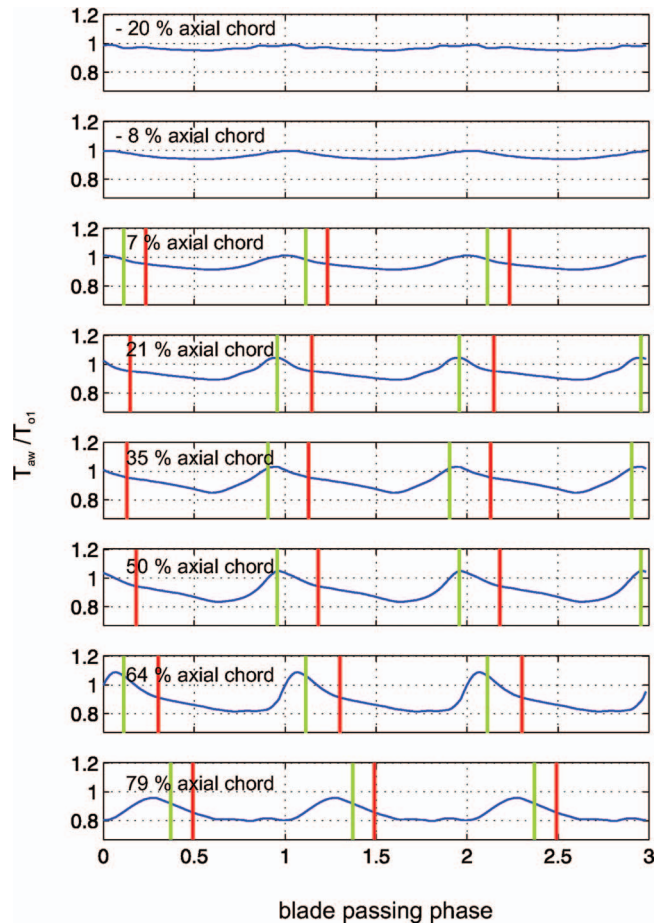


Fig. 5 The time-resolved adiabatic wall temperature at various axial locations as a function of blade-passing phase (green line indicates blade suction surface, and the red line the blade pressure surface)

on the casing wall. Generally, the structure of the time-resolved data is similar to that of the heat flux shown in Fig. 3, as might be expected. As was observed in the heat flux and h data, it is evident that fluctuations in flow temperature occur upstream of the blade row in the vane-rotor axial gap: Fluctuations in temperature of around 25 K are observed at -8% axial chord, with the peak being associated with the presence of a blade leading edge immediately downstream. The spatial structure of these fluctuations can be appreciated from the contour plot presented in Fig. 6(c). It is interesting to note that a region of higher temperature extends axially upstream of the blade suction surface (Label C). This region of elevated temperature explains the high heat flux also observed in this region in Fig. 6(a).

The variations in the casing T_{aw} are due to the distribution of work transfer within the turbine rotor (this is discussed in detail by Thorpe et al. [14]). As the flow passes through the blade passage, it is turned and decelerated in the absolute frame of reference. The absolute total temperature of the flow drops as energy is extracted and its absolute circumferential velocity is reduced. This is clearly seen in the contour plot in Fig. 6(c) (Label B). The reduction in T_{aw} in the blade passage produces a correspondingly strong attenuation of heat flux, as seen in Fig. 6(a) (Label B). It is interesting to note that the highest measured T_{aw} occurs within the tip gap and is actually higher than the value seen at rotor inlet. This increase in absolute temperature is caused by work transfer to the fluid, that is, energy addition to the tip-leakage fluid [14].

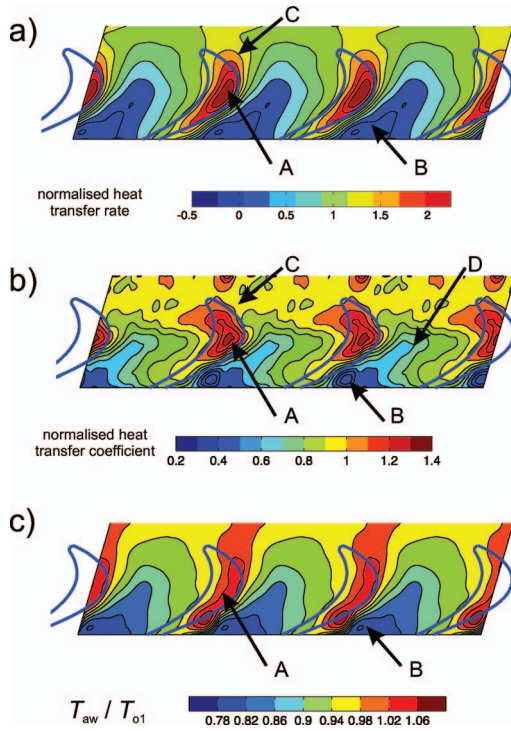


Fig. 6 Contour plots of the time-resolved conditions on the overtip casing wall: (a) heat transfer rate, (b) heat transfer coefficient, and (c) adiabatic wall temperature

The regions of high T_{aw} in the tip gap are also associated with high heat flux, which can be appreciated by comparing Figs. 6(a) and 6(c).

Further Discussion of Results

To summarize the experimental findings, (1) higher heat transfer to the casing occurs in the blade-tip gap, while lower heat transfer occurs in the blade passage; (2) the heat transfer in the passage decreases as the absolute flow temperature and heat transfer coefficient and flow temperature in the tip gap are generally high, while those in the blade passage are lower. The factors giving rise to these observations will now be discussed.

It is normal for aerodynamicists to consider the flow through the rotor blade passages in the blade-relative frame of reference. However, it is essential to use the flow conditions in the absolute frame when considering heat transfer to the overtip casing. This allows the effects of the blade/casing relative motion to be taken into account, as well as the effect of changing flow total temperature. Shown in Fig. 7 is a schematic diagram of typical velocity vectors at a few points of interest on the casing wall: red vectors are absolute, and black vectors are blade relative. The measured static pressure distribution on the casing wall is shown in Fig. 8 in an equivalent manner to the heat transfer data presented in Fig. 6(a). The nozzle guide vane exit flow (Label “a”) and the blade-tip gaps (Labels “b” and “d”) are regions of high absolute flow velocity. At position a, the nozzle guide vane exit flow is close to sonic, as revealed in the static pressure distribution shown in Fig. 8. In a transonic turbine, the pressure ratio across some parts of the blade-tip gap is sufficient to drive sonic and even supersonic flow speeds in the blade-relative frame of Ref. [23]. Also, the tip-leakage flow vector may have a component in the direction of blade movement. As a consequence, the flow speed in the tip gap in the absolute frame of reference can be particularly high. These regions of high flow speed are seen in Fig. 6(b) to be areas of high heat transfer coefficient also. In the blade passage, the flow is

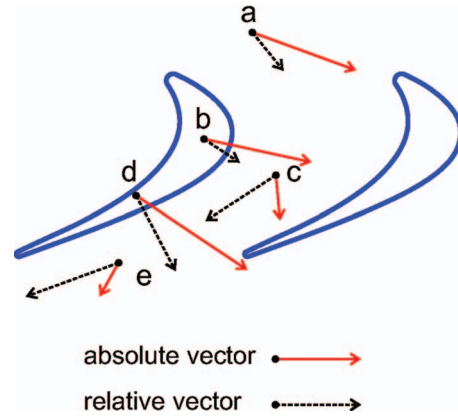


Fig. 7 A schematic diagram illustrating typical flow vectors in the blade-tip region

turned and accelerated in the blade relative frame of reference, leading to a reduction of static pressure, as seen in Fig. 8. When viewed in the absolute frame, this leads to a reduction in flow speed, as shown by the red vectors at labels a, c, and e in Fig. 7. This reduction in absolute speed is associated with a reducing heat transfer coefficient, as seen in Fig. 6(b) at Label “D.” In addition to these flow speed changes, the schematic diagram in Fig. 7 also suggests that the flow direction on the casing wall oscillates over a wide angular range during the blade-passing period. In addition, the regions of high absolute flow velocity also tend to be associated with high T_{aw} , as seen in Fig. 6(c). Overall, this means the tip gap transfers a disproportionate quantity of heat to the casing wall. Consequently, consideration of the effect of tip-leakage aerodynamics and blade-tip design is important to casing heat load.

Heat Transfer in the Presence of Periodic Temperature Fluctuations. The data in the previous sections have clearly demonstrated that both h and T_{aw} on the casing wall fluctuate in a cyclical manner at the blade-passing frequency. This section will consider the implications of this for the experimental investigation of casing heat transfer.

The time-resolved heat flux at a point on the casing wall can be expressed by Eq. (1), where the time-varying quantities are expressed as functions of the blade-passing phase, ϕ . Considering h , T_{aw} , and \dot{Q} to be composed of a time mean and periodic unsteady (deterministic) component, we can then write

$$\dot{Q}(\phi) = \bar{\dot{Q}} + \dot{Q}'(\phi)$$

$$T_{aw}(\phi) = \bar{T}_{aw} + T'_{aw}(\phi)$$

$$h(\phi) = \bar{h} + h'(\phi)$$

where the deterministic components have a zero time-mean value. Substituting these into Eq. (1), and taking the time-mean of the

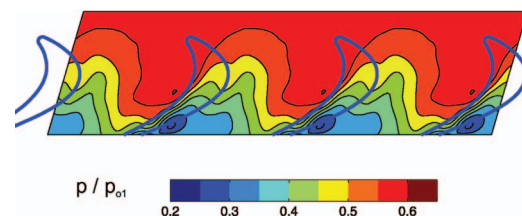


Fig. 8 A contour plot of the time-resolved casing static pressure

Table 1 Steady and unsteady heat flux contributions to casing heat load (expressed as a percentage of total heat load at each axial position)

| Axial position (%) | Steady heat flux (%) | Unsteady heat flux (%) |
|--------------------|----------------------|------------------------|
| -20 | 100 | 0 |
| -8 | 100 | 0 |
| 7 | 99 | 1 |
| 21 | 98 | 2 |
| 35 | 87 | 13 |
| 50 | 86 | 14 |
| 64 | 83 | 17 |
| 79 | 25 | 75 |

resulting equation, the following expression for the time-mean heat flux is obtained:

$$\underbrace{\bar{Q}}_{\text{time-mean heat flux}} = \underbrace{\bar{h}(\bar{T}_{aw} - T_w)}_{\text{steady heat flux}} + \underbrace{\overline{h'T'_{aw}}}_{\text{unsteady heat flux}} \quad (2)$$

This equation shows that the time-mean heat transfer rate can be considered to consist of two parts: (1) the steady part based on the time-mean heat transfer coefficient and adiabatic wall temperature, and (2) the unsteady part arising from the fluctuations in these parameters. This equation shows that the time-mean heat flux is not just dependent on the time-mean heat transfer coefficient (\bar{h}) and time-mean driver temperature ($\bar{T}_{aw} - T_w$). In fact, in a case where $\overline{h'T'_{aw}} \neq 0$, the fluctuating components also contribute to the net heat transfer rate: even in the case where $T_w = \bar{T}_{aw}$, the time-mean heat flux may still be nonzero. This point serves to emphasize that when both h and T_{aw} fluctuate, experimental simulation of the heat transfer conditions needs to be carefully considered. In the current investigation, the blade-passing events impose just such time-varying flow conditions on the casing wall. It is instructive then to determine the relative magnitude of the two terms on the right hand side of Eq. (2). Such an analysis can be achieved using the time-resolved data obtained in this study, and this is summarized in Table 1 (this being for a $T_{o1}/T_w = 1.18$). The data show that in regions of small amplitude fluctuations (-20% to 21% axial chord), the unsteady heat flux term is small, and the heat transfer can be described using time-mean quantities. In regions of high amplitude fluctuations and positions where the wall temperature is close to the time-mean adiabatic wall temperature ($35\text{--}79\%$ axial chord), the unsteady heat flux becomes a significant contributor to the overall heat load.

In light of these findings, it is suggested that when conducting experiments related to overtip casing heat transfer, the aim of the experiments needs to be carefully considered. Such experiments can be divided (roughly speaking) into two broad families: (1) fully scaled simulations of engine conditions that allow estimation of the heat transfer in an engine application (e.g., the turbine stage experiments reported here); (2) simplified experiments that allow the detailed investigation of design parameters but which do not incorporate the full scaling of the turbine problem (e.g., the use of low-Mach number cascade-style facilities). Low-Mach number cascade experiments are essentially isothermal and do not simulate the temperature fluctuations associated with work transfer ($T'_{aw} = 0$). Such testing is useful for ascertaining the effect of factors such as blade-tip design on \bar{h} . However, when deterministic fluctuations in both T_{aw} and h are present, the use of mean temperatures and mean heat transfer coefficients can be misleading when trying to predict engine heat transfer, as indicated by the discussion relating to Eq. (2).

Conclusions

Experimental measurements have shown that the overtip casing wall of a transonic turbine is exposed to large temporal fluctuations in heat transfer rate that are associated with blade-passing events. By adopting a new measurement strategy in a short-duration test facility, it has been possible to measure the time-resolved heat transfer coefficient and time-resolved adiabatic wall temperature associated with this blade passing. These data have allowed the aerodynamic causes of the fluctuating heat transfer rate to be assessed, that is, to separate the effects of heat transfer coefficient and flow temperature.

At some points on the casing wall, the ratio of maximum to minimum heat transfer coefficient during the blade-passing period can be in excess of 2. This large fluctuation is most pronounced in the midaxial chord region of the blade. At all measurement locations, the maximum value of the heat transfer coefficient is observed when a blade tip passes over a particular point. Lower levels of heat transfer coefficient have been seen during the transit of a blade passage, reaching a minimum just before the arrival of the blade suction surface. A steep rise in the local heat transfer coefficient is observed as the suction surface passes over the point in question. The effect of the moving blades propagates upstream into the vane-blade gap, producing changes in heat transfer coefficient and flow temperature. These are relatively small compared to the fluctuations seen in regions where the blade tip passes directly over the point in question. An explanation of the distribution of heat transfer coefficient based on the changes in absolute flow velocity has been proposed.

The overtip casing experiences flow conditions in the absolute frame of reference, and as a consequence is exposed to time-varying flow temperatures that are dictated by the distribution of work transfer within the rotor. Consideration of situations where both flow temperature and heat transfer coefficient are varying in time has shown that the net heat load to the casing is affected by both time-mean and time-varying quantities. Due to the elevated heat transfer coefficient in the tip gap, a disproportionate quantity of heat is transferred from the tip-leakage fluid to the casing wall. This suggests that the aerodynamic design of the blade tip is particularly important to casing heat load.

Acknowledgment

The authors would like to acknowledge the support of Rolls-Royce plc and the UK Government Department of Trade and Industry, and their permission to publish this article.

Nomenclature

| | |
|------------|--|
| h | = heat transfer coefficient |
| \bar{h} | = time-mean heat transfer coefficient |
| h' | = fluctuating component of heat transfer coefficient |
| p | = pressure |
| \dot{Q} | = wall heat flux |
| \bar{Q} | = time-mean wall heat flux |
| \dot{Q}' | = fluctuating component of wall heat flux |
| t | = time |
| T | = temperature |
| \bar{T} | = time-mean temperature |
| T' | = fluctuating component of temperature |
| ϕ | = blade-passing phase angle |

Subscripts

| | |
|----|--------------------------------|
| aw | = adiabatic wall |
| w | = wall |
| o1 | = stage inlet total conditions |

References

- [1] 2004, Turbine Blade Tip Design and Tip Clearance Treatment, von Karman Institute for Fluid Dynamics Lecture Series, T. Arts, ed., von Karman Institute for Fluid Dynamics, Brussels.
- [2] Yamamoto, A., 1989, "Endwall Flow/Loss Mechanisms in a Linear Turbine Cascade With Blade Tip-Clearance," *ASME J. Turbomach.*, **111**, pp. 264–275.
- [3] Heyes, F. J. G., Hodson, H. P., and Dailey, G. M., 1992, "The Effect of Blade Tip Geometry on the Tip Leakage Flow in Axial Turbine Cascades," *ASME J. Turbomach.*, **114**(3), pp. 643–651.
- [4] Kim, Y. W., and Metzger, D. E., 1995, "Heat Transfer and Effectiveness on Film Cooled Turbine Blade Tip Models," *ASME J. Turbomach.*, **117**(1), pp. 12–21.
- [5] Papa, M., Goldstein, R. J., and Gori, F., 2003, "Effects of Tip Geometry and Tip Clearance on the Mass/Heat Transfer From a Large-Scale Gas Turbine Blade," *ASME J. Turbomach.*, **125**(1), pp. 90–96.
- [6] Srinivasan, V., and Goldstein, R. J., 2003, "Effect of Endwall Motion on Blade Tip Heat Transfer," *ASME J. Turbomach.*, **125**(2), pp. 267–273.
- [7] Cho, H. H., Rhee, D. H., and Choi, J. H., 2001, "Heat/Mass Transfer Characteristics on Turbine Shroud With Blade Tip Clearance," *Ann. N.Y. Acad. Sci.*, **934**, pp. 281–288.
- [8] Guenette, G. R., Epstein, A. H., Norton, R. J. G., and Yuzhang, C., 1985, "Time-Resolved Measurements of a Turbine Rotor Stationary Tip Casing Pressure and Heat Transfer Field," AIAA Paper No. 85-1220.
- [9] Chana, K. S., and Jones, T. V., 2001, "An Investigation on Turbine Tip and Shroud Heat Transfer," *ASME J. Turbomach.*, **125**(3), pp. 513–520.
- [10] Polanka, M. D., Hoying, D. A., Meininger, M., and MacArthur, C. D., 2003, "Turbine Tip and Shroud Heat Transfer and Loading Part A: Parameter Effects Including Reynolds Number, Pressure Ratio, and Gas to Metal Temperature Ratio," *ASME J. Turbomach.*, **125**(1), pp. 97–106.
- [11] Ameri, A. A., and Steinthorsson, E., 1996, "Analysis of Gas Turbine Rotor Blade Tip and Shroud Heat Transfer," ASME Paper No. 96-GT-189.
- [12] Ameri, A. A., Steinthorsson, E., and Rigby, D. L., 1999, "Effects of Tip Clearance and Casing Recess on Heat Transfer and Stage Efficiency in Axial Turbines," *ASME J. Turbomach.*, **121**, pp. 683–693.
- [13] Thorpe, S. J., Yoshino, S., Ainsworth, R. W., and Harvey, N. W., 2004, "An Investigation of the Heat Transfer and Static Pressure on the Over-Tip Casing Wall of an Axial Turbine Operating at Engine Representative Flow Conditions—Part II: Time-Resolved Results," *Int. J. Heat Fluid Flow*, **25**(6), pp. 945–960.
- [14] Thorpe, S. J., Miller, R. J., Yoshino, S., Ainsworth, R. W., and Harvey, N. W., 2007, "The Effect of Work Processes on the Casing Heat Transfer of a Transonic Turbine," *ASME J. Turbomach.*, **129**, pp. 84–91.
- [15] Chyu, M. K., 2001, "Heat Transfer Near Turbine Nozzle Endwall," *Ann. N.Y. Acad. Sci.*, **934**, pp. 27–36.
- [16] Ainsworth, R. W., Schultz, D. L., Davies, M. R. D., Forth, C. J. P., Hilditch, M. A., Oldfield, M. L. G., and Sheard, A. G., 1988, "A Transient Flow Facility for the Study of the Thermofluid-Dynamics of a Full Stage Turbine Under Engine Representative Conditions," ASME Paper No. 8-GT-144.
- [17] Miller, R. J., Moss, R. W., Ainsworth, R. W., and Harvey, N. W., 2001, "Time-Resolved Vane-Rotor-Vane Interaction in a Transonic One-and-a-Half Stage Turbine," *Proc. Inst. Mech. Eng., Part A*, **215**(6), pp. 675–685.
- [18] Thorpe, S. J., Yoshino, S., Thomas, G. A., Ainsworth, R. W., and Harvey, N. W., 2005, "Blade-Tip Heat Transfer in a Transonic Turbine," *Proc. Inst. Mech. Eng., Part A*, **219**(A6), pp. 421–430.
- [19] Payne, S. J., Ainsworth, R. W., Miller, R. J., Moss, R. W., and Harvey, N. W., 2003, "Unsteady Loss in a High Pressure Turbine Stage," *Int. J. Heat Fluid Flow*, **24**(5), pp. 698–708.
- [20] Atkins, N. R., and Ainsworth, R. W., 2005, "The Measurement of Shaft Power in a Fully Scaled Transient Turbine Test Facility," ASME Paper No. GT2005-68998.
- [21] Thorpe, S. J., Yoshino, S., Ainsworth, R. W., and Harvey, N. W., 2004, "Improved Fast-Response Heat Transfer Instrumentation for Short Duration Wind Tunnels," *Meas. Sci. Technol.*, **15**(9), pp. 1897–1909.
- [22] Schultz, D. L., and Jones, T. V., 1973, "Heat-Transfer Measurements in Short-Duration Hypersonic Facilities," AGARDograph 165, North Atlantic Treaty Organization.
- [23] Moore, J., Moore, J. G., Henry, G. S., and Chaudhry, U., 1989, "Flow and Heat Transfer in Turbine Tip Gaps," *ASME J. Turbomach.*, **111**, pp. 301–309.

Combined Effects of Wakes and Jet Pulsing on Film Cooling

Kristofer M. Womack

Ralph J. Volino

e-mail: volino@usna.edu

Mechanical Engineering Department,
United States Naval Academy,
Annapolis, MD 21402

Michael P. Schultz

Naval Architecture and Ocean Engineering
Department,
United States Naval Academy,
Annapolis, MD 21402

Pulsed film cooling jets subject to periodic wakes were studied experimentally. The wakes were generated with a spoked wheel upstream of a flat plate. Cases with a single row of cylindrical film cooling holes inclined at 35 deg to the surface were considered at blowing ratios B of 0.50 and 1.0 with jet pulsing and wake Strouhal numbers of 0.15, 0.30, and 0.60. Wake timing was varied with respect to the pulsing. Temperature measurements were made using an infrared camera, thermocouples, and constant current (cold wire) anemometry. The local film cooling effectiveness and heat transfer coefficient were determined from the measured temperatures. Phase locked flow temperature fields were determined from cold-wire surveys. With $B=0.5$, wakes and pulsing both lead to a reduction in film cooling effectiveness, and the reduction is larger when wakes and pulsing are combined. With $B=1.0$, pulsing again causes a reduction in effectiveness, but wakes tend to counteract this effect somewhat by reducing jet lift-off. At low Strouhal numbers, wake timing had a significant effect on the instantaneous film cooling effectiveness, but wakes in general had very little effect on the time averaged effectiveness. At high Strouhal numbers, the wake effect was stronger, but the wake timing was less important. Wakes increased the heat transfer coefficient strongly and similarly in cases with and without film cooling, regardless of wake timing. Heat transfer coefficient ratios, similar to the time averaged film cooling effectiveness, did not depend strongly on wake timing for the cases considered. [DOI: 10.1115/1.2812335]

Introduction

Film cooling has been studied extensively to provide improved cooling of the airfoils in gas turbine engines and thus increase their life and allow for higher turbine inlet temperatures. Approximately 20–25% of compressor air is used for cooling of high performance turbine engines (Ekkad et al. [1]). If the amount of required coolant air could be reduced, engine efficiency would increase. Most investigations have focused on steady flow cases. The flow in a gas turbine engine, however, is inherently unsteady. The main flow is unsteady, with high freestream turbulence and periodic unsteadiness caused by the interaction between vane and blade rows in the turbine. Upstream airfoils shed wakes, which periodically impinge on the airfoils downstream. The wakes include a mean velocity deficit and increased turbulence, with effects similar to those of high freestream turbulence. Wakes can disrupt film cooling jets, reducing the film cooling effectiveness in some areas and possibly enhancing it in others. Wake induced turbulence may also increase heat transfer coefficients, thereby reducing the overall benefit of film cooling.

A few studies have investigated the effect of wakes on film cooling. Funazaki et al. [2,3] considered flow around the leading edge of a blunt body subject to wakes produced by a spoked wheel. In a series of studies, Ou et al. [4], Mehendale et al. [5], Jiang and Han [6], Ekkad et al. [7], Du et al. [8,9], and Teng et al. [10–12] used a linear cascade with an upstream spoked wheel to generate wakes. Film cooling effectiveness, heat transfer coefficients, and time averaged flow temperature fields were documented for cases with various blowing ratios, hole locations and geometries, density ratios, and freestream turbulence levels. Heidmann et al. [13] used a rotating facility to investigate the effect of wakes on showerhead film cooling. They report time averaged film effectiveness. Wolff et al. [14] utilized a linear cascade in a high speed facility with cooling holes on the suction side

and pressure side of their center blade. Wakes were generated with rods fastened to belts, which traveled around the cascade and two pulleys. Phase averaged velocity and turbulence levels were documented in multiple planes on both sides of the airfoil. Adami et al. [15] did numerical simulations of the flow through this cascade. Deinert and Hourmouziadis [16] conducted an experimental study in which they investigated the effects of main flow unsteadiness, but without wakes. The test surface was a flat plate, and a rotating flap downstream of the plate created the unsteadiness. Film cooling acted to suppress a separation bubble on the surface. Documentation included phase averaged velocity and temperature fields in the flow.

Further discussion of the studies listed above is available in Womack et al. [17], who documented the unsteady temperature field in a film cooling flow on a flat plate disturbed by wakes from a spoked wheel. The spokes rotated toward the plate, simulating the wake effect on an airfoil suction surface. Phase averaged temperature fields showed how the wake causes the film cooling jet to disperse. The jet returned to a steady condition between wakes at low wake Strouhal numbers, but there was insufficient time for full recovery at higher Strouhal numbers. At low blowing ratios ($B=0.25$ and 0.5), the wakes resulted in lower film cooling effectiveness, but at a higher blowing ratio ($B=1.0$), the wakes helped to mitigate jet lift-off effects by pushing the film cooling fluid back toward the wall and increasing the effectiveness. Heat transfer coefficients increased with wake passing frequency, with nearly the same percentage increase in the cases with and without film cooling. Unsteady near-wall flow temperature measurements were used to approximate the unsteady film cooling effectiveness during the wake passing cycle. During the wake passing, the unsteady effectiveness was low and approximately equal for cases at all Strouhal numbers. Variation during the rest of the cycle depended on the time available for recovery between wakes. At the lowest Strouhal number considered, the unsteady effectiveness during the wake passing dropped to less than 50% of the between wake value at some locations.

In addition to shedding wakes, airfoils passing both upstream and downstream of a turbine passage cause periodic flow blockage, inducing pressure fluctuations, which could cause film cool-

Contributed by the International Gas Turbine Institute of ASME for publication in the JOURNAL OF TURBOMACHINERY. Manuscript received June 6, 2007; final manuscript received June 22, 2007; published online August 1, 2008. Review conducted by David Wisler. Paper presented at the ASME Turbo Expo 2007: Land, Sea and Air (GT2007), Montreal, Quebec, Canada, May 14–17, 2007.

ing jets to pulsate. Only a few studies have considered the effects of pulsed jets. Bons et al. [18] used a loudspeaker to induce pulsations in their jets and examined the effects on film cooling of a flat plate. They found that pulsation resulted in reduced film cooling effectiveness for low blowing ratios, and that the effectiveness increased slightly as the blowing ratio increased to 1.5. Ligrani et al. [19], Seo et al. [20], and Jung et al. [21] used static pressure pulsations of the main flow to induce jet pulsing. They showed that pulsations cause the film cooling jet to spread more uniformly across the test surface.

Ekkad et al. [1] were the first to consider direct control of the coolant jets to improve film cooling. They controlled the pulsing using solenoid valves. Their geometry had a single film cooling hole angled at 20 deg to the surface and 90 deg to the streamwise direction, located on the leading section of a cylinder. Ekkad et al. [1] stated that pulsed jets increase the ability to effectively protect the surface and slightly lower heat transfer coefficients compared to continuous jets in some cases. Ou and Rivir [22] also found promising results in a study of shaped cooling holes using the same facility. Nikitopoulos et al. [23] did a numerical study of pulsed film cooling.

Coulthard et al. [24,25] considered pulsed film cooling from a row of holes on a flat plate. Solenoid valves were used to cyclically turn the jets on and off. Film cooling effectiveness, heat transfer coefficients, and unsteady flow temperature fields were documented. Pulsing the film coolant resulted in higher heat transfer coefficients, but the change was generally small compared to the changes in the film cooling effectiveness. Pulsing induced a high startup velocity, which momentarily increased jet lift-off. Higher pulsing frequencies tended to result in lower effectiveness. At the highest frequencies tested, however, this trend was reversed. There was insufficient time for the jets to turn fully off, resulting in some low momentum flow from the hole during the "off" portion of the cycle. At high blowing ratios, this low momentum fluid helped mitigate jet lift-off, thereby increasing the effectiveness.

Whether or not controlled pulsing can improve film cooling, natural pulsation occurs in engines and occurs in combination with wakes. To the authors' knowledge, the combined effects have not been studied in detail. The incomplete knowledge of unsteady cooling flow behavior is typically overcome by supplying enough cooling air to prevent damage to all components in the turbine. This can lead to overcooling in some areas, reducing engine efficiency. Better documentation of the unsteady behavior may lead to more efficient use of cooling air and increased engine efficiency. Given the large change in unsteady film cooling effectiveness during wake passing events documented by Womack et al. [17], the timing of pulses relative to wakes may be very important. If the pulse timing could be controlled, it might be advantageous to provide coolant only when it would be effective. Alternatively, Womack et al. [17] noted that wakes tend to mitigate jet lift-off by pushing film cooling jets back toward the surface. If wakes were timed to coincide with the start of a pulse, they might help to control the lift-off associated with startup noted by Coulthard et al. [24]. Since film cooling jets pulse in response to pressure fluctuations in engines, it might be possible through clocking to control the timing.

In the present study, the effects of pulsed jets and wakes on film cooling are combined. Experiments were conducted in a flat plate facility with a single row of five streamwise oriented round holes inclined at 35 deg to the surface and spaced $3D$ apart. The geometry has been used in many studies including Bons et al. [18], Burd and Simon [26], Pedersen et al. [27], and Kohli and Bogard [28]. Blowing ratios of 0.5, and 1.0 were investigated with various wake passing frequencies and pulse timings relative to the wakes. In all cases, the wake passing and pulsing frequencies were equal. Phase averaged flow temperature distributions and time averaged film cooling effectiveness and heat transfer results are presented below.

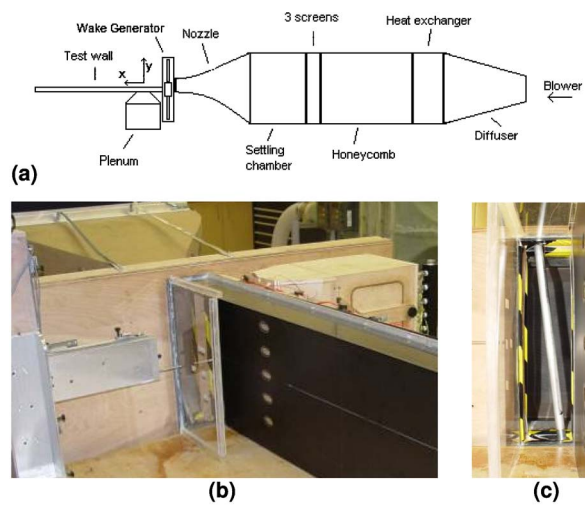


Fig. 1 Wind tunnel configuration: (a) schematic, (b) photograph of test wall with sidewalls, (c) photograph looking upstream at rod moving across main flow

Experimental Facility and Measurements

Experiments were conducted in the facility constructed by Coulthard et al. [24,25,29] to study pulsing effects and modified by Womack et al. [17] to include wakes. It consists of an open loop subsonic wind tunnel with a test plate at the exit of the contraction, and a plenum to supply the film cooling jets. The wind tunnel, shown in Fig. 1, was comprised of a blower, a diffuser with three screens, a heat exchanger to maintain air nominally at 20°C, a honeycomb, a settling chamber with three screens, and a nozzle with an 8.8 area reduction. The nozzle exit area was $0.38 \times 0.10 \text{ m}^2$. The exiting mainstream air was uniform in temperature and velocity to within 0.1°C and 1%, respectively. The freestream turbulence intensity at the nozzle exit was 1%. This value is lower than typical intensity levels in engines. Air exiting the nozzle forms a wall jet at $U_\infty = 8 \text{ m/s}$ along the flat plate test wall. The mainstream velocity remained at 8 m/s $18D$ downstream of the film cooling holes. At this downstream location, the velocity outside the boundary layer was uniform up to the edge of the free shear layer, which was located $3D$ from the wall. The freestream unsteadiness level (rms streamwise fluctuations normalized on freestream velocity) gradually increased in the streamwise direction to 6%. This increase is due to the growth of the shear layer at the edge of the wall jet. Spectral measurements indicate that the freestream fluctuations are nearly all at frequencies between 5 Hz and 50 Hz, with a peak at 22 Hz. These low frequencies are associated with large scale structures formed in the shear layer, which buffet the boundary layer, but do not promote significant turbulent mixing. The boundary layer is therefore expected to behave as if subject to low freestream turbulence, and the heat transfer coefficient results in Coulthard et al. [29] are typical of low freestream turbulence conditions. The wall jet configuration is based on the facility of Burd and Simon [26].

The film cooling supply plenum was a box with $0.38 \times 0.18 \times 0.36 \text{ m}^3$ inside dimensions. It was supplied by a manifold connected to a high pressure air source. The supply pressure was adjusted to vary the blowing ratio from $B=0.5$ to 1.0. The air passed through small diameter, fast response solenoid valves (General Valve Series 9 valves with Iota 1 controllers), which choked the flow between the manifold and the plenum. For a given supply pressure, the film cooling mass flow remains constant, independent of downstream conditions. Nine valves operating in parallel provided the desired coolant mass flow. The valves could be opened for continuous blowing or set to cycle between fully open and fully closed positions. In the present pulsed cases,

they were set for a 50% duty cycle, i.e., the valves were open and closed for equal intervals during the jet pulsing cycle. The plenum contained a finned tube heat exchanger, midway between the valves and the film cooling holes. Warm water at 30°C circulated through the tubes, heating the air to approximately 27°C. Details of the capacitance of the plenum and the response of the film cooling jets to the valve actuation are available in Coulthard et al. [24].

The test wall was constructed of polyurethane foam with a thermal conductivity of 0.03 W/mK. The dimensions were 0.38 m wide, 44 mm thick, and 1.17 m long, with a starting length of 13.3*D* upstream of the row of film cooling holes. A wall opposite the starting length and sidewalls along the length of the test wall, as shown in Fig. 1(b), helped limit interaction between the wind tunnel flow and the still air in the room. Foil heating elements were placed on the foam surface to provide a uniform heat flux condition, and are described in more details in Coulthard et al. [25,29]. Heaters were located both upstream and downstream of the film cooling holes. The heaters were covered with a 0.79 mm thick sheet of black Formica® laminate to provide a smooth test surface. The film cooling geometry consisted of a single row of five round holes inclined at 35 deg to the surface. The sharp edged holes had a diameter of $D=19.05$ mm, a length to diameter ratio $L/D=4$, and were spaced $3D$ apart, center to center. A 1.6 mm thick trip was installed $11D$ upstream of the leading edge of the film cooling holes, producing a fully turbulent boundary layer.

Wakes were generated with a spoked wheel between the contraction and the test plate. The hub of the wheel was driven by an electric motor and had 24 threaded holes around its circumference, into which 38 cm long, 1.905 cm diameter hollow aluminum rods could be installed. When the hub was rotated, the rods cut through the main flow, generating wakes. The rods were intended to produce wakes simulating those shed from the trailing edges of upstream airfoils. In an engine, the diameter of an airfoil trailing edge is of the same order as the diameter of typical film cooling holes. The rods in the present study, therefore, were chosen to have the same diameter as the film cooling holes in the test plate. The wake passing velocity in a turbine is of the same order as the main flow velocity, so the rotation speed of the spoked wheel was set at 200 rpm, which produced rod velocities of 8 m/s at the spanwise centerline of the test section. Combinations of 3, 6, and 12 rods were used to produce wake passing frequencies of 10 Hz, 20 Hz, and 40 Hz. When nondimensionalized using the rod diameter and main flow velocity, these frequencies correspond to Strouhal numbers, $Sr=2\pi fD/U_\infty$, of 0.15, 0.30, and 0.60. These Sr are typical of engine conditions and match the range considered by Heidmann et al. [13]. The direction of rotation was set so that the rods moved toward the test plate (clockwise when looking upstream in Figs. 1(b) and 1(c)), to simulate wakes impacting the suction side of an airfoil. Further details of the wake generator are available in Womack et al. [17].

Measurements. Thermocouples were placed in the film cooling plenum, at the plenum-side end of the outermost film cooling hole, at the wind tunnel exit, on the back of the test plate, in the ambient air, on the wall of the room to measure the surrounding temperature for radiation corrections, and in ice water as a reference. Constant current (cold-wire) and constant temperature (hot-wire) anemometry were used to measure flow temperature and velocity, respectively. Boundary layer probes with 1.27 μm diameter platinum sensors (TSI model 1261A-P.5) were used for temperature measurements, and boundary layer probes with 3.81 μm diameter tungsten sensors (TSI model 1218-T1.5) were used for the velocity. An infrared (IR) camera (FLIR Systems Merlin model) with a Stirling cooled detector was used to measure the surface temperature field of the test wall. The temperature resolution of the camera was 0.05°C. The camera had a 255 × 318 pixel detector and was positioned such that each pixel corresponded to a 1 × 1 mm² area on the test wall. The field of view

on the test wall corresponded to 13.4*D* × 16.7*D*.

An infrared sensor was used to detect the passing of the wake generator rods. The pulse train from this sensor was digitized along with the instantaneous anemometer voltages (typically 13 s long traces at a 10 kHz sampling rate) to allow phase averaging of the flow velocities and temperatures relative to the wake passing events. Phase averaged results were typically computed at 24 increments during the wake passing cycle. The pulse train from the sensor was also used as the input to a circuit, which controlled the valves for cases with pulsed jets and wakes. The delay between the wake passing and pulse start, and the duration of the pulse were independently adjustable.

The film cooling effectiveness and Stanton number were defined, respectively, as follows:

$$\eta = \frac{T_{aw} - T_\infty}{T_{jet} - T_\infty} \quad (1)$$

$$St = \frac{q''_{conv}}{\rho c_p U_\infty (T_w - T_{aw})} \quad (2)$$

The jet, freestream, and wall (T_w) temperatures were measured. The convective heat flux q''_{conv} was determined based on the power input to the heaters, with corrections for conduction and radiation losses. Measurements were made for each flow condition with the wall heaters on and off, to determine local T_{aw} , η , and St . The procedure is described in more details in Coulthard et al. [25]. Stanton numbers were determined for cases with film cooling (St_f), and in cases without film cooling (St_o) but otherwise similar main flow, wake, and surface heating conditions. Stanton number ratios (St_f/St_o) were computed to determine the effect of film cooling on heat transfer coefficients.

The thermocouples and IR camera were calibrated against a precision blackbody source, and the cold-wire probe was calibrated against the thermocouples. The uncertainty in the measured temperature is 0.2°C, and the uncertainty in the measured velocity is 3%. The uncertainty in the film cooling effectiveness was determined to be 6% and the uncertainty in the Stanton number is 8%. The uncertainty in the ratio of two Stanton numbers is 11%, based on a standard propagation of error with a 95% confidence interval.

As documented in Coulthard et al. [25] before installation of the wake generator, the boundary layer 0.8*D* upstream of the film cooling hole leading edge had a momentum thickness Reynolds number of 550 and a shape factor of 1.48. The local skin friction coefficient at this location was 5.4×10^{-3} and the enthalpy thickness Reynolds number was 470. The Reynolds number based on hole diameter and mainstream velocity was 10,000. Womack et al. [17] confirmed that with the wake generator operating at low Sr , the phase averaged velocity profile between wakes matched the profile acquired before installation of the wake generator.

As shown in Womack et al. [17], the freestream turbulence level rose from about 1% between wakes to about 19% in the wakes. For the $Sr=0.15$ case, the freestream settled to its undisturbed state between wakes, and this undisturbed condition occupied about 60% of the cycle. The influence of the wake on the turbulence extended all the way to the wall. When the leading edge of the wake arrived at the hole, the freestream turbulence level rose sharply. About 5 ms later, a similar rise in turbulence was observed near the wall. About 15 ms later, the near-wall turbulence level had fallen. About 20 ms after this, the freestream turbulence level returned to its undisturbed condition. The duration of the wake, therefore, was about 40 ms in the freestream, with the strongest near-wall influence lasting about 15 ms. At the higher Strouhal numbers, the dimensional timing of the wakes was about the same, since the freestream velocity and wake generator speed were unchanged. The time between wakes was reduced, however, so the disturbed flow occupied a larger fraction of the cycle. At $Sr=0.3$, the calm flow between wakes occupied

Table 1 Naming convention for pulse/wake combinations

| Name | Description |
|------|---|
| P/NW | Pulsed jets, No wakes (steady freestream) |
| P/WO | Pulsed jets, wakes impact out of (between) pulses |
| P/WI | Pulsed jets, wakes impact In (during) pulses |
| S/W | Steady jets with wakes |
| S/NW | Steady jets, no wakes (steady freestream) |

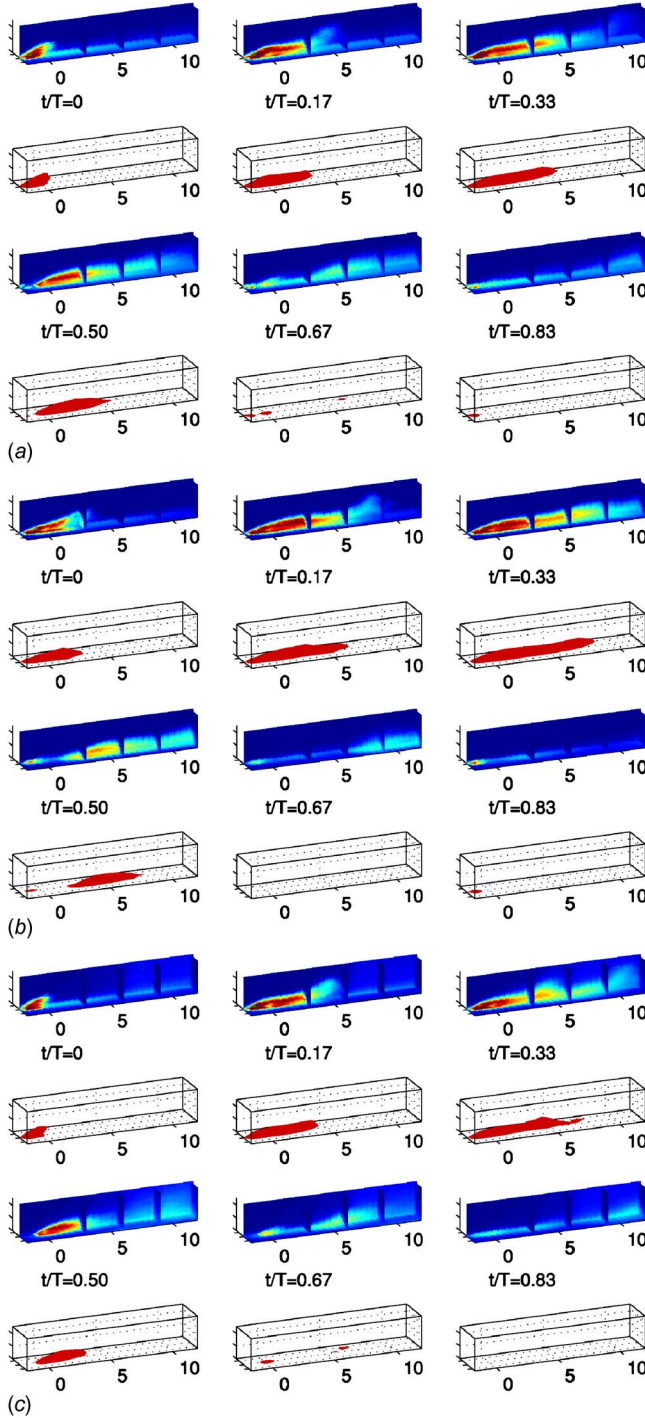


Fig. 2 Dimensionless temperature field, ϕ , for $B=0.5$, $Sr=0.15$, upper image shows temperature contours in various planes, color range 0 (blue) to 0.6 (red); lower image shows isothermal surface with $\phi=0.3$; axis limits: $x=-1.74D$ to $12D$, $z=-1.5D$ to $1.5D$, $y=0$ to $2.55D$; (a) P/NW, (b) P/WO, (c) P/WI (see Table 1 for names)

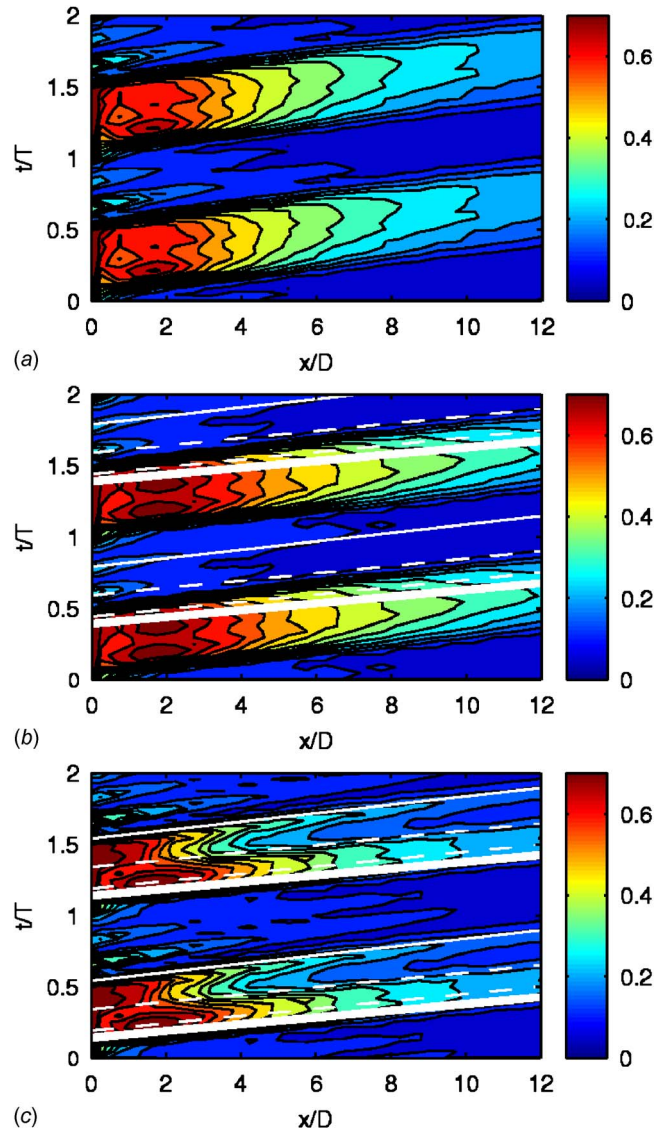


Fig. 3 Phase averaged η^* for $B=0.5$, $Sr=0.15$, white lines indicate wake duration in freestream (solid) and near-wall (dashed); (a) P/NW, (b) P/WO, (c) P/WI

about 20% of the cycle. At $Sr=0.6$, the wakes merged, and the freestream turbulence level cycled between a low of about 10% and a high of 19%.

Velocity profiles acquired at multiple streamwise locations showed that the propagation speed of the leading edge of the wake was about equal to the undisturbed freestream velocity, $U_\infty = 8$ m/s. The trailing edge of the wake was somewhat slower, at about $0.8U_\infty$. Near the wall, the leading and trailing edges of the disturbed flow traveled at about $0.9U_\infty$. Further details of the wake including velocity and turbulence profiles are available in Womack et al. [17].

The film cooling jet velocity and temperature distributions at the hole exit plane were documented in Coulthard et al. [24]. The jet temperature was very uniform and matched the plenum temperature to within 0.2°C . With steady blowing, the velocity was highest in the upstream section of the hole, and agreed with the results of Burd and Simon [26], who considered the same geometry. Phase averaged velocity distributions were also shown in Coulthard et al. [24]. Since the jets were only heated to approximately 7°C above the mainstream temperature, the density ratio of jets to mainstream was 0.98. Hence the blowing and velocity

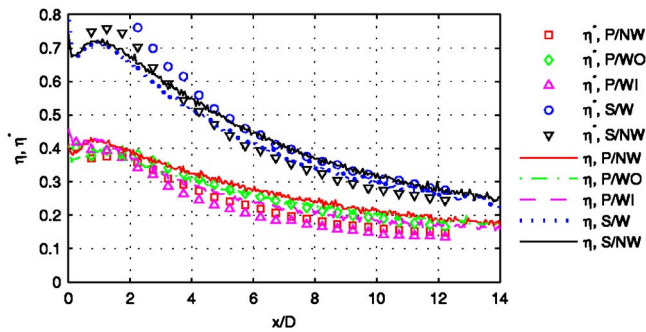


Fig. 4 Time averaged centerline η and η^* for $B=0.5$, $Sr=0.15$

ratios were essentially equal.

Three-dimensional surveys of the flow temperature were measured using the cold-wire probe. Each survey consisted of a $29 \times 11 \times 5$ grid with 1595 measurement locations. In the streamwise direction, 29 evenly spaced locations extended from $x=-1.74D$ (the leading edge of the film cooling holes) to $12.2D$. In the wall normal direction, there were 11 evenly spaced locations extending from $y=0$ to $2.55D$. Coulthard et al. [24] confirmed that the flow was symmetric about the spanwise centerline in this facility, so spanwise locations were all on one side of the centerline, with five evenly spaced points extending from $z=0$ to the midpoint between adjacent holes at $z=1.5D$.

Results and Discussion

$B=0.5$ Cases

$Sr=0.15$. The nominal blowing ratio in the discussion below refers to the blowing rate when the jets are turned on. For the pulsed cases, this means the time averaged blowing ratio is about

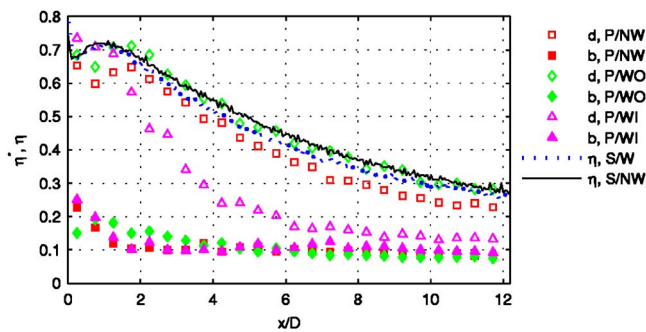


Fig. 5 Phase averaged centerline η^* for $B=0.5$, $Sr=0.15$, d =during pulse, b =between pulses

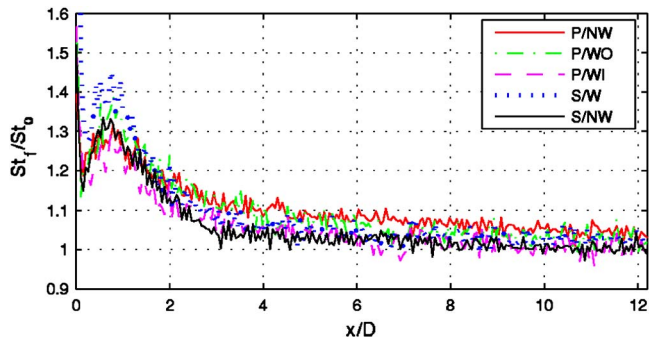


Fig. 6 Centerline Stanton number ratio, St_t/St_0 , for $B=0.5$, $Sr=0.15$

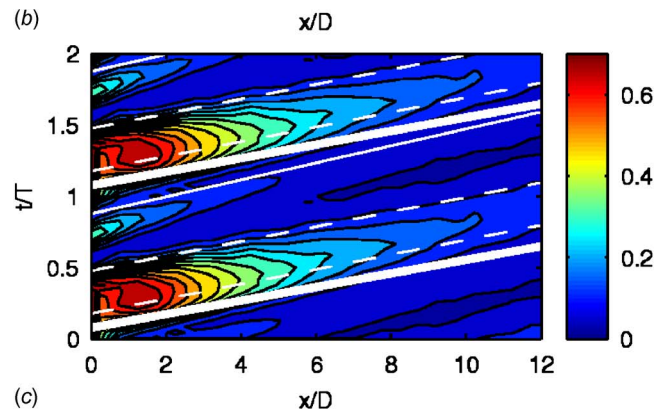
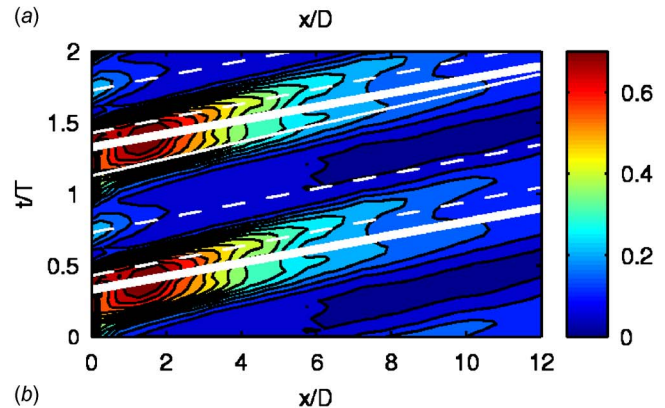
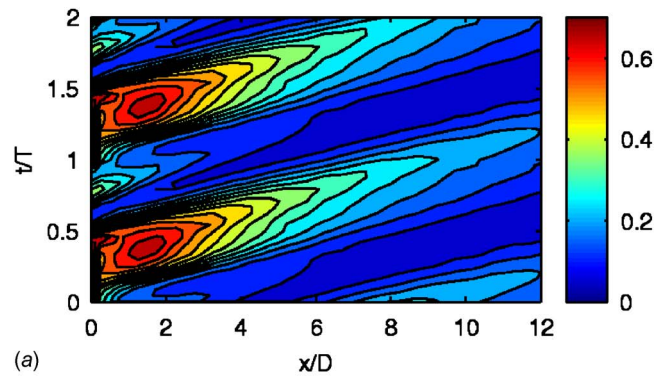


Fig. 7 Phase averaged η^* for $B=0.5$, $Sr=0.30$; (a) P/NW, (b) P/WO, (c) P/WI

0.25 for the nominal $B=0.5$ cases. Various pulsing/wake combinations were tested for each blowing ratio as described by the naming convention in Table 1. The three-dimensional temperature fields for the nominal $B=0.5$ cases with Strouhal number equal 0.15 are shown in Fig. 2. Six phases of the jet pulsing cycle are shown for each case, labeled with the time t normalized on the

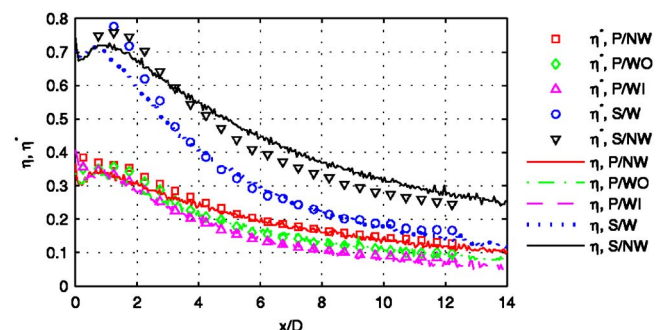


Fig. 8 Time averaged centerline η and η^* for $B=0.5$, $Sr=0.30$

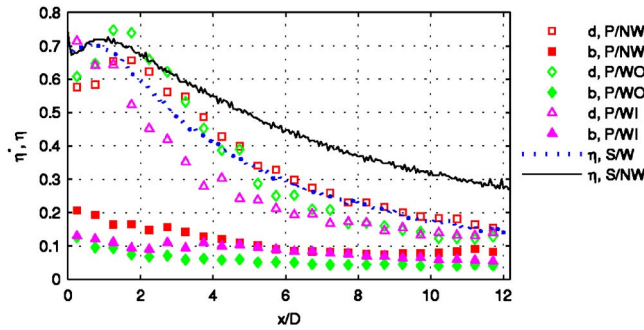


Fig. 9 Phase averaged centerline η^* for $B=0.5$, $Sr=0.30$

period T . As explained in Coulthard et al. [24], the plenum dynamics result in about a 4 ms delay between the opening of the solenoid valves and the first appearance of the jet at the hole exit plane. Another 10 ms elapses before the jet is of sufficient strength for significant coolant to be observed at the trailing edge of the hole. This delay is accounted for in all the figures that follow, so $t/T=0$ corresponds to the arrival of the jet at $x=0$. The top image at each phase shows dimensionless temperature contours, $\phi=(T-T_\infty)/(T_{jet}-T_\infty)$, in multiple planes arranged to provide a three-dimensional image of the temperature field. The color range is from $\phi=0$ (blue) to $\phi=0.6$ (red), and the axes extend from $-1.74D$ to $12D$ in the streamwise direction, $-1.5D$ to $1.5D$ in the spanwise direction, and 0 to $2.55D$ in the wall normal direction. The lower image in each figure shows an isothermal surface with $\phi=0.3$. This value of ϕ was found to give a good visual representation of the jet position. The axis limits are the same as in the upper figure. Some of the axis labels have been removed to unclutter the figures. Figure 2(a) shows the case with pulsed jets and a steady freestream. The jet is emerging from the hole at $t/T=0$ and shows some signs of lift-off. The lift-off does not continue beyond the startup, and in the next two frames, the jet is near the wall as its extent increases along the surface. At $t/T=0.5$ the jet has turned off, and the coolant convects downstream and out of the field of view in the next two frames. The pulsing is the same in Fig. 2(b), but a wake arrives at the hole at $t/T=0.39$. The wake has been timed to largely miss the jet pulse. Comparing Figs. 2(a) and 2(b), there is little difference at the first three phases, as expected since the wake is not yet present. The wake does appear to increase the dispersal of the jet somewhat at $t/T=0.5$ and 0.67, but by this point there is little jet fluid present and the film cooling effectiveness will already be low even without the wake. In Fig. 2(c), the wake is timed to disrupt the jet pulse and arrives at the hole at $t/T=0.14$. Comparing Figs. 2(a) and 2(c), it appears that the jet has been disrupted somewhat be-

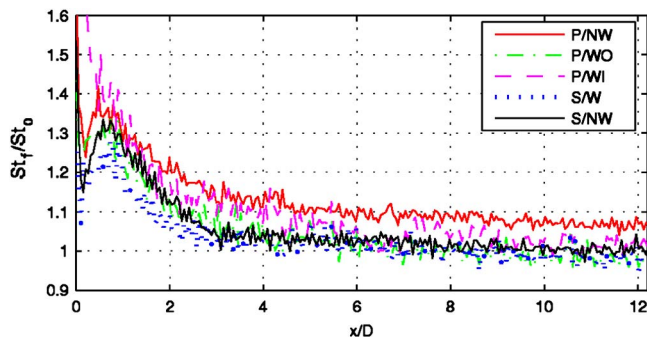
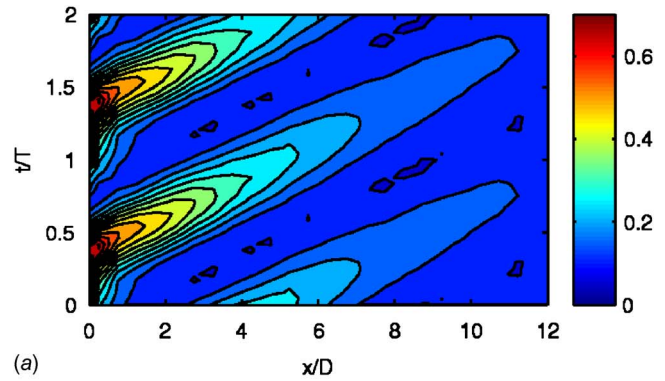
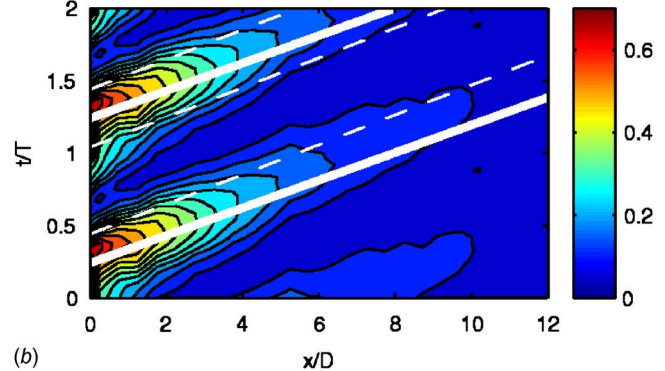


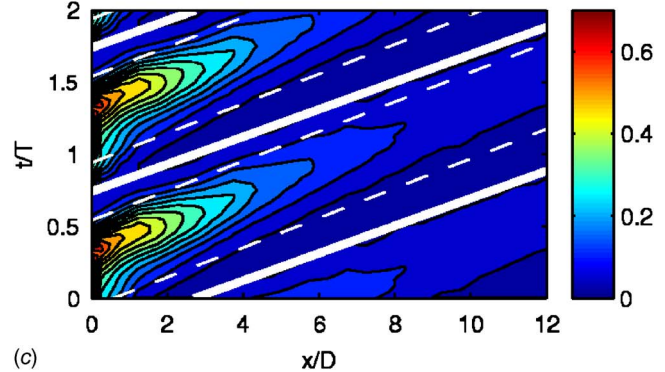
Fig. 10 Centerline Stanton number ratio, St_f/St_0 , for $B=0.5$, $Sr=0.30$



(a)



(b)



(c)

Fig. 11 Phase averaged η^* for $B=0.5$, $Sr=0.60$; (a) P/NW, (b) P/WO, (c) P/WI

tween $t/T=0.17$ and 0.50.

Womack et al. [17] defined an approximate unsteady film cooling effectiveness,

$$\eta^* = \phi(y=0.08D) = \frac{T(y=0.08D) - T_\infty}{T_{jet} - T_\infty} \quad (3)$$

based on the near-wall phase averaged flow temperature at $y/D=0.08$. Womack et al. [17] found that time averaged η^* agreed very closely with η based on surface temperature measurements, in agreement with Kohli and Bogard [28] who showed that the time averaged flow temperature at $y/D=0.1$ agreed with the wall temperature to within 0.02 in ϕ . Because of the thermal mass of the wall, its surface temperature cannot respond rapidly enough to follow the fluctuations induced by pulsing or wakes. The flow temperature above the wall does respond rapidly, however, so phase averaged η^* provides an estimate of the instantaneous film cooling effectiveness during the wake and pulsing cycles. Figure 3 shows phase averaged η^* from the spanwise centerline on a time-space plot for the cases of Fig. 2. The vertical axis indicates the phase, with the data repeated to show 2 cycles. A horizontal line on the figure shows the value of η^* at a particular phase. The

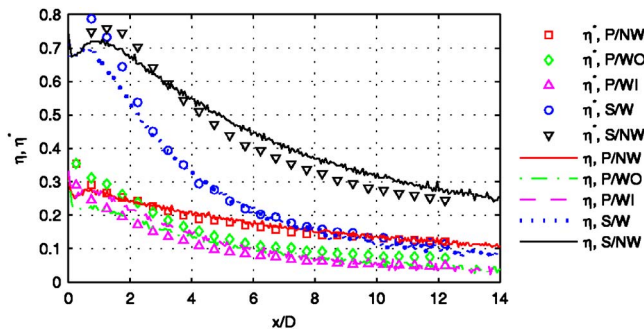


Fig. 12 Time averaged centerline η and η^* for $B=0.5$, $Sr=0.60$

white lines in Figs. 3(b) and 3(c) show the location of the wake. The thicker solid line corresponds to the leading edge of the wake in the freestream, and the thinner solid line indicates the trailing edge in the freestream. The dashed lines indicate the leading and trailing edges of the period of strong wake turbulence near the wall. The effect of the pulsing is clear. The effectiveness is high during the pulse and drops to near zero between pulses. In Fig. 3(b), the wake lies largely between pulses and appears to have little effect on the film cooling. In Fig. 3(c), the wake cuts through the pulse and appears to have a large effect in reducing the effectiveness.

The actual centerline effectiveness η along with the time averaged η^* is shown for all the $B=0.5$, $Sr=0.15$ cases in Fig. 4. Included are cases with and without wakes, with steady and pulsed jets, and also the steady $B=0.5$ case without wakes for comparison. The agreement between η and η^* is good in all cases, and is within the experimental uncertainty at most locations. Pulsing has a large impact in lowering the effectiveness, as shown in Coulthard et al. [24]. This is expected since the coolant mass flow is reduced by a factor of 2 and the effectiveness between pulses is near zero, as shown in Fig. 3. The wakes appear to have only a small effect on η , in agreement with the results of Womack et al. [17] at this Strouhal number. The case with the seemingly large disruption of the jet shown in Fig. 2(c) (P/WI in Fig. 4) does have the lowest η , but it is only slightly lower than the other pulsed cases.

Figure 5 shows η^* for the cases of Fig. 4 at particular phases either during (d) or between (b) pulses. These data were extracted from Fig. 3 along diagonal lines with slopes corresponding to the convection velocity. Also shown for reference in Fig. 5 are the corresponding steady blowing cases with and without wakes. Between pulses, η^* is near zero. It is not exactly zero, however, since the near-wall fluid is heated by the wall between pulses, making η^* only an approximation to the instantaneous adiabatic effectiveness. For the P/NW and P/WO cases, the effectiveness during the pulse is about equal to η for the steady blowing cases.

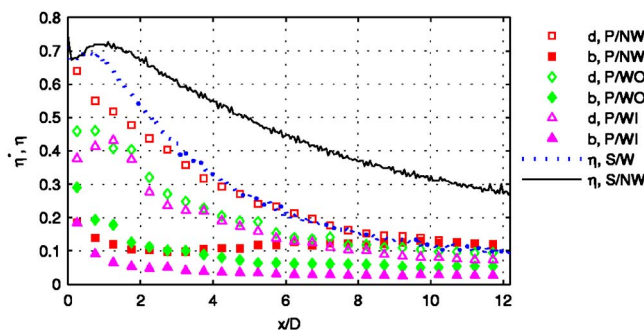


Fig. 13 Phase averaged centerline η^* for $B=0.5$, $Sr=0.60$

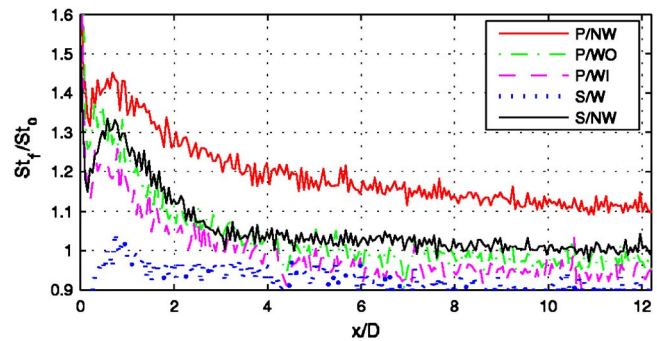


Fig. 14 Centerline Stanton number ratio, St_f/St_o , for $B=0.5$, $Sr=0.60$

The effectiveness during the pulse for the P/WI case, however, is reduced by about 50% when the wake impacts. Depending on its timing, the wake can have a large role in disrupting the film cooling flow and reducing the instantaneous effectiveness, but for the $Sr=0.15$ cases, this disruption occupies a relatively small fraction of the cycle, so the overall impact on η is small.

Figure 6 shows the centerline Stanton number ratio, St_f/St_o , for the $B=0.5$, $Sr=0.15$ cases. Womack et al. [17] showed that wakes significantly increase the Stanton number, but the relative percentage increase is nearly the same with and without film cooling. Hence, St_f and St_o both increase such that the ratio St_f/St_o is about the same with and without wakes. This is seen in Fig. 6, where all cases agree with each other and wake timing does not play a noticeable role. Film cooling causes a rise in Stanton number just downstream of the holes, which drops off a few diameters downstream. More discussion of this Stanton number behavior is available in Coulthard et al. [25,29].

Spanwise averaged results show the same trends as the centerline data of Figs. 3–6 and are not included in the present paper. Spanwise averaged results are included in Coulthard et al. [24,25] and Womack et al. [17] for the cases with separate pulsing and wakes. As discussed below for the centerline data, the separate effects of pulsing and wakes are additive, and the same is true for the spanwise averaged results.

$Sr=0.30$. Figures 7–10 show results for the $B=0.5$, $Sr=0.3$ cases in the format of Figs. 3–6. Comparison of the time-space plots in Figs. 7(a) and 7(c) shows reduction of the effectiveness by the wake. The effect is actually stronger than in the $Sr=0.15$ case of Fig. 3(c), but is less distinct because the wake is spread over a larger fraction of the cycle in Fig. 7(c). Figure 8 shows time averaged η and η^* , which again agree very well with each other. Wakes with $Sr=0.3$ reduce the effectiveness by 30–50% for the steady blowing case, which is more significant than the small change observed for the $Sr=0.15$ cases of Fig. 4. Pulsing alone reduces η by a factor of about 2 compared to the steady blowing case. Combined pulsing and wakes reduce the effectiveness by about 65–75%, which suggests that the individual effects of pulsing and wakes are additive (i.e., if pulsing reduces η to 0.5 its steady value and wakes reduce the 0.5 another 30% to 0.35, then the combined effect is a 65% reduction below the S/NW case). The same additive behavior was observed in all cases. The P/WI case has the lowest η , as expected, although the differences in η with different wake timings are within the uncertainty. Figure 9 shows the phase averaged η^* during and between pulses. As in the $Sr=0.15$ case, the effectiveness is near zero between pulses. During the pulses, η^* never achieves the steady freestream value, even in the P/NW case, in contrast to the $Sr=0.15$ results. The P/WI case had the lowest η^* during pulses, as expected, but the difference between timings was lower than in the $Sr=0.15$ case. The higher Strouhal number results in less recovery time between wakes, so the jet never fully reaches steady conditions. Some

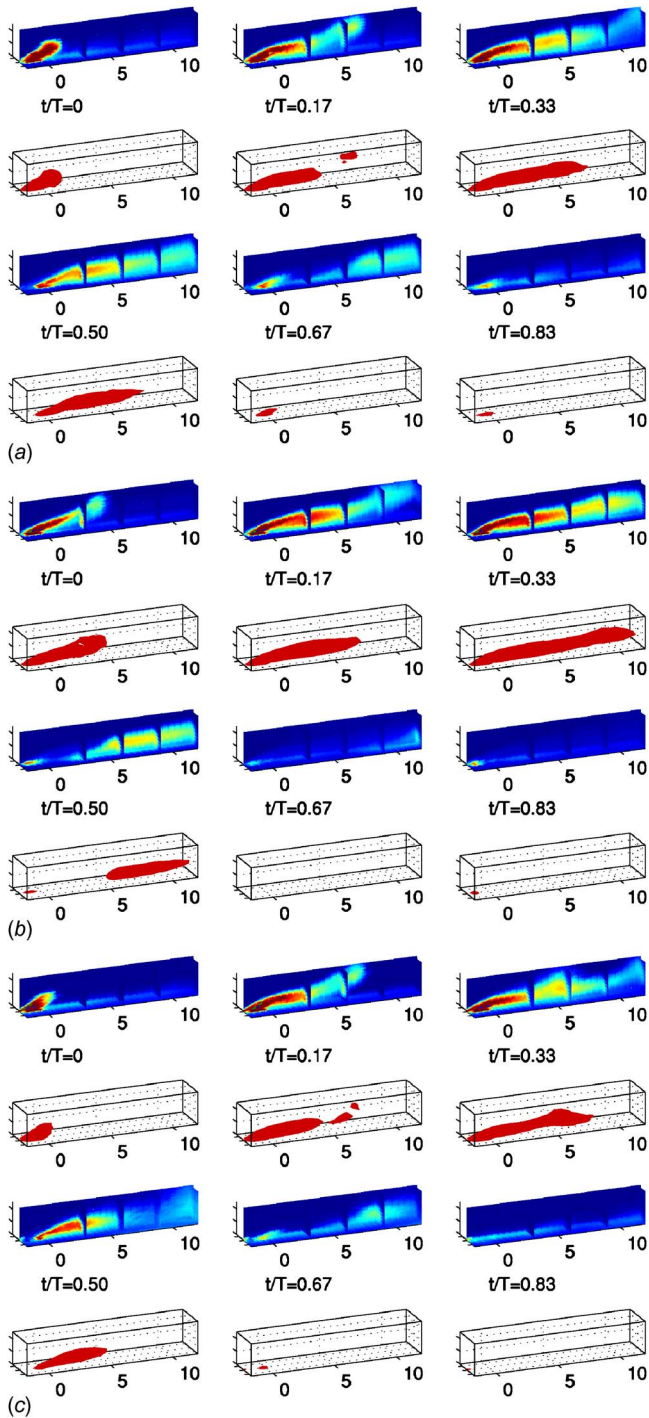


Fig. 15 Dimensionless temperature field, ϕ for $B=1.0$, $Sr=0.15$; (a) P/NW, (b) P/WO, (c) P/WI

disturbance is present for most of the cycle, regardless of wake timing, so the distinction between the various timings is also reduced. The Stanton number ratio for the $B=0.5$, $Sr=0.3$ cases are shown in Fig. 10. As at $Sr=0.15$, the difference between cases is small.

$Sr=0.60$. The $B=0.5$, $Sr=0.6$ case results are shown in Figs. 11–14. Pulsing results in jet lift-off during the startup of each pulse, and for the $Sr=0.6$ cases, the startup period occupies a large fraction of the pulse. This is seen in the time-space plots of Fig. 11 as reduced effectiveness during most of the pulse, followed by a short period of higher η^* just as the jet turns off. The thin white

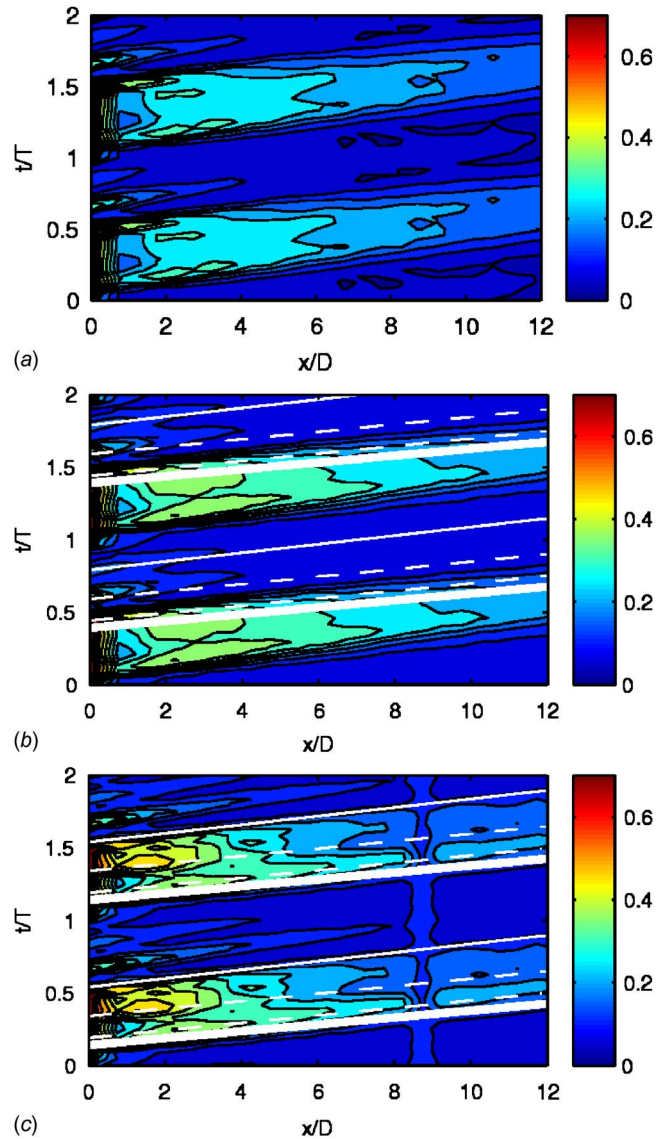


Fig. 16 Phase averaged η^* for $B=1.0$, $Sr=0.15$; (a) P/NW, (b) P/WO, (c) P/WI

line indicating the trailing edge of the wake is not shown in Fig. 11 since the wakes overlap each other. The wakes reduce the effectiveness, but the timing does not appear to matter. Since the wake disturbance occupies the full pulsing cycle, little variation with timing should be expected. Figure 12 shows that pulsing alone reduces η by about 60% (due to the combined effects of lower coolant mass flow and increased lift-off), and wakes alone reduce η by 60% or more, particularly at downstream locations. The combined effects are commensurate with the individual reductions. Effectiveness in the P/WI case was reduced by as much as 85% from the steady blowing case without wakes. Figure 13 shows the phase averaged η^* during and between pulses. As in the lower Sr cases, η^* is low between pulses, as expected. During pulses, the effectiveness is much lower than in the steady blowing case, even without wakes, due to jet lift-off during pulse startup. Wakes reduce η^* further, and again the results are about equal for the two wake timings. Stanton number ratios for the $B=0.5$, $Sr=0.6$ cases are shown in Fig. 14. Most of the cases agree with each other and are about equal to those at the lower Sr in Figs. 6 and 10. Wake timing effects again appears insignificant. The Stanton ratios for the P/NW case are noticeably higher than those of the other cases. Pulsing raises Stanton numbers, but the effect is

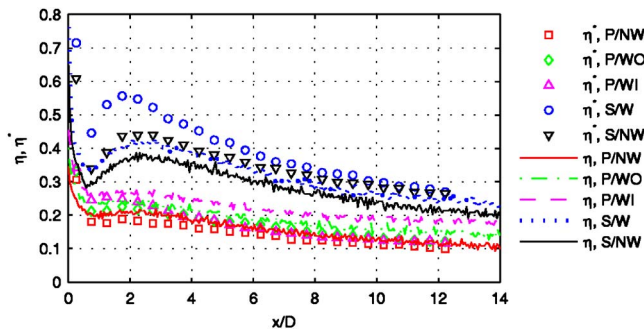


Fig. 17 Time averaged centerline η and η^* for $B=1.0$, $Sr=0.15$

relatively small in comparison with the effect of the wakes. Since the wake effect is present in both St_f and St_o , the pulsing effect is less apparent in the ratios for the cases with wakes.

$B=1.0$ Cases

$Sr=0.15$. Figure 15 shows phase averaged temperature fields for the $B=1.0$, $Sr=0.15$ cases in the same format as Fig. 2. With higher mass flow, the jets extend farther down the surface before being dispersed than in the lower B cases, but there is also more jet lift-off and, therefore, less coolant near the wall. The wake timings are the same as in Fig. 2. The wake disturbs the jet at $t/T=0.5$ and $t/T=0.67$ in Fig. 15(b), and at $t/T=0.17-0.5$ in Fig. 15(c). The near-wall effect of this is shown in the time-space plots of Fig. 16. Effectiveness is lower than in the $B=0.5$ case of Fig. 3 due to lift-off, which is particularly apparent at $x/D < 1$. When the wakes pass during the pulses, they momentarily increase η^* in the upstream region by suppressing lift-off. The wake effect farther downstream appears slight, since the jet fluid is largely away from the wall and dispersed even without wakes. Figure 17 shows that the time averaged effectiveness drops by about 50% between the steady and pulsed jets, as expected with the 50% mass flow reduction. Wakes raise the effectiveness slightly both with steady and pulsed jets, and this rise is slightly larger for the P/WI case. The differences with wakes are small, however, and within the experimental uncertainty. The phase averaged η^* results of Fig. 18 show that the effectiveness is low between jet pulses, and approaches the steady blowing results during the pulses, in agreement with the $B=0.5$ results in Fig. 5. The wake enhances η^* at $x/D < 2$ by reducing lift-off, but has little effect farther downstream. Stanton number ratios for the $B=1.0$, $Sr=0.15$ cases are shown in Fig. 19. All agree with each other, as in the $B=0.5$ cases.

$Sr=0.30$ and 0.60 . Figures 20–23 show results for the $B=1.0$, $Sr=0.3$ cases and Figs. 24–27 are for the $B=1.0$, $Sr=0.6$ cases. As in the $B=1.0$, $Sr=0.15$ cases, during the pulses the wakes tend to increase effectiveness upstream of $x/D=2$, particularly in the

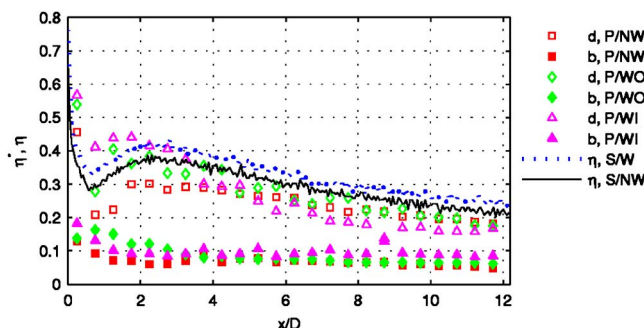


Fig. 18 Phase averaged centerline η^* for $B=1.0$, $Sr=0.15$

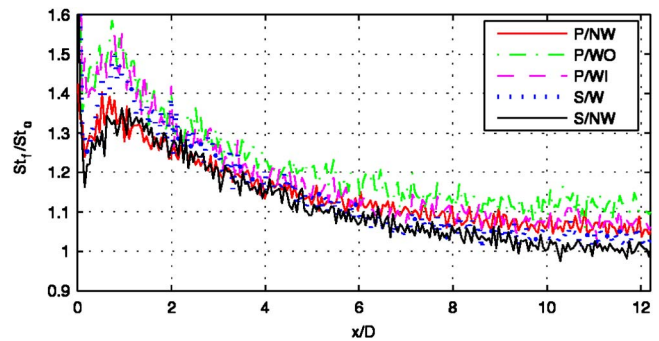


Fig. 19 Centerline Stanton number ratio, St_f/St_o , for $B=1.0$, $Sr=0.15$

P/WI case, and reduce effectiveness farther downstream. The time averaged results show that the wake effect is relatively small. Stanton number ratios show no significant differences with wake timing, but the ratios are about 10% higher for the P/NW cases.

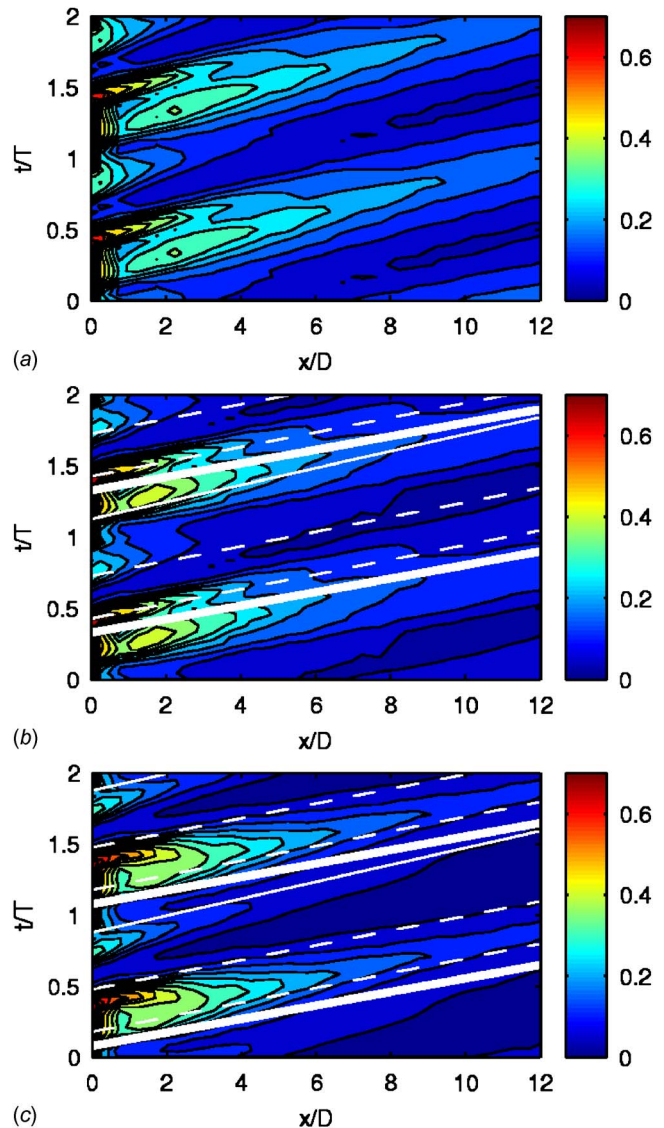


Fig. 20 Phase averaged η^* for $B=1.0$, $Sr=0.30$; (a) P/NW, (b) P/WO, (c) P/WI

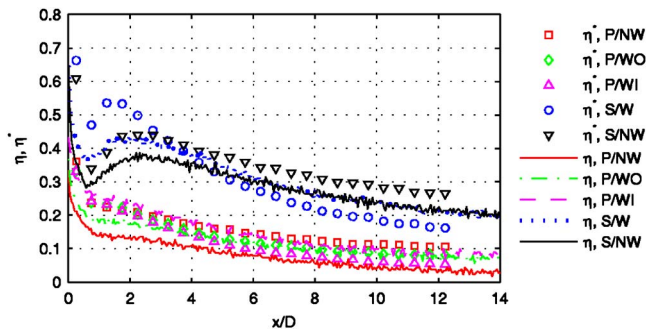


Fig. 21 Time averaged centerline η and η^* for $B=1.0$, $Sr=0.30$

As in the $B=0.5$ case of Fig. 14, pulsing increases Stanton numbers, but the effect is hidden by the larger wake effect in the cases with wakes.

It should be noted that wakes increase the lateral spreading of the film cooling jets. When combined with a reduction in lift-off, this results in a significant increase in the spanwise averaged effectiveness in the $B=1.0$ cases, as shown in Womack et al. [17]. The wakes, therefore, help to mitigate the reduction in η caused by pulsing. As noted above, the pulsing and wake effects are additive, so the combined effects on the spanwise averaged data can be deduced from the separate effects presented in Coulthard et al. [24] and Womack et al. [17]. Direct measurements of the combined effects show that wake timing has little effect on the spanwise averaged results, in agreement with the centerline results discussed above.

Conclusions

With $B=0.5$, film cooling jet pulsing and passing wakes both act to reduce the film cooling effectiveness. In combination, the reduction in effectiveness is greater than with either effect alone.

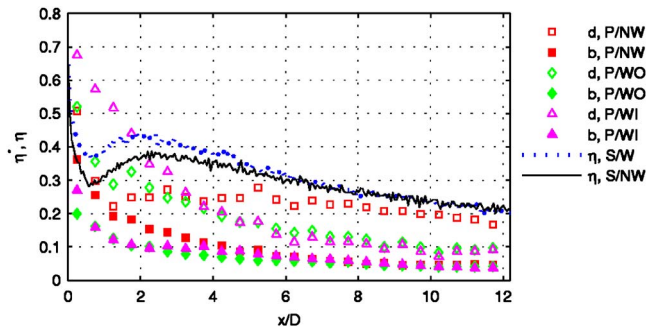


Fig. 22 Phase averaged centerline η^* for $B=1.0$, $Sr=0.30$

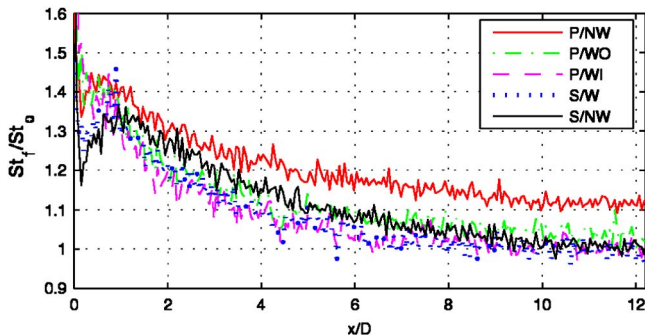


Fig. 23 Centerline Stanton number ratio, St_f/St_o , for $B=1.0$, $Sr=0.30$

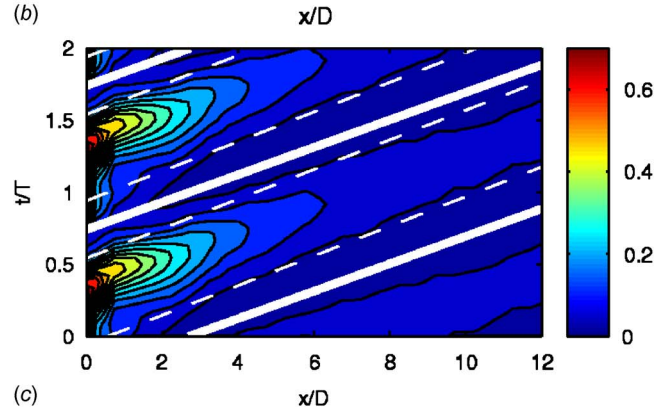
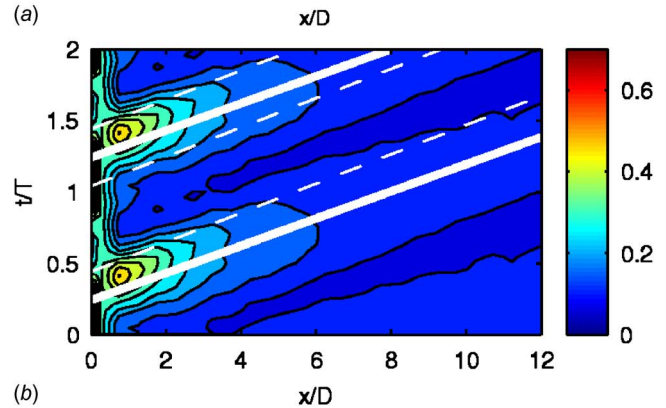
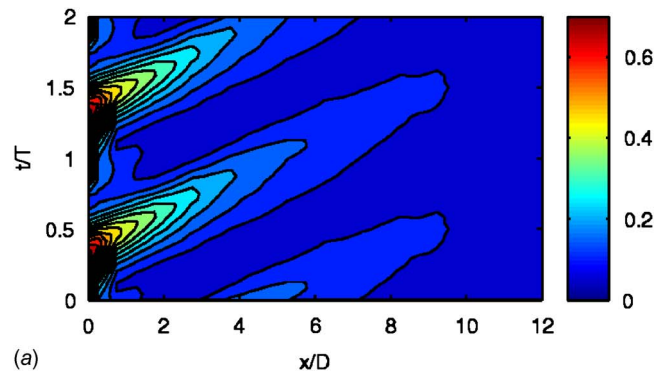


Fig. 24 Phase averaged η^* for $B=1.0$, $Sr=0.60$; (a) P/NW, (b) P/WO, (c) P/WI

With $B=1.0$, the film cooling was dominated by jet lift-off. Pulsing reduced effectiveness by decreasing mass flow, but wakes tended to increase effectiveness somewhat by forcing more jet fluid closer to the wall, particularly near the film cooling holes.

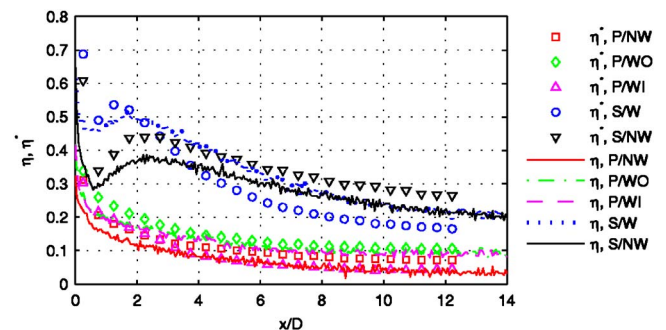


Fig. 25 Time averaged centerline η and η^* for $B=1.0$, $Sr=0.60$

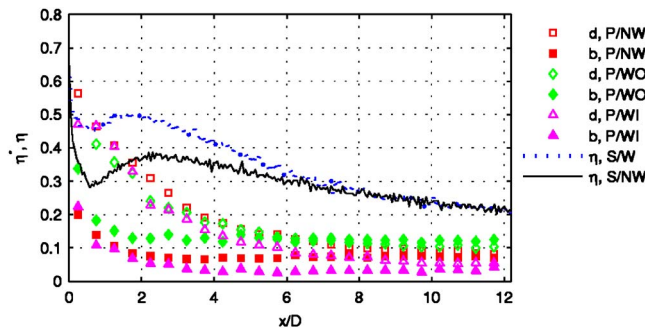


Fig. 26 Phase averaged centerline η^* for $B=1.0$, $Sr=0.60$ cases

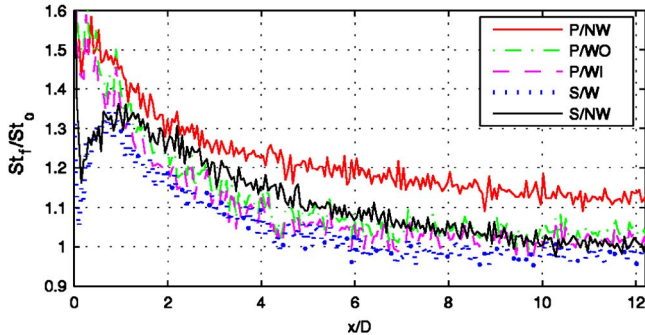


Fig. 27 Centerline Stanton number ratio, St_f/St_o , for $B=1.0$, $Sr=0.60$ cases

At low Strouhal numbers, the wake timing had a significant impact on the instantaneous film cooling effectiveness, but the effect of the wakes on the time averaged η was small. At higher Strouhal numbers, the wakes caused a greater reduction in time averaged effectiveness, but the shorter period of calm flow between wakes resulted in less variation during the cycle, thereby reducing the importance of wake timing. The time averaged effectiveness, therefore, did not depend strongly on wake timing at any Strouhal number.

Wakes caused a significant increase in heat transfer coefficient, but the effect was the same in cases with and without film cooling, and with all combinations of pulsing and wake timing. Stanton number ratios, therefore, showed no significant dependence on wake timing.

The present results indicate that there is no clear benefit to imposing pulsation on film cooling jets for the geometry considered. If pulsation occurs naturally in response to wakes, the present results provide some insight into how it affects the film cooling behavior.

Acknowledgment

The first author gratefully acknowledges the Office of Naval Research for partial support of this work, via the Naval Academy Trident Scholar Program, on funding Document No. N0001406WR20137. The second author gratefully acknowledges partially support by the Naval Air Systems Command.

Nomenclature

- $B = \rho_{jet} U_{jet} / \rho_{\infty} U_{\infty}$, blowing ratio
- c_p = specific heat at constant pressure
- D = film cooling hole and wake generator rod diameter
- f = frequency, Hz
- L = length of film cooling hole channel
- q'' = heat flux

- Sr = Strouhal number, $Sr = 2\pi f D / U_{\infty}$
- St = Stanton number, $q''_{conv} / [\rho c_p U_{\infty} (T_w - T_{aw})]$
- T = temperature or wake passing period
- t = time
- U = velocity
- x = streamwise coordinate, distance from trailing edge of film cooling holes
- y = normal coordinate, distance from the wall
- z = spanwise coordinate, distance from the centerline of the center hole
- η = film cooling effectiveness, $(T_{aw} - T_{\infty}) / (T_{jet} - T_{\infty})$
- η^* = approximate unsteady film cooling effectiveness, Eq. (3)
- ρ = density
- ϕ = dimensionless temperature $(T - T_{\infty}) / (T_{jet} - T_{\infty})$

Subscripts

- aw = adiabatic wall
- conv = convective
- f = with film cooling
- jet = film cooling jet
- o = without film cooling, same wakes as corresponding f case
- w = wall
- ∞ = mainstream

References

- [1] Ekkad, S. V., Ou, S., and Rivir, R. B., 2006, "Effect of Jet Pulsation and Duty Cycle on Film Cooling From a Single Jet on a Leading Edge Model," ASME J. Turbomach., **128**, pp. 564–571.
- [2] Funazaki, K., Yokota, M., and Yamawaki, S., 1997, "Effect of Periodic Wake Passing on Film Cooling Effectiveness of Discrete Cooling Holes Around the Leading Edge of a Blunt Body," ASME J. Turbomach., **119**, pp. 292–301.
- [3] Funazaki, K., Koyabu, E., and Yamawaki, S., 1998, "Effect of Periodic Wake Passing on Film Cooling Effectiveness of Inclined Discrete Cooling Holes Around the Leading Edge of a Blunt Body," ASME J. Turbomach., **120**, pp. 70–78.
- [4] Ou, S., Han, J. C., Mehendale, A. B., and Lee, C. P., 1994, "Unsteady Wake Over a Linear Turbine Blade Cascade With Air and CO₂ Film Injection: Part I—Effect on Heat Transfer Coefficients," ASME J. Turbomach., **116**, pp. 721–729.
- [5] Mehendale, A. B., Han, J. C., Ou, S., and Lee, C. P., 1994, "Unsteady Wake Over a Linear Turbine Blade Cascade With Air and CO₂ Film Injection: Part II—Effect on Film Effectiveness and Heat Transfer Distributions," ASME J. Turbomach., **116**, pp. 730–737.
- [6] Jiang, H. W., and Han, J. C., 1996, "Effect of Film Hole Row Location on Film Effectiveness on a Gas Turbine Blade," ASME J. Turbomach., **118**, pp. 327–333.
- [7] Ekkad, S. V., Mehendale, A. B., Han, J. C., and Lee, C. P., 1997, "Combined Effect of Grid Turbulence and Unsteady Wake on Film Effectiveness and Heat Transfer Coefficients of a Gas Turbine Blade With Air and CO₂ Film Injection," ASME J. Turbomach., **119**, pp. 594–600.
- [8] Du, H., Han, J. C., and Ekkad, S. V., 1998, "Effect of Unsteady Wake on Detailed Heat Transfer Coefficients and Film Effectiveness Distributions for a Gas Turbine Blade," ASME J. Turbomach., **120**, pp. 808–817.
- [9] Du, H., Ekkad, S. V., and Han, J. C., 1999, "Effect of Unsteady Wake With Trailing Edge Coolant Ejection on Film Cooling Performance for a Gas Turbine Blade," ASME J. Turbomach., **121**, pp. 448–455.
- [10] Teng, S., Sohn, D. K., and Han, J. C., 2000, "Unsteady Wake Effect on Film Temperature and Effectiveness Distributions for a Gas Turbine Blade," ASME J. Turbomach., **122**, pp. 340–347.
- [11] Teng, S., Han, J. C., and Poinatte, P. E., 2001, "Effect of Film-Hole Shape on Turbine-Blade Heat-Transfer Coefficient Distribution," J. Thermophys. Heat Transfer, **15**, pp. 249–256.
- [12] Teng, S., Han, J. C., and Poinatte, P. E., 2001, "Effect of Film-Hole Shape on Turbine-Blade Film-Cooling Performance," J. Thermophys. Heat Transfer, **15**, pp. 257–265.
- [13] Heidmann, J. D., Lucci, B. L., and Reshotko, E., 2001, "An Experimental Study of the Effect of Wake Passing on Turbine Blade Film Cooling," ASME J. Turbomach., **123**, pp. 214–221.
- [14] Wolff, S., Fottner, L., and Ardey, S., 2002, "An Experimental Investigation on the Influence of Periodic Unsteady Inflow Conditions on Leading Edge Film Cooling," ASME Paper No. GT-2002-30202.
- [15] Adami, P., Belardini, E., Montomoli, F., and Martelli, F., 2004, "Interaction Between Wake and Film Cooling Jets: Numerical Analysis," ASME Paper No. GT2004-53178.
- [16] Deinert, M., and Hourmouziadis, J., 2004, "Film Cooling in Unsteady Flow With Separation Bubble," ASME Paper No. GT2004-53075.
- [17] Womack, K. M., Volino, R. J., and Schultz, M. P., 2007, "Measurements in

Film Cooling Flows With Periodic Wakes,” ASME J. Turbomach., to be published.

- [18] Bons, J. P., Rivir, R. B., MacArthur, C. D., and Pestian, D. J., 1996, “The Effect of Unsteadiness on Film Cooling Effectiveness,” Wright Laboratory Technical Report No. WLTR-96-2096.
- [19] Ligrani, P. M., Gong, R., Cuthrell, J. M., and Lee, J. S., 1996, “Bulk Flow Pulsations and Film Cooling—I, Injectant Behavior, II. Flow Structure and Film Effectiveness,” *Int. J. Heat Mass Transfer*, **39**, pp. 2271–2292.
- [20] Seo, H. J., Lee, J. S., and Ligrani, P. M., 1999, “Effects of Bulk Flow Pulsations on Film Cooling From Different Length Injection Holes at Different Blowing Ratios,” ASME J. Turbomach., **121**, pp. 542–550.
- [21] Jung, I. S., Lee, J. S., and Ligrani, P. M., 2002, “Effects of Bulk Flow Pulsations on Film Cooling With Compound Angle Holes: Heat Transfer Coefficient Ratio and Heat Flux Ratio,” ASME J. Turbomach., **124**, pp. 142–151.
- [22] Ou, S., and Rivir, R. B., 2006, “Shaped-Hole Film Cooling With Pulsed Secondary Flow,” ASME Paper No. GT2006-90272.
- [23] Nikitopoulos, D. E., Acharya, S., Oertling, J., and Muldoon, F. H., 2006, “On Active Control of Film-Cooling Flows,” ASME Paper No. GT2006-90051.
- [24] Coulthard, S. M., Volino, R. J., and Flack, K. A., 2007, “Effect of Jet Pulsing on Film Cooling—Part 1: Effectiveness and Flowfield Temperature Results,” ASME J. Turbomach., **129**, pp. 232–246.
- [25] Coulthard, S. M., Volino, R. J., and Flack, K. A., 2007, “Effect of Jet Pulsing on Film Cooling—Part 2: Heat Transfer Results,” ASME J. Turbomach., **129**, pp. 247–257.
- [26] Burd, S., and Simon, T. W., 2000, “Effects of Hole Length, Supply Plenum Geometry, and Freestream Turbulence on Film Cooling Performance,” NASA Report No. CR-2000-210336.
- [27] Pedersen, D. R., Eckert, E. R. G., and Goldstien, R. J., 1977, “Film Cooling With Large Density Differences Between the Mainstream and the Secondary Fluid Measured by the Heat-Mass Transfer Analogy,” ASME J. Heat Transfer, **99**, pp. 620–627.
- [28] Kohli, A., and Bogard, D. G., 1998, “Fluctuating Thermal Field in the Near-Hole Region for Film Cooling Flows,” ASME J. Turbomach., **120**, pp. 86–91.
- [29] Coulthard, S. M., Volino, R. J., and Flack, K. A., 2006, “Effect of Unheated Starting Lengths on Film Cooling Experiments,” ASME J. Turbomach., **128**, pp. 579–588.

The Influence of Sweep on Axial Flow Turbine Aerodynamics in the Endwall Region

Graham Pullan

Whittle Laboratory,
Department of Engineering,
University of Cambridge,
Cambridge CB3 0DY, UK
e-mail: gp10006@cam.ac.uk

Neil W. Harvey

Rolls-Royce plc,
Derby DE24 8BJ, UK

Sweep, when the stacking axis of the blade is not perpendicular to the axisymmetric stream surface in the meridional view, is often an unavoidable feature of turbine design. In a previously reported study, the authors demonstrated that sweep leads to an inevitable increase in midspan profile loss. In this paper, the influence on the flowfield close to the endwalls is investigated. Experimental data from two linear cascades, one unswept, and the other swept at 45 deg but having the same overall turning and midspan pressure distribution, are presented. It is shown that sweep causes the blade to become more rear loaded at the hub and fore loaded at the casing. This is further shown to reduce the penetration of the secondary flow at the hub, and to produce a highly unusual secondary flow structure, with low endwall overturning, at the casing. A computational study is then presented in which the development of the secondary flows of both blades is studied. The differences in the endwall flowfields are found to be caused by a combination of the effect of sweep on both the endwall blade loading distribution and on the bulk movements of the primary irrotational flow. [DOI: 10.1115/1.2812337]

Introduction

There are alternative definitions of blade sweep. In this paper, we adopt the convention that the sweep angle (λ) is the deviation of the blade stacking axis from the normal to the axisymmetric stream surface in the meridional view (meridional sweep); see Fig. 1. A second option is to measure the sweep angle when viewed in the direction perpendicular to the true chord line (true sweep).

Sweep has long been a feature of steam turbine design. The large increase in volume flow rate through the machine necessitates changes in annulus area to maintain the required meridional velocities. This can lead to casing radial angles (flare) of over 40 deg. The need to stack rotor blades on a radial line for mechanical reasons then automatically gives rise to high levels of sweep. In general, designers of aeroengine turbines have, up to now, been able to avoid such large sweep angles. However, the continuing trend for large bypass ratios leads to a small radius core turbine and, if no gearbox is employed, a large radius low pressure turbine. The latter is needed to achieve a high blade speed, and hence reduce the number of required stages, with the relatively low rotational speed of the low pressure spool (limited by fan tip speed). With radially stacked blades, this change in radius leads to sweep.

The effects of sweep on turbomachinery blading aerodynamics can be traced to one cause: the tendency of the spanwise velocity component (V_s) to remain constant through the blade row. Smith and Yeh [1] noted that an infinite swept blade can exert no force on the flow in the spanwise direction so that V_s must remain unchanged. Although this is easy to see for an infinite blade, the same effect occurs in high aspect ratio blading, as shown in Fig. 2.

Smith and Yeh [1] showed that the persistence of V_s has two consequences. First, the two-dimensional profile should not be designed on an axisymmetric stream surface section, but on a section perpendicular to the stacking axis. Second, the inlet stream

surface becomes twisted and is discontinuous in the circumferential direction at the trailing edge of the row. Potts [2] used three-dimensional CFD to calculate the distortion of stream surfaces through a cascade of swept turbine blades. Close to the endwalls, however, the stream surface is constrained to follow the hub or casing of the machine and it has been shown that this can significantly modify the blade pressure distributions in these regions, Denton and Xu [3].

Recently, Pullan and Harvey [4] investigated the consequences of sweep for turbine blade profile loss. Assuming a constant spanwise velocity, they showed that, in order to maintain a fixed lift coefficient, the pitch-chord ratio must reduce as the sweep angle increases. Based on simplified velocity distributions and an assumption of fully turbulent boundary layers, an analytical expression was developed for the estimation, at the preliminary design stage, of the profile loss increase due to sweep. This result was then validated in cascades of unswept and highly swept ($\lambda = 45$ deg) low pressure turbine blades.

The purpose of the present work is to provide, for the first time, a description of the changes in the endwall secondary flow caused by sweep. A large body of research has investigated the flow structures and loss caused by secondary flows in unswept blading (Sieverding [5], Langston [6]) but it is not known how such flows compare to those of swept blades. The paper presents experimental data from two cascades, one unswept, and the other a novel swept cascade designed to perform exactly the same aerodynamic duty as the first. CFD is then used to develop an understanding of the different mechanisms of secondary flow development in the two blades.

Experimental Method

Blading. The experimental work presented in this paper was performed on the same two low-speed linear cascades first described by Pullan and Harvey [4]. One cascade is unswept, and the other has the high sweep angle of $\lambda = 45$ deg. The blade profile in the unswept cascade, Blade H, is typical of the “high-lift” thin-solid blading used in low pressure turbines of modern civil aeroengines and has been the subject of other work ([7–9]). The swept cascade uses a different profile, Blade HS, designed to achieve the same pressure distribution and lift coefficient as Blade H. Table 1 lists some details of the blading. Since the spanwise

Contributed by the International Gas Turbine Institute of ASME for publication in the JOURNAL OF TURBOMACHINERY. Manuscript received June 7, 2007; final manuscript received June 27, 2007; published online August 1, 2008. Review conducted by David Wisler. Paper presented at the ASME Turbo Expo 2007: Land, Sea and Air (GT2007), Montreal, Quebec, Canada, May 14–17, 2007.

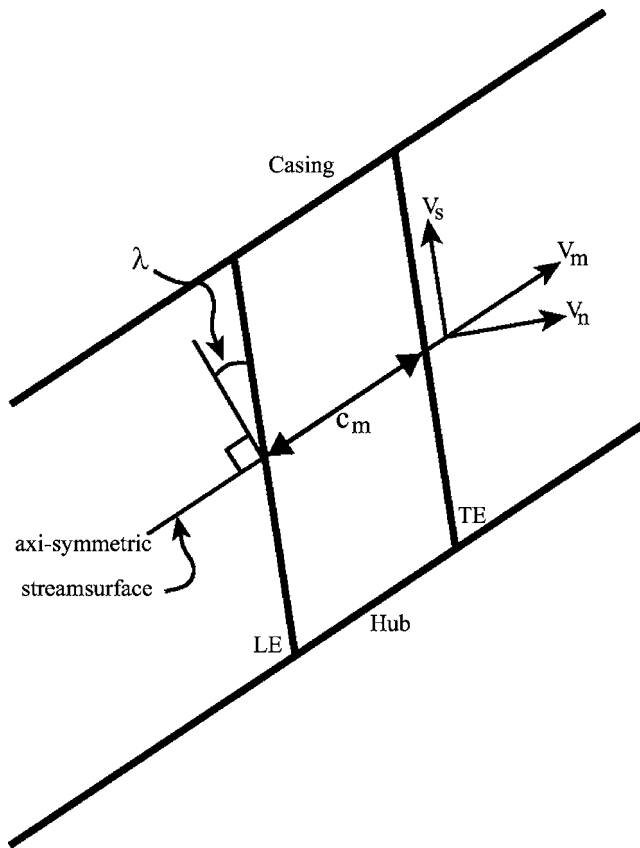


Fig. 1 Meridional view of blade to define sweep angle λ

component of the inlet velocity cannot be turned by the blade (strictly, this applies for an infinite blade) the designer is unable to utilize this component of dynamic head in the creation of lift. As a result, it was shown by Pullan and Harvey [4] that a reduced pitch-chord ratio must be employed by the swept aerofoil as compared to the unswept one in order to maintain the same lift coefficient; this is shown in the values in Table 1.

Cascades. Both cascades were first reported by Pullan and Harvey [4]. The unswept cascade is of a conventional design typical of many low-speed open-circuit turbomachinery cascades. By contrast, the simple addition of sweep causes several complications. Figure 3 shows a side view of the Blade HS cascade. In this view, the meridional and tangential directions are in the plane of the page, as are the endwalls. The introduction of sweep results in the displacement of the blade profile on one endwall relative to the other in the meridional direction. It can be seen that, if the inlet angle, α_{m1} , is nonzero, sweep will cause the upper and lower walls of the cascade inlet to be inclined from the horizontal plane. A transition duct is employed to smoothly join the rectangular outlet of the wind tunnel to the inlet of the swept cascade (which has a parallelogram cross section). This "twisted" inlet gives rise to cross flows in the tunnel boundary layers. However, traverses of the full inlet plane of the cascade with a five-hole probe were used to show that a parallel inlet flow with uniform endwall boundary layers could be restored by bleeding off air immediately downstream of the transition duct.

Instrumentation. The instrumentation used was similar in each cascade. A reference inlet total pressure, p_{01} , was obtained with a Pitot probe in the inlet duct (the variation of p_{01} across the whole inlet plane, outside the boundary layers, was measured to be within $\pm 0.2\%$ of the exit dynamic head). The periodicity of the cascade was assessed using rows of endwall static pressure tapings located 35% of meridional chord upstream and downstream

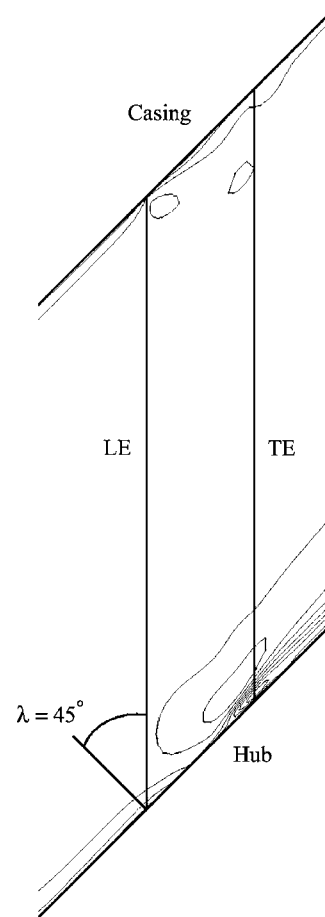


Fig. 2 Pitchwise averaged V_s , $\Delta_{con}=0.05 V_2$, $\lambda=45$ deg, meridional view (Pullan and Harvey [2])

of the blades, and also by midspan wake traverses over the central three blades. Fine-tuning of the periodicity was achieved by adjustment of tailboards (not shown in Fig. 3). The center blade of each cascade was instrumented with 44 static pressure tapings at nine different spanwise locations: 2%, 5%, 10%, 15%, 50%, 85%, 90%, 95%, and 98% span. Inlet boundary layer traverses, using a flattened pitot probe of size 0.3 mm, were performed at 50% of meridional chord upstream of the leading edge; see Fig. 4. Outlet area traverses were done at 3% and 25% of chord downstream of the trailing edge using a five-hole probe of 2.0 mm tip diameter. These exit traverses were performed in two halves with a measurement grid of 45 (one pitch) \times 47 (half-span) points.

The five-hole probe was calibrated in a uniform jet at incidences up to ± 30 deg of yaw and pitch at increments of 2 deg. It is estimated that the probe is able to discern flow angle to within ± 0.5 deg, stagnation pressure to within $\pm 0.2\%$ of exit dynamic

Table 1 Blade parameters

| | Blade H | Blade HS |
|--|-------------------|-------------------|
| Reynolds number Re_{cm} | 2.9×10^5 | 2.9×10^5 |
| Inlet turbulence | 0.5% | 0.5% |
| Air inlet angle (from axial) α_{m1} | -30.4 deg | -30.4 deg |
| Design exit air angle (from axial) α_{m2} | 62.8 deg | 62.8 deg |
| Sweep angle λ | 0 deg | 45 deg |
| Meridional chord c_m | 94 mm | 133 mm |
| Nominal exit velocity V_2 | 46 m/s | 33 m/s |
| Pitch-meridional chord ratio P/c_m | 0.97 | 0.87 |

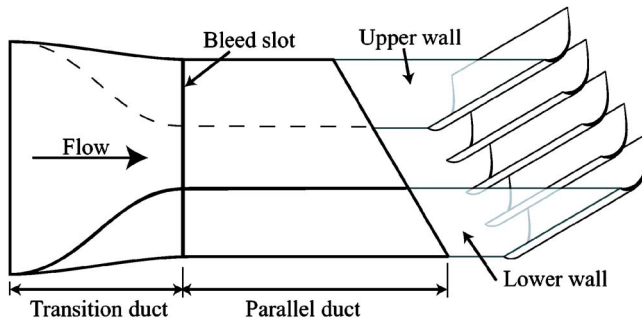


Fig. 3 Schematic of swept cascade (Blade HS), side view

head, and local dynamic head to within $\pm 1\%$ of exit dynamic head. Normalized Y_p can be determined to within approximately ± 0.1 . These estimates of uncertainty apply to the traverses made at $x_m/c_m=1.25$, where the spatial gradients in the flow are generally larger than the scale of the probe tip. The measurement errors at $x_m/c_m=1.03$ will be larger (trailing edge thickness is comparable to probe tip diameter) and quantitative interpretation of these data are not made in this paper.

Data Processing. The blade surface static pressures are presented as pressure coefficients:

$$c_p = \frac{p_{01} - p}{p_{01} - p_2} \quad c_{p\lambda} = \frac{p_{01} - (1/2)\rho V_s^2 - p}{p_{01} - (1/2)\rho V_s^2 - p_2} \quad (1)$$

where p_{01} is from the inlet reference Pitot and p_2 is taken as the ambient pressure. $c_{p\lambda}$ can be used to directly compare the midspan pressure distributions of Blade H and Blade HS since it takes into account the effective reduction in inlet total pressure caused by the inability to stagnate the spanwise component of velocity.

The loss coefficient is evaluated using

$$Y_p = \frac{p_{01} - p_0}{p_{01} - p_3} \quad (2)$$

where p_3 is the static pressure obtained after the flow at the $x_m/c_m=1.25$ plane is mixed out at constant area. All values of Y_p are presented normalized by the midspan profile loss of Blade H.

Numerical Method

The CFD simulations presented in this paper were performed with Denton's structured multiblock solver, TBLOCK. The code is described in detail in Refs. [10,11]. Wall functions are used to calculate the surface skin friction, turbulence is modeled with a simple mixing length approach, and transition location, though not predicted, can be specified. Although TBLOCK can use any structured multiblock grid topology, the authors opted to employ a

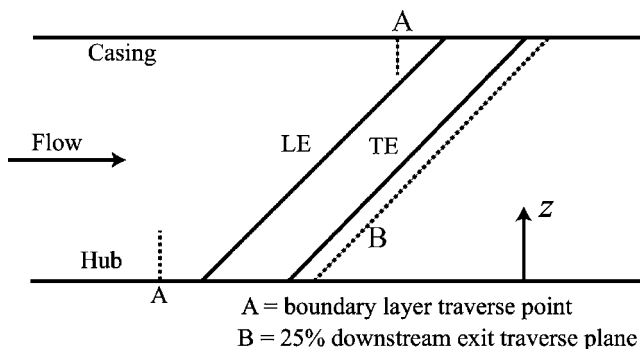


Fig. 4 Schematic of swept cascade (Blade HS), meridional view showing traverse planes and z coordinate direction

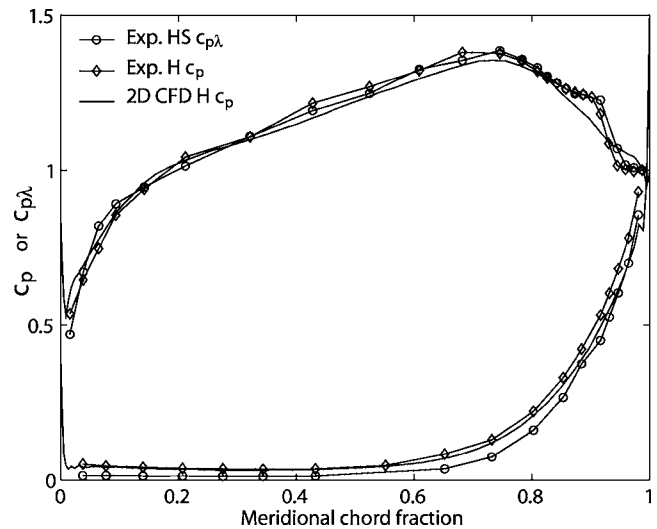


Fig. 5 Midspan pressure distributions for both blades

single sheared H-mesh block for the present study. In addition, since we cannot hope to capture any vortex shedding in the steady-state simulations used in this work, a trailing edge cusp is employed to avoid unphysical spikes in the blade pressure distribution. The authors have, therefore, deliberately used TBLOCK in as simple a configuration as possible, but it will be shown, by comparison to the measured data, to achieve accurate results provided that sensible estimates can be made for the location of boundary layer transition.

Experimental Results

Midspan Results. It was shown by Pullan and Harvey [4] that the blading of the swept cascade, operating between the same inlet and exit flow angles, has the same midspan pressure distribution as the unswept blade, Fig. 5. Despite having the same lift distribution, Pullan and Harvey [4] demonstrated that the swept blade had a 20% higher profile loss than that of the unswept cascade.

Presentation of Endwall Data. The flows in the endwall regions of Blade H and Blade HS will be presented as if from three separate cascades: Blade H, Blade HS "hub" and Blade HS "casing." "Hub" refers to the end of the blade where an obtuse angle is formed between the leading edge and the endwall, as in Fig. 2. In taking this approach, we assume that the aspect ratio of the cascade is sufficiently large for the endwall flows to be separated by a significant region (more than one meridional chord of span) of two-dimensional flow—this will be shown to be the case. In order to compare the secondary flows from the three endwalls, the distance perpendicular to the endwalls is shown nondimensionalized by the meridional chord of the blade. This approach is justified by two separate arguments: First, the blades were designed to operate in the same duct between the same inlet and exit states and at the same Reynolds number based on meridional chord. This means that an inlet stream surface at the same z/c_m on all three endwalls encloses the same mass flow per unit pitch (provided that δ^*/c_m is the same for each inlet boundary layer). Second, in the absence of secondary flow, the stream surfaces close to the endwall must remain parallel to the endwall whether the blade is swept or not. Therefore, the appropriate measure of the scale of the blade is the chord parallel to the endwall, i.e., the meridional chord. All the contour plots presented in this paper have a circumferential extent of one blade pitch, and a spanwise extent of $z/c_m=1$ (i.e., measured perpendicular to the endwall).

In compliance with the above arguments, the inlet boundary layer thickness at each endwall was controlled, by trial-and-error positioning of a boundary layer trip, so as to maintain the same

Table 2 Inlet endwall boundary layers, integral parameters

| | δ^* | θ | H |
|-----------------|------------|------------|------|
| Blade H | $0.030c_m$ | $0.022c_m$ | 1.36 |
| Blade HS hub | $0.028c_m$ | $0.021c_m$ | 1.35 |
| Blade HS casing | $0.029c_m$ | $0.022c_m$ | 1.32 |

δ^*/c_m , θ/c_m , and H , as measured at the inlet boundary layer traverse station $0.5c_m$ upstream of the leading edge. Table 2 shows that this intent was achieved and the associated boundary layer profiles are shown in Fig. 6.

Blade H (Unswept Cascade)

Flow Visualization. Figure 7 shows the results of an oil-and-dye flow visualization experiment. The photograph shows a meridional view of the suction surface and the separation bubble at $x_m/c_m=0.85$ extends over most of the span of the blade. Close to the hub and casing, the separation bubble disappears where the turbulent endwall boundary layer has penetrated up the suction surface as a result of secondary flow. As expected for Blade H, the secondary flows at each endwall are approximately symmetric.

Surface Pressure Distributions. The variation in surface pressure distribution close to the endwall is shown in Fig. 8. The midspan pressure distribution is maintained until approximately 5% span. At 2% and 5% spans, upstream of 75% chord, the suction-surface pressure is increased due to the impingement of the cross flow from the pressure surface. Aft of 75% chord, the suction-surface pressure is reduced at 5% span and this is likely due to the high velocities caused by the proximity of the passage vortex in this region.

Exit Traverses. Data from exit area traverse at two stations, $x_m/c_m=1.03$ and $x_m/c_m=1.25$, are presented in Figs. 9 and 10. Note that, in common with the traverses for Blade HS presented later, the spanwise extent of the contour plots is restricted to $z/c_m=1$ to show the detail of the secondary flow structure (the circumferential extent is one blade pitch). The narrow white zone at the bottom of each plot indicates the region not traversed by the probe.

Figure 9 shows contours of normalized total pressure loss coefficient. In Fig. 9(a), the wake is still radial and a distinct island

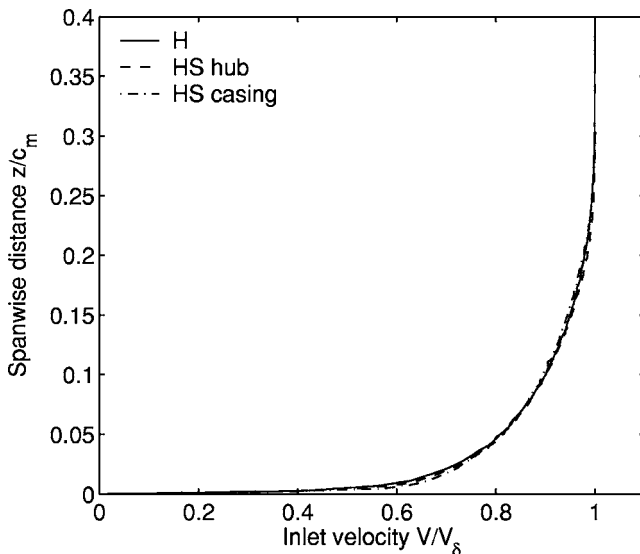


Fig. 6 Inlet endwall boundary layer profiles, swept and unswept cascades

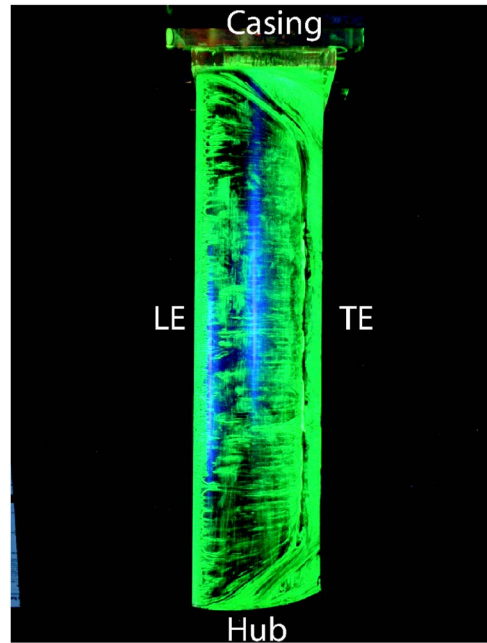


Fig. 7 Blade H suction-surface flow visualization, meridional view

of high loss is visible at $z/c_m=0.2$. This is the core of the passage vortex and it contains the inlet endwall boundary layer fluid, see Sieverding [5] and Gregory-Smith et al. [12]. Below this core, the

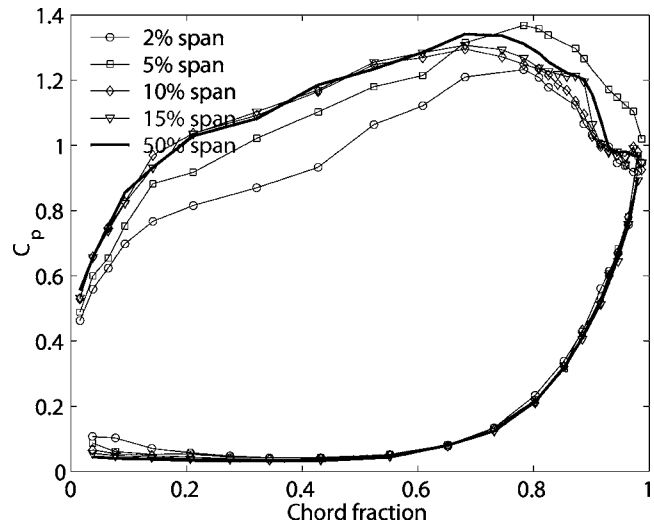


Fig. 8 Blade H, surface pressure distributions

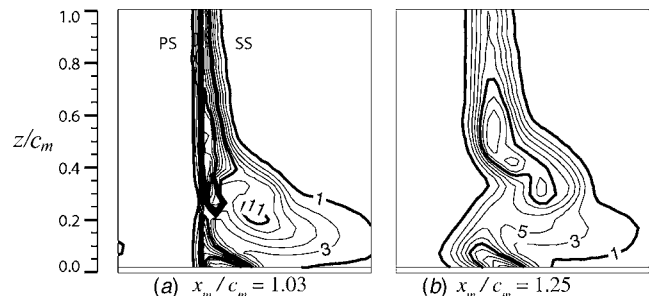


Fig. 9 Blade H, measured normalized Y_p , $\Delta_{con}=2$

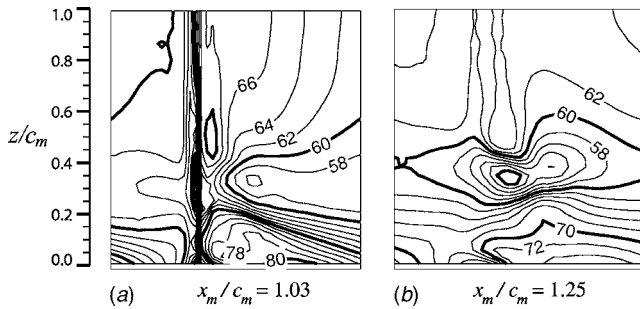


Fig. 10 Blade H, measured yaw angle (deg), $\Delta_{con}=2$ deg

flow is overturned, and above it is underturned by this vortex, Fig. 10(a). At $x_m/c_m=1.25$, the secondary flows have distorted the wake. Concentrations of loss are seen at the center of the passage vortex and trailing shed vortex. The latter forms downstream of the trailing edge as a result of the opposing spanwise velocities on the suction surface and pressure surface generated by the secondary flows.

When pitchwise mass averaged, the results at $x_m/c_m=1.25$ form the curves of Fig. 11. In these plots, the spanwise range is greater than in the contour maps described above (midspan for the Blade H cascade is at $z/c_m=2.0$). It can be seen that the flow above $z/c_m=1$ is two dimensional. Figure 11(b) shows the classical under- and overturning signatures of secondary flow.

Blade HS (Swept Cascade)

Flow Visualization. Results of an oil-and-dye flow visualization test are shown in Fig. 12. Three points are noteworthy: First, as was the case for Blade H, the separation bubble on the late suction surface is clearly seen over all but the 20% of span closest to each endwall. Second, the flow on the suction surface is seen to accelerate in the plane normal to the blade stacking axis, so that just upstream of the separation bubble (peak suction) it is almost perpendicular to the trailing edge. As the flow approaches the lift-off line of the separation bubble, it begins to turn back toward the meridional direction. At the trailing edge, the flow returns to its initial direction but it is displaced radially from its position at inlet to the cascade. Finally, the secondary flows are not symmetric with a greater spanwise penetration seen at the casing than at the hub.

Surface Pressures. Figures 13 and 14 show surface pressure distributions measured close to the hub and casing, respectively. The analysis of Denton and Xu [3] predicts that the leading edge loading should reduce at the hub and increase at the casing, while the opposite should occur at the trailing edge. Figure 13 clearly

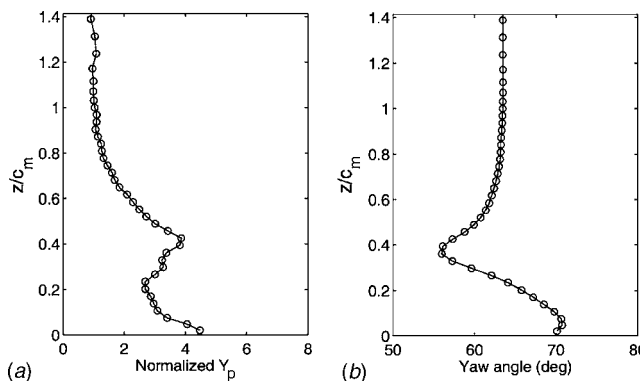


Fig. 11 Blade H, pitchwise mass-averaged distributions, $x_m/c_m=1.25$

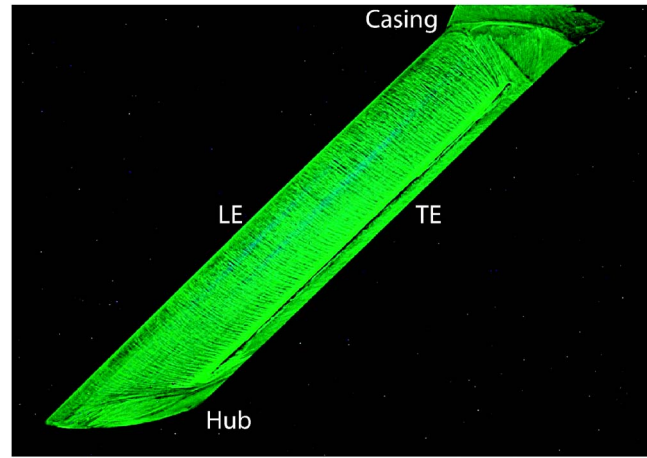


Fig. 12 Blade HS suction-surface flow visualization, meridional view

shows a gradual reduction of leading edge loading from 15% span down to the wall. At 2% span, the lift distribution is highly aft loaded. As was the case for Blade H, the pressure distribution at 5% span shows a reduced suction-surface static pressure downstream of 75% chord. Again, this is thought to be caused by the presence of the passage vortex. At the casing, the leading edge loading is increased, but the effect is weaker than that at the hub and is restricted to a smaller spanwise zone. No significant increase in loading at the trailing edge near the hub can be seen, but a raised pressure-surface pressure contributes to a reduced trailing edge loading near the casing. No influence of the passage vortex is evident in the casing pressure distributions.

Exit Traverses. The authors anticipated that the exit traverses would show that the aft-loaded hub produced weaker secondary flow than Blade H, whereas the increased leading edge loading at the casing would produce stronger secondary flow in this region. However, the exit traverse data in Figs. 15 and 16 reveal that the reality is not so straightforward.

Figures 15 and 16 show contour plots of loss coefficient and yaw angle, respectively. In the plots at the casing, the spanwise direction has been reversed so that the endwall is always at the bottom of the figure.

In Fig. 15(a), the radial wake is joined by two additional loss

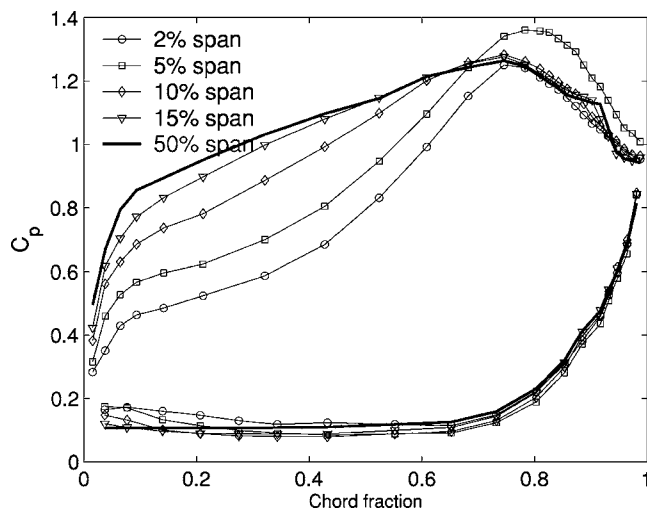


Fig. 13 Blade HS, surface pressure distributions close to the hub

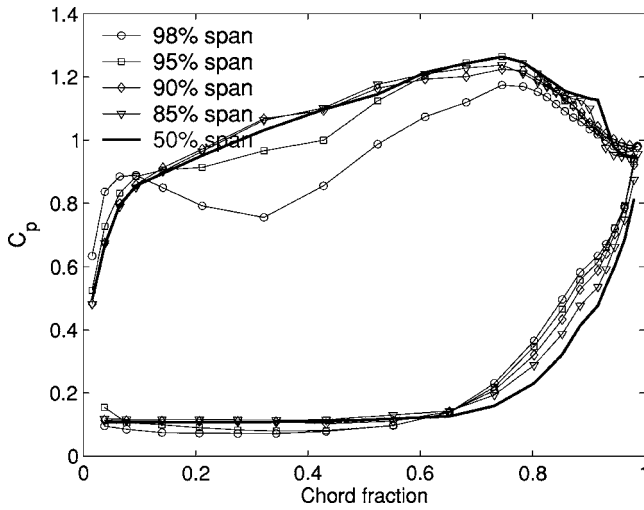


Fig. 14 Blade HS, surface pressure distributions close to the casing

contributions close to the suction surface. The upper one contains inlet endwall boundary layer fluid in the core of the passage vortex (noticeably closer to the hub than was the case for Blade H). The lower region of increased loss is in the suction-surface/endwall corner. At $x_m/c_m=1.25$, the under- and overturnings have distorted the wake into an “S” shape with the deepest loss occurring next to the endwall. Again, the penetration is much reduced as compared to the corresponding traverse for Blade H, Fig. 9.

At the casing, the flow structure is very different. The high leading edge loading has caused cross flow in the early passage so that the inlet endwall boundary layer fluid has been driven clear from the endwall by the trailing edge, Fig. 15(c). However, there is minimal additional loss in the suction-surface/endwall corner. In addition, the overturning at the endwall is greatly reduced compared to both the hub of Blade HS and to Blade H. Indeed, the wake at $x_m/c_m=1.25$ has remained substantially undistorted. This

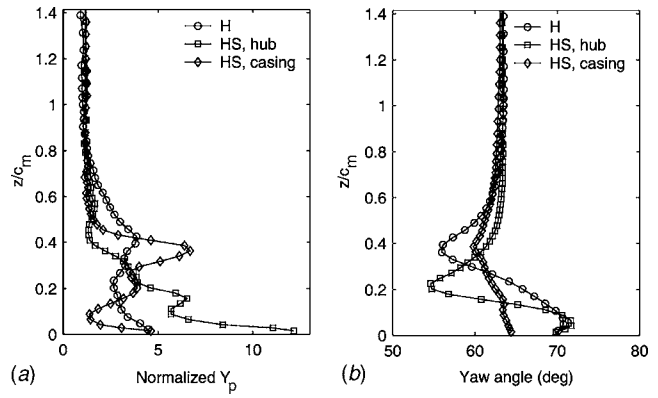
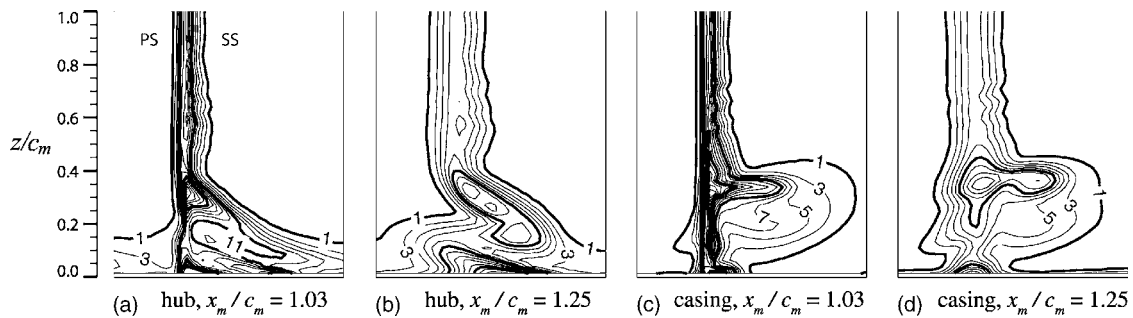


Fig. 17 Blade HS, pitchwise mass-averaged distributions, $x_m/c_m=1.25$

flow structure was unexpected and is difficult to explain using the conventional secondary flow understanding of unswept blades. Further insight is gained, however, through the application of CFD later in this paper.

Figure 17 compares pitchwise mass-averaged data for both ends of Blade HS with that for Blade H. In Fig. 17(a), the 20% increase in midspan profile loss for Blade HS, reported by Pullan and Harvey [4], can be seen. The marked increase in loss close to the hub of Blade HS is also apparent. Figure 17(b) clearly shows both the reduced penetration of the secondary flow at the hub of Blade HS and the unusual flow angle signature at the casing.

Loss Audit. The losses associated with the three endwall flows are now compared. The approach taken was to mass average the inlet and exit Y_p over a spanwise distance enclosing the same mass flow. For Blade HS, it was found that the mass flow at blade exit in each half-span ($z/c_m=1.41$) differed by only 1% and so it was legitimate to integrate the inlet loss up to midspan as well. Note that it had originally been planned to integrate the exit flows up to $z/c_m=1$ but it will be shown later, in Fig. 24, that the inlet



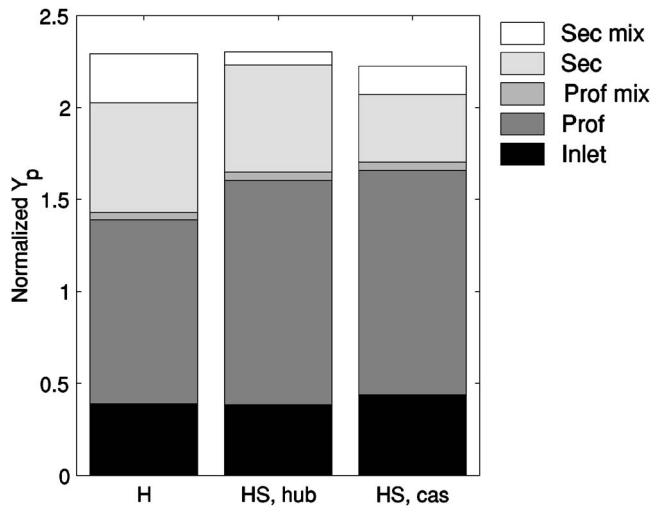


Fig. 18 Blades H and HS, measured loss audit

boundary layer is predicted to climb the pressure surface at the hub almost to this height. For Blade H, the mass flow up to $z/c_m=1.41$ at inlet (midspan for Blade H is at $z/c_m=2$) was used to find the appropriate z/c_m at exit. All three loss audits were therefore based on the same inlet and exit mass flows.

Figure 18 shows an audit of the measured loss at all three endwalls. The breakdown has been performed in the following way. The total unmixed loss is obtained by mass averaging the traverse data at $x_m/c_m=1.25$. The inlet loss is obtained from the inlet endwall boundary layer traverse. The profile loss is given by the fine resolution traverse data used in Ref. [4]. The profile mixing loss is the small increment obtained by constant area mixing of the midspan wake. The secondary loss is given by the total unmixed loss with the inlet and profile loss subtracted. Finally, the secondary mixing loss is obtained by mixing out the traverse data to pitchwise uniformity and subtracting all the other loss components.

The overall loss of all three audits is very similar. The increased profile loss of the swept blade is evident. It is clear, however, that *both* endwalls of Blade HS contribute less secondary and secondary mixing loss than Blade H. For the Blade HS hub, the sum of these components is 76% of that for Blade H. At the casing of Blade HS, the value is 61% of the Blade H figure. It should be noted that, because of the reduced pitch-chord ratio of Blade HS, these reductions have been achieved despite an increase in blade wetted area of 12% as compared to Blade H.

Numerical Results

Introduction. In this section, TBLOCK is used to provide further understanding of the experimental results discussed above. First, the distortion of the axisymmetric inlet stream surfaces as they pass through Blade HS is calculated using an inviscid solution. Second, a viscous simulation is presented to give confidence that TBLOCK is able to capture the real flowfield. Finally, the development of the secondary flows in both Blade H and Blade HS is studied.

Stream Surfaces. The midspan stream surface for Blade HS is shown in Fig. 19. The view is from upstream with the blade radially stacked. The stream surface was calculated from a two-dimensional simulation of the Blade HS profile with a superimposed constant spanwise velocity such that the sweep angle $\lambda=45$ deg. The stream surface in Fig. 19 is similar to those calculated by Potts [2]. In the present case, however, the very low two-dimensional velocity close to the pressure surface leads to severe distortion in this region.

Figure 20 tracks stream surfaces through the three-dimensional

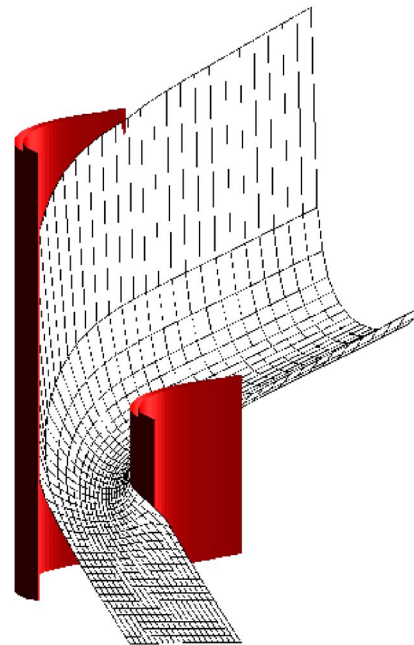


Fig. 19 Deformation of midspan stream surface, axial view from upstream

blade row using inviscid CFD with no inlet endwall boundary layer (no conventional secondary flow). At the leading edge, the velocity in the plane normal to the spanwise direction stagnates but the spanwise component persists. This causes the stream surfaces on both sides of the passage to curve upwards in Fig. 20(a). By $x_m/c_m=0.25$, Fig. 20(b), the blade curvature causes V_n , the velocity component normal to the stacking axis in the meridional view, to reduce greatly near the pressure surface and to increase near the suction surface. This causes further upwards movement of the stream surface close to the pressure surface and downwards movement near the suction surface. This process continues through $x_m/c_m=0.5$, Fig. 20(c). At the trailing edge, the stream surface is highly distorted and discontinuous in the circumferential direction.

The stream tube thickness is seen to remain constant with pitchwise position over much of the span. In this region, the flow is two-dimensional and can be closely approximated by the infinite swept blade model. The endwalls are observed to influence the flow within approximately one blade pitch of the hub and casing.

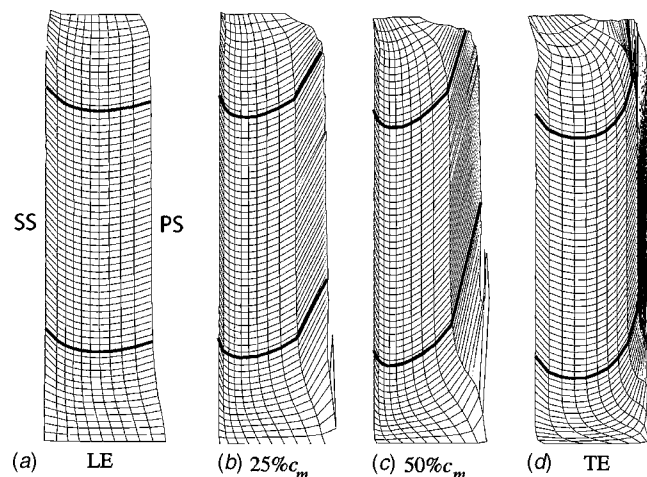


Fig. 20 Stream surface deformation through Blade HS

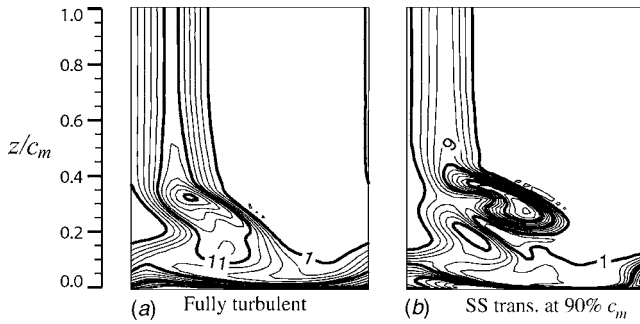


Fig. 21 Blade HS, CFD predictions of normalized Y_p at hub

The effect on the blade loading at the endwalls can be assessed qualitatively by considering the stream tube formed between the inlet stream surface one pitch from the endwall (shown in bold) and the endwall itself. We now examine the thickness of this stream tube close to the suction surface. At the leading edge, this thickness is increased at the hub and reduced at the casing; this leads to the suction-surface velocities being lowered at the hub (reduced loading) and raised at the casing (increased loading). The reverse is true at the trailing edge.

Flowfield: Calibration. The effect of changing two aspects of the numerical modeling, mesh refinement, and transition location, on the accuracy of the solution, was assessed. It was found that a grid of $125 \times 49 \times 129$ (axial \times pitchwise \times spanwise) nodes was sufficient to resolve the secondary flow structures. Note that the spanwise distribution of points was concentrated in the secondary flow region so that 58 points were within $z/c_m = 1$ of the endwall. Figure 21 shows the predicted loss coefficient at the hub of Blade HS for a simulation with fully turbulent blade surface boundary layers, Fig. 21(a), and for one having a fully laminar pressure surface and transition specified on the suction surface at the location observed in the midspan surface pressure measurements. The structure of the secondary flow in Fig. 21(a) is closer to the experimental data shown in Fig. 15(b) but the two-dimensional wake depth is, as expected, too great. In Fig. 21(b), the wake depth is well reproduced but the secondary flows are different to those observed in reality. The flow visualization results of Fig. 12 indicate that the suction surface close to the endwalls, where the secondary flows penetrate, is turbulent. To simulate this, a passive scalar was added to the inlet endwall boundary layers of the fully turbulent calculation and tracked through the blade row. The location of this tracer on the suction surface was used as a marker for transition onset, Fig. 22(a), and the resultant flowfield is shown in Fig. 22(b). The shape of the secondary flow and the two-dimensional wake depth agree closely with the experiment. However, the loss core is too deep in Fig. 22(b), deeper than in Fig. 21(a), which indicates that more of the suction surface close to the hub is turbulent than was specified. This could be achieved

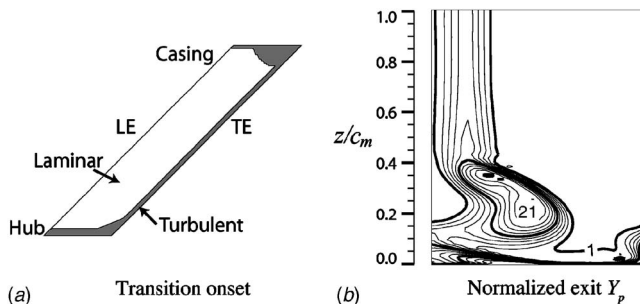


Fig. 22 Blade HS, CFD, spanwise varying transition onset

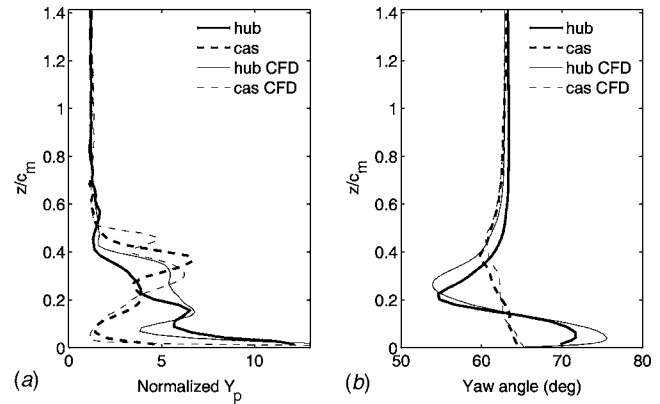


Fig. 23 Pitchwise mass-averaged distributions, $x_m/c_m = 1.25$

in the calculation by altering the passive scalar threshold used to generate Fig. 22(a), but the trends of the impact of boundary layer state on the secondary flows, of this blade at least, have been established.

Figure 23 compares pitchwise mass-averaged computational and experimental data for Blade HS. Apart from the loss discrepancy at the hub noted above, the agreement is very good. In particular, the ability to reproduce both the conventional over- and underturnings observed at the hub and the unusual yaw angle distribution seen at the casing is clear.

Flowfield: Analysis. CFD simulations are now used to investigate the flowfield structure within the passage where measurements have not been taken. For clarity, inviscid simulations (including free slip on all walls) with the measured inlet boundary layer profile were performed. Any vorticity present within the passage is then the result of turning of the vorticity of the inlet flow, not viscous effects. Figures 24(a)–24(c) show these calculations for Blade H, the hub of Blade HS, and the casing of Blade HS, respectively. Data from three planes are shown. At each plane, plots of pitch angle (defined to be positive when away from the local endwall) and streamwise vorticity (positive when clockwise) are presented. The streamwise vorticity from the CFD is calculated using the midspan, midpitch flow as the streamwise direction. At the third plane shown, $x_m/c_m = 1.25$, measured contours of streamwise vorticity are presented. The vorticity is calculated using the method used by Gregory-Smith et al. [12] and Yaras and Sjolander [13]. Here, the primary direction is taken to be the design exit angle. The streamwise vorticity shown is non-dimensionalized by the inlet freestream meridional velocity and meridional chord:

$$\omega'_{sw} = \frac{\omega_{sw}}{4\pi V_m/c_m} \quad (3)$$

In discussion of Fig. 24, it is helpful to think of the flowfield as the superposition of a primary irrotational flow, and a perturbation flow (secondary flow). The primary flows for the two blades differ fundamentally in that the unswept blade has a primary flow with zero spanwise velocity component but the swept blade has a primary flow, which has large spanwise velocities that lead to pitch angles of up to ± 40 deg.

Figure 24(a) shows the endwall flow of Blade H. At $x_m/c_m = 0.5$, Fig. 24(a)(i) shows that the pressure-side leg of the horseshoe vortex, “A,” has crossed the passage to the suction surface. The inner portion of the inlet boundary layer is contained within A, the rest is seen as streamwise vorticity to the right of A in Fig. 24(a)(i). By Fig. 24(a)(ii) at $x_m/c_m = 0.95$, the passage vortex (this is what A has now become) is well developed. Immediately downstream of the trailing edge, the passage vortex is joined by vorticity of the opposite sense that has been shed from the blade, “C.” Note that the position of the trailing edge in the contour plots

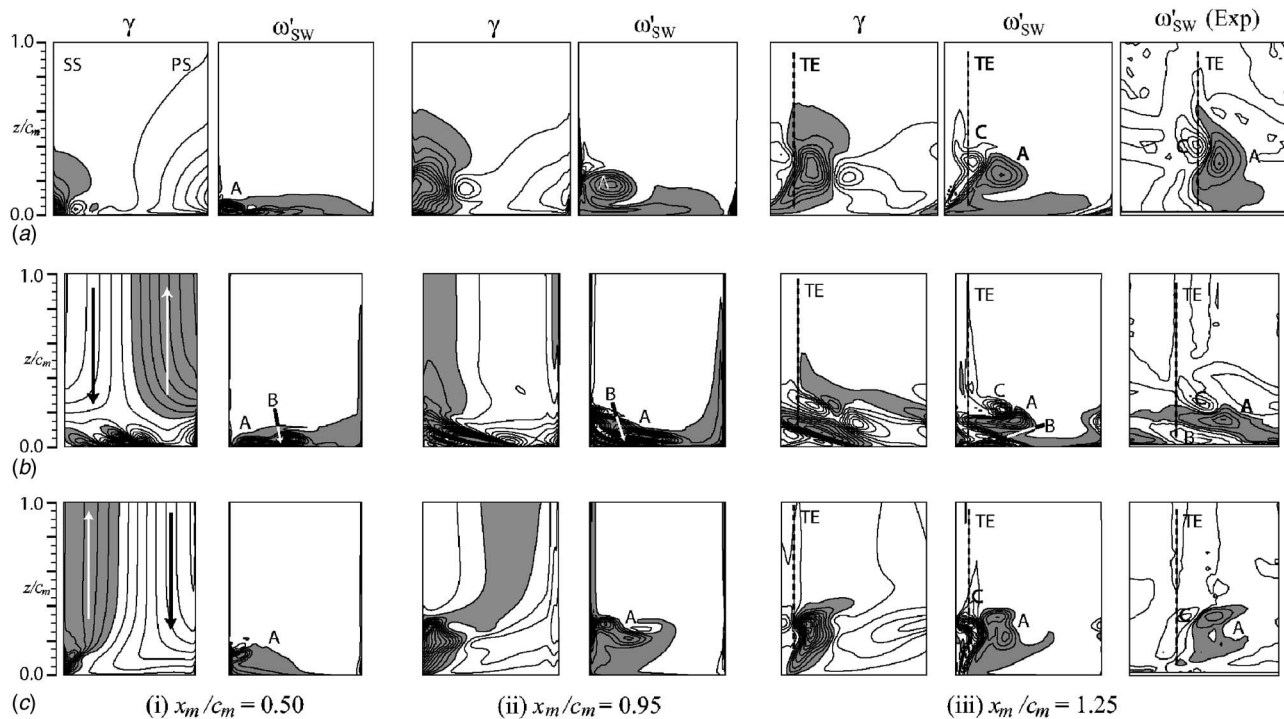


Fig. 24 Results of inviscid calculations (with measured inlet boundary layer) (a) Blade H, (b) Blade HS hub, (c) Blade HS casing. Pitch angle γ , $\Delta_{con}=5$ deg, $\gamma>2.5$ deg shown gray. Normalized streamwise vorticity ω'_{sw} , $\Delta_{con}=0.4$, $\omega'_{sw}>0.2$ shown gray.

differs in the calculations and experimental results but the approximate location is indicated in the figure. The fact that the inviscid predictions and the measured results are similar illustrates that the main features of secondary flow are generated by the inviscid transport of the vorticity present in the inlet flow. The secondary flow depicted in Fig. 24(a) is similar to that seen by many investigators, e.g., Langston et al. [14] and Gregory-Smith et al. [12].

The flow at the hub of Blade HS is shown in Fig. 24(b). The strong pitch angle variations of the primary flow are clearly evident in Fig. 24(b)(i), which shows flow moving away from the endwall on the pressure surface and toward the endwall on the suction surface. This bulk movement of the primary flow is in the opposite direction to the secondary flow and so should be expected to hinder or delay its development. Two islands of positive streamwise vorticity are visible in Fig. 24(b)(i). These later form the passage vortex. Between them, a small zone of negative streamwise vorticity, “B,” is just discernible. Examination of the CFD revealed that the fluid at B is part of the inlet boundary layer that was swept up the pressure surface by the primary flow before being driven back down and across the passage by the secondary flow. This small zone of negative vorticity is still visible in Fig. 24(b)(ii) where it is also apparent that the primary flow has hampered the development of the passage vortex so that it is much closer to the endwall than was the case for Blade H. Furthermore, positive vorticity can be seen next to the pressure surface almost up to $z/c_m=1$ and this is inlet boundary layer fluid swept up the pressure surface by the primary flow. Satisfactory agreement with the experimental data is again observed in Fig. 24(b)(iii), although B is larger in the measured data than in the inviscid predictions.

It has been shown that the secondary flow at the casing of Blade HS is highly unusual, with minimal overturning next to the endwall. It can be seen in Fig. 24(c)(i) that the cross-passage movement of the inlet endwall boundary layer is helped by the bulk primary flow motion. In the streamwise vorticity plot of Fig. 24(c)(i), virtually no inlet boundary layer fluid is visible in the pressure-surface half of the passage. As the inlet boundary layer

moves across the endwall, it is replaced by *primary flow from the pressure-surface half of the passage*. This flow continues in a predominantly streamwise direction (i.e., out of the page of Fig. 24)—it is not overturned. By contrast, in the conventional secondary flow of Blade H, the flow that “fills the space” left by the inlet boundary layer comes from much closer to the pressure surface and so itself becomes overturned as it moves toward the suction surface. This is the explanation for the much reduced overturning of the flow at the endwall at the exit of the casing of Blade HS compared to Blade H.

Conclusions

This paper has examined the influence of high levels of sweep on the secondary flow structure, and associated losses, of a turbine blade. Two blades, designed to perform the same aerodynamic duty, have been investigated both experimentally and computationally. The first, Blade H, is unswept, and the second, Blade HS, is highly swept ($\lambda=45$ deg). As compared to the unswept blade, the following have been found:

1. The hub of Blade HS generates secondary flows, which penetrate a smaller distance up the suction surface from the endwall. This is shown to have been caused by a delay in the endwall cross flow resulting from a combination of two effects of the sweep. First, the leading edge loading at the hub of Blade HS is greatly reduced. Second, the bulk motion of the primary flow acts to oppose the secondary flow by pushing the inlet endwall boundary layer toward and up the pressure surface. The overall effect on performance is a reduction of the measured secondary loss of 24%.
2. The casing of Blade HS generates secondary flows with a similar spanwise penetration to those at the hub but with, very distinctively, greatly reduced endwall overturning at row exit. This time, it is shown that sweep encourages cross-passage flow by increasing the leading edge blade loading. However, once the inlet boundary layer has swept on to the suction surface, it is replaced on the endwall by irrotational

primary flow, which arrives at the casing over the pressure-side half of the passage. At this endwall, the measured secondary loss is 39% of that for Blade H.

In addition, it has been shown that accurate predictions for both the structure and loss of the endwall flows of high-lift low Reynolds number blading can be achieved, even with simple turbulence modeling, provided that an estimate can be made for the transition onset location.

This work should prove useful to the turbine aerodynamicist because it suggests the following:

1. A trade-off exists between the increased profile loss and reduced secondary loss of highly swept blading as the aspect ratio is varied.
2. The reduced overturning at the casing of Blade HS will create a more uniform flow for the downstream row. This has been shown to be beneficial for stage efficiency when achieved through three-dimensional blade design, Wallis and Denton [15].
3. Introducing sweep in annuli with little radial flow, by restacking the blade, could be used to reduce secondary losses

Acknowledgment

The authors are grateful for the numerous discussions that this work has stimulated. In particular, conversations with John Denton of the Whittle Laboratory and Simon Gallimore of Rolls-Royce have been very helpful. The authors would also like to thank Trevor Chandler, Bill Gurney, and Nick Hooper for the construction of the cascades.

Nomenclature

| | |
|----------------|--|
| c | = chord |
| c_d | = dissipation coefficient |
| c_p | = $(p_{01} - p)/(p_{01} - p_2)$ pressure coefficient |
| $c_{p\lambda}$ | = $(p_{01} - 0.5\rho V_s^2 - p)/(p_{01} - 0.5\rho V_s^2 - p_2)$ sweep pressure coefficient |
| H | = blade height (perpendicular to endwalls) |
| p | = pressure |
| P | = blade pitch |
| r | = radius |
| V | = velocity |
| x_m | = meridional distance (from LE) |
| Y_p | = $(p_{01} - p_0)/(p_{01} - p_3)$ (normalized by Blade H midspan Y_p) |
| z | = perpendicular distance from endwall |
| α | = yaw angle |

| | |
|-----------------------|--------------------------|
| δ^* | = displacement thickness |
| Δ_{con} | = contour interval |
| γ | = pitch angle |
| λ | = sweep angle |
| ρ | = density |
| θ | = momentum thickness |
| ω_{SW} | = streamwise vorticity |

Subscripts

| | |
|----------|--|
| m | = meridional |
| n | = normal to spanwise in meridional plane |
| s | = spanwise |
| θ | = pitchwise, tangential |
| 0 | = stagnation quantity |
| 1, 2, 3 | = inlet, exit, exit (mixed out) |

References

- [1] Smith, L. H., and Yeh, H., 1963, "Sweep and Dihedral Effects in Axial-Flow Turbomachinery," ASME J. Basic Eng., **85**, pp. 401–416.
- [2] Potts, I., 1987, "The Importance of S-1 Stream Surface Twist in the Analysis of Inviscid Flow Through Swept Linear Turbine Cascades," IMechE, **C258/87**pp. 231–248.
- [3] Denton, J., and Xu, L., 1999, "The Exploitation of 3D Flow in Turbomachinery Design," IMechE, **213**, pp. 125–137.
- [4] Pullan, G., and Harvey, N. W., 2006, "The Influence of Sweep on Axial Flow Turbine Aerodynamics at Mid-Span," ASME Paper No. GT2006-91070.
- [5] Sieverding, C. H., 1985, "Recent Progress in the Understanding of Basic Aspects of Secondary Flows in Turbine Blade Passages," ASME J. Eng. Gas Turbines Power, **107**, pp. 248–257.
- [6] Langston, L., 2001, "Secondary Flows in Axial Turbines—A Review," Ann. N.Y. Acad. Sci., **934**, pp. 11–26.
- [7] Curtis, E., Hodson, H., Baniaghbal, M., Denton, J., Howell, R., and Harvey, N., 1997, "Development of Blade Profiles for Low Pressure Turbine Applications," ASME J. Turbomach., **119**, pp. 531–538.
- [8] Howell, R., Ramesh, O., Hodson, H., Harvey, N., and Schulte, V., 2001, "High Lift and Aft-Loaded Profiles for Low-Pressure Turbines," ASME J. Turbomach., **123**, pp. 181–188.
- [9] Harvey, N., Cox, J., Schulte, V., Howell, R., and Hodson, H., 1999, "The Role of Research in the Aerodynamic Design of an Advanced Low-Pressure Turbine," IMechE, **C557/043**, pp. 123–132.
- [10] Rosic, B., Denton, J., and Pullan, G., 2006, "The Importance of Shroud Leakage Modelling in Multistage Turbine Flow Calculations," ASME J. Turbomach., **128**, pp. 699–707.
- [11] Pullan, G., Denton, J., and Curtis, E., 2006, "Improving the Performance of a Turbine With Low Aspect Ratio Stators by Aft-Loading," ASME J. Turbomach., **128**, pp. 492–499.
- [12] Gregory-Smith, D., Graves, C., and Walsh, J., 1988, "Growth of Secondary Losses and Vorticity in an Annular Turbine Cascade," ASME J. Turbomach., **110**, pp. 1–8.
- [13] Yaras, M., and Sjolander, S., 1990, "Development of the Tip-Leakage Flow Downstream of a Planar Cascade of Turbine Blades: Vorticity Field," ASME J. Turbomach., **112**, pp. 609–617.
- [14] Langston, L., Nice, M., and Hooper, R., 1977, "Three-Dimensional Flow Within a Turbine Cascade Passage," ASME J. Eng. Power, **99**, pp. 21–28.
- [15] Wallis, A., and Denton, J., 1988, "Comparison of Design Intent and Experimental Measurements in a Low Aspect Ratio Axial Flow Turbine with Three-Dimensional Blading," ASME Paper No. 98-GT-516.

Effects of Regular and Random Roughness on the Heat Transfer and Skin Friction Coefficient on the Suction Side of a Gas Turbine Vane

Jason E. Dees

David G. Bogard

The University of Texas at Austin,
Austin, TX 78712

Skin friction coefficients and heat transfer coefficients are measured for a range of regular and random roughnesses on the suction side of a simulated gas turbine vane. The skin friction coefficients are calculated using boundary layer data and the momentum integral method. High resolution surface temperature data measured with an IR camera yield local heat transfer values. 80 grit, 50 grit, 36 grit, and 20 grit sandpapers along with a regular array of conical roughness elements are tested. Measured skin friction coefficient data show that the conical roughness array behaves very similar to the 50 grit, 36 grit, and 20 grit sandpapers in terms of the effect of the roughness on the hydrodynamic boundary layer. In terms of heat transfer, the conical roughness array is most similar to the 80 grit sandpaper, which are both lower than the roughest sandpapers tested. These data show that the particular regular array of roughness elements tested has fundamentally different behavior than randomly rough surfaces for this position on the simulated turbine vane. In addition, this difference is in the opposite direction as seen in previous experimental studies. In order to draw a more general conclusion about the nature of random and regular roughness, a parametric study of regular roughness arrays should be performed. [DOI: 10.1115/1.2812338]

Introduction

Increased surface roughness levels on operational turbine components have been shown to significantly degrade the performance of gas turbine engines. The degradation in performance occurs due to augmentation of surface heat transfer and skin friction. This augmentation can be quite large if the smooth surface is laminar, and roughness causes an earlier boundary layer transition. These results lead to higher operating costs and lower lifetimes for engines and engine components.

Simulating the roughness has traditionally been approached in one of two ways. One way that turbine roughness is simulated is by using a regular array of roughness elements that matches a real roughness sample in terms of some roughness quantity. Bogard et al. [1] examined samples of two turbine vanes that had been significantly roughened by operation in the field. They developed an array of cones designed to match the equivalent sandgrain roughness k_s of the sample roughness. The equivalent sandgrain roughness is by definition the roughness height, which would yield the same skin friction coefficient as a sandgrain surface (as quantified by Nikuradse [2]) for the surface being analyzed. The presumption made by Bogard et al. was that by matching the equivalent sandgrain roughness with the array of cones, the heat transfer and skin friction drag for the real rough surface can be accurately simulated. Other studies [3,4] have also used regular arrays of roughness elements to simulate the behavior of real rough surfaces.

Bons et al. [5] analyzed over 100 used turbine components and concluded that due to the various roughness characteristics

present, no one roughness element (cones, hemispheres, etc.) would be adequate to simulate the real roughness found on the components. A later study by Bons [6] looked at six scaled up real roughness models chosen to represent a range of types and levels of the roughness seen in the previous study. Skin friction coefficient and heat transfer coefficient were measured for all of the real rough surfaces. When a standard correlation was used to compare the measured heat transfer values for the realistic rough surfaces to the predicted value, the predicted values were found to overpredict the heat transfer by about 10%. An ordered array was constructed to match the skin friction coefficient of one of the realistic rough surfaces, and the heat transfer coefficient was measured to be 10% lower than that for the realistic rough surface. However, the measured heat transfer for the ordered array matched the predicted heat transfer within 1%. Due to this result, the author suggested that ordered arrays may be used to simulate either skin friction effects or heat transfer effects of real roughness, but not both simultaneously.

A similar study was performed by Belnap et al. [7] that showed the same overprediction of heat transfer for real rough surfaces. In this study, two examples of real component roughness were tested in a fully developed channel flow. Measurement of the average pressure drop was used to determine the skin friction of each rough surface. When a correlation was used to predict the Stanton number based on the measured C_f , the predicted Stanton number values overpredicted the measured values by about 10%.

The study presented in the paper also involved a comparison of random roughness and ordered array roughness. Measurements were made of skin friction and heat transfer coefficient so that the relative augmentation of these two parameters could be determined. However, this study was done on the suction side of a simulated turbine vane where the strong favorable pressure gradi-

Contributed by the International Gas Turbine Institute of ASME for publication in the JOURNAL OF TURBOMACHINERY. Manuscript received June 7, 2007; final manuscript received August 15, 2007; published online August 1, 2008. Review conducted by David Wisler. Paper presented at the ASME Turbo Expo 2007: Land, Sea and Air (GT2007), Montreal, Quebec, Canada, May 14–17, 2007.

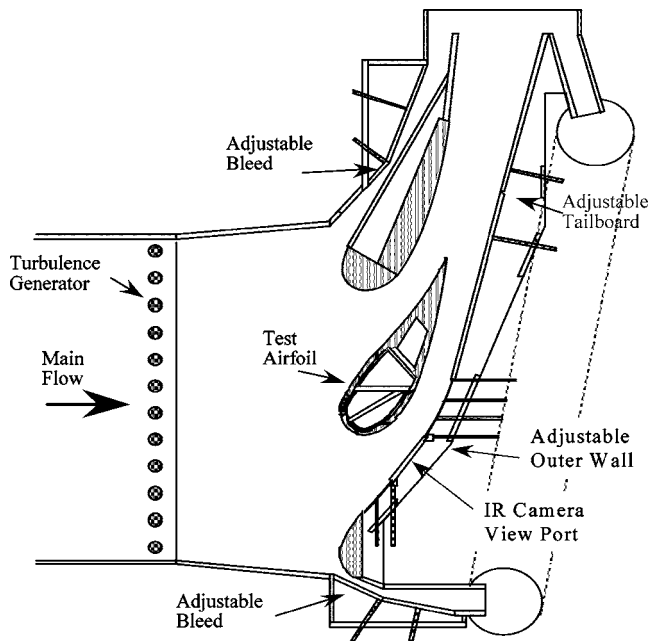


Fig. 1 Schematic of the simulated turbine vane test section

ent had a strong effect on boundary layer transition. Consequently, roughness samples were tested in a region where the roughness would affect the transition process.

Experimental Facilities and Procedures

Experiments were conducted in a closed loop wind tunnel driven by a 50 hp adjustable speed blower. The test section, shown in Fig. 1, simulated a three vane, two passage cascade. The vane geometry was taken from an actual turbine inlet guide vane scaled up nine times. The center vane, shown in Fig. 2, was instrumented with pressure taps to measure the pressure distribution around the vane.

Adjustable bypass flows outside of the two half vanes were designed to match the passage flow of three vanes. The outer wall of the test section had movable walls in order to control the pressure distribution around the test vane. The chord length of the scaled up test vane was 59.4 cm and the span was 54.9 cm. The vane cascade had a pitch of 45.7 cm. For the experiments per-

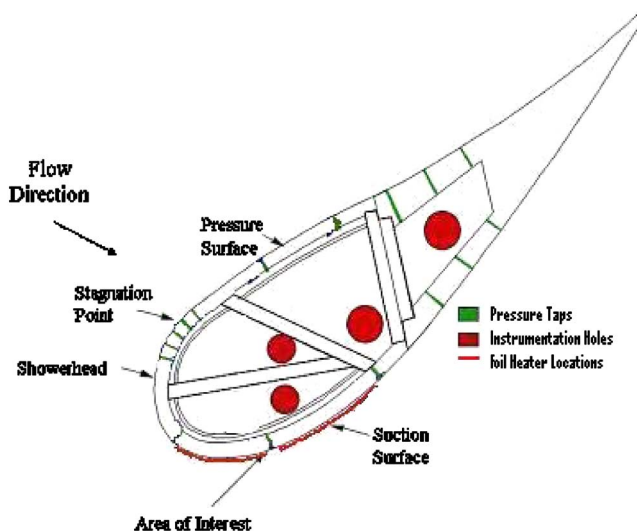


Fig. 2 Schematic of test vane detail

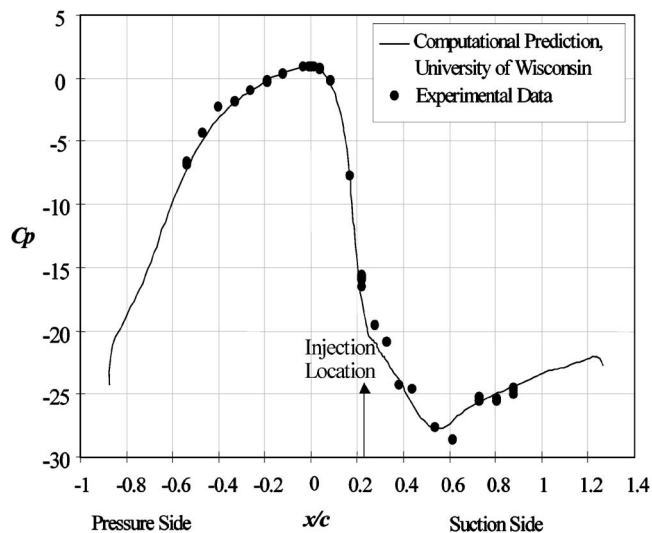


Fig. 3 C_p distribution for the vane (from Ref. [9])

formed in this study, the mainstream approach flow was held at 5.8 m/s. This resulted in a cascade exit velocity of 28 m/s and a Reynolds number based on exit velocity and chord length of $Re = 1.06 \times 10^6$. Previous measurements [8] showed that the mainstream turbulence was $Tu = 5.2\%$ at $0.18c$ upstream of the vane's leading edge. The vane was constructed of low conductivity polyurethane foam with thermal conductivity $k = 0.048$ W/m K. The area studied was between $s/C = 0.37$ and $s/C = 0.57$ on the suction side of the vane. The pressure coefficient distribution around the vane was measured in a previous study [9], and is shown in Fig. 3. Note that the region over which these tests were conducted was immediately downstream of a strong favorable pressure gradient.

This study examined the effects of regular roughness arrays and random, "real" rough surfaces. A regular array of conical roughness elements was constructed by punching cones in a thin stainless steel foil, distributed as shown in Fig. 4. The cones had a height $k = 1$ mm, base diameter $d = 4$ mm, and a pitch $p = 4.3$ mm. The equivalent sandgrain roughness value for this array of cones was estimated to be $k_s = 0.5$ mm using the roughness shape density parameter of Sigal and Danberg [10]. Sandpaper was chosen to simulate real rough surfaces due to its low cost, availability, and wide range of roughness levels. Preliminary boundary layer measurements were conducted to determine which sandpaper levels had hydrodynamic effects that were most similar to the regular roughness array discussed above. As a result of these measurements, 20 grit, 36 grit, 50 grit, and 80 grit sandpapers were chosen for further study.

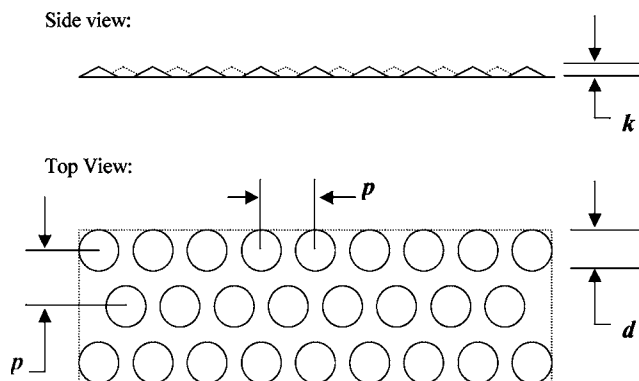


Fig. 4 Schematic of regular roughness array

All rough surfaces were attached to the surface of a heating foil using double sided tape. In order to make the conical roughness array similar to the sandpaper roughness, the conical roughness was first attached to a paper backing using double sided tape. The paper backing with the conical roughness attached was then taped to the vane in the same way the sandpaper was attached. In all cases, the roughness extended from the stagnation line to $s/C \approx 0.60$.

Boundary layer measurements were performed using an A.A. Lab Systems Ltd. AN-1003 hot wire/hot film anemometry system. Mean velocity profiles and fluctuating velocity profiles were measured at $s/C=0.37$ and $s/C=0.57$ for all rough surfaces and a smooth base line. For the smooth surface condition, a smooth piece of vinyl cardstock was taped to the vane surface over $0 < s/C < 0.60$ to make the surface as smooth as possible. For some experiments, a tripwire of 0.61 mm diameter was installed at $s/C=0.29$ for the smooth case only, in order to promote tripping the boundary layer to become turbulent. The data were acquired using a National Instruments data acquisition system. When measuring boundary layers over the rough surfaces, an effective origin, or $y=0$, must be established. In this study, the effective origin was taken to be the midpoint between the surface and the top of the roughness elements. While performing hot wire measurements, the vane was not heated.

For the heat transfer measurements, a uniform heat flux foil was used on the surface of the vane, underneath the surface roughness or smooth cardstock. The surface temperature distribution, T_0 , between $s/C=0.37$ and $s/C=0.57$ was measured using a FLIR ThermoCAM P20 infrared camera. The camera was calibrated in situ using two type E thermocouples located at the rear of the test area, prior to the attachment of the surface roughness. A uniform heat flux was applied using electrical heating of the stainless steel foil attached to the vane in the region of interest as well as upstream of the region of interest (upstream heating took place over the range $0.21 < s/C < 0.37$). The upstream heat flux foil produced a heat flux that was nominally 1.25 times the heat flux produced by the heat flux foil in the area of interest. All rough surfaces were painted with flat black spray paint to obtain a consistent surface emissivity. After painting the surface roughness, a binocular microscope was used to visually verify that the thin coat of paint did not affect the surface roughness level.

During heat transfer tests, nonuniformities in temperature distributions were observed for all roughness levels. This nonuniformity was found to be due to the nonuniform attachment of sandgrains for the commercial sandpaper used. However, tests with different sandpaper samples, and different orientations of the sandpaper, showed that the laterally averaged heat transfer coefficients were essentially the same for all samples.

The convective heat transfer coefficient was determined through the following equation:

$$h = \frac{q_{\text{electrical}} - q_{\text{radiation}} - q_{\text{conduction}}}{T_o - T_\infty} \quad (1)$$

where $q_{\text{radiation}}$ and $q_{\text{conduction}}$ are the heat fluxes lost due to radiation from the surface and conduction through the foam substrate. The mainstream temperature, T_∞ , was measured using a type E thermocouple near the leading edge of the vane. The conduction correction and radiation correction were calculated using Eqs. (2) and (3) as follows:

$$q_{\text{conduction}} = \frac{-k}{l} (T_o - T_i) \quad (2)$$

$$q_{\text{radiation}} = \varepsilon \sigma (T_o^4 - T_\infty^4) \quad (3)$$

T_i was measured by attaching a surface thermocouple to the inside surface of the test vane.

Uncertainty in the boundary layer momentum thickness measurements was established by measuring the boundary layer pro-

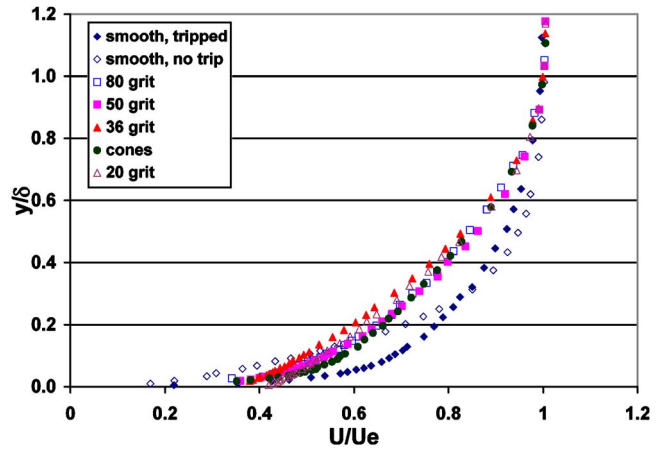


Fig. 5 Mean velocity profiles at $s/C=0.37$ for varying surface roughnesses

file at three different spanwise locations and calculating the momentum thickness for each profile. Mean velocity and fluctuating velocities for all three spanwise locations were compared directly and no significant differences were observed at any surface roughness level. The maximum deviation from the average momentum thickness was found to be about 2% for all surfaces. Uncertainties in the mean velocities, U_{rms} values, and the skin friction coefficient were found to be about $\pm 0.5\%$, $\pm 3\%$, and $\pm 5\%$, respectively. Bias uncertainties in the hot wire measurements arise from any uncertainty in the Pitot probe used to calibrate the hot wire system. The uncertainty in the Pitot probe measurement was estimated to be about 0.2 m/s at the test velocity of 5.8 m/s. In addition, drift in the hot wire calibration was checked by performing the calibration before and after the experiment. The maximum differences in calibration were less than 0.1 m/s at the freestream velocity. The bias uncertainty in the temperature measurements was estimated to be less than 1 K. The overall uncertainty in the heat transfer coefficient was established by repeating the heat transfer tests on four different days. From these four tests, the uncertainty was found to be $\pm 3\%$ for all sandpaper samples and $\pm 5\%$ for cone surface.

Results

Mean velocity profiles and fluctuating velocity profiles were measured for all of the rough surfaces as well as the smooth tripped and untripped base line conditions at positions $s/C=0.37$ and $s/C=0.57$. The normalized mean velocity profiles at each position are shown in Figs. 5 and 6. The nominal values for the edge velocities were $U_e=32$ m/s at $s/C=0.37$ and $U_e=33.5$ m/s at $s/C=0.57$. As seen in both Figs. 5 and 6, the rough surfaces caused a much greater velocity defect when compared to the smooth base line case. However, there was little variation among the different grit sandpapers and the cones.

Boundary layer thicknesses, momentum thickness, and shape parameters were determined from the velocity profile measurements, and are reported in Table 1. The influence of the tripwire on the smooth case was to increase the boundary layer thickness by a factor of about 2 at both streamwise positions. Table 1 also shows the trend of increasing boundary layer thickness with increasing roughness level. One exception to this trend is that the boundary layer thickness for the 36 grit sandpaper was thicker than that of the 20 grit sandpaper at the $s/C=0.37$ position, although the 20 grit sandpaper had a larger thickness at the $s/C=0.57$ position. An interesting observation is that the smooth, tripped boundary layer thickness was thicker than both the 80 grit and 50 grit sandpapers at the $s/C=0.37$ position, but thinner than the 80 grit sandpaper at the $s/C=0.57$ position. The conical

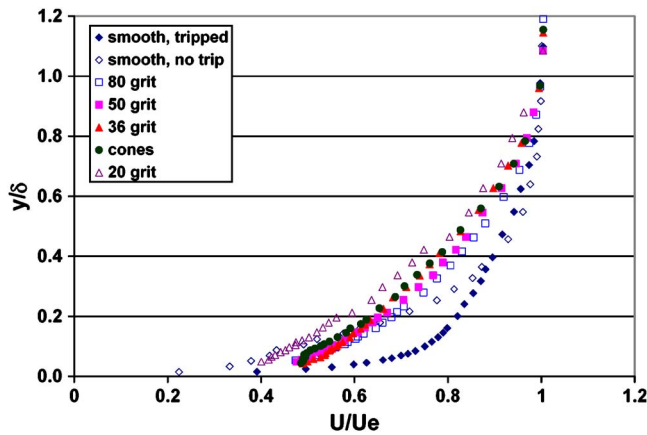


Fig. 6 Mean velocity profiles at $s/C=0.57$ for varying surface roughnesses

roughness was shown to be most similar to the 36 grit sandpaper at the upstream position in terms of boundary layer thickness, but is most similar to the 20 grit sandpaper at the downstream position.

The profiles of normalized fluctuating velocity (U_{rms}/U_e) are shown in Figs. 7 and 8. Generally, the fluctuating velocity values increase as the surface roughness increases for the $s/C=0.37$ position, except in the case of the conical roughness, which has lower fluctuating velocity values than all of the sandpapers. The smooth, no-trip case had a peak at about $y/\delta=0.2$, while the smooth case with the tripwire had a small peak much closer to the wall. The peak very close to the wall is a characteristic of a fully turbulent boundary layer. Furthermore, shape factor for the untripped smooth case was significantly larger than would be expected for a turbulent boundary layer, but much lower than what would be expected of a laminar boundary layer, indicating a transitional boundary layer.

At the $s/C=0.57$ position, the different roughness levels have fluctuating velocity profiles that are grouped more closely together, except for the 20 grit sandpaper, which has higher fluctuating velocity values than any other roughness level. The magnitudes of the fluctuating velocity for the rough surfaces were very similar to the magnitudes at the $s/C=0.37$ position. For the

Table 1 Boundary layer data

| | Location | δ (mm) | θ (mm) | H | Re_θ |
|------------------|------------|---------------|---------------|------|-------------|
| Smooth w/o trip | $s/C=0.37$ | 1.26 | 0.13 | 1.64 | 593 |
| | $s/C=0.57$ | 2.08 | 0.19 | 1.68 | 406 |
| Smooth with trip | $s/C=0.37$ | 3.28 | 0.28 | 1.28 | 572 |
| | $s/C=0.57$ | 4.02 | 0.41 | 1.37 | 877 |
| 80 grit | $s/C=0.37$ | 2.79 | 0.29 | 1.38 | 593 |
| | $s/C=0.57$ | 3.17 | 0.49 | 1.48 | 1048 |
| 50 grit | $s/C=0.37$ | 3.06 | 0.38 | 1.42 | 777 |
| | $s/C=0.57$ | 5.27 | 0.68 | 1.49 | 1455 |
| 36 grit | $s/C=0.37$ | 3.53 | 0.46 | 1.42 | 940 |
| | $s/C=0.57$ | 5.36 | 0.77 | 1.56 | 1647 |
| 20 grit | $s/C=0.37$ | 3.17 | 0.43 | 1.55 | 879 |
| | $s/C=0.57$ | 5.48 | 0.76 | 1.56 | 1626 |
| Cones | $s/C=0.37$ | 3.43 | 0.45 | 1.46 | 920 |
| | $s/C=0.57$ | 5.65 | 0.76 | 1.45 | 1626 |

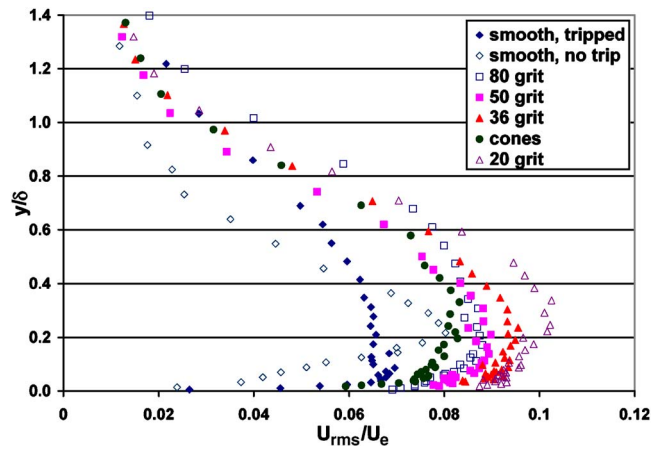


Fig. 7 Fluctuating velocity profiles, $s/C=0.37$

smooth cases, the magnitudes increase at the downstream position relative to the upstream position for both the tripped and untripped cases.

Using the measured momentum thickness values and taking into account pressure gradients, the average skin friction coefficient was calculated for each surface using the momentum integral equation. To check whether the tripped smooth boundary layer was fully turbulent, a Clauser fit was done to see if it would yield the correct skin friction coefficient. The average skin friction coefficient for the smooth tripped case as calculated by the momentum integral was found to be $C_f/2=0.0012$.

The Clauser fit indicated $C_f/2=0.0029$ and $C_f/2=0.0022$ for the upstream and downstream profiles, respectively. Since the value given by the momentum integral is an average between the upstream and the downstream skin friction values, the values calculated by the Clauser plot should bracket the average value from the momentum integral equation, if the flow is fully turbulent. Consequently, these data indicate that the boundary layer was transitional, not fully turbulent in this region.

As an additional check of the accuracy of the momentum integral technique to determine average skin friction, the same procedure was used to determine the average skin friction between the $s/C=0.57$ position and a farther downstream position of $s/C=1.0$. The local skin friction values were also obtained using a Clauser fit. The average value of $C_f/2=0.0018$ obtained from the momentum integral technique was bracketed by the Clauser fit

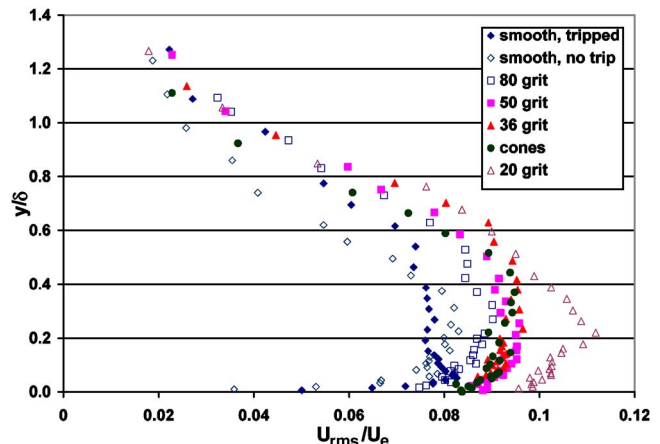


Fig. 8 Fluctuating velocity profiles, $s/C=0.57$

Table 2 Smooth case skin friction data

| Skin friction coefficient value $C_f/2$ | | |
|---|--------------|-------------------|
| s/C | Clouser plot | Momentum integral |
| 0.37 | 0.0029 | 0.0012 |
| 0.57 | 0.0022 | 0.0018 |
| 1.0 | 0.0017 | |

values of $C_f/2=0.0022$ and $C_f/2=0.0017$ at $s/C=0.57$ and $s/C=1.0$, respectively. This confirmed the accuracy of the momentum integral technique.

A likely cause of the boundary layer remaining transitional in spite of the presence of a trip is the significant pressure gradient accelerating the flow in the area of interest. The acceleration parameter was found to be $K=0.40 \times 10^{-6}$ at the upstream position and $K=0.45 \times 10^{-8}$ for the $s/C=0.57$ position. Similarly, Keller and Wang [11] showed that a flow with $K=0.25 \times 10^{-6}$ caused a significant delay in transition onset and widened the transition region. This clearly shows that the acceleration parameter value for the current vane is significant. A summary of the smooth skin friction data discussed above is presented in Table 2.

Average skin friction coefficient values were calculated using the momentum integral equation for $0.37 < s/C < 0.57$. The calculated values are shown in Fig. 9. As can be seen in this figure, there are two values shown for the smooth case skin friction coefficient. The highest value was determined from the momentum integral with a tripwire present. The lowest value represents the skin friction coefficient calculated from the momentum integral equation for a smooth vane without any tripwire present and can give a good idea of what the skin friction coefficient on a new, smooth turbine vane is. The skin friction coefficient data suggest that the 50 grit, 36 grit, and 20 grit sandpapers, and conical roughness all have similar hydrodynamic effects. Within experimental uncertainty, no distinction can be made between these samples.

Figure 10 shows the augmentation in the skin friction coefficient for each rough surface relative to the smooth tripped value as calculated by the momentum integral equation. The conical roughnesses, 50 grit, 36 grit, and 20 grit sandpapers, all have the same augmentation of about 300% relative to the tripped smooth base line. The 80 grit sandpaper shows an increase in skin friction of about 200%. The increases in skin friction are due to the surface roughness as well as causing boundary layer transition earlier along the test vane, since the tripped flow was not fully turbulent due to the significant pressure gradient. Stripf et al. [12] also observed different levels of roughness having different effects on the transition of the boundary layer on the suction side of a vane.

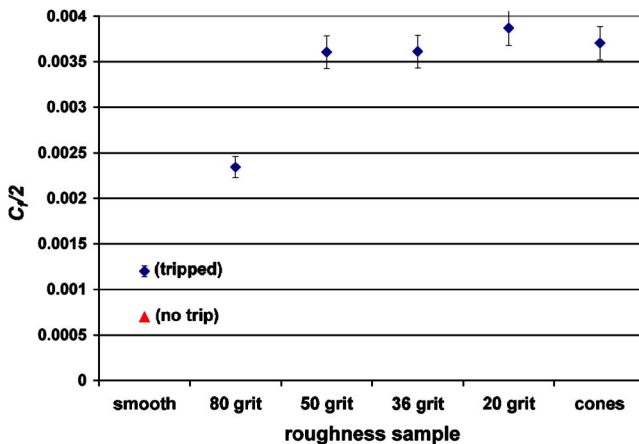


Fig. 9 Skin friction coefficient values for various roughness levels

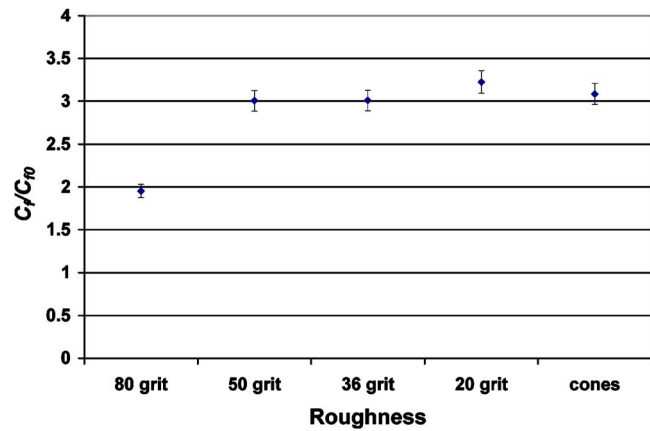


Fig. 10 Skin friction augmentation factors for various surface roughness levels

In this study, low levels of roughness were seen to have very small effects on the transition location and larger roughness levels were seen to move the transition point well upstream of the smooth base line case. An interesting point to note is that if the skin friction values were normalized to the smooth untripped case, even higher augmentation factors will be seen. These augmentation factors may be interesting in that they may provide more insight into what the total effect of the roughness is relative to a new turbine vane.

By using the measured momentum thickness for the tripped smooth case, an estimation of what the fully turbulent skin friction coefficient would have been was made using a standard correlation. The predicted skin friction coefficients for the $s/C=0.37$ and 0.57 positions were found to be $C_f/2=0.0029$ and 0.0024 , respectively. These levels of skin friction coefficient would result in an average of about $C_f/2=0.0026$ over the test range. When referenced to this higher value of C_{f0} (rather than the much lower value found from the momentum integral calculation), the rough surface skin friction augmentation is about 50% for the four roughest surfaces. This is roughly the same augmentation due to roughness seen by both Bons [6] and Belnap et al. [7]. This reduction in skin friction augmentation shows the importance of the reference condition when trying to determine the effect of surface roughness on skin friction on an airfoil where significant pressure gradient effects may be present.

Roughness Reynolds number values, Re_k , were predicted using the skin friction augmentation for each rough surface relative to a representative fully turbulent smooth base line and the correlation from White [13] shown below:

$$Re_x \approx 1.73(1 + 0.3Re_k)e^Z \left[Z^2 - 4Z + 6 - \frac{0.3Re_k}{1 + 0.3Re_k}(Z - 1) \right] \quad (4)$$

where $Z = \kappa(2/C_f)^{0.5}$.

The correlation is implicit in three variables; C_f , k_s (in the form of Re_k), and downstream distance x . Values of C_f were obtained from measurements. The effective downstream distance x was unknown, but was approximated as the development distance needed for a turbulent boundary layer over a flat plate to have a certain skin friction coefficient. A flat plate correlation was used to determine the x value for the case of $C_f/2=0.0026$, since this was believed to be most representative of a fully turbulent case. The calculated Re_k and k_s values are shown in Table 3. For comparison, this table also includes values for the CAMI published grit sizes for the sandpapers used. The equivalent sandgrain roughness levels were consistently lower than the grit sizes, sometimes by a factor of 2.

Table 3 Equivalent sandgrain roughness and roughness Reynolds number values

| | k_s (mm) | Re_k | CAMI grit size (mm) | $C_f/2$ |
|---------|------------|--------|---------------------|---------|
| 80 grit | 0.004 | ~0 | 0.19 | 0.0023 |
| 50 grit | 0.30 | 39 | 0.35 | 0.0036 |
| 36 grit | 0.30 | 39 | 0.54 | 0.0036 |
| 20 grit | 0.42 | 57 | 0.90 | 0.0039 |
| Cones | 0.34 | 45 | — | 0.0037 |

Laterally averaged heat transfer coefficient data were obtained and are presented in Fig. 11 for each rough surface in the area of interest. These data show the effect that the roughness has on heat transfer. The 50 grit and 36 grit sandpapers have identical heat transfer coefficient values, but the cones, which were identical to 50 grit and 36 grit in terms of skin friction coefficient, have a lower heat transfer value. Also shown on the chart is the effect of the tripwire on the heat transfer coefficient for the smooth case. The tripwire clearly caused the smooth case boundary layer to become more turbulent, increasing the heat transfer by a factor of 2.

Figure 12 shows the augmentation in heat transfer coefficient due to the rough surfaces in terms of a spatially averaged Stanton number. The augmentations for the 50 grit, 36 grit, and 20 grit sandpapers were all about 1.7–1.8. The 80 grit sandpaper and

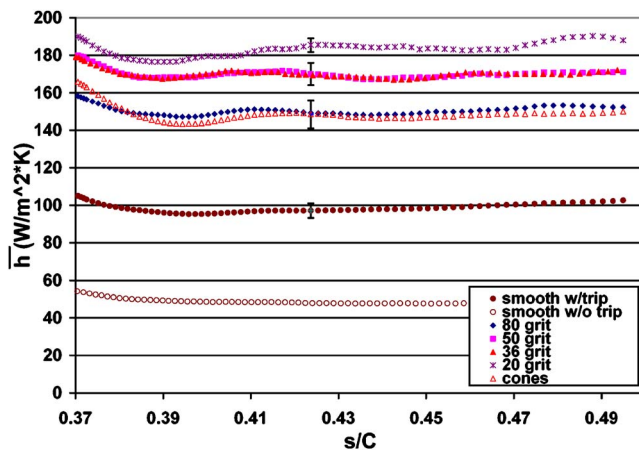


Fig. 11 Laterally averaged heat transfer coefficient for various surface roughness levels

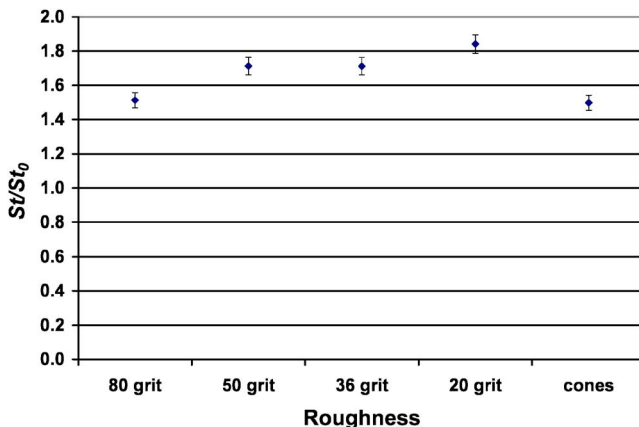


Fig. 12 Stanton number augmentation for various surface roughness levels

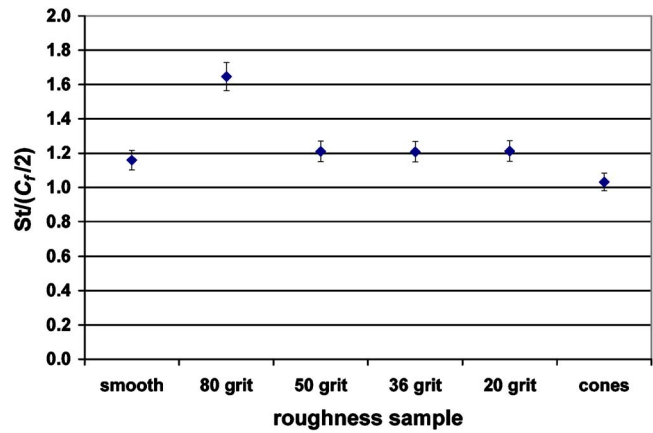


Fig. 13 Combined $St/(C_f/2)$ value for various surface roughness levels

conical roughness array both had St augmentation of about 1.5. The combined effect of each roughness level on skin friction and heat transfer can be seen in terms of a Reynolds analogy, $2St/C_f$ value. This is shown in Fig. 13. This quantity is important in that it quantifies the relative increase in skin friction coefficient due to roughness. The conical roughness elements can clearly be seen to have an augmentation relative to the smooth base line that is about 20% lower than the hydrodynamically similar sandpaper roughness levels. This is in contrast to the differences seen by both Bons [6] and Belnap et al. [7] where the regular roughness array caused an elevation in heat transfer coefficient relative to the hydrodynamically similar randomly rough surface. However, these previous studies were not done with a transitional boundary layer, and this may be a significant factor for this study.

Expected values for $2St/C_f$ can be determined using representative skin friction coefficient values of $C_f=0.003$ and 0.006 and the following correlation for St [7]:

$$St = \frac{C_f}{2} \left/ \left[1 + \left(\frac{C_f}{2} \right)^{0.5} (5.19Re_k^{0.2}Pr^{0.44} - 8.48) \right] \right. \quad (5)$$

The $C_f/2=0.003$ value was chosen to be representative of a fully turbulent boundary layer while the $C_f/2=0.006$ value was also included to show the effect of varying $C_f/2$ on the predicted value of St . Figure 14 shows the predicted values plotted along with the measured values from this study and studies from Refs. [6,7]. The regular roughness array falls within 5% of the predicted value, while the randomly rough surfaces are all higher by 20% or more

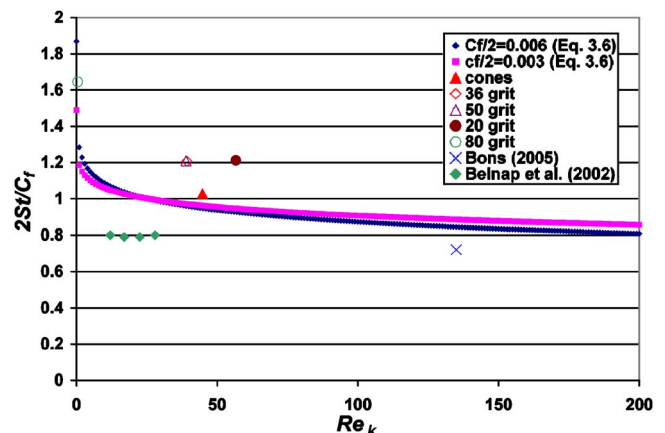


Fig. 14 $St/(C_f/2)$ versus roughness level

than the predicted value. The randomly rough surfaces from Bons [6] and Belnap et al. [7] had $2St/C_f$ 20% lower than that predicted by the correlation.

Conclusions

Heat transfer and skin friction coefficients were measured for a range of rough surfaces on the suction side of a simulated gas turbine vane. The unique aspect of this study is the transitional nature of the smooth base line case even when a trip is used. The pressure gradient in this region of the airfoil is significant enough to prevent complete boundary layer transition for the smooth reference case. Consequently, roughness effects are magnified by the effects of roughness in promoting transition to a fully turbulent boundary layer.

The results show different effects between one regular array and a set of random rough surfaces on the heat transfer coefficient and skin friction coefficient on this region of the vane. The measured skin friction and heat transfer coefficients were combined into a $2St/C_f$ value so that the relative effects of each roughness level could be directly compared to one another. The most interesting result was the difference between the conical roughness elements and the roughest sandpapers. The 50 grit, 36 grit, and 20 grit sandpapers all had $2St/C_f$ values of about 1.2. The conical roughness had a value of about 1.0, representing a 20% decrease when compared to the sandpaper. This was a direct result of the conical roughness having a similar hydrodynamic effect when compared to the 50 grit, 36 grit, and 20 grit sandpapers, but much lower heat transfer. Clearly, the conical roughness does not behave the same way that sandpaper does for this region of the vane. These results contrasted with previous studies which showed an increase in heat transfer for regular array roughness. However, these previous studies had fully turbulent flows and did not involve effects due to transition of the boundary layer. While involving interactions with a transitioning boundary layer complicates the understanding of roughness effects, such effects on transition are, in fact, more realistic for actual turbine airfoils. A fuller understanding of the regular array effects is still needed through a parametric study of other regular roughness types.

Acknowledgment

The authors gratefully acknowledge support from the University Turbine Systems Research (UTSR) program (Contract No. 03-01-SR110) directed through the South Carolina Institute for Energy Studies.

Nomenclature

| | |
|-------|--|
| C | = vane chord length |
| C_f | = skin friction coefficient |
| d | = conical roughness element cone diameter |
| h | = heat transfer coefficient |
| k | = roughness height or thermal conductivity |
| k_s | = equivalent sandgrain roughness |
| H | = shape factor, δ^*/θ |
| K | = acceleration parameter, $(\nu/U_e^2)(dU_e/dx)$ |

| | |
|-------------|---|
| l | = thickness of vane wall |
| Pr | = Prandtl number |
| q'' | = heat flux |
| p | = spacing between conical roughness elements |
| Re_k | = roughness Reynolds number, $u_r k_s / \nu$ |
| Re_θ | = momentum thickness Reynolds number, $U\theta/\nu$ |
| Re_x | = Reynolds number based on development length, Ux/ν |
| s | = streamwise surface distance from stagnation |
| St | = Stanton number, $h/\rho c_p U_\infty$ |
| T | = temperature |
| U | = flow velocity |

Greek

| | |
|---------------|-------------------------------------|
| δ | = 99% boundary layer thickness |
| ε | = emissivity |
| Λ_s | = roughness density parameter |
| θ | = boundary layer momentum thickness |
| σ | = Stephan-Boltzmann constant |

Subscripts

| | |
|----------|----------------------|
| e | = edge |
| i | = inner vane surface |
| o | = outer vane surface |
| ∞ | = freestream |
| rms | = root mean squared |

References

- [1] Bogard, D. G., Schmidt, D. L., and Tabbita, M., 1998, "Characterization and Laboratory Simulation of Turbine Airfoil Surface Roughness and Associated Heat Transfer," *ASME J. Turbomach.*, **120**, pp. 337–342.
- [2] Nikuradse, J., 1933, "Stromungsgesetze in Rauchen Rohren," *Forschungsheft* 361, Vol. B, VDI Verlag, Berlin.
- [3] Kithcart, M. E., and Klett, D. E., 1996, "Heat Transfer and Skin Friction Comparison of Dimpled Versus Protusion Roughness," *J. Enhanced Heat Transfer*, **3**(4), pp. 273–280.
- [4] Stripf, M., Schulz, A., and Wittig, S., 2005, "Surface Roughness Effects on External Heat Transfer of a HP Turbine Vane," *ASME J. Turbomach.*, **127**, pp. 200–208.
- [5] Bons, J. P., Taylor, R. P., McClain, S. T., and Rivir, R. B., 2001, "The Many Faces of Turbine Surface Roughness," *ASME Paper No. 2001-GT-0163*.
- [6] Bons, J. P., 2002, "St and c_f Augmentation for Real Turbine Roughness With Elevated Freestream Turbulence," *ASME Paper No. GT-2002-30198*.
- [7] Belnap, B. J., van Rij, J. A., and Ligrani, P. M., 2002, "A Reynolds Analogy for Real Component Surface Roughness," *Int. J. Heat Mass Transfer*, **45**, pp. 3089–3099.
- [8] Rutledge, J. L., Robertson, D. R., and Bogard, D. G., 2005, "Degradation of Film Cooling Performance on a Turbine Vane Suction Side Due to Surface Roughness," *ASME Paper No. GT2005-69045*.
- [9] Bogard, D. G., Snook, D., and Kohli, A., 2003, "Rough Surface Effects on Film Cooling of the Suction Side Surface of a Turbine Vane," *ASME Paper No. IMECE2003-42061*.
- [10] Sigal, A., and Danberg, J. E., 1990, "New Correlation of Roughness Density Effect on the Turbulent Boundary Layer," *AIAA J.*, **28**(3), pp. 554–556.
- [11] Keller, F. J., and Wang, T., 1993, "Flow and Thermal Structures in Heated Transitional Boundary Layers With and Without Streamwise Acceleration," Final Report, Clemson University.
- [12] Stripf, M., Schulz, A., and Bauer, H.-J., 2006, "Modeling of Rough Wall Boundary Layer Transition and Heat Transfer on Turbine Airfoils," *ASME Paper No. GT2006-90316*.
- [13] White, F. M., 1991, *Viscous Fluid Flow*, 2nd ed., McGraw-Hill, New York.

Bump and Trench Modifications to Film-Cooling Holes at the Vane-Endwall Junction

N. Sundaram

Mechanical Engineering Department,
Virginia Polytechnic Institute
and State University,
Blacksburg, VA 24061
e-mail: nasundar@vt.edu

K. A. Thole

Mechanical and Nuclear Engineering Department,
The Pennsylvania University,
University Park, PA 16802

The endwall of a first-stage vane experiences high heat transfer and low adiabatic effectiveness levels because of high turbine operating temperatures and formation of leading edge vortices. These vortices lift the coolant off the endwall and pull the hot mainstream gases toward it. The region of focus for this study is the vane-endwall junction region near the stagnation location where cooling is very difficult. Two different film-cooling hole modifications, namely, trenches and bumps, were evaluated to improve the cooling in the leading edge region. This study uses a large-scale turbine vane cascade with a single row of axial film-cooling holes at the leading edge of the vane endwall. Individual hole trenches and row trenches were placed along the complete row of film-cooling holes. Two-dimensional semi-elliptically shaped bumps were also evaluated by placing the bumps upstream and downstream of the film-cooling row. Tests were carried out for different trench depths and bump heights under varying blowing ratios. The results indicated that a row trench placed along the row of film-cooling holes showed a greater enhancement in adiabatic effectiveness levels when compared to individual hole trenches and bumps. All geometries considered produced an overall improvement to adiabatic effectiveness levels. [DOI: 10.1115/1.2812933]

Introduction

A higher demand in power output for modern gas turbines have resulted in an increase in combustor exit temperatures. Higher temperatures in turn have resulted in flatter profiles at the combustor exit [1] warranting the need for sufficient cooling of endwall surfaces. In addition to these flat profiles, the endwall surfaces also experience high heat transfer due to the formation of leading edge vortices, which tend to lift the coolant off the surface. Friedrichs et al. [2–4] showed that the leading edge on the endwall is the most difficult region to cool. Studies by Thole and Knost [5] showed that even with an upstream leakage flow, the leading edge-endwall junction around the stagnation region remains uncooled.

To achieve higher adiabatic effectiveness levels at the leading edge, it is important to ensure that there is a uniform spread of coolant exiting the film-cooling holes. Typical film-cooling hole designs on a surface give low adiabatic effectiveness levels near and in between the hole exits causing localized regions of hot spots. This study focuses on eliminating these hot spots by improving the adiabatic effectiveness levels at the leading edge region of a vane endwall.

Since effective cooling at the leading edge is a challenge to a turbine designer, new cooling methods are desired. This study is aimed at understanding the effect of modifying the coolant jet trajectory at the cooling hole exit and how it enhances the adiabatic effectiveness levels. The work presented in this paper compares the effect of two different modifications on the adiabatic effectiveness levels at the leading edge, namely, trenches and bumps.

Relevant Past Studies

Effective cooling of a turbine surface is highly important for its improved operational life and the performance of the engine as a

whole. With regard to that, a number of studies have focused on developing alternate methods to cool a surface in addition to placing film-cooling holes.

An early study was carried out by Blair [6] in which he showed that coolant flow from an upstream slot resulted in higher cooling near the suction side and reduced cooling near the pressure side. This nonuniform cooling was as a result of the coolant being swept from the pressure side to the suction side caused by the secondary flow within the vane passage. Knost and Thole [7] studied the effect of leakage flow through the combustor-vane interface onto the endwall adiabatic effectiveness levels. Similar to Blair [6], they also showed that the coolant exits the upstream slot in a nonuniform fashion. The nonuniformity was associated with the formation of a hot ring around the stagnation region toward the pressure side of the vane. Cardwell et al. [8] showed that the size of this hot ring can be reduced by decreasing the width of the upstream slot, which results in a more uniform spread of coolant. Burd and Simon [9] studied the effects of slot bleed injection over the contoured endwall of a nozzle guide vane. They concluded from their measurements that bleed cooling from upstream of the leading edge of the vane provides considerable thermal protection within the passage. These studies of coolant flow through a slot showed that effective cooling can be achieved by injecting a 2D layer of film cooling over the surface.

Searching for better cooling techniques, Bunker [10] measured improved film-cooling effectiveness levels on a flat plate using discrete holes placed within a transverse slot with varying widths. Bunker [10] showed that the narrowest possible slot width relative to the interior cooling hole diameter is most desirable. As placing cooling holes in slots basically modifies the hole exit, there have been few studies that have investigated this particular effect. Lu et al. [11] investigated the effect of slot exit area and edge shape on film effectiveness measurements made on a flat plate. They found that a straight edge exit performed the best at a blowing ratio of $M=1.0$, whereas a ramped exit enhanced the adiabatic effectiveness levels at lower blowing ratios. Wayne and Bogard [12] applied the trench configuration on the suction side of a first-stage vane with varying slot exit configurations. They tested a narrow trench where the trench wall was at the film-cooling hole exit, a wide trench where the trench wall was at a distance of one cooling hole

Contributed by the International Gas Turbine Institute of ASME for publication in the JOURNAL OF TURBOMACHINERY. Manuscript received June 6, 2007; final manuscript received June 26, 2007; published online August 1, 2008. Review conducted by David Wisler. Paper presented at the ASME Turbo Expo 2007: Land, Sea and Air (GT2007), Montreal, Quebec, Canada, May 14–17, 2007.

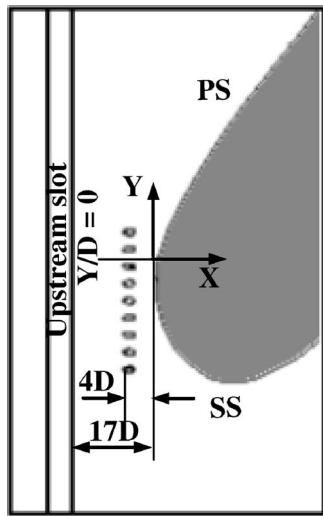


Fig. 1 Illustrates the endwall design studied at the leading edge

diameter from the hole exit, and a trench with an angled exit. They also found that the narrow trench performed the best relative to a wide trench and angled exit trench and the adiabatic effectiveness levels peaked for blowing ratios beyond $M=1.0$.

A recent study was carried out by Sundaram and Thole [13] to understand the effect of placing semi-elliptically shaped deposits downstream of a row of cooling holes. While their study was aimed at understanding how deposits could adversely affect cooling levels, their results indicated improved cooling performance for some geometries. They carried out this study at the leading edge of a first-stage vane endwall on a rough surface and found that smaller deposits enhanced adiabatic effectiveness levels. As the deposit height was increased, the effectiveness levels were reduced below that of the baseline with no bumps.

In summary, different modifications have been applied to film-cooling holes to enhance the adiabatic effectiveness levels. Most of these studies have been on a flat plate with no studies carried out at the leading edge of a first-stage vane endwall with the exception of the authors' previous work [13].

Bump and Trench Descriptions

Previous studies by Bunker [10] and Wayne and Bogard [12] showed that holes in a slot are effective in forming a layer of protective film over the surface. These studies also showed that the edges of the slot were very close to the exit of the film-cooling hole for enhanced cooling. The effect of placing cooling holes in a trench was found to show a significant enhancement in effectiveness levels. The trench on the surface can be manufactured during the thermal barrier coating (TBC) application process [14] and its effect can differ with varying trench depths as the thickness of the TBC can be varied. Similarly, studies by Sundaram and Thole [13] also showed that when the edges of the semi-elliptical deposits (bumps) were close to the cooling hole exit, the cooling effectiveness levels were enhanced.

Motivated from these studies, modifications were applied to the leading edge region of the first-stage vane endwall, as shown in Fig. 1. The endwall of the vane was constructed of foam because of its low thermal conductivity (0.033 W/m K). The endwall surface was covered with a thin layer of Balsa wood to simulate a smooth TBC. All of the different configurations were tested on a smooth endwall surface. The endwall leading edge consisted of a single row of axial film-cooling holes with a hole spacing corresponding to $P/D=3$. The cooling row was placed four cooling hole diameters ($4D$) upstream from the stagnation location. An upstream slot, representing the combustor-turbine gap, was placed

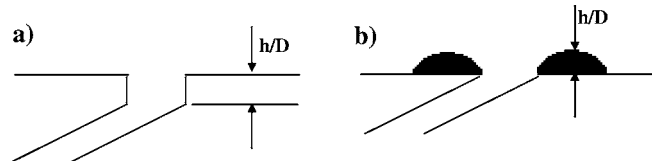


Fig. 2 Illustrates the (a) trench geometry and (b) bump geometry studied at the leading edge

$17D$ from the stagnation location. Note that it is important to simulate the upstream slot since this interface exists in most turbines and the exiting slot flow influences the upstream boundary condition. Figures 2(a) and 2(b) show the geometries of the two modifications studied at this leading edge location. Figure 2(a) illustrates the trench geometry and Fig. 2(b) illustrates the bump geometry previously described by Sundaram and Thole [13]. For the trench configuration, three different depths were studied corresponding to $h/D=0.4, 0.8,$ and 1.2 . The trench depths were controlled by varying the thickness of the Balsa wood covering the endwall surface. Three different bump heights were also tested at the leading edge. Similar to Sundaram and Thole [13], these heights corresponded to $h/D=0.5, 0.8,$ and 1.2 .

Based on the above two concepts, four different cooling hole configurations were tested at varying blowing ratios, as shown in Figs. 3(a)–3(d). Figure 3(a) illustrates the baseline case, which simulated a smooth endwall without any surface modifications. It consisted of a row of axial film-cooling holes placed 30 deg to the endwall surface. Figure 3(b) simulates the individual hole trench configuration, where the trench surrounded each individual cooling hole. Figure 3(c) is the row trench configuration, similar to the one tested by Bunker [10] on a flat plate, where the trench runs along the entire length of the cooling row. Bunker [10] studied only a single trench depth of $h/D=0.43$ for the axial hole geometry. Figure 3(d) is the bump configuration, in which two semi-elliptical bumps were placed at the upstream and downstream locations of the film-cooling hole. The geometries shown in Figs. 3(b)–3(d) will be compared with the baseline case to see if these modifications result in any enhancement.

Experimental Methodology

The experimental section was placed in a closed loop wind tunnel facility, as shown in Fig. 4. The flow encounters an elbow downstream of the fan and passes through a primary heat exchanger used to cool the bulk flow. The flow is then divided into three channels including the center passage and two cooled secondary passages located above and below the test section. Note that only the top secondary passage was used for this study. The primary core flow, located in the center passage, convects through a heater bank where the air temperature is increased to about 60°C . The secondary flow, in the outer passage, was cooled to about 20°C , thereby maintaining a temperature difference of 40°C between the primary and secondary flows. The secondary flow provided the coolant through the film-cooling holes and through the upstream slot. Also, for all the tests carried out in this study, a density ratio of 1.1 was maintained between the coolant

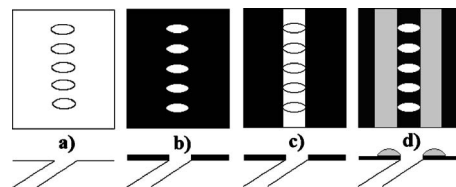


Fig. 3 Schematic of the four configurations: (a) baseline, (b) individual trench, (c) row trench, and (d) bumps tested at the leading edge

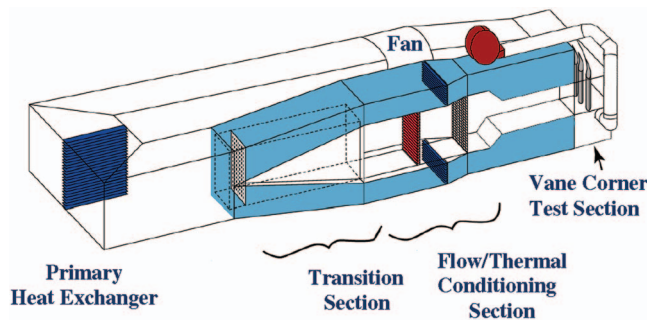


Fig. 4 Illustration of the wind tunnel facility

and mainstream flows. As the density ratios are not being matched to that of the engine, velocity ratios for the cooling holes will be significantly higher than those found in an engine for the same mass flux or momentum flux ratios. While there have been studies indicating that momentum flux scales jet lift-off for flat plate film cooling, it is unknown as to whether it best scales lift-off for endwall film cooling.

Downstream of the flow/thermal conditioning section is the test section that consists of two full passages with one center vane and two half vanes. Table 1 provides a description of the turbine vane geometry and operating conditions. Table 1 also gives the inlet boundary layer characteristics. The boundary layer approaching the vane cascade was measured at 0.63C upstream of the vane stagnation. The measurement was done far upstream from the stagnation as the upstream slot flow influences the boundary layer approaching the vane cascade. The vane geometry used in the current study is a commercial first-stage vane previously described by Radomsky and Thole [15]. The passage under study consisted of an endwall surface with film-cooling holes and leakage paths simulating the combustor-vane interface (upstream slot) and vane-to-vane interface. A detailed description of the endwall construction has been previously described by Knost and Thole [5].

The inlet turbulence intensity and length scales were measured to be 1.3% and 4 cm, respectively. These tests were carried out at a low turbulence intensity of 1.3% to isolate the effects of trenches and bumps on endwall adiabatic effectiveness levels. For every test condition, the dimensionless pressure coefficient distribution was verified to ensure periodic flow through the passages. Two separate plenums were used to control the coolant flowrate through the upstream slot and through the film-cooling holes, respectively. The upstream slot flow was assumed to have a discharge coefficient of 0.6, which is the assumed value for a flow through a sharp-edged orifice, and the blowing ratio was calculated accordingly. The coolant flowrate through the film-cooling holes was set based on an average ideal blowing ratio. This blow-

ing ratio was based on an inviscid calculation through the holes and the inlet mainstream velocity. It should be noted that an average discharge coefficient was not assumed to set the coolant flow through the film-cooling holes as it varies from hole to hole.

Instrumentation and Temperature Measurements. A FLIR P20 infrared camera was used to spatially resolve adiabatic wall temperatures on the endwall. Measurements were taken at six different viewing locations to ensure that the entire endwall surface was mapped. The camera was placed perpendicular to the endwall surface at a distance 55 cm from the endwall. Each picture covered an area $24 \times 18 \text{ cm}^2$ with the area being divided into 320×240 pixel locations. The spatial integration of the camera was 0.715 mm (0.16 hole diameters). Thermocouples were also placed on the endwall surface at different locations to directly measure the temperature to postcalibrate the infrared images. For the post-calibration, the emissivity was set at a constant value of 0.92 and the background temperature ($\sim 45^\circ\text{C}$) was adjusted until the temperatures from the infrared camera images were within 0.05°C of the corresponding thermocouple data. Six images were taken at each of the viewing locations to obtain an averaged picture using an in-house MATLAB program. The same program was also used to assemble the averaged pictures at all locations to give a complete temperature distribution along the passage endwall.

Freestream temperatures were measured at multiple locations along the pitch and the average was determined by using a thermocouple rake consisting of three thermocouples along the span. It was found that the variations along the pitch were less than 0.2°C and that along the span were less than 1.5°C . Voltage outputs from the thermocouples were acquired by a 32 channel data acquisition module that was used with a 12 bit digitizing card. The temperature data were compiled after the system reached steady state.

A 1D conduction correction as described by Ethridge et al. [16] was applied to all adiabatic effectiveness measurements to account for conduction losses through the endwall surface. The conduction correction was applied by measuring the endwall surface effectiveness with no blowing through the film-cooling holes. This was done by blocking the film-cooling holes on the endwall passage under study while maintaining similar flowrates through the adjacent passage to ensure the correct boundary condition under the endwall. At the entrance to the flow passage for a measured value of $\eta=0.9$, a correction of 0.16 was typical while along the pressure side for a measured value of $\eta=0.1$, a correction of 0.03 was applied.

Experimental Uncertainty. An uncertainty analysis was performed on the measurements of adiabatic effectiveness and blowing ratio using the partial derivative method described at length by Moffat [17].

For adiabatic effectiveness measurements, the precision uncertainty was determined by taking the standard deviation of six measurement sets of IR camera images with each set consisting of six images. The precision uncertainty of the measurements was $\pm 0.014^\circ\text{C}$. The bias uncertainty was $\pm 1.0^\circ\text{C}$ based on the uncertainty in the IR camera measurements specified by the manufacturer. The bias uncertainty of the thermocouples was $\pm 0.5^\circ\text{C}$ as specified by the manufacturer and the bias uncertainty associated with the digitizing card was $\pm 0.35^\circ\text{C}$. Then, the total bias uncertainty of the temperature measurement due to the thermocouple and the digitizing card was calculated to be $\pm 0.61^\circ\text{C}$. The total uncertainty was then calculated as $\pm 1.02^\circ\text{C}$ for the images and $\pm 0.62^\circ\text{C}$ for the thermocouple measurements. Uncertainty in effectiveness η was found based on the partial derivative of η with respect to each temperature in the definition and the total uncertainty in the measurements. Uncertainties in adiabatic effectiveness were calculated to be $\partial\eta = \pm 0.032$ at a η value of 0.2 and $\partial\eta = \pm 0.033$ at a η value of 0.9.

To calculate the uncertainty in blowing ratio, the uncertainties associated with the pressure transducers, the Pitot probe, and the

Table 1 Geometric and flow conditions

| | |
|--|-------------------|
| Scaling factor | 9 |
| Scaled up chord length (C) | 59.4 cm |
| Pitch/chord (P/C) | 0.77 |
| Span/chord (S/C) | 0.93 |
| Hole diameter (D) | 0.46 cm |
| Hole L/D | 8.3 |
| Re_{in} | 2.1×10^5 |
| Inlet and exit angles | 0 deg and 72 deg |
| Inlet and exit Mach numbers | 0.017 and 0.085 |
| Inlet mainstream velocity | 63 m/s |
| Boundary layer thickness/span (δ/S) | 0.18 |
| Displacement thickness/span (δ^*/S) | 0.025 |
| Momentum thickness/span (θ/S) | 0.020 |
| Upstream slot width | 0.024C |

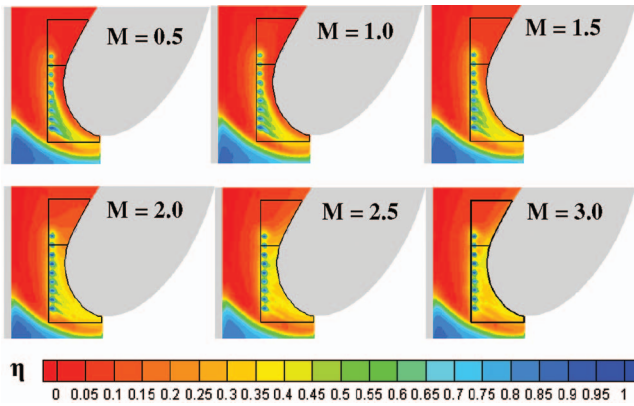


Fig. 5 Contours of adiabatic effectiveness comparing the baseline case at different blowing ratios

thermocouples were taken into account. The pressure transducer had a total uncertainty of ± 0.13 Pa and the pitot probe which was used to measure the inlet mainstream velocity had a total uncertainty of ± 0.22 Pa. The total uncertainty of the thermocouples as explained earlier was $\pm 0.62^\circ\text{C}$. The uncertainties in blowing ratio were then calculated to be $\partial M = \pm 0.045$ at a value of $M=0.5$ and $\partial M = \pm 0.052$ at a value of $M=3.0$.

Discussion of Results

As mentioned previously, the baseline case was measured on a smooth endwall surface. baseline tests were carried out at six film-cooling blowing ratios varying from $M=0.5$ to $M=3.0$, as shown in Fig. 5. A flowrate corresponding to an inlet blowing ratio of $M_{in}=0.3$ was set through the upstream slot for all the tests.

It can be seen from the contours in Fig. 5 that at low blowing ratios, the adiabatic effectiveness levels are higher on the suction side of the endwall than on the pressure side. This is because of the lower static pressure on the suction side, which enables more coolant to exit the cooling holes near the suction side. With an increase in blowing ratio up to $M=2.0$, there is a gradual increase in effectiveness levels along the pressure and suction sides. A further increase beyond $M=2.0$ results in an increase in effectiveness levels on the pressure side with subsequent decrease on the suction side when compared to the lower blowing ratio. It can also be seen that at higher blowing ratios, there is a reduction in effectiveness levels just downstream of the cooling holes. At high blowing ratios, the coolant jets are associated with high momentum resulting in jet lift-off from the surface. It is also seen that at these high blowing ratios, the adiabatic effectiveness levels increase near the vane-endwall junction. The adiabatic effectiveness levels also increase because of the horseshoe vortex formed at the leading edge, which pulls the coolant injected into the mainstream flow back to the surface. As a result, the adiabatic effectiveness levels increase at the vane-endwall junction along both the pressure and suction sides.

Figure 6 compares the lateral average effectiveness ($\bar{\eta}$) at varying blowing ratios for the baseline case. Adiabatic effectiveness values were laterally averaged in the streamwise (X direction), direction as shown in Fig. 1. Figure 1 also shows the stagnation location along the pitch where $Y/D=0$. Lateral averaging was calculated for two areas on either side of the stagnation location; suction side extending from $Y/D=0$ to $Y/D=-25$ and pressure side extending from $Y/D=0$ to $Y/D=10$ (refer to Fig. 5). For calculating the lateral average, the area under consideration was divided into many small divisions starting at different pitch (Y/D) locations. The adiabatic effectiveness values were then averaged along each of these divisions to give the laterally averaged adiabatic effectiveness along the pitch. Note that lateral averaging was

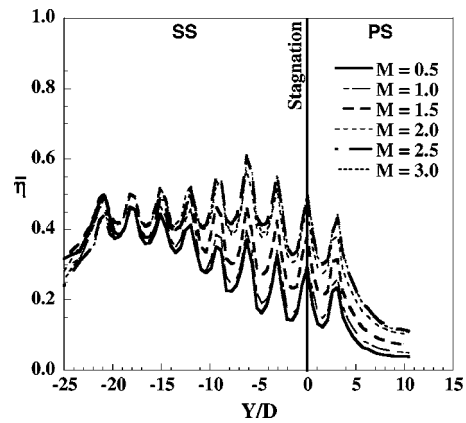


Fig. 6 Lateral average effectiveness plots of the baseline case

carried out for the same vane surface length of $x/S=0.15$ along the suction and pressure sides from the vane stagnation.

From Fig. 6, it can be seen that for blowing ratios from $M=0.5$ to $M=2.0$, the effectiveness levels increase on the suction side until $Y/D=-10$. Any subsequent increase in blowing ratio caused an increase on the pressure side and a decrease on the suction side. It is interesting to note that at a blowing ratio of $M=2.0$, the effectiveness levels are the highest on the suction side as well on the pressure side when compared to other blowing ratios. The formation of peaks and valleys in the lateral average plot clearly show that at every blowing ratio, there is a variation in adiabatic effectiveness levels between the film-cooling holes. The variation in effectiveness levels is because of the formation of hot spots as a result of nonuniform coolant spread on the endwall surface.

The variation in adiabatic effectiveness levels on the suction and pressure sides can also be studied by comparing their area-averaged effectiveness ($\bar{\eta}$). Figure 7 compares the area-averaged effectiveness for the baseline cases at different blowing ratios. An overall area-averaged effectiveness was calculated for the combined (SS+PS) region by averaging the adiabatic effectiveness values extending from the suction side to the pressure side ($Y/D=-25$ to $Y/D=10$). Note that lateral averaging was carried out for the same vane surface length of $x/S=0.15$ along the suction and pressure sides from the vane stagnation. The area-averaged effectiveness of the combined region increases until a blowing ratio of $M=2.0$ and then steadies out with any further increase. By looking at the individual effectiveness levels, on the suction side, it peaks at $M=2.0$ and then decreases and plateaus,

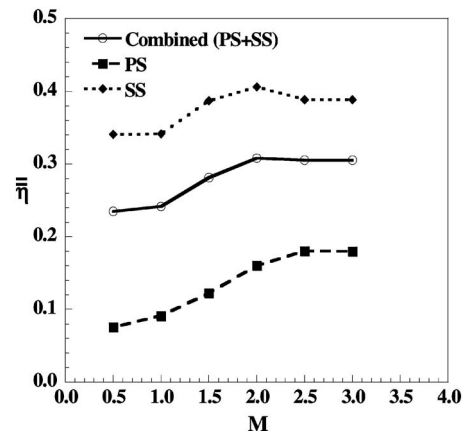


Fig. 7 Area-averaged effectiveness for the baseline geometry along suction, pressure, and the whole leading edge region

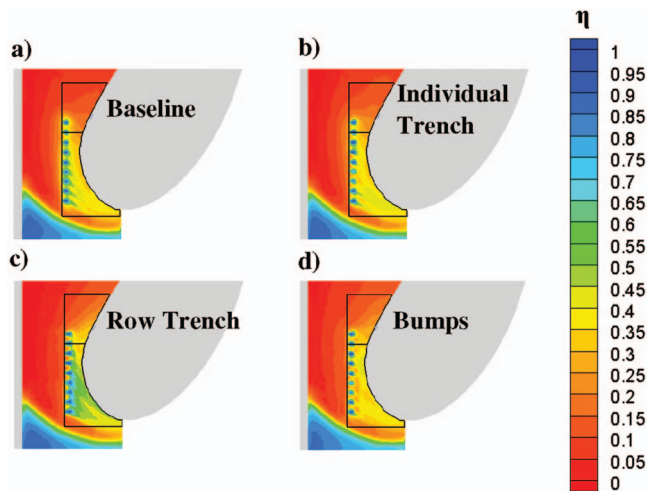


Fig. 8 Contours of adiabatic effectiveness comparing the baseline case with the other configurations at a blowing ratio of $M=2.0$

whereas on the pressure side, the effectiveness levels keep increasing with an increase in blowing ratio. So, for the baseline case with a smooth endwall surface, a blowing ratio of $M=2.0$ was found to have the highest effectiveness levels.

Effect of Modifying the Film-Cooling Hole Exit. An individual hole trench, a row trench, and a bump configuration upstream and downstream of the cooling row were tested on a smooth endwall surface. These modifications were carried out at a constant coolant flowrate through the upstream slot. It was shown by Thole and Knost [5] that for a two passage study, the coolant flow from the upstream slot is an important characteristic to simulate given that it provides the correct incoming boundary conditions to the vane cascade. Their study showed that due to secondary flows in the vane passage, the coolant flow from the upstream slot was swept from the pressure side to the suction side, creating a low adiabatic effectiveness zone around the stagnation region. They also found that in the presence of leading edge film-cooling holes, the variation in adiabatic effectiveness levels around the stagnation region was solely the result of coolant flow from the film-cooling holes. Hence, it was concluded that the upstream slot did not influence the comparisons with respect to trenches and bumps. Note that for these comparisons, the same pressure ratio was used to set the blowing ratio through the film-cooling holes for the baseline and the trench and bump modifications.

Figures 8(a)–8(d) compare the contours of adiabatic effectiveness of the three modified film-cooling hole exit configurations with the baseline case at a blowing ratio of $M=2.0$. In this section, the baseline is compared with the smallest trench depth and bump height. The smallest trench depth studied corresponded to $0.4D$ and the smallest bump height corresponded to $0.5D$. Comparing the individual hole trench (Fig. 8(b)) at $M=2.0$ to the baseline case (Fig. 8(a)), it is seen that due to a presence of a vertical wall at the cooling hole exit, the jets are detached from the surface but reattach further downstream of the holes. Hence, the adiabatic effectiveness levels are lower at the exit of the cooling holes. The row trench in Fig. 8(c) showed the maximum enhancement in effectiveness levels on the leading edge. The trench walls upstream and downstream of the holes allow the coolant to spread laterally within the trench area, resulting in enhancements in adiabatic effectiveness levels. It is speculated by Bunker [10] that the trench walls reduce the typical vortex motion of the coolant jets and thereby preventing the hot gases from getting pulled underneath the coolant jets.

Placing bumps on the smooth surface caused varied results. From Fig. 8(d), it can be seen that relative to the baseline case, it

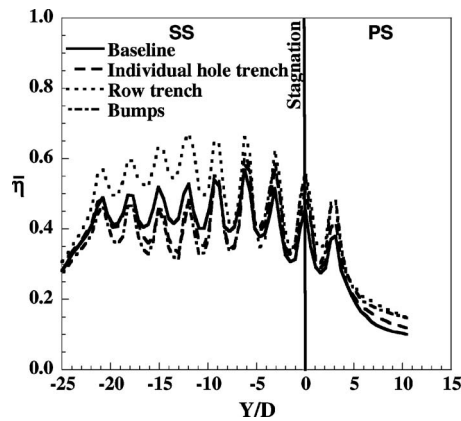


Fig. 9 Laterally averaged adiabatic effectiveness comparing the effect of trenches and bumps at the leading edge at $M=2.0$

lowered the effectiveness levels on the suction side, whereas it increased the effectiveness levels on the pressure side. Bumps downstream of the cooling holes deflected the coolant jets off the surface, thereby lowering the adiabatic effectiveness levels on the suction side, but caused an increase in effectiveness on the pressure side.

The effects of these modifications are quantified by calculating the laterally averaged effectiveness downstream of the film-cooling holes. From Fig. 9, it can be seen that row trench performed the best on the suction and pressure sides. The individual hole trench and the bumps showed a reduction in adiabatic effectiveness levels from $Y/D=-25$ to $Y/D=-5$ and showed an improvement in effectiveness levels from $Y/D>-5$. The lateral averaged effectiveness curves for the baseline and individual trench seem to coexist with little variation. Their effects at varying blowing ratios can be seen in Fig. 10, which compares the area-averaged effectiveness for the three modifications. At a blowing ratio of $M=2.0$, the area-averaged adiabatic effectiveness of the trenched hole, bumps, and the baseline coexists, showing that their overall effectiveness levels downstream of the cooling holes are the same. Trenches show an improvement over the whole range of blowing ratios tested with the maximum enhancement at a blowing ratio of $M=2.5$.

This initial study was to ascertain which geometry has the maximum effect on the effectiveness levels at the leading edge. Trenches showed an overall enhancement in effectiveness levels and the bumps showed an improvement along the pressure side.

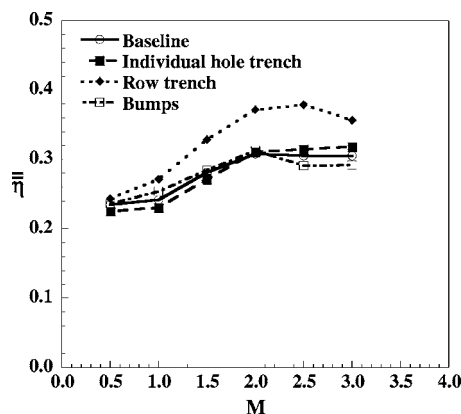


Fig. 10 Area-averaged effectiveness showing the effect of trenches and bumps on film-cooling effectiveness

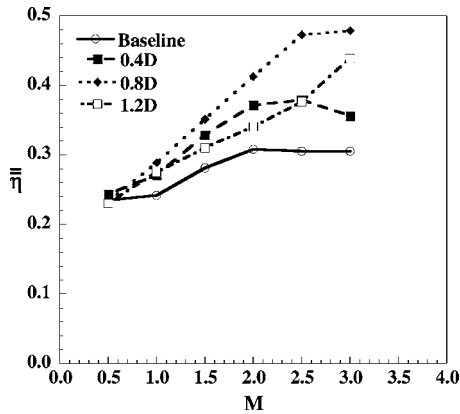


Fig. 11 Area-averaged effectiveness showing the effect of different trench depths for the row trench configuration at varying blowing ratios

The sensitivity of varied bump heights and trench depths to blowing ratios will be presented in the following sections.

Effect of Trench Depths on Adiabatic Effectiveness Levels.

Three different row trench depths corresponding to $0.4D$, $0.8D$, and $1.2D$ were tested on a smooth endwall surface. This study was conducted to investigate the trench depth sensitivity to adiabatic effectiveness levels. Figure 11 compares the area-averaged adiabatic effectiveness of the different trench depths. At the smallest trench depth of $0.4D$, the enhancements in adiabatic effectiveness levels were seen for all blowing ratios. The adiabatic effectiveness levels for $0.4D$ trench increased with increasing blowing ratio up to a blowing ratio of $M=2.5$. Upon a further increase in blowing ratio to $M=3.0$, the effectiveness levels slightly dropped as a result of higher jet momentum associated with the coolant flow.

As the trench depth was further increased to $0.8D$, higher enhancements in effectiveness levels were seen for all blowing ratios. Contrary to the $0.4D$ trench, the adiabatic effectiveness for the $0.8D$ trench depth increased until a blowing ratio of $M=2.5$, and then stayed nearly the same with a further increase to $M=3.0$. Compared to the baseline, the enhancement in effectiveness varied from $\eta=0.24$ at $M=1.0$ to a high value of almost $\eta=0.48$ at $M=3.0$.

An increase in trench depth to $1.2D$ also showed enhancements compared to the baseline case but the effectiveness levels were comparatively lower than the $0.8D$ trench, as seen in Fig. 11. Also, the effectiveness levels at $1.2D$ depth were similar or lower than the $0.4D$ depth for blowing ratios less than $M=2.5$ and showed higher levels only at $M=3.0$. At a higher depth and low blowing ratio, the walls of the trench prevent the coolant from exiting uniformly resulting in lower effectiveness levels. As the blowing ratio is increased, the jets exit at a higher momentum making the trench more effective in the spreading of the coolant. From Fig. 11, it can also be seen that the adiabatic effectiveness levels for the $1.2D$ trench follow a different pattern when compared to the $0.4D$ and $0.8D$ trenches.

Figure 12 compares the adiabatic effectiveness levels for three blowing ratios at $M=1.0$, $M=2.0$, and $M=3.0$ for different trench depths. The downstream edge of the trench forms a wall at the film hole exit, which forces the coolant to spread laterally within the trench before convecting over the endwall surface. At a smaller trench depth of $0.4D$, it is seen that with an increase in blowing ratio, the coolant spreads downstream of the cooling holes in a more uniform manner until the blowing ratio is high enough resulting in jet lift-off. At a high blowing ratio of $M=3.0$, there is less lateral spreading of coolant within the trench resulting in a deterioration in effectiveness levels.

An increase in trench depth to $0.8D$ results in a better lateral

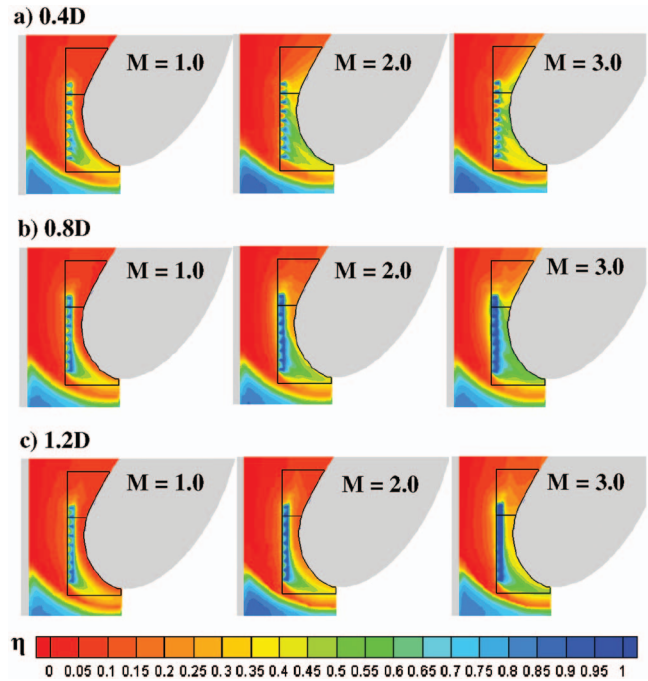


Fig. 12 Contours of adiabatic effectiveness showing the effect of varying the trench depth for the row trench configuration at three different blowing ratios

spread of coolant within the trench as there is less interaction between the mainstream gases and the coolant than when a set of axial holes are placed on a flat endwall surface. The contours of the $0.8D$ trench show that there are fewer hot spots between the cooling holes when compared to the $0.4D$ trench at the same blowing ratios. It is speculated that with an increase in trench depth, the vortical nature of the flow leaving the cooling holes at the exit is less intense preventing the hot gases from getting pulled down to the surface resulting in a better lateral spread within the trench. Lateral spreading within the trench causes the coolant to exit the trench in a more uniform manner onto the endwall surface. When the trench depth is further increased to $1.2D$, it is seen that at low blowing ratios, there is an increase in the coolant retention within the trench. A higher depth causes a recirculation of coolant within the trench preventing it from convecting over the surface. With an increase in blowing ratio, the amount of coolant spreading onto the surface increases. As this study was done only until a maximum blowing ratio of $M=3.0$, it is speculated that the $1.2D$ trench will perform better at a blowing ratio of $M=3.0$ or higher.

The uniform spread of coolant as a result of trenches can also be seen by comparing the laterally averaged effectiveness at different blowing ratios for the $0.8D$ trench, as shown in Fig. 13. For the baseline cases (refer to Fig. 6), the laterally averaged adiabatic effectiveness levels showed definite peaks and valleys indicating regions of low effectiveness between the cooling holes. With the trench, it is seen from Fig. 13 that the height between the peaks and valleys is smaller and this height becomes smaller as the blowing ratio is increased, thus indicating a more uniform spread of coolant over the endwall surface. Also, the $0.8D$ trench was found to be the optimum depth from the three trench depths tested, and the performance is highly sensitive to blowing ratio.

Effect of Bump Heights on Adiabatic Effectiveness Levels.

Three different bump heights corresponding to $0.5D$, $0.8D$, and $1.2D$ were also evaluated at the leading edge on a smooth endwall surface. Figure 14 compares the area-averaged effectiveness for the varying bump heights with the baseline case. The $0.5D$ and

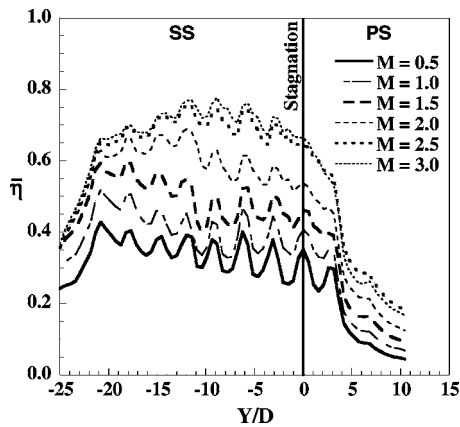


Fig. 13 Lateral averaged effectiveness showing the effect of the $0.8D$ trench depth at different blowing ratios

$0.8D$ bumps showed little effect on modifying the adiabatic effectiveness levels downstream of the film-cooling holes. When the bump height was increased to $1.2D$, there was an increase in effectiveness levels up to a blowing ratio of $M=2.0$ and a further increase in blowing ratio resulted in lower effectiveness levels.

The variation in effectiveness levels caused by the $1.2D$ bumps can be explained by the adiabatic effectiveness contours shown in Fig. 15. The increase in blowing ratio results in an increase in coolant mass flow rate, which in turn increases the effectiveness levels. At lower blowing ratios of $M=0.5$ and $M=1.0$, the jets are more attached to the surface and they are obstructed by the presence of the bumps. As a result, the coolant accumulates between the cooling holes thereby preventing it from spreading downstream. As the blowing ratio is increased, it can be seen that there is less coolant accumulation between the cooling holes. With the increase in blowing ratio, the coolant injects directly into the mainstream resulting in the formation of hot spots at the exit of the cooling holes. At high blowing ratios, the effectiveness levels further downstream of the cooling holes are higher than at low blowing ratios as a result of jet reattachment. $M=2.0$ was found to be an optimum blowing ratio where there is minimal coolant accumulation between the cooling holes and more spreading downstream of the cooling holes.

The performance of the $1.2D$ bumps along the pressure and suction sides at different blowing ratios can be compared using the laterally averaged effectiveness shown in Fig. 16. Similar to the baseline study, the bumps performed better on the suction side at lower blowing ratio, whereas the effectiveness levels were

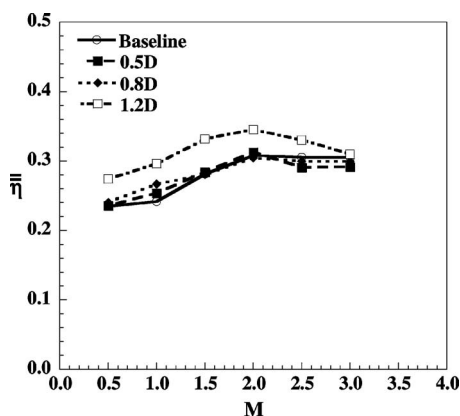


Fig. 14 Area-averaged effectiveness showing the effect of varying bump heights

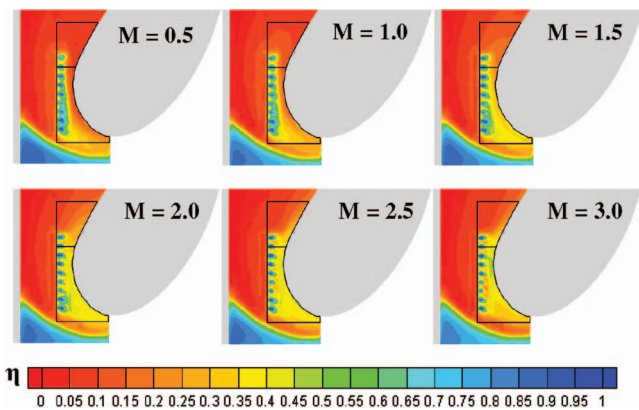


Fig. 15 Contours of adiabatic effectiveness showing the effect of the $1.2D$ bumps at different blowing ratios

higher on the pressure side at higher blowing ratios. As mentioned previously, the bumps performed the best at a blowing ratio of $M=2.0$.

Summary of Cooling Enhancements

To summarize the results, Fig. 17 shows the percent increase in area-averaged adiabatic effectiveness levels as a result of placing trenches of different depths at the leading edge. Figure 18 shows the enhancements in adiabatic effectiveness levels as a result of placing bumps of different heights at the leading edge. Trenches showed an enhancement for all depths tested, whereas bumps performed better only at higher heights when compared to the baseline cases.

Trenches typically showed little effect at the lowest blowing ratio of $M=0.5$. For a blowing ratio of $M=1.0$ and higher, the percent enhancements ranged from 10% to almost as high as 60%. The enhancement caused by the $0.8D$ trench was the highest at a blowing ratio of $M=2.5$, beyond which there was a small increase in effectiveness at $M=3.0$. The $1.2D$ trench showed a different trend compared to $0.4D$ and $0.8D$. The cooling enhancement of the $1.2D$ trench was similar up to a blowing ratio of $M=2.0$. At blowing ratios greater than $M=2.0$, the $1.2D$ trench resulted in higher effectiveness levels than seen at the low blowing ratios.

Contrary to trenches, the bumps at heights of $0.5D$ and $0.8D$ showed very little effect on adiabatic effectiveness levels. Bumps of height $1.2D$ showed higher enhancements at lower blowing ratios and the enhancement levels dropped with an increase in blowing ratio beyond $M=1.0$. The maximum enhancement shown by the $1.2D$ bump was about 20%. From the baseline study, it was

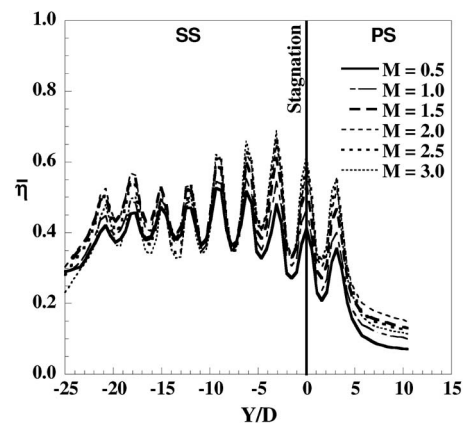


Fig. 16 Laterally averaged effectiveness showing the effect of the $1.2D$ bump at different blowing ratios

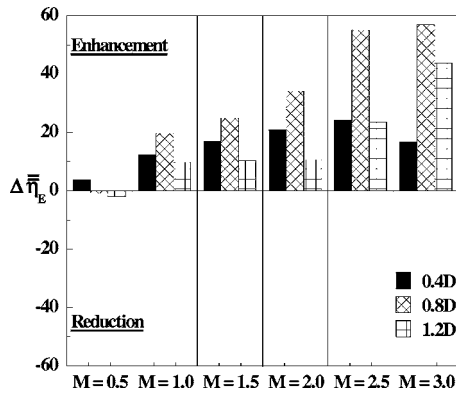


Fig. 17 Comparison of percent enhancement on area-averaged adiabatic effectiveness as a result of placing trenches at the leading edge

seen that without any modification at the leading edge, the maximum effectiveness was achieved at a blowing ratio of $M=2.0$. As bumps and trenches both showed an enhancement, it is important to see if these modifications at lower blowing ratios can show any enhancement when directly compared to the baseline case of $M=2.0$. This is important as it will ascertain if it will require less coolant, which in turn will increase the efficiency of the engine.

Figure 19 compares the enhancements resulting from the 0.8D trench and 1.2D bump relative to a baseline case of effectiveness achieved at $M=2.0$. The 0.8D trench and 1.2D bump were chosen as these were found to show the maximum enhancement for a particular geometry. For both the trenches and bumps, enhancements were only measured for $1.5 \leq M \leq 2.5$ and beyond $M=2.5$, only trenches were measured to have a positive augmentation. Even in this comparison, as previously discussed, the trenches performed better than the bumps. It needs to be seen whether a reduction in blowing ratio to $M=1.5$, showing an enhancement of only 10–15%, is more favorable than operating at the same blowing ratio of $M=2.0$ to achieve an enhancement of 35% (trenches).

Conclusions

Measurements of adiabatic effectiveness levels were presented at the leading edge-endwall junction where cooling is made difficult by the presence of a horseshoe vortex. In an attempt to improve cooling performance from a row of film-cooling holes placed near the junction, incorporating bumps and trenches were evaluated.

Trenches were applied in two different configurations. Individual hole trenches and row trenches were evaluated for a range

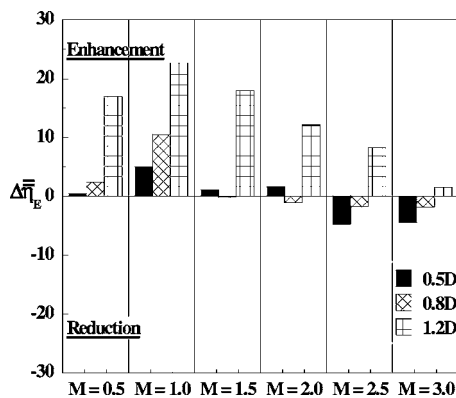


Fig. 18 Comparison of percent enhancement on area-averaged adiabatic effectiveness as a result of placing bumps at the leading edge

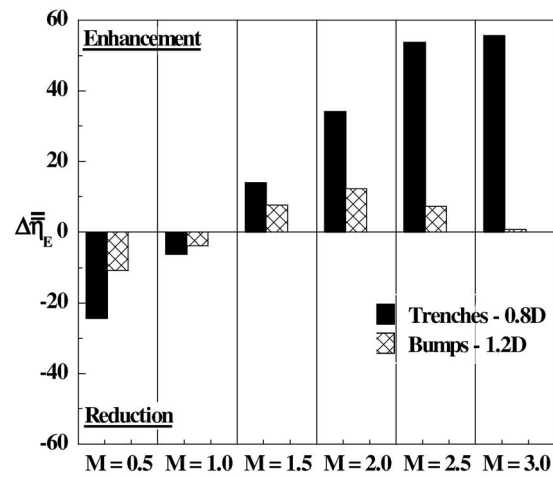


Fig. 19 Comparison of percent enhancement on area-averaged adiabatic effectiveness on trenches and bumps when compared to the baseline case at $M=2.0$

of blowing ratios and trench depths. Individual hole trenches showed very little effect on adiabatic effectiveness levels, whereas the row trenches showed a considerable enhancement. The 0.8D trench depth was found to be an optimum relative to the three depths studied at different blowing ratios. It was also found that the success of the trench on improving effectiveness levels is highly sensitive to blowing ratio for a particular trench depth.

Bumps with heights of 0.5D and 0.8D did not produce a major effect on effectiveness, although a bump height of 1.2D did show an enhancement of approximately 20% at a blowing ratio of $M=1.0$. Overall, this study has shown that it is possible to achieve improved film cooling at the vane-endwall junction through the use of small surface modifications near the cooling hole exits.

Acknowledgment

This publication was prepared with the support of the US Department of Energy, Office of Fossil Fuel, and National Energy Technology Laboratory. The authors thank Mike Blair (Pratt & Whitney), Ron Bunker (General Electric), and John Weaver (Rolls-Royce) for their input on the modeling of realistic turbine features.

Nomenclature

- C = true chord of stator vane
- D = diameter of film-cooling hole
- h = height/depth of trenches and bumps
- M = blowing ratio based on inlet mainstream velocity $M = \rho_j U_j / \rho_\infty U_\infty$
- P = vane pitch; hole pitch
- PS = pressure side
- Re_{in} = Reynolds number defined as $Re_{in} = CU_{in} / \nu$
- S = span of stator vane; total vane surface length
- SS = suction side
- T = temperature
- x = length along the vane surface
- X, Y, Z = local coordinates
- U = velocity

Greek

- η = adiabatic effectiveness, $\eta = (T_\infty - T_{aw}) / (T_\infty - T_c)$
- $\bar{\eta}$ = laterally averaged effectiveness
- $\bar{\eta}_E$ = area-averaged effectiveness
- $\Delta \bar{\eta}_E$ = percent reduction in area-averaged effectiveness, $\Delta \bar{\eta}_E = [(\bar{\eta}_{effect} - \bar{\eta}_{base\ line}) / \bar{\eta}_{base\ line}] \times 100$
- ν = kinematic viscosity

Subscripts

- aw = adiabatic wall
c = coolant conditions
in = inlet conditions
j = coolant flow through film-cooling holes
 ∞ = local freestream conditions
E = enhancement

References

- [1] Chyu, M. K., 2001, "Heat Transfer Near Turbine Nozzle Endwall," *Ann. N.Y. Acad. Sci.*, **934**, pp. 27–36.
- [2] Friedrichs, S., Hodson, H. P., and Daws, W. N., 1996, "Distribution of Film-Cooling Effectiveness on a Turbine Endwall Measured Using Ammonia and Diazo Technique," *ASME J. Turbomach.*, **118**, pp. 613–621.
- [3] Friedrichs, S., Hodson, H. P., and Dawes, W. N., 1997, "Aerodynamic Aspects of Endwall Film-Cooling," *ASME J. Turbomach.*, **119**, pp. 786–793.
- [4] Friedrichs, S., Hodson, H. P., and Dawes, W. N., 1999, "The Design of an Improved Endwall Film-Cooling Configuration," *ASME J. Turbomach.*, **121**, pp. 772–780.
- [5] Thole, K. A., and Knost, D. G., 2005, "Heat Transfer and Film-Cooling for the Endwall of a First Stage Turbine Vane," *Int. J. Heat Mass Transfer*, **48**, pp. 5255–5269.
- [6] Blair, M. F., 1974, "An Experimental Study of Heat Transfer and Film-Cooling on Large-Scale Turbine Endwalls," *ASME J. Heat Transfer*, **96**, pp. 524–529.
- [7] Knost, D. G., and Thole, K. A., 2005, "Adiabatic Effectiveness Measurements of Endwall Film-Cooling for a First Stage Vane," *ASME J. Turbomach.*, **127**, pp. 297–305.
- [8] Cardwell, N. D., Sundaram, N., and Thole, K. A., 2007, "The Effects of Varying the Combustor-Turbine Gap," *ASME J. Turbomach.*, **129**, pp. 756–764.
- [9] Burd, S. W., and Simon, T. W., 2000, "Effects of Slot Bleed Injection Over a Contoured Endwall on Nozzle Guide Vane Cooling Performance—Part II: Thermal Measurements," ASME Paper No. 2000-GT-0200.
- [10] Bunker, R. S., 2002, "Film-Cooling Effectiveness Due to Discrete Holes Within a Transverse Surface Slot," ASME Paper No. GT2002-30178.
- [11] Lu, Y., Nasir, H., and Ekkad, S. V., 2005, "Film-Cooling From a Row of Holes Embedded in Transverse Slots," ASME Paper No. GT2005-68598.
- [12] Wayne, S. K., and Bogard, D. G., 2007, "High Resolution Film-Cooling Effectiveness Measurements of Axial Holes Embedded in a Transverse Trench With Various Trench Configurations," *ASME J. Turbomach.*, **129**, pp. 294–302.
- [13] Sundaram, N., and Thole, K. A., 2007, "Effects of Surface Deposition, Hole Blockage, and Thermal Barrier Coating Spallation on Vane Endwall Film Cooling," *ASME J. Turbomach.*, **129**, pp. 599–607.
- [14] Bunker, R. S., 2001, "A Method for Improving the Cooling Effectiveness of a Gaseous Coolant Stream," U.S. Patent No. 6,234,755.
- [15] Radomsky, R., and Thole, K. A., 2002, "Flowfield Measurements for a Highly Turbulent Flow in a Stator Vane Passage," *ASME J. Turbomach.*, **122**, pp. 255–262.
- [16] Ethridge, M. I., Cutbirth, J. M., and Bogard, D. G., 2000, "Scaling of Performance for Varying Density Ratio Coolants on an Airfoil With Strong Curvature and Pressure Gradient Effects," *ASME J. Turbomach.*, **123**, pp. 231–237.
- [17] Moffat, R. J., 1988, "Describing the Uncertainties in Experimental Results," *Exp. Therm. Fluid Sci.*, **1**, pp. 3–17.

Prestall Behavior of a Transonic Axial Compressor Stage via Time-Accurate Numerical Simulation

Jen-Ping Chen
The Ohio State University,
Columbus, OH 43210

Michael D. Hathaway

Gregory P. Herrick

Army Research Laboratory,
Vehicle Technology Directorate,
Cleveland, OH 44135

Computational fluid dynamics calculations using high-performance parallel computing were conducted to simulate the prestall flow of a transonic compressor stage, NASA compressor Stage 35. The simulations were run with a full-annulus grid that models the 3D, viscous, unsteady blade row interaction without the need for an artificial inlet distortion to induce stall. The simulation demonstrates the development of the rotating stall from the growth of instabilities. Pressure rise performance and pressure traces are compared with published experimental data before the study of flow evolution prior to the rotating stall. Spatial fast Fourier transform analysis of the flow indicates a rotating long-length disturbance of one rotor circumference, which is followed by a spike-type breakdown. The analysis also links the long-length wave disturbance with the initiation of the spike inception. The spike instabilities occur when the trajectory of the tip clearance flow becomes perpendicular to the axial direction. When approaching stall, the passage shock changes from a single oblique shock to a dual shock, which distorts the perpendicular trajectory of the tip clearance vortex but shows no evidence of flow separation that may contribute to stall. [DOI: 10.1115/1.2812968]

Introduction

Advances in gas turbine engine technology have made possible the production of highly efficient engines. However, the useful operating range of a gas turbine engine is limited by the stable operation of the compressor. The limiting instability can be characterized by either rotating stall or surge. Surge is the zeroth order planar oscillation mode resulting from overall imbalance of the entire propulsion system, thus, analysis would have to include full volume and ducting. This violent system instability may be preceded by a rotating stall, which sets up alternating stress on the blades. Rotating stall and surge can cause destructive damage to engines and should be avoided. Understanding the physical process of the onset of rotating stall can aid in the design of a better control method to stabilize the system and enhance engine performance.

Stall inception has been an active research effort for the past five decades. The events leading to rotating stall have been traditionally classified according to two different types of wave disturbances moving around the annulus: long-length (modal) and short-length (spike) waves. Long-length wave disturbances are those with length on the order of the rotor circumference. This type of disturbance is caused by the characteristic frequencies of the compression system. Theories to model the long-length instability were developed by Moore and Greitzer [1]. The assumption is that the disturbance length scale is much larger than one blade pitch, and that the entire blade row can be modeled, both spatially and temporally, without the knowledge of the detailed flow inside the blade passages. This approach predicts the existence of long-length waves leading to stall. McDougall [2] demonstrated the existence of the modal waves through experiments, and Garnier et al. [3] supported the validity of the Moore and Greitzer model with detailed measurements. Unsteady pressure or axial velocity

measurements from probes placed around the annulus are usually used to track the development of modal waves. Modal oscillations often have an axial extent from inlet to exit. It is typically a 2D (θ, x) phenomenon, which is not an early form of stall cell but instead represents harmonic oscillations of the flow field. It usually appears when the shape of the total-to-static pressure rise characteristic becomes horizontal.

The second type of stall inception mechanism is the short-length, or spike, disturbances. These are disturbances with length scale on the order of blade passage breadth. Spikes can be viewed as embryonic stall cells with flow breakdown in local regions (Camp and Day [4]); it is a 3D phenomenon whose development depends on the flow structure within the blade passage. A common scenario for the spike stall inception process is that localized, 3D pockets of instability in multiple blade passages erupt first to form small-sized multicell rotating stall. These stall cells rotate at 30–85% rotor speed initially and then merge into a single rotating stall cell within a few rotor revolutions (Day [5]). The final speed of the consolidated stall cell is nearly half or less of the rotor speed (Cumpsty [6]). A spike disturbance more frequently occurs when the slope of the pressure rise characteristic is still negative. That is, the pressure still rises as the mass flow reduces.

The above discussions indicate that the slope of the pressure rise characteristic may correlate with the stall inception type. Spike and mode can also be the different aspects of the stall inception process and can exist in the same machine (Day [5]). Day indicated that modal waves may be measurable in the machine for as many as 200 rotor revolutions before stall. A spike disturbance, on the other hand, once formed, can lead to rotating stall quickly, usually within a few rotor revolutions.

Numerical simulation using computational fluid dynamics (CFD) techniques has been shown as an alternative way to analyze aerodynamic problems and is a complement to experiments in the understanding of complex flow phenomena. Flow structure can be examined in detail where experimental measurements are difficult or impossible. During the past ten years, steady-flow simulations have provided an increasingly accurate prediction of the flow up to the point of compressor stall. Attempts to study stall

Contributed by the International Gas Turbine Institute of ASME for publication in the JOURNAL OF TURBOMACHINERY. Manuscript received June 7, 2007; final manuscript received August 20, 2007; published online August 1, 2008. Review conducted by David Wisler. Paper presented at the ASME Turbo Expo 2007: Land, Sea and Air (GT2007), Montreal, Quebec, Canada, May 14–17, 2007.

through unsteady simulations of a periodic subset of the blades in a compressor blade row (Hoying et al. [7], Vo et al. [8], Davis and Yao [9]) or through reduced-order unsteady-flow models (Gong et al. [10]) have reached valuable findings of the flow structure leading to stall. However, since the temporal flow field variations that occur during stall inception are not harmonics of blade passing frequency, a full-annulus model should be used to remove the constraint of the periodic model in order to study the transition from a steady flow into the unsteady stalling flow, and to resolve flow features of length scale on the order of the rotor circumference. Such simulations have been done two dimensionally (He [11], Saxer-Felici et al. [12]), but stall and the instabilities leading to stall are inherently three-dimensional phenomena. Predicting stall phenomena may thus require three-dimensional unsteady full-annulus simulations, which is a daunting computational endeavor requiring considerable computational resources. Due to the rapid advance of high-performance computing in the past decade, advanced CFD codes have benefited from the almost-unlimited computing potential of parallel computing. Recently, Chen et al. [13] demonstrated the ability to conduct a full-annulus 3D unsteady computation of an entire compressor stage while Hah et al. [14] also conducted a full-annulus 3D computation of an isolated rotor. This trend indicates that large-scale simulation using parallel computing is within reach.

Previous comparisons of the time averages of unsteady phase-lag and partial annulus predictions to measurements have shown the validity of the TURBO code to capture the 1D and 2D characteristics of this compressor (Hathaway et al. [15]). The intent of this work is to use the available experimental data to provide assessment of the code and to show evidence that the computational model reasonably captures the inherent behavior of compressors as they are throttled into stall. It is recognized that some features of the actual tested compressor are not captured by the computational model, for example, the leakage gap at the rotor/stator hub interface, the actual blade tip profile, and the geometry of the upstream and downstream ducting between the plenum and throttle valve locations. Although these features might influence the actual compressor stall, they are not considered requisite to understanding fundamental stall inception characteristics.

Axial Compressor, Stage 35

NASA research single-stage compressor Stage 35, representative of the advanced transonic core compressor, is used in this investigation. A schematic of the compressor test rig and compressor geometry is provided in Fig. 1 and the design parameters are provided in Table 1. Stage 35 produces 1.8 total pressure ratio at a mass flow rate of 20.2 kg/s at the design speed of 17,189 rpm. Details of the Stage 35 geometry, operating conditions, and the experimental results are provided by Reid and Moore [16].

Relevant Experimental Work

Time-resolved pressure measurement of Stage 35 near stall was reported by Bright et al. [17]. The experiment was performed at 85% design speed. Several configurations, including a clean-inlet case, were reported in that paper. For the interest of this study we will focus on the clean-inlet case. The compressor was transitioned into stall using a continuous throttle maneuver. Time-resolved pressure was recorded by high-frequency-response transducers at eight locations equally spaced around the annulus. Figure 2 reproduces the pressure traces of the clean-inlet case for 180 revolutions prior to stall reported in that paper (the original data are not available to us). Based on the pressure disturbance, Bright et al. [17] commented that the compressor with the clean-inlet stalls due to modal instabilities, and at 40 revolutions before stall, there appear to be spikes on top of the modal wave. They concluded that, "This indicates that our high-speed stage under normal stalling condition is considered a 'modal' machine, since modal instabilities dominate the pre-stall behavior with some added pin instabilities present just before stall."

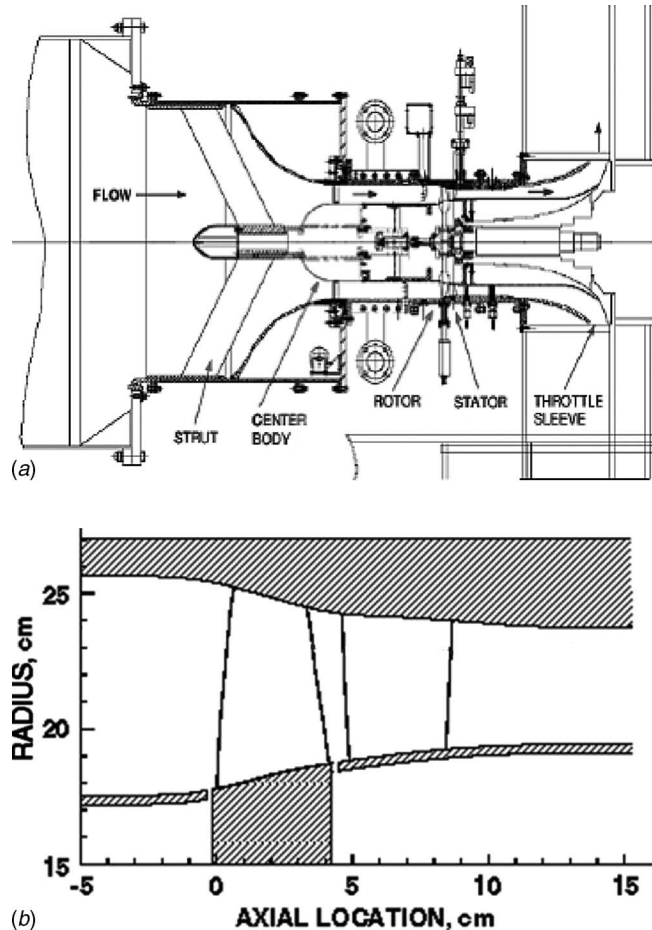


Fig. 1 NASA high-speed compressor Stage 35

In the following, we take a closer look at these experimental data. The shapes of the modal disturbances indicated in Fig. 2 resemble sinusoidal waves with a temporal period of ten rotor revolutions. The speed of the modal disturbances, as indicated by the slope of Line A, connecting the peaks of the pressure wave, is zero. This indicates that the modal disturbance is caused by axisymmetric longitudinal system disturbances. The system includes all ducting and volumes of the experimental facility. This modal disturbance is the *surge mode* that oscillates at a frequency of 10% rotor speed—equivalent to the ten rotor revolutions period it covers. Unlike a typical rotating modal wave, the surge mode does not rotate. The surge mode is a compression system wide resonance that cannot be modeled with the current simulation because the computational grid does not include the ducting of the test facility, which is quite substantial, as shown in Fig. 1.

As the compressor throttles closer to stall at about ten revolutions before stall, there is a secondary disturbance, much like a spike in the time scale of Fig. 2. Looking more closely, this secondary disturbance covers a circumferential distance of one rotor circumference, as indicated in the enlarged image. It sits on top of

Table 1 Design parameters of Stage 35

| | |
|-------------------------|----------|
| Rotor rpm at 100% speed | 17,188.7 |
| Tip speed (m/s) | 454.456 |
| Hub/tip radius | 0.7 |
| Rotor aspect ratio | 1.19 |
| Stator aspect ratio | 1.26 |
| Number of rotor blades | 36 |
| Number of stator blades | 46 |

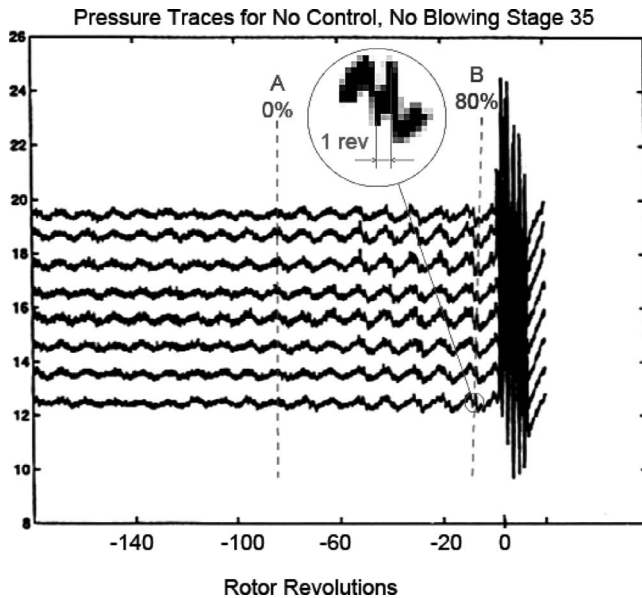


Fig. 2 Experiment pressure traces for clean inlet, 85% design speed, Stage 35, Bright et al. [17]

the surge mode and rotates around the annulus at about 80% rotor speed, indicated by Line B. Because the length scale of this disturbance is the entire annulus, which is much larger than that of a typical spike, it is classified as a mode. For discussions in the rest of the paper, this *rotating long-length disturbance* is also referred to as a *rotating modal disturbance*. This long-length disturbance is followed by the eventual flow breakdown. Due to the picture quality, we are unable to discern the transition between the start of the rotating long-length disturbance and the final breakdown. The long-length disturbance has a length scale of *one* rotor circumference. The rotating long-length disturbance, because of its length scale, can only be resolved by a full-annulus simulation.

The simulation reported in this work is part of an overall effort to examine steady tip injection stall flow control for Stage 35 at design speed with the clean inlet. As such, the simulation was conducted at design speed. To our knowledge, there are no pressure trace data available at design speed as that shown in Fig. 2. Therefore, we will use the 85% speed case to compare with the simulated results. While the speeds are different, the two cases are both transonic compressors and share common features as we explore the flow behavior prior to stall. The experimental characteristics at 85% and 100% speeds are compared in Fig. 3. Both cases stall at the peak of static pressure rise. More importantly is that their slopes near stall are similar. These similarities justify the use of the 85% speed case for comparison.

Numerical Methodology

TURBO is a physics-based simulation tool for multistage turbomachinery. The solver computes the fluid conservation laws without ad hoc modeling of any flow phenomenon other than models required for turbulence. This code solves the unsteady Reynolds-averaged Navier–Stokes equations and a decoupled $k-\varepsilon$ turbulence model. The code is implemented in a portable, scalable form for distributed-memory parallel computers using message passing interface (MPI). The parallel implementation employs domain decomposition and supports general multiblock grids with arbitrary grid-block connectivity. The solution algorithm is a Newton iterative implicit time-accurate scheme with characteristics-based finite-volume spatial discretization. The Newton subiterations are solved using a concurrent block-Jacobi symmetric Gauss–Seidel (BJ-SGS) relaxation scheme. Because all of the fundamental fluid mechanics are computed, the code is capable of capturing the

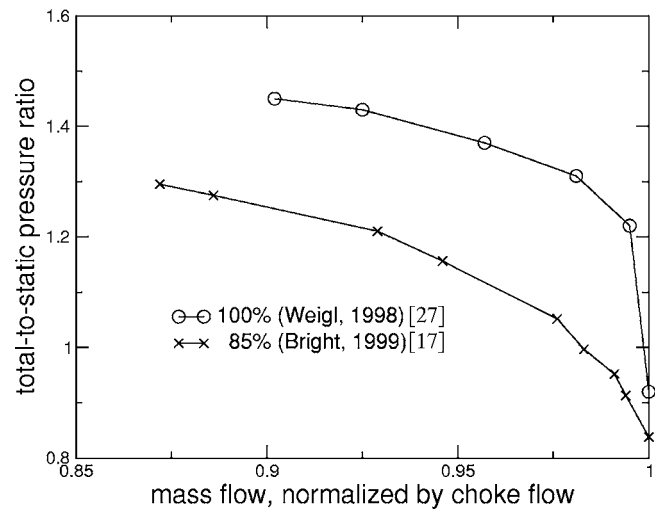


Fig. 3 Comparison of characteristics at 85%, Bright et al. [17], and 100%, Weigl et al. [27], speeds, Stage 35

nonlinear characteristics of the flow fields of interest. With the actual modeling of blade rows in relative motion, this code is capable of computing the unsteady interactions between blade rows. Details of the flow solver can be found from Chen and Whitfield [18]. The approach to parallelization for large-scale, complex problems is discussed by Chen and Briley [19]. In the following, we discuss several issues applied to the code in the simulation of rotating stall.

Full Compressor Stage Simulation. The intent to simulate the inception and maturation of long-wavelength circumferential modes, with wave numbers as low as unity, requires full-annulus simulations. A time-accurate sliding interface (Chen and Barter [20]) is implemented, in which pressure waves in all directions (axial, radial, and circumferential) are passed unaltered between the rotor and the stator. This attribute is necessary to examine the temporal and spatial responses associated with blade row interaction during stall inception.

Inlet Boundary Condition. An isentropic inlet condition (Chen and Whitfield [18]) is applied, where the spanwise total condition is prescribed. This boundary condition preserves the upstream total conditions at test facility level but can potentially reflect outgoing pressure waves back to the computational domain.

Exit Boundary Condition. The traditional choice of exit boundary for stable flow is the radial equilibrium condition. This boundary condition uses a preset exit static pressure. In near-stall or during-stall conditions, compressor pressure rise drops and a preset exit pressure cannot match the pressure drop. In this study, we relieve the situation by the use of a “choked” throttle model that specifies corrected mass flow at the exit. This boundary condition allows variation of exit static pressure to match the compressor exit mass corrected to the exit total condition.

Tip Clearance Model. The tip gap was modeled by the tip clearance model of Kirtley [21]. This model ensures the conservation of mass and momentum through the tip gap without the need of a tip clearance grid. A gridding strategy suggested by Van Zante et al. [22] is adopted in this study where ten points are placed in the tip gap region. Although the detailed physics of the development of the leakage vortex are not captured, the tip clearance model was considered adequate for predicting the first order effects of the leakage vortex strength, extent, and direction (Chima [23]).

Gridding. This compressor stage consists of 36 rotor blades

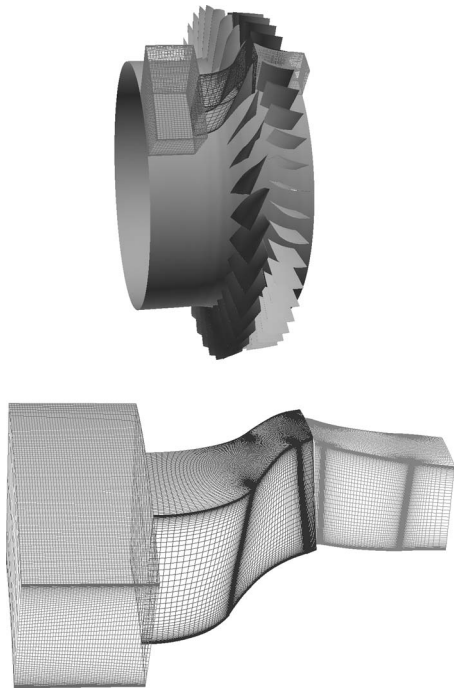


Fig. 4 Three-blade-row grid model for the Stage 35 simulation

and 46 stator blades. For the purpose of conducting simulations with tip injectors in another effort, we built a three-blade-row grid as shown in Fig. 4. The injector row has 12 injectors (not activated in this study) that are equally spaced in the circumferential direction. The grid size of the rotor is $151(x)$, $71(r)$, and $56(\theta)$ with $81(x)$ and $61(r)$ points on the blade. The grid size of the stator is $141(x)$, $71(r)$, and $79(\theta)$ with $81(x)$ and $53(r)$ points on the blade. The rotor tip clearance is 1% of rotor tip chord. The grids are replicated around the annulus to generate a full-annulus grid with a total of 67×10^6 grid points. The grid is then partitioned into 328 blocks. The simulations were run on an IBM P4 cluster at NAVO MSRC using 328 CPUs with 24 h (wall clock) computation time for one rotor revolution. In the simulation of the development of rotating stall, ten revolutions were needed. Ideally, each operating point should be run at least ten revolutions to ensure convergence, especially for points close to stall. The time for each speedline would then be 0.5×10^6 CPU hours (six operating points).

Constrained by the computational resources for the full-annulus simulations, very short upstream and downstream computational domains were used here. This choice prompts two caveats: (1) The exclusion of the test facility volume effect prevents the modeling of the surge mode. Any modal activity showing up in the simulation should be a result of the compound effect of the blades (both rotor and stator if the interaction of the two matters) and the limited volume effect present in the ducting of the current grid. (2) Limiting the axial extent of the computational domain can potentially disrupt long-length modes due to the reflective inlet boundary. Because pressure waves (with length λ) decay $e^{-L/\lambda}$ through a distance L , it is preferred to place the inlet boundary away from the rotor so that pressure waves, especially with long wavelengths, decay sufficiently before reaching the inlet. Typically, the modal instability shows up hundreds of revolutions prior to stall. Complete simulation of the evolution of such modal instability is beyond the computational resources available in this study. Our intent, therefore, is to examine the development of the modal disturbances as they first emerge before reaching the inlet rather than the complete resolution of the modal stall process. In this aspect, a shorter upstream domain (2.5 rotor chords) is justified.

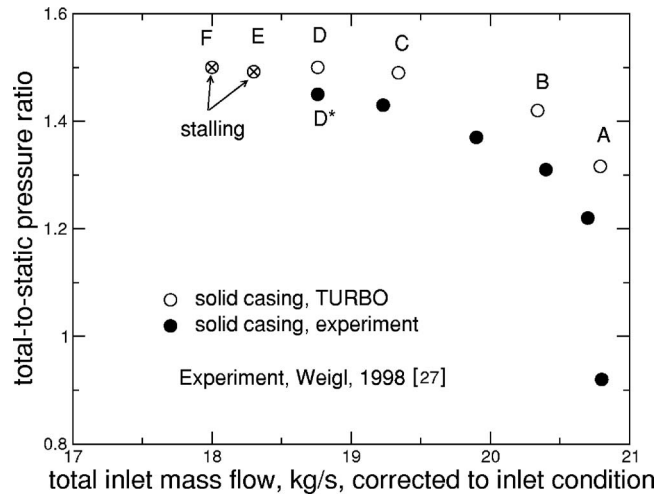


Fig. 5 Stage 35 computed and measured speedlines, design speed

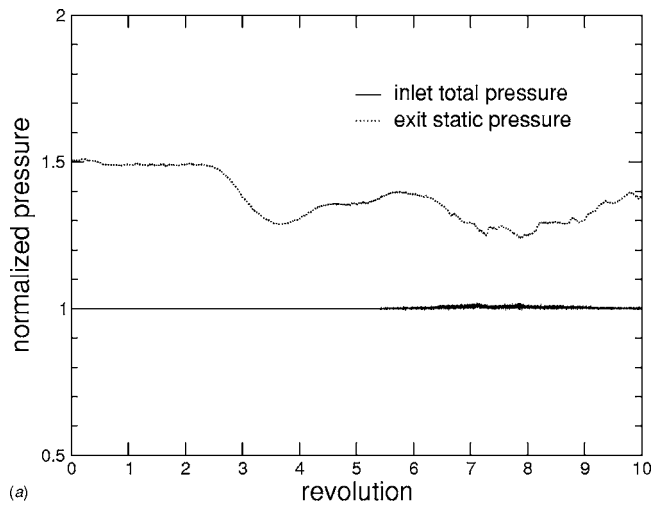
Results and Discussions

The difference of the throttling processes in the simulation and the experiment is that in the simulation, the exit boundary condition is changed in discrete steps, while in the experiment, the compressor transitioned to stall through a continuous throttling maneuver. In this simulation, a new throttle setting restarts from the solution of a previous throttle setting. Due to computational resources, each throttle setting was only run for a few revolutions before moving to the next. Generally, it was sufficient to reach convergence within four revolutions while away from stall. As stall was approached, more (six or more) revolutions were required to assure convergence.

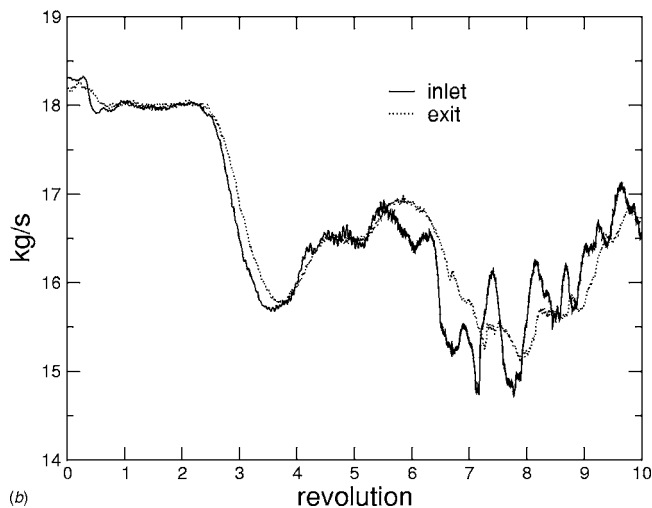
Stage Characteristics. The computed and experimental characteristics (speedlines) are shown in Fig. 5. The data used in this figure are the ratio of exit static pressure to inlet total pressure versus mass rate corrected to inlet total condition. The computed speedline is generated by incrementally closing the throttle setting (decreasing exit corrected mass flow) from A to F. The overall shape of the computed characteristic before stall is similar to the experimental data, so is the slope of the characteristic near the peak pressure (throttle Point D). Since the slope of the compressor characteristic correlates with the type of stall inception, we consider the simulation reasonable to capture the stall inception mechanisms.

Point D in Fig. 5 is the last stable throttle setting. Points E and F both restart from Point D and develop into a rotating stall. In both cases, the exit pressure changes from the peak at D into a transitional peak and then drops to a much lower level during rotating stall, as shown in Fig. 6(a). This demonstrates the throttling effect of the corrected mass exit boundary condition by allowing the exit pressure to vary as the flow condition changes. The pressure ratios shown in Fig. 5 for E and F are the transitional peak pressures before entering rotating stall. Point D* is the approximate stall point from the experiment. The actual simulated stall point should occur between D and E. The actual stall point depends on many issues, such as tip clearance height, deviation of real blade geometry from designed geometry, as well as the type of turbulence modeling in the numerical simulation. These details may not be correctly represented in this simulation. Even though the exact stall point is important, for the intent of this study, the simulation is considered adequate to examine the general physical trends leading to stall.

In the following sections, we first present the entire evolution of the rotating stall as the throttle setting changes from D to F. This



(a)



(b)

Fig. 6 Pressure and mass variation during rotating stall at throttle Setting F: (a) Pressure (b) mass flow

is followed by a closer examination of the prestall flow development from D to E, with E being closer to the stable point D.

Evolution of the Rotating Stall. This result was reported by Chen et al. [13] and is outlined here for completeness. The rotating stall was captured by the time variation of static pressure at eight pressure transducers circumferentially spaced upstream of the rotor. The probes are located 44% chord upstream of the rotor leading edge at 98% span. The circumferential locations are 10 deg, 70 deg, 100 deg, 160 deg, 190 deg, 250 deg, 280 deg, and 340 deg. The history of pressure variations are shown in Fig. 7, in which the pressure levels are offset by the probe circumferential locations. Because the volume effect is not modeled in the simulation, the pressure disturbance of Fig. 7 should be viewed as a filtered version of Fig. 2 by removing the surge mode oscillations.

Small, periodic pressure variations caused by the rotor blade passing, as indicated by the thickness of the curves, are present in all curves of Fig. 7. A smooth disturbance is visible at $t=0.7T$ (T =time for one rotor revolution) traveling at full rotor speed. This disturbance, analyzed in further detail later, has a length scale of one rotor circumference, thus is classified as a modal disturbance. The rotating modal disturbance continues to grow in magnitude but the speed slows to 84% rotor speed in approximately one revolution. After $2T$, it transforms into several spike disturbances around the annulus, each with a smaller length scale of a

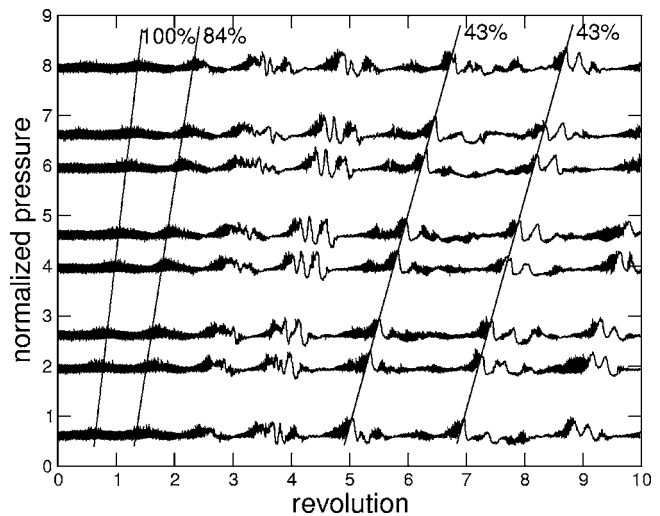


Fig. 7 Time history of static pressure variation at eight locations around the annulus located 44% chord ahead of the rotor of Stage 35, throttling Setting F

few blade passages. The spike disturbances then grow in magnitude and slow down to 43% in four revolutions. Inlet and exit mass flow histories during the same period are shown in Fig. 6(b), in which the mass flow remains relatively flat in the first two revolutions at 18 kg/s before it drops sharply and sustains large variations of 14% of the peak mass flow.

In Figs. 8 and 9, the entropy on a surface of revolution near the casing is shown at two instants in time. The full-annulus surface is illustrated by two half-annulus surfaces. At $t=3.8T$, Fig. 8, the early phase of the stall inception, three separate high entropy (red color) regions can be seen, with the axial extent covering from one chord upstream to aft of the stator leading edges. The radial extent of the stall cell is shown in the axial cut plane at 16% chord before the rotor, where the high entropy region shows the stall cell extending about 30% span from the casing. At $t=10T$, Fig. 9, the stall cell evolves into the final stage as its rotating speed becomes stabilized. The three-cell stall has merged into a single-cell stall with the axial extent covering all the way from the inlet of the computation domain to aft of the stator trailing edge. The radial extent of the stall cell has now extended about 70% span from casing.

The evolution of the simulated rotating stall cell is similar to the spike stall inception mechanism commonly observed in that localized, three-dimensional pockets of instability in multiple rotor passages break up to form the initial phase of a rotating stall cell, usually with several small-sized stall cells. These small stall cells move fast at the beginning and then merge into a single rotating stall cell within a few revolutions before slowing down to about half of the rotor speed as the rotating stall becomes fully developed.

In the previous section, we gave a brief description of the overall evolution of the rotating stall using throttle Setting F. In the following sections, we will examine the process that leads to the initial flow breakdown, i.e., the stall inception process. Restarting from the stable solution of D, the simulation was repeated with throttle Setting E, the mass flow history during the transition from D to E is shown in Fig. 10. The simulation shows that after four revolutions from restart, the mass flow starts to decrease, leading to the rotating stall. Three time stamps marked E1 (1.7T), E2 (3.2T), and E3 (4.3T) will be referenced in the following discussions.

Development of Long-Length Disturbance. Both experimental (Spakovszky et al. [24] and Suder et al. [25]) and computational studies (Chen et al. [13], Davis and Yao [9]) indicate that

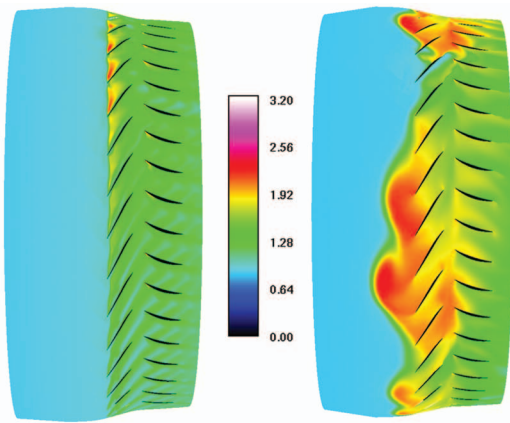


Fig. 8 Entropy of Stage 35 during stall inception, $t=3.87$: Left half annulus and right half annulus, 16% chord upstream of rotor leading edge

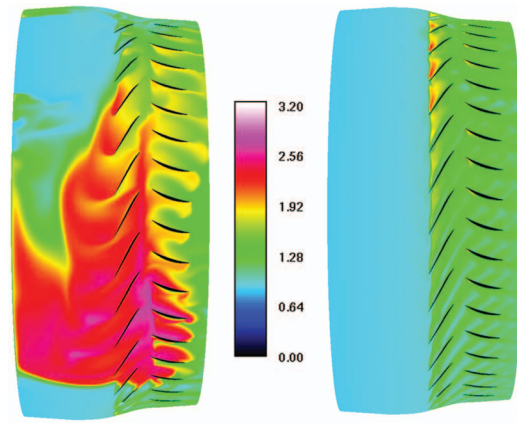
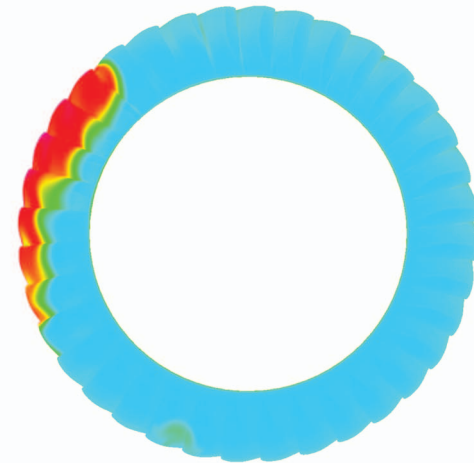
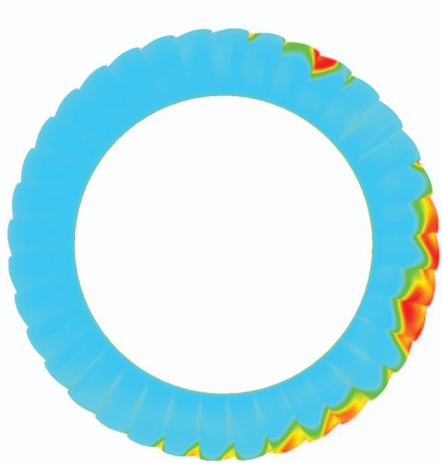


Fig. 9 Entropy of Stage 35 during stall inception, $t=107$: Left half annulus and right half annulus, 16% chord upstream of rotor leading edge



the rotating stall of this compressor initiates in the rotor tip region, so the analysis will focus on the rotor tip. Instantaneous pressure profiles around the annulus near the rotor tip leading edge are shown in Fig. 11. The three curves correspond to different phases at throttle Settings D and E during the transition from stable operation to stall (Fig. 10). Phase 1 is the last stable point before stall, which will be used as the base line for comparison. Phases 2 and 3 are the same throttle Setting E, but at two different instants: one before stall (Time E1) and the other at the beginning of stall (Time E2). Spatial fast Fourier transforms (FFTs) of the pressure profile are shown in Fig. 12. The most dominant harmonic is the 36th mode (its magnitude is at least one order of magnitude larger than those of others), which corresponds to the number of rotor blades. This disturbance is caused by the periodic flow features between blades and thus has the length scale associated with the rotor blade pitch. Not shown here is the strength of the 46th mode, which is negligible. This indicates that the influence of the stator on the potential field at rotor leading edge can be ignored. Therefore we will focus the study only on the rotor.

Modal disturbances, if any, should exist in the low harmonics with longer wavelengths that are on the order of the rotor circumference. At Phase 1 (D), only the 36th mode prevails. This indicates that when away from stall, the only disturbance to the otherwise uniform annulus flow is that from the periodic rotor passing and there is no modal activity. At Phase 2 (Time E1), the early phase of the rotating stall, there exists an identifiable 1st mode along with the 36th mode. There are also weaker but identifiable modes between the 1st and 36th modes. As the simulation

proceeds, bringing the compressor even closer to stall at Phase 3 (Time E2), the magnitude of the first mode increases even more. The magnitudes of the modes in between remain relatively similar to those in the previous two phases but fluctuate over the spectrum. The only mode that grows persistently during the prestall phase is the first mode. This disturbance rotates at 100% rotor speed. This observation is the same as that of throttle Setting F, where the speed of rotating mode is indicated in the pressure history of Fig. 7. This finding is similar to the experiment (see Fig. 2) in that the one rotor circumference disturbance, which sits on top of the surge mode (not modeled in this simulation), starts to rotate at 80% rotor speed right before stall. It suggests perhaps that the simulation is adequately modeling the one rotor circumference modal disturbance before the compressor enters rotating stall.

A possible explanation of the origin of the first mode can be derived from the following observations: (1) While the grid in our simulation does not include the complete ducting system, it does include the limited ducting that contains the rotor and the stator. (2) The speed of the rotating mode is 100% rotor speed; in other words, the first mode is fixed to the rotor. This makes it likely that the disturbance is associated with the rotor. The two observations suggest that the first mode may originate from a compound effect of the rotor blades and the limited volume effect present in the ducting of the current grid.

Development of Mode and Spike. To better understand the development of the first mode and the spike disturbance, we focus

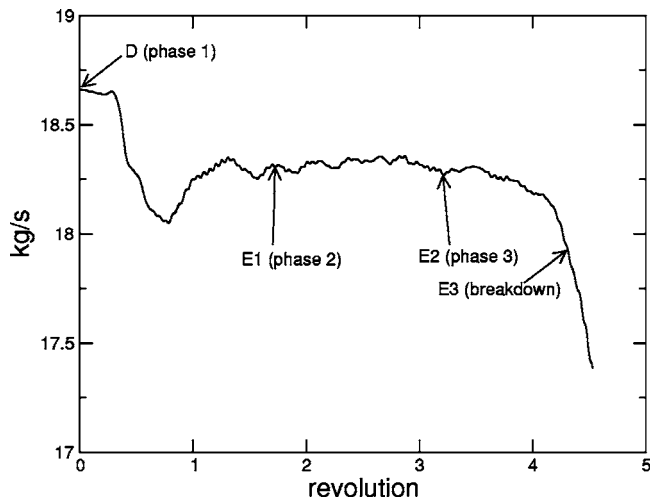


Fig. 10 Mass flow history at throttle Setting E

on the evolution of the flow during the transient right before stall. Since stall is likely to be associated with the reverse flow (negative axial flow), we will monitor the development of the negative axial velocity of the flow during the transition. Figures 13(a)–13(c) illustrate the axial velocity of the stage at three radial cut planes at the three time instants E1, E2, and E3 during the transient. The three cut planes are located at 4 clearance heights (4ϵ) below casing (Cut plane 1), 1.5 clearance heights (1.5ϵ) below casing (Cut plane 2), and 0.5 clearance heights (0.5ϵ) below casing (Cut plane 3). Figure 13(d) illustrates the front views of Cut plane 3 at the three time instants. The contours of the axial velocity have been truncated so that only the negative velocity has a color. All positive velocities are colored white.

At Time E1, Fig. 13(a), about 2.5 revolutions before breakdown, the reverse flow is seen in all rotor passages with a radial coverage of at least four clearance heights below the casing, as indicated by the reverse flow being visible on all cut planes. The rotor reverse flow is formed by the tip clearance vortex flow, which will be explained in detail later. The boundary and magnitude of the reverse flow region depicts the boundary and the strength of the tip vortex. The patterns of the reverse flow are not the same in every passage, with the reverse flow zone larger on the back side of the view (210 deg). This can be readily seen on Cut planes 1 and 2. The overall shape of rotor reverse flow cor-

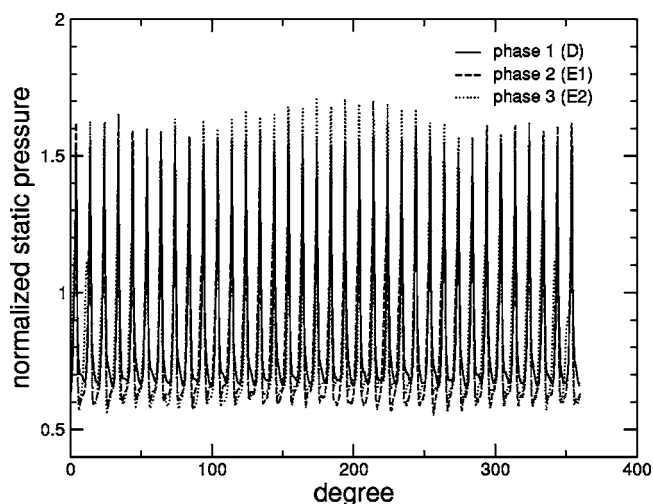


Fig. 11 Instantaneous pressure profile at rotor tip

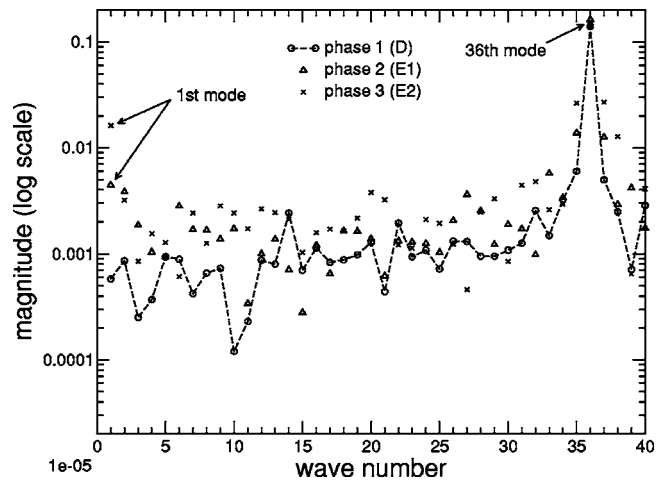


Fig. 12 FFT of Fig. 11

responds well with the harmonics of Fig. 12 in that the 1st mode coexists with the 36th mode. The speed of the 1st mode is the same as that of the 36th mode, both rotate at the rotor speed. The flow at this phase has already shown the instability.

At Time E2, by comparing the front view of Cut plane 3 at Times E1 and E2 [Fig. 13(d)], we see that the front boundary of the reverse flow moves forward and becomes perpendicular to the axial direction. The magnitude of the negative velocity at Time E2 is also higher than that at Time E1 as is shown by more green spots at Time E2. This is consistent with the short-length stall inception mechanism described by Hoying et al. [7] that spike stall initiates when the tip clearance vortex trajectories align perpendicularly to the axial direction. The larger reverse flow zone now rotates to the front side of the view (0 deg), Fig. 13(b), better seen on Cut planes 1 and 2. Also seen on the two cut planes is the appearance of reverse flow in the stator. Different from the reverse flow in the rotor, which is caused by tip clearance vortex, the stator reverse flow is caused by suction surface flow separation.

At Time E3, 1.1 revolutions after Time E2, the flow formally enters the rotating stall. A zone of extended reverse flow covering five rotor passages can now be seen in the front view of Cut plane 3 (330 deg) in Figs. 13(c) and 13(d). This zone sits in the middle of the less extensive reverse flow characterized by the green colored tip clearance flow on Cut plane 3. This less extensive reverse flow correlates with the first mode. The five-passage reverse flow zone initiates a spikelike disturbance on top of the first mode and finally leads to the rotating stall.

Further analysis of the simulation also indicates the correlation between the first mode disturbance of axial momentum and the appearance of spike. The circumferential profile of the axial momentum near the rotor tip leading edge is low-pass filtered to remove high-frequency noise so only the first mode stays. Figure 14 shows the results at Times E1, E2, and E3. The magnitude of the first mode disturbance grows from E1 to E3 as it rotates around the annulus. The locations of the trough of the waves (marked in Fig. 14) are where the flow has the lowest axial momentum. These locations match the regions of the larger reverse flows in all three cut planes mentioned previously. This is consistent with the observation of Day [5] that spikes can grow out of the trough of the axial velocity modal waves if critical incidence is reached.

As we pointed out before, it is difficult to discern the actual transition from the rotating modal wave to the start of the rotating stall in Fig. 2. The simulation provides the details to complement the experiment. It is demonstrated here that a spike of five passages long does occur. It evolves smoothly out of the rotating mode and eventually leads to the breakdown (rotating stall).

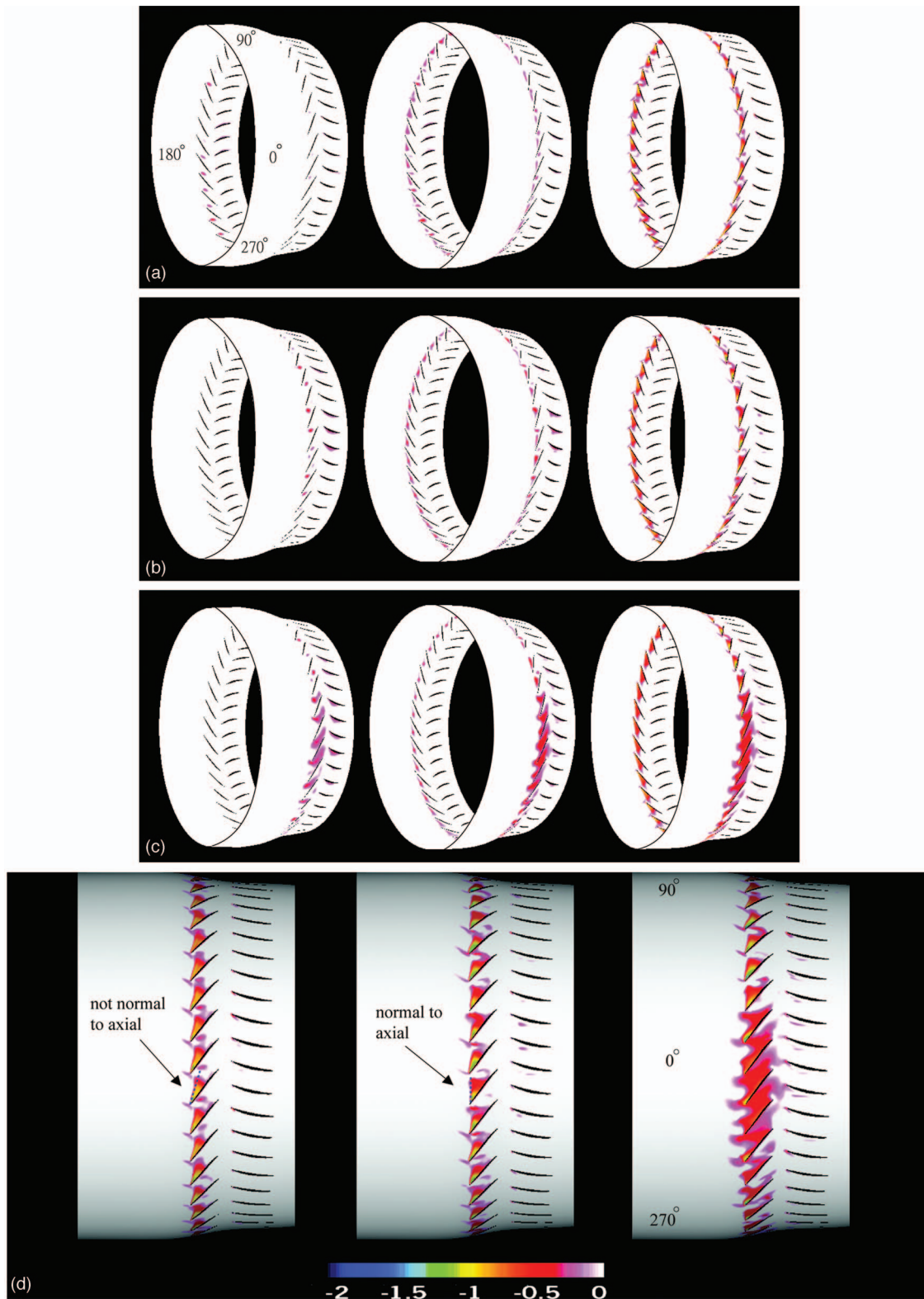


Fig. 13 Negative axial velocity at three cut planes, three time instants: (a) Time E1 ($2.5T$ before rotating stall), (b) Time E2 (beginning of rotating stall), and (c) Time E3 (during rotating stall); Left to right, cut plane 1 (4ε), cut plane 2 (1.5ε), cut plane 3 (0.5ε). (d) Left to right, front views of cut-plane 3 (0.5ε) at three time instants, E1, E2, and E3, negative axial velocity.

Interaction of Shock and Tip Clearance Flow. Interaction between the tip clearance flow and shock in transonic compressor has been cited as one of the initiators of spike disturbance. As

noted by Day [5], short-length spikes can be viewed as embryonic stall cells with flow breakdown in local regions; it is a 3D phenomenon. Computational simulations using a single blade passage

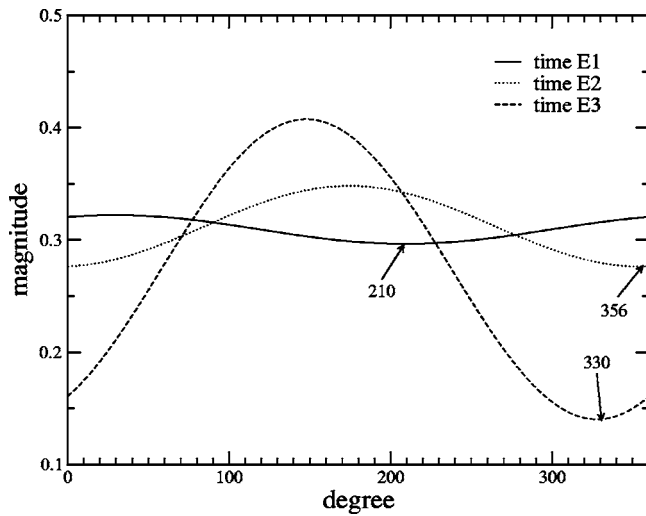


Fig. 14 First mode disturbances of axial momentum at rotor tip

to study the effect of the tip clearance flow on the onset of stall were reported by Adamczyk et al. [26]. One generally agreed conclusion is that the tip clearance vortex moves forward from stable to stall condition. Using vortex kinematics arguments, Hoying et al. [7] developed a criterion for stall inception when the trajectory of the tip clearance vortex becomes perpendicular to the axial direction. Vo et al. [8] also demonstrated that stall inception is most likely accompanied by the forward spillage of tip clearance vortex. One might ask the following: How does the shock interact with the tip clearance flow? Does the shock directly cause flow separation that may contribute to the stall inception?

To answer these questions, we take a closer look at the flow within the rotor passage. A comparison of pressure contours near the casing between the stable and near-stall (Time E1) conditions is made in Fig. 15. In the stable condition, the pressure fields in the two passages shown are almost identical. There exists a distinguishable attached oblique passage shock, which originates from the leading edge of the rotor blade and extends across the passage to 80% chord on the suction surface of the adjacent blade. At Time E1, the pressure fields between passages are no longer identical. Even though the flow structure is not identical among

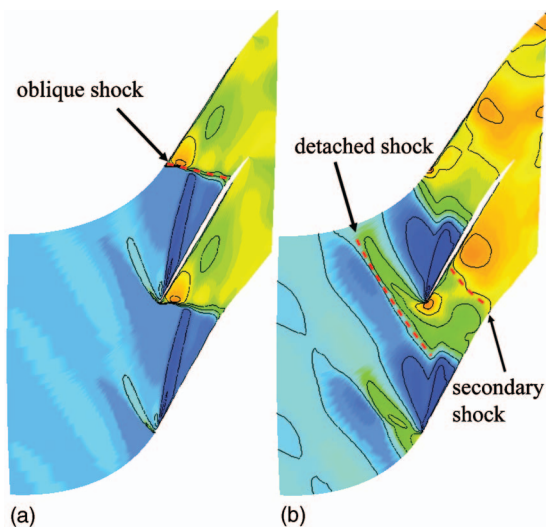


Fig. 15 Pressure contour near casing: (a) Stable condition and (b) near-stall condition (Time E1)

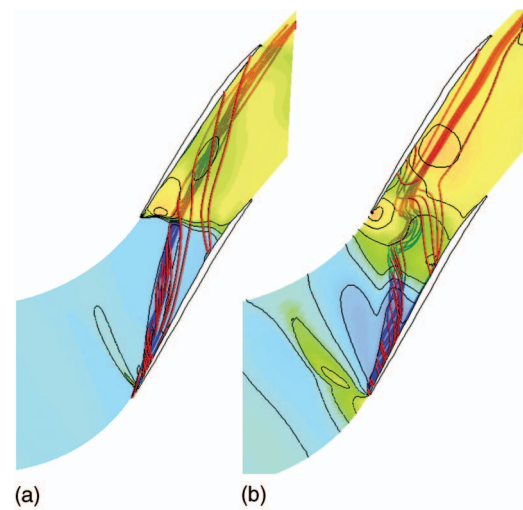


Fig. 16 Streamlines forming the tip clearance vortex: (a) Stable condition and (b) near-stall condition (Time E1)

passages, there is still similarity between them before the flow breakdown. We will discuss the common features that are generic for the rotor passages before stall. Examining the pressure field at Time E1, we see that the single attached oblique shock now changes to a more complicated dual-shock system: A strong detached shock followed by a weaker secondary shock. The strong detached shock, together with the stagnant flow around the leading edge, creates a high pressure region near the leading edge of the pressure surface. The pressure outside this area is relatively low until aft of the secondary shock where the pressure level rises again to fill uniformly between the blades.

Streamlines forming the tip clearance vortex for both stable and near-stall (Time E1) conditions are shown in Fig. 16. The pressure contour near the casing is overlaid in the background to help the discussion. First, take a look at the stable condition. Only the forward 15% portion of the tip clearance flow emerges to form the core of the tip clearance vortex. The trajectory of the tip clearance vortex is not perpendicular to the axial direction. The oblique shock intersecting the vortex only slightly alters the shape of the vortex. The vortex moves away from the pressure surface of the adjacent blade without impinging it.

At the near-stall condition (Time E1), Fig. 16(b), the core vortex, again formed by the forward 15% of the tip clearance flow, now moves forward. The center portion of the vortex trajectory becomes perpendicular to the axial direction. This trend follows well with the stall inception criterion of Hoying et al. [7]. However, the shape of the vortex trajectory is first pushed backward by the high pressure near the pressure surface leading edge and then forward by the high pressure behind the secondary shock as it proceeds downstream. This distortion of the vortex trajectory is caused by the dual-shock system. The criterion of Hoying et al. [7], developed for low-speed machines, still holds for areas not affected by the dual shock. It is unclear whether or not the distorted vortex can accelerate the flow breakdown, but it is clear that the distortion occurs as the flow is close to stall with the existence of the dual shock.

Flow is likely to separate due to the shock-boundary layer interaction, in which the low momentum flow in the boundary layer is subjected to the sudden pressure rise across the shock. Thus, it is of interest to examine whether shock-induced flow separations occur in the simulation. There are two possible locations for flow separation in the rotor passage: One is on the suction surface and the other is on the casing surface. By examining the streamlines in Fig. 16, we rule out the suction surface separation. To search for the casing separation, the velocity vector in the meridional view is examined. Figure 17(a) shows such a plane 30% pitch off the

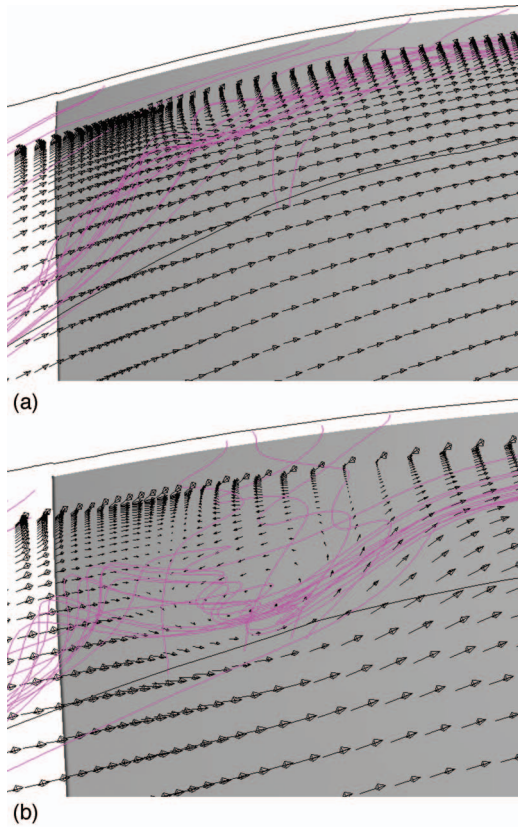


Fig. 17 Velocity vector on a meridional plane 30% pitch off pressure surface: (a) Stable condition and (b) near-stall condition (Time E1)

pressure surface. There is no observable reverse flow in this view. This indicates that the vortex moves straight downstream and that the flow remains attached to the casing. At Time E1, the reverse flow associated with the distorted vortex can be seen in Fig. 17(b). The velocity vector shows that the flow reversal occurs beneath the casing and is caused by the organized spiraling fluids of the distorted vortex. There is no indication of casing separation at this instant. The cross section of the vortex, however, is larger than the stable condition. This also shows that the negative axial velocity of the rotor flow shown in Fig. 13 is caused by the spiraling fluids of the tip clearance vortex and has no association with casing or blade separation. With the above observations, we conclude that there is no shock-induced separation in this during the stall inception.

As the compressor proceeds more into stall between Times E2 and E3, the flow breaks down, i.e., the mass flow rate through the compressor is declines. The reverse flow in a few passages combines to form the large blockage as shown in Figs. 13(b) and 13(c), which in turn expels flow to adjacent blades. The blockage creates the spike-type disturbance over a few passages. The expelled flow entering the adjacent blade passages brings in extra axial momentum to the casing areas of these passages. The additional axial momentum behaves like tip injection, which reduces rotor incidence levels, relative to Time E1. The vortex shape and shock structure of two passages at Time E2 are compared in Fig. 18. Figure 18(a) is a passage where the spike occurs. The shape of the vortex trajectory and shock structure is similar to those at Time E1, Fig. 16(b), only that the vortex continues to grow and the high pressure behind the detached shock pushes the vortex backward so the trajectory moves away from being perpendicular to the axial direction. Spillage of tip clearance flow forward of the leading edge can be seen in Fig. 19(a), where it is colored by the

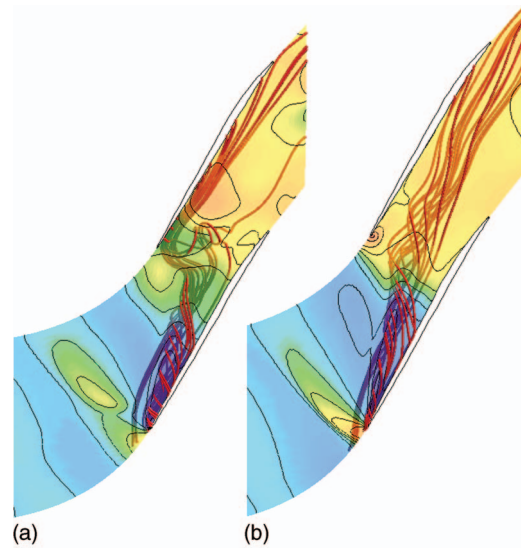


Fig. 18 Tip clearance vortex at Time E2: (a) Deteriorating passage and (b) improving passage

pink stream lines. In the passage where the flow condition improved, as shown in Fig. 18(b), the dual-shock system returns to a single shock and the vortex trajectory is not distorted. There is no spillage of the tip clearance flow forward of the leading edge, Fig. 19(b).

Simulation Summary

1. The simulation results of the high-speed axial compressor Stage 35 provide evidence that the current numerical procedure may be adequate for predicting the onset of flow instabilities and their subsequent growth into a fully developed rotating stall. The simulation results clearly show a full-annulus first mode disturbance starting to travel at 100% rotor speed at the peak of the pressure rise transitioning to a spike disturbance traveling at 84%

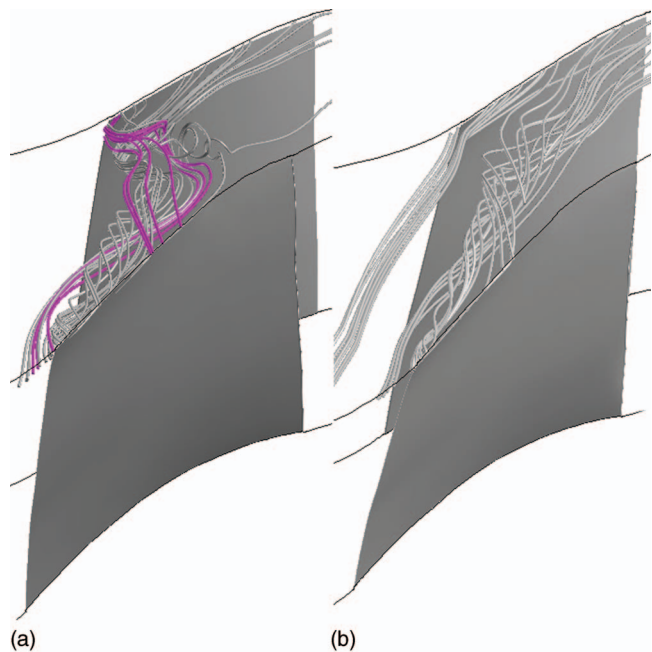


Fig. 19 Tip clearance flow showing spillage over rotor leading edge at Time E2 (a) spillage in deteriorating passage and (b) no spillage in improving passage

rotor speed. This spike disturbance then splits into multiple stall cells while their speeds reduce. Finally the multiple stall cells coalesce into a large single stall cell that rotates at 43% of rotor speed when fully developed. This simulation models the natural growth of the stall process without the use of an artificial inlet distortion.

2. As the simulation is throttled to stall, small amplitude long-length waves of 1st mode and high-order modes between the 1st and the 36th can be discerned. The magnitudes of the high-order modes fluctuate but do not grow much during the transition to stall. The first mode wave, however, persistently grows before breakdown. A short-length disturbance covering five rotor passages bursts into a spike like disturbance during the breakdown. This spike disturbance then grows into a rotating stall.

3. The computed first mode disturbance has a length scale closely resembling the one rotor circumference disturbance prior to stall in the experiment. The computed speed of the first mode disturbance (100% rotor speed) is also similar to the measured speed (80% rotor speed) of the first mode disturbance from the experiment, estimated from the results of Fig. 2. The difference is within the resolution of the picture quality of the published data.

4. The first mode of the axial momentum correlates well with the appearance of the growing reverse flow. The trough of the axial momentum matches the region of the larger reverse flow that leads to the birth of the initial spike.

5. The interaction of the shock and tip clearance vortex is examined. As the compressor approaches stall, the trajectory of the tip clearance vortex moves forward to become perpendicular to the axial direction. The shock system, in the meantime, also moves forward, changing from an attached oblique single shock to a dual shock. The pressure field of the dual-shock system distorts the trajectory of the tip clearance vortex, creating a large reverse flow region in the distorted vortex. The reverse flow in the rotor is the outward tip clearance vortex as no shock-induced casing or blade separation is found.

6. During the flow breakdown, spillage of the tip clearance flow forward of the rotor leading edge is found in several passages, where the flow condition is deteriorating. A large blockage region is formed in the deteriorating passages; this in turn impels flow to enter into adjacent passages. The influx of fluid momentum in the adjacent passages improves the flow condition there.

Conclusions

The TURBO code has been applied to the 3D full-annulus simulation of a transonic compressor stage NASA Stage 35 to investigate the flow evolution prior to stall. This simulation does not include the system volume, and therefore cannot model the surge mode oscillation that arises from the test facility ducting system. With the surge mode removed, the stalling flow first takes the form of a rotating long-length (modal) disturbance; it then changes into a spike. The spike seems to grow out of the long-length disturbance and eventually leads to stall. The spike emerges when the tip clearance vortex becomes perpendicular to the axial direction and, in some passages, with forward spillage. The passage shock changes from single shock to dual shock when approaching stall. The dual shock distorts the trajectory of the vortex but does not cause flow separation that directly contributes to the stall. The simulation correlates well with the experiment data excluding the surge mode. The computational resources involved in conducting such a simulation are prohibitively large at the time and are not suitable for routine executions. While this is certainly an issue, the key point is that the simulations of this type

generate qualitatively and quantitatively accurate flow field data that can support our understanding and inferences of the unsteady compressor flow field, including support and interpretation of experimental work.

Acknowledgment

The authors would like to acknowledge the invaluable discussions and technical advises from Dr. John Adamczyk, Dr. Dale Van Zante, Dr. Gerard Welch, and Dr. Tony Strazisar of NASA Glenn Research Center, and Dr. Choon Tan, Dr. Yifang Gong, and Professor Edward Greitzer of MIT Gas Turbine Laboratory. Thanks to Mr. Sean Barrows, Mr. Trevor Goerig, and Mr. Benjamin Johnson of The Ohio State University for their hard work in preparing the manuscript. The high-performance computing resources are provided by DoD Grand Challenge Project, Ohio Supercomputing Center, and IBM. Financial support comes from AVETEC, with Robert Evans Miller as project manager, and Army Research Office, with Thomas Doligalski as project manager. These supports are greatly appreciated.

References

- [1] Moore, F. K., and Greitzer, E. M., 1986, "A Theory of Post-Stall Transients in Axial Compressors—Part I: Development of the Equations," *ASME J. Eng. Gas Turbines Power*, **108**, pp. 68–76.
- [2] McDougall, N. M., 1988, "Stall Inception in Axial Compressors," Ph.D. thesis, Cambridge University, Cambridge.
- [3] Garnier, V. H., Epstein, A. H., and Greitzer, E. M., 1991, "Rotating Waves as a Stall Inception Indication in Axial Compressors," *ASME J. Turbomach.*, **113**, pp. 290–302.
- [4] Camp, T. R., and Day, I. J., 1998, "Study of Spike and Modal Stall Phenomenon in a Low-Speed Axial Compressor," *ASME J. Turbomach.*, **120**(3), pp. 393–401.
- [5] Day, I. J., 1993, "Stall Inception in Axial Flow Compressors," *ASME J. Turbomach.*, **115**, pp. 1–9.
- [6] Cumpsty, N. A., 2004, *Compressor Aerodynamics*, Krieger, Malabar, FL.
- [7] Hoying, D. A., Tan, C. S., Vo, H. D., and Greitzer, E. M., 1998, "Role of Blade Passage Flow Structures in Axial Compressor Rotating Stall Inception," *ASME J. Turbomach.*, **121**, pp. 735–742.
- [8] Vo, H. D., Tan, C. S., and Greitzer, E. M., 2005, "Criteria for Spike Initiated Rotating Stall," ASME Paper No. GT2005-68374.
- [9] Davis, R. L., and Yao, J., 2006, "Prediction of Compressor Stage Performance From Choke Through Stall," *J. Propul. Power*, **22**(3), pp. 550–557.
- [10] Gong, Y., Tan, C. S., Gordon, K. A., and Greitzer, E. M., 1999, "A Computational Model for Short Wavelength Stall Inception and Development in Multistage Compressors," *ASME J. Turbomach.*, **121**, pp. 726–734.
- [11] He, L., 1997, "Computational Study of Rotating-Stall Inception in Axial Compressors," *J. Propul. Power*, **13**(1) pp. 31–38.
- [12] Saxer-Felici, H. M., Saxer, A. P., Inderbitzin, A., and Gyarmathy, G., 2000, "Numerical and Experimental Study of Rotating Stall in an Axial Compressor Stage," *AIAA J.*, **38**(7) pp. 1132–1141.
- [13] Chen, J. P., Webster, R. S., Hathaway, M. D., Herrick, G. P., and Skoch, G. J., 2006, "Numerical Simulation of Stall and Stall Control in Axial and Radial Compressors," AIAA Paper No. AIAA-2006-418.
- [14] Hah, C., Bergner, J., and Schiffer, H.-P., 2006, "Short Length-Scale Rotating Stall Inception in a Transonic Axial Compressor—Criteria and Mechanisms," ASME Paper No. GT2006-90045.
- [15] Hathaway, M. D., Chen, J., Webster, R., and Herrick, G. P., 2004, "Time Accurate Unsteady Simulations of the Stall Inception Process in the Compression System of a U.S. Army Helicopter Gas Turbine Engine," 2004 DoD High Performance Computing Modernization Program User's Group Conference, Williamsburg, VA, June 7–10.
- [16] Reid, L., and Moore, R. D., 1978, "Performance of Single-Stage Axial-Flow Transonic Compressor with Rotor and Stator Aspect Ratios of 1.19 and 1.26, Respectively, and With Design Pressure Ratio of 1.82," NASA Technical Report No. TP-1338.
- [17] Bright, M. M., Qammar, H. K., and Wang, L., 1999, "Investigation of Pre-Stall Mode and Pip Inception in High-Speed Compressors Through the Use of Correlation Integral," *ASME J. Turbomach.*, **121**, pp. 743–750.
- [18] Chen, J. P., and Whitfield, D. L., 1993, "Navier-Stokes Calculations for the Unsteady Flowfield of Turbomachinery," AIAA Paper No. AIAA-93-0676.
- [19] Chen, J. P., and Briley, W. R., 2001, "A Parallel Flow Solver for Unsteady Multiple Blade Row Turbomachinery Simulations," ASME Paper No. GT-2001-348.
- [20] Chen, J. P., and Barter, J., "Comparison of Time-Accurate Calculations for the Unsteady Interaction in Turbomachinery Stage," AIAA Paper No. AIAA-98-3293.
- [21] Kirtley, K. R., Beach, T. A., and Adamczyk, J. J., 1990, "Numerical Analysis of Secondary Flow in a Two-Stage Turbine," AIAA Paper No. AIAA-90-2356.
- [22] Van Zante, D. E., Strazisar, A. J., Wood, J. R., Hathaway, M. D., and Okishi, T. H., 2000, "Recommendations for Achieving Accurate Numerical Simulation

- of Tip Clearance Flows in Transonic Compressor Rotors," ASME J. Turbomach., **122**, pp. 733–742.
- [23] Chima, R. V., 1998, "Calculation of Tip Clearance Effects in a Transonic Compressor Rotor," ASME J. Turbomach., **120**, pp. 131–140.
- [24] Spakovszky, Z. S., Weigl, H. J., Paduano, J. J., van Schalkwyk, C. M., Suder, K. L., and Bright, M. M., 1999, "Rotating Stall Control in a High-Speed Stage With Inlet Distortion: Part I—Radial Distortion," ASME J. Turbomach., **121**, pp. 510–516.
- [25] Suder, K. L., Hathaway, M. D., Thorp, S. A., Strazisar, A. J., and Bright, M. M., 2001, "Compressor Stability Enhancement Using Discrete Tip Injection," ASME J. Turbomach., **123**, pp. 14–23.
- [26] Adamczyk, J. J., Celestina, M. L., and Greitzer, E. M., 1993, "The Role of Tip Clearance in High-Speed Fan Stall," ASME J. Turbomach., **115**, pp. 28–38.
- [27] Weigl, H. J., Paduano, J. D., Frechette, L. G., Epstein, A. H., Greitzer, E. M., Bright, M. M., and Strazisar, A. J., 1998, "Active Stabilization of Rotating Stall and Surge in a Transonic Single Stage Axial Compressor," ASME J. Turbomach., **120**(4), pp. 625–636.

Large Eddy Simulation of Leading Edge Film Cooling—Part II: Heat Transfer and Effect of Blowing Ratio

Ali Rozati

Danesh K. Tafti

High Performance Computational Fluid-Thermal
Sciences and Engineering Laboratory,
Mechanical Engineering Department,
Virginia Polytechnic Institute and State
University,
Blacksburg, VA 24061

Detailed investigation of film cooling for a cylindrical leading edge is carried out using large eddy simulation (LES). The paper focuses on the effects of coolant to mainstream blowing ratio on flow features and, consequently, on the adiabatic effectiveness and heat transfer coefficient. With the advantage of obtaining unique, accurate, and dynamic results from LES, the influential coherent structures in the flow are identified. Describing the mechanism of jet-mainstream interaction, it is shown that as the blowing ratio increases, a more turbulent shear layer and stronger mainstream entrainment occur. The combined effects lead to a lower adiabatic effectiveness and higher heat transfer coefficient. Surface distribution and span-averaged profiles are shown for both adiabatic effectiveness and heat transfer (presented by Frossling number). Results are in good agreement with the experimental data of Ekkad et al. [1998, "Detailed Film Cooling Measurement on a Cylindrical Leading Edge Model: Effect of Free-Stream Turbulence and Coolant Density," ASME J. Turbomach., 120, pp. 799–807].
[DOI: 10.1115/1.2812411]

1 Introduction

Detailed knowledge of film cooling flow physics is necessary to improve cooling efficiency. The dynamics of coolant and mainstream mixing are dependent on various factors such as mass flux ratio, mainstream turbulence, angle of injection, and shape of the coolant hole. Among these factors, investigation of the effect of mass flux ratio is not only important to obtain the maximum film cooling effectiveness but also essential to determine the minimum amount of coolant flow needed for effective surface protection from hot free stream gases.

Early studies investigated the effects of blowing ratio on flat plate film cooling, such as the experimental study of Honami and Shizawa [1], in which the coolant was laterally injected on a flat plate. Time averaged data of the temperature field were measured on the cross-sectional planes downstream of the coolant hole. These data showed the existence of an asymmetric coolant jet, with mainstream hot gas entrainment occurring from the coolant jet's aftside. They observed that mainstream entrainment strengthened as the mass flux ratio increased and caused more coolant lift-off from the surface downstream of the coolant hole, resulting in lower effectiveness. Mayhew et al. [2] also investigated the effect of blowing ratio on a flat plate with compound angle of injection. Their observations on film cooling effectiveness were similar to that of Honami and Shizawa. They suggested that the asymmetric counter-rotating vortex pair governs the enhancement of heat transfer coefficient. In low free stream turbulence, as blowing increased, the counter-rotating vortex pair became stronger and augmented the heat transfer coefficient.

In another study on flat plate film cooling with streamwise coolant injection, Kaszeta and Simon [3] investigated the transport of turbulence by measuring the eddy diffusivity of momentum in the spanwise and cross-stream directions. The primary structure of the counter-rotating vortex pair appeared to be slightly asymmetric.

The cross-stream to spanwise eddy diffusivity ratio showed values up to 2.5, which indicated an anisotropic flow even for the streamwise injection. Their results showed that the anisotropy in the turbulent transport is too complex to be modeled by simple anisotropy models such as the model of anisotropy of Bergeles et al. [4], although previous studies had shown some success (see Refs. [5,6]).

The experimental setup of Honami and Shizawa was also simulated by Lakehal et al. [7] and they showed that a standard $k-\epsilon$ model could not predict the flow accurately. Namely, it underpredicted the lateral coverage of the coolant and the strength of the vortex pair. A two layer approach was used to resolve the near-wall region with a one-equation model. However, it led to overprediction of the strength of the vortex pair, while the lateral coverage was still underpredicted. Muldoon and Acharya [8] applied the direct numerical simulation (DNS) method on a flat plate film cooling flow field to compare the exact and modeled turbulent diffusions. The comparison showed that $k-\epsilon$ models tend to overpredict the eddy viscosity. They proposed a damping function to reduce the eddy viscosity.

Understanding the details of flow physics of flat plate film cooling sheds some light on the phenomenon. However, to investigate film cooling physics on the blade leading edge, the geometry should represent the complexity of the region while maintaining domain simplicity to enable to conduct experimental measurements and numerical simulations. A cylindrical leading edge with a flat afterbody provides such features. Mouzon et al. [9], Yuki et al. [10], and Cruse et al. [11] used an experimental setup of a cylindrical leading edge with three rows of film cooling holes placed at stagnation and ± 25 deg from the stagnation line to investigate leading edge film cooling. Film cooling adiabatic effectiveness measurements were conducted in Refs. [9,11] with a coolant to mainstream density ratio of 1.8, and heat transfer measurements in Refs. [9,10] were conducted at a density ratio of 1.0. Additionally, Mouzon et al. [9] used fan-shaped holes in their study. Despite this difference, results showed that the heat transfer coefficient increased with increase in the blowing ratio for both low and high freestream turbulences. At density ratio of 1.8, adia-

Contributed by the International Gas Turbine Institute of ASME for publication in the JOURNAL OF TURBOMACHINERY. Manuscript received June 8, 2007; final manuscript received June 20, 2007; published online August 4, 2008. Review conducted by David Wisler. Paper presented at the ASME Turbo Expo 2007: Land, Sea and Air (GT2007), Montreal, Quebec, Canada, May 14–17, 2007.

batic effectiveness increased with increase of blowing ratio, but the augmentation was not considerable in the presence of high free stream turbulence.

Ekkad et al. [12] observed that the jet-mainstream interaction and Frossling number increased with increase of the blowing ratio. Adiabatic effectiveness dropped with an increase in blowing ratio at a density ratio of 1.0. However, as observed in Refs. [9,11], at a density ratio of 1.5, an increase in blowing ratio increased the effectiveness.

Azzi and Lakehal [13] observed that applying an isotropic $k-\epsilon$ model to predict leading edge film cooling resulted in an exaggerated size of the kidney shape vortex and an underprediction of the lateral spreading of the coolant. The discrepancies with experimental results grew with increase of the blowing ratio. This problem arises due to the stronger transport of turbulence in the lateral direction rather than normal to the wall. They improved their results by applying a two layer approach, which resolves the near-wall region with a one-equation DNS based anisotropic model. However, this method required high grid resolution near the surface and, therefore, their results for the leading edge film cooling were not as satisfactory as the results for flat plate film cooling.

Based on the limitations and inaccuracies in film cooling simulations with Reynolds-Averaged Navier-Stokes (RANS) models, an alternative approach to simulate this phenomenon is large eddy simulation (LES), which resolves the large anisotropic turbulent scales of the flow field while only modeling the smaller isotropic scales. The availability of accurate time-dependent results from LES enables the identification of key elements in the flow physics and their contribution to film cooling efficiency.

2 Objective of the Study

LES is proposed to investigate the leading edge film cooling flow. The primary goal is to achieve a thorough understanding of the film cooling dynamics with the temporal resolution provided by LES. In particular, identifying coherent structures and their role in driving the hot gas entrainment is of interest. Since all previous numerical studies at the leading edge have applied RANS models to simulate the flow field, this investigation is the first to report on the dynamic flow structures that are not resolved with the same clarity in steady simulations.

Additionally, the effects of the coolant to mainstream blowing ratio on adiabatic effectiveness and heat transfer are investigated. These effects have been studied experimentally and numerically (using the RANS method) before. However, the current work elucidates how the variation in blowing ratio affects the flow features and consequently the adiabatic effectiveness and heat transfer coefficient.

3 Solution Methodology

The governing flow and energy equations are nondimensionalized by the characteristic length and velocity scales of cylinder diameter (D) and free stream velocity (u_∞), respectively. Characteristic temperatures of ($T_\infty - T_c$) and $q_w'' D / k$ are selected when calculating the adiabatic effectiveness and heat transfer coefficient, respectively. The dynamic Smagorinsky model is used to obtain the eddy viscosity of the subgrid scales. The nondimensional time-dependent Navier-Stokes and energy equations in transformed coordinates are given in Ref. [14]. The governing equations of momentum and energy are discretized with a conservative finite volume formulation using a second-order central difference scheme. The temporal advancement is performed with a predictor-corrector algorithm. Detailed information can be found from Tafti [15].

The computational domain is adopted from an experimental study by Ekkad et al. [12], where the leading edge is represented by a cylinder with a tailboard placed at the rear of the cylinder. Rozati and Tafti [14] established that this geometry can be repre-

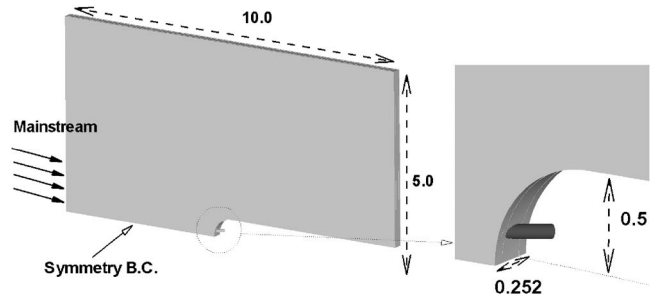


Fig. 1 Computational domain

sented by the domain shown in Fig. 1, where a symmetry boundary condition is imposed along the stagnation line.

The free stream Reynolds number is 100,000 based on the cylinder diameter, coolant to mainstream blowing ratios are 0.4 and 0.8, and density ratio is unity. In calculations of the adiabatic effectiveness, the nondimensional temperature of the coolant and mainstream are set to zero and unity, respectively. An adiabatic no-slip wall boundary condition is imposed on the surface. Adiabatic effectiveness is defined as

$$\eta = \frac{T_{ad,w} - T_\infty}{T_c - T_\infty} = 1 - \theta_{ad,w} \quad (1)$$

where θ is the nondimensional temperature:

$$\theta = \frac{T - T_c}{T_\infty - T_c} \quad (2)$$

In the calculation of the heat transfer coefficient, both the coolant and mainstream nondimensional temperatures are set to zero, while the blade surface has a constant nondimensional heat flux of unity. The local Nusselt number is calculated as the local temperature difference between the surface and reference temperatures:

$$Nu = \frac{1}{\theta_i - \theta_{ref}} \quad (3)$$

where the free stream temperature is selected as the reference temperature and $\theta_{ref} = 0.0$.

The coolant pipe inlet boundary condition is provided from an auxiliary fully developed, time-dependent, turbulent pipe flow calculation, from which time-dependent profiles of the velocity field are extracted and fed into the coolant pipe inlet. Effects of the coolant inlet velocity profile, accuracy, and validity of the auxiliary calculation are given in Ref. [14]. The grid contains 62 hybrid structured/unstructured blocks with the total size of 3,211,264 cells. The grid is highly resolved in the vicinity of the coolant hole and coolant pipe and normal to the cylinder blade surface. A posteriori results show that the value of y^+ at the first point from the surface is less than 1 and adequate numbers of grid points lie within the distance of $0 < y^+ < 10$ [14].

4 Results and Discussion

The calculations are carried out on Virginia Tech's Terascale computing facility, SystemX, on 2.3 GHz PowerPC 970FX processors on 62 processors. The nondimensional time step is set to 2×10^{-5} . Each time step takes approximately 4.5 s of wall clock time. The flow is allowed to develop for approximately three time units before averaging for time mean quantities is activated. The results explain the flow physics of film cooling, coherent structures, adiabatic effectiveness, and heat transfer coefficients for two blowing ratios of 0.4 and 0.8.

4.1 Coherent Structures. The dominant coherent structures for a classical jet in cross flow are a counter-rotating vortex pair in the wake of the jet, a horseshoe vortex on the windward side of the jet, and shear layer vortices (see Refs. [16,17]). To identify the

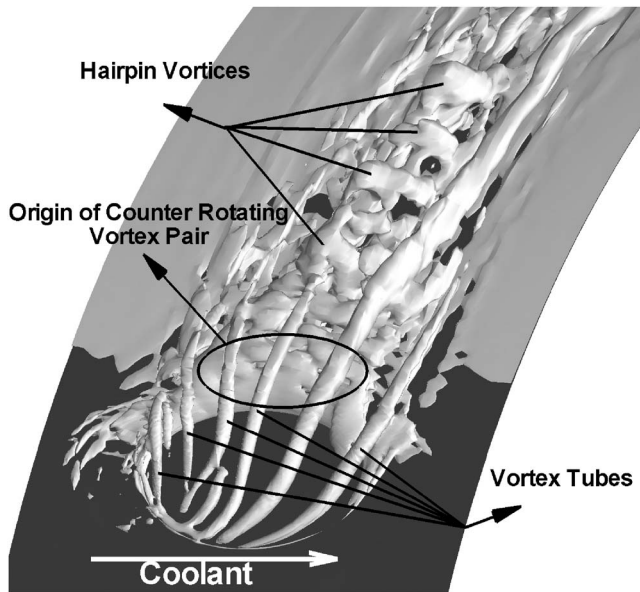


Fig. 2 Coherent structures, B.R.=0.4 (isosurface value=18)

coherent structures in the present study, the vortex eduction technique proposed by Chong et al. [18] is used. In this method, in regions dominated by vortical motion, the velocity gradient tensor exhibits two eigenvalues that are complex conjugate. The magnitude of the eigenvalue is indicative of the strength of the vortex. The structures identified by this method are referred to as “coherent vorticity” in this paper and the magnitude of the eigenvalue is identified as the strength of the vortices.

The following definition is used to describe the location of flow/structures. In the lateral direction, the side that the jet blows from is specified with “aft” and the side the jet blows to is specified with “fore.” In the streamwise direction along the blade surface, “leeward” is used to denote the downstream side of the jet and “windward” is used to denote the upstream side of the jet. Figure 2 shows an instantaneous snapshot of coherent vorticity for blowing ratio (B.R.)=0.4. An immediate observation is the complete absence of a horseshoe vortex. This is due to the combination of the low injection ratio and the compound angle injection. Immediately downstream of the coolant hole, a low pressure region exists, which was shown in Ref. [14] and is repeated in Fig. 3. The existence of a low pressure region was also observed in a flat plate film cooling study by Muldoon and Acharya [8]. This low pressure region is responsible for creating a strong counter-rotating vortex pair, which entrains hot mainstream gases underneath the jet. The primary structure forms immediately at the leeward edge of the hole (Fig. 2) and is transported downstream to form packets of hairpin vortices. This agrees with the observations of Tyagi and Acharya [16] for a jet in cross flow in a flat plate boundary layer. However, due to the asymmetry of the low pressure region, the strength of these counter-rotating vortices is not equal, and the structure at the aft side of the jet has considerably higher strength and size due to the lateral direction of coolant injection.

Compared to a classical jet in cross flow, additional structures in the form of vortex tubes appear at the windward side of the jet. They are instabilities produced by the interaction of the transverse jet velocity and the mainstream flow. These vortex tubes originate from the windward side of the coolant hole and bend toward the mainstream direction, on top of the hairpin vortices. It is noted that the vortex tubes are not stationary structures but constantly move fore to aft along the windward rim of the hole. Vortex tubes on the top of the coolant jet break down within one to two diameters downstream of the jet, while the tubes at the aft and fore

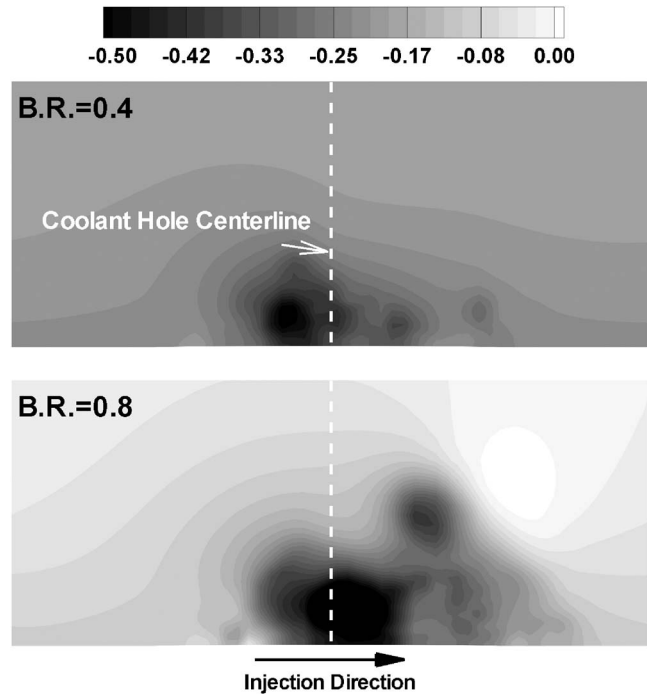


Fig. 3 Pressure contour at $x/d=1.0$ downstream of the coolant hole

edges of the hole are stronger and directly participate in the jet-mainstream dynamics. One of these tubes is seen to extend at least $6d$ downstream of the jet, aiding the entrainment of hot gases.

Figure 3 compares the size and magnitude of the low pressure region at $x/d=1.0$ downstream of the coolant hole for the two B.R.'s. Contours show the instantaneous distribution of pressure with the same level in coloring. As shown, with an increase of the B.R., the low pressure region is shifted to the fore side due to higher lateral momentum of the coolant. The pressure difference within and outside of the coolant core increases drastically at B.R.=0.8, which results in much stronger entrainment from the aft side of the coolant jet.

A snapshot of the coherent structures at the B.R. of 0.8 is shown in Fig. 4. The magnitude of the vorticity isosurface is the

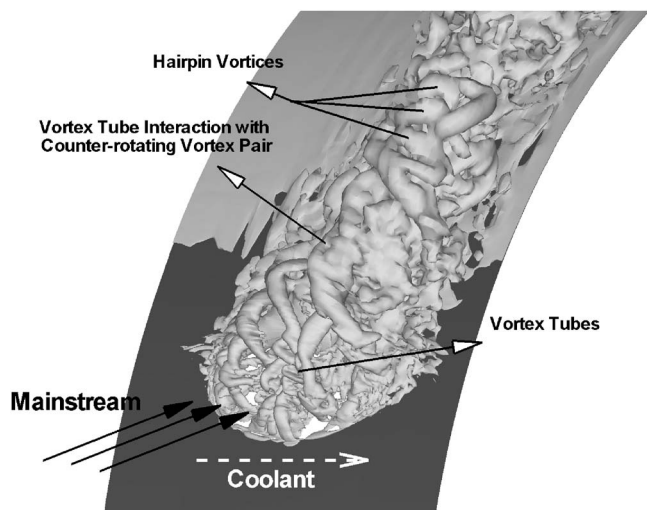


Fig. 4 Coherent structures, B.R.=0.8 (isosurface value=18)

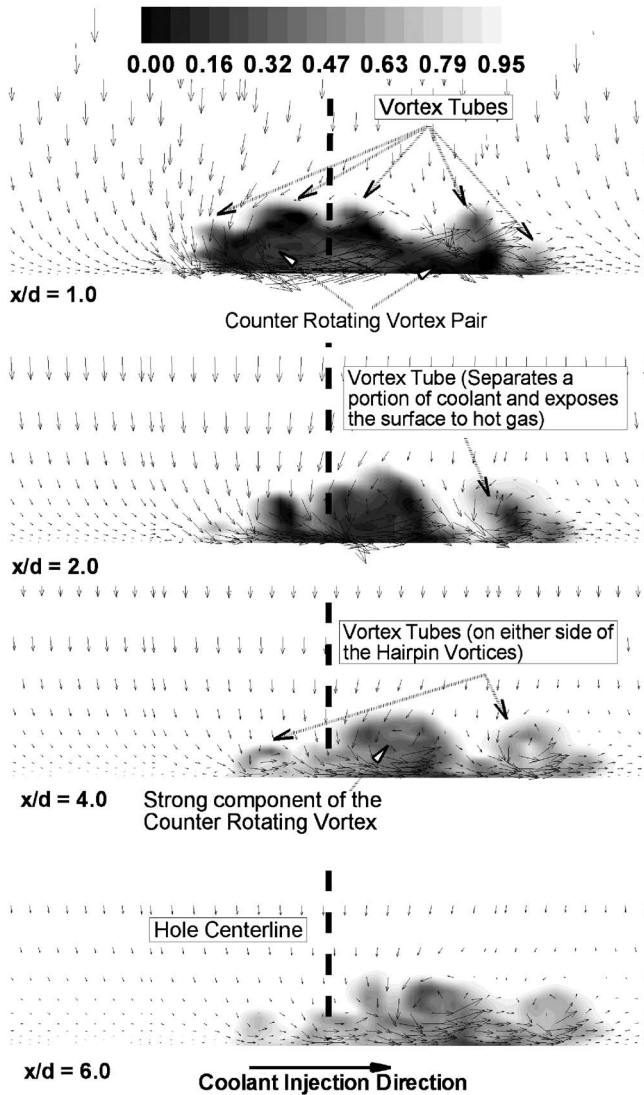


Fig. 5 Temperature contour and velocity vectors on cross-sectional planes normal to the surface and downstream the hole (B.R.=0.4)

same as for Fig. 2. An intensified turbulent region with smaller scale eddies is observed at the coolant hole exit. Vortex tubes now originate inside the coolant hole versus at the jet-mainstream interface outside the hole at the low B.R. Contrary to the previous case where the vortex tubes bent toward the surface, at B.R.=0.8, vortex tubes do not maintain their streamwise trajectory. Strong entrainment from the aft side of the coolant hole disrupts and twists some of the vortex tubes in that direction and the remaining take a hairpin shape and transport downstream of the coolant hole. Contrary to the results at the lower B.R., vortex tubes do not have any discernible individual effect in entraining hot gases at the aft/fore side of the coolant jet.

4.2 Coolant-Mainstream Mixing Mechanism. Figure 5 explains the jet-mainstream interaction mechanism by means of instantaneous temperature contours and velocity vectors in planes normal to the blade surface and downstream of the jet. At $x/d = 1.0$, one can identify vortex tubes on the top and sides of the counter-rotating vortex pair. The strength of the main counter-rotating vortex aided by the outer vortex tubes near the aft side causes the bulk of the hot gas entrainment. As the jet travels downstream ($x/d = 2.0$), the strength of the primary counter-

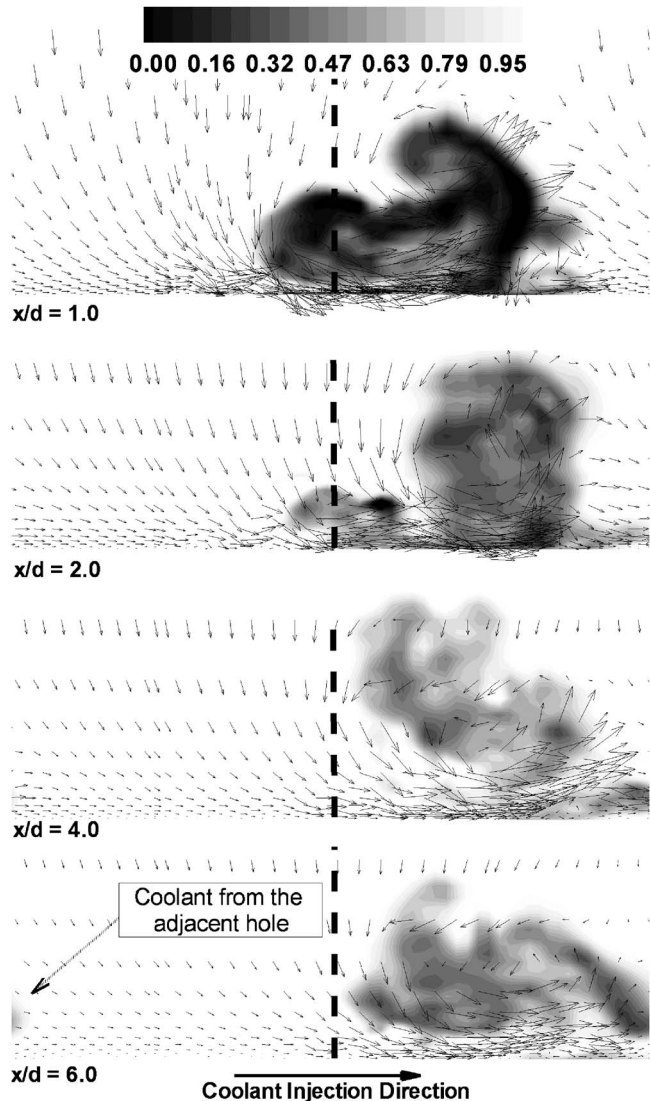


Fig. 6 Temperature contour and velocity vectors on cross-sectional planes normal to the surface and downstream the hole (B.R.=0.8)

rotating vortex decreases. Eventually, at $x/d = 4.0$, the weak component of the counter-rotating vortex pair, at the fore side of the jet, disappears. As mentioned earlier, vortex tubes travel on the top and sides of the primary vortex structure. The tubes located at the top join with the stronger component of the counter-rotating vortex pair and contribute to entraining hot gas into the coolant from the aft side. Vortex tubes located at the sides of the primary structure remain intact and separate. At $x/d = 2.0$, the vortex tube on the fore edge of the coolant is seen to entrain hot gases. The side vortex tubes periodically cause the coolant flow to break off and join again with the main portion of the coolant jet. Due to the lateral velocity component of the coolant, it is observed that at $x/d = 6.0$, the jet completely shifts to the fore side.

The instantaneous results of temperature contours and velocity vectors are presented at the same cross-sectional planes for the B.R. of 0.8 (Fig. 6). The planes in both Figs. 5 and 6 have the same scale in the spanwise and cross-stream directions. One can immediately notice that at the higher B.R., the coolant jet has a stronger infiltration into the mainstream and stronger shear interaction with the mainstream. The primary vortex is stronger and larger compared to the same structures (aft component of the counter-rotating vortex) at the lower B.R. As a result, a stronger

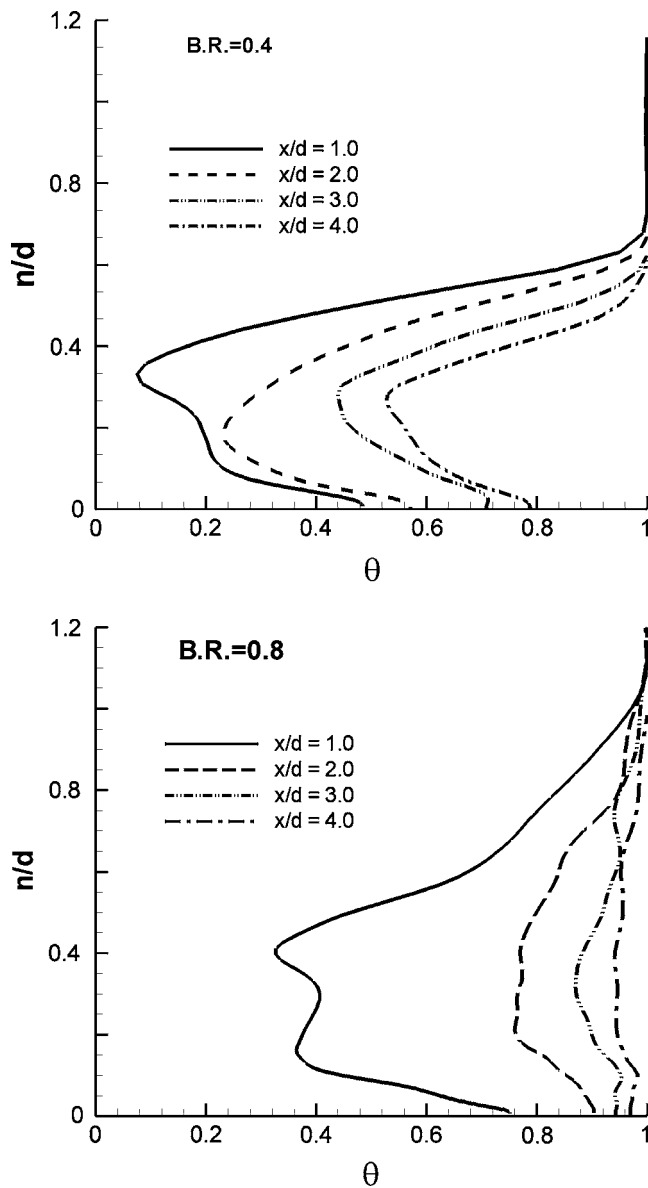


Fig. 7 Time averaged temperature profile normal to the wall at jet centerline

entrainment is observed from the aft side. Vortex tubes on the top of the coolant core merge with the primary structure at $x/d=2.0$. At $x/d=4.0$, the lateral momentum of the coolant shifts it to the fore side of the coolant hole completely. Unlike for the lower B.R., the coolant does not remain attached to the surface and at $x/d=6.0$, it is completely detached from the surface due to the stronger hot mainstream gas entrainment. Stronger shear layer mixing, entrainment of hot gases, and detachment of the coolant result in lower effectiveness of leading edge film cooling at the higher B.R. of 0.8 compared to 0.4. Additionally, due to the coolant jet lift-off from the surface, a narrower span coverage exists at $x/d=4.0$ and 6.0 downstream of the hole.

4.3 Mean Profiles. Figure 7 shows temperature profiles at the hole centerline and downstream of the hole for the two B.R.'s of 0.4 and 0.8. As observed in the previous section, at B.R.=0.8 and $x/d=2.0$, the higher momentum of the coolant has pushed it to the fore side of the coolant hole centerline. Therefore, the surface temperature on the centerline is close to the mainstream temperature after $x/d=2.0$ downstream of the hole, which results in low

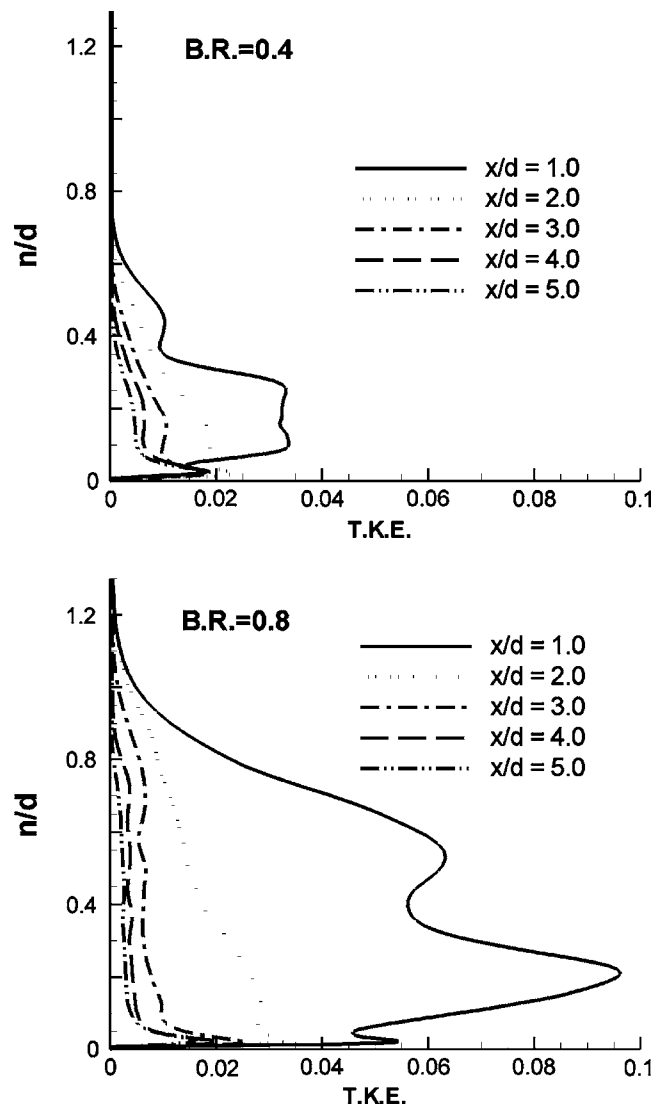


Fig. 8 T.K.E. profile normal to the wall at jet centerline

adiabatic effectiveness on the centerline. A stronger hot gas entrainment can also be observed close to the coolant hole at $x/d=1.0$. The coolant jet penetrates more into the free stream at the higher B.R. with the formation of a thicker thermal boundary layer. Temperature profile at $x/d=1.0$ shows that the core of the coolant is located at the distance of $0.1d-0.4d$ from the surface, where the mean temperature of the coolant core is much higher at B.R.=0.8. Temperature profile at $x/d=1.0$ also shows the stronger mixing at the coolant-mainstream shear layer for B.R.=0.8, while at B.R.=0.4, the local minimum at $0.3d$ from the surface is much lower than the local minimum at $0.1d$, and at B.R.=0.8, the two local minima have almost the same values due to the stronger mixing.

4.4 Turbulent Statistics and Kinetic Energy. Turbulent Kinetic Energy (T.K.E.) behavior along the streamwise direction is shown in Fig. 8 for both B.R.'s. The distributions are along the hole centerline, normal to the surface, and are only shown at five locations downstream of the coolant hole to aid in describing the flow development and identifying the major features of the turbulent field. Compared to the results with B.R.=0.4, the primary noticeable difference at B.R.=0.8 is the significantly higher values of T.K.E. especially at $x/d=1.0$ downstream of the coolant hole. At the same location, the thickness of the turbulent layer for

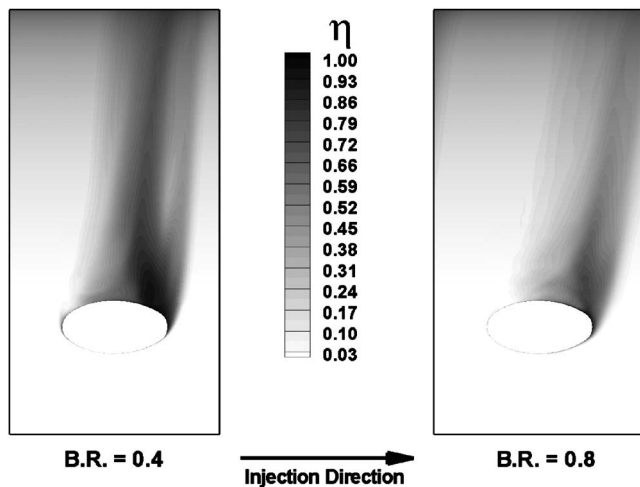


Fig. 9 Surface distribution of adiabatic effectiveness

B.R.=0.8 is two times larger than that at B.R.=0.4.

The highest values of T.K.E. at $x/d=1.0$ for both cases are located at a normal distance of $0.2d$ from the wall and are 0.03 and 0.1 for B.R.'s of 0.4 and 0.8, respectively. This peak is caused by the strong interaction of hot mainstream gases with the underbelly of the coolant jet. The peak close to the wall (0.02 and 0.055 at $x/d=1.0$ for B.R.=0.4 and 0.8, respectively) signals the formation of a turbulent boundary layer and is a result of the strong disturbances created by the lateral entrainment of flow. The merging and interaction of vortex tubes on the top of the primary vortex is responsible for the additional peak in the T.K.E. profile ($n/d=0.45$ and 0.6 for B.R.=0.4 and 0.8, respectively).

The low values of T.K.E. further downstream for B.R.=0.8 are a result of the shifting of the coolant core to the fore side of the centerline. However, in spite of this shift, a turbulent boundary layer is clearly represented in the profile very close to the surface, as it is for the lower B.R.

4.5 Adiabatic Effectiveness. Figure 9 compares the distribution of adiabatic effectiveness at the two B.R.'s of 0.4 and 0.8. While at B.R.=0.4, a portion of the coolant remains attached at the fore side and leeward rim of the coolant hole, at higher B.R.=0.8, it does not due to the combination of increased mixing and jet lift-off. At low B.R., mainstream momentum is much stronger than the coolant momentum and pushes the coolant toward the surface immediately downstream of the coolant hole. At higher B.R., stronger momentum of the coolant causes more mixing with the mainstream and stronger entrainment of hot gases, as discussed earlier. This entrainment eventually detaches the coolant from the surface and causes a narrower coverage of the coolant on the surface at B.R.=0.8. Also, the stronger lateral momentum of the coolant shifts it further to the fore side when compared to the lower B.R.

As expected, the spanwise average adiabatic effectiveness decreases as the B.R. increases (Fig. 10). Results at higher B.R. shows some discrepancies with the experimental data especially far downstream of the coolant hole ($x/d=6-7$). The experimental data show an increase in the adiabatic effectiveness at these locations. However, considering the experimental uncertainty of $\pm 6.8\%$ for the film cooling effectiveness measurements and the unavailability of the jet inlet conditions in the experiments, the results show acceptable agreement at both B.R.'s.

4.6 Heat Transfer Coefficient. Surface distribution of the Frossling number (Fig. 11) shows that for both B.R.'s a small region with high heat transfer is located at the fore side of the coolant hole rim. At B.R.=0.4, the counter-rotating vortex pair

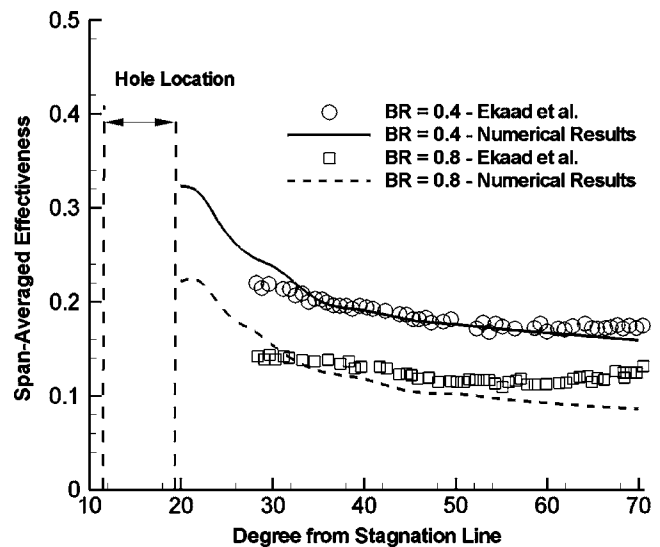


Fig. 10 Spanwise averaged adiabatic effectiveness distribution

and vortex tubes create high heat transfer regions at the fore and aft sides of the coolant hole centerline. At B.R.=0.8, the extent of the high heat transfer region is increased due to the stronger coherent structures, stronger entrainment, and jet-mainstream interaction, which lead to higher T.K.E. near the surface. In particular, compared to the lower B.R., higher values of Frossling number are observed at the aft side and close to the coolant hole. This is the direct effect of stronger entrainment of hot mainstream gases underneath the coolant at this location, as illustrated before.

The spanwise averaged Frossling number distribution (Fig. 12) shows good agreement with the experimental data (with $\pm 4.5\%$ uncertainty in heat transfer coefficient measurement). The heat transfer coefficient decreases downstream of injection due to the weakening of the coherent structures and the decay of near-wall turbulent intensities. An increase in B.R. enhances the heat transfer coefficient.

5 Summary and Conclusions

LES is used to investigate leading edge film cooling for two B.R.'s. For both B.R.'s, hot mainstream gases entrain underneath the coolant from the aft side of the coolant jet. However, this

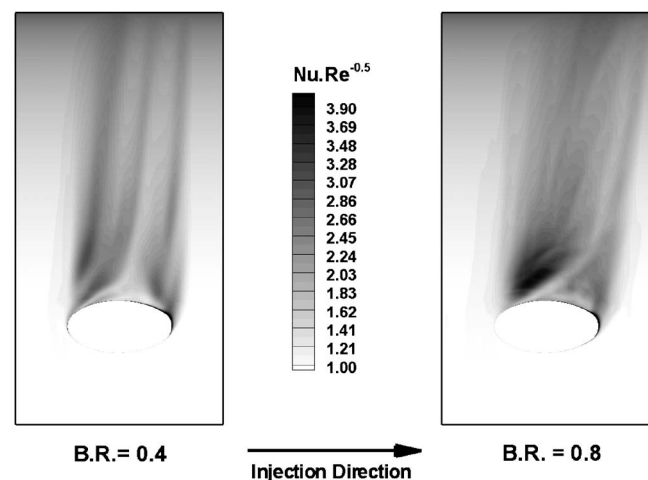


Fig. 11 Surface distribution of the Frossling number

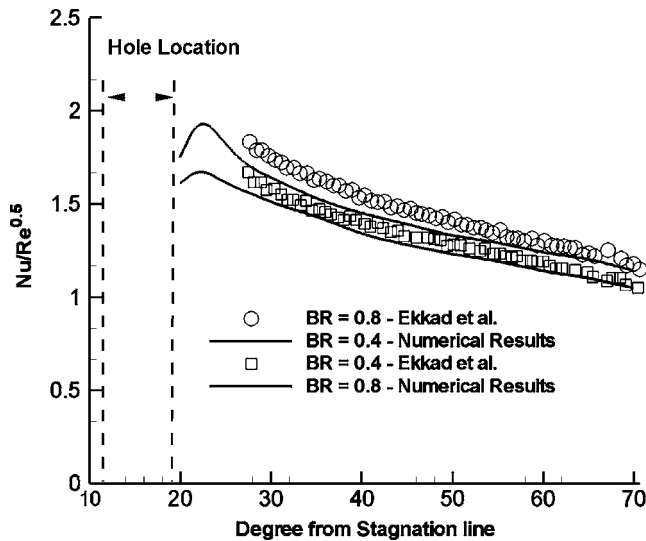


Fig. 12 Spanwise averaged Frossling number distribution

entrainment is much stronger at the higher B.R.=0.8 considered in this study. Unlike for B.R.=0.4, where the coolant remains attached to the surface, at B.R.=0.8, the larger momentum and strong entrainment of the hot mainstream gases underneath the coolant detach it from the surface at $x/d=4.0$. The higher lateral momentum of the coolant shifts it to the fore side of the hole centerline as the coolant reaches $x/d=2.0$. Due to the stronger ejection from the hole at B.R.=0.8, the coolant penetrates further into the mainstream.

Coherent structures are identified for both B.R.'s. At B.R.=0.4, three types of structures are identified. An asymmetric counter-rotating vortex pair forms at the leeward rim of the coolant hole due to the existence of a low pressure region. The aft side component of this vortex pair is significantly stronger than the other component and dominates the jet-mainstream interaction further downstream of the hole. The vortex pair transports downstream in the form of a packet of hairpin vortices. At the windward rim of the hole, vortex tubes form as a result of the transverse velocity of the coolant and its interaction with the mainstream flow. The momentum of the mainstream flow bends these vortex tubes toward the counter-rotating vortex. A number of vortex tubes extend only $1.0d-2.0d$ downstream of the hole. However, the vortex tubes on the fore and aft sides of the hole have an individual effect on entraining mainstream hot gases. At B.R.=0.8, vortex tubes exhibit a different behavior as they are drawn toward and merge with the strong primary vortex immediately downstream of the coolant hole. Additionally, the origin of these vortices, which have smaller scales compared to B.R.=0.4, is from the entire surface of the coolant hole instead of only the windward rim.

At B.R.=0.8, mixing of coolant with mainstream increases due to stronger entrainment and higher values of T.K.E. in the jet-mainstream interaction region. T.K.E. profile at the coolant hole centerline and $1.0d$ downstream of the hole shows peaks of 3% and 10% for B.R.'s of 0.4 and 0.8, respectively. The thickness of the turbulent boundary layer increases from $0.6d$ to $1.2d$ as well with an increase in B.R.

As a result, the averaged values of effectiveness decrease and the span coverage of the coolant becomes narrower with an increase in the B.R. Unlike the effectiveness, the spanwise average values and surface distribution of the Frossling number increases as the B.R. increases. The highest values of Frossling numbers are observed at the immediate downstream aft side of the coolant jet due to the strong mainstream entrainment.

Nomenclature

| | |
|----------|--|
| A | = area |
| B.R. | = blowing ratio (u_c/u_∞) |
| D | = leading edge diameter |
| d | = coolant hole diameter |
| L | = coolant hole length to diameter ratio |
| k | = Thermal conductivity |
| n | = normal wall distance |
| Nu | = Nusselt number |
| q'' | = heat flux |
| Re | = Reynolds number |
| T | = temperature |
| u | = Cartesian velocity vector/streamwise velocity |
| w | = wall |
| x | = streamwise direction (parallel to the surface) |
| θ | = nondimensional temperature |
| η | = adiabatic effectiveness |

Subscripts

| | |
|----------|---------------|
| ad | = adiabatic |
| b | = bulk |
| c | = coolant |
| ∞ | = free stream |

References

- Honami, S., and Shizawa, T., 1992, "Behavior of the Laterally Injected Jet in Film Cooling: Measurement of Surface Temperature and Velocity/Temperature Field Within the Jet," ASME Paper No. 92-GT-180.
- Mayhew, J. E., Baughn, J. W., and Byerley, A. R., 2004, "The Effect of Free Stream Turbulence on Film Cooling Heat Transfer Coefficient and Adiabatic Effectiveness Using Compound Angle Holes," ASME Paper No. GT2004-53230.
- Kaszeta, R. W., and Simon, T. W., 2000, "Measurement of Eddy Diffusivity in Film Cooling Flows With Stream-Wise Injection," ASME J. Turbomach., **122**, pp. 178-183.
- Bergeles, G., Gosman, A. D., and Launder, B. E., 1978, "The Turbulent Jet in a Cross Stream at Low Injection Rates: A Three-Dimensional Numerical Treatment," Numer. Heat Transfer, **1**, pp. 217-242.
- Sathyamurthy, P., and Patankar, S. V., 1992, "Film Cooling Studies Using a Three-Dimensional Parabolic Procedure," University of Minnesota Supercomputer Institute Research Report No. 92/44.
- Xu, J. Z., Ko, S. Y., Chen, S. J., and Tsou, F. K., 1990, "Computer Simulation of Film Cooling With Coolants From One and Two Rows of Holes," ASME Paper No. 90-WA/HT-7.
- Lakehal, D., Theodoridis, G. S., and Rodi, W., 1998, "Computation of Film Cooling of a Flat Plate by Lateral Injection From a Row of Holes," Int. J. Heat Fluid Flow, **19**, pp. 418-430.
- Muldoon, F., and Acharya, S., 2004, "Direct Numerical Simulation of a Film Cooling Jet," ASME Paper No. GT2004-53502.
- Mouzon, B. D., Albert, J. E., Terrell, E. J., and Bogard, D. G., 2005, "Net Heat Flux Reduction and Overall Effectiveness for a Turbine Blade Leading Edge," ASME Paper No. GT2005-69002.
- Yuki, U. M., Bogard, D. G., and Cutbirth, J. M., 1998, "Effect of Coolant Injection on Heat Transfer for a Simulated Turbine Airfoil Leading Edge," ASME Paper No. 98-GT-431.
- Cruse, M. W., Yuki, U. M., and Bogard, D. G., 1997, "Investigation of Various Parametric Influences on Leading Edge Film Cooling," ASME Paper No. 97-GT-296.
- Ekkad, S. V., Han, J. C., and Du, H., 1998, "Detailed Film Cooling Measurement on a Cylindrical Leading Edge Model: Effect of Free-Stream Turbulence and Coolant Density," ASME J. Turbomach., **120**, pp. 799-807.
- Azzi, A., and Lakehal, D., 2001, "Perspective in Modeling Film Cooling of Turbine Blades by Transcending Conventional Two-Equation Turbulence Model," Proceedings of IMECE'01, Nov. 11-16, New York.
- Rozati, A., and Tafti, D. K., 2007, "Large Eddy Simulation of Leading Edge Film Cooling Part—I: Computational Domain and Effect of Coolant Inlet Condition," ASME Paper No. GT2007-27689.
- Tafti, D. K., 2001, "GenIDLEST—A Scaleable Parallel Computational Tool for Simulating Complex Turbulent Flows," Proceedings of the ASME Fluid Engineering Division (FED), Vol. 25, ASME, New York.
- Tyagi, M., and Acharya, S., 2003, "Large Eddy Simulation of Film Cooling Flow From an Inclined Cylindrical Jet," ASME J. Turbomach., **125**, pp. 734-742.
- Iourokina, I. V., and Lele, S. K., 2005, "Towards Large Eddy Simulation of Film Cooling Flows on a Model Turbine Blade Leading Edge," 43rd AIAA Aerospace Science Meeting and Exhibit, Jan. 10-13, Reno, NV.
- Chong, M. S., Perry, A. E., and Cantwell, B. J., 1990, "A General Classification of Three Dimensional Flow Fields," Phys. Fluids A, **2**(5), pp. 765-777.

Large Eddy Simulation Investigation of Flow and Heat Transfer in a Channel With Dimples and Protrusions

Mohammad A. Elyyan

Danesh K. Tafti

High Performance Computational Fluids-Thermal Sciences and Engineering Laboratory, Mechanical Engineering Department, Virginia Polytechnic Institute and State University, Blacksburg, VA 24061

Large eddy simulation calculations are conducted for flow in a channel with dimples and protrusions on opposite walls with both surfaces heated at three Reynolds numbers, $Re_H = 220, 940, \text{ and } 9300$, ranging from laminar, weakly turbulent, to fully turbulent, respectively. Turbulence generated by the separated shear layer in the dimple and along the downstream rim of the dimple is primarily responsible for heat transfer augmentation on the dimple surface. On the other hand, augmentation on the protrusion surface is mostly driven by flow impingement and flow acceleration between protrusions, while the turbulence generated in the wake has a secondary effect. Heat transfer augmentation ratios of 0.99 at $Re_H = 220$, 2.9 at $Re_H = 940$, and 2.5 at $Re_H = 9300$ are obtained. Both skin friction and form losses contribute to pressure drop in the channel. Form losses increase from 45% to 80% with increasing Reynolds number. Friction coefficient augmentation ratios of 1.67, 4.82, and 6.37 are obtained at $Re_H = 220, 940, \text{ and } 9300$, respectively. Based on the geometry studied, it is found that dimples and protrusions may not be viable heat transfer augmentation surfaces when the flow is steady and laminar. [DOI: 10.1115/1.2812412]

Introduction

Increasing the inlet temperature of gas turbines increases the thermal efficiency. In modern turbines, the inlet temperature is above the melting point of the high temperature alloys used in manufacturing inlet guide vanes and turbine blades. Hence, effective cooling of these components is critical to durability. In order to achieve effective cooling, the blades are cooled by circulating cooler bypass air from the compressor through internal passages in the channel (internal cooling) and ejecting the coolant onto the surface to form a protective layer (film cooling).

Improving the internal blade cooling has been the topic of significant research. Different patterns and shapes of ribbed turbulators and pin fins have found widespread use in enhancing heat transfer from the internal blade passages. Depending on the flow disturbance introduced by the augmented surfaces, typical heat transfer augmentation ratios (over a smooth duct) between 2 and 3 have been obtained at a significant pressure drop penalty that varies anywhere from 10 to 20 times that in a smooth duct [1].

Introducing concave/convex surfaces, or in other words dimples and protrusions, is a practical and effective way of heat transfer enhancement that has gained much attention recently. While the augmentation in heat transfer using this technique is about the same as that obtained from conventional ribs and pins, the pressure loss can be significantly lower. In addition, surfaces with dimples and protrusions are also easy to manufacture. Application of dimples and protrusions is not limited to internal cooling channels but they can also be applied to other heat transfer surfaces such as in cooling of combustor liners and in direct skin cooling of turbine blades using microchannels.

An early investigation on the effect of dimples on heat transfer was by Afanasyev et al. [2], who investigated the effect of shallow dimples on flat plate heat transfer for high Reynolds number. Re-

sults showed a significant increase in heat transfer (30–40%) with negligible friction augmentation. Chyu et al. [3] reported heat transfer augmentation of 2.5 for two concavity shapes, hemisphere and teardrop in the Reynolds number range of 10,000–50,000.

Mahmood et al. [4] experimentally studied the flow structure and heat transfer for a one side dimpled channel ($Re_H = 1200\text{--}61,000$). The results showed vortex shedding from the downstream half of the dimple. Maximum heat transfer regions at the downstream rim of the dimple and the flat landing downstream of the dimple cavity were observed.

For a dimpled surface channel, Ligrani et al. [5] identified a primary vortex pair ejection from the dimple cavity into the flow normal to the streamwise direction and secondary vortex pair ejection from the span wise edges of the dimple. Reduction of the channel height was found to intensify the secondary structures in the flow.

The effect of channel height and dimple depth on heat transfer in the turbulent regime was studied by Moon et al. [6] and Burgess and Ligrani [7]. They reported that heat transfer and friction factor augmentation increased with decreasing channel height and increasing dimple depth.

Ligrani et al. [8] and Mahmood et al. [9] investigated the effect of dimples and protrusions on opposite walls of a channel on heat transfer and flow structure. Higher heat transfer and friction coefficient augmentation were observed for Reynolds number range of 5000–20,000. More intensified secondary flows with different patterns resulted from the presence of the protrusions.

Borisov et al. [10] studied heat transfer and pressure loss for internal flow in a channel with dimples on two opposite walls. Maximum heat transfer augmentation of the dimples was reported at the maximum dimple density tested.

A few computational investigations have also been performed, most using Reynolds-Averaged Navier-Stokes (RANS) modeling. Lin et al. [11] used $k\text{-}\epsilon$ turbulence model without wall functions and predicted flow over dimples for $Re = 23,000$ and 46,000.

Isaev and Leont'ev [12] used Menter's shear stress transport model and showed the vortical structures in the dimple for various depth. Park et al. [13] used a realizable $k\text{-}\epsilon$ model. Steady-state

Contributed by the International Gas Turbine Institute of ASME for publication in the JOURNAL OF TURBOMACHINERY. Manuscript received June 11, 2007; final manuscript received June 23, 2007; published online August 4, 2008. Review conducted by David Wisler. Paper presented at the ASME Turbo Expo 2007: Land, Sea and Air (GT2007), Montreal, Quebec, Canada, May 14–17, 2007.

results showed the existence of a counter-rotating vortex pair originating upstream and inside each dimple and another pair at the spanwise edges of the dimple.

Won and Ligrani [14] studied the effect of dimple depth to imprint diameter ratio on flow structure and local heat transfer in a channel with one surface dimpled using realizable $k-\epsilon$ model for the case of $Re_H=10,000$. An increase of vorticity magnitude with the increase of dimple depth was reported.

Patrick and Tafti [15] applied direct numerical simulation (DNS)-large eddy simulation (LES) to predict the heat transfer and friction coefficient augmentation in a channel with one dimpled wall at low Reynolds numbers ($Re_H=50-2000$). The result showed that up to $Re_H=1000$, the flow was laminar, with no augmentation in either the heat transfer or the friction. Self-sustained flow oscillations appeared at $Re_H>1000$, with shedding of coherent structures from the dimple leading to heat transfer augmentation.

Elyyan et al. [16] numerically studied the flow structure and heat transfer distribution in a channel with dimples/protrusions using LES. The study was for a fully turbulent flow of $Re_H=15,500$. High heat transfer regions on the protrusion and dimple surfaces were identified.

Objective

The objective of this study is to apply high-fidelity time-dependent simulation methodologies based on LES to elucidate on the unsteady flow structure and to predict friction and heat transfer in a channel with dimple and protrusions on opposing walls. Three Reynolds numbers, covering a range of applications from minichannel heat transfer to high Reynolds number internal cooling ducts, are investigated: $Re_H=220, 940, \text{ and } 9300$, covering laminar to fully turbulent flow.

Past experimental studies (see, Refs. [8,9]) have only studied the heat transfer on the dimpled surface in the presence of protrusions on the opposite wall. The goal of this investigation is to provide a detailed analysis of the flow structure in different flow regimes and to clearly identify flow features responsible for heat transfer augmentation on both surfaces. In addition, a detailed breakdown of heat transfer and pressure loss components is identified.

Governing Equations and Computational Model

The nondimensional incompressible time-dependent Navier–Stokes and energy equations are solved in a generalized coordinate system assuming fully developed hydrodynamic and thermal conditions. Both channel walls are heated by applying a constant heat flux boundary condition (q''). The nondimensionalization is carried out by using the height of the channel (H) as the characteristic length scale, a characteristic velocity scale given by the friction velocity (u_τ), and a characteristic temperature scale given by $q''H/k$.

The governing equations for momentum and energy are discretized with a conservative finite-volume formulation using a second-order central difference scheme on a nonstaggered grid topology [17]. Turbulent subgrid stresses are modeled using the dynamic Smagorinsky model [18], which is activated for $Re_H=940$ and 9300 .

The computer program GENIDLEST (generalized incompressible direct and large eddy simulations of turbulence) used for these simulations has been applied extensively to study flow and heat transfer in stationary and rotating internal ducts used for cooling gas turbine blades (e.g., Refs. [19,20]) and other heat transfer augmentation geometries.

Channel Geometry and Boundary Conditions. The fin geometry is shown in Fig. 1. All the dimensions are nondimensionalized by channel height, $H=1.0$. Dimple/protrusion pitches in spanwise and streamwise directions are $P=S=3.24$. Dimple im-

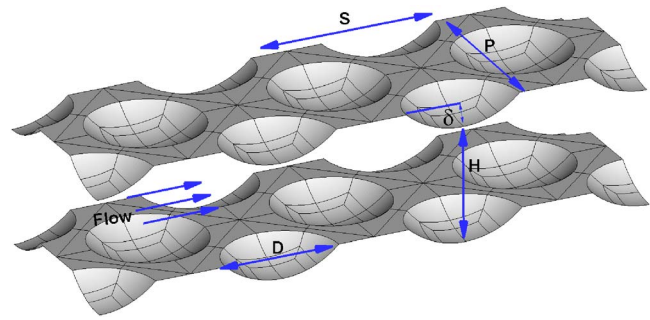


Fig. 1 Geometry specifications

print diameter D is 2.0 and dimple depth δ is 0.4. Dimples and protrusions are staggered without any offset with respect to each other. The geometry dimensions match the experimental setup of Ligrani et al. [5], Ligrani et al. [8], and Mahmood et al. [9].

The domain is periodic in the streamwise and spanwise directions. No slip wall boundary condition with constant heat flux is applied at the channel surfaces (dimple and protrusion surfaces). Further details about how the boundary conditions are applied can be found from Zhang et al. [21].

Domain Size and Grid Resolution. An initial study was conducted to determine the minimum periodic domain size possible, which will admit all the important unsteady modes into the solution. A periodic domain of size $H \times P/2 \times S$ was chosen in this study, Fig. 2. The selection procedure and the different domain sizes are explained by Elyyan et al. [16]. The adopted domain consists of 28 structured grid blocks with 1,575,864 cells.

A fine grid at an average distance of $\Delta y=6.67 \times 10^{-3}$ is placed at the walls based on an estimated $y_1^+=\Delta y Re_\tau=0.5$. An a posteriori calculation of the local friction velocity places $y_1^+<0.5$ at both surfaces and provides five to six grid points within $y^+=10$.

Baseline Nu and C_f . In the present study, the laminar Fanning friction coefficient and Nusselt number for flow between smooth parallel plates and the Petukhov and Gnielinski correlations for a smooth channel are used to calculate the baseline Fanning friction coefficient and Nusselt number, respectively [22]. The choice of correlations is dictated by their validity and accuracy over the range of Reynolds numbers of interest in this study.

Validation. The computer code GENIDLEST has been validated with experiments extensively in past studies (e.g., Refs. [20,23]) with very close matches with experiments in the literature. For the purposes of this study, the code is further validated in a canonical turbulent channel flow at $Re_\tau=360$ (based on H). A grid of $64 \times 64 \times 64$ computational cells is used in the $x, y, \text{ and } z$ directions,

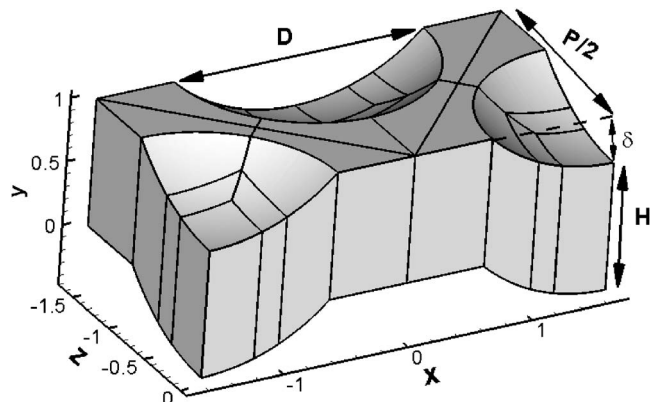


Fig. 2 Adopted computational domain

Table 1 Results compared with DNS and correlations

| | GENIDLEST | DNS | Correlations |
|-----------------------------------|-----------------------|-----------------------|---------------------------------|
| $Re_\tau = u_\tau H / \nu$ | 360 | 360 | |
| $Re_c = u_c H / \nu$ | 6516 | 6696 | |
| $Re_H = u_m H / \nu$ | 5616 | 5600 | |
| $C_f = \tau_w / (1/2 \rho u_m^2)$ | 8.21×10^{-3} | 8.18×10^{-3} | Petukhov: 7.62×10^{-3} |
| $Nu_H = hH/k$ | 18.5 | ... | Dittus-Boelter: 17.34 |

respectively. The first grid point in the inhomogeneous y direction was placed at $y_1^+ = 0.9$ with five grid points within $y^+ < 10$. The maximum spacing at the center of the channel was $\Delta y^+ = 6$. The nondimensional time step used was 1×10^{-3} .

The results obtained using GENIDLEST were compared to previously published DNS data, to results of Kim et al. [24], and to correlations in the literature. Table 1 shows that all predictions obtained using GENIDLEST are within a few percent of the DNS data of Kim et al. [24] and within 10% of the correlations in the literature.

In order to further validate the prediction accuracy of the calculations, the results are compared to the experimental data of Mahmood et al. [9] for a channel with dimples and protrusions, in which the protrusion side is not heated. A constant heat flux boundary condition is applied to the dimpled surface and an adiabatic wall boundary condition is applied to the protrusion surface to match the wall boundary conditions of the experiment. The Reynolds number based on the channel height, Re_H , is 14,600.

Table 2 summarizes the comparisons. While the Nusselt number augmentation shows excellent agreement with experiments, the augmentation of C_f is more than twice the value reported by Mahmood et al. [9]. The reason for this discrepancy is believed to be a result of the selected baseline used for friction coefficient normalization in the experiments. In the same paper, Mahmood et al. [9], using a smooth channel experiment to calculate the baseline friction factor, report a friction factor augmentation of about 1.6 at $Re_H = 15,000$ for a channel with only dimples on one side. Ekkad and Nasir [25], using smaller and shallower dimples on one side of a smooth channel with $D = 0.75$ and $\delta = 0.125$, reported a friction factor augmentation of 3.1 for flow at $Re_H = 13,000$ when their baseline friction factor was obtained from Moody's chart (which agrees with the sentence with the baseline C_f of the current study). By comparison, in ribbed ducts, for an overall heat transfer augmentation of 2.0, the friction augmentation is about 9 [23].

Results and Discussion

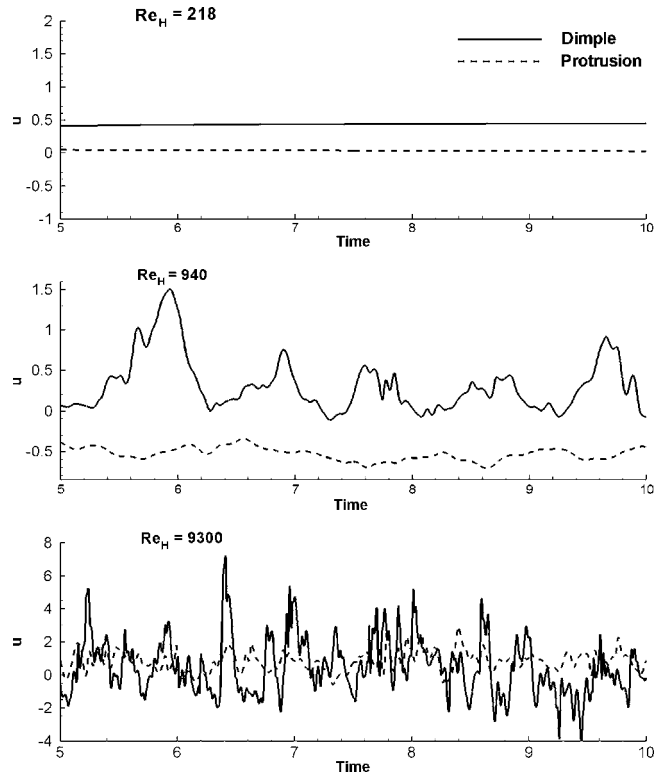
The calculations considered in the following sections discuss the flow structure and heat transfer inside the channel at low, medium, and high Reynolds number flows, $Re_H = 250, 940$, and 9300.

Each Reynolds number was run until a statistically stationary state was established in the computation domain, after which time-averaged quantities relating to the mean flow and turbulent quantities were obtained. All results are nondimensionalized by the mean bulk velocity and the channel height.

Unsteady Characteristics and Flow Structure. Figure 3 shows the instantaneous flow velocities of two probes in the wake of the dimple and protrusion located at $\Delta y = 0.0163$ normal to the

Table 2 Comparison between numerical and experimental results

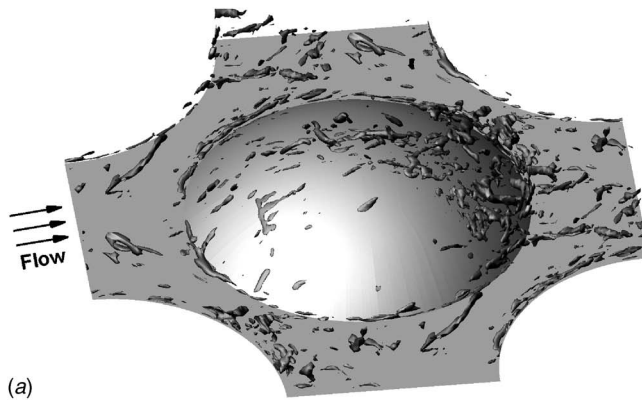
| | Re_H | Nu/Nu_0 | C_f/C_{f0} |
|------------------|--------|-----------|--------------|
| Present study | 14,600 | 2.31 | 6.54 |
| Experimental [9] | 15,000 | 2.23 | 3.08 |

**Fig. 3 Instantaneous flow velocities**

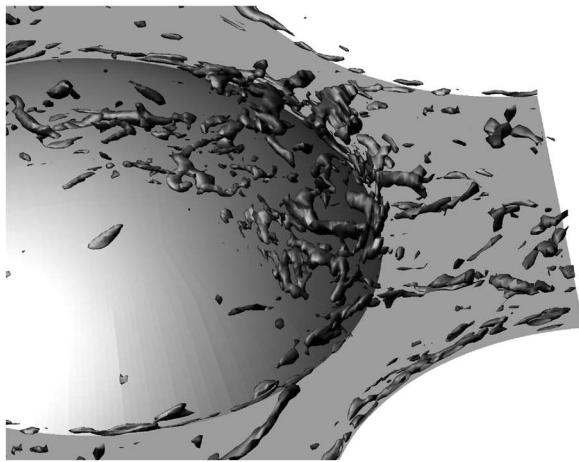
fin surface and $0.2D$ downstream of the dimple/protrusion. While the flow is steady and laminar at $Re_H = 220$, flow instabilities develop in the dimple cavity by $Re_H = 940$, which is captured in the instantaneous streamwise velocity downstream of the dimple. Smaller amplitude oscillations are also present in the wake of the protrusion. By $Re_H = 9300$, the flow is fully turbulent at both surfaces.

Figures 4 and 5 show the instantaneous single-valued isosurfaces of the coherent vorticity structure in the domain for the fully turbulent case of $Re_H = 9,300$ on the protrusion and dimple surfaces, respectively, at a single-valued level of 40. To identify the coherent structures in the present study, the vortex eduction technique proposed by Chong et al. [26] is used. In this method, in regions dominated by vortical motion, the velocity gradient tensor exhibits two eigenvalues that are complex conjugate. The magnitude of the eigenvalue is indicative of the strength of the vortex. The structures identified by this method are referred to as "coherent vorticity" in this paper, and the magnitude of the eigenvalue is referred to as the strength of the vortices. Figure 4 shows the instantaneous coherent flow structures on the protrusion side of the channel. The flow separation from the protrusion is characterized by vortex shedding seen at the back of the protrusion. These vortices reattach to the channel surface immediately downstream. A close-up view at that region is seen in Fig. 4(b).

Figure 5 shows the instantaneous coherent vorticity on the dimple side of the channel. Flow separates at the upstream rim of the dimple creating an unstable separated free shear layer inside the dimple, characterized by the intense vortices in the upstream half of the dimple. The shear layer vortices impinge in the reattachment region at the back end of the dimple. As the flow ejects out of the dimple cavity, the vortices are stretched, tilted, and directed in the direction of the mainstream flow. Additional small scale vorticity is also generated at the downstream rim of the dimple as the flow ejects out. Another shear layer forms and separates from the surface with a small recirculation region as shown in Fig. 5(b). The vortices then reattach to the channel surface or



(a)

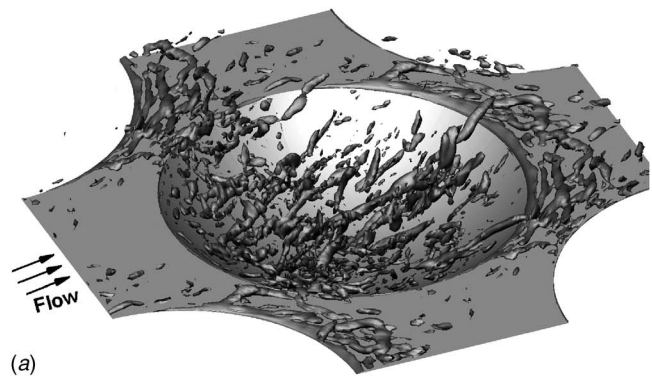


(b)

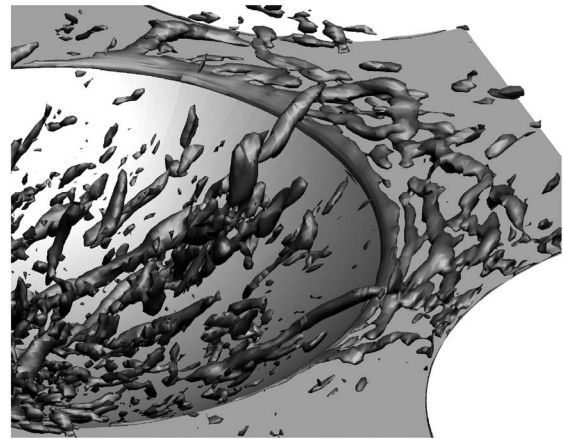
Fig. 4 Instantaneous coherent vorticity isosurfaces (level = 40) for flow at $Re_H=9300$: (a) at protrusion side; (b) vortex shedding from the back of the protrusion

flat landing downstream of the dimple. It is clear that at both surfaces, the energetic structures exist at a very small scale and are representative of fine scale turbulence.

Mean Flow Characteristics. The mean flow structure is described with the aid of 3D mean velocity streamlines in the vicinity of the dimple and protrusion surfaces for the three Reynolds numbers. Figure 6 shows the mean 3D velocity streamlines close to the protrusion surface for $Re_H=220$, 940, and 9300 with x -velocity contours for a 3D surface located at $\Delta y=0.0016$ from the protrusion surface. The velocity streamlines show a smooth flow on the protrusion surface for the laminar flow at $Re_H=220$. The flow impinges on the front of the protrusion and then accelerates smoothly on the protrusion surface; no flow separation or recirculation is observed for the flow at this Reynolds number. As the flow Reynolds number increases, flow impingement at the front of the protrusion becomes stronger and the flow separates at the back of the protrusion at $Re_H=940$. In spite of the separation, the flow exhibits very weak oscillations (see Fig. 3). At $Re_H=9300$, the flow separates at the same location on the protrusion but the turbulent wake reattaches immediately downstream of the protrusion, as can be seen by the x -velocity contours. A small flow recirculation region at the front of the protrusion is observed at $Re_H=9300$; this is due to a pressure gradient setup in a direction normal to the channel surface at impingement, which leads to velocity recirculation. The large blockage resulting from the protrusions causes flow acceleration in the passage between the protrusions, as can be clearly seen in the x -velocity contours for the $Re_H=940$ and 9300 flows. An additional feature is the movement of fluid along the side rims of the protrusions into the low pressure



(a)



(b)

Fig. 5 Instantaneous coherent vorticity isosurfaces (level = 40) for flow at $Re_H=9300$: (a) at dimple side; (b) vortex shedding and reattachment at downstream of dimple

wake.

Figure 7 shows the mean 3D velocity streamlines close to the dimple surface for $Re_H=220$, 940, and 9300 with x -velocity contours for a 3D surface located at $\Delta y=0.00067$ from the dimple surface. The mean structure shows flow separation at the upstream rim of the dimple with flow recirculation inside the dimple cavity. The size of this recirculation zone shrinks as the flow becomes more turbulent, promoting early reattachment. Another feature of the mean structure is flow ejection from the side rim of the dimple toward the adjacent dimples. At $Re_H=9300$, a mean helical vortex exists around the downstream rim of the dimple, which is the manifestation of the unsteady vortices shed by the separated shear layer (Fig. 5) along the rim.

Turbulent Kinetic Energy Distribution. Since in most instances heat transfer augmentation is intimately correlated to the level of turbulent kinetic energy (T.K.E.) near surfaces, in this section the T.K.E. distribution of the fully turbulent flow at $Re_H=9300$ and T.K.E. profiles at selected locations for $Re_H=940$ and 9300 are analyzed in connection with the flow structures identified earlier.

Figure 8 shows the distribution of T.K.E. at selected spanwise planes across the domain starting from and ending at the center of the dimple. The locations $x=-1.62$ and $x=0$ represent the center of the dimple cavity and protrusion and the flat landing half-pitch between streamwise dimples and protrusions, respectively. Four main structures that generate high turbulence intensity are identified:

- (1) The separated turbulent shear layer that forms at the upstream rim of the dimple exhibits T.K.E. intensities as high as 12% when normalized by the bulk mean velocity squared. The early part of the shear layer is located at $x=$

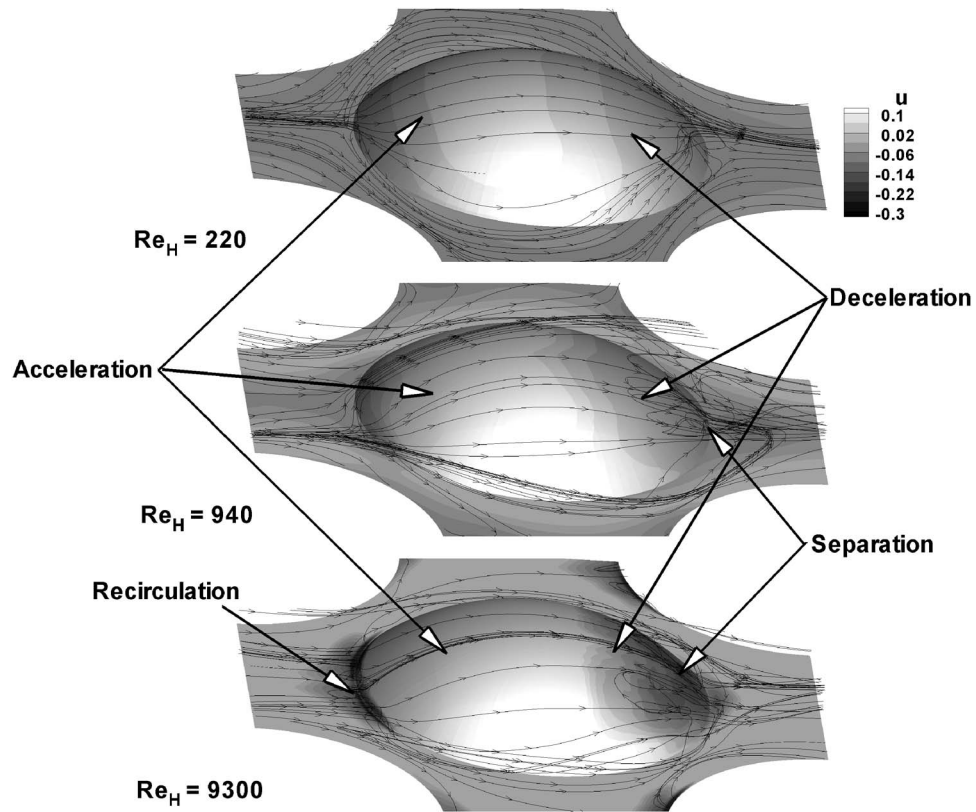


Fig. 6 Mean 3D velocity streamlines close to the protrusion surface with x -velocity contours very close to channel surface for $Re_H=220, 940, \text{ and } 9300$

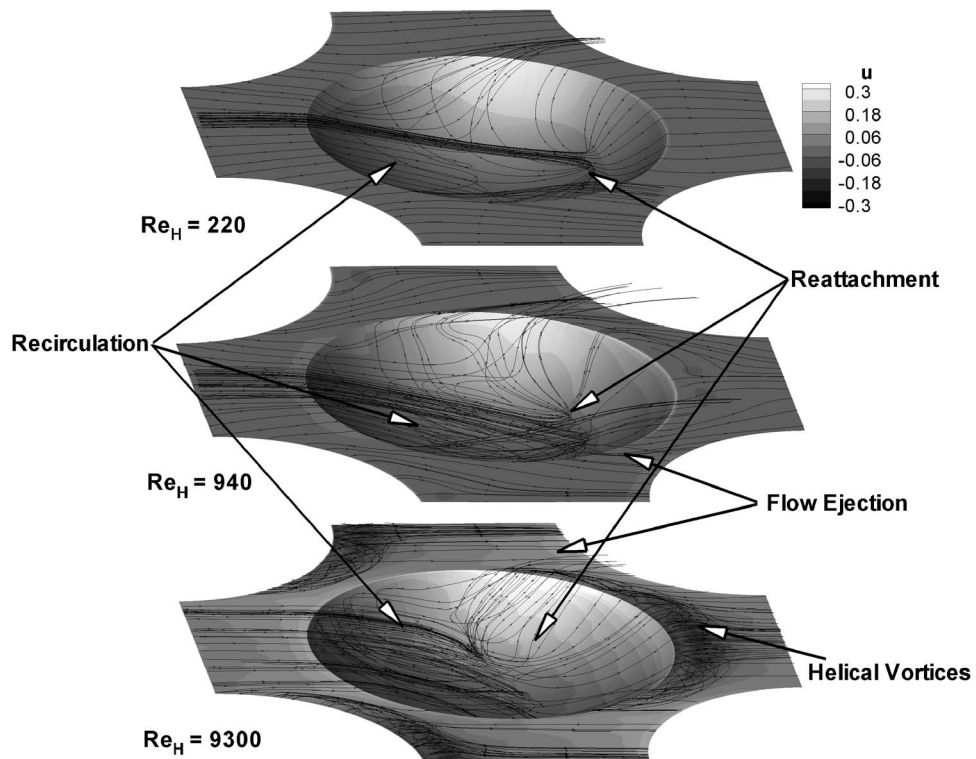


Fig. 7 Mean 3D velocity streamlines close to the dimple surface with x -velocity contours very close to channel surface for $Re_H=220, 940, \text{ and } 9300$

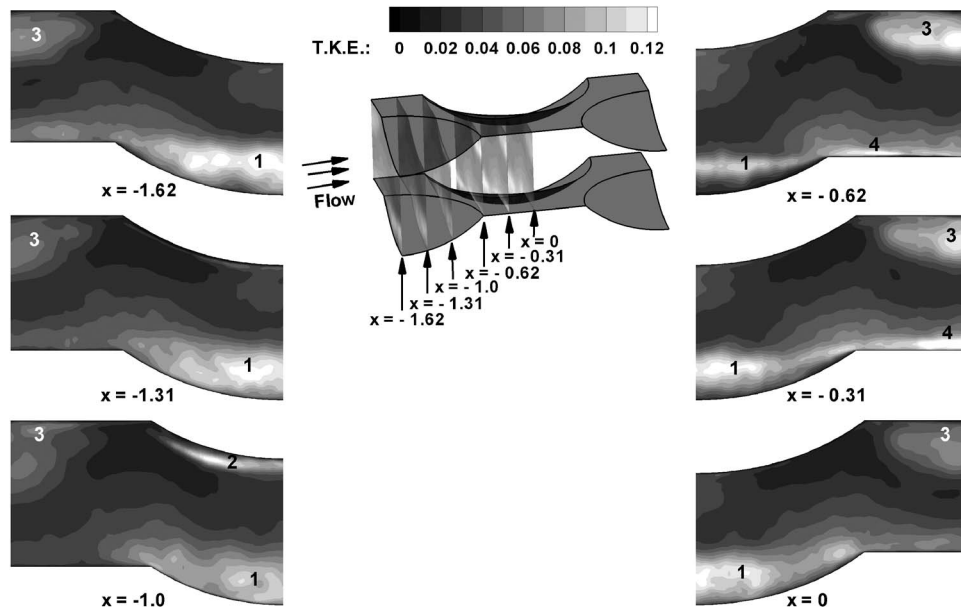


Fig. 8 Mean T.K.E. distribution at different spanwise planes across the computational domain for flow at $Re_H=9300$. See text for explanation of labels.

- 0.62, which grows ($x=-0.31, 0, -1.62, -1.31$, and -1.0) and reattaches in the latter half of the dimple cavity.
- (2) The turbulent separated shear layer on the protrusion also exhibits high T.K.E. values of up to 10%, the early stages of which can be seen at $x=-1.0$.
 - (3) The separated turbulent shear layer on the protrusion leads to a highly turbulent wake behind the protrusion, which can be identified by the high T.K.E. values at $x=-0.62$ and $x=-0.31$, which subsequently decays further downstream ($x=0, -1.62, -1.31$).
 - (4) The strong flow ejection from the dimple cavity creates a separated shear layer at the downstream rim, generating turbulent eddies. In the mean, these can be identified by the helical streamlines along the rim of the dimple. The turbulence generated in this region is further augmented by the turbulence (vorticity) ejected out of the dimple cavity and is tilted by the main flow toward the flat landing behind the dimple. The regions of high T.K.E. at $x=-0.62$ and $x=-0.31$ represent these phenomena.

To investigate the effect of Reynolds number on flow structure, T.K.E. profiles at locations in the immediate wake of the dimple and protrusion are shown for $Re_H=940$ and 9300 . Figure 9 shows the T.K.E. profile at the centerline of the domain, $z=0$, at (i) $x=-0.62$, at the downstream rim of the dimple, (ii) $x=-0.31$, at the flat landing downstream of the dimple, and (iii) $x=0$, at the half-way location between two streamwise dimples or protrusions.

Two major differences exist between the Reynolds numbers. The first is that the maximum T.K.E. values at these locations is about two to three times higher at $Re_H=9300$, indicating that at $Re_H=940$, the flow is not fully turbulent. The peaks, respectively, capture the wake turbulence on the protrusion side and the turbulence generated within the dimple and at the downstream rim of the dimple. While there is a sharp growth in the peak T.K.E. near $y=0.0$, between $x=-0.62$ and $x=-0.31$ at $Re_H=9300$, at $Re_H=940$ the peak does not grow substantially but remains at a value between 0.04 and 0.05 for all three x locations. This implies that the dynamics related to vorticity generation and ejection downstream of the dimple is much weaker at $Re_H=940$. This can also be concluded from the mean flow in Fig. 7, in which the helical streamlines indicative of strong instantaneous vorticity is absent at

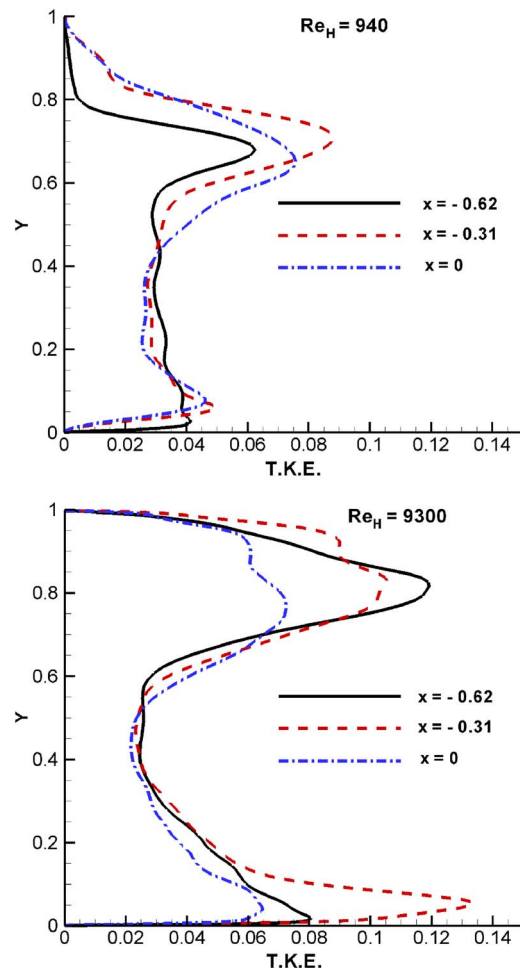


Fig. 9 Normalized mean T.K.E. profile at different locations in the domain along the center of the domain, $z=0$, for $Re_H=940$ and 9300

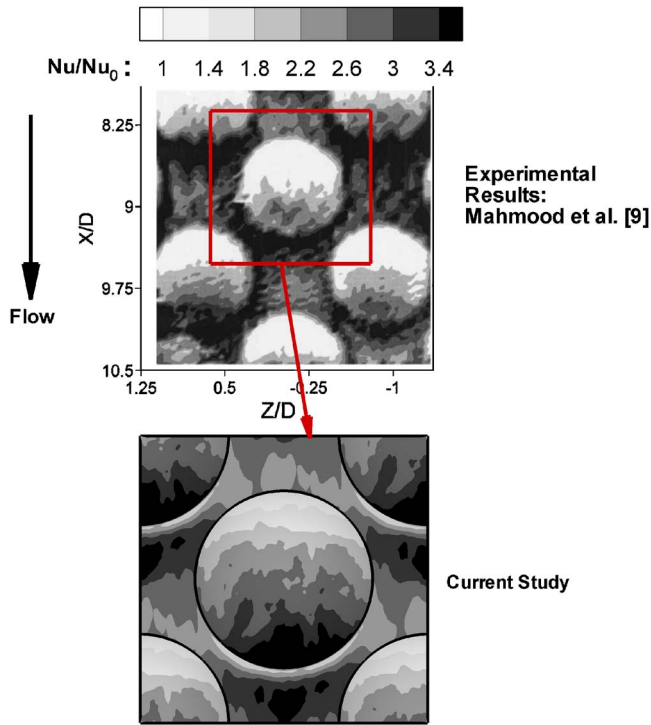


Fig. 10 Mean Nu/Nu_0 distribution on dimple surface for experimental data at $Re_H=10,400$ for channel with aligned dimple and protrusion, Mahmood et al. [9] (reprinted by permission of the American Institute of Aeronautics and Astronautics, Inc.) and current study at $Re_H=9300$. Flow direction is from top to bottom.

the lower Reynolds number. Another major difference between the two Reynolds numbers is the magnitude of T.K.E. in the immediate vicinity of the channel surfaces. At $Re_H=940$, the T.K.E. values near the channel walls is much smaller than those at the higher Reynolds numbers. For instance, the turbulence generated in the wake of the protrusion does not diffuse to the channel walls as it does at the higher Reynolds number.

Heat Transfer and Friction Augmentation. Figure 10 shows a comparison between the experimental results obtained by Mahmood et al. [9] at $Re_H=10,400$ for a channel with aligned dimples and protrusions and present results at $Re_H=9300$ (flow is from top to bottom). In the dimple cavity, the heat transfer augmentation (versus a smooth channel) increases from the leading to the trailing edge of the dimple, with low augmentation in the separated region and high augmentation at reattachment in the cavity. Immediately downstream of the dimple cavity, there is a region of reduced augmentation, which is a result of flow separation at the downstream rim of the dimple. As vortices from the shear layer and dimple cavity touch down or reattach on the flat landing, the heat transfer augmentation increases once again.

The predictions show an excellent match with the experimental results. In contrast, RANS calculations by Park et al. [13] underpredict the heat transfer coefficient by nearly 100% (predicted range of Nusselt numbers are from 0.9 to 2.1 versus experimental measurements in the range of 1.4–3.4).

Figure 11 shows the distribution of Nusselt number augmentation on the protrusion surface for the different Reynolds number flows. The laminar flow at $Re_H=220$ shows a uniform heat transfer augmentation at the flat surface on the protrusion side, which is near or less than that of a smooth channel. Some heat transfer augmentation occurs as the flow accelerates over the protrusion. For the turbulent flows at $Re_H=940$ and 9300, low heat transfer regions are observed on the flat surface immediately upstream of

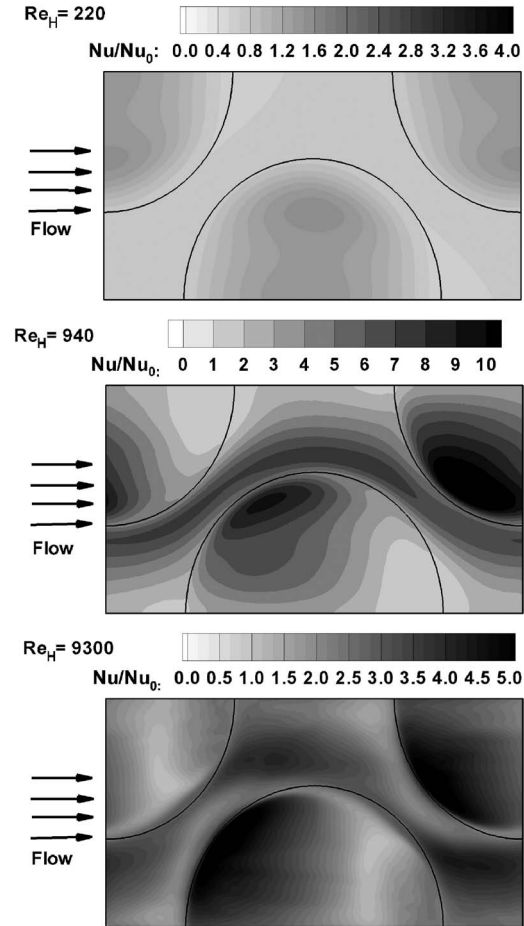


Fig. 11 Mean Nusselt number augmentation on the protrusion surface for $Re_H=220$, 940, and 9300

the protrusion, which is a result of the low momentum wake of the upstream protrusion and the recirculation region upstream of the protrusion that was observed earlier in the mean flow structure. By far, the highest values of heat transfer augmentation are observed in regions where the flow directly impinges on the protrusion. High heat transfer regions are also observed in regions of flow acceleration between the protrusions.

Figure 12 shows the distribution of Nusselt number augmentation on the dimple surface. Low heat transfer regions appear in the upstream half of the dimple cavity, where flow recirculates inside the dimple. The size of the recirculation zone inside the dimple shrinks as the flow becomes more turbulent. High heat transfer augmentation appears in the downstream half of the dimple where the flow reattaches to the dimple surface and accelerates toward the downstream rim of the dimple. The highest heat transfer appears at the boundary layer regeneration region at the downstream rim of the dimple; this is most obvious for the low and medium Reynolds number flows. For the fully turbulent flow at $Re_H=9300$, the downstream rim of the dimple is followed by a small low augmentation region caused by flow separation observed earlier. After this small separation region, flow reattaches at the flat landing and a region of high heat augmentation is observed.

Table 3 summarizes the overall time mean and area weighted average Nusselt numbers for the dimple and protrusion surfaces for the different Reynolds numbers studied. Unlike many experimental investigations, the actual dimple/protrusion area is used in the calculation of the Nusselt number, not the projected flat plate area. At $Re_H=220$, the protrusion surface exhibits a Nusselt number that is lower than that of a smooth channel because of the detrimental effect of the low momentum wake of the protrusion

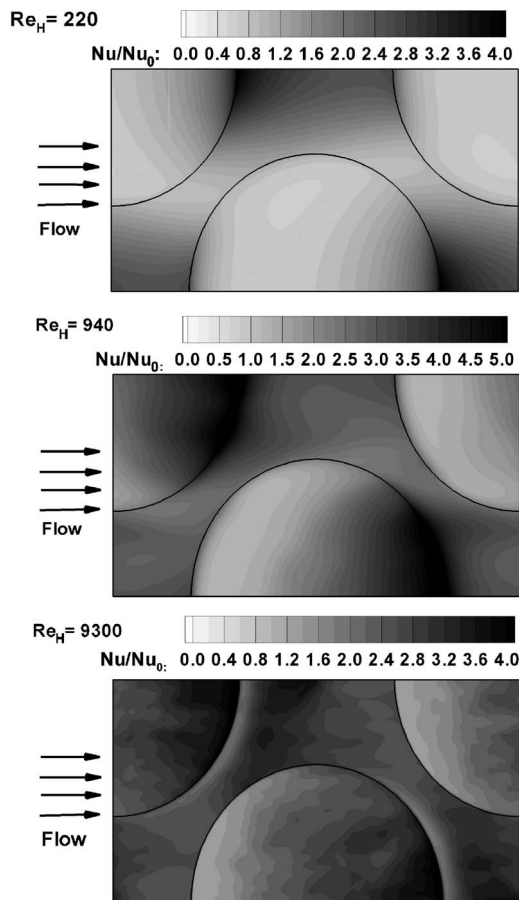


Fig. 12 Mean Nusselt number augmentation on the dimple surface for $Re_H=220$, 940, and 9300

on surface heat transfer. The dimple surface on the other hand exhibits some augmentation, but clearly the use of dimples and protrusions for low Reynolds number applications does not seem viable for heat transfer augmentation. These results are in agreement with previous work by Patrick and Tafti [15] for shallower dimples. As the Reynolds number increases to 940, the flow is no longer laminar and exhibits turbulentlike characteristics but is not yet fully turbulent. At this Reynolds number, the protrusion surface exhibits significantly higher heat transfer coefficients than the

Table 3 Heat transfer from protrusion and dimpled surfaces

| Re_H | $Nu_{\text{protrusion}}$ | Nu_{dimple} | Nu_{ave} | Nu/Nu_0 |
|--------|--------------------------|----------------------|-------------------|-------------------|
| 220 | 3.67 | 4.47 | 4.07 | 0.99 |
| 940 | 15.24 | 9.77 | 12.50 | 2.94 |
| 9300 | 62.70 | 59.83 | 61.27 | 2.53 ^a |

^aTurbulent baseline correlation used for normalization.

Table 4 Pressure drop contribution from the protrusion and dimple surfaces and overall friction coefficient augmentation

| Re_H | Protrusion | | | Dimple | | | C_f | C_f/C_{f0} |
|--------|------------|-------|--------|--------|-------|--------|-------|-------------------|
| | %form | %fric | %total | %form | %fric | %total | | |
| 220 | 15 | 32 | 47 | 29 | 24 | 53 | 0.092 | 1.67 |
| 940 | 23 | 28 | 51 | 41 | 8 | 49 | 0.065 | 4.82 |
| 9300 | 26 | 14 | 40 | 54 | 6 | 60 | 0.042 | 6.37 ^a |

^aTurbulent baseline correlation used for normalization.

dimple surface. This is mostly due to flow impingement on the protrusion surface and flow acceleration between protrusions. The overall Nusselt number augmentation relative to a smooth laminar channel is 2.94 in this case. In the fully turbulent regime, the heat transfer coefficients on the two sides of the channel are similar in magnitude, providing an overall augmentation of 2.53 based on a turbulent baseline correlation.

Table 4 summarizes the form and friction drag contribution to the total pressure drop for the protrusion and dimple surfaces in addition to the average friction coefficient and friction coefficient augmentation with respect to a smooth channel. At the low and medium Reynolds numbers, both the dimple and the protrusion surface contribute almost equally to the overall pressure drop. However, at $Re_H=9300$, the dimpled surface exhibits a much larger contribution to total pressure drop, most of it coming from an increase in form drag. In general, the overall form drag contribution increases from 44% at $Re_H=220$ to 80% at $Re_H=9300$, which is consistent with trends on other augmentation surfaces as well. Interestingly, the contribution of dimples to overall form drag dominates over protrusions, which is quite an unexpected result. The overall friction coefficient augmentation ranges from 1.67 at the lowest Reynolds number studied to a high value of 6.37 at the highest Reynolds number studied.

Summary and Conclusions

LES is applied to predict and analyze the flow structure and heat transfer in a channel with dimpled surfaces for low, medium, and high Reynolds numbers assuming fully developed flow and thermal conditions.

The following important conclusions are made:

- Heat transfer augmentation on the dimple surface is primarily a result of turbulence generated in the separated shear layer at the upstream rim of the dimple. Turbulent vortices shed from the shear layer impinge in the downstream half of the dimple in the reattachment zone to augment heat transfer. Flow ejection out of the dimple cavity along the side and downstream rim of the dimple further aids in the generation of turbulence (small scale vorticity), particularly at high Reynolds numbers. Both the turbulence generated at the rim and that ejected out of the dimple cavity aid in augmenting heat transfer on the flat landing immediately downstream of the dimple. Because of the strong dependence of heat transfer augmentation on turbulence generation, dimple surfaces may not be viable for heat transfer augmentation at low Reynolds numbers in the steady laminar regime. The onset of unsteadiness is found to augment heat transfer, which can be controlled by the dimple geometry.
- In contrast, heat transfer augmentation on the protrusion side is mostly a result of flow impingement on the protrusion and resulting acceleration between protrusions. The turbulence generated in the separated shear layer and wake of the protrusions has some effect on heat transfer augmentation on the flat landing immediately downstream of the protrusion. In spite of the lesser dependence of protrusions on turbulence generation for heat transfer augmenta-

tion, they too do not seem to be viable as heat transfer augmentation surfaces in the steady laminar regime based on the results in this study.

- (iii) Both form and friction drag contribute to the overall pressure losses, with form drag contributing from 44% in the laminar regime to 80% in the fully turbulent regime. Contrary to expectations, dimples contribute more to form losses than protrusions across the full range of Reynolds numbers. Overall friction augmentation factors range from 1.67 in the laminar regime to 6.37 in the turbulent regime.
- (iv) Finally, it can be concluded that channels with dimples and protrusions are quite competitive with other heat transfer augmentation surfaces in the turbulent regime and benefit from a lower pressure drop penalty than other augmentation surfaces.

Acknowledgment

This work is a result of support provided by the U.S. Army RDECOM, Fort Belvoir, VA and Modine Manufacturing Co., Passenger Thermal Management, Racine, WI for air-side heat transfer enhancement in next generation compact heat exchangers. The support is gratefully acknowledged. The calculations were performed on Virginia Tech's Advanced Research Computing facility, System-X. The allocation grant and support provided by the staff are also gratefully acknowledged.

Nomenclature

| | | |
|-----------|---|--|
| D | = | dimple imprint diameter |
| C_f | = | Fanning friction coefficient |
| k | = | thermal conductivity |
| S | = | streamwise pitch |
| P | = | spanwise pitch |
| H | = | channel height |
| Nu | = | Nusselt number |
| p | = | fluctuating, modified, or homogenized pressure |
| q'' | = | constant heat flux on channel walls |
| Re | = | Reynolds number |
| u | = | streamwise velocity component |
| x, y, z | = | Cartesian coordinates |
| δ | = | dimple depth |

Subscripts

| | | |
|--------|---|-----------------------------------|
| b | = | bulk |
| o | = | smooth channel |
| τ | = | values based on friction velocity |

Superscript

| | | |
|-----|---|------------------|
| $+$ | = | wall coordinates |
|-----|---|------------------|

References

- [1] Ligrani, P. M., Oliveira, M. M., and Blaskovich, T., 2003, "Comparison of Heat Transfer Augmentation Techniques," *AIAA J.*, **41**(3), pp. 337–362.
- [2] Afanasyev, V. N., Chudnovsky, Ya. P., Leontiev, A. I., and Roganov, P. S., 1993, "Turbulent Flow Friction and Heat Transfer Characteristics for Spherical Cavities on a Flat Plate," *Exp. Therm. Fluid Sci.*, **7**(1), pp. 1–8.
- [3] Chyu, M. K., Yu, Y., Ding, H., Downs, J. P., and Soechting, F. O., 1997,

- "Concavity Enhanced Heat Transfer in an Internal Cooling Passage," ASME Paper No. 97-GT-437.
- [4] Mahmood, G. I., Hill, M. L., Nelson, D. L., and Ligrani, P. M., 2000, "Local Heat Transfer and Flow Structure on and above a Dimpled Surface in a Channel," ASME Paper No. 2000-GT-230.
 - [5] Ligrani, P. M., Harrison, J. L., Mahmood, G. I., and Hill, M. L., 2001, "Flow Structure Due to Dimple Depressions on a Channel Surface," *Phys. Fluids*, **13**(11), pp. 3442–3451.
 - [6] Moon, H. K., O'Connell, T., and Sharma, R., 2003, "Heat Transfer Enhancement Using a Convex-Patterned Surface," *ASME J. Turbomach.*, **125**, pp. 274–280.
 - [7] Burgess, N. K., and Ligrani, P. M., 2004, "Effects of Dimple Depth on Nusselt Numbers and Friction Factors for Internal Cooling Channel," ASME Paper No. GT2004-54232.
 - [8] Ligrani, P. M., Mahmood, G. I., Harrison, J. L., Clayton, C. M., and Nelson, D. L., 2001, "Flow Structure and Local Nusselt Number Variation in a Channel With Dimples and Protrusions on Opposite Walls," *Int. J. Heat Mass Transfer*, **44**, pp. 4413–4425.
 - [9] Mahmood, G. I., Sabbagh, M. Z., and Ligrani, P. M., 2001, "Heat Transfer in a Channel With Dimples and Protrusions on Opposite Walls," *J. Thermophys. Heat Transfer*, **15**(3), pp. 275–283.
 - [10] Borisov, I., Khalatov, A., Kobzar, S., and Glezer, B., 2004, "Comparison of Thermo-Hydraulic Characteristics for Two Types of Dimpled Surfaces," ASME Paper No. GT2004-54204.
 - [11] Lin, Y. L., Shih, T. I.-P., and Chyu, M. K., 1999, "Computations of Flow and Heat Transfer in a Channel With Rows of Hemispherical Cavities," ASME Paper No. 99-GT-263.
 - [12] Isaev, S. A., and Leont'ev, A. I., 2003, "Numerical Simulation of Vortex Enhancement of Heat Transfer Under Conditions of Turbulent Flow Past a Spherical Dimple on the Wall of a Narrow Channel," *High Temp.*, **41**(5), pp. 655–679.
 - [13] Park, J., Desam, P. R., and Ligrani, P. M., 2004, "Numerical Predictions of Flow Structure Above a Dimpled Surface in a Channel," *Numer. Heat Transfer, Part A*, **45**(1), pp. 1–20.
 - [14] Won, S. Y., and Ligrani, P. M., 2004, "Numerical Predictions of Flow Structure and Local Nusselt Number Ratios Along and Above Dimpled Surfaces With Different Dimple Depths in a Channel," *Numer. Heat Transfer, Part A*, **46**(6), pp. 549–570.
 - [15] Patrick, W. V., and Tafti, D. K., 2004, "Computations of Flow Structures and Heat Transfer in a Dimpled Channel at Low to Moderate Reynolds Number," ASME Paper No. HT-FED2004-56171.
 - [16] Elyyan, M., Rozati, A., and Tafti, D. K., 2006, "Study of Flow Structures and Heat Transfer in Parallel Fins With Dimples and Protrusions Using Large Eddy Simulation," ASME Paper No. FEDSM2006-98113.
 - [17] Tafti, D. K., 2001, "GENIDLEST—A Scalable Parallel Computational Tool for Simulating Complex Turbulent Flows," *Proceedings of ASME Fluids Engineering Division (FED)*, Vol. 256, ASME, New York.
 - [18] Germano, M., Piomelli, U., Moin, P., and Cabot, W. H., 1991, "A Dynamic Subgrid-Scale Eddy Viscosity Model," *Phys. Fluids A*, **3**, pp. 1760–1765.
 - [19] Viswanathan, A. K., and Tafti, D. K., 2005, "Detached Eddy Simulation of Turbulent Flow and Heat Transfer in Ribbed Duct," *ASME J. Fluids Eng.*, **127**, pp. 888–896.
 - [20] Sewall, E. A., Tafti, D. K., Graham, A. B., and Thole, K. A., 2006, "Experimental Validation of Large Eddy Simulation of Flow and Heat Transfer in a Stationary Ribbed Duct," *Int. J. Heat Fluid Flow*, **27**, pp. 243–258.
 - [21] Zhang, L. W., Tafti, D. K., Najjar, F. M., and Balachander, S., 1997, "Computations of Flow and Heat Transfer in Parallel-Plate Fin Heat Exchangers on the CM-5: Effects of Flow Unsteadiness and Three-Dimensionality," *Int. J. Heat Mass Transfer*, **40**(6), pp. 1325–1341.
 - [22] Incropera, F., and DeWitt, D. P., 1996, *Fundamentals of Heat and Mass Transfer*, 4th ed., Wiley, New York.
 - [23] Tafti, D. K., 2005, "Evaluating the Role of Subgrid Stress Modeling in a Ribbed Duct for Internal Cooling of Turbine Blades," *Int. J. Heat Fluid Flow*, **26**, pp. 92–104.
 - [24] Kim, J., Moin, P., and Moster, R., 1987, "Turbulence Statistics in Fully Developed Channel Flow at Low Reynolds Number," *J. Fluid Mech.*, **177**, pp. 133–166.
 - [25] Ekkad, S. V., and Nasir, H., 2003, "Dimple Enhanced Heat Transfer in High Aspect Ratio Channels," *J. Enhanced Heat Transfer*, **10**(4), pp. 395–405.
 - [26] Chong, M. S., Perry, A. E., and Cantwell, B. J., 1990, "A General Classification of Three-Dimensional Flow Fields," *Phys. Fluids A*, **2**, pp. 765–777.

Transition on the T106 LP Turbine Blade in the Presence of Moving Upstream Wakes and Downstream Potential Fields

Maciej M. Opoka¹

e-mail: maciej.opoka@rolls-royce.com

Howard P. Hodson

Whittle Laboratory,
University of Cambridge,
Madingley Road,
Cambridge CB3 0DY, UK

Boundary layer measurements were performed on a cascade of the T106 high lift low-pressure (LP) turbine blades that was subjected to upstream wakes and a moving downstream potential field. Tests were carried out at a low level of inlet freestream turbulence (0.5%) and at a higher (4.0%). It is found that perturbations in the freestream due to both disturbances are superposed on each other. This affects the magnitude of the velocity perturbations at the edge of the boundary layer under the wakes as well as the fluctuations in the edge velocity between the wakes. Furthermore, the fluctuations in the adverse pressure gradient on the suction surface depend on the relative phase of the upstream and downstream disturbances, providing an additional stimulus for clocking studies. Time-mean momentum thickness values calculated from laser Doppler anemometry (LDA) traverses performed near the suction surface trailing edge are used to identify the optimum relative phase angle of the combined interaction. Unsteady suction surface pressures, quasiwall shear stress and LDA data illustrate the resulting multimode process of transition, which is responsible for the observed clocking effects. The optimum relative phase angle of the upstream wake and the downstream potential field can produce 0.25% of efficiency improvement through the reduction of the suction surface boundary layer loss. This reduction is mainly related to the calmed region and the laminar flow benefits that can be more effectively utilized than when only the upstream wakes are present. During the remaining parts of the cycle, the features that are usually associated with the wake and the potential field effects are still present. [DOI: 10.1115/1.2812415]

Introduction

The relative motion of the adjacent blade rows in turbomachines gives rise to a variety of unsteady interactions. The potential influence of a blade extends both upstream and downstream. It decays exponentially with a length scale of the order of blade pitch. Wakes form as the boundary layers shed from upstream blades and mix while convected downstream. Their rate of decay is much lower than that of the potential influence in the downstream direction. As a result, the interaction of wakes with downstream blade rows has received far more attention in the literature. Much of this work has been concerned with the effect of the velocity and turbulent fluctuations on the transition processes within the suction side boundary layer. This is important because the blade suction side boundary layers are responsible for most of the loss of efficiency (Curtis et al. [1]).

Studies of the effects of upstream wakes on a downstream blade row capture the most important unsteady interaction in the low-pressure (LP) turbine. However, there are anywhere between 2 and 14 blade rows in LP turbines. Consequently, there is an opportunity for interactions to take place across several blade rows. Binder et al. [2], for example, found that the fluctuations in the mean quantities caused by wakes persist through more than one blade row and their maximum values are relatively undiminished.

When the neighbouring stators or rotors have equal numbers of blades, the efficiency can be affected by changing the relative circumferential position (i.e., clocking) of these blade rows. Ex-

periments on clocking in LP turbines have been carried out by Halstead et al. [3] and by Solomon [4] using two stage LP turbines. Arnone et al. [5] performed numerical calculations for a LP turbine with three stages. The first two studies illustrated changes of the boundary layer on the second stator suction surface arising due to different clocking positions of the first stator. It was shown that wakes from the first stator were capable of inducing a separate transition process on the second stator in addition to that induced by the wakes of the first rotor. Arnone and his co-workers numerically investigated rotor as well as stator clocking effects showing that both clocking strategies could give similar benefits. The optimum clocking position was observed (as in many earlier clocking studies, see Refs. [3–5], for example) when wake segments of an upstream rotor/stator impinge on the leading edge of a downstream blade of the same type.

None of the above clocking studies makes reference to the effects of the upstream propagating potential field. However, the data of Binder et al. [2], Schröder [6] and Arndt [7] suggest that upstream potential field interactions do exist.

Today, there is a trend of increasing the lift coefficient and therefore the pitch-chord ratio of LP turbine blades. Since the axial blade row spacing in these machines can be less than 40% of the blade pitch, the unsteady perturbations in the velocity field due to an upstream propagating potential field of the downstream blade row can be of a comparable magnitude to the unsteady perturbations caused by an upstream wake, as shown by Opoka et al. [8]. In these circumstances, the successful design of blade rows with low solidity and reduced axial spacing will require a detailed understanding of the interaction between wakes and potential field disturbances. This will include the effects of blade row clocking but in a context that may be different to that previously studied.

¹Present address: Rolls Royce Deutschland, Dahlewitz, Germany.

Contributed by the International Gas Turbine Institute of ASME for publication in the JOURNAL OF TURBOMACHINERY. Manuscript received July 11, 2007; final manuscript received July 2, 2007; published online August 4, 2008. Review conducted by David Wilser. Paper presented at the ASME Turbo Expo 2007: Land, Sea and Air (GT2007), Montreal, Quebec, Canada, May 14–17, 2007.

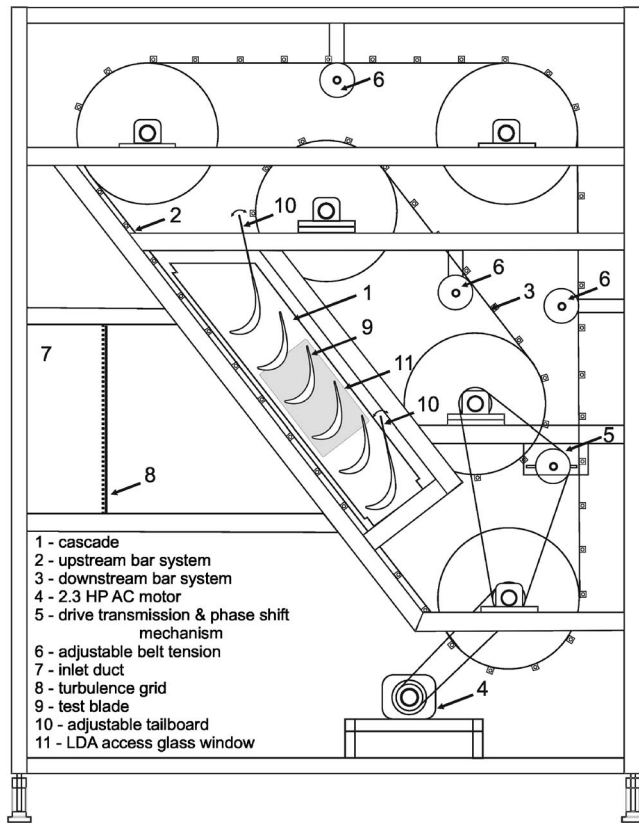


Fig. 1 T106A LP turbine bar passing rig

The current paper considers the combined effects of upstream wakes and downstream potential fields, as they appear in a multistage environment of LP turbines.

Experimental Setup

Previous studies of LP turbine cascades at the Whittle Laboratory have used a single system of moving belts and bars, see, for example, Curtis et al. [1] and Stieger et al. [9]. These experiments produced flows representative of a single stage of a turbomachine in the context of wake-boundary layer interactions. In order to facilitate replication of a downstream potential field, Opoka et al. [8] redesigned the facility of Stieger et al. [9] to accommodate a system of moving belts and large diameter bars situated downstream of the cascade.

Bar Passing Rig. The general arrangement of the test facility is shown in Fig. 1. The basic rig characteristics are summarized in Table 1. The cascade (1) consists of six T106 profiles, assembled with a pitch-chord ratio known as configuration “A.” The T106 profile is a high lift LP turbine blade. It is a high turning profile with a design exit Mach number of 0.59. Here, the same profile is tested at incompressible conditions. As shown in the schematic of the velocity triangles (see Fig. 2), the inlet conditions were chosen to reproduce those of a 50% reaction turbine. The Zweifel coefficient is of the order of 1.05.

The upstream moving bar system (2) that is shown in Fig. 1 is used to generate viscous wakes. The downstream moving bar system (3) was designed to reproduce the stator suction surface pressure oscillations associated with the potential fields of a downstream rotor. This dual belt system was driven by a 2.3 HP ac motor (4) with feedback control. The drive from the upstream system was transmitted onto the downstream system through the belt (5). The test facility was attached to the outlet of an open cycle low-speed wind tunnel, where a centrifugal fan supplied the

Table 1 Characteristic dimensions of T106A cascade

| Cascade properties | |
|--|-------|
| Number of blades in the cascade | 6 |
| Real chord— C (mm) | 198 |
| Axial chord— C_{ax} (mm) | 170 |
| Cascade pitch— s (mm) | 158.2 |
| Pitch to chord ratio— $s/C=\tau$ | 0.799 |
| Blade aspect ratio— h/C | 1.884 |
| Design inlet flow angle α_1 (deg) | -37.7 |
| Design exit flow angle α_2 (deg) | 63.2 |
| Upstream bar diameter— d (mm) | 2.05 |
| Downstream bar diameter— D (mm) | 47.5 |
| Upstream bar to trailing edge (mm) | 70 |
| Downstream bar to trailing edge (mm) | 112 |
| Bars pitch in both systems (mm) | 237 |

airflow. The set of gauzes and honeycomb inserts in the tunnel made the flow uniform before delivering it into the cascade test section through the inlet duct (7).

Because the propagation of the unsteady potential field depends on the flow Mach number, it is impossible to reproduce an exactly equivalent unsteady pressure field in a low-speed facility such as the one used here. Being conscious of the limitation of such an approach, inviscid numerical predictions for the T106 LP turbine repeating stage design, with pitch and chord ratios of 1:1.5 and a blade row gap equal to 43% of the downstream rotor blade pitch (40% of rotor C_{ax}), were carried out by Antoranz and de la Calzada [10]. These were followed by a series of simulations in which the downstream rotor was replaced with a cylindrical bar. The bar diameter and the spacing between stator trailing edge and the bar center were chosen to match the amplitude of pressure oscillations seen on the stator suction surface as induced by the real rotor blade. The downstream bar system was designed following the results of these simulations. Opoka et al. [8] have measured the influence of moving downstream potential fields on the

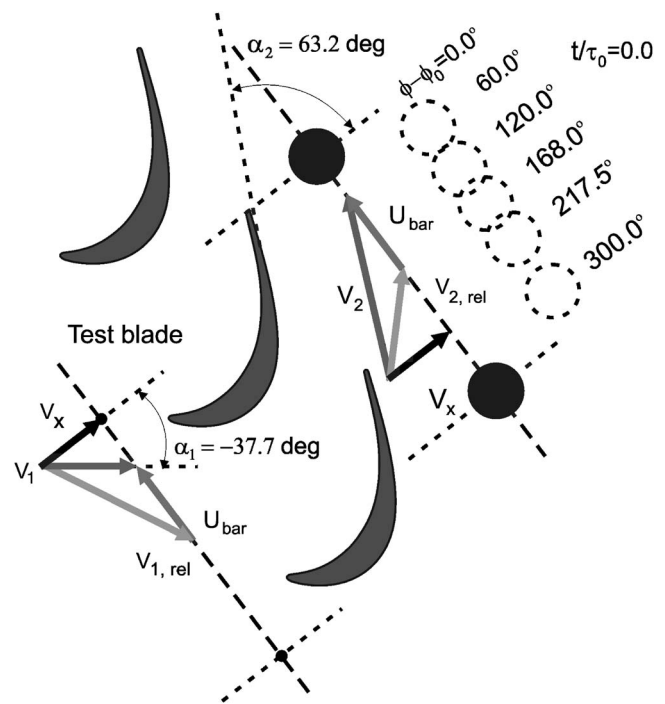


Fig. 2 T106A cascade, with upstream and downstream bars shown at time $t/\tau_0=0.0$ and relative phase angle $\phi-\phi_0=0.0$ deg, 60.0 deg, 120.0 deg, 168.0 deg, 217.5 deg, 300.0 deg

suction surface boundary layer, using this test facility. Their unsteady surface pressure data have shown similar trends to those observed by Dring et al. [11], who studied this type of rotor-stator interaction on a large-scale turbine rig.

Test Conditions and Cascade Equipment. The flow delivered from the wind tunnel is characterized by low turbulence levels of the order of 0.5%. To reach levels of inlet freestream turbulence intensity more representative of the multistage environment (2–4%, see Halstead et al. [3]), a turbulence grid was used in half of the experiments. The turbulence grid (see (8) in Fig. 1) was based on the work of Roach [12]. The grid was located at a distance of three axial chords upstream of the test blade (9). This provided an inlet freestream turbulence intensity (FSTI) of 4.0%, measured in the absence of the cascade, at a location corresponding to the leading edge of the test blade. It should be mentioned that the turbulence grid was not parallel to the cascade inlet plane. Therefore, the decay of turbulence varies across the cascade in the pitchwise direction. The correlation of Roach predicts the turbulence levels at the leading edges of the top and bottom blades to be equal to 5.65% and 2.95%, respectively. Although these turbulence levels differ, the levels are such that the differences in blade boundary layer behavior, which result from the varying inlet turbulence intensity, do not seriously affect the cascade periodicity at the Reynolds number investigated here.

Total and static pressure probes at the inlet and wall tapings at the outlet from the cascade were used to monitor the flow conditions and check the level of inlet uniformity and outlet periodicity. Adjustable tailboards (10), shown in Fig. 1, extending from the trailing edge of the top and bottom blades were used to ensure that the outlet flow was periodic.

The pitch ratio for the upstream bar system, the cascade and the downstream bar system was 1:0.667:1, as shown in Fig. 2, for which the initial position of time ($t/\tau_0=0.0$) has been presented. A ratio of 1:0.667:1 is similar to that found in many LP turbines.

Measuring Techniques and Data Presentation. The cascade flow conditions were monitored with a Scanivalve DSA 3017 16 channel pressure scanner.

The T106 test blade (9) shown in Fig. 1 was equipped with surface pressure tapings. The tapings had a diameter of 0.3 mm and were located at 45% of the span. The time-mean levels of surface static pressure were measured using a Scanivalve system. Surface flush-mounted, fast response Kulite pressure transducers (model XCS-062) were used to acquire unsteady suction surface pressures at blade midspan. A detailed description of the Kulite signal acquisition procedure may be found in Stieger et al. [9].

A sheet of 50 hot film sensors spaced at intervals of 2.54 mm in the streamwise direction was fitted on the blade suction surface at midspan. The array was manufactured by Senflex. The sensors were used to measure the quasiwall shear stress distribution using the procedure described in Hodson et al. [13]. Each sensor was connected to a Dantec C-series anemometer. The signal outputs from each anemometer were first acquired with filter settings that provided only the mean component. Then, a bandpass filter was used to acquire the fluctuating part.

During the acquisition of the hot film and pressure transducer data, the logging frequency was 10 kHz and 128 ensembles of 4096 samples were acquired. The bar passing frequency was equal to approximately 28 Hz. The pressure data in this paper are presented as an ensemble averaged pressure coefficient. This is defined in Eq. (1). Raw hot film signals were extracted from the first ensemble of acquired data.

$$\langle C_{p2iss} \rangle = \frac{P_{01} - \langle P_{S(s,t)} \rangle}{P_{01} - P_{S2}} \quad (1)$$

One of the cascade sidewalls was equipped with a glass window (11) to allow laser beam access (see Fig. 1). Two-dimensional, suction surface boundary layer surveys were per-

formed with a Dantec LDA system. This included a 5 W argon ion laser (Coherent Innova 70) and Dantec FibreFlow System with a beam expander. To avoid interruption of the laser beams by the blade surface, the laser probe axis was inclined with respect to the blade suction surface. The size of the measuring volume was equal to approximately $0.08 \times 0.08 \times 1.00 \text{ mm}^3$.

The laser Doppler anemometry (LDA) system was operated in backscatter mode. The Dantec burst spectrum analyzers (BSAs) and photomultiplier tubes were controlled with LABVIEW software. The acquisition was triggered by each bar passing event. Data were collected in the dead time mode with a dead time interval that ensured statistical independence of the acquired data.

The seeding for the LDA was generated using a TSI Six Jet Atomizer with Shell Odina Oil. The mean particle size was approximately $1.5 \mu\text{m}$. The data rate during the acquisition varied between 1.5 kHz and 5 kHz.

During the postprocessing of laser signals, a coincidence filter was used. The velocity bias resulting from periods of higher or lower velocity was removed using a residence time weighting factor as defined in Eq. (2), (see George [14]).

$$\eta_i = \frac{t_{ri}}{N} \quad (2)$$

$$\sum_{j=1}^N t_{rj}$$

The LDA data were ensemble averaged by first dividing the wake passing period into 128 time bins. Each time bin was evaluated based on a nominal average of 500 samples. The weighting factor and mean were then calculated for each time bin according to Eqs. (2) and (3).

$$\langle u \rangle = \sum_{i=1}^N \eta_i u_i \quad (3)$$

The traverses were performed perpendicular to the suction surface, in the boundary layer region, between 0.1 mm and 16 mm above the wall at 45% of the blade span. The complete traverse consisted of 21 stations, with the first millimeter above the wall being traversed in five steps. From these LDA measurements, the time dependent ensemble mean momentum thickness value was derived using Eq. (4). The edge of the boundary layer was defined as the height where the velocity was equal to 98% of the freestream value. The LDA velocity data were nondimensionalized with the cascade isentropic exit velocity (V_{2is}).

$$\langle \theta \rangle = \int_{y=0}^{\langle \delta_{98} \rangle} \frac{\langle u \rangle}{\langle U_e \rangle} \left(1 - \frac{\langle u \rangle}{\langle U_e \rangle} \right) dy \quad (4)$$

The data presented in this paper were acquired at a Reynolds number of $Re_{2is}=1.6 \times 10^5$, based on the exit isentropic velocity and the real chord, as given by Eq. (5). The flow coefficient, defined by Eq. (6), was equal to 0.83. The reduced frequency of wake and potential field disturbances, defined by Eq. (7), was set to 0.46. The background flow was characterized by two levels of inlet freestream turbulence intensity ($Tu_1=0.5\%$ and 4.0%).

$$Re_{2, is} = \frac{\rho V_{2, is} C}{\mu} \quad (5)$$

$$\phi = \frac{V_{x1}}{U_{bar}} \quad (6)$$

$$F_{red} = \frac{f_{bar} C}{V_{2, is}} \quad (7)$$

Uncertainty Analysis. At the exit from the cascade, the exit dynamic pressure varied by less than 2.5% over the five passages. Over the central passages, the variation was less than 1%.

The inclination of the laser probe with respect to the suction

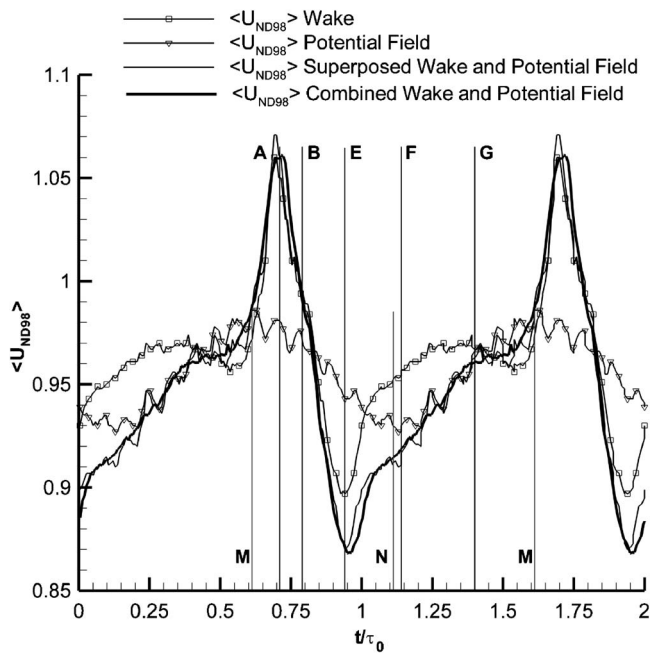


Fig. 3 Nondimensional ensemble averaged velocity at the boundary layer edge due to separate and combined effects $Re_{2is}=1.6 \times 10^5$, $F_{red}=0.46$, and $Tu_1=0.5\%$, $s/S_0=0.96$, $\phi-\phi_0=0.0$ deg

surface of the blade was of the order of 5 deg. This was to avoid any obstruction of the laser beams by the blade wall. The velocity measured with the inclined LDA probe is insignificantly different from that measured with a noninclined probe (less than 0.5%) and for this reason it was considered unnecessary to apply a correction to the measurements. The 2D LDA data were processed with a coincidence window set to 0.005 ms. The step resolution of the traversing system was 0.025 mm.

The mean pressure levels were measured using the Scanivalve DSA 3107 array with a ± 2500 Pa range. The discretization error on this measurement is 0.17 Pa, which corresponds to 0.2% of the exit dynamic pressure at $Re_{2is}=1.6 \times 10^5$. The sensitivity of the Kulite transducer system was approximately equal to 500 Pa/V with a discretization error of 0.05 Pa.

Discussion of Results

Freestream Velocity. Figure 3 shows ensemble averaged time traces of nondimensional velocity, measured at the boundary layer edge at $s/S_0=0.96$ for the case of $Tu_1=0.5\%$. Two of the lines represent the separate cases of the upstream wakes (rectangles) and the downstream potential disturbances (triangles). The black-thick line represents the measured velocity during a combined interaction at the relative phase angle of $\phi-\phi_0=0.0$ deg, as shown in Fig. 2. The black-thin line shows the superposed effects of the wake and the potential field perturbation on the time mean flow measured during a combined interaction. The upper set of labels (A–G) is used to describe the wake effects as in Refs. [15,16]. Points A, B, and E placed at particular times (t/τ_0) indicate the maximum positive velocity perturbation in the freestream, which occurs in the leading portion of the wake, the centreline of the wake and the maximum negative velocity perturbation in the free stream, which occurs in the trailing portion of the wake. The remaining Labels F and G refer to the calmed region that will receive more attention and will be explained in the discussion of the hot film results. The lower set of Labels M and N is used to indicate the occurrence of the velocity maximum and minimum induced by the single downstream potential field (see Ref. [8]).

Figure 3 shows that perturbations due to separate upstream

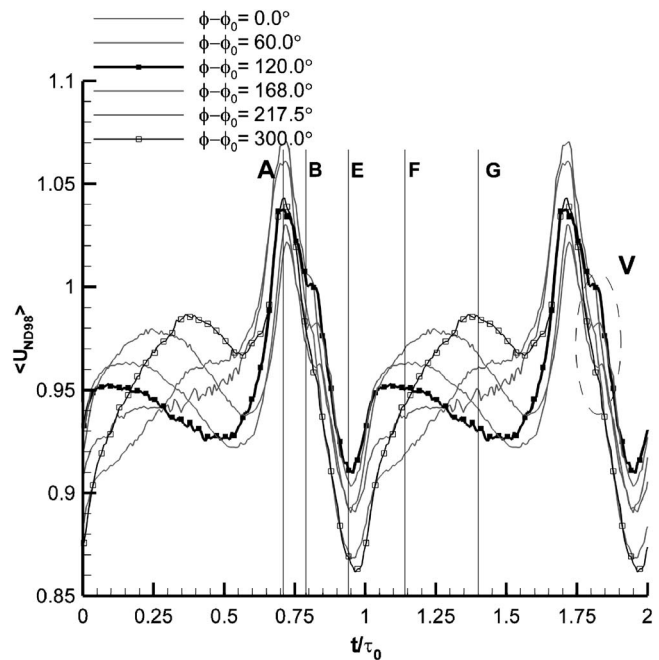


Fig. 4 Influence of the relative phase angle ($\phi-\phi_0$) of combined interactions illustrated with nondimensional ensemble averaged velocity at the boundary layer edge. $Re_{2is}=1.6 \times 10^5$, $F_{red}=0.46$, and $Tu_1=0.5\%$, $s/S_0=0.96$, $\phi-\phi_0=0.0$ deg, 60.0 deg, 120.0 deg, 168.0 deg, 217.5 deg, 300.0 deg

wakes and downstream potential fields can be superposed, at least to a first order. The most significant difference between the measured (black-thick) and superposed (black-thin) time traces is a lack of the high frequency component in the measured data. The high frequency oscillations seen during the potential field experiments (triangles) were due to the breakdown of vortices shed by the separation bubble. Although these vortex breakdowns occurred further upstream in those tests, their effects on the velocity field are still seen near the trailing edge. The lack of such perturbations in the case of the combined interaction (black-thick) might suggest that the wakes modify the transition.

Boundary layer traverses were performed at $s/S_0=0.96$ for six clocking positions (as defined in Fig. 2). Figure 4 shows ensemble averaged time traces of the nondimensional velocity measured at the boundary layer edge for the case of $Tu_1=0.5\%$. Velocity changes during one period of the cycle illustrate the effects of the relative phase angle of the combined interaction.

In Fig. 4, between the wakes ($t/\tau_0=0.0-0.6$), the velocity varies as the clocking settings are changed. Here, at $s/S_0=0.96$, within the region (E–G), two extreme clocking cases are characterized by the first having approximately linear velocity increase ($\phi-\phi_0=0.0$ deg) with a more sinusoidal tendency. Later in time, between $t/\tau_0=0.6-1.0$, the upstream wake is passing over the measurement location (A–E). This is manifested on all presented traces as an acceleration-deceleration process (indicative of the so-called negative jet behavior of the wake). Depending on the phase of the downstream potential field into which the wake enters (i.e., the relative phase angle), the combined result is modified. Traces at $\phi-\phi_0=0.0$ deg and $\phi-\phi_0=168.0$ deg represent the strongest (Velocity maxima A and M are in phase, see Fig. 3) and the weakest (out of phase) velocity perturbations between Times A and E.

The data for the $Tu_1=4.0\%$ are not presented here; however, measurements did not show significant differences between the low and high freestream turbulence cases with respect to the freestream velocity at this surface position, except for the region labeled V, shown in Fig. 4. This perturbation in the velocity (V)

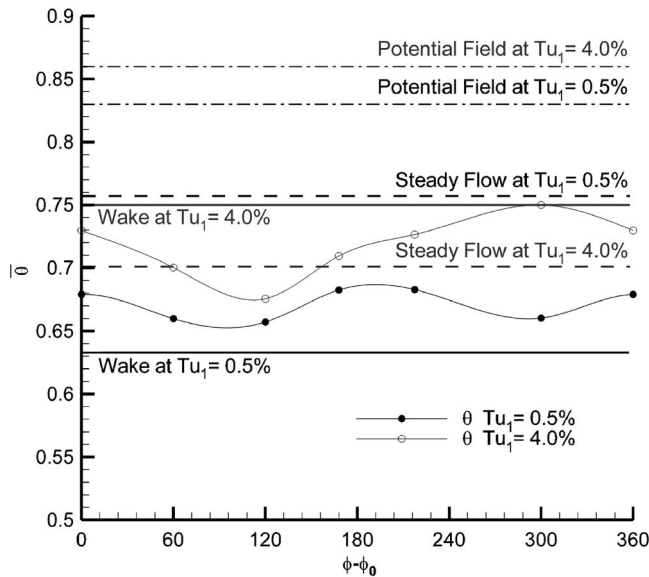


Fig. 5 Effect of Clocking—Time mean of momentum thickness, at trailing edge location at $Tu_1=0.5\%$ and 4.0% , $Re_{2is}=1.6 \times 10^5$, $F_{red}=0.46$ at surface distance of $s/S_0=0.96$, steady flow, wake-only, potential field-only, and combined interaction at $\phi-\phi_0=0.0$ deg, 60.0 deg, 120.0 deg, 168.0 deg, 217.5 deg, 300.0 deg

during a deceleration phase (A–E) was observed only at $Tu_1=0.5\%$. It is a result of the breakdown of roll-up vortices that were formed further upstream due to the wake negative jet (flow history).

Time-Mean Trailing Edge Momentum Thickness. Curtis et al. [1] presented a loss breakdown for LP turbines. The profile loss can represent about 60% of the total inefficiency, being mainly affected (60%) by the suction surface boundary layer. Strictly, the entropy that has been created in the boundary layer upstream of the trailing edge is measured by their entropy or energy thickness (Denton, [17]). Here, however, the momentum thickness (θ) near the trailing edge will be used to provide a measure of the suction surface loss. This is because it is related to the mixed out loss of the boundary layer far downstream of the trailing edge [17]. In practice, the conclusions are unchanged whether the momentum thickness or the energy thickness is considered.

The background for the clocking work was established by documenting the effects of separate upstream [16] and downstream [8] disturbances. In Fig. 5, horizontal (solid and dashed-dotted) lines indicate time-mean levels of the momentum thickness measured for separate effects of the upstream wakes and the downstream potential disturbances. The dashed lines indicate the time-mean levels of momentum thickness in steady flow. The black and gray colours are used to differentiate between the lower and higher levels of FSTI. The data shown in Fig. 5 were taken at $s/S_0=0.96$.

Figure 5 shows that at the lower FSTI (black) for the wake-only case, the time-mean momentum loss significantly decreases when compared to steady flow. This benefit is due to the low losses that are produced in the calmed region and its effect in limiting the growth of the separation bubble in between the wakes to below its steady flow dimensions. On the contrary, for the wake-only case at the higher FSTI (gray), the loss in the boundary layer rises above steady flow values. This loss increase occurs because the negative effects of transition in the wake path are not counterbalanced by the benefits of calmed region, and because the boundary layer in between the wakes regained its steady flow character and loss

level.

In the cases of only the downstream potential field, for both levels of FSTI, transition onset occurred close to the steady flow location or was forced upstream. This produced an extended turbulent wetted area. Figure 5 shows that this was responsible for a significant increase in the trailing edge momentum thickness.

The filled and empty symbols in Fig. 5 represent time mean θ for each of the six relative phase angles of the combined interaction that were investigated at a low (0.5% black) and at a high (4.0% gray) FSTI. The data points are joined by curves that have been fitted to the data. Figure 5 shows that for both FSTI cases, the minimum in the boundary layer loss exists at a relative phase angle of $\phi-\phi_0=120.0$ deg. This clocking position was characterized by one of the smallest variations in velocity measured at the trailing edge between A and E (see Fig. 4). While the minimum loss occurs at the same relative phase angle for both cases of FSTI, there is no common value of $\phi-\phi_0$ for which a maximum of the boundary layer loss would be generated. At a relative phase angle of $\phi-\phi_0=300.0$ deg, the maximum momentum thickness was measured for the case of the higher FSTI. In the case of the lower FSTI, a second minimum occurs at this same relative phase angle.

At the lower level of FSTI, with the combined interactions, the lowest time-mean momentum thickness ($\phi-\phi_0=120.0$ deg) is 5% less than the highest level ($\phi-\phi_0=217.5$ deg). At the higher FSTI, the clocking effect can be used to produce a 10% reduction when compared to the worst case. The minimum value is now below the steady flow level. The reasons for these observations are related to the competing effects of transition and calming. These will be discussed in the following sections.

Current designs of LP turbines have an efficiency of the order of 93%. Using the aforementioned breakdown of losses of Curtis et al. [1], the suction side boundary layer loss is equivalent to a reduction in the efficiency of approximately 2.5%. Therefore, using the results of Fig. 5, the maximum benefit in machine efficiency due to clocking can be of the order of 0.25%. Furthermore, the mean benefit resulting from the combined wake and potential field interactions will be of the order of 0.125%. This would be the benefit in the case of mismatched blade numbers, since the entire range of relative phase angles would then exist.

Given that the flow in LP turbines is mainly two dimensional, so that the flow properties do not vary significantly across central part of the span (25–75%), the clocking of the transition patterns might be possible.

Surface Pressure Variations. The cases of $\phi-\phi_0=120.0$ deg and $\phi-\phi_0=300.0$ deg were chosen for a further discussion on the effects of the relative phase angle for the combined interaction cases. In Fig. 6, a compilation of surface pressure data is presented in form of the surface pressure coefficient $C_{p,2is}$ as defined by Eq. (1). Again, black and gray colors are, respectively, attributed to the lower (0.5%) and the higher (4.0%) level of FSTI. The lower part of distributions that represents the pressure side (dashed lines), and the very front of the suction side are data that were measured in steady flow with surface pressure tappings. The remaining part of the suction surface is represented by ensemble-averaged data that were acquired with a system of surface pressure tappings (mean) and Kulite transducers (fluctuating component). For each case of FSTI, time-mean distributions of the ensemble-averaged data are shown together with a set of vertical lines that represents the extent of the local pressure perturbations. Furthermore, for each level of FSTI, both sets of data (time mean and envelope) are shown at two relative phase angles. The case of $\phi-\phi_0=120.0$ deg is represented with thick lines, and $\phi-\phi_0=300.0$ deg with thin lines. To avoid overlapping of vertical lines, only the lines for the case of $\phi-\phi_0=120.0$ deg at $Tu_1=0.5\%$ are placed at the correct surface distances. The remaining three cases were shifted by a fraction of s/S_0 to the left or to the right.

The time-mean $C_{p,2is}$ distributions, which are shown in Fig. 6,

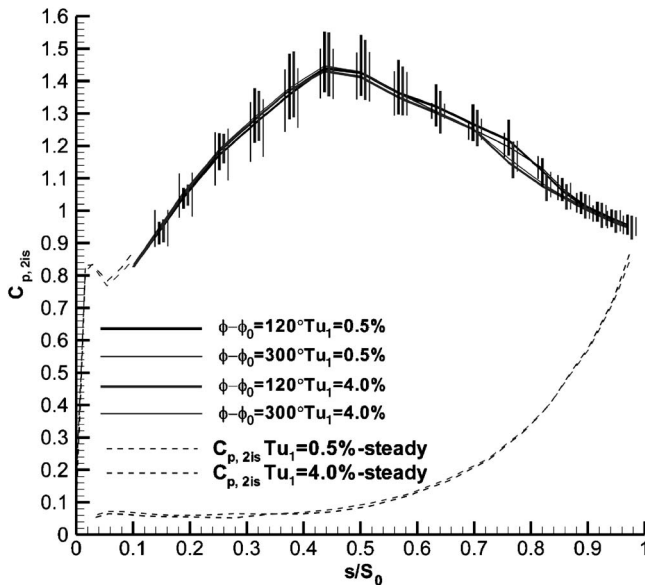


Fig. 6 Effect of Clocking—Surface pressure coefficient measured at $\phi-\phi_0=120.0$ deg and $\phi-\phi_0=300.0$ deg for both $Tu_1=0.5\%$ and $Tu_1=4.0\%$, $Re_{2is}=1.6 \times 10^5$, $F_{red}=0.46$

do not differ significantly between the two relative phase angles (thick lines: $\phi-\phi_0=120.0$ deg and thin lines: $\phi-\phi_0=300.0$ deg). This is true for both FSTI. The most pronounced change appears at the lower FSTI, in the region between $s/S_0=0.60-0.76$. This is where the boundary layer separated. Within this region, at the $\phi-\phi_0=300.0$ deg (thin black line), the time-mean values of $C_{p,2is}$ are smaller than at $\phi-\phi_0=120.0$ deg. This indicates that the time-mean blockage caused by the boundary layer (i.e., the height of the separation bubble) was reduced. With respect to the suppression of the separation, the effect of the relative phase angle is smaller than the effect of the FSTI. (More details on the latter can be found in Ref. [16].)

Although the time-mean data do not differ significantly at the corresponding cases of freestream turbulence shown on Fig. 6, the magnitudes of the local peak-to-peak pressure perturbations revealed a strong dependence on the relative phase angle of the combined interaction. The effect of freestream turbulence is insignificant with respect to the local peak-to-peak pressure perturbations. The maximum peak-to-peak surface pressure perturbations for both relative phase angles appeared at $s/S_0=0.375$. They are of the order of 20% of the exit dynamic pressure. On the front part of the suction surface, higher pressure perturbations were observed for the case of $\phi-\phi_0=300.0$ deg (thin lines), while on the rear part of the suction surface (between $s/S_0=0.60$ and 0.76) perturbations for the case of $\phi-\phi_0=120.0$ deg were approximately twice those for the case of $\phi-\phi_0=300.0$ deg. Surprisingly for $\phi-\phi_0=120.0$ deg, even in the region between $s/S_0=0.60-0.76$, the magnitude of the peak-to-peak pressure perturbations were independent of the FSTI. In each case, these reached approximately 12% of the exit dynamic pressure. In the case of only upstream wakes [9] (low FSTI), the magnitude of the peak-to-peak pressure perturbations reached 30% in the separation bubble. This was attributed to the effects of the rolling-up into vortices of the separated shear layer, which was triggered by the negative jet behavior of the wake. This might indicate that the sizes of the roll-up vortices were significantly reduced at the lower FSTI and are more comparable to those that were observed in Ref. [16] in the case where only upstream wakes were present at the higher FSTI. In that case, the peak-to-peak pressure perturbations at corresponding surface distances reached 10% of the exit dynamic pressure.

The data for the cases of the lower FSTI presented in Fig. 6 are

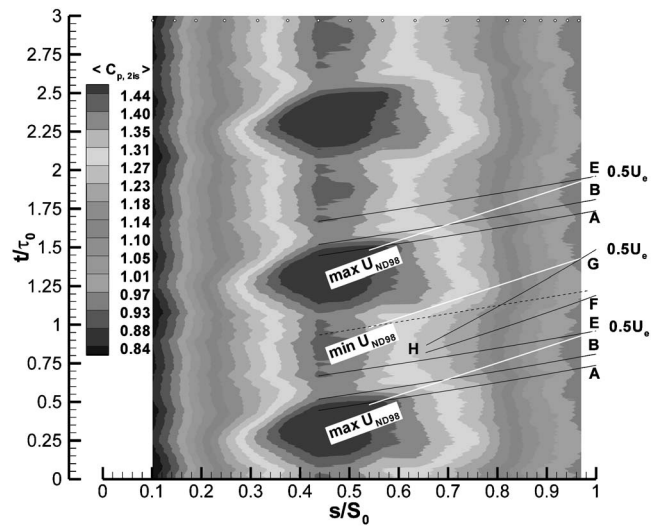


Fig. 7 Ensemble averaged distribution of surface pressure coefficient $C_{p,2is}$ measured at $Re_{2is}=1.6 \times 10^5$, $F_{red}=0.46$, $Tu_1=0.5\%$, and $\phi-\phi_0=120.0$ deg

redrawn as distance-time diagrams in Fig. 7 ($\phi-\phi_0=120.0$ deg) and Fig. 8 ($\phi-\phi_0=300.0$ deg). In these diagrams, the abscissa represents the nondimensional surface length and the ordinate shows the nondimensional time. Here, three periods of the combined interactions are shown. The contour field represents values of the surface pressure coefficient $C_{p,2is}$. The definition of the pressure coefficient (see Eq. (1)) is such that high values represent low values of the surface pressure. The symbols at the top of the diagrams indicate the sensor positions. The solid black lines imposed on the contour field indicate trajectories of the wake in the freestream (A, B, and E). The white lines show the paths of the velocity minima and maxima observed during tests with only downstream potential field disturbances. The lines between points H and F and H and G will be used later when describing particular transition patterns.

Figure 7 shows that at the lower FSTI, the value of $C_{p,2is}$ at the peak suction point ($s/S_0=0.44$) strongly oscillates. The maximum value occurs between $t/\tau_0=0.06-0.56$. In the remaining part of

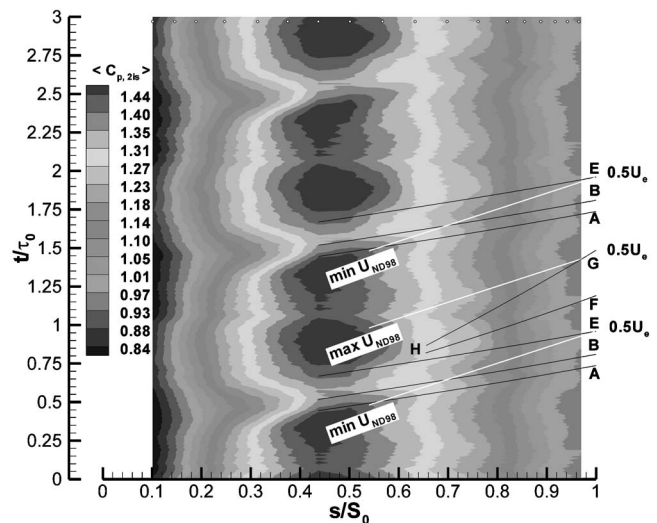


Fig. 8 Ensemble averaged distribution of surface pressure coefficient $C_{p,2is}$ measured at $Re_{2is}=1.6 \times 10^5$, $F_{red}=0.46$, $Tu_1=0.5\%$, and $\phi-\phi_0=300.0$ deg

the cycle, the value was reduced by as much as 20% when compared to the maximum. Near the trailing edge, the pressure oscillations are much smaller than those at the peak suction point (see also Fig. 6). Therefore, the severity of the adverse pressure gradient will oscillate. In Fig. 7, following the wake passage (above line E), the adverse pressure gradient first reduced during time $t/\tau_0=0.56-1.06$ and then increased during time $t/\tau_0=1.06-1.56$.

The strong oscillations that are seen within the region between $s/S_0=0.40-0.76$ appear because the phases of the perturbations in pressure or in velocity associated with the separate disturbances are of the same sign. For example, Line A, which represents the maximum positive velocity perturbation due to wake intersects with the line of maximum velocity due to the downstream potential field disturbances at $s/S_0=0.55$. When the relative phase angle is changed by 180 deg (see Fig. 8), the temporal variation of the surface pressure is reduced. This is because the phases of the perturbations in pressure or in velocity associated with the separate disturbances are now of the opposite sign. As a result, each of the upstream and downstream disturbances creates its own peak in the values of $C_{p,2is}$ at the peak suction point ($s/S_0=0.44$). As a consequence, the severity of the adverse pressure gradient is significantly reduced. However, the more adverse pressure gradient now occurs twice as often during one cycle of the combined interaction.

In Fig. 8, following the passage of the wake, above Line E, the value of the surface pressure coefficient rises again (lower surface pressure) due to the accelerative phase of the potential field interaction that extends up to the line of maximum velocity. This reveals an important difference between the cases of $\phi-\phi_0=120.0$ deg and $\phi-\phi_0=300.0$ deg, with respect to the conditions at which the rear portion of the wake induces transition (point H), and where the calmed region develops. For the case of $\phi-\phi_0=120.0$ deg, the wedge formed between Lines H-F and H-G (it will be shown below that this is where the calmed region can be found) lays within the decelerative period of the potential field cycle and will experience a reduced severity of the adverse pressure gradient. However, for $\phi-\phi_0=300.0$ deg, the wedge between Lines H-F and H-G is within the accelerative period, where the steeper adverse pressure gradient is present. Both separation and wake induced transition might be promoted further upstream in the presence of more severe adverse pressure gradients. Also, the potential of calmed regions to remain attached or laminar can be challenged by more aggressive adverse pressure gradients.

In Fig. 9, five sets of surface pressure coefficient are presented, at equally spaced time intervals within 1 cycle period. Only a portion of the suction surface distributions is illustrated. The lower set of circles above the abscissa indicates the Kulite sensor positions. The meaning of upper circles and of a black dashed line will be explained in the following paragraphs. In Fig. 9, the presence of regions of almost constant static pressure suggests that the separation bubble may be present at many of the time instants shown, in all of the presented cases. Its position and size vary in time, depending on $\phi-\phi_0$ and the FSTI. These distributions will be referred to in the discussion of the transition processes in the following section.

Transition Mechanisms at Minima and Maxima of Loss Due to Clocking. Time traces of raw hot film signals acquired at five streamwise locations are presented in Figs. 10 and 11. The position of the hot film sensors is indicated in Fig. 9 with black circles placed above the abscissa. In Figs. 10 and 11, the effect of the relative phase angle on the transition process is illustrated for both FSTI levels. In each figure, the thick (top) traces represent the case of $\phi-\phi_0=120.0$ deg, while the thin (bottom) traces are for $\phi-\phi_0=300.0$ deg. There are two ordinates for each plot, the total range on each one is the same although the mean is shifted to avoid an overlapping of the traces. The left ordinate is for $\phi-\phi_0=120.0$ deg. The vertical lines, with corresponding labels, represent the same events as in previous figures.

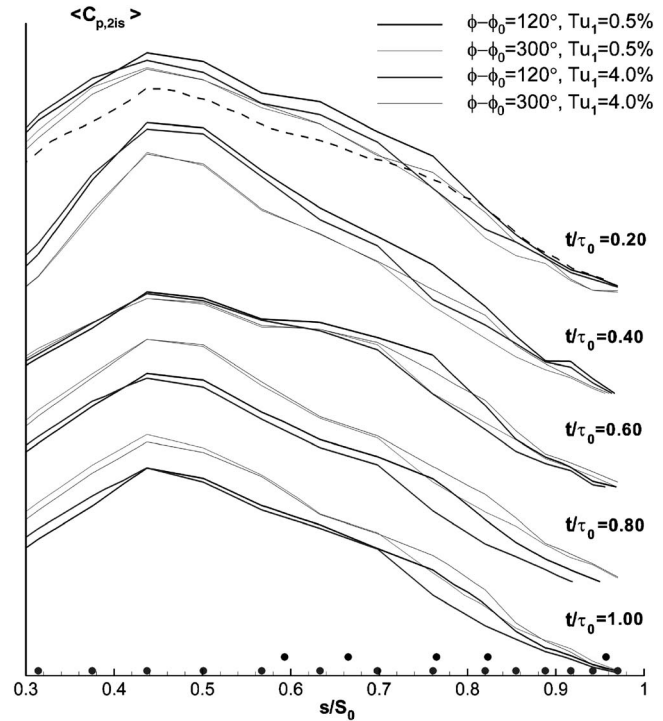


Fig. 9 Ensemble averaged of suction surface pressure coefficient $C_{p,2is}$ at five time instants within one period of the combined interaction. Data measured at $Re_{2is}=1.6 \times 10^5$, $F_{red}=0.46$, $Tu_1=0.5\%$ and 4.0% and $\phi-\phi_0=120.0$ deg and 300.0 deg

Lower Freestream Turbulence Intensity Case. In Fig. 10, at the most upstream surface location of $s/S_0=0.593$, the boundary layer as the wake arrives (shortly before Point A) is separated in both cases of $\phi-\phi_0$ (see Fig. 9, $t/\tau_0=0.40$ and $t/\tau_0=0.60$). In such inflexional boundary layers, which are experiencing a strong perturbation due the wake negative jet, the first significant growth in the amplitude of instability waves appears anywhere between A and E. Evidence of these waves at $s/S_0=0.593$ can also be found in Figs. 7 and 8. These figures also contain evidence of a similar type of the wave activity upstream of the peak suction point. This indicates a Tollmien–Schlichting (TS) convective wave character. The presence of the TS waves upstream of the separation point suggests that the separation at these times is of a transitional type (Hatman and Wang [18]).

In Fig. 10 between A and E, the amplitudes of the shear stress perturbations at $s/S_0=0.593$ are comparable in both cases of $\phi-\phi_0$. In time after E, only for the case of $\phi-\phi_0=120.0$ deg, the growth of instability waves continues almost up to Point N. This point indicates the end of a decelerative phase due to the downstream potential field disturbances. On the contrary, the waves are attenuated after Point E for the case of $\phi-\phi_0=300.0$ deg. This is believed to result from the accelerative phase of the potential field cycle that lasts to the Point M. Following the time of $t/\tau_0=1.00$, and up to the next wake front ($t/\tau_0=1.52$), the trace representing $\phi-\phi_0=300.0$ deg, remains flat indicating a laminar flow that just separates. For the case of $\phi-\phi_0=120.0$ deg, the upper trace shows reducing shear stress values that is representative of an attached flow ($t/\tau_0=1.00$) that tends to a separation ($t/\tau_0=1.20$). The above statements can be confirmed in Fig. 9. These very subtle differences in the behavior of separation point are due to changed severity of the adverse pressure gradient in between the wakes (see Figs. 7 and 8).

At the next surface location of $s/S_0=0.65$, most of the fluctuations between A and E in both cases of $\phi-\phi_0$ have developed into higher frequency components indicating that the breakdown of the

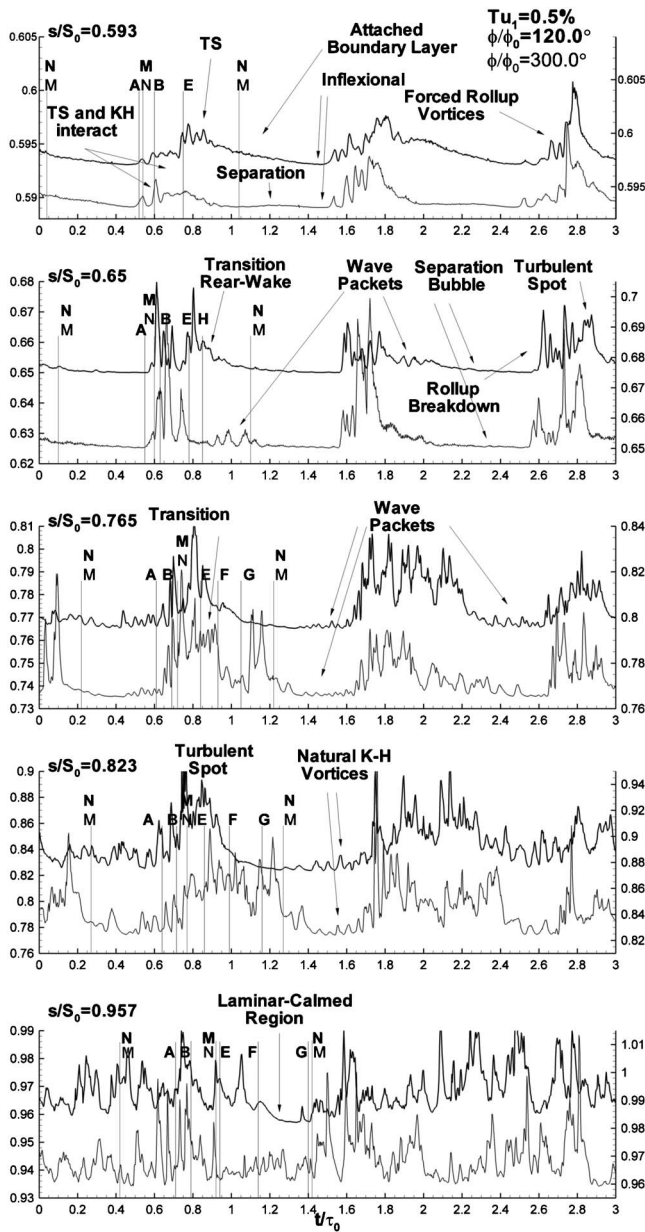


Fig. 10 Combined Interaction—raw hot film signals, $Re_{2is} = 1.6 \times 10^5$, $F_{red} = 0.46$, $Tu_1 = 0.5\%$, $\phi - \phi_0 = 120.0$ deg—first minimum of momentum loss, $\phi - \phi_0 = 300$ deg—second minimum of momentum loss

waves into turbulent spots has occurred. The magnitude of the peak-to-peak pressure perturbation shown in Fig. 6, at about $s/S_0 = 0.63$ and further downstream, for the case of $\phi - \phi_0 = 300.0$ deg was half of that seen for $\phi - \phi_0 = 120.0$ deg. The higher pressure perturbation measured at $\phi - \phi_0 = 120.0$ deg, is related to stronger inflexional tendencies invoked by the “in-phase” configuration of upstream and downstream disturbances (higher $C_{p,2is}$ in front of Line A in Fig. 7 than in Fig. 8, or in Fig. 9 at $t/\tau_0 = 0.60$). Increasing the height of the inflexion point in the velocity profile and a longer stream wise distance along which inflexional profiles develop would promote the growth of Kelvin–Helmholtz instabilities and could lead to coherent structure formation, see [16]. In fact, both types of instabilities that coexist in a transitional separated shear layer (TS and Kelvin–Helmholtz (KH)) may be accompanied by vortex formation [18].

For the case of combined unsteady effects discussed here, at

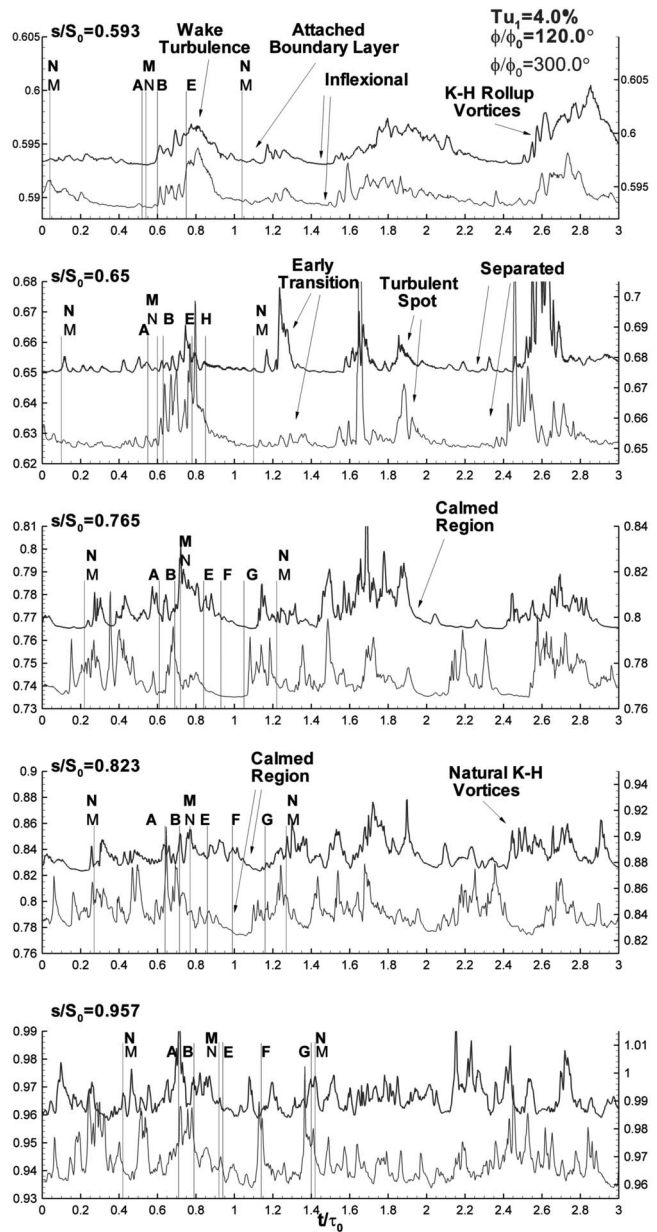


Fig. 11 Combined Interaction—raw hot film signals, $Re_{2is} = 1.6 \times 10^5$, $F_{red} = 0.46$, and $Tu_1 = 4.0\%$, $\phi - \phi_0 = 120$ deg—minimum of momentum loss, $\phi - \phi_0 = 300$ deg—minimum of momentum loss

$\phi - \phi_0 = 120.0$ deg, the shear layer does roll up to form KH type vortices between $s/S_0 = 0.65$ and $s/S_0 = 0.761$. Going back to Fig. 4, in the case of $\phi - \phi_0 = 300.0$ deg, within region labeled V, there is no perturbation in velocity, while for the case of $\phi - \phi_0 = 120.0$ deg the “kink” is one of the most pronounced, among all of the clocking configurations. Such a velocity perturbation is indicative of the formation of roll-up vortex occurring further upstream and can serve here as an evidence of the presence of a roll-up vortex. Finally, when compared to the case of the single wake [9], the weaker pressure pulse ($\approx 1/3$) induced by the vortex indicates that the vortex currently being described is smaller than these previously observed and/or was formed in the upper region of the boundary layer.

In Fig. 10 at $s/S_0 = 0.65$, for the case of $\phi - \phi_0 = 120.0$ deg, at time H, while the boundary layer still feels the effects of the rear part of the wake that is accompanied by the decelerative phase of

the potential field disturbance, the first TS waves that were seen after the time E , at $s/S_0=0.593$, breakdown, and turbulent spots are formed. The characteristics of a turbulent spot can be seen in the first and the third period. In the region between H and M ($\phi-\phi_0=300.0$ deg), wave packets appear later in time and while being under the influence of an accelerative phase of the potential field cycle, they remain ordered. During the remaining portion of the period between $t/\tau_0=1.20-1.58$ laminar separation is present without visible TS waves, in both cases of $\phi-\phi_0$.

More than 10% of surface length further downstream, at $s/S_0=0.765$, instability waves were seen throughout most of the time between the wakes ($t/\tau_0=0.10-0.60$). This is true for both cases of $\phi-\phi_0$. For $\phi-\phi_0=300.0$ deg, the waves between $t/\tau_0=1.05-1.40$ have broken down. Due to this transition, the surface static pressure has recovered for $\phi-\phi_0=300.0$ deg, as shown in Fig. 9, at $t/\tau_0=0.40$. For the case of $\phi-\phi_0=120.0$ deg, the boundary layer at a distance of $s/S_0=0.765$ is separated for a quarter of the cycle before the wake arrives. For this case, transition between $t/\tau_0=0.10-0.40$ just begins (the waves are being amplified) or has already occurred (e.g., between $t/\tau_0=2.10-2.40$), while for the second wake event, the flow remains still laminar. This aperiodic behavior in the raw hot film data, between $t/\tau_0=0.10-0.40$ and in the successive periods at the same phase, is typical of the separation bubble. The ensemble averaged pressure data in Fig. 9 shows that the surface pressure just starts to recover, indicating the onset of transition.

Between the time of $t/\tau_0=0.40-0.60$ at a surface distance of $s/S_0=0.765$, the hot film data are very similar for both cases of the relative phase angle ($\phi-\phi_0$). In both cases, the boundary layer is once again separated. However, the wave activity in this portion of time is still weak. Later in time, as the front of the wake arrives (Point A), random fluctuations at a significantly higher frequency appear, indicating a turbulent character of the near wall region of the boundary layer. The turbulence persists up to time F. This is because transitional flow between Points A and B and behind E induced beneath the front and the rear portions of the wake, respectively, have merged together. The later and more regular wave breakdown seen for the case of $\phi-\phi_0=300.0$ deg, behind Line F and before M might be essential with respect to loss considerations, as it coincides with the time when a combination of calmed and laminar region could be seen for the case of $\phi-\phi_0=120.0$ deg.

Further downstream at $s/S_0=0.823$, in both cases of the relative phase angle, between the wakes, at times $t/\tau_0=0.40-0.60$, the waves have grown in amplitude. Such waves during tests with downstream potential field disturbances were associated with naturally occurring KH vortices that were shed by the separation bubble. At this surface position, the peak-to-peak pressure perturbations were similar for all cases presented in Fig. 6 (not more than 10% of the exit dynamic pressure), indicating that shedding from the rear part of the separation bubble does not significantly differ between the two relative phase angles. Once again the vortices are smaller than those that formed during the interaction with only a downstream potential field disturbance [8]. In the latter case, the peak-to-peak pressure perturbations were of the order of 15% of the exit dynamic pressure. The kinks in the pressure data in Fig. 9 seen between $s/S_0=0.823$ and $s/S_0=0.957$ at times $t/\tau_0=0.40$ and $t/\tau_0=0.60$ are characteristic of vortex shedding.

At a surface distance of $s/S_0=0.957$ in Fig. 10, both hot film traces exhibit a turbulent character for most of the time. However, only in the case of $\phi-\phi_0=120.0$ deg, the remains of the laminar-like calmed region (F-G) was observed following the pattern of transition due to the rear portion of the wake negative jet (E-F). The exceptional persistence of the laminar flow and the KH vortex formation at $s/S_0=0.65$ in the case of $\phi-\phi_0=120.0$ deg are the most important differences with respect to the case of $\phi-\phi_0=300.0$ deg at the lower FSTI.

The persistence of the calmed region far downstream is due to

a reduced adverse pressure gradient. A sample of such a pressure distribution with a gentle slope is shown in Fig. 9, (dashed-line) with the distributions representing the case of $t/\tau_0=0.20$. This line represents the surface pressure coefficient extracted from the pressure data of Fig. 7. The trajectory along which those data were extracted is indicated with a black-dashed line in Fig. 7. This trajectory corresponds to the history and the arrival of the laminar-like calmed flow at $s/S_0=0.957$ in Fig. 10.

In summary, at the lower FSTI, the front portion of the wake forced the formation of large shear layer roll-up vortices, while the wake turbulence, which arrives later, led to the initiation of turbulent spots. Calmed regions followed the turbulent spots. The effect of the potential field on those wake-associated features is to promote/prevent the formation of large vortices and to enhance/degenerate the calmed region, depending on the relative phase angle between both disturbances.

Higher Freestream Turbulence Intensity Case. Figure 11 presents some of the hot film data obtained in the case of the higher FSTI. One of the main differences between the cases of the lower and the higher FSTI appears in between the wakes ($t/\tau_0=1.15-1.30$). At this time, already at a surface distance of $s/S_0=0.593$, additional periods of disturbed flow exist between the main wake-induced events. These additional events lead to an early attachment of the flow before $s/S_0=0.65$ as this portion of the flow becomes transitional. However, for the case of $\phi-\phi_0=120.0$ deg these events appear to be less regular in their occurrence. Therefore, periods of laminar (and sometimes separated) flow (see Fig. 9 at $t/\tau_0=0.20$ and $t/\tau_0=0.40$) can be seen as far downstream as $s/S_0=0.765$ (see Fig. 11; $t/\tau_0=2.10-2.40$). On average, the greater regularity of these additional transitional events in the case of $\phi-\phi_0=300.0$ deg, will lead to an extended turbulent wetted area as the calmed region is eroded. Even though this will prevent the growth of the separation bubble (see Fig. 9 at $t/\tau_0=0.20$), it results in a higher loss. This is probably because in the case of $\phi-\phi_0=120.0$ deg, the separation bubble does not significantly contribute to the loss at the higher FSTI, as it is a relatively shallow separation.

For the higher level of FSTI presented in Fig. 11, the transitional behavior of the near wall region between A and N ($\phi-\phi_0=120.0$ deg) or A and M ($\phi-\phi_0=300.0$ deg) at the first two streamwise positions does not differ significantly from that observed for the case of the lower FSTI. This is because of the dominant influence of the wake and because a similar pressure distribution is seen when the front of the wake is present (see Fig. 9; $t/\tau_0=0.60$). The extent of the local pressure perturbation shown in Fig. 6 also does not differ. At the higher FSTI, for the case of wake-only tests [16], an occasional single vortex was seen, and the level of peak-to-peak surface pressure perturbation induced by the vortex reached 10% of exit dynamic pressure, which is similar to the currently measured values. This suggests that even for these flow conditions, which are more representative of a real LP turbine environment ($Tu_1=4.0\%$), roll-up vortices will form shortly behind the central part of the wake (B) at $\phi-\phi_0=120.0$ deg. In the time between $t/\tau_0=0.60-0.75$ (B-E) when comparing the state of the hot film signals at $s/S_0=0.593$ and $s/S_0=0.65$ shown in Figs. 10 and 11, it is seen that in the case of the higher FSTI, there is a greater higher frequency content. This indicates that the breakdown to turbulence for both cases of $\phi-\phi_0$ at $Tu_1=4.0\%$ has occurred further upstream than at the lower level of FSTI. This is due to the combination of the higher level of background turbulence and the wake turbulence.

In Fig. 11, downstream of $s/S_0=0.65$, the calmed regions are more distinct between F and G than at the lower FSTI. They can still be present as far as $s/S_0=0.823$, occurring anywhere between $t/\tau_0=0.00-0.20$. However, for the case of $\phi-\phi_0=300.0$ deg, they seem to be corrupted sooner than at $\phi-\phi_0=120.0$ deg, due to transition that develops in between the wakes (see region between G and N or G and M at $s/S_0=0.823$). This corrupting effect on the

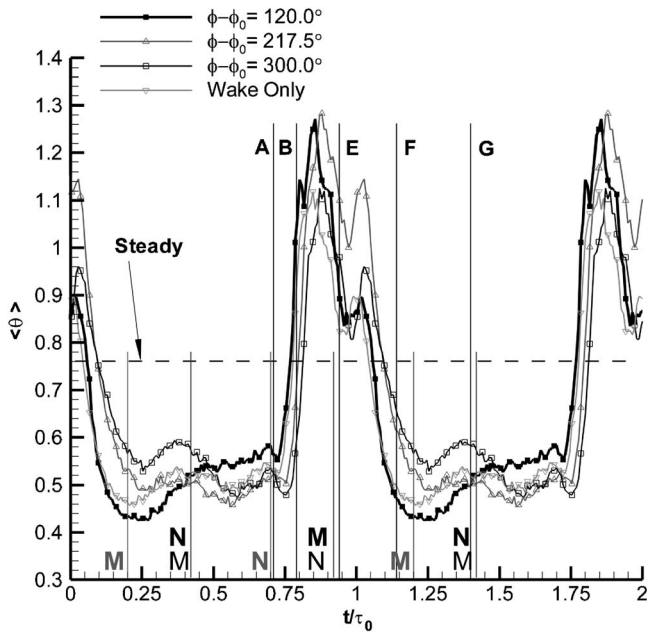


Fig. 12 Traces of ensemble averaged momentum thickness measured at $s/S_0=0.96$, $Re_{2is}=1.6 \times 10^5$, $F_{red}=0.46$, $Tu_1=0.5\%$, $\phi-\phi_0=120.0$ deg, $\phi-\phi_0=300.0$ deg, and single wake

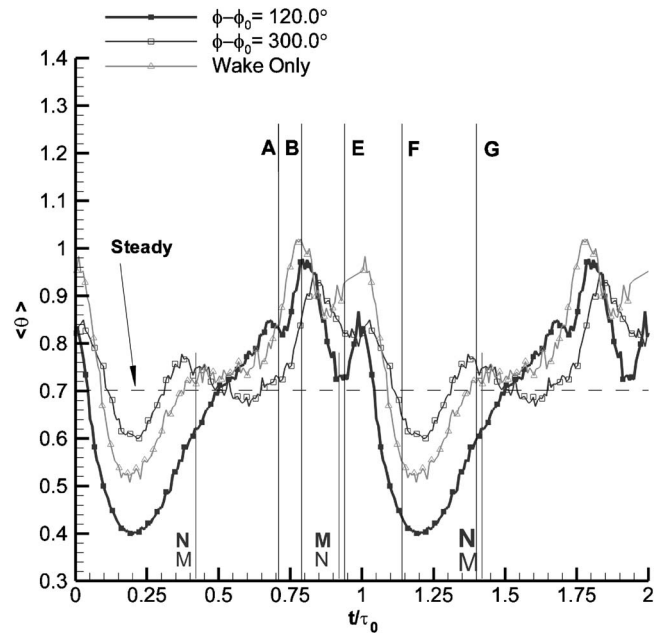


Fig. 13 Traces of ensemble averaged momentum thickness measured at $s/S_0=0.96$, $Re_{2is}=1.6 \times 10^5$, $F_{red}=0.46$, $Tu_1=4.0\%$, $\phi-\phi_0=120.0$ deg, $\phi-\phi_0=300.0$ deg, and single wake

calmed region is similar to that at the lower FSTI case.

The hot film data, particularly between $t/\tau_0=2.20-2.60$ at $s/S_0=0.823$, show a set of oscillations that are similar to those seen at the lower FSTI case. These shear stress fluctuations are once again an indication of roll-up vortices naturally occurring in the separation bubble.

In Fig. 11, near the trailing edge at $s/S_0=0.957$, in both cases of the relative phase angle, the flow in boundary layer is almost fully turbulent throughout the whole period of the wake-passing cycle.

In summary, at the higher FSTI the wake associated features appear at similar phases of the cycle and streamwise distances. However, because of the higher FSTI, the breakdown of roll-up vortices beneath the front of the wake occurred further upstream than at the lower FSTI. The main difference between the lower and the higher FSTI case is that the boundary layer between the wakes undergoes transition further upstream at the higher FSTI. This earlier transition prevents the inflexional tendencies of the boundary layer in between the wakes and result in a shorter streamwise extent of the transitional separation. The effect of the potential field is similar to that observed at the lower FSTI.

Trailing Edge Boundary Layer. The raw hot film signals have delivered a detailed insight into the unsteady transition process. The understanding of the wall shear stress patterns will be applied to the ensemble averaged momentum thickness measured near the trailing edge. This is to allow discussion of the boundary layer loss budget and to deduce the reasons for the observed clocking effects.

In Figs. 12 and 13, time traces of the ensemble averaged momentum thickness measured at a surface distance of $s/S_0=0.96$ are shown for both levels of FSTI. Both previously discussed cases of relative phase angles ($\phi-\phi_0=120.0$ deg thick black-filled rectangles, $\phi-\phi_0=300.0$ deg thin black-empty rectangles) are compared to traces that were measured during single wake interaction (delta). The black dashed lines represent time-mean levels of momentum thickness that were measured in steady flow.

For the case of the lower FSTI (Fig. 12), both cases of the relative phase angle discussed previously (120.0 deg and 300.0 deg) brought similar levels of time-mean momentum thickness (see Fig. 5). This is because of a specific balance in the loss

contributions of particular (transitional) periods of the flow. Here at low FSTI, the case of $\phi-\phi_0=120.0$ deg does not differ significantly from the case of a single wake. Higher loss levels than in the wake-only case are observed in the region between B and E (due an earlier breakdown of roll-up vortices). In the region between E and F (transition beneath the rear portion of the wake), the loss levels are not changed. At these times between E and F, the transition occurs due to a combination of TS instability and wake turbulence that while diffusing through the boundary layer may act as a catalyst in process of TS breakdown.

Figure 12 also shows that in region between F and G, the loss for the case of the $\phi-\phi_0=120.0$ deg is reduced when compared to the case of a single wake. This is due to the calmed region that persists further downstream, due to the milder adverse pressure gradient, which exists between F and G at this relative phase angle. Following G, where the potential field influence switches between decelerative and accelerative phases, the loss rises above the wake-only levels.

In the region between G and A ($t/\tau_0=1.50-1.70$), the loss in the case of $\phi-\phi_0=300.0$ deg remains at the wake-only levels. Later in time (i.e., after $t/\tau_0=0.75$), the loss rapidly rises. This rise, however, occurs later in time (by approximately 0.05) than in the wake-only and $\phi-\phi_0=120.0$ deg cases. The shorter temporal extent of this high loss region between A and E is related to the lack of roll-up vortices at $\phi-\phi_0=300.0$ deg.

For the case of $\phi-\phi_0=300.0$ deg, the most pronounced loss increase occurred in the time between $t/\tau_0=1.05-1.50$. Hot film data have shown that the transition beneath the rear part of the wake on average has occurred not only further upstream than in the case of $\phi-\phi_0=120.0$ deg (higher peak value in Region E-F) but also later in time. Furthermore, the instability waves seen at $s/S_0=0.65$ and $s/S_0=0.761$ further downstream have corrupted the calmed region, thereby promoting its transition at a further upstream position than in the case of $\phi-\phi_0=120.0$ deg (see Fig. 10 at $s/S_0=0.823$ at G).

The maximum loss at the lower FSTI has occurred for the case of $\phi-\phi_0=217.5.0$ deg. The time trace of the momentum thickness (triangles in Fig. 12) shows a significantly increased loss between B and G when compared with trace for $\phi-\phi_0=120.0$ deg (minimum loss). Unfortunately, there are no other data for this relative

phase angle. However, based on the behavior observed for the other two cases of $\phi-\phi_0$, it is postulated that the higher loss in region between B and G results from a combination of the more upstream occurrence of the rollup vortices (the Period B–E is similar to the case of 120.0 deg) and a further upstream and earlier in time occurrence of the transition responsible for the loss beneath the rear part of the wake (E–F). The earlier breakdowns could be due to a more severe adverse pressure gradient.

For the case of the higher FSTI, which is presented in Fig. 13, the relative contribution to the mean level of loss from the particular regions is similar to that discussed above for the case of the low FSTI. For the relative phase angle of $\phi-\phi_0=300.0$ deg, the benefit of the calmed region is much reduced compared to the wake-only case. This degeneration of the calmed region occurs due to an increased adverse pressure gradient caused by the downstream potential field. This is unlike the case of $\phi-\phi_0=120.0$ deg, where between $t/\tau_0=0.85-1.50$ the loss is significantly reduced. This reduction of the loss is due to a significantly decreased severity of the adverse pressure gradient that results from in-phase behavior at the peak suction point (see Fig. 7). Such configuration enables the laminar flow to exist as far as $s/S_0=0.823$ ($t/\tau_0=0.10-0.40$) (see Fig. 11). Furthermore, the equal peak values of θ between E and F suggest that at the higher FSTI the onset of the wake-induced transition beneath the rear portion of the wake (around H in Fig. 11 at $s/S_0=0.65$) is insensitive to the pressure gradient and velocity variation such as those resulting from the relative phase angle setting. Therefore, the main effect of the downstream potential field is to extend or corrupt the calmed region by decreasing or increasing, respectively, the severity of the adverse pressure gradient during times when the calmed region is present. This directly affects the profile loss.

Conclusions

The experimental data presented in this paper have shown that for closely spaced blade rows, downstream moving wakes and upstream propagating potential fields interact in the blade passage of an intermediate blade row. The resulting interaction will affect the profile loss.

It has been shown that velocity perturbation fields due to the two types of disturbance are superposed. The effect on the profile loss depends on the relative phase angle of the two disturbances. When the periodic perturbations in velocity and pressure due to each type of disturbance are in phase near to the peak suction point on the blade surface, a strong oscillation of the downstream adverse pressure gradient occurs. On the other hand, when the perturbations are out of phase, the peak-to-peak perturbations in the pressure along the rear part of the suction surface are reduced. Although, the magnitude of perturbations reduces, the more adverse pressure gradient now occurs twice as often during 1 cycle of the combined interaction.

The boundary layer in both cases of FSTI tends to separate in response to the approaching wake. Independently of the FSTI, the loss in the wake path constitutes the highest contribution to the suction surface loss budget. Clocking can be used to reduce this loss in the wake path. This is achieved by reducing the adverse pressure gradient before the wake arrival. This is achieved with an “out-of-phase” arrival of upstream and downstream disturbances at the peak suction point. In these circumstances, the resulting reduced severity of the adverse pressure gradient limits the inflexional tendency in the boundary layer. This helps in avoiding the formation of large roll-up vortices, and the higher loss that is associated with the vortex breakdown.

Reducing the severity of the adverse pressure gradient in front of the wake means that it is increased when the wake has passed. This promotes a further upstream transition and extends the turbulent wetted area. Therefore, the relative phase angle between wakes and potential field disturbance can be chosen (optimized) to reduce the suction surface boundary layer loss.

The effect in a multistage LP turbine of the combined interactions can be to alter the performance. The maximum efficiency improvement can be of the order of 0.25%, while the mean benefit resulting from combined interaction will be equal to 0.125%. This mean level will occur in the case of the mismatched blade numbers due to the variation around the annulus in the relative phase angle between the upstream and downstream disturbances.

Acknowledgment

The work reported in this paper was conducted as a part of the project on “Unsteady Transitional Flows in Turbomachines” (UTAT), which was funded by European Commission under Contract No. G4RD-CT-2001-00628. Authors would like to thank to the partners of the UTAT consortium for their permission to publish presented data.

Nomenclature

| | | |
|----------|---|------------------------------------|
| C | = | profile chord (m) |
| D | = | downstream bar diameter (mm) |
| F | = | reduced frequency |
| P | = | pressure (Pa) |
| S | = | surface length (mm) |
| T | = | period (s) |
| U | = | velocity (m/s) |
| Re | = | Reynolds number |
| Tu | = | turbulence intensity (%) |
| d | = | upstream bar diameter (mm) |
| h | = | blade span (mm) |
| s | = | blade pitch, surface length (mm) |
| t | = | time (s) |
| α | = | flow angle (deg) |
| θ | = | momentum thickness (mm) |
| ϕ | = | flow coefficient or phase angle |
| ρ | = | density (kg/m^3) |
| τ | = | shear stress or period (s) |

Subscripts

| | | |
|----------|---|------------|
| ∞ | = | freestream |
| 0 | = | total |
| 1 | = | inlet |
| 2 | = | outlet |
| p | = | pressure |
| w | = | wall |
| ax | = | axial |
| is | = | isentropic |
| red | = | reduced |

Others

| | | |
|---------------------|---|------------------------|
| $\langle x \rangle$ | = | ensemble averaged- x |
| \bar{x} | = | time mean- x |

References

- [1] Curtis, E. M., Hodson, H. P., Baniaghbal, M. R., Howell, R. J., and Harvey, N. W., 1997, “Development of Blade Profiles for Low Pressure Turbine Applications,” *ASME J. Turbomach.*, **119**, pp. 531–538.
- [2] Binder, A., Schröder, T., and Hourmouziadis, J., 1989, “Turbulence Measurements in a Multistage Low-Pressure Turbine,” *ASME J. Turbomach.*, **111**, pp. 153–161.
- [3] Halstead, D. E., Wisler, D. C., Okiishi, T. H., Walker, G. J., Hodson, H. P., and Shin, H. W., 1997, “Boundary Layer Development in Axial Compressors and Turbines, Part 3LP Turbines,” *ASME J. Turbomach.*, **119**, pp. 225–237.
- [4] Solomon, W. J., 2000, “Effects of Turbulence and Solidity on the Boundary Layer Development in a LPT,” Paper No. 2000-GT-0273.
- [5] Arnone, A., Marconcini, M., Pacciani, R., Schipani, C., and Spano, E., 2002, “Numerical Investigation of Airfoil Clocking in a Three Stage LPT,” *ASME J. Turbomach.*, **124**, pp. 375–384.
- [6] Schröder, Th., 1991, “Investigations of Bladerow Interaction and Boundary Layer Transition Phenomena in a Multistage Aeroengine Low Pressure Turbine by Measurements With Hot-film Probes and Surface-Mounted Hot-Film Gauges,” *VKI Lecture Series No 9 Boundary Layers in Turbomachines*, Von Karman Institute.
- [7] Arndt, N., 1993, “Bladerow Interaction in a Multistage Low-Pressure Tur-

- bine," ASME J. Turbomach., **115**, pp 137–146.
- [8] Opoka, M. M., Hodson, H. P., and Thomas, R. L., 2006, "Boundary Layer Transition on the High Lift T106A LP Turbine Blade With an Oscillating Downstream Pressure Field," ASME Paper No. GT2006-91038.
- [9] Stieger, R., Hollis, D., and Hodson, H. P., 2004, "Unsteady Surface Pressures Due to Wake Induced Transition in a Laminar Separation Bubble on a LP Turbine Cascade," ASME J. Turbomach., **126**, pp. 544–550.
- [10] Antoranz, A., and de la Calzada, P., 2002, "Downstream Cylindrical Rods Design for Whittle Lab Low Velocity Cascade," ITP Internal Report in UTAT Project 13/05/02.
- [11] Dring, R. P., Joslyn, H. D., Hardin, L. W., and Wagner, J. H., 1982, "Turbine Rotor-Stator Interaction," ASME J. Eng. Power, **104**, pp. 729–742.
- [12] Roach, P. E., 1987, "The Generation of Nearly Isotropic Turbulence by Means of Grids," Int. J. Heat Fluid Flow, **8**(2), pp. 82–92.
- [13] Hodson, H. P., Huntsman, I., and Steele, A. B., 1994, "An Investigation of Boundary Layer Development in a Multistage LP Turbine," ASME J. Turbomach., **116**, pp. 375–383.
- [14] George, W. K., 1975, "Limitations to Measuring Accuracy Inherent in the Laser-Doppler Signal," (A76-45326 23–35) *Proceedings LDA-Symposium Copenhagen*, Skovlunde, Denmark, pp. 20–63.
- [15] Stieger, R., and Hodson, H. P., 2004, "The Transition Mechanism of Highly Loaded LP Turbine Blade," ASME J. Turbomach., **126**, pp. 536–543.
- [16] Opoka, M. M., and Hodson, H. P., 2005, "An Experimental Investigation on the Unsteady Transition Process on the High Lift T106A Turbine Blade," Paper No 1277.
- [17] Denton, J. D., 1993, "The 1993 IGTI Scholar Lecture Loss Mechanisms in Turbomachines," ASME J. Turbomach., **115**, pp. 621–656.
- [18] Hatman, A., and Wang, T., 1998, "Separated-Flow Transition, Part 3-Primary Modes and Vortex Dynamics," ASME Paper No. 98-GT-463.

Numerical Study of Turbulent-Spot Development in a Separated Shear Layer

Brian R. McAuliffe¹

e-mail: brian.mcauliffe@nrc-cnrc.gc.ca

Metin I. Yaras

e-mail: metin_yaras@carleton.ca

Department of Mechanical and Aerospace
Engineering,
Carleton University,
1125 Colonel By Drive,
Ottawa, ON, K1S 5B6, Canada

The development of turbulent spots in a separation bubble under elevated freestream turbulence levels is examined through direct numerical simulation. The flow Reynolds number, freestream turbulence level, and streamwise pressure distribution are typical of the conditions encountered on the suction side of low-pressure turbine blades of gas-turbine engines. Based on the simulation results, the spreading and propagation rates of the turbulent spots and their internal structure are documented, and comparisons are made to empirical correlations that are used for predicting the transverse growth and streamwise propagation characteristics of turbulent spots. The internal structure of the spots is identified as a series of vortex loops that develop as a result of low-velocity streaks generated in the shear layer. A frequency that is approximately 50% higher than that of the Kelvin–Helmholtz instability is identified in the separated shear layer, which is shown to be associated with the convection of these vortex loops through the separated shear layer. While freestream turbulence is noted to promote breakdown of the laminar separated shear layer into turbulence through the generation of turbulent spots, evidence is found to suggest coexistence of the Kelvin–Helmholtz instability, including the possibility of breakdown to turbulence through this mechanism. [DOI: 10.1115/1.2812948]

1 Introduction

Laminar-to-turbulent transition in a separated shear layer has been shown to occur under both the natural and bypass modes of transition. In the natural mode, where transition occurs through the receptivity of the shear layer to small disturbances, a roll-up of spanwise vorticity in the separated shear layer is observed, and subsequent breakdown to turbulence occurs within a region of high shear between these vortices [1]. When elevated levels of environmental disturbances are present, be it in the form of freestream turbulence, surface roughness, or periodic passing of turbulent wakes, bypass transition occurs whereby turbulent spots are produced, grow, and merge within the separated shear layer, leading to reattachment in the form a turbulent boundary layer [2–4].

The structure of turbulent spots in attached boundary layers has been examined by many researchers dating back to the work of Emmons [5] and Schubauer and Klebanoff [6]. Early work consisted of identifying the shape and growth characteristics of spots in mild pressure gradients and providing conceptual ideas regarding the cause for spot growth and turbulence generation. Yaras [7] provided a brief review of turbulent-spot research in regards to attached boundary-layer transition. Recent studies such as those of Schröder and Kompenhans [8] and Yaras [7] have focused on identifying coherent substructures within turbulent spots. These studies provide strong evidence of the presence of organized patterns of hairpin vortices and associated streaky patterns in the streamwise velocity field within a turbulent spot.

The presence of turbulent spots in separated shear layers has been observed under conditions with elevated environmental disturbances [2,9–11], from single-point measurements. The internal structure of the spots has been documented mainly based on arti-

ficially generated spots through phase-averaged measurements. Averaging of phase-locked measurements tends to smear out details of the substructure, unless the spots develop under strongly favorable pressure gradients, relatively low flow Reynolds numbers, and low levels of environmental disturbances such as freestream turbulence [7]. Artificially generated spots in separated shear layers have been examined by D’Ovidio et al. [12,13] and by Watmuff [14] through excitation of a wave packet introduced upstream of the separation, although Watmuff referred to them as “vortex loops” rather than “turbulent spots.” In both of these studies, a dominant frequency emerges from the wave packet as it convects through the separated shear layer. Watmuff identified a roll-up of vorticity from this amplified instability, which leads to a series of vortex loops the structures of which remain coherent as they convect through the reattached turbulent boundary layer. The presence of a dominant frequency within the turbulent spot is also identified in the measurements of D’Ovidio et al. [12,13].

For the purposes of modeling the streamwise and transverse growth rates of turbulent spots, which are then used as part of semiempirical schemes for estimating the length of the transition zone, Gostelow et al. [15] and D’Ovidio et al. [13] proposed models for the spot spreading half angle α and the spot propagation parameter σ respectively. The spot propagation parameter is defined as

$$\sigma = \tan(\alpha) \left(\frac{1}{b} - \frac{1}{a} \right) \quad (1)$$

where $a = U_{le}/U_e$ and $b = U_{te}/U_e$ are the leading-edge and trailing-edge celerities of the spot, respectively. The models provide the spot growth parameters as a function the local pressure gradient parameter λ_θ and are based on measurements of artificially generated turbulent spots under accelerating and decelerating freestream conditions. The spot spreading half angle is modeled as

$$\alpha = 4 + \frac{22.14}{0.79 + 2.72e^{(47.63\lambda_\theta)}} \quad (2)$$

and the spot propagation parameter is modeled as

¹Present address: Aerodynamics Laboratory, Institute for Aerospace Research, National Research Council of Canada, 1200 Montreal Road, Building M-2, Ottawa, ON, K1A 0R6, Canada.

Contributed by the International Gas Turbine Institute of ASME for publication in the JOURNAL OF TURBOMACHINERY. Manuscript received June 12, 2007; final manuscript received August 3, 2007; published online August 4, 2008. Review conducted by David Wisler. Paper presented at the ASME Turbo Expo 2007: Land, Sea and Air (GT2007), Montreal, QB, Canada, May 14–17, 2007.

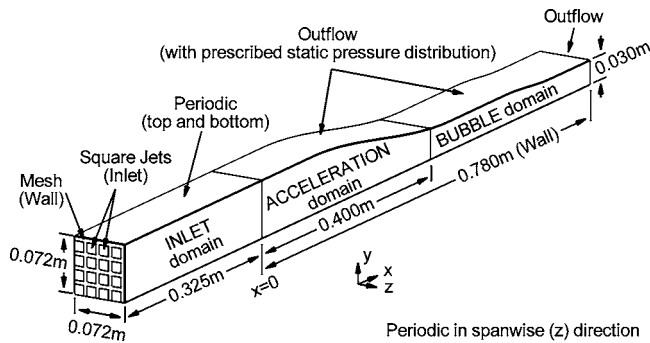


Fig. 1 Schematic of computational domain

$$\sigma = 0.024 + \frac{0.604}{1 + 5e^{(66\lambda_\theta)}} \quad (3)$$

These models have been validated in the range $-0.12 \leq \lambda_\theta \leq 0.06$ [13].

In the present study, the characteristics and internal structure of naturally occurring turbulent spots in a separation bubble are examined. The study is performed using the results of a direct numerical simulation (DNS) in which the streamwise pressure distribution and turbulence levels are representative of those prevailing over the suction surface of low-pressure turbine airfoils. An analysis of the simulation results provides considerable insight into the internal structure of the turbulent spot as well as its spreading and convection rates, which are then used to evaluate the accuracy of semiempirical correlations that are used for estimating the growth and convection characteristics of turbulent spots.

2 Numerical Method

2.1 Computational Domain and Boundary Conditions.

The computational domain used for the present study is shown in Fig. 1 and was selected to capture the complete boundary-layer development along a flat plate with a prescribed streamwise pressure distribution under elevated freestream turbulence conditions. The configuration is based on an experimental setup used by this research group in a series of experiments on separated and attached-flow transition, as outlined by Roberts and Yaras [3]. The spanwise extent of the computational domain is considerably smaller than the width of the flat plate used in the experiments. The inflow boundary condition consists of a 4×4 array of square, uniform-velocity jets of 13 mm width, and 18 mm spacing to simulate the flow through a turbulence-generating grid that was used in the experiments. The jet velocity was set to 8.13 m/s, which provides a mixed-out mean velocity of 4.24 m/s upstream of the plate leading edge. The leading edge of the no-slip, smooth-wall computational-domain boundary was placed 325 mm downstream of the inflow boundary. Over this streamwise distance, the simulated grid turbulence decayed to 5% intensity with an integral length scale of 7 mm, thereby approximating the conditions measured at the test plate leading edge in the experiments. Over this initial turbulence-decay region, the computational domain is bounded in the y (wall-normal) and z (spanwise) directions by surfaces with periodic flow conditions.

The no-slip smooth-wall boundary of 780 mm length represents a large streamwise portion of the flat test plate used in the experiments and extends to the computational-domain outlet yielding a complete domain length of 1105 mm. In the experimental setup, the pressure distribution was imposed upon the flat test surface through the use of a contoured shape for the ceiling of the wind-tunnel test section. For computational efficiency, in the y -axis direction, the computational domain does not extend up to this contoured ceiling. Instead, the upper boundary of the computational

domain was set to an outflow condition with a prescribed static pressure distribution. The boundary was shaped such that fluid does not enter the domain through this boundary, allowing the use of the outflow boundary condition. This shaping was accomplished by first estimating the contraction and expansion required by a wall-bounded domain based on the desired freestream velocity distribution using a one-dimensional flow assumption. The surface shape selected for the upper domain boundary provides a greater contraction than that estimated, ensuring no streamlines enter the upper domain surface.

An area-averaged constant static pressure condition was specified for the outflow boundary at the downstream end of the computational domain. The location of this boundary was chosen such that the absence of a convective boundary condition, which allows for transient flow structures to leave the domain with minimal deformation, does not affect the flow field within and immediately downstream of the region of interest.

The domain width of 72 mm was selected such that multiple turbulent spots can convect and spread through the transition region without a significant artificial influence of the periodic boundary conditions imposed on the surfaces bounding the domain in the spanwise direction.

2.2 Solution Method. The simulation was performed using the ANSYS-CFX commercial computational fluid dynamics (CFD) software package (version 10). Central differencing was used for discretization of the spatial derivatives, and time discretization was realized through second-order Euler backward differencing. Solutions of the continuity and momentum equations at each time step were converged through an algebraic multigrid scheme within eight iterations such that the maximum residuals at the end of each time step were lower than 6×10^{-5} , except very near the inlet boundary where the maximum residuals were on the order of 10^{-4} . rms residual levels were on the order of 10^{-6} after each time step. A general description of the algebraic multigrid method implemented in ANSYS-CFX is given by Raw [16], and the method makes use of the additive correction technique of Hutchinson and Raithby [17]. The method uses a W cycle with a coarsening rate of approximately 10, thus requiring six grid levels for the present simulation, which consists of 4.2×10^6 grid elements. The spatial and temporal resolutions summarized below were chosen such that the turbulence scales in the turbulent boundary layer downstream of the separation bubble are resolved down to about 35 times the Kolmogorov scale. Roberts and Yaras [18] and McAuliffe and Yaras [1] demonstrated that this level of resolution is sufficient to perform DNS of the transition process in separation bubbles, i.e., without explicit modeling of subgrid turbulence. Their simulations demonstrated a good agreement with experiment with regard to the shape and extent of the separation bubble, the streamwise velocity spectra, and the laminar-to-turbulent breakdown process in a low-disturbance environment. The present simulations were therefore performed in this DNS framework.

2.3 Spatial Grid. In mapping a structured spatial grid onto the computational domain, the domain was subdivided into three subdomains, as shown in Fig. 1. The inlet subdomain was discretized using 262, 57, and 57 nodes in the streamwise, spanwise, and wall-normal directions, respectively. Equal node spacing of 1.25 mm was used in the streamwise direction for the first 315 mm, and a reduction factor of 0.977 was used in the last 10 mm to ensure minimal node-spacing discontinuity at the plate leading edge. A near-uniform node spacing of 1.263 mm was used in the transverse directions, with slight variations implemented in these spacings to conform to the boundaries of the jets at the inflow plane.

The acceleration domain was discretized using 401, 73, and 59 nodes in the streamwise, spanwise, and wall-normal directions, respectively. Equal node spacing of 1 mm was used in the streamwise and spanwise directions, and nodes in the wall-normal directions were clustered closer to the wall to place a sufficient number

Table 1 Node spacings used in DNS studies involving separation bubbles (all have $y_1^+ < 1$)

| Investigators | Δx^+ | Δz^+ |
|------------------------|--------------|--------------|
| Current study | 19 | 19 |
| Na and Moin [19] | 18 | 11 |
| Alam and Sandham [20] | 14,20 | 6 |
| Michelassi et al. [21] | 10 | 3 |
| Kalitzin [22] | 28 | 19 |

of nodes in the boundary layer.

The bubble domain was discretized using 404, 73, and 59 nodes in the streamwise, spanwise, and wall-normal directions, respectively. The streamwise node spacing in the regions $0.40 \text{ m} < x < 0.55 \text{ m}$ and $0.64 \text{ m} < x < 0.78 \text{ m}$ was set to 1 mm and was reduced to 0.75 mm in the region $0.576 \text{ m} < x < 0.626 \text{ m}$, using a node-spacing stretch factor no greater than 2%. The wall-normal spacing was varied along the streamwise direction to ensure that nodes were clustered within the shear layer.

Based on the turbulent boundary layer near the domain outlet, y^+ of the first node off the wall is about 0.5. The corresponding Δz^+ value is 19, and the Δx^+ value varies between 14 and 19 through the separation bubble region. As shown in Table 1, the present streamwise node spacing is comparable to published DNS studies involving separation bubbles. Furthermore, the present spatial resolution has been found to be adequate in resolving the transitional flow structures associated with separation bubbles in a low freestream disturbance environment [1,18].

2.4 Simulation Time Step and Simulation Duration. A time step of 0.15 ms was used for the simulation, corresponding to a Courant number ($U\Delta t/\Delta x$) in the freestream over the separated shear layer of approximately 1.0. The simulation was started on a two-dimensional grid with a slip wall replacing the no-slip wall to establish the freestream velocity and pressure field, which was then used as an initial condition for the computations in the three-dimensional domain. With this initialization, approximately 5600 time steps were required to reach a “steady-state” condition in which the freestream turbulence distribution and large-scale properties of the separation bubble did not change, after which the simulation was continued for another 4100 time steps. The presented results are based on data from the last 3200 time steps. Over this period, running averages of the autocorrelation and cross correlation of velocity fluctuations within the transition region show variation by no more than a few percent, providing confidence that the dominant physical aspects of the transition process were captured.

3 Results and Discussion

The present discussion of turbulent-spot development in a separated shear layer is focused on results of a DNS for which the streamwise pressure distribution and flow Reynolds number are representative of those observed over the suction surface of low-pressure turbine airfoils. Figure 2 presents the freestream velocity distribution and turbulence levels observed in the simulation. The Reynolds number based on the momentum thickness and boundary-layer edge velocity at the time-averaged location of boundary-layer separation ($x_s = 0.518 \text{ m}$) is 335. At this streamwise location, the freestream Mach number is 0.02, and the freestream turbulence integral length scale and intensity are 0.011 m and 1.45%, respectively. The streamwise rate of decay of freestream turbulence downstream of the simulated turbulence grid at the inflow boundary is consistent with grid-generated turbulence in wind tunnels [23], and a slight anisotropy of the turbulence is observed. Above the plate leading edge ($x=0 \text{ m}$, $y=0.015 \text{ m}$) where the turbulence intensity is 5.1%, the streamwise fluctuation levels are 10% higher than those in the other two

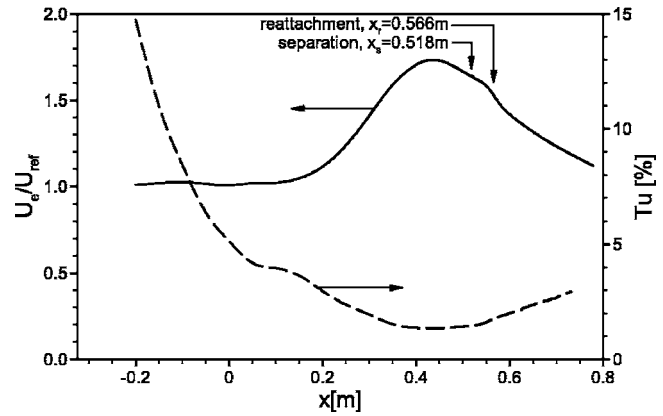


Fig. 2 Streamwise distributions of freestream velocity and turbulence intensity

coordinate directions, which is consistent with what has been observed downstream of turbulence-generating grids of similar configuration [23]. The strong streamwise acceleration over the forward part of the flat plate causes a reduction in this streamwise turbulence intensity, providing a streamwise turbulence level at x_s that is 10% lower than those associated with the wall-normal and spanwise components of velocity.

In the present simulation, transition in the separated shear layer is observed to occur through the bypass mode. In this mode, disturbances that penetrate the shear layer undergo an algebraic growth followed by viscous decay, unless they manage to grow to sufficiently high amplitudes to yield a turbulent spot. This path to transition is also referred to as transient growth or nonmodal growth, with the latter referring to the fact that this mode is not predicted as one of the eigenmodes of the solution of linearized theories based on the Orr–Sommerfeld and Squire equations. A velocity time trace from within the transition region is shown in Fig. 3 and compared with a time trace from an experimentally measured separation bubble under very similar Reynolds number and freestream turbulence conditions. The two traces in Fig. 3 are representative of signals from their respective cases with an intermittency level of approximately 0.5. A good agreement is observed for both the occurrence and the time duration of turbulent spots convecting past the particular location. In the present case, the generation of turbulent spots is observed to occur over a range of streamwise locations. Figure 4 shows a histogram of turbulent-spot origins along with the streamwise intermittency distribution. The vertical height of bars in the histogram represent the fraction

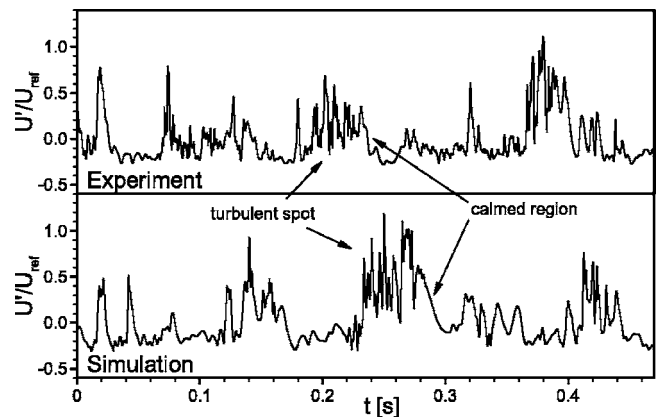


Fig. 3 Comparison of simulated and measured velocity time traces with an intermittency of 0.5 (experimental data from a test case of Roberts and Yaras[2])

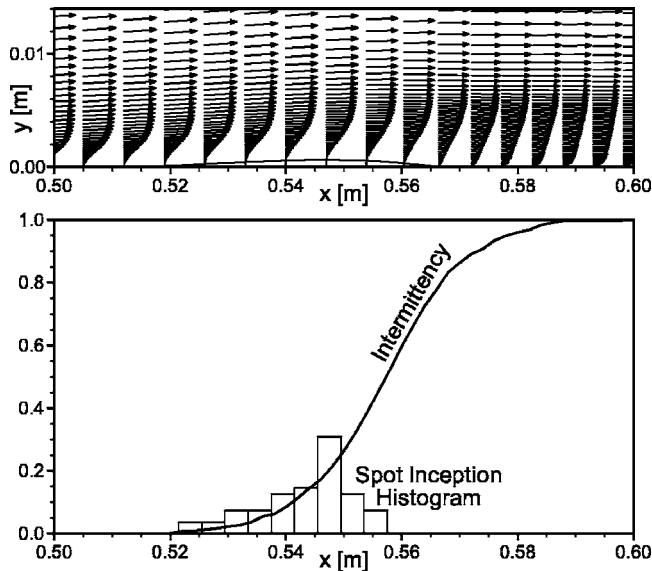


Fig. 4 Velocity profiles, intermittency distribution, and spot origin histogram through the bubble region

of observed spots that are produced within the streamwise range defined by the bar width. This histogram is based on the observation of more than 50 distinct turbulent spots in the separated shear layer, which is on the same order as the number of spots required for statistical averaging, as identified by Yaras [7] in an experimental analysis of artificially generated turbulent spots. Averaged velocity profiles through the bubble region, along with a line containing the reverse-flow region, are also shown in this figure for reference, with the coordinate normal to the surface having been stretched to better illustrate the structure of the separation bubble. Turbulent spots are noted to be produced along the entire length of the reverse-flow region. This result is consistent with the experimental results on bypass transition in attached boundary layers [24]. These observations suggest that extending the concentrated breakdown hypothesis, often utilized in the modeling of natural transition in attached boundary layers, to apply to the bypass transition mode cannot be readily justified. It is also noted that transition completion occurs approximately 50% of the reverse-flow length downstream of reattachment.

Unlike separated shear layers in low-disturbance environments, where separation generally occurs at a fixed streamwise location [1,25], the instantaneous separation point under elevated freestream turbulence varies both in time and in the spanwise direction. This variation is demonstrated in Fig. 5(a), which shows an x - z plane corresponding to the location of the first node off the wall, and in Fig. 5(b), which shows a z - y plane at the time and spanwise-averaged streamwise location of separation. Figure 5(a) shows streamwise streaks of alternating forward and reverse flow along the averaged streamwise location of separation, with the latter represented by the white contour regions. These streaks are associated with streamwise vorticity in the shear layer which transfers low-momentum fluid away from the wall and high-momentum fluid toward the wall. The fluctuations and vortical structures associated with these streamwise streaks are identifiable in the y - z plane of Fig. 5(b) by the v' and w' fluctuation vectors. In this plane, the white contour regions near the surface represent reverse flow. Through a theoretical analysis, Ustinov [26] concluded that a laminar boundary layer is most receptive to low-frequency longitudinal vorticity modes of disturbances. The dominant presence of longitudinal vortical structures in the boundary layer of the present results, as observed in Fig. 5(b), does indeed suggest that the component of freestream turbulence fluctuations with longitudinal vorticity is most readily received by the bound-

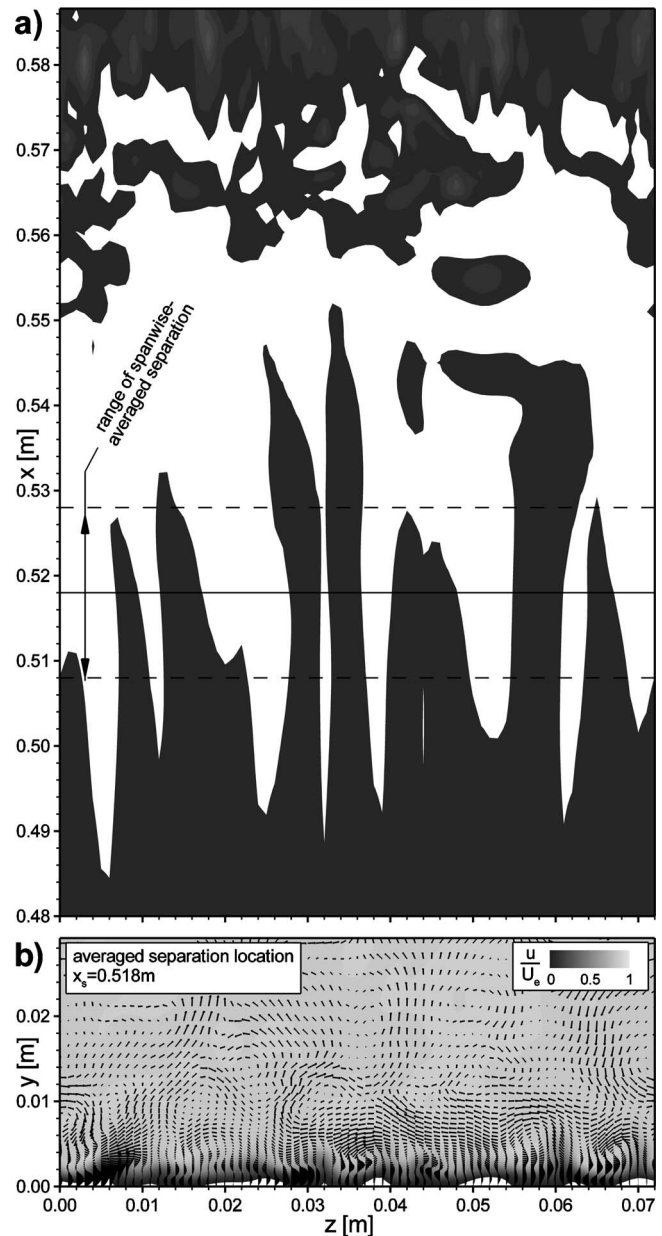


Fig. 5 Unsteadiness of separation location: (a) x - z near-wall plane and (b) z - y plane at the averaged separation location

ary layer. A variation in time of the spanwise-averaged separation location is observed to occur over a range of 0.02 m (42% of time-averaged bubble length). A similar variation was observed by Alam and Sandham [20] in a DNS study of a separation bubble where perturbations were introduced through the wall upstream of separation, providing a disturbance level similar to freestream turbulence.

The streaks shown in Fig. 5 have also been observed in attached laminar boundary layers exposed to freestream turbulence, starting with the work of Klebanoff [27], hence the identification of these flow structures as Klebanoff modes in some of the published literature. They originate near the leading edge of the flat plate, as this is a receptivity site where the mean flow changes rapidly [28]. Spanwise spacing of the streamwise streaks is comparable to the boundary-layer thickness prior to separation. This is similar to what has been observed by Matsubara and Alfredsson [29] in attached laminar boundary layers under elevated freestream turbulence conditions.

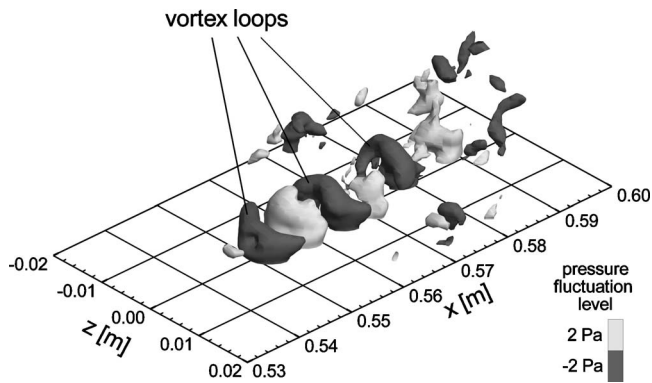


Fig. 6 Vortex loops within a turbulent spot

As the aforementioned streamwise streaks convect through the separated shear layer, a secondary instability develops and provides conditions that are favorable for turbulent-spot generation.

As a low-speed streak passes through the shear layer, a localized roll-up of vorticity occurs around the streak, resulting in a series of vortex loops, which provide an exchange of momentum toward the surface. In the early stage of spot development, these vortex loops closely resemble those generated by Watmuff [14] by a low-disturbance wave packet convecting through a separated shear layer. Figure 6 shows the structure of one such spot. The vortex loops are identified by isosurfaces of negative pressure fluctuation (dark contour surfaces). The small-scale structures apparent to the sides and downstream of the spot are associated with turbulence activity downstream of reattachment.

Within the turbulent spot, the vortex loops provide the mechanism for momentum exchange across the shear layer. In a series of y - t and z - t plots, the internal structure of the turbulent spot from Fig. 6 is presented in Fig. 7. The low-speed streak is apparent as dark contour regions in both the y - t and z - t planes. A roll-up of vorticity occurs around this low-speed streak, which pulls fluid inward, resulting in a patch of reattached fluid that convects through the separated shear layer. This patch is identified by the time interval in the y - t plots during which light contour regions are observed very close to the surface. The structure within the

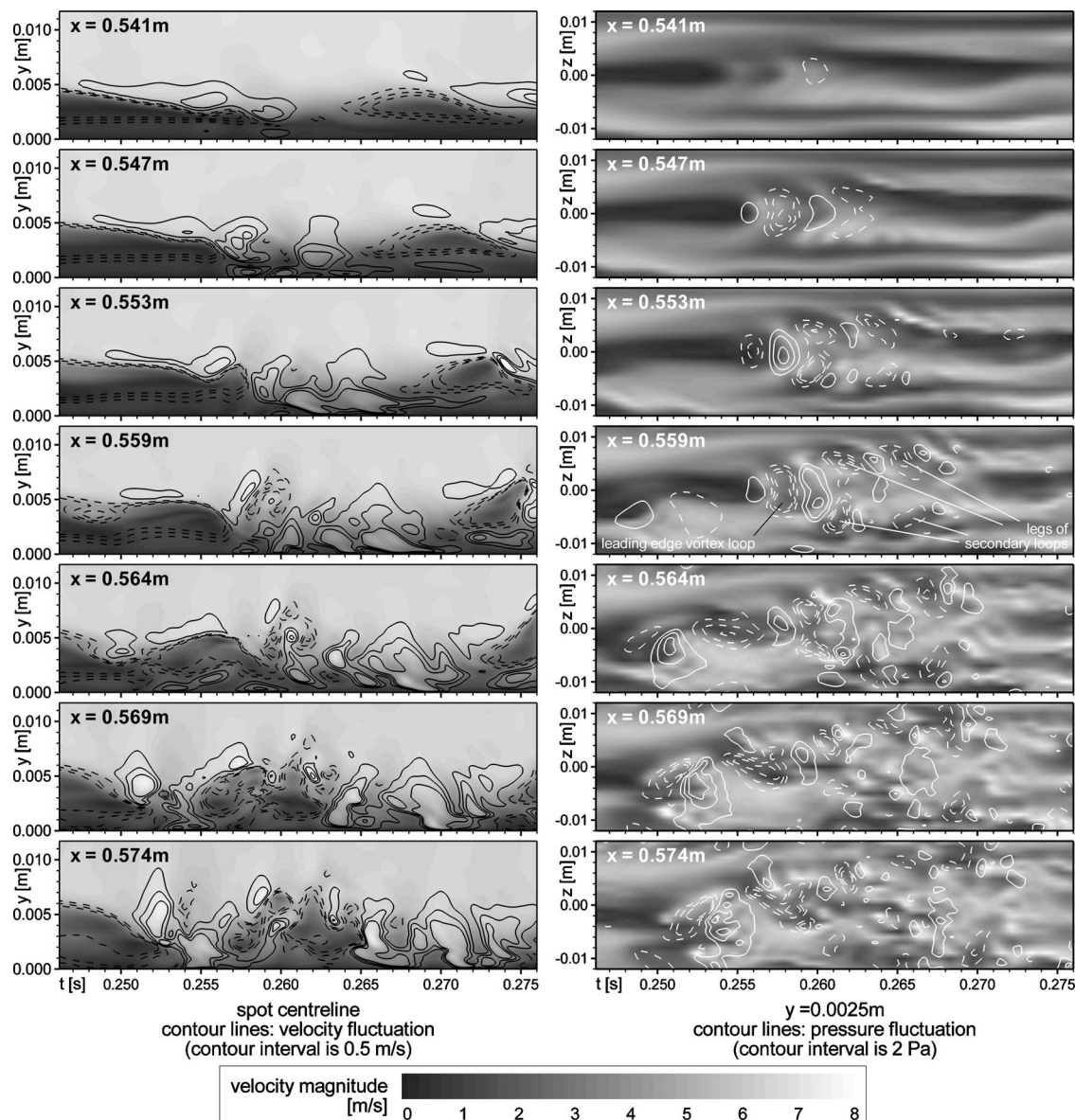


Fig. 7 Turbulent-spot growth as observed in the y - t and z - t planes

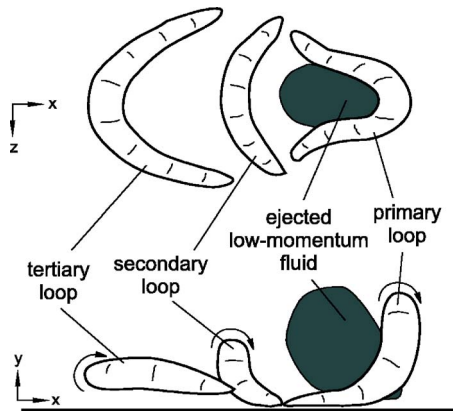


Fig. 8 Schematic of vortex loop structure during the early development of a turbulent spot

spot is dominated by the vortex loops shown in Fig. 6, which can be identified by the pressure perturbation contour lines in the z - t plots of Fig. 7. Although the spot originates near $x=0.54$ m, the primary vortex loop located at the leading edge of the spot is not clearly identified until after $x=0.55$ m. In the z - t plot for $x=0.559$ m, this vortex loop is identified, and the legs of the other two dominant vortex loops are visible. As the spot propagates downstream into the reattached boundary layer, its structure begins to contort and break down due to vortical diffusion within the surrounding boundary layer and freestream. However, the basic vortex-loop structure of the spot remains coherent downstream of reattachment, with loop legs still being identifiable at $x=0.574$ m in Fig. 7.

Of the spots observed in the simulation, generally three dominant vortex loops develop about the low-speed streak, as seen in Fig. 6. Figure 8 shows a schematic of the vortex-loop structures within a turbulent spot during an early phase of its growth. This schematic has been interpreted from examining multiple spots occurring in the present simulation. The primary vortex loop located at the leading edge of the spot is lifted away from the surface, and is reminiscent of the hairpin vortex substructure observed in turbulent boundary layers [30]. Upon lifting away from the surface, the primary vortex loop extends further into the freestream than the subsequent loops, where it convects at a relatively higher rate due to the higher freestream velocity. The legs of the primary vortex loop extend toward the wall where they point in the upstream direction. The secondary and tertiary vortex loops are oriented with their legs pointing in the downstream direction. The primary vortex loop induces a velocity in the flow region between its legs such that low-momentum fluid in close vicinity of the wall is ejected upward, away from the wall. This creates a blockage for the shear-layer fluid upstream of the primary vortex loop, resulting in wrapping of the vorticity associated with that fluid around this ejected fluid, thereby forming the secondary and tertiary vortex loops with their legs pointing in the downstream direction. Although three vortex loops are shown in the schematic of Fig. 8, sometimes only the primary and secondary loops are observed and sometimes there are signs of a weak fourth loop upstream of the tertiary loop. The internal structure identified here for a turbulent spot in a separation bubble shares similarities with the vortex-loop patterns observed by Watmuff [14] in an experiment of artificially generated spots in a separated shear layer and, apart from consisting of vortical structures, does not show a strong resemblance to a turbulent spot developing in an attached boundary layer [7,8].

The dominant mechanism of transition in the present case is the production and growth of turbulent spots. However, the Kelvin-Helmholtz (KH) instability mechanism that occurs under low-disturbance conditions is still active. Near and downstream of the time-averaged reattachment, there are no distinct turbulent spots

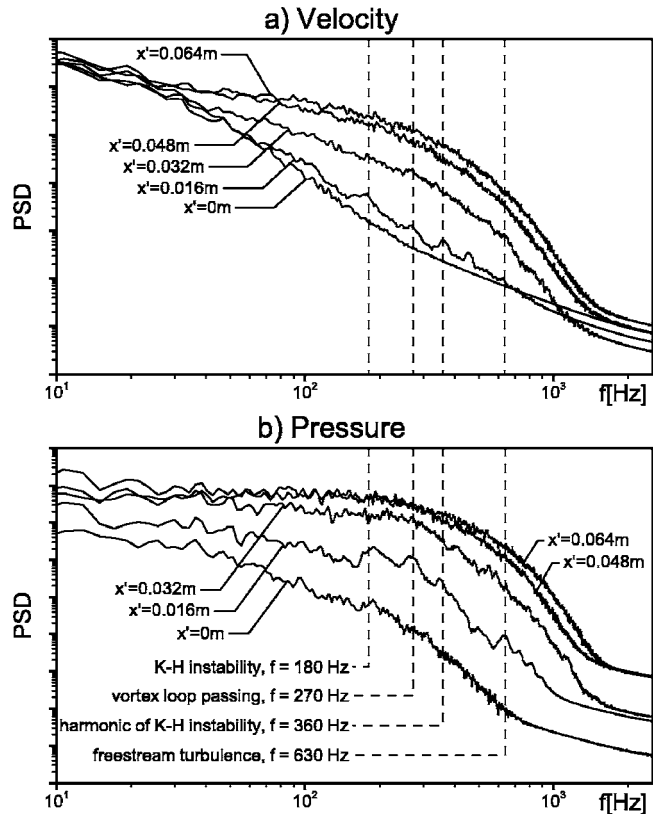


Fig. 9 Power spectra of (a) velocity and (b) static pressure

produced (as observed in the spot origin histogram of Fig. 4), but turbulence is still observed in the interspot regions. This turbulence may be linked to the rapid breakdown process that is typical of KH dominated transition [1]. The distinct large-scale spanwise-oriented vortices (also known as Kelvin cat eyes) generally associated with KH instability growth are difficult to discern within the spatial structure of the shear layer. However, the frequency of the KH instability is observed in a spectral analysis of the separation bubble. Figure 9 presents the power spectra of both velocity and static pressure at several streamwise locations through the separation bubble region, with x' representing the streamwise distance from the averaged separation location ($x' = x - x_s$). Shortly downstream of the separation ($x' = 0.016$ m), during the early stages of transition, several peaks are observed and identified in the power spectrum. These peaks are more pronounced in the spectrum of static pressure (Fig. 9(b)), and the four most dominant peaks are identified. The frequencies about which these peaks appear are 180 Hz, 270 Hz, 360 Hz, and 630 Hz and are associated with the maximum amplified frequency of the KH instability (180 Hz) along with its harmonic (360 Hz), the vortex loop passing frequency (270 Hz), and the frequency corresponding to the integral time scale of freestream turbulence (630 Hz). The KH frequency observed in Fig. 9 corresponds to a Strouhal number, based on separation conditions ($Sr_{0s} = f \theta_s / U_{es}$), of 0.018, which is in close agreement to the value of 0.016 identified by Ho and Huerre [31] for planar free shear layers in which the KH instability mechanism dominates. The identification of the frequency associated with the integral time scale of freestream turbulence was not expected, as the power spectrum of the freestream turbulence is smooth with no distinct peaks. This peak may be linked to some other mechanism and warrants further investigation. There is also an additional peak at 460 Hz in the spectrum of velocity at $x' = 0.016$ m. In examining the spectra for the individual velocity components (not presented), this peak is only present in that for

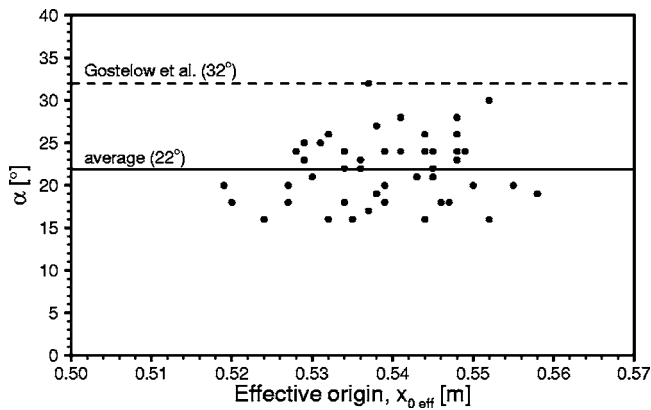


Fig. 10 Spot spreading half angles

the streamwise component of velocity and it is yet unknown what causes this peak to emerge. At and downstream of the time-averaged reattachment ($x' \geq 0.048$ m), a broad spectrum is observed with no distinct peaks.

One goal of the present study is to validate the turbulent-spot growth models of Gostelow et al. [15] and D'Ovidio et al. [13] used in the semiempirical intermittency-based transition model of Roberts and Yaras [32]. Figure 10 shows the variation in spot spreading half angles observed in the simulation, as compared with the value obtained from Eq. (2). The "effective origin" $x_{0, \text{eff}}$ plotted on the abscissa is the streamwise location from which lines emanating at \pm the spot spreading half angle align with the spot extremities. This is upstream of the true streamwise origin, which, as seen in Fig. 7, is not a point source. However, the use of an effective origin allows an assessment of any spot spreading variation with downstream distance. The spot extremities have been identified using the wall-normal component of velocity fluctuation (v'), with a threshold value of ± 0.2 m/s (3% of U_e). For the levels of Thwaites' pressure gradient parameter observed in the initial part of the separation bubble ($\lambda_\theta \approx -0.2$), the model of Gostelow et al. predicts a spot spreading half angle α of 32 deg, whereas the average value in the present simulation is 22 deg. Although the threshold used by Gostelow et al. in identifying the spot edge is slightly different (4% of U_e), they observed negligible sensitivity to this threshold over a range of 2–15% of U_e . The spot spreading half angles identified in the current case are consistently lower than that predicted by the model and do not show an apparent trend with streamwise distance. In the present case, the spot spreading angles have been extracted while the spot propagates and grows in a nonturbulent region of the separated shear layer. Identifying the spot extremities in a turbulent surrounding is difficult and highly subjective. Upon closer inspection of the data from which D'Ovidio et al. extracted α for their separation bubble cases, the spreading angle prior to the spot entering the turbulent part of the undisturbed separation bubble is observed to be lower than that in the turbulent region by about 5–10 deg. Thus, in the region of the separated shear layer where the turbulent spots grow in the absence of any other turbulence activity in the interspot regions, the spreading rate observed in the present simulations and that extracted from the experimental data of D'Ovidio et al. are in good agreement. On this basis, the present simulation results are judged to be supportive of the use of Eq. (2) for estimating the transverse spreading rate of turbulent spots in separated shear layers.

The leading- and trailing-edge celerities of the observed turbulent spots were extracted to assess the spot propagation parameter model of D'Ovidio et al. (Eq. (3)). The experiments from which this model was developed used phase-averaged measurements of artificially generated turbulent spots, from which distinct spot boundaries can be identified. Such phase averaging is not possible

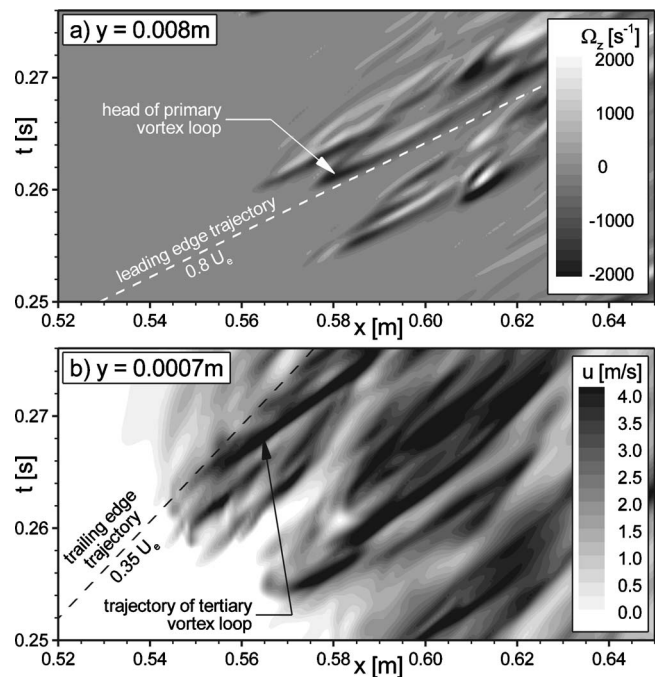


Fig. 11 Identification of spot celerities: (a) leading edge and (b) trailing edge

for the present case due to the range in streamwise spot origins and the difficulty in identifying and matching a specific phase during the spot growth period. The identification of the leading and trailing edges of the spots in the present case is therefore more difficult and subjective. Figure 11 shows x - t plots along the centerline of the spot previously examined in Figs. 6 and 7. The celerities shown as dashed lines in Fig. 11 are a "best fit" based on many of the spots identified in the simulation, and happen to provide a very good match to the spot shown through the flood plots. The spot leading edge has been identified as the downstream side of the primary vortex loop head, which is convected through the shear layer at the highest rate of any point in the turbulent spot. In Fig. 11(a), the primary vortex loop head is identified by high negative values of the spanwise component of vorticity (dark contour regions). The leading-edge celerity based on this criterion is 0.8 ± 0.05 .

Gostelow et al. [15] and D'Ovidio et al. [13] identified the spot trailing edge based on rms fluctuation levels within the spot. In examining their data, the trailing edge is noted to be consistent with the trajectory of the high-velocity phase-locked perturbation peak leading the calmed region. From the spots identified in the present case (see Fig. 11(b)), a distinct trajectory can be identified, upstream of which near-wall streamwise velocity levels are significantly reduced from those observed within the turbulent spot. The spot trailing-edge celerity is quantified on the basis of this trajectory. While the vortex loops within the spot convect at a higher rate than the spot trailing edge, which was also observed by D'Ovidio et al., weaker vortex loops and/or random fluctuations are evident between the tertiary vortex loop and the spot trailing edge. The best fit trailing-edge celerity of the present case is 0.35 ± 0.05 .

The spot propagation parameter for the present case is $\sigma = 0.65 \pm 0.2$. The high uncertainty in σ is due to subjectivity associated with identifying the leading-edge and trailing-edge celerities. However, the extracted value agrees well with Eq. (3), which predicts a value of 0.63 for the pressure gradient parameter observed through the bubble region of the present investigation ($\lambda_\theta = -0.2$).

4 Conclusions

Transition in a separation bubble associated with the production and growth of turbulent spots has been examined through DNS. The computational model was set up to approximate a wind-tunnel test case, and the computed transition process was confirmed to be consistent with experimental observations. The freestream turbulence that was produced through a turbulence grid in the wind-tunnel experiments was reproduced in the computations by extending the computational domain in the upstream direction to the location of the turbulence grid, where the inflow boundary was set up in the form of an array of square jets to mimic the flow behavior through the actual turbulence grid.

Transition is observed to occur through the production, growth, and propagation of turbulent spots within the separated shear layer. The production of the spots occurs through the interaction of freestream turbulence eddies with the separated shear layer. In this bypass mode of transition, a distributed streamwise breakdown is observed, with turbulent spots produced along the entire length of the separated shear layer. Transition completion is observed approximately 50% of the bubble length downstream of the time-averaged reattachment location.

The internal structure of a turbulent spot in the separated shear layer is identified as a series of vortex loops, which develop around low-speed streaks within the separated shear layer. The primary vortex loop has a structure similar to the hairpin vortex structures observed in the inner regions of turbulent boundary layers. Unlike the primary vortex loop whose legs extend in the upstream direction, the legs of the secondary and tertiary vortex loops extend in the downstream direction as a result of being dragged and stretched around a column of low-momentum fluid ejected upward between the legs of the primary loop. Once the spot convects into the turbulent boundary layer, much of the coherence in the vortex loops is lost due to vortex stretching, mixing with other turbulent spots, and/or mixing with turbulence generated through the KH breakdown process. While in this present case of elevated freestream turbulence the transition process in the separated shear layer appears to be dominated by the production of turbulent spots through the bypass mechanism, in the rear portion of the separation bubble there is evidence of breakdown in the interspot regions that resembles the pattern observed in KH-type instability of separated shear layers in low-disturbance environments. In each turbulent spot, a distinct frequency has been identified with the passing of vortex loops, which in the current case is approximately 50% higher than that associated with the KH instability of the separated shear layer.

A good agreement with the spot spreading half-angle model of Gostelow et al. [15] and the spot propagation parameter model of D'Ovidio et al. [13] has been observed. These models are therefore further recommended for use in semiempirical intermittency-based transition models.

Acknowledgment

The authors gratefully acknowledge the financial support of Pratt & Whitney Canada in this project. The first author would also like to thank the Natural Sciences and Engineering Research Council of Canada (NSERC) for financial support through a post-graduate scholarship. The Gas Turbine Laboratory (GTL) of the National Research Council of Canada (NRC) and Dr. J. E. D. Gauthier of Carleton University are also acknowledged for providing the computational resources for the simulation.

Nomenclature

| | |
|------|---|
| a | = leading-edge celerity = U_{1e}/U_e |
| b | = trailing-edge celerity = U_{2e}/U_e |
| f | = frequency |
| t | = time |
| Tu | = turbulence intensity |
| U | = velocity magnitude |

| | |
|--------------------|--|
| u | = x -velocity component |
| v | = y -velocity component |
| w | = z -velocity component |
| x | = streamwise coordinate |
| x' | = separation-referenced streamwise coordinate = $x - x_s$ |
| $x_{0\text{ eff}}$ | = hypothetical point origin of turbulent spot |
| y | = wall-normal coordinate |
| z | = spanwise coordinate |
| α | = spot spreading half angle |
| λ_θ | = Thwaites' pressure gradient parameter = $(\theta^2/\nu)(dU_e/dx)$ |
| ν | = kinematic viscosity |
| Ω_z | = spanwise vorticity = $\partial v/\partial x - \partial u/\partial y$ |
| θ | = momentum thickness |
| σ | = spot propagation parameter (Eq. (1)) |

Subscripts

| | |
|-----|---|
| e | = boundary-layer edge |
| r | = reattachment |
| ref | = reference condition ($x=0$ m, $y=0.036$ m, $z=0$ m) |
| s | = separation |

Superscripts

| | |
|-----|-------------------------|
| $+$ | = wall-scale coordinate |
| $'$ | = fluctuation quantity |

References

- [1] McAuliffe, B. R., and Yaras, M. I., 2008, "Numerical Study of Instability Mechanisms Leading to Transition in Separation Bubbles," *ASME J. Turbomach.*, **130**(3), pp. 021006.
- [2] Roberts, S. K., and Yaras, M. I., 2003, "Effects of Periodic Unsteadiness, Free-Stream Turbulence and Flow Reynolds Number on Separation-Bubble Transition," *ASME Paper No. GT2003-38626*.
- [3] Roberts, S. K., and Yaras, M. I., 2005, "Boundary-Layer Transition Affected by Surface Roughness and Free-Stream Turbulence," *ASME J. Fluids Eng.*, **127**, pp. 449–457.
- [4] Zhang, X. F., and Hodson, H., 2005, "Combined Effects of Surface Trips and Unsteady Wakes on the Boundary Layer Development of an Ultra-High-Lift LP Turbine," *ASME J. Turbomach.*, **127**, pp. 479–488.
- [5] Emmons, H. W., 1951, "The Laminar-Turbulent Transition in a Boundary Layer—Part I," *J. Aeronaut. Sci.*, **18**, pp. 490–498.
- [6] Schubauer, G. B., and Klebanoff, P. S., 1955, "Contributions on the Mechanics of Boundary-Layer Transition," *NACA Report No. 1289*.
- [7] Yaras, M. I., 2007, "An Experimental Study of Artificially-Generated Turbulent Spots Under Strong Favorable Pressure Gradients and Freestream Turbulence," *ASME J. Fluids Eng.*, **129**, pp. 563–572.
- [8] Schröder, A., and Kompenhans, J., 2004, "Investigation of a Turbulent Spot Using Multi-Plane Stereo Particle Image Velocimetry," *Exp. Fluids*, **36**, pp. 82–90.
- [9] Volino, R. J., 2002, "Separated Flow Transition Under Simulated Low-Pressure Turbine Airfoil Conditions—Part I: Mean Flow and Turbulence Statistics," *ASME J. Turbomach.*, **124**, pp. 645–655.
- [10] Volino, R. J., 2002, "Separated Flow Transition Under Simulated Low-Pressure Turbine Airfoil Conditions—Part II: Turbulence Spectra," *ASME J. Turbomach.*, **124**, pp. 656–664.
- [11] Roberts, S. K., and Yaras, M. I., 2006, "Effects of Surface Roughness Geometry on Separation-Bubble Transition," *ASME J. Turbomach.*, **128**, pp. 349–356.
- [12] D'Ovidio, A., Harkins, J. A., and Gostelow, J. P., 2001, "Turbulent Spots in Strong Adverse Pressure Gradients—Part I: Spot Behavior," *ASME Paper No. 2001-GT-0194*.
- [13] D'Ovidio, A., Harkins, J. A., and Gostelow, J. P., 2001, "Turbulent Spots in Strong Adverse Pressure Gradients—Part II: Spot Propagation and Spreading Rates," *ASME Paper No. 2001-GT-0406*.
- [14] Watmuff, J. H., 1999, "Evolution of a Wave Packet Into Vortex Loops in a Laminar Separation Bubble," *J. Fluid Mech.*, **397**, pp. 119–169.
- [15] Gostelow, J. P., Melwani, N., and Walker, G. J., 1996, "Effects of Streamwise Pressure Gradients on Turbulent Spot Development," *ASME J. Turbomach.*, **118**, pp. 737–743.
- [16] Raw, M., 1996, "Robustness of Coupled Algebraic Multigrid for the Navier-Stokes Equations," *AIAA Paper No. 96-0297*.
- [17] Hutchinson, B. R., and Raithby, G. D., 1986, "A Multigrid Method Based on the Additive Correction Strategy," *Numer. Heat Transfer*, **9**, pp. 511–537.
- [18] Roberts, S. K., and Yaras, M. I., 2006, "Large-Eddy Simulation of Transition in a Separation Bubble," *ASME J. Fluids Eng.*, **128**, pp. 232–238.
- [19] Na, Y., and Moin, P., 1998, "Direct Numerical Simulation of a Separated Turbulent Boundary Layer," *J. Fluid Mech.*, **374**, pp. 379–405.

- [20] Alam, M., and Sandham, N. D., 2000, "Direct Numerical Simulation of 'Short' Laminar Separation Bubbles With Turbulent Reattachment," *J. Fluid Mech.*, **403**, pp. 223–250.
- [21] Michelassi, V., Wissink, J., and Rodi, W., 2002, "Analysis of DNS and LES of Flow in a Low Pressure Turbine Cascade With Incoming Wakes and Comparison with Experiments," *Flow, Turbul. Combust.*, **69**, pp. 295–330.
- [22] Kalitzin, G., 2003, "DNS of Fully Turbulent Flow in a LPT Passage," *Int. J. Heat Fluid Flow*, **24**, pp. 636–644.
- [23] Roach, P. E., 1987, "The Generation of Nearly Isotropic Turbulence by Means of Grids," *Int. J. Heat Fluid Flow*, **8**, pp. 82–92.
- [24] Johnson, M. W., and Ercan, A. H., 1999, "A Physical Model for Bypass Transition," *Int. J. Heat Fluid Flow*, **20**, pp. 95–104.
- [25] McAuliffe, B. R., and Yaras, M. I., 2005, "Separation-Bubble-Transition Measurements on a Low-Re Airfoil Using Particle Image Velocimetry," ASME Paper No. GT2005-68663.
- [26] Ustinov, M. V., 2003, "Receptivity of the Flat-Plate Boundary Layer to Free-Stream Turbulence," *Fluid Dyn.*, **38**, pp. 397–408.
- [27] Klebanoff, P. S., 1971, "Effect of Free-Stream Turbulence on a Laminar Boundary Layer," *Bull. Am. Phys. Soc.*, **16**, p. 1323.
- [28] Saric, W. S., Reed, H. L., and Kerschen, E. J., 2002, "Boundary-Layer Receptivity to Freestream Disturbances," *Annu. Rev. Fluid Mech.*, **34**, pp. 291–319.
- [29] Matsubara, M., and Alfredsson, P. H., 2001, "Disturbance Growth in Boundary Layers Subjected to Free-Stream Turbulence," *J. Fluid Mech.*, **430**, pp. 149–168.
- [30] Panton, R. L., 2001, "Overview of the Self-Sustaining Mechanisms of Wall Turbulence," *Prog. Aerosp. Sci.*, **37**, pp. 341–383.
- [31] Ho, C., and Huerre, P., 1984, "Perturbed Free Shear Layers," *Annu. Rev. Fluid Mech.*, **16**, pp. 365–424.
- [32] Roberts, S. K., and Yaras, M. I., 2005, "Modeling Transition in Separated and Attached Boundary Layers," *ASME J. Turbomach.*, **127**, pp. 402–411.

The Effect of Combustor-Turbine Interface Gap Leakage on the Endwall Heat Transfer for a Nozzle Guide Vane

S. P. Lynch

Mechanical Engineering Department,
Virginia Polytechnic Institute
and State University,
Blacksburg, VA 24061

K. A. Thole

Mechanical and Nuclear Engineering Department,
The Pennsylvania State University,
University Park, PA 16802

To enable turbine components to withstand high combustion temperatures, they are cooled by air routed from the compressor, which can leak through gaps between components. These gaps vary in size from thermal expansions that take place. The leakage flow between the interface of the combustor and the turbine, in particular, interacts with the flowfield along the endwall. This study presents measurements of adiabatic cooling effectiveness and heat transfer coefficients on the endwall of a first vane, with the presence of leakage flow through a flush slot upstream of the vane. The effect of axial contraction of the slot width due to thermal expansion of the engine was tested for two blowing rates. Contracting the slot width, while maintaining the slot mass flow, resulted in a larger coolant coverage area and higher effectiveness values, as well as slightly lower heat transfer coefficients. Matching the momentum flux ratio of the leakage flow from the nominal and contracted slot widths lowered both cooling effectiveness and heat transfer coefficients for the contracted slot flow. Comparison of the coolant coverage pattern to the measured endwall shear stress topology indicated that the trajectory of the slot coolant was dictated by the complex endwall flow. [DOI: 10.1115/1.2812950]

Introduction

To achieve high efficiency and maximum power output, the temperature of the combustion gases entering the turbine section of a gas turbine engine must be as high as possible, while acknowledging the limitations of material strength and durability. This subjects the turbine section components to high heat loads, which must be managed by cooling, since turbine inlet temperatures are generally well above the melting point of the metal. Relatively cool air is bled from the compressor and routed to the turbine components, where it provides internal and external cooling. Cooling is particularly important on the endwall of a turbine vane or blade, since the complex flow in that region results in high heat transfer rates, and also tends to sweep coolant away from the endwall surface.

Assembly of individual turbine components inherently results in gaps between parts. The large operational range of a gas turbine results in significant thermal expansion, making these gaps difficult to seal. Furthermore, the temperature profile exiting the combustor may not be uniform, leading to additional thermal expansion issues. Since leakage of the hot combustion gases into the gaps is detrimental to engine durability, high-pressure compressor bleed air is purged through the gaps. Purge flow, however, results in a loss in turbine efficiency since it does no useful work, and it is desirable to minimize this flow.

One gap that must be considered is between the combustor and the first stage of the turbine section. In addition to preventing hot gas ingestion, purge flow through the combustor-turbine interface gap can provide some cooling to the endwall of the turbine vane. However, the trajectory of this coolant is influenced by the complex endwall flowfield. Thermal expansion of the combustor-

turbine interface gap during engine operational cycling also influences purge flow and changes the heat transfer experienced by the endwall.

This paper discusses the effects of leakage flow on turbine vane-end-wall heat transfer, for a combustor-turbine interface gap with axial thermal expansion. Also considered is the effect of moving the interface far upstream of the turbine vanes.

Relevant Past Studies

The endwall flowfield of a first stage turbine vane consists of unique features that contribute to high heat transfer and aerodynamic losses. Although there are slight differences in detail, flowfield studies by Langston [1], Sharma and Butler [2], Goldstein and Spores [3], and others concur on the dominant structures in the endwall region for an approach flow that is uniform with a two-dimensional boundary layer. The incoming boundary layer on the endwall rolls up into a horseshoe vortex at the leading edge of the vane. The horseshoe vortex splits into suction and pressure side legs where the pressure side leg develops into a passage vortex. These vortical structures and their interaction (generally termed "secondary flows") are sources of aerodynamic loss in the cascade; furthermore, they sweep coolant from the endwall and increase endwall heat transfer coefficients.

Graziani et al. [4], Kang et al. [5], and Ames et al. [6] presented results of endwall heat transfer influenced by secondary flows. Measurements of heat transfer coefficients indicated regions of high heat transfer at the blade leading edge, and adjacent to the suction side of the airfoil downstream of the passage throat. All of the investigators attributed the high heat transfer coefficients to the effects of the horseshoe and passage vortices. Goldstein and Spores [3] used naphthalene mass transfer to infer heat transfer coefficients and deduced the existence of additional corner vortices along the suction side of the vane.

Coolant leakage was investigated by Blair [7] who presented endwall heat transfer from flow through a two-dimensional slot upstream of a linear cascade. Measured endwall heat transfer coefficients were similar with and without the additional slot flow. However, measurements of adiabatic effectiveness over a range of

Contributed by the International Gas Turbine Institute of ASME for publication in the JOURNAL OF TURBOMACHINERY. Manuscript received June 15, 2007; final manuscript received June 26, 2007; published online August 4, 2008. Review conducted by David Wisler. Paper presented at the ASME Turbo Expo 2007: Land, Sea and Air (GT2007), Montreal, Quebec, Canada, May 14–17, 2007.

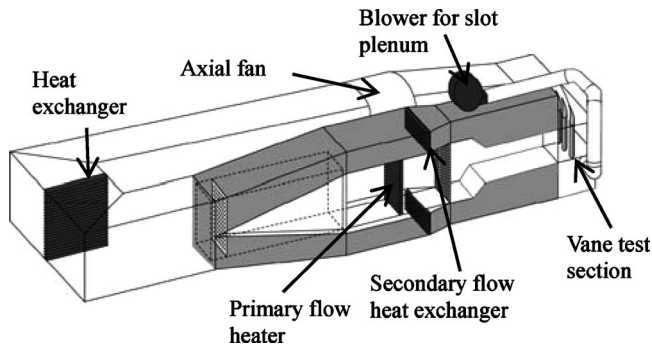


Fig. 1 Large low-speed wind tunnel with separate flow conditioning paths and corner test section

blowing ratios revealed that coolant accumulated along the suction side of the vane in the passage. Granser and Schulenberg [8] and Knost and Thole [9] reported similar trends of coolant accumulation. Computational predictions by Knost and Thole [10] indicated that streamline paths near the endwall became increasingly more directed toward the pressure side of the vane passage as flow rates increased through their upstream slot configuration.

Studies have been completed with upstream leakage in a contoured endwall vane cascade, where the contour serves to accelerate the flow and thin the boundary layer with the aim of reducing secondary flows. Burd et al. [11] found that coolant effectiveness levels and coolant coverage were increased for higher coolant ejection rates from an upstream flush slot on their contoured endwall. They conjectured that the momentum of the slot coolant at higher flow rates enabled it to avoid being entrained into the secondary flow vortices.

The only known study of thermal expansion of the combustor-turbine gap in the axial direction is Cardwell et al. [12]. Cardwell et al. found that adiabatic cooling effectiveness coverage area was a function of slot momentum flux ratio, but effectiveness levels were dependent on the slot mass flow ratio.

The axial location of an upstream slot has also been shown to be important in the interaction of slot flow with secondary vortices. Kost and Nicklas [13] and Nicklas [14] presented aerodynamic and heat transfer measurements for upstream slot and passage discrete hole film cooling in a transonic cascade. For slot coolant ejection at 1.3% of the core flow rate and no passage film cooling, they found that the slot flow intensified the horseshoe vortex and increased heat transfer coefficients by nearly three times that of no slot flow. They attributed this dramatic increase to the fact that their slot, at $0.2C_{ax}$ upstream of the vane, was intensifying the horseshoe vortex by injecting at the separation location on the endwall. Kost and Mullaert [15] studied the same airfoil geometry, but moved the flush slot to $0.3C_{ax}$ upstream of the vane. They found that for this configuration, slot flow stayed closer to the endwall and provided better cooling than flow from the slot located at $0.2C_{ax}$ upstream of the vane.

The study reported in our paper expands upon the work of Cardwell et al. [12] by including heat transfer coefficient and shear stress measurements. It is also important to note that the slot locations relative to the vane differ between this study and that of Cardwell et al. [12], which will be addressed.

Experimental Facility and Methodology

Endwall friction coefficients, adiabatic effectiveness, and heat transfer coefficients were measured in a closed-loop, low-speed wind tunnel, depicted in Fig. 1 and previously described by Cardwell et al. [12]. The flow was driven by a 50 hp axial fan, and passed through a heat exchanger. A porous plate with 25% open area diverted flow into the secondary path from the primary flow path. Note that the tunnel has upper and lower secondary flow paths; only the top secondary flow path was used in this study. For

Table 1 Vane geometry and flow conditions

| | |
|--|-------------------|
| Scaling factor | 9 |
| Scaled vane chord (C) | 59.4 cm |
| Axial chord/chord (C_{ax}/C) | 0.48 |
| Pitch/chord (P/C) | 0.77 |
| Span/chord (S/C) | 0.93 |
| Inlet Reynolds number (Re_{in}) | 2.2×10^5 |
| Inlet mainstream velocity ($U_{\infty, in}$) | 6.3 m/s |
| Inlet, exit angle | 0 deg, 78 deg |
| Inlet, exit Mach number | 0.017, 0.085 |

adiabatic effectiveness measurements, the primary path was heated with a 55 kW electrical resistance heater bank to increase the flow temperature to 45°C . The secondary path was further cooled with a heat exchanger to 20°C to increase the temperature differential between the mainstream and coolant leakage flow. To measure the convective heat transfer coefficients, the coolant and mainstream temperatures were matched with no primary flow heating or additional secondary flow cooling needed.

Downstream of the heat exchanger shown in Fig. 1, the primary flow next passed through several screens and a contraction section. The contraction, located 2.9 vane chords upstream of the vane, reduced the flow area from 1.11 m^2 to 0.62 m^2 through symmetric 45 deg bounding walls. The primary flow area remained constant up to the corner test section.

The corner test section contained two full nozzle guide vanes and a third partial vane connected to a flexible wall to maintain the desired pressure distribution along the center vane. The vane design was a three-dimensional extrusion of a two-dimensional midspan airfoil geometry. The vanes were scaled up by a factor of 9 to allow for high measurement resolution. The vanes were manufactured from low-density closed-cell polyurethane foam for low conductivity. A description of the turbine vane parameters is given in Table 1.

The boundary layer entering the cascade was measured at a location $0.63C$ upstream of the vane stagnation. Table 2 lists the turbulent inlet boundary layer parameters, which were maintained throughout this study. The measured inlet turbulence intensity and length scales were 0.7% and 4 cm ($0.07C$), respectively. Although the turbulence intensity is lower than that typically found in an engine, the effect of turbulence was considered to be of secondary interest and was not examined in this study.

To simulate the leakage interface between a combustor and a turbine, a two-dimensional slot was placed upstream of the turbine vane bottom endwall, as illustrated in Fig. 2. This combustor-turbine interface gap was based on the geometry presented by Cardwell et al. [12], and will be referred to as an upstream slot in this paper. Cardwell et al. [12] based their upstream slot design on discussions with several industrial contacts. The primary difference in the slot geometry between our study and that of Cardwell et al. [12] is the location of the slot relative to the vane stagnation ($0.38C_{ax}$ for Cardwell et al. [12] compared to $0.77C_{ax}$ for this study). The much larger upstream placement of the slot for this study was necessary to accommodate other end-wall-airfoil geometries.

Table 2 Inlet boundary layer characteristics

| | |
|--|-------|
| Boundary layer thickness/span (δ/S) | 0.18 |
| Displacement thickness/span (δ^*/S) | 0.025 |
| Momentum thickness/span (θ/S) | 0.020 |
| Shape factor (δ^*/θ) | 1.26 |
| Momentum thickness | 4138 |
| Reynolds number (Re_θ) | |

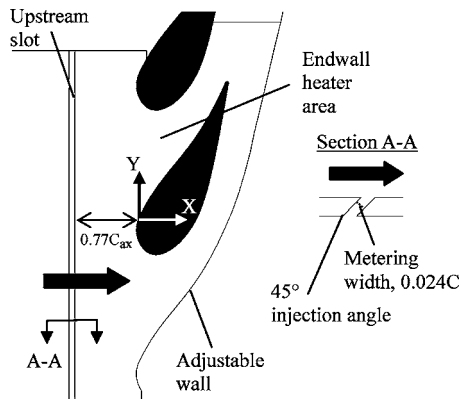


Fig. 2 A schematic of the endwall and the combustor-turbine leakage interface (upstream slot) modeled in this study

Two upstream slot widths were chosen to model the combustor-turbine interface. The nominal metering width, at a scale that is nine times that of the engine, was 1.43 cm (0.024C) with a flow length-to-width ratio of 1.9. The contracted slot metering width was 50% of the nominal slot width, and will be referred to as the half slot. The distance of the slot centerline to the vane stagnation was maintained for both slot widths. Both slots had an injection angle of 45 deg relative to the endwall.

Coolant was extracted from the top secondary channel of the wind tunnel by a 2 hp blower and fed to a plenum located below the upstream slot. To calculate the average mass flow exiting the slot, the inviscid blowing ratio from the slot was multiplied by an assumed discharge coefficient of 0.6, which is the commonly accepted value for flow from a sharp-edged orifice [16]. Note that the coolant-to-mainstream density ratio was fixed at 1.1 for all adiabatic cooling effectiveness measurements. The density ratio in this study is lower than that typically found in an engine; however, past film cooling research has indicated that jet behavior best scales with momentum flux ratio. The leakage mass flow ratios and nominal slot metering width for this study were selected based on input from industrial contacts, so the blowing and momentum flux ratios are expected to be representative of engine values. For the convective heat transfer coefficient measurements, the coolant was maintained to within 0.1°C of the mainstream temperature, resulting in a density ratio of 1.0. Table 3 lists the coolant settings investigated for this paper. Mass flow from the upstream slot is reported as a percentage of the mass flow entering a single vane passage.

Endwall Friction Coefficient Measurements. Endwall friction coefficient measurements were made using oil film interferometry; see the review by Naughton and Sheplak [17], and implementation of the method in linear cascades by Harrison [18] and Holley and Langston [19]. Oil-film interferometry (OFI) is based on the dynamic behavior of a thin oil film. OFI is similar in concept to oil flow visualization, except that the oil layer is extremely thin (on the order of visible light wavelengths), and the height of the oil film is quantified to enable calculation of wall friction coefficients. The equation used in this study to determine the friction coefficient is

Table 3 Slot coolant settings

| | MFR | <i>M</i> | <i>I</i> |
|--------------------|------|----------|----------|
| Nominal slot width | 1.0% | 0.36 | 0.13 |
| | 0.5% | 0.19 | 0.03 |
| Half slot width | 1.0% | 0.73 | 0.50 |
| | 0.5% | 0.36 | 0.13 |

$$C_f = L/2h_{oil} \int \frac{\rho U_{z,in}^2}{2\mu_{oil}} dt \quad (1)$$

To derive Eq. (1), a mass and momentum balance is performed on a differential control volume aligned with the endwall (limiting) streamline. The mass balance gives the height of the oil and its average convective velocity as functions of time and distance along the streamline. Based on an order-of-magnitude analysis for the oil film, the streamwise momentum can be simplified by recognizing that the Reynolds number for the oil film is much less than 1 (thus, the inertial terms are negligible). Then, the momentum equation can be solved for the oil velocity (retaining the pressure gradient, gravity, and shear terms) by applying no-slip boundary conditions at the wall-oil interface, and the desired shear at the air-oil interface. Combining the momentum and mass balance results yields the thin oil-film equation

$$\frac{\partial h_{oil}}{\partial t} + \frac{\partial}{\partial s} \left(\frac{\tau_{w,s} h_{oil}^2}{2\mu_{oil}} - \frac{h_{oil}^3}{3\mu_{oil}} \right) = 0 \quad (2)$$

For representative values pertinent to this study ($h_{oil}=1 \mu\text{m}$, $\nu_{oil}=100 \text{ cS}$, $\tau_{w,s}=10 \text{ Pa}$, $\rho_{oil}=1000 \text{ kg/m}^3$, $dP/ds=100 \text{ Pa/m}$, $g_s=10 \text{ m/s}^2$), order-of-magnitude analysis on the terms in the parentheses of Eq. (2) shows that the shear stress term is at least two orders of magnitude larger than the other terms, which are then neglected. For spatially constant shear stress over the region of interest (reasonable assumptions in this study because of the large scale and small measurement sizes), the reduced oil-film equation can be solved by separation of variables for the height of the oil in terms of the shear stress, distance along the streamline, and time. Note that the shear stress is nondimensionalized by the inlet dynamic pressure before performing separation of variables, so that the dynamic pressure appears in the integral in Eq. (1). The solution requires measurement of the oil height only at the end of the wind tunnel run, since the conditions leading to the final oil-film thickness are integrated over time.

Fizeau interferometry provides a means of measuring the height of the oil. Light strikes the surface of the oil film and is reflected and refracted. The phase difference (φ) between the initially reflected and refracted rays will attenuate or augment the rays, creating interference bands (fringes). The phase difference is related to the height of the oil by the wavelength of the light rays, the optical properties of air and oil, and the incident light angle:

$$h_{oil} = \frac{\lambda \varphi}{4\pi} \left(\frac{1}{\sqrt{n_{oil}^2 - n_{air}^2 \sin^2 \theta_i}} \right) \quad (3)$$

The phase difference between successive fringes is an integer multiple of 2π . The average spacing between successive fringes (L) is determined by a least-squares cosine fit to the pixel intensity profile of the fringe pattern [19] to determine the period of the intensity profile. The location of the friction coefficient measurement in the interferogram is taken as the center of the intensity profile.

To measure endwall friction coefficients in the cascade, small silicone oil droplets, nominally less than 5 mm in diameter, were placed on 0.05 mm thick rectangular sheets of nickel foil that had been adhered to the endwall (see Fig. 3). For the entire endwall, three viscosities of silicone oil (100 cSt, 500 cSt, and 1000 cSt) were used to maximize the range of the OFI method throughout the vane passage. The oil viscosity was corrected for temperature variation during a test (generally less than 4°C) by the correlation of Naughton and Sheplak [17]. The time history of the cascade inlet dynamic pressure and the flow temperature were recorded over the entirety of a test, which nominally took 20 min. The foil patches were carefully removed after a test and imaged in a fixture with a nearly monochromatic sodium vapor lamp ($\lambda=589$, 589.6 nm) to obtain the interferograms. Several tests were required to obtain over 400 data points on the endwall.

Shear stress vectors were obtained by examining the progres-

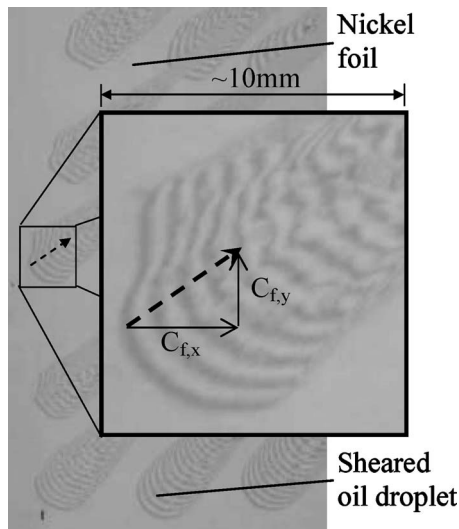


Fig. 3 Example of oil film interferograms on nickel foil, used to determine endwall friction coefficient magnitude and direction

sion of features in the fringe pattern. For example, a notch in a fringe will propagate downstream in the direction of the limiting streamline. Note, however, that measurements were only obtained on the portion of a fringe that was undisturbed by dust particle wakes or upstream oil droplets.

The OFI method was benchmarked by measuring friction factors in fully developed flow in a square channel. Friction factor measurements agreed with textbook correlations to within 5% over a wide range of channel Reynolds numbers ($25,000 < Re_{Dh} < 45,000$).

The partial derivative method described by Moffat [20] was used to calculate uncertainties for the measurements of friction coefficients. Uncertainty was estimated as $\partial C_f = \pm 5.8\%$ for both low ($C_f = 0.004$) and high ($C_f = 0.126$) values of friction coefficients, and was dominated by uncertainty in the interferogram spacing.

Adiabatic Effectiveness Measurements. Adiabatic wall temperatures for endwall effectiveness of upstream slot coolant were obtained from infrared thermography measurements of the bottom endwall surface. The endwall was manufactured from a 2.54 cm thick sheet low-density closed-cell polyurethane foam, which has a low thermal conductivity (0.0287 W/m K) to minimize conduction errors. The endwall was instrumented with type-E thermocouples throughout the vane passages for calibration of infrared thermography images. The endwall and thermocouples were painted with flat black paint, which has a nominal emissivity of 0.96 and enabled good resolution of surface temperatures with the infrared camera. Infrared-reflective finishing nails were used as image transformation markers.

An infrared camera was used to capture spatially resolved surface temperatures on the bottom endwall. Based on an uncertainty analysis, five images were taken at each location and averaged, where each image is also an average of 16 frames taken by the camera. The camera's spatial integration was approximately 0.17 mm (0.0012C). Images were postcalibrated by determining the emissivity and background temperature of the image through matching of the image temperatures with the acquired thermocouple measurements. The thermocouples and the calibrated images generally agreed to within 0.3°C. An in-house MATLAB routine was developed to assemble the individual images into a single endwall map.

A one-dimensional correction for endwall conduction effects

was applied to all adiabatic effectiveness measurements. The resulting η correction was 0.14 at $\eta = 0.75$ measured downstream of the slot, and 0.05 for $\eta = 0.07$ measured at the exit of the vane passage.

The partial derivative method was used to calculate uncertainties for the measurements of adiabatic cooling effectiveness. For adiabatic surface temperatures, a precision uncertainty of $\pm 0.33^\circ\text{C}$ was determined by taking the standard deviation of six measurement sets of IR camera images, with each set consisting of five images. Since the IR images were calibrated as closely as possible to the thermocouples in each image, the bias uncertainty for an image was assumed to be the root sum square of the thermocouple bias uncertainty ($\pm 0.2^\circ\text{C}$) and the average deviation of the calibrated images from the thermocouples ($\pm 0.34^\circ\text{C}$). In this way, a bias uncertainty of $\pm 0.39^\circ\text{C}$ was determined. Using the bias and precision uncertainties, a total uncertainty of $\pm 0.51^\circ\text{C}$ was estimated for the IR surface temperature measurements. Overall uncertainty in adiabatic effectiveness was calculated to be $\partial\eta = \pm 0.036$ at a η value of 0.1, and $\partial\eta = \pm 0.026$ at a η value of 0.8.

Heat Transfer Measurements. Endwall heat transfer measurements were taken by imaging surface temperatures on a constant heat flux plate attached to a 2.54 cm thick sheet of the closed-cell polyurethane foam. The heat flux plate consisted of a 37 μm copper layer on top of a 75 μm thick kapton layer, in which 25 μm Inconel elements were embedded in a serpentine pattern. The heater covered the entire endwall, from immediately downstream of the slot to 0.3C downstream of the vane trailing edge, as shown in Fig. 2. E-type thermocouples, embedded in the foam endwall, were placed in thermal contact with the bottom surface of the heater by thermal cement. A conduction bias between the bottom-mounted thermocouple and the infrared top-surface measurement was accounted for by a one-dimensional calculation of the thermal resistance of the heater. The infrared camera was also used to capture surface temperatures on the heat flux plate.

The input heat flux to the endwall was calculated by measuring the voltage across the heater circuit, as well as the voltage across a precision resistor (1 Ω) in series with the circuit, which gave the current. This flux was corrected for conduction and radiation losses, which accounted for a maximum of 0.2% and 21% of the input power, respectively. Note that the conduction and radiation corrections varied locally with the highest correction occurring at the highest surface temperatures. Uncertainty in Stanton numbers was dominated by the uncertainty in surface temperature measurements. For those measurements, a precision uncertainty of $\pm 0.22^\circ\text{C}$ was estimated from the standard deviation of six IR image measurement sets, and a bias uncertainty of $\pm 0.88^\circ\text{C}$ was determined in the same way as for the adiabatic effectiveness measurements. Overall uncertainty in Stanton numbers was $\partial St = \pm 0.00011$ (3.3%) at a St value of 0.003, and $\partial St = \pm 0.0009$ (7.5%) at a St value of 0.011.

Discussion of Results

Endwall friction coefficient measurements without any upstream slot flow over the endwall will be presented first, followed by adiabatic cooling effectiveness results with upstream slot flow. Heat transfer coefficient measurements with and without upstream slot flow are then discussed. Finally, the net heat flux reduction parameter, which incorporates both heat transfer coefficients and adiabatic cooling effectiveness, is presented.

Friction Coefficients Without an Upstream Slot. OFI measurements of endwall friction coefficients were linearly interpolated to a uniform grid, and then downsampled to create the vector plot in Fig. 4. Several unique features due to secondary flow are visible in the vector field. Shear decreases as flow approaches the vane leading edge and begins to stagnate. A saddle point is also visible upstream of the vane, where flow diverges around the lead-

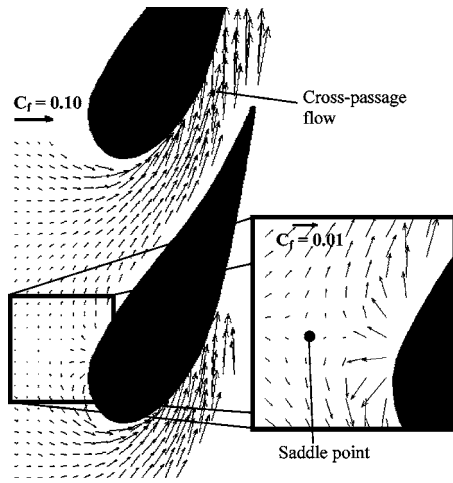


Fig. 4 Measured friction coefficient vectors for no upstream slot flow, which illustrate the features of secondary flow over the endwall

ing edge. The saddle point is the intersection of flow attachment and separation lines on the endwall. At the separation line, the incoming boundary layer separates from the endwall and rolls up into the horseshoe vortex. The vortex rollup causes flow to wash down the airfoil toward the endwall and then move upstream, away from the airfoil-end-wall junction.

Further in the passage, cross-passage flow from the passage vortex sweeps from the pressure side of the lower airfoil to the suction side on the adjacent airfoil. Because of this, the exit turning angle of the airflow near the endwall is much larger than the exit turning angle of inviscid flow away from the wall. The measured friction coefficient magnitudes near the passage throat have increased relative to the inlet values, resulting from the flow acceleration in the vane passage.

Figure 5 shows a prediction of inviscid streamlines near the midspan of the vane using FLUENT 6.2 [21], which are superimposed upon the endwall streamlines computed from the friction coefficient measurements. The endwall streamlines are representative of the flow streamlines in the limit as the wall is approached, and thus are also known as limiting streamlines. Figure 5 shows the endwall separation line also computed from the endwall friction coefficient vector measurements. The separation line was obtained by computing multiple streamline paths starting very near to the saddle point, and taking the mean of the paths. Note that since the saddle point is a location of zero shear stress, its exact location could not be found since the OFI method requires some detectable amount of oil flow.

Adiabatic Effectiveness Levels From an Upstream Slot. Contours of adiabatic cooling effectiveness for upstream slot flow

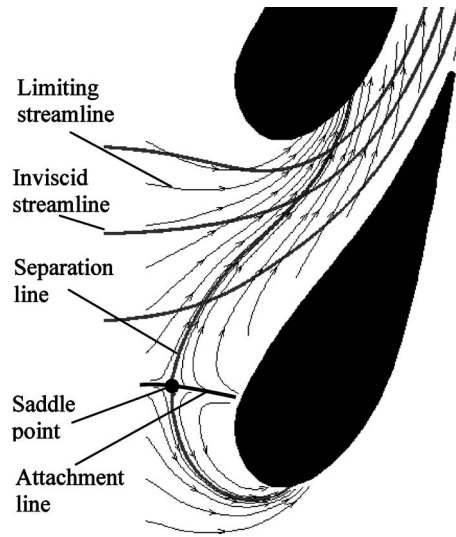


Fig. 5 Endwall limiting streamlines and the separation line calculated from the friction coefficient vectors in Fig. 4, with inviscid streamlines from FLUENT [21] overlaid

at various flow rates and metering widths are presented in Fig. 6. Note that for all cases in this study, there is a hot region around the vane-end-wall junction where slot coolant is not present. This pattern is caused by the rollup of the horseshoe vortex at the vane leading edge, which brings hot mainstream gases down to the endwall, and sweeps coolant off of the endwall. Further downstream, the combination of the horseshoe and passage vortices entrains coolant and sweeps it to the suction side of the vane.

To visualize endwall results in a more quantitative sense, values were extracted from the endwall data along the paths of inviscid streamlines obtained from a CFD prediction of the vane flowfield with FLUENT 6.2 [21]. Streamlines were released at midspan of the vane from three pitch locations, corresponding to $Y/P=0.25$, 0.50 , and 0.75 , as shown in Fig. 6(a). These streamlines are denoted as $0.25P$, $0.50P$, and $0.75P$, respectively. Figure 7 presents the adiabatic effectiveness levels on the endwall resulting from the upstream slot flow, along each of the three streamline paths. The abscissa of the plots is nondimensionalized distance along the streamline, shifted so that $s/C=0$ corresponds to where the streamline would cross an imaginary pitchwise line connecting adjacent vane stagnation points. Note that the plots in Fig. 7 have different abscissas, since the streamlines have different lengths through the vane passage. In the shifted streamline coordinate system, the upstream slot is located at $s/C=-0.35$. Data are not plotted directly downstream of the slot, but rather starting at $s/C=-0.3$, in order to avoid the high measurement uncertainty at the start of the thermal boundary layer in the heat transfer coeffi-

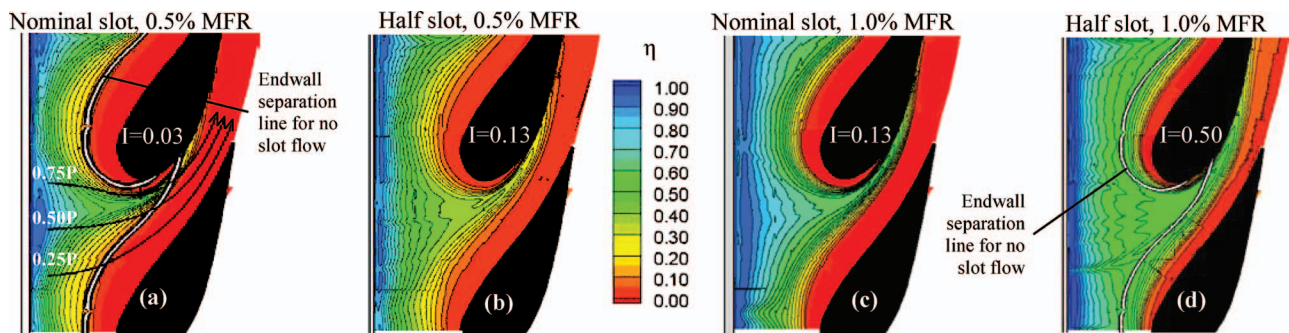


Fig. 6 Contours of endwall effectiveness from upstream slot flow for (a) nominal slot, MFR=0.5%; (b) half slot, MFR=0.5%; (c) nominal slot, MFR=1.0%; and (d) half slot, MFR=1.0%

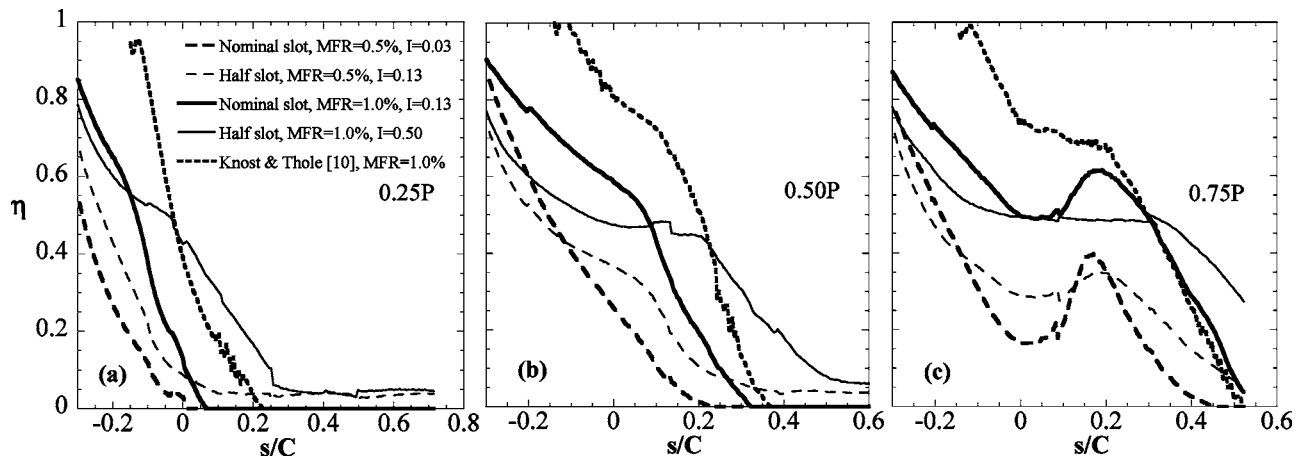


Fig. 7 Adiabatic cooling effectiveness on the endwall from upstream slot flow, sampled along an inviscid streamline released from (a) 25% pitch, (b) 50% pitch, and (c) 75% pitch

cient measurements.

In Fig. 7, effectiveness values eventually become zero as each streamline path crosses into the hot region. Note that in most cases, the path of the 0.75P streamline crosses the hot ring region around the suction side of the vane, passes through the narrow band of coolant being swept to the suction side by the passage vortex, and reenters the pressure side hot region (refer to Fig. 6(a)). These crossings explain why effectiveness along the 0.75P path decays, increases, and then progressively decays.

As described earlier, the slot in this study was positioned at $0.77C_{ax}$ upstream of the vane stagnation. A slot located far upstream, away from the influence of the vane, can reduce or eliminate the potential for hot gas path ingestion into the slot, but from a practical point of view may be difficult to implement in an engine. The effect of moving the slot upstream is shown in Fig. 8. A similar lack of coolant coverage around the base of the vane is seen between this study's results and those of Knost and Thole [10], for 1% slot flow from a nominal slot. The horseshoe and passage vortices control the distribution of coolant in the passage, despite the differences in slot location. Note that the upstream slot for the case in Fig. 8 had the same geometry as the slot tested by Knost and Thole [10], but Knost and Thole positioned their slot at $0.38C_{ax}$ from the vane leading edge. In the contours of Fig. 8, and along the inviscid streamline paths in Fig. 7, Knost and Thole's [10] slot blowing at 1.0% mass flow ratio (MFR) exhibits higher local effectiveness than the nominal slot blowing at 1.0% MFR. Coolant ejected farther upstream interacts more with the mainstream and thus is less effective when it reaches the vane passage. However, the slot in Knost and Thole's [10] study also results in

more poorly distributed effectiveness levels across the endwall than for a slot ejecting farther upstream (see Fig. 8). High effectiveness gradients would be a durability concern since they could lead to large gradients in endwall metal temperature and increased thermal stresses.

The effect of increasing the coolant flow rate can be seen by comparing the contours in Figs. 6(a) and 6(c) for the nominal slot at two coolant flow rates, as well as in Figs. 6(b) and 6(d) for the half slot at two coolant flow rates. For a given upstream slot width, effectiveness levels from upstream slot coolant over the endwall increase with increasing slot mass flow rates. Also, coolant coverage is more uniform downstream of the slot and is better able to penetrate into the hot ring around the vane-end-wall junction for a slot MFR of 1% as compared to a slot MFR of 0.5%. Figures 7(a) and 7(b) show that for a given upstream slot width, the location of zero effectiveness along the 0.25P and 0.50P inviscid streamline paths moves farther downstream (convects farther into the passage) as the slot mass flow rate is increased from 0.5% to 1.0%.

Matching the upstream slot leakage flow while decreasing the slot width increases the coolant momentum, with the effect of increasing overall coolant coverage in the passage. Comparison of Fig. 6(a) with Fig. 6(b) for the same mass flux ratios with differing slot widths (differing momentum flux ratios), and Fig. 6(c) with Fig. 6(d) also for the same mass flux ratios with differing slot widths, shows that the half slot at a given mass flow rate produces more uniform coolant coverage upstream and around the vane-end-wall junction than the nominal slot at the same mass flow rate. Along the streamline paths in Fig. 7, for a given mass flow rate, coolant from the half slot generally has higher levels of effectiveness than the nominal slot as the coolant enters the vane passage (downstream of $s/C=0$). Maintaining the mass flow rate from the slot, while decreasing the metering area of the slot, requires a larger plenum-to-freestream pressure differential, which forces coolant out of the slot more evenly. This finding is in agreement with the conclusions of Cardwell et al. [12], even though the upstream slot in this study was located farther upstream of the vane leading edge than that of Cardwell et al.

The effect of matching the slot momentum flux ratio for the nominal and half slot is perhaps a more realistic situation for a turbine engine. Generally, the coolant will be supplied at a constant pressure relative to the mainstream. The effect of reducing the upstream slot width will be to reduce the coolant mass flow rate, but the average momentum flux ratio will remain the same. The coolant coverage region in Fig. 6(b) for the half-width slot at a MFR of 0.5% appears similar to the coverage region from the nominal slot at the same momentum flux ratio (Fig. 6(c)). How-

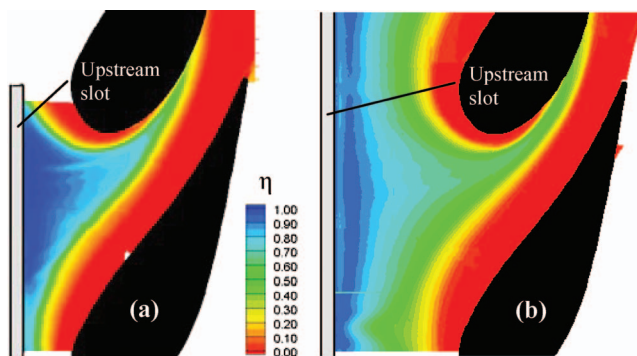


Fig. 8 Contours of effectiveness for the nominal slot at 1.0% MFR for (a) Knost and Thole [10] (slot at $X/C_{ax}=-0.38$), and (b) this study (slot at $X/C_{ax}=-0.77$)

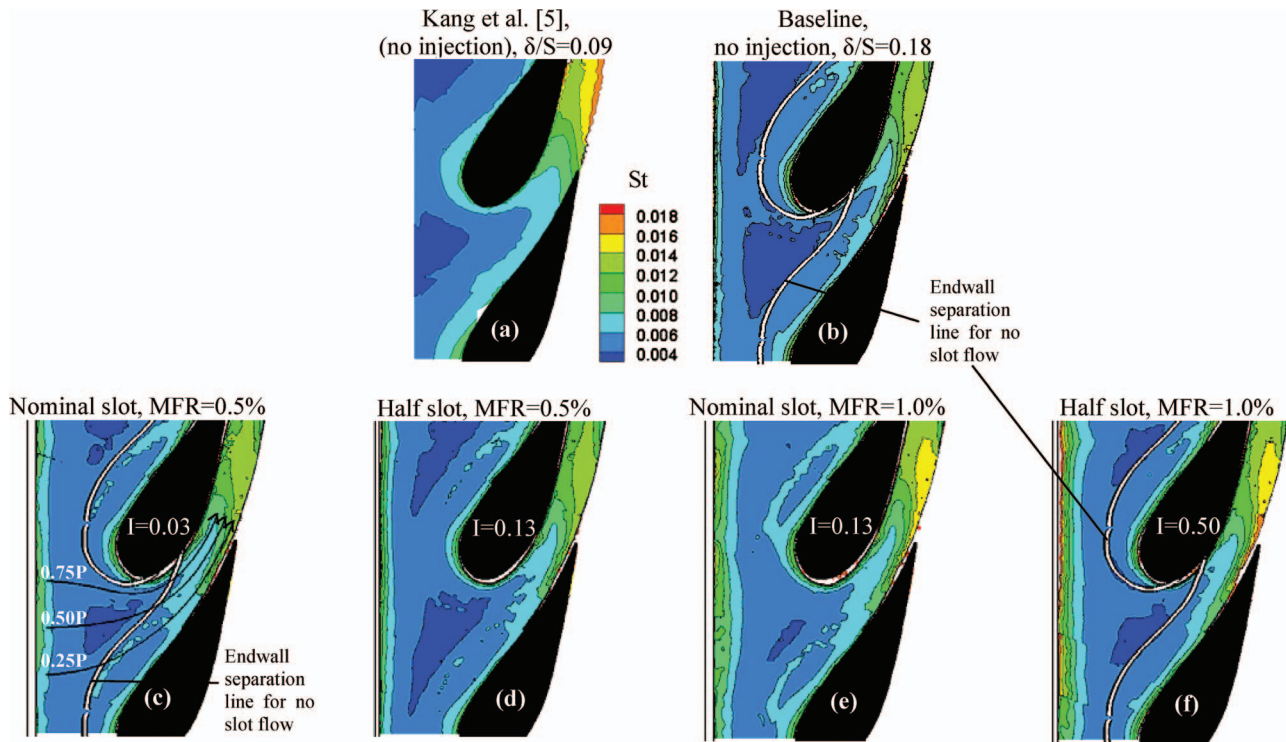


Fig. 9 Contours of St for (a) Kang et al. [5] (no upstream slot); (b) base line (no upstream slot); (c) nominal slot, MFR=0.5%; (d) half slot, MFR=0.5%; (e) nominal slot, MFR=1.0%; and (f) half slot, MFR=1.0%

ever, coolant effectiveness levels from the half slot flow are lower relative to the nominal slot at the same momentum flux ratio, since the nominal slot is ejecting more coolant.

When the endwall separation line for no upstream blowing is overlaid on the adiabatic cooling effectiveness contours in Figs. 6(a) and 6(d), it is apparent that for low slot coolant momentum, the trajectory of the coolant is dictated by the secondary flow vortices. For the highest momentum flux ratio tested, however, some coolant penetrates downstream of the separation line, indicating that the coolant has a more significant interaction with end-wall secondary flow in this case.

Heat Transfer Coefficients for an Upstream Slot. Endwall heat transfer coefficients were measured with and without an upstream slot flow. For the baseline with no slot flow, a qualitative comparison was made to Kang et al. [5], who used the same

airfoil geometry. Similar results were achieved, as can be seen in Figs. 9(a) and 9(b) for both baselines with no slot flow, despite differences in the upstream tunnel geometry and inlet boundary layer thicknesses ($\delta/S=0.09$ for Kang et al. [5] and $\delta/S=0.18$ for our work). High heat transfer coefficients are seen in Figs. 9(a) and 9(b) near the vane stagnation region resulting from the horseshoe vortex. The effects of the passage vortex are seen further downstream as the contours sweep to the suction surface.

Figures 9(b)–9(f) compare heat transfer coefficients with and without upstream slot flow for the various slot widths and flow rates. The overall effect of injection along the endwall is that the heat transfer coefficients are slightly increased in the cases with injection, relative to the baseline without injection. Figure 10 shows endwall heat transfer augmentation levels relative to the no

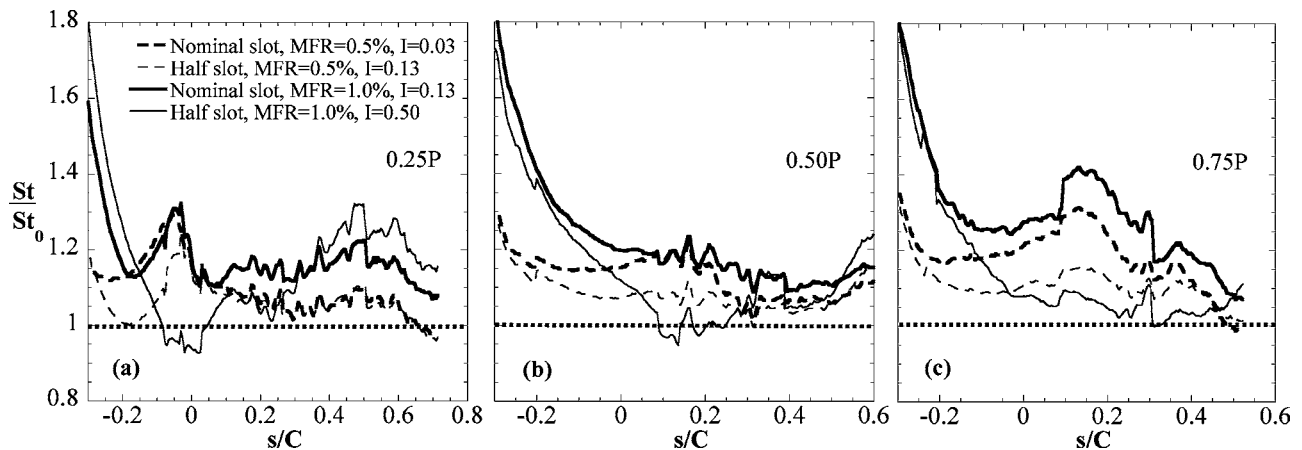


Fig. 10 Heat transfer augmentation on the endwall from upstream slot flow, sampled along an inviscid streamline released from (a) 25% pitch, (b) 50% pitch, and (c) 75% pitch

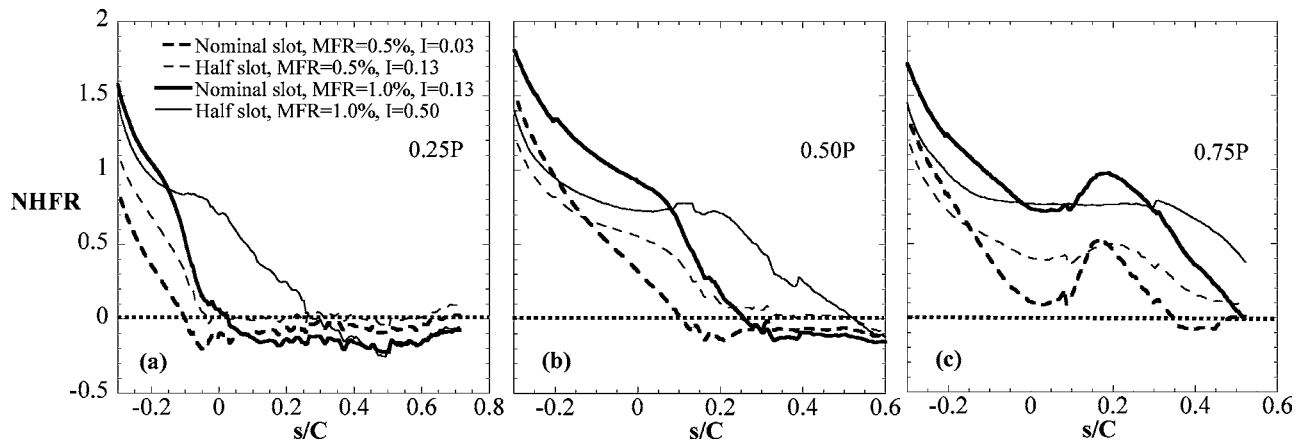


Fig. 11 NHFR to the endwall from upstream slot flow, sampled along an inviscid streamline released from (a) 25% pitch, (b) 50% pitch, and (c) 75% pitch

leakage flow case along the $0.25P$, $0.50P$, and $0.75P$ streamline paths. Note that overall, augmentation levels with upstream slot blowing indicate higher heat transfer throughout most of the passage.

The effect of increasing the slot mass flow rate, while maintaining the slot width, is illustrated for the nominal slot in Figs. 9(c) and 9(e) and for the half slot in Figs. 9(d) and 9(f). Stanton numbers increase slightly throughout the passage when the slot mass flow rate is increased from 0.5% to 1.0% for a given slot width. Heat transfer augmentation levels along the inviscid streamline paths (Fig. 10) are generally higher as the mass flow rate increases through a given slot width. An exception to this trend, however, is the region around $s/C = -0.05$ on the $0.25P$ streamline path (Fig. 10(a)) and the region around $s/C = 0.10$ on the $0.50P$ streamline path (Fig. 10(b)). At these locations, there is no difference in heat transfer augmentation for the nominal slot injecting coolant at either mass flow rate. It was noted that the $0.25P$ streamline path crosses the separation line for no upstream slot blowing at $s/C = -0.07$, while the $0.50P$ streamline path crosses the separation line at $s/C = 0.11$ (refer to Fig. 9(c)). These results indicate that the separated flow dictates the heat transfer augmentation near the endwall separation line rather than the injection itself. However, for the half slot, increasing its mass flow from 0.5% to 1.0% increases the coolant momentum to the point that the injection begins to interfere with the horseshoe vortex.

As mentioned earlier, for a turbine engine, a decrease in upstream slot width would result in a decrease in slot mass flow rate, but nominally the same momentum flux ratio. The effect of decreasing the slot width while maintaining the same momentum flux is seen by comparing the contours of Figs. 9(d) and 9(e). Stanton numbers are slightly lower for the half slot at a MFR of 0.5%, compared to the nominal slot at a MFR of 1.0%, even though both have the same momentum flux.

The endwall separation line, deduced from the measured friction coefficients with no upstream slot blowing, is overlaid on the heat transfer coefficient results for no upstream slot blowing (Fig. 9(b)), and for blowing at the lowest and highest momentum flux ratios in Figs. 9(c) and 9(f), respectively. There is a region of low heat transfer between the vanes near the passage entrance that persists farther downstream for the case with the highest momentum flux ratio (Fig. 9(f)) relative to the lowest momentum flux ratio (Fig. 9(c)). These behaviors suggest that the upstream slot injection at a high momentum flux ratio reduces horseshoe vortex strength.

Net Heat Flux Reduction for an Upstream Slot. The determination of convective heat transfer to a turbine endwall with film cooling requires knowledge of the film heat transfer coefficient, the metal wall temperature, and the adiabatic wall (recovery) tem-

perature. The addition of coolant to the endwall reduces the adiabatic wall temperature and thus the driving potential for heat transfer. The mixing and flow disturbance induced by the coolant injection, however, generally increases the convective heat transfer coefficients. The net heat flux reduction (NHFR) parameter incorporates the effects of convective heat transfer coefficients and coolant effectiveness on the overall augmentation to the heat load to the component. To deduce the NHFR parameter, the component wall metal temperature must also be known, since it is the other driving temperature for heat transfer into the part. The non-dimensional form (denoted as φ) relates the wall temperature to the freestream and coolant temperatures. Since the wall temperature is dependent on the vane metal conductivity and internal cooling scheme, it had to be assumed for this study, which used adiabatic materials for the endwall. A value of $\varphi = 1.6$ was assumed based on typical film-cooled engine conditions (Sen et al. [22]). Note that values of $\text{NHFR} < 0$ indicate that the film cooling scheme is causing an increase in the overall heat flux experienced by the surface.

Figure 11 presents the NHFR calculated along each of the inviscid streamline paths. For the cases that have been studied, it is clear that there is a strong benefit of the leakage coolant at the entrance to the vane passage. Downstream, however, the cooling benefit of the leakage flow produces a detrimental effect where no coolant is present but the heat transfer coefficients have been increased. This increase is caused by alterations to the secondary flows that in turn increase the overall convective heat transfer coefficients. The $0.25P$ and $0.50P$ streamline paths, shown in Figs. 11(a) and 11(b), respectively, indicate that the addition of upstream slot flow at any mass flow rate or slot width causes NHFR values that are less than zero near the exit of the vane passage. The lack of coolant penetration into the hot ring around the vane, combined with slight heat transfer coefficient augmentations from slot flow, leads to an increased net heat flux that would be experienced by the part.

It is apparent that the trends of NHFR along the streamline paths in Fig. 11 parallel the trends of the effectiveness levels, and many of the same conclusions about the effects of slot flow can be made. Although increasing the slot flow rate tends to increase heat transfer coefficients, the additional coolant from a given slot width at 1.0% MFR relative to 0.5% MFR results in a net heat flux reduction. Also, the better coolant coverage from a half-width slot at a given mass flow rate reduces net heat flux, as compared to the nominal slot at the same mass flow rate. Finally, the case of matched momentum flux ratios for the nominal and half slots shows that, despite reduced Stanton number augmentations from the half slot blowing versus the nominal slot blowing, the lower

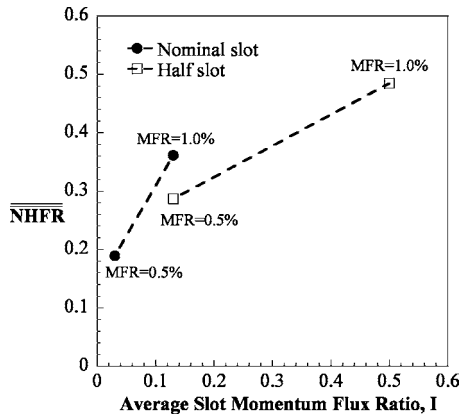


Fig. 12 Area-averaged NHFR to the endwall as a function of upstream slot momentum flux ratio

amount of coolant ejected from the half slot at a MFR of 0.5% is not as effective in reducing heat flux into the endwall as is the coolant from the nominal slot at a MFR of 1.0%.

An overall, area-averaged NHFR is shown in Fig. 12 as a function of slot momentum flux ratio. Coolant ejection from the half slot does a better job in decreasing average heat flux into the endwall than coolant from the nominal slot, when both are ejecting coolant at a given mass flow ratio. However, blowing from the half slot at a momentum flux ratio of 0.13 (MFR=0.5%) increases the average net heat flux (decreases NHFR parameter) by 26%, compared to the nominal slot blowing at the same momentum flux ratio ($I=0.13$, MFR=1.0%). Thus, axial contraction of the upstream slot, in a situation where the slot momentum flux is maintained, would increase endwall heat transfer.

Conclusions

Measurements of adiabatic cooling effectiveness and heat transfer coefficients on the endwall, from leakage flow through a two-dimensional upstream slot representing a combustor-turbine interface gap, were presented. Two slot flow rates and two slot widths were tested to determine the effect of the contraction of the slot on the endwall heat transfer.

The dominance of the endwall secondary flow on upstream slot coolant coverage was demonstrated by moving the slot further upstream. The coverage area of the slot coolant, when the slot was located $0.77C_{ax}$ upstream of the vane, was similar to the coverage area for a slot located $0.38C_{ax}$ upstream. It was noted, however, that effectiveness levels in the passage were lower for the slot placed farther upstream since the coolant had more distance to interact with the mainstream flow.

For a fixed slot width, increasing the slot mass flow resulted in slightly increased heat transfer coefficients, but also higher adiabatic cooling effectiveness levels. Coolant exited the slot more uniformly at the higher slot flow rates, since the higher flow rate required an increase in slot pressure ratio. Overall, the net heat flux to the endwall was reduced, since more coolant was present at the higher flow rates.

Decreasing the slot width while maintaining a constant slot mass flow resulted in larger coolant coverage areas and increased local effectiveness levels. Moreover, heat transfer coefficient augmentations from the half-width slot were lower than augmentations from the nominal slot. Area-averaged values of the NHFR parameter indicated that the coolant from the half slot width reduced the net heat flux to the endwall compared to the nominal slot, when both were ejecting coolant at the same mass flow rate. The higher momentum of slot coolant from the half-width slot enabled it to penetrate farther into the passage.

Overlaying the endwall separation line for no blowing on contours of effectiveness and heat transfer coefficients revealed that

for low slot momentum, the endwall secondary flow dictated the coolant trajectory in the passage. At the highest momentum flux ratio tested, a significant amount of coolant penetrated downstream of the endwall separation line, and heat transfer coefficients were reduced compared to the low momentum slot flow. The high coolant momentum in this case is suspected to have reduced the horseshoe vortex strength.

These results indicate that leakage flow through the combustor-turbine interface can provide cooling to the endwall, with a more uniform distribution of coolant when the interface is placed farther upstream. More uniform coverage reduces the spatial temperature variation in the turbine endwall metal, which is beneficial for durability. The effects of thermal expansion of the interface, however, need to be carefully considered since higher heat loads can result when the combustor-turbine interface gap contracts. Understanding how a leakage interface expansion impacts the heat transfer and cooling effectiveness of the leakage flow may help a designer to protect the part during unwanted thermal expansion incidents with the least amount of coolant.

Acknowledgment

The authors would like to thank the National Science Foundation's GOALI program for funding this research (Grant No. 0412971). They would also like to acknowledge their partners in the GOALI program: Joel Wagner and Peter Tay (Pratt & Whitney), and Dr. Lee Langston and Brian Holley (University of Connecticut).

Nomenclature

- C = true chord of stator vane
- C_{ax} = axial chord of stator vane
- C_f = friction coefficient, see Eq. (1)
- C_p = heat capacity at constant pressure
- g = gravitational acceleration (9.81 m/s²)
- h = heat transfer coefficient
- h_{oil} = height of oil film
- I = average momentum flux ratio, $I = \rho_c U_c^2 / \rho_\infty U_\infty^2$
- L = spacing between oil film interferogram bands (fringes)
- M = average blowing ratio, $M = \rho_c U_c / \rho_\infty U_\infty$
- MFR = mass flow ratio, $MFR = \dot{m}_c / \dot{m}_{in}$
- n = index of refraction
- NHFR = net heat flux reduction, $NHFR = 1 - (h_f / h_0)(1 - \eta\phi)$
- \overline{NHFR} = area-averaged NHFR
- P = pitch of stator vane, or pressure
- Re_{Dh} = Reynolds number based on hydraulic diameter
- Re_{in} = inlet Reynolds number, $Re_{in} = CU_{\infty, in} / \nu$
- Re_θ = momentum thickness Reynolds number, defined as $Re_\theta = \theta U_{\infty, in} / \nu$
- s = distance along a streamline
- S = span of stator vane
- St = Stanton number, $St = h / \rho C_p U_{\infty, in}$
- t = time
- T = temperature
- U = axial velocity
- X, Y, Z = vane coordinates, where X is turbine axial direction

Greek

- δ = boundary layer thickness
- η = adiabatic effectiveness, $\eta = (T_\infty - T_{aw}) / (T_\infty - T_c)$
- θ = momentum thickness
- θ_i = incident light angle
- λ = light wavelength of sodium vapor lamp
- μ_{oil} = dynamic viscosity of oil
- ν = kinematic viscosity

ρ = density
 τ_w = wall shear stress
 ϕ = phase difference of light rays, or nondimensional vane metal temperature,
 $\phi = (T_\infty - T_c) / (T_\infty - T_w)$

Subscripts

0 = baseline conditions (no blowing)
aw = adiabatic wall
c = coolant conditions
in = inlet conditions
s = streamline coordinate
w = conductive (metal) wall
 ∞ = local freestream conditions

References

- [1] Langston, L. S., 1980, "Crossflows in a Turbine Passage," ASME J. Eng. Power, **102**, pp. 866–874.
- [2] Sharma, O. P., and Butler, T. L., 1987, "Predictions of Endwall Losses and Secondary Flows in Axial Flow Turbine Cascades," ASME J. Turbomach., **109**, pp. 229–236.
- [3] Goldstein, R. J., and Spores, R. A., 1988, "Turbulent Transport on the Endwall in the Region Between Adjacent Turbine Blades," ASME J. Heat Transfer, **110**, pp. 862–869.
- [4] Graziani, R. A., Blair, M. F., Taylor, J. R., and Mayle, R. E., 1980, "An Experimental Study of Endwall and Airfoil Surface Heat Transfer in a Large Scale Turbine Blade Cascade," ASME J. Eng. Power, **102**, pp. 257–267.
- [5] Kang, M., Kohli, A., and Thole, K. A., 1999, "Heat Transfer and Flowfield Measurements in the Leading Edge Region of a Stator Vane Endwall," ASME J. Turbomach., **121**, pp. 558–568.
- [6] Ames, F. E., Barbot, P. A., and Wang, C., 2003, "Effects of Aeroderivative Combustor Turbulence on Endwall Heat Transfer Distributions Acquired in a Linear Vane Cascade," ASME J. Turbomach., **125**, pp. 210–220.
- [7] Blair, M. F., 1974, "An Experimental Study of Heat Transfer and Film Cooling on Large-Scale Turbine Endwalls," ASME J. Heat Transfer, **96**, pp. 524–529.
- [8] Granser, D., and Schulenberg, T., 1990, "Prediction and Measurement of Film Cooling Effectiveness for a First-Stage Turbine Vane Shroud," ASME Paper No. 90-GT-95.
- [9] Knost, D. G., and Thole, K. A., 2004, "Adiabatic Effectiveness Measurements of Endwall Film-Cooling for a First Stage Vane," ASME Paper No. GT2004-53326.
- [10] Knost, D. G., and Thole, K. A., 2005, "Adiabatic Effectiveness Measurements of Endwall Film-Cooling for a First Stage Vane," ASME J. Turbomach., **127**, pp. 297–305.
- [11] Burd, S. W., Satterness, C. J., and Simon, T. W., 2000, "Effects of Slot Bleed Injection Over a Contoured Endwall on Nozzle Guide Vane Cooling Performance: Part II—Thermal Measurements," ASME Paper No. 2000-GT-200.
- [12] Cardwell, N. D., Sundaram, N., and Thole, K. A., 2007, "The Effects of Varying the Combustor-Turbine Gap," ASME J. Turbomach., **129**, pp. 756–764.
- [13] Kost, F., and Nicklas, M., 2001, "Film-Cooled Turbine Endwall in a Transonic Flow Field—Part I: Aerodynamic Measurements," ASME J. Turbomach., **123**, pp. 709–719.
- [14] Nicklas, M., 2001, "Film-Cooled Turbine Endwall in a Transonic Flow Field—Part II: Heat Transfer and Film-Cooling Effectiveness," ASME J. Turbomach., **123**, pp. 720–729.
- [15] Kost, F., and Mullaert, A., 2006, "Migration of Film-Coolant From Slot and Hole Ejection at a Turbine Vane Endwall," ASME Paper No. GT2006-90355.
- [16] Munson, B. R., Young, D. F., and Okiishi, T. H., 2002, *Fundamentals of Fluid Mechanics*, 4th ed., Wiley, New York, p. 514.
- [17] Naughton, J. W., and Sheplak, M., 2002, "Modern Developments in Shear Stress Measurement," Prog. Aerosp. Sci., **38**, pp. 515–570.
- [18] Harrison, S., 1990, "Secondary Loss Generation in a Linear Cascade of High-Turning Turbine Blades," ASME J. Turbomach., **112**, pp. 618–624.
- [19] Holley, B., and Langston, L. S., "Surface Shear Stress and Pressure Measurements in a Turbine Cascade," ASME Paper No. GT2006-90580.
- [20] Moffat, R. J., 1988, "Describing the Uncertainties in Experimental Results," Exp. Therm. Fluid Sci., **1**, pp. 3–17.
- [21] FLUENT, Version 6.2.1, Fluent Inc., Lebanon, NH.
- [22] Sen, B., Schmidt, D. L., and Bogard, D. G., 1996, "Film Cooling With Compound Angle Holes: Heat Transfer," ASME J. Turbomach., **118**, pp. 800–806.

A Comparative Investigation of Round and Fan-Shaped Cooling Hole Near Flow Fields

James S. Porter

Jane E. Sargison

Gregory J. Walker

Alan D. Henderson

School of Engineering,
University of Tasmania,
Hobart 7001, Australia

This study presents velocity and turbulence data measured experimentally in the near field of a round and a laterally expanded fan-shaped cooling hole. Both holes are fed by a plenum inlet, and interact with a turbulent mainstream boundary layer. Flow is Reynolds number matched to engine conditions to preserve flow structure, and two coolant to mainstream blowing momentum ratios are investigated experimentally. Results clearly identify regions of high shear for the round hole as the jet penetrates into the mainstream. In contrast, the distinct lack of high shear regions for the fan-shaped hole points to reasons for improvements in cooling performance noted by previous studies. Two different computational fluid dynamics codes are used to predict the flow within and downstream of the fan-shaped hole, with validation from the experimental measurements. One code is the commercially available ANSYS CFX 10.0, and the other is the density-based solver with low Mach number preconditioning, HYDRA, developed in-house by Rolls-Royce plc for high speed turbomachinery flows. Good agreement between numerical and experimental data for the center-line traverses was obtained for a steady state solution, and a region of reversed flow within the expansion region of the fan-shaped hole was identified. [DOI: 10.1115/1.2812952]

Introduction

Film cooling of turbine components continues to be one of the most successful cooling techniques used in the gas turbine industry. Yet, for all its importance, and the amount of research invested in the process, many key mechanisms involved in the coolant flow path are still not fully understood. Due to the broad range of circumstances where a round jet in a crossflow is encountered, this configuration has been more thoroughly researched than other hole geometries. Significant features of the flow field, such as the counter-rotating vortex pair, have been identified through various studies. The transition from round holes to the use of various configurations of fan-shaped cooling holes has resulted in improved lateral coverage and extended centerline effectiveness largely due to the reduced momentum of the exiting coolant jet for an equivalent mass of coolant.

Most experimental work with fan-shaped holes has examined the effects of various parameters on film cooling effectiveness or discharge coefficient. Both of these parameters are important for evaluating a configuration's performance. Their values are, however, the end result of a complex flow path through the cooling system, and a three dimensional interaction between the jet and the mainstream. A more detailed understanding of the internal and exit region flow field for shaped cooling holes is therefore essential for improvements in cooling hole design to be made.

The present paper is primarily concerned with shaped holes, in particular, the laterally expanded or fan-shaped hole commonly used in gas turbine blade and guide vane cooling. Its performance is compared to a cylindrical hole as a reference case. Measurements from both geometries complement currently available data on jet-in-crossflow configurations. In addition, these new data are used to partially validate Reynolds-averaged Navier-Stokes (RANS) based numerical solutions of the flow field using a mesh based directly on the experimental domain. Two different compu-

tational fluid dynamics (CFD) solvers have been applied to the same problem, using the same mesh and boundary conditions, and where possible the same initial flow conditions. One of the solvers, ANSYS CFX, is a commercially produced code, with robust solution techniques and a good suite of pre- and postprocessing tools. The second code, HYDRA, is a Rolls-Royce plc in-house developed numerical solver used in aeroengine applications, and optimized for the solution of high speed turbomachinery flows.

Literature Review

Experimental Studies. Experimental work on the performance of shaped film cooling holes has grown strongly in past years. However, the majority of studies have concentrated on the distribution of heat transfer coefficient and cooling effectiveness on the surface downstream of the hole exit. Goldstein et al. [1] first reported the improvements in adiabatic effectiveness obtained by using holes with a laterally expanded exit, attributing the main cause of these improvements to a reduction in effective blowing rate at the hole exit due to the area expansion of the fan. More recently, Gritsch et al. [2] presented cooling effectiveness for single, large scale, round and fan-shaped holes; as with Goldstein et al., the results indicated significantly improved cooling performance, particularly in laterally averaged results. These authors also identified significant effects of the coolant flow conditions at the hole inlet on cooling performance. This agrees with previous findings presented by Pietrzyk et al. [3], who highlighted the important effects of the hole inlet flow on developments further downstream. Many other studies are available that present valuable data on the thermal performance and benefits of fan-shaped cooling holes, including several more by Gritsch et al. [4–6] and Dittmar et al. [7]. However, these studies do little to expose the features of the flow field that control this performance, and thus provide only a partial picture.

There are few experimental studies that focus attention on the flow field created by the jet-mainstream interaction for fan-shaped holes. Thole et al. [8] used laser Doppler velocimetry to compare the velocity and turbulence field of a round, laterally expanded, and forward-laterally expanded fan-shaped hole. They found that velocity gradients were significantly reduced for the fan-shaped

Contributed by the International Gas Turbine Institute of ASME for publication in the JOURNAL OF TURBOMACHINERY. Manuscript received June 19, 2007; final manuscript received July 3, 2007; published online August 4, 2008. Review conducted by David Wisler. Paper presented at the ASME Turbo Expo 2007: Land, Sea and Air (GT2007), Montreal, Quebec, Canada, May 14–17, 2007.

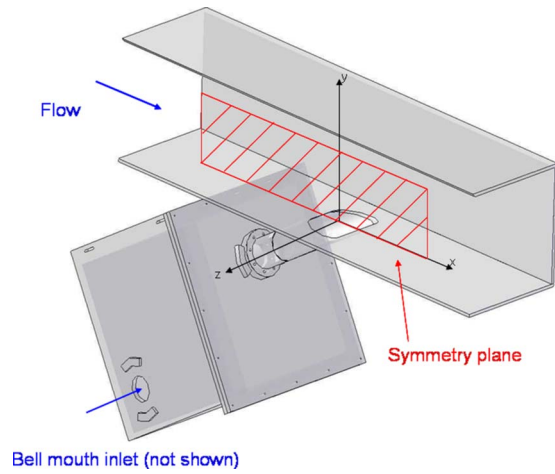


Fig. 1 Working section and cooling hole with plenum supply

holes when compared with the round hole, which resulted in less turbulence downstream. High levels of turbulence were measured above the exit, however, and this was attributed to the large expansion angle of the fans. Other studies, such as Hale et al. [9,10], make tentative assumptions on the flow structure based on thermal measurements and visualizations, but the focus of the research is again on cooling performance. Clearly, there is a need for more detailed experimental flow field data for shaped cooling holes.

Computational Studies. One of the more extensive computational investigations into the flow field of round and shaped film cooling holes was a series of papers by Leyelek and co-workers that used a systematic computational methodology, and looked at both round and shaped holes. Hyams and Leyelek [11] produced one in a series of four papers looking at the physics of film cooling for round and shaped cooling holes. The authors examined four different shaped hole configurations, including the traditional laterally expanded fan-shaped hole, and identified this configuration as having the best overall cooling performance of all those tested. They presented velocity field data in the exit region and provided an analysis using components of vorticity, based on a proposition by Moussa et al. [12]. This approach was used to explain the sources of the well-documented counter-rotating vortex pair for the round hole; it demonstrated that the laterally and forward diffused holes significantly reduce the axial aligned vorticity, thus discouraging mainstream ingestion downstream.

Kohli and Thole [13] examined the flow field of a round and fan-shaped hole inclined at 35 deg. They concentrated on the effects of inlet crossflows, finding that for the cases considered, a large separation region occurred within the expanded portion of the fan. This study also found that the shaped hole produced no counter-rotating vortices at exit, and had a maximum in turbulence intensity at the downstream edge of the hole. Due to the flexibility of CFD, these studies and others have provided useful information on the flow field for shaped holes in conjunction with cooling performance data. However, the need for experimental validation of computational studies is still high.

Experimental Facility and Instrumentation

The low speed wind tunnel at the University of Tasmania that was used for this research is shown schematically in Fig. 1. The wind tunnel has a 225×225 mm working section of 1 m length. It is preceded by a smooth two-dimensional vertical contraction, utilizing a sixth order polynomial profile that optimizes the flow uniformity at the working section midplane, and prevents separation in the contraction. Details of this contraction design are presented by Sargison et al. [14]. At 200 mm upstream of the working section inlet, the boundary layer is tripped to ensure a fully

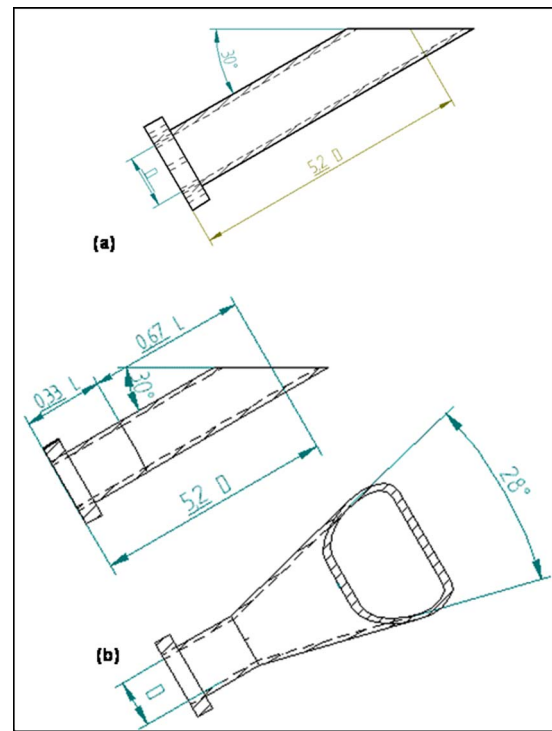


Fig. 2 Hole geometries: (a) round hole and (b) laterally expanded hole

developed and stable turbulent boundary layer through the working section. The maximum working section flow speed is 20 ms^{-1} , and calibration of the wind tunnel is reported by Sargison et al. [14] and Rossi [15]. The mainstream turbulence is 0.6%, flow direction is uniform to within ± 0.5 deg, and velocity is uniform to within $\pm 2\%$.

The hole configurations tested in this study consist of a round, or cylindrical, reference geometry, and a laterally expanded fan-shaped hole. The round hole and the fan-shaped hole throat both have a 50 mm diameter inlet nozzle to meter the coolant flow. Both holes are inclined at 30 deg to the mainstream. The length/diameter ratio for both holes was 5.2. The length L is measured along the hole centerline, with the fan-shaped hole expansion starting at $1/3L$ at an included angle of 28 deg. The geometries are shown in Fig. 2. Both the coolant and mainstream air were drawn from atmosphere, giving a temperature and density ratio of unity for all cases. Coolant air was drawn into the coolant supply plenum by the difference in static pressure between the working section and local atmospheric pressure, and the blowing ratio was varied by introducing varying grades of mesh at the plenum entrance to increase the flow resistance and hence reduce the flow rate through the hole. Using this method, blowing ratios of $M = 0.7, 0.6,$ and 0.5 were achievable, with the coolant flow rate measured by a bellmouth inlet to the plenum.

Flow through the hole is Reynolds number matched to engine conditions based on hole throat diameter. The velocity profile at $x/D = -1.2$ indicates a mainstream boundary layer thickness of $\delta/D = 0.4$, which is similar to that of a real turbine blade on the early pressure surface. The momentum thickness Reynolds number at the same location is approximately 2000. Other parameters of the flow were limited by laboratory capabilities at the time of the experimental work. However, this paper aims to provide an insight into the fundamental flow physics of the fan-shaped hole in crossflow, and add to the available data for validation of CFD predictions. The satisfaction of complete engine condition modeling is not required for this purpose.

Velocity and turbulence intensity measurements were made us-

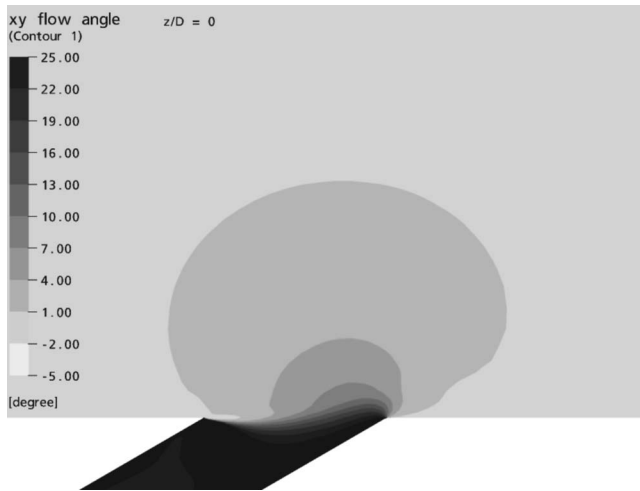


Fig. 3 Contour plot of deviation from pure x -direction flow for the fan-shaped hole. Angle is measured anticlockwise.

ing a single sensor Dantec type 55P11 miniature hot-wire probe with wire axis normal to the average mainstream flow direction. The probe was operated by a DISA 55M constant temperature anemometer with standard bridge, and calibrated in situ against a Pitot tube and wall static tapping in the plane of the sensor tip. Turbulence intensity values were calculated from the measured velocity rms scaled by the mean velocity value at the measurement location. Measurements were corrected for electrical noise in the anemometer; however, the inherent nonlinearity of the hot-wire anemometer introduced errors in calculated mean velocity and turbulence intensity values. Investigation into these errors indicated that for the majority of the measurement domain, errors due to nonlinearity were less than 3%. This uncertainty increased to almost 10% in regions of very high measured turbulence intensity. However, the latter regions were small.

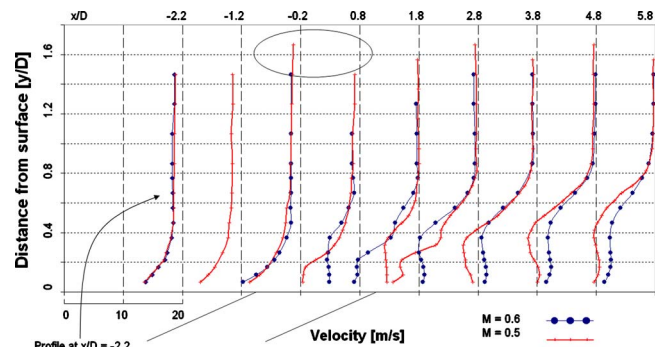
Due to limitations in the traverse setup, the hot-wire tip could only be positioned within 3 mm ($0.06D$) of the wall. As a result, the boundary layer profile is not fully captured down to the wall. However, a fully turbulent boundary layer velocity profile is still clearly identifiable in the main flow upstream of the hole, and measurements compare well with the $1/7$ th power law.

The use of a single axis probe in a highly three-dimensional flow brings with it errors in measured values due to the insensitivity to flow direction of the probe. Positioning the sensor along the plane of symmetry effectively eliminates the influence of z -component velocities, and thus it is only deviation from a purely x -direction flow in the x - y plane that will cause errors in the measured u velocity. Far from the jet-mainstream interaction region, it can be expected that the dominant flow direction is indeed streamwise along the x axis. However, closer to the hole, where the three dimensionality of the flow is more pronounced, the measured u -velocity magnitude will include some y -component velocity.

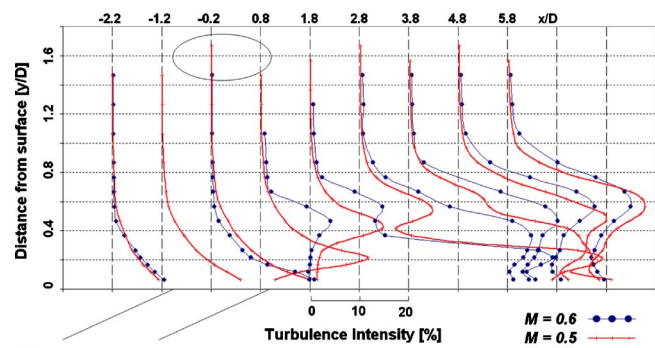
CFD predictions of the flow enable a view of the expected flow directions, and a contour plot of the deviation in degrees from a purely u -component flow is presented in Fig. 3. It can be seen that the region of largest variation is around the hole exit, with a maximum value of approximately 15 deg at the downstream edge. This corresponds to a maximum u -velocity magnitude error of 3.4% in this region. The deviation angle for the majority of the domain is less than 5 deg, giving a measured velocity error of less than 0.4%.

Experimental Results

Experimental results provided velocity and turbulence intensity profiles at up to 10 x/D locations along the symmetry plane



(a)



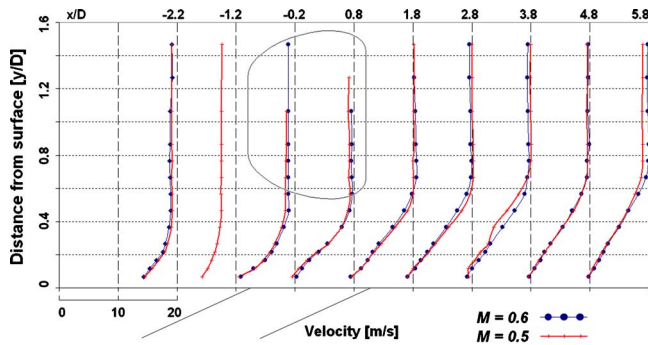
(b)

Fig. 4 Centerline velocity (a) and turbulence intensity (b) profiles for the round hole geometry

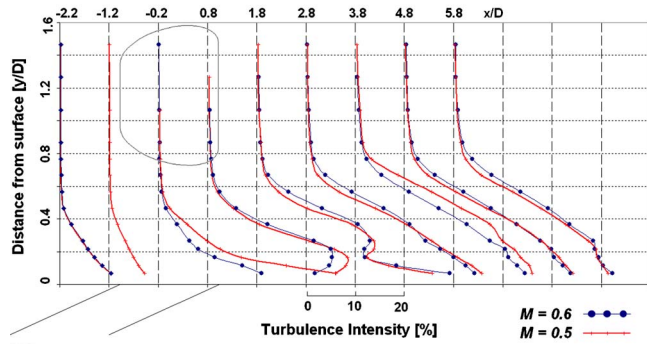
($z/D=0$) ranging from 4 diameters upstream to 5 diameters downstream. The coordinate system used in this study has its origin at the center of the cooling hole exit, as shown in Fig. 1. The plot format used to present data facilitates visualization of the streamwise flow development. The vertical axis shows dimensionless distance y/D from the exit plane. The values across the top of the chart denote the streamwise measurement location x/D . The bottom horizontal axis provides a sliding scale, representing velocity or turbulence intensity, with 20 m/s and 0% values, respectively, aligning with the x/D location of a profile. The location of the cooling hole is indicated by the exit plane x - z outline; the lines at the bottom of the plots indicate the centerline section of the cooling hole passage in the x - y plane.

Round Hole. Examining Fig. 4, the effects of the ejected round jet on the flow field are clearly visible, with a distinct lifting of the mainstream flow away from the wall indicated by the increase in height of the $u/U=99\%$ location downstream of $x/D=-0.2$ for both blowing ratios. At $x/D=0.8$, the penetration of the jet fluid into the mainstream starts to become evident, with a region of almost uniform lower velocity fluid near $y/D=0$. For the $M=0.5$ case, the lower momentum fluid penetrates vertically only about half as far as for the higher blowing ratio case; the flow acts as if a partially inclined “cover” was positioned over the hole exit as described by Andreopoulos and Rodi [16]. At $x/D=0.8$, the velocity gradient between $y/D=0.2$ and 0.4 is pronounced, and is reflected in the large rise in turbulence intensity at the corresponding location in Fig. 4(b). This velocity gradient and increase in turbulence can be attributed to the existence of a strong shear layer between the jet and mainstream fluid, as identified by Pietrzyk et al. [3] and supported by Walters and Leyeck [17]. It remains evident for the whole extent of the measurement domain downstream.

The exit velocity of the jet is somewhat higher just downstream of exit than expected from the velocity ratio (equal to M for constant density). This can be attributed to the acceleration experi-



(a)



(b)

Fig. 5 Centerline velocity (a) and turbulence intensity (b) profiles for the fan-shaped hole geometry

enced by the jet fluid as it is turned by the mainstream. Continuing downstream, the wake-like behavior of the flow can be seen, with a clear velocity deficit for both blowing ratios. Near the wall, the velocity is seen to increase, and a negative velocity gradient occurs. This can be explained by the lateral ingestion of higher momentum mainstream fluid into the wake region, indicating the existence of the well-documented counter-rotating vortices. An interesting feature of the lower blowing ratio velocity profile at $x/D=2.8$ occurs near the wall. A distinct drop in the velocity magnitude occurs at about $y/D=0.3$, which would appear to be within the jet fluid region. At $y/D=0.2$, the velocity gradient reverses to a peak before reverting once again closer to the wall. This peak in velocity is consistent with a rectification of the velocity in a reversed flow region as a consequence of the directional insensitivity of a single axis probe.

The presence of a reversed flow region is further supported by the very high turbulence intensity values measured at the corresponding locations in Fig. 4(b). A similar occurrence is seen for the higher blowing ratio case, but at one measurement location upstream of the $M=0.5$ case. The flow structure in this region is present for both blowing ratio cases, as evidenced in the $x/D=1.8$ profile for $M=0.6$. However, the flow development is “delayed” in the lower blowing ratio case as the lower momentum jet fluid is swept downstream more rapidly. The turbulence level contours start to flatten at $x/D=4.8$, as the two fluid streams mix out, but the overall level is still high as the wake region develops. The differences between the two blowing ratio cases become somewhat less with downstream distance, although the $M=0.6$ case maintains a higher average velocity in the wake region due to the higher momentum jet fluid.

Fan-Shaped Hole. From Fig. 5, it can be seen that the fan-shaped hole exhibits far less variation with downstream distance in both velocity and turbulence when compared with the round hole cases. The jet fluid exiting the hole is decreased in velocity compared with the round hole case, more notably for $M=0.6$, due

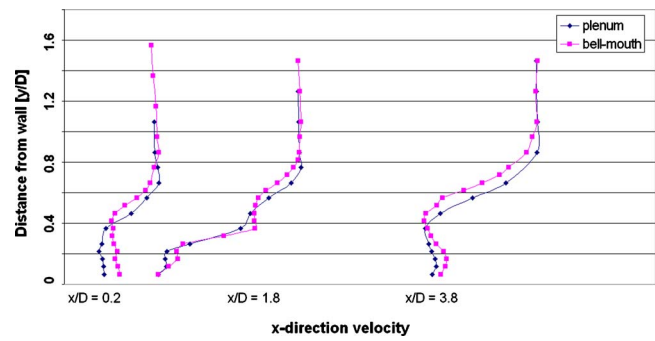


Fig. 6 Comparison of velocity profiles for different hole inlet conditions (round hole)

to the reduced momentum of the flow as a result of the area expansion of the fan. As with the round hole, the mainstream is seen to be lifted away from the surface by the jet over the exit region. However, the deflection for the fan-shaped case is less than that of the round hole by $y/d=0.2$. This points to the fact that the jet fluid is spread laterally across the surface downstream of the hole rather than penetrating far into the mainstream. A decrease in velocity near the wall can be seen between $x/D=1.2$ and -0.2 as the mainstream experiences a blockage by the jet fluid. At $x/D=0.8$, just upstream of the hole trailing edge, a flattened velocity profile near the wall indicates that this region is occupied by jet fluid.

There does not appear to be a strong velocity gradient near the wall downstream of the hole as seen in the round hole case, indicating that a reversed flow region is not present. This is again due to the lower momentum jet fluid remaining close to the surface and not allowing mainstream fluid to enter laterally. The velocity gradient is almost constant from near the wall all the way out to the freestream, with a wake-type region of constant shear existing as the top edge of the jet is accelerated by the mainstream flow. This large shear region creates the high levels of turbulence seen in Fig. 5(b). Another major contributor to the high turbulence levels downstream is the unsteadiness created in the flow as a result of the overexpansion of the fan. The half angle of the current fan geometry is 14 deg. Combined with the effects of the sharp edged entry to the hole, the high turbulence levels at exit are not unrealistic; but, it should be noted that these values are still significantly lower than for the round hole case. At $x/D=5.8$, the turbulence intensity profiles appear to be approaching a typical boundary layer shape, suggesting that the effects of the jet-mainstream interaction on the surface flow have diminished by about $x/D=6$. The differences between blowing ratio cases are small for both velocity and turbulence profiles. This suggests that the effects of blowing ratio may be more evident away from the symmetry plane for the fan-shaped hole.

Effect of Coolant Supply Configuration. In addition to the variation of blowing ratio, two different inlet conditions were tested for the round hole to reveal differences in the flow field as a direct result of the hole inlet condition. These conditions were a tube with bellmouth entry, and a plenum chamber. The bellmouth nozzle, of the same diameter as the hole and with length $5D$, was mounted directly to the hole inlet, effectively doubling the length to diameter (L/D) ratio.

The differences in velocity and turbulence profiles for each inlet case at a blowing ratio of 0.5 are shown in Fig. 6 for three x/D locations. The velocity profiles demonstrate little variation, with both intake conditions producing very similar profiles. The velocity profiles for the plenum inlet condition do, however, seem to exhibit lower values near the wall and higher values through the mainstream boundary layer away from the wall. At $x/D=0.2$, the flow at low y/D values is primarily jet fluid; the increase in ve-

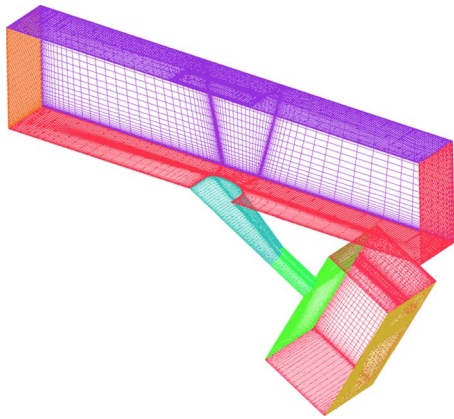


Fig. 7 Computational mesh (~500,000 cells)

Locality for the bellmouth inlet case can be explained by a more developed boundary layer within the hole, resulting in a contraction of effective flow area and thus an increase in velocity of the core fluid region. Further downstream the differences are less pronounced, with the bellmouth inlet case maintaining higher velocity values near the wall.

Computational Investigation

In addition to the experimental measurements, a preliminary RANS-based CFD study was conducted to investigate the flow within the cooling hole, and also to validate and compare two different CFD solvers. The details of this investigation are presented below.

Numerical Codes. Documentation on the numerical schemes used in CFX is easily accessible from the user manual. One of the strengths of this program is that all of the industry-accepted first and second order advection schemes are offered [18]. A fully implicit time-stepping scheme and a blended first and second order advection scheme are used here, together with the industry standard two equation $k-\varepsilon$ turbulence model. This model is implemented with scalable wall functions to improve robustness and accuracy for fine near-wall meshes.

HYDRA is a density-based solver to align with the normal application of the code to high speed compressible flows in turbomachinery. A density-based solver uses the value and gradients of density at a mesh node to calculate other flow variables. Due to the inherent invariability of density in a flow considered to be incompressible, density-based solvers often struggle to provide accurate solutions for incompressible flows, and usually require some form of preconditioning to improve numerical robustness. Low Mach number preconditioning is available in HYDRA and was used in conjunction with the $k-\varepsilon$ turbulence model. However, cases run in HYDRA presented here used the one-equation Spalart-Allmaras turbulence model as it was stable and produced converged steady state solutions with sensible flow fields, without the need for preconditioning.

Computational Method. A structured hexahedral mesh was fitted to the CAD geometry of the physical wind tunnel working section using ANSYS ICEM, with cell determinant values above 0.6. The determinant gives an indicator of cell skewness and warpage and is based on the internal angles of the opposing edges within a cell. A more orthogonal mesh provides more accurate results. A grid independence study was performed and revealed no change to the cooling hole flow field for higher resolution meshes. Thus, the current mesh with approximately 500,000 cells was used in the computations, and is shown in Fig. 7. The wall-element y^+ values were reduced to 4 for this study at all hole boundaries and also the mainstream hole surface boundary.

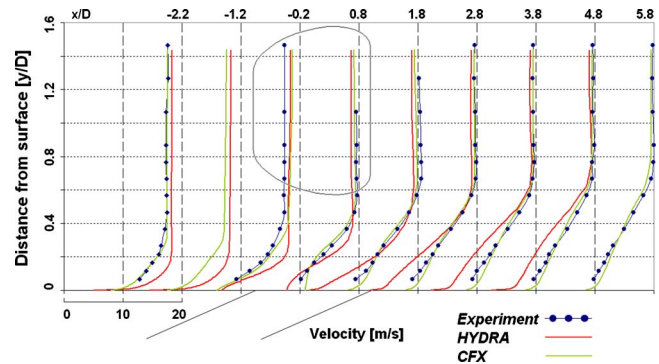


Fig. 8 Comparison of centerline velocity profiles from experiment, HYDRA, and CFX for fan-shaped hole

For the HYDRA case, a uniform mass flow inlet condition was specified for both the mainstream flow and plenum inlet planes, thus controlling the blowing ratio. The static pressure at outlet was adjusted until the main flow average velocity upstream of the cooling hole was close to experimental values. Turbulence modeling was kept simple for this initial computational study, with the one-equation Spalart-Allmaras turbulence model, due to greater robustness. For the CFX cases, a velocity profile was applied at the mainstream inlet based on experimental data to ensure that the numerical solution was closely representative of the actual flow. A uniform mass flow was specified at the plenum inlet, and the industry standard $k-\varepsilon$ two equation model was used.

The main parameters for the numerical problem were set to match the experimental conditions. These were a blowing ratio of $M=0.6$, density and temperature ratio of 1, and a mesh modeled on the working section as described above. Inlet turbulence levels were set to 1% to reflect measured results.

Computational Fluid Dynamics Results

Comparison With Experimental Data. In order to provide a degree of validation for the numerical solutions, velocity profiles were extracted during postprocessing at locations within the domain that corresponded to those used in acquiring the experimental data. A comparison of the numeric and experimental profiles was then made. Figure 8 shows the experimental data for the fan-shaped hole at a blowing ratio of $M=0.6$ together with the values extracted from the HYDRA and CFX solutions. The agreement is good overall, particularly downstream of the hole, and mainstream values are in good agreement away from the surface. Moving down toward the surface, the HYDRA curves tend to diverge from the experimental values, while the CFX values remain similar and demonstrate a tendency to overpredict the velocity near the wall. This near-wall difference can be partially attributed to nonlinearity errors of the hot wire, which result in experimental velocity values less than the actual value, by up to 3%.

Looking upstream of the hole at $x/D=-2.2$, a large difference between the HYDRA and experimental velocity profiles in the boundary layer region can be seen. This part of the domain is a fairly simple bounded flow and the numerical code would be expected to provide a good solution here. For the CFX case, a velocity profile based on the $1/7$ th power law through the boundary layer was specified, and the agreement of the upstream profiles is excellent. This agreement continues downstream with very little deviation. Unfortunately, the same profile could not be specified at the time HYDRA calculations were made, and thus the results from this solver cannot be expected to match experimental values accurately. The discrepancy in values at inlet to the domain is propagated downstream and can be attributed with many of the differences seen as the jet fluid starts to interact with the mainstream. It is interesting to notice that the HYDRA solution still demonstrates a similar progression of velocity profiles to the other cases, and

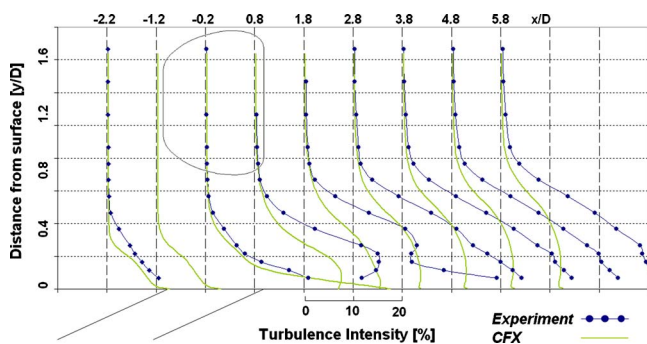


Fig. 9 Comparison of centerline turbulence intensity profiles from experiment and cfx for fan-shaped hole

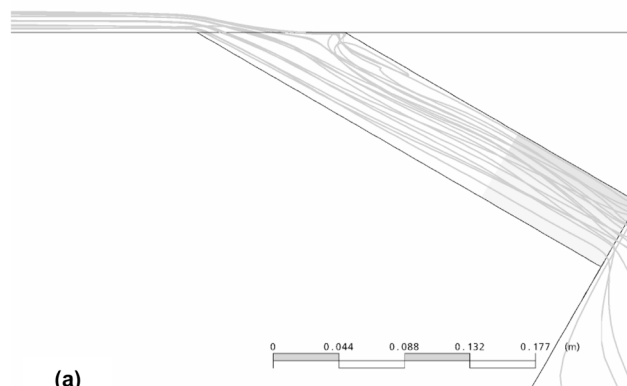
indicates that the solver is capable of capturing the main flow features.

For the CFX solution, a measure of turbulence intensity was extracted from the data to compare with experimental values. The turbulence intensity was calculated from the equation for turbulent kinetic energy with the assumption of isotropic turbulence. Figure 9 shows the centerline turbulence intensity profiles from experimental measurements alongside the values taken from the CFX solution. The agreement with experimental values for the profiles upstream of and directly above the hole is excellent, and in line with the velocity profile results. Further downstream, it is evident that the standard $k-\varepsilon$ turbulence model consistently underpredicts the experimental values. Nonetheless, the effects of the jet on the flow field are evident, with a large region of increased turbulence present downstream, indicating that the wake-type region seen in the experimental results is identified in the numerical solution. However, this region is not as full as in the experimental case, and points to the turbulence model failing to capture the full dynamics of the jet-mainstream interaction. This is evident right from the start of the shear layer where the two curves consistently diverge.

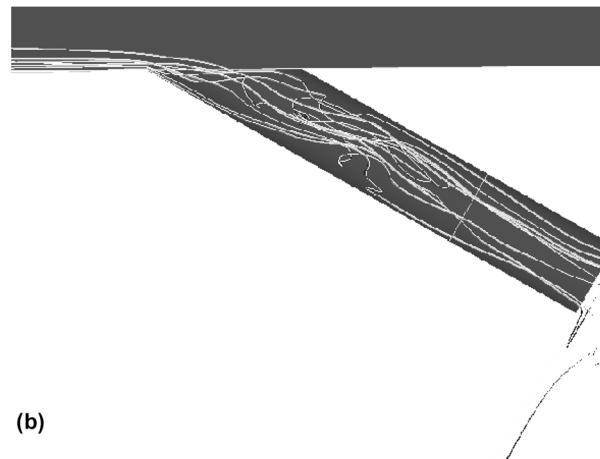
It should be noted here that nonlinearity errors in the hot-wire data gave higher than actual values of turbulence in areas of reported high turbulence. Account of this would bring the curves closer, though the limitations of the two equation model will continue to produce underpredicted values. The profiles are much smoother than experiment, and this is possibly due to the RANS approach averaging out the turbulent quantities. Closer to the wall and downstream of the hole exit, the numerical solution shows a marked decrease in turbulence intensity. This is in contrast to the experimental results which show increasing intensity with decreasing distance from the wall, and the development of a turbulent boundary layer profile near the wall downstream of $x/D = 3.8$.

The CFX case clearly shows the limitations of the two equation $k-\varepsilon$ turbulence model when applied to flows with regions of high shear and boundary layer separation. The assumption of isotropic turbulence is very approximate and must be considered when comparing to experimental results. The RANS-based approach combined with the anisotropy of the real flow turbulence contribute a significant portion to the discrepancies observed. Future work aims to apply a large eddy simulation (LES) approach to resolve the turbulent structures and improve correlation with experimental data.

A comparison between the two numerical codes is difficult, as the numerical scheme, turbulence model, and main inlet velocity profile are dissimilar. Nevertheless, the results from both CFD codes are encouraging, particularly for the HYDRA solver, as the density-based scheme appears to deal quite well with the very low speed ($Ma=0.06$) flow. This suggests that regions of low Mach number flow in nominally high speed turbomachinery problems will be well represented at the required level. The partial validation of both solvers permits a degree of confidence in the numeri-



(a)



(b)

Fig. 10 Comparison of in-hole streamlines for (a) cfx and (b) HYDRA

cal solution across the entire domain based on the centerline plane results.

In-Hole Region. Streamlines within the hole for both solvers are shown in Fig. 10. The most immediately obvious difference between the two images is the level of disturbance of the flow within the expanded section. Both images show a region of recirculating fluid within the expansion but the CFX case has a much smoother velocity field, with the recirculation region confined to an area at the edge of the expanded section. The HYDRA results, however, have a much more turbulent flow field within the hole, beginning as far upstream as the hole inlet, where the sharp edge creates a separated region and high turbulence levels. The HYDRA results suggest that the expansion flow is unsteady, and a time averaged solution of smoothed streamlines presented here is not realistic. Experimental investigations using a wool tuft indicate that a region of recirculating flow does indeed exist at the sides of the expanded portion, inline with the CFX predictions. Tufting also revealed that the flow in the main body of the expansion is indeed highly unsteady, supporting the results from HYDRA.

Near Field. The predicted flow downstream of the hole and around the exit area was very similar for both solvers, despite the differences in flow within the hole. Examining the streamlines in Fig. 11, it can be seen that in both cases, the mainstream streamlines are deflected around the side of the hole and also over the ejecting jet fluid. Figure 11(b) shows a highlighted region at the upstream edge of the domain indicating the area of origin of the streamlines, which is also applicable to Fig. 11(a). Both images show a streamline leaving the edge of the hole at an angle to the mainstream and being subsequently driven back toward the cen-

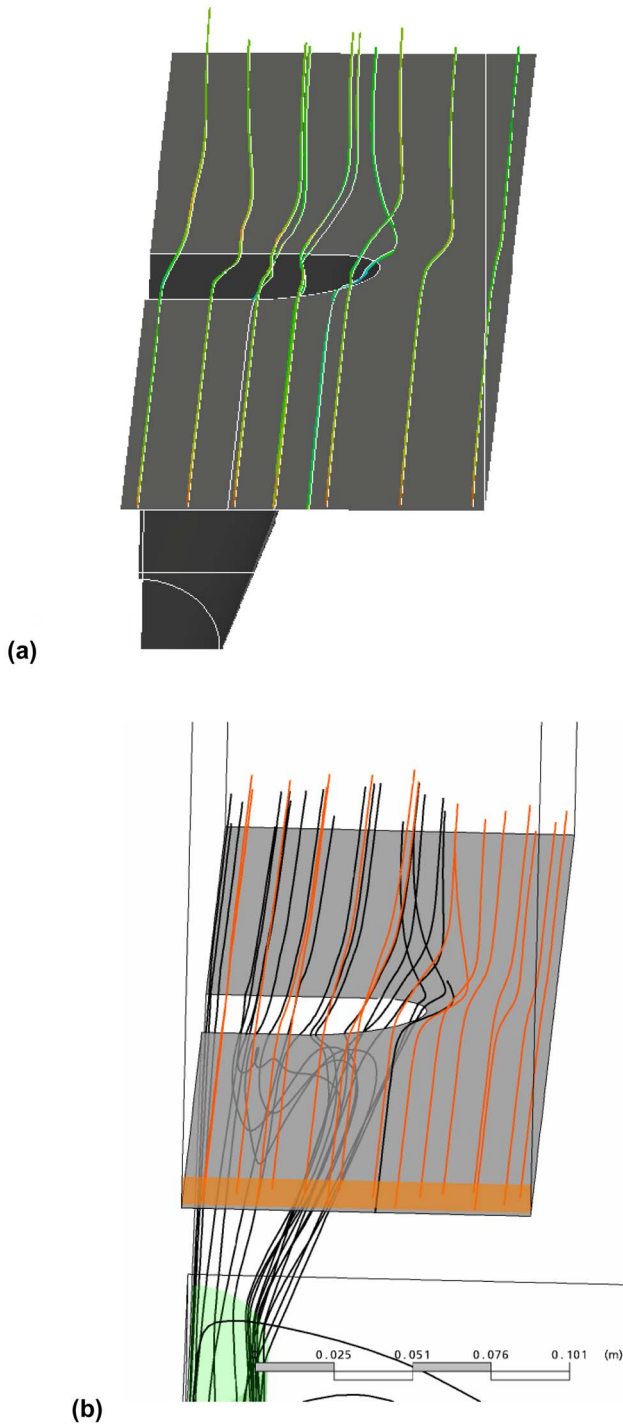


Fig. 11 Near hole region streamlines: (a) HYDRA and (b) CFX

terline of the hole by the mainstream fluid. A notable feature of the downstream flow field is the lateral contraction of the jet fluid as the higher momentum mainstream fluid accelerates around the jet and in turn accelerates the jet fluid through the shear layer. This flow pattern is consistent with surface streak marks on real blades from dirt deposition.

Although not clearly shown in these images, some ingestion of the mainstream fluid into the cooling hole near the upstream outside edge of the hole was noticed, and agrees with findings of Kohli and Thole [13] in their CFD study. Such ingestion is detrimental to film cooling performance.

Conclusions

Experimental flow field data have been presented for the centerline plane in the near field of both a round and a laterally expanded fan-shaped hole. Profiles of velocity and turbulence in this plane have shown that the round jet ejection creates regions of high shear and turbulence production, and a low pressure region in the lee of the jet that encourages entrainment of mainstream fluid near the surface. The fan-shaped hole, in contrast, produces a much more uniform flow field downstream, with reduced mixing between fluid streams and less vertical deflection of the mainstream flow.

Preliminary computational results have been presented for the fan-shaped geometry from two RANS-based numerical solvers using different turbulence models and numerical schemes. Both solvers produced centerline plane profiles in agreement with experimental data, with the CFX results being particularly good over the whole domain. Improvements in specified inlet boundary conditions and use of a higher order turbulence model would increase the accuracy of the HYDRA solution. The flow within the expansion demonstrated a clear region of recirculating flow near the edge of the hole, and results indicated unstable flow throughout the expanded section.

This study has contributed to the database of available film cooling flow field data, and provides new information for the fan-shaped hole. The need for further detailed experimental investigation within the film cooling hole itself is clear.

Acknowledgment

The authors gratefully acknowledge support from Rolls-Royce plc UK for financial assistance, access to HYDRA, and technical advice and guidance. ANSYS is thanked for the provision of an academic license to the CFX 10.0 suite. The author also acknowledges support through receipt of an Australian Postgraduate Award.

Nomenclature

- L = length of cooling hole
- D = diameter of cooling hole
- M = blowing ratio $\rho_j U_j / \rho_\infty U_\infty$
- Re = Reynolds number ($\rho U D / \mu$)
- Tu = turbulence (%)
- U = average velocity

Subscripts

- ∞ = mainstream
- j = cooling jet

References

- [1] Goldstein, R. J., Eckert, E. R. G., and Burggraf, F., 1974, "Effects of Hole Geometry and Density on Three-Dimensional Film Cooling," *Int. J. Heat Mass Transfer*, **17**, pp. 595–607.
- [2] Gritsch, M., Schulz, A., and Wittig, S., 1998, "Adiabatic Wall Effectiveness Measurements of Film-Cooling Holes With Expanded Exits," *ASME J. Turbomach.*, **120**(3), pp. 549–556.
- [3] Pietrzyk, J. R., Bogard, D. G., and Crawford, M. E., 1989, "Hydrodynamic Measurements of Jets in Crossflow for Gas Turbine Film Cooling Applications," *ASME J. Turbomach.*, **111**(2), pp. 139–145.
- [4] Gritsch, M., Schulz, A., and Wittig, S., 2003, "Effect of Internal Coolant Crossflow on the Effectiveness of Shaped Film-Cooling Holes," *ASME J. Turbomach.*, **125**(3), pp. 547–554.
- [5] Gritsch, M., Schulz, A., and Wittig, S., 2000, "Film-Cooling Holes With Expanded Exits: Near-Hole Heat Transfer Coefficients," *Int. J. Heat Fluid Flow*, **21**(2), pp. 146–155.
- [6] Gritsch, M., Colban, W., Schär, H., and Döbbling, K., 2005, "Effect of Hole Geometry on the Thermal Performance of Fan-Shaped Film Cooling Holes," *ASME J. Turbomach.*, **127**(4), pp. 718–825.
- [7] Dittmar, J., Schulz, A., and Wittig, S., 2002, "Assessment of Various Film Cooling Configurations Including Shaped and Compound Angle Holes Based on Large Scale Experiments," ASME Paper No. GT2002-30176.
- [8] Thole, K., Gritsch, M., Schulz, A., and Wittig, S., 1998, "Flowfield Measurements for Film-Cooling Holes With Expanded Exits," *ASME J. Turbomach.*, **120**(2), pp. 327–336.
- [9] Hale, C. A., Plesniak, M. W., and Ramadhyani, S., 2000, "Film Cooling Ef-

- fectiveness for Short Film Cooling Holes Fed by a Narrow Plenum," ASME J. Turbomach., **122**(3), pp. 553–557.
- [10] Hale, C. A., Plesniak, M. W., and Ramadhyani, S., 2000, "Structural Features and Surface Heat Transfer Associated With a Row of Short-Hole Jets in Crossflow," *Int. J. Heat Fluid Flow*, **21**(5), pp. 542–553.
- [11] Hyams, D. G., and Leylek, J. H., 2000, "Detailed Analysis of Film Cooling Physics: Part III—Streamwise Injection With Shaped Holes," ASME J. Turbomach., **122**(1), pp. 122–132.
- [12] Moussa, Z. M., Trischka, J. W., and Eskinazi, S., 1977, "Near Field in the Mixing of a Round Jet With a Cross-Stream," *J. Fluid Mech.*, **80**, pp. 49–80.
- [13] Kohli, A., and Thole, K. A., 1997, "A CFD Investigation on the Effects of Entrance Crossflow Directions to Film-Cooling Holes," paper presented at the ASME Heat Transfer Division meeting, HTD, ASME, New York, pp. 223–232.
- [14] Sargison, J. E., Walker, G. E., and Rossi, R., 2004, "Design and Calibration of a Wind Tunnel With a Two Dimensional Contraction," paper presented to 15th Australasian Fluid Mechanics Conference, University of Sydney, Dec. 13–17.
- [15] Rossi, R., 2004, *Blade-Cooling Mechanism: Calibration of the Open Circuit Wind Tunnel*, University of Tasmania/Ecole Polytechnique Nantes, France.
- [16] Andreopoulos, J., and Rodi, W., 1984, "Experimental Investigation of Jets in a Crossflow," *J. Fluid Mech.*, **138**, pp. 93–127.
- [17] Walters, D. K., and Leylek, J. H., 2000, "A Detailed Analysis of Film-Cooling Physics: Part I—Streamwise Injection With Cylindrical Holes," ASME J. Turbomach., **122**(1), pp. 102–112.
- [18] ANSYS 2005, *CFX Advanced Solver Technology*, viewed 30th July 2006, <http://www.ansys.com/products/cfx-advanced-solver.asp>

Mixed Flow Turbine Research: A Review

Srithar Rajoo

e-mail: srithar.rajoo@imperial.ac.uk

Ricardo Martinez-Botas

e-mail: r.botas@imperial.ac.uk

Department of Mechanical Engineering,
Imperial College London,
London SW7 2AZ, United Kingdom

Research on mixed flow turbines spans over 50 years with substantial literature available in the public domain. Mixed flow turbines were initially used as an alternative rotor design for gas turbines and later extended to automotive turbocharger applications. The characteristics of a mixed flow turbine resemble a radial turbine but with some significant performance improvements, giving this design an edge to satisfy the ever increasing demand in the automotive sector. The initial research focus was mainly experimental but in recent years, there have been significant contributions in computational analysis. This paper is intended to provide readers with a comprehensive review of the past and present research into the design, performance, and use of mixed flow turbines. Additionally, the future research direction of the mixed flow turbine is discussed in view of the current turbocharger and automotive demand. [DOI: 10.1115/1.2812326]

Keywords: turbocharger, mixed flow turbine, variable geometry turbine

1 Introduction

One of the earliest contributions using a mixed flow concept in turbomachinery was presented by Hamerick et al. [1], where they presented one of the earliest methods to analyze the compressible flow in an arbitrary mixed flow impeller intended for a compressor design. Stewart [2] used the method proposed by Hamerick et al. [1] to analyze the flow in a mixed flow turbine and showed possible improvements when compared to a radial and an axial turbine. The work by Stewart [2] focused on the use of a mixed flow impeller in gas turbines for the aerospace industry. Thus, the design of the mixed flow turbine was derived from an axial turbine point of view. The benefits of a mixed flow turbine from a radial turbine point of view were demonstrated by Wallace [3] focusing on the automotive turbocharging application. The pulsating nature of the exhaust flow in an internal combustion engine requires a turbocharger turbine to operate efficiently at higher pressure ratio conditions, which in turn leads to better energy extraction during the peak of the exhaust pulses. The velocity ratio is inversely proportional to the turbine's pressure ratio, as shown by the equation.

$$\frac{U}{C_{is}} = \frac{U}{\sqrt{2c_p T_{0inlet} [1 - (P_{exit}/P_{0inlet})^{(\gamma-1)/\gamma}]}} \quad (1)$$

Thus, the need for an efficient high pressure ratio operation requires a turbine to operate in lower velocity ratio region. A radial turbine, despite its many advantages, has less flexibility in coping

with the lower velocity ratio demand due to the radial inlet requirement. Figure 1 shows the turbine velocity ratio in relation to the inlet absolute and relative flow angles. Due to the radial inlet requirement ($\beta_2=0$), the peak efficiency of a radial turbine is limited to a velocity ratio of about 0.7. In contrast, the nonradial inlet of a mixed flow turbine enables it to achieve peak efficiency at a lower velocity ratio (Fig. 1), which gives more freedom in the design and operation of the turbine. A typical mixed flow turbine efficiency curve is superimposed in Fig. 2(b) to show its peak efficiency at a lower velocity ratio compared to a radial turbine. Figure 2 also demonstrates the performance difference between an axial turbine and a radial or a mixed flow turbine (from Refs. [4,5]). A radial turbine is preferred for an automotive turbocharger because of its ability to maintain high efficiency at a range of pressure ratios. A mixed flow turbine has a similar ability with the benefit of lower velocity ratio operation. As an additional comment, it has been shown in Fig. 2(c) that the operational range of a mixed flow turbine is similar to a radial turbine but can be extended slightly to an axial turbine region. For further investigation, readers can refer to Japikse and Baines [6] for a comprehensive comparison of axial, radial, mixed flow, and other types of turbomachines.

Since the 1970s, research has been undertaken by a number of groups to demonstrate the benefits of mixed flow turbines. The following discussion will explore the progress in the past 50 years and will also suggest future research directions involving mixed flow turbines.

2 Definition of a Mixed Flow Turbine

A mixed flow turbine can be viewed as a cross design between a radial and an axial turbine, as it possesses the features of both. The basic schematic of a mixed flow turbine is shown in Fig. 3 with a comparison to its radial counterpart. The inlet flow of a mixed flow turbine is at an angle between the complete axial and the radial design. In comparison to a radial turbine, this reduces the flow path curvature, as seen in Fig. 4, and effectively reduces the formation of secondary flow. This can be attributed as one of the main advantages of the mixed flow turbine compared to its radial counterpart.

The defining characteristics of a mixed flow turbine are the blade angle, cone angle, and camber angle, as shown in Fig. 5. The distinction between a mixed flow and a radial turbine (see Fig. 3) is the cone angle at the blade inlet. The cone angle of a radial turbine is fixed at 90 deg due to the blade radial fiber requirement. By radially sweeping the blade inlet as in a mixed flow rotor, a nonzero blade angle can be achieved and still maintain the radial fiber. Figure 5 also shows the 3D view of a mixed flow rotor in which the nonzero inlet blade angle can be noticed. This enables a forward sweep at the inlet without jeopardizing the structural stability, which improves its performance compared to the radial counterpart. There is no definitive optimum cone angle for a mixed flow rotor and different values are usually used. Nevertheless, the values used by researchers in the past as shown in Table 1 can be used as a basic reference. The relationship between the blade angle, cone angle, and camber angle can be derived as in Eq. (2) from Ref. [5],

$$\tan \beta_B = \cos \lambda \tan \phi \quad (2)$$

Figure 6 shows the variation of the inlet blade angle with different combinations of cone angle and camber angle. For a radial turbine, in which the cone angle is restricted to 90 deg, the blade angle is zero regardless of the camber angle. By introducing a cone angle, positive blade angle can be achieved at the inlet, which is beneficial in terms of the turbine velocity ratio and loading. The velocity ratio and loading of a turbine are given in Eqs. (3) and (4), respectively,

$$\frac{U}{C_{is}} = \frac{1}{\sqrt{2}} \sqrt{1 - \left(\frac{\tan \beta_2}{\tan \alpha_2} \right)} \quad (3)$$

Contributed by the Turbomachinery Division of ASME for publication in the JOURNAL OF TURBOMACHINERY. Manuscript received March 28, 2006; final manuscript received July 17, 2007; published online June 27, 2008. Review conducted by Aspi Wadia.

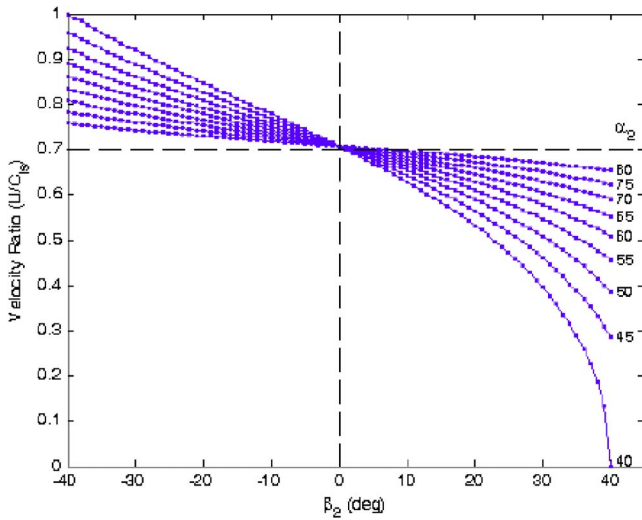


Fig. 1 Velocity ratio variation with blade inlet relative (β) and absolute (α) angles

$$\psi = 1 / \left[1 - \left(\frac{\tan \beta_2}{\tan \alpha_2} \right) \right] \quad (4)$$

Assuming zero incidence, the inlet relative flow angle equals the inlet blade angle; the effects of inlet blade angles on the velocity

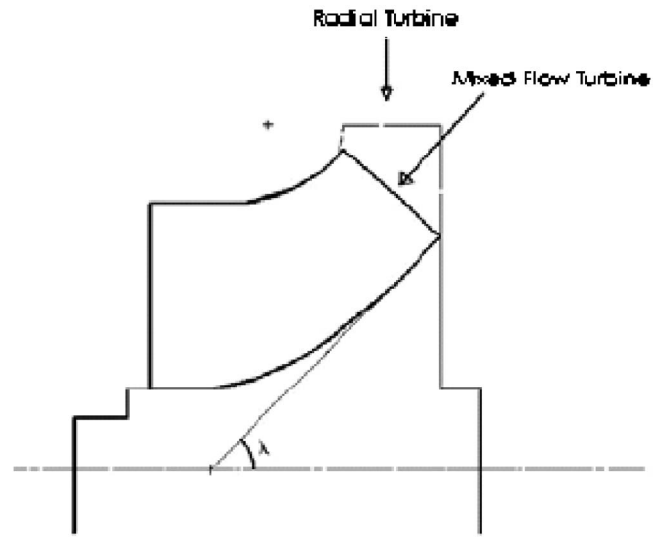
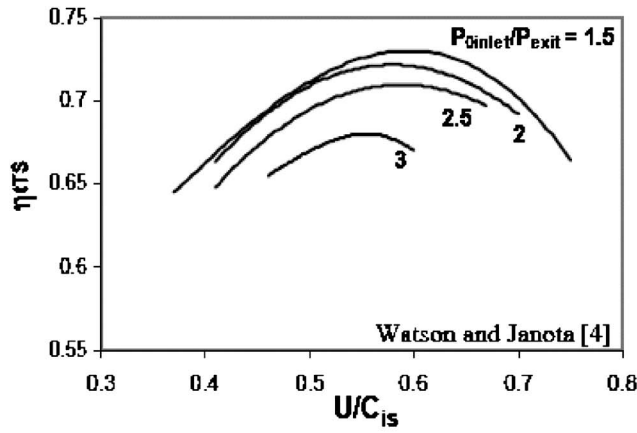
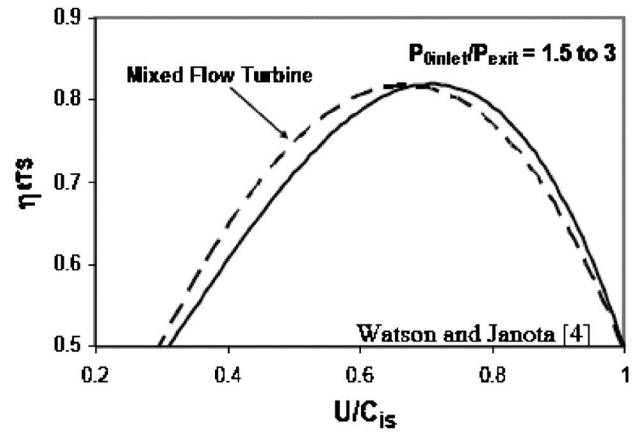


Fig. 3 Schematic description of radial and mixed flow turbines

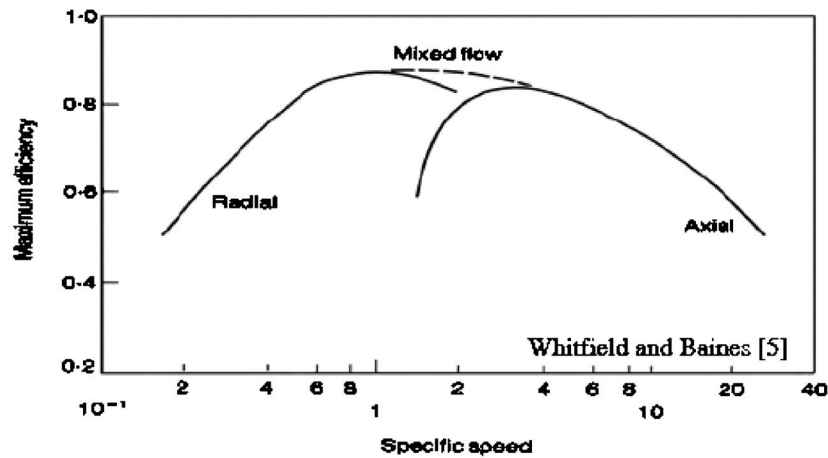
ratio and turbine loading are shown in Figs. 1 and 7 calculated based on Eqs. (3) and (4). A positive blade angle reduces the velocity ratio and increases the turbine loading capacity, thus allowing a turbine to operate at its optimum, consequently extract-



(a) Axial Flow



(b) Radial Flow



(c) Axial, Radial and Mixed Flow

Fig. 2 Efficiency of axial, radial, and mixed flow turbines against [(a) and (b)] velocity ratio and (c) specific speed adapted from Refs. [4,5], respectively

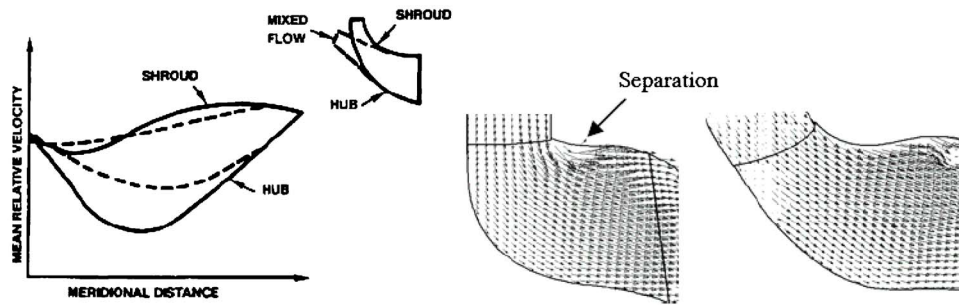


Fig. 4 Radial and mixed flow turbine passage velocities [7] and meridional flow separation [8]

ing more work at higher pressure instances in an exhaust pulse. Figure 8, which is a mirror of Fig. 2(b) with the turbine loading coefficient as a parameter, shows the higher loading characteristics of a mixed flow turbine compared to its radial counterpart.

3 Design of a Mixed Flow Turbine

The design method of a mixed flow turbine was first studied parametrically by Wallace and Pasha [9]. They aimed to increase the swallowing capacity and achieved a modified radial turbine with swept leading edge and a mean cone angle of 45 deg. They showed analytically and experimentally the higher swallowing capacity of the mixed flow turbine at various pressure ratios, as shown in Fig. 9. The improvement was more significant in the higher speed and pressure ratio region, where the radial turbine shows a drastic drop in the swallowing capacity. Baines et al. [10] adopted a method similar to Wallace and Pasha [9] but with a loss factor included to design and test two mixed flow turbines. Baines et al. [10] documented similar performance results to these of Wallace and Pasha [9]. Abidat et al. [13] extended the mixed flow turbine design approach of Baines et al. [10] by including the blade incidence effect. Furthermore, Abidat et al. [13] used the Bezier polynomial for the blade geometry profile design rather than the Lamé oval technique used by Baines et al. [10]. Nevertheless, the results agreed well with the previous work [9,10], achieving an improved understanding of the inlet incidence effects.

Following the initial development of the mixed flow turbine [9,10], there was a need to direct the research emphasis toward an engine application. The design effort for the practical application of a mixed flow turbine in an internal combustion engine was brought to light through research by Yamaguchi et al. [11], Chou and Gibbs [12], Naguib [14], and Minegashi et al. [15]. The major motivation for these efforts was to utilize the higher swallowing

capacity of the mixed flow turbine, thus resulting in a smaller turbine for a given performance target. This consequently reduces the inertia of the turbine rotor and yields a better turbocharger response. Nonetheless, the design method used was similar to the previous work [9,10], which is the modification from a well established radial turbine design.

By the 1990s, years of research and development have resulted in a comprehensive design methodology for mixed flow turbines. Chen and Baines [16] have documented an optimization method in the design of a mixed flow turbine, which concentrated on the turbine loading factor and the exit loss. The basis of the optimization is to reduce loss by reducing the velocity components at the inlet and the exit of the rotor [16,17]. In the design of a mixed flow turbine, it is conventional to assume zero exit swirl angle (as in the radial turbine design) but Chen and Baines [16] found that a positive exit swirl angle will reduce overall turbine losses but at the expense of a reduced specific power.

4 Experimental Works on Mixed Flow Turbines

Although the idea of a mixed flow turbine arose in the 1950s, the actual experimental work was not available until the 1970s. Wallace and Pasha [9] documented one of the earliest experimental research with a mixed flow turbine. Most of the experimental work on a mixed flow turbine was carried out through a stand-alone cold flow test. Nevertheless, there are few documented works that include an engine-coupled testing where a mixed flow turbine was used as part of the turbocharger. In general, the experimental work on mixed flow turbines can be grouped as steady- and unsteady-state testings.

4.1 Steady-State Experiments. Most of the early experimental works on mixed flow turbines were confined to steady state as the focus was to explore the benefits of a mixed flow design

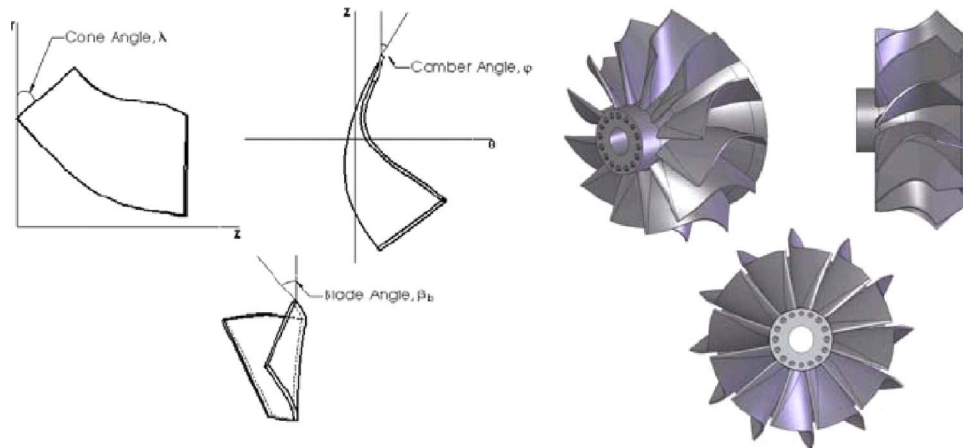


Fig. 5 Mixed flow blade configurations and the rotor's 3D view

Table 1 Cone angle values used by past researchers

| Authors | Cone angle (deg) |
|-----------------------|------------------|
| Wallace and Pasha [9] | 45 |
| Baines et al. [10] | 50 |
| Yamaguchi et al. [11] | 60 |
| Chou and Gibbs [12] | 55 |
| Abidat et al. [13] | 50 |

against the radial design. Numerous research groups in the last three decades have conducted steady-state experiments on mixed flow turbines and agreed on two facts: a mixed flow turbine has higher swallowing capacity and the peak efficiency is at a lower velocity ratio compared to a radial turbine. Results from two such researches, by Baines et al. [10] and Abidat et al. [13], are shown in Fig. 10. With the mixed flow turbine's benefits established from the past researches, Abidat et al. [13] and Chen et al. [18,19] took a step further to optimize the mixed flow design itself. A series of rotors was designed and tested to deduce and compare their performances. Apart from the performance, Abidat et al. [13] and Chen et al. [18,19] also carried out comprehensive measurements

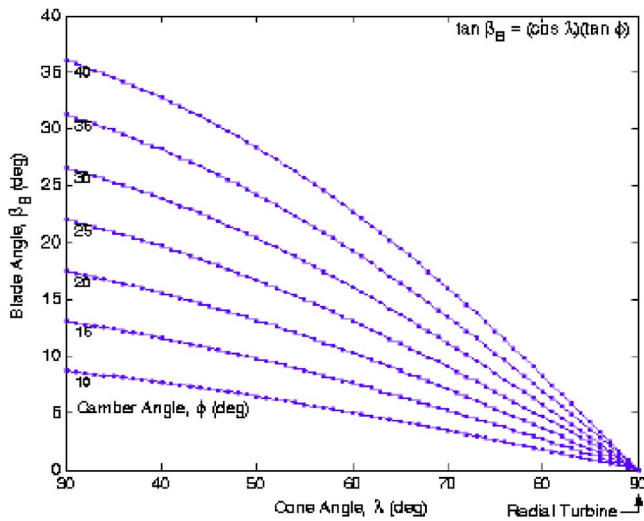


Fig. 6 Inter-relations of mixed flow turbine leading edge defining angles

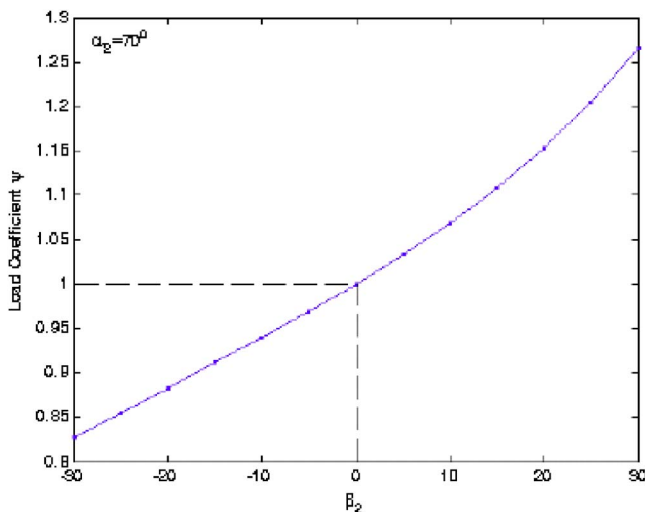


Fig. 7 Effect of inlet relative flow angle on turbine loading

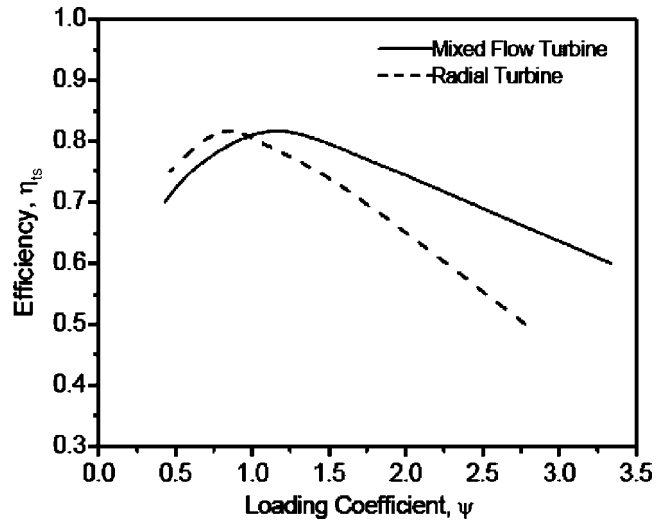


Fig. 8 Efficiency versus loading coefficient of a mixed flow and a radial turbine

to study the characteristics of the inlet incidence and the exit flow in a mixed flow turbine rotor. The optimization process resulted in the improvement of the turbine efficiency (see Fig. 10).

Following the successful stand-alone testing, mixed flow turbines were put into engine testing. In agreement with the stand-alone testing, a mixed flow turbine produced very promising results in improving the engine power and, importantly, the specific fuel consumption, as shown in Fig. 11. The advantage of a mixed flow turbine is noticeable especially in the lower speed region, which is one of the critical improvement factors sought by engine and turbocharger manufacturers. This is due to the improvement of the pressure ratio and swallowing capacity with a mixed flow turbine, which leads to a better turbocharger boost as shown in Fig. 12. Furthermore, the lower inertia of a mixed flow rotor enables better turbocharger response [15] and the desired performance was achieved at lower specific speed [14].

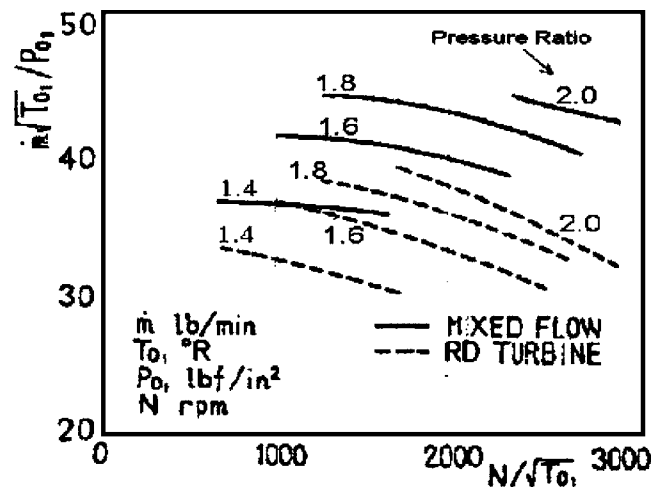


Fig. 9 Mass flow improvement of mixed flow turbine at various pressure ratios [9]

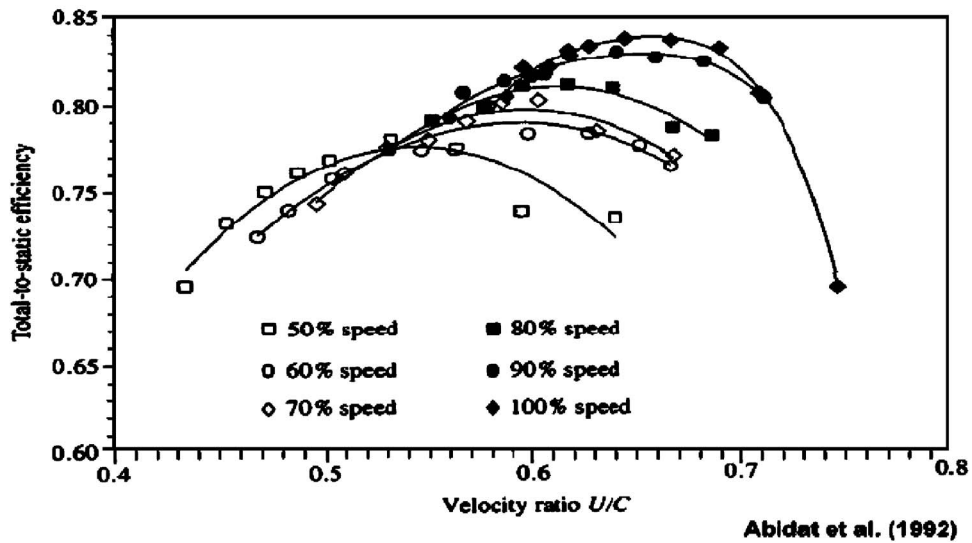
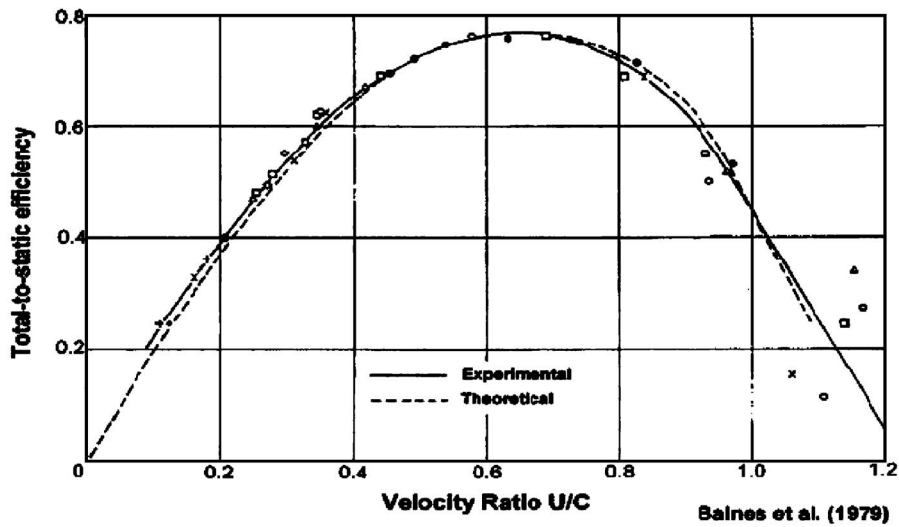


Fig. 10 Mixed flow turbine efficiency [10,13]

With the increase use of computational analysis in the mixed flow turbine design process, reliable experimental data were needed for validation. Baines et al. [10] and Kim and Civinskas [20] documented experimental work for the purpose of validating their own computational analysis. Both the works of Baines et al.

[10] and Kim and Civinskas [20] were limited to steady state as it was adequate to address the turbine design effort, which is mainly based on a steady-state assumption.

Nevertheless, the advancement of the computational capacity soon enabled the prediction of the unsteady effects in a turbine

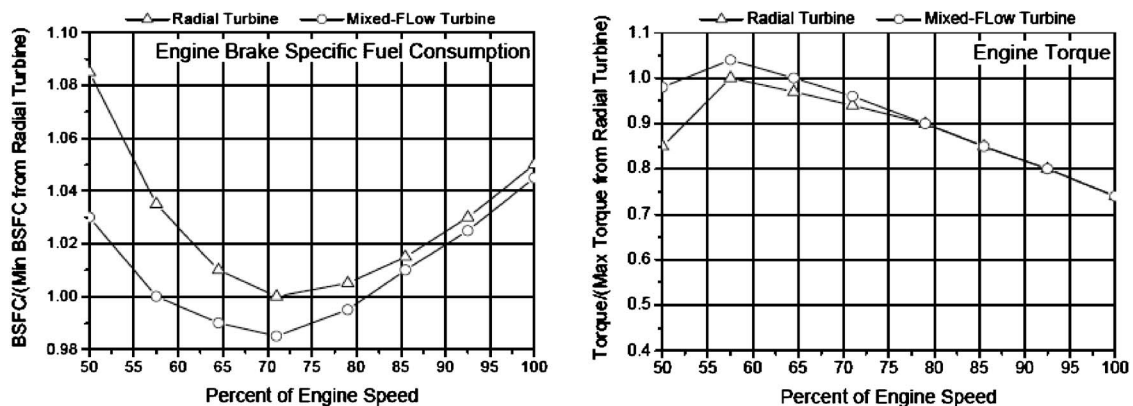


Fig. 11 Diesel engine performance with turbocharger on a radial and a mixed flow turbine [12]

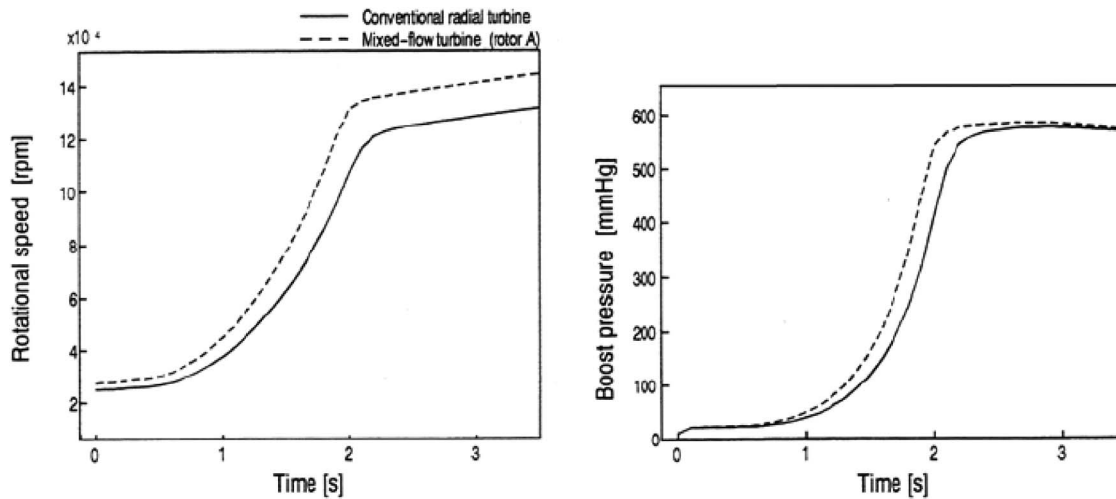


Fig. 12 Turbocharger speed and boost with radial and mixed flow turbines [15]

flow, thus requiring more challenging experimental results. The upcoming sections will elaborate the work on the turbine unsteady flow from the experimental and computational points of view.

4.2 Unsteady-State Experiments. A turbocharger turbine in an engine constantly operates under unsteady condition due to the pulsating exhaust flow. Thus, there is a need for experimental work to understand the turbine unsteady-state performance. In comparison to the steady-state experiments, the unsteady flow measurements require extra complexity with a higher response rate. Three decades ago, this might have been a difficult task in order to achieve reliable results, but with the advances in measuring techniques, unsteady work has been reported with full unsteady characterization in the past 15 years. Turbine unsteady experiments are generally carried out using cold flow tests at equivalent nondimensional engine conditions. A pulse generator is usually used to create the flow unsteadiness similar to an engine exhaust gas pulse. Even though the unsteady flow experiments in a radial turbine were documented a while ago, similar work on a mixed flow turbine has only been reported since the 1990s, Arcoumanis et al. [21] and Szymko et al. [22].

One difficulty in most of the turbine unsteady flow experiments is the time difference between the instantaneously measured isentropic conditions and the actual turbine conditions. This is due to the difference in the location of the measurements; the isentropic conditions were measured before the volute entry, while the actual conditions were measured at the turbine rotor. To resolve the time difference, it is important to phase shift the measurements in order to accurately relate the turbine's isentropic and actual parameters.

Dale and Watson [23] and Arcoumanis et al. [21] used the sonic velocity for phase shifting, while Winterbone et al. [24] and Baines et al. [25] used the bulk flow velocity. However, in a very recent study, Szymko et al. [22] showed that good agreement can be achieved by assuming the pulse traveling at a speed equal to the sum of sonic and bulk flow velocities.

In a radial turbine performance testing, the unsteady swallowing capacity and efficiency of the turbine were observed to produce a hysteresis loop around the steady-state profile [24,26]. Similar observation was also seen in the mixed flow turbine unsteady testing by Arcoumanis et al. [21], Karamanis and Martinez-Botas [27], and Szymko et al. [22]. The observed looping behavior is attributed to the emptying and filling of the turbine volute due to the pulsation and finite volume of the turbine stage, producing lower and higher capacity, respectively, than the steady-state condition. A mixed flow turbine's instantaneous efficiency for a complete pulse cycle is shown in Fig. 13, as reported by Szymko et al. [22]. It can be observed that in some instances, the efficiency is higher than unity, attributed to the inertial effect of the turbine rotor, which causes its rotation to continue even when the mass flow rate is low. It is important to note that the unsteady efficiency's value is also dependent on the phase shifting methodology and might lead to the unrealistic efficiency values. Arcoumanis et al. [21] and Karamanis and Martinez-Botas [27] employed sonic velocity phase shift and recorded higher than unity efficiencies in all pulsating frequencies. However Szymko et al. [22], who employed the sum of sonic and bulk flow velocity phase shift, recorded higher than unity efficiencies only at the higher

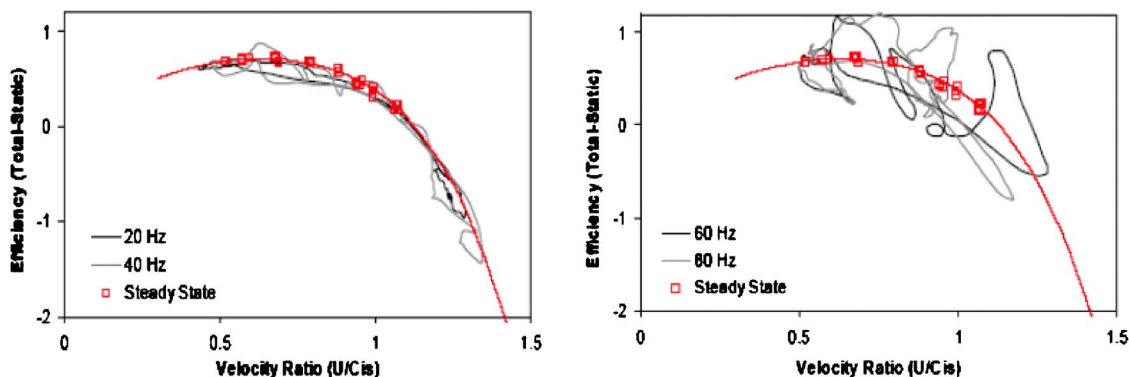


Fig. 13 Mixed flow turbine instantaneous efficiency for a complete pulse cycle during unsteady flow [22]

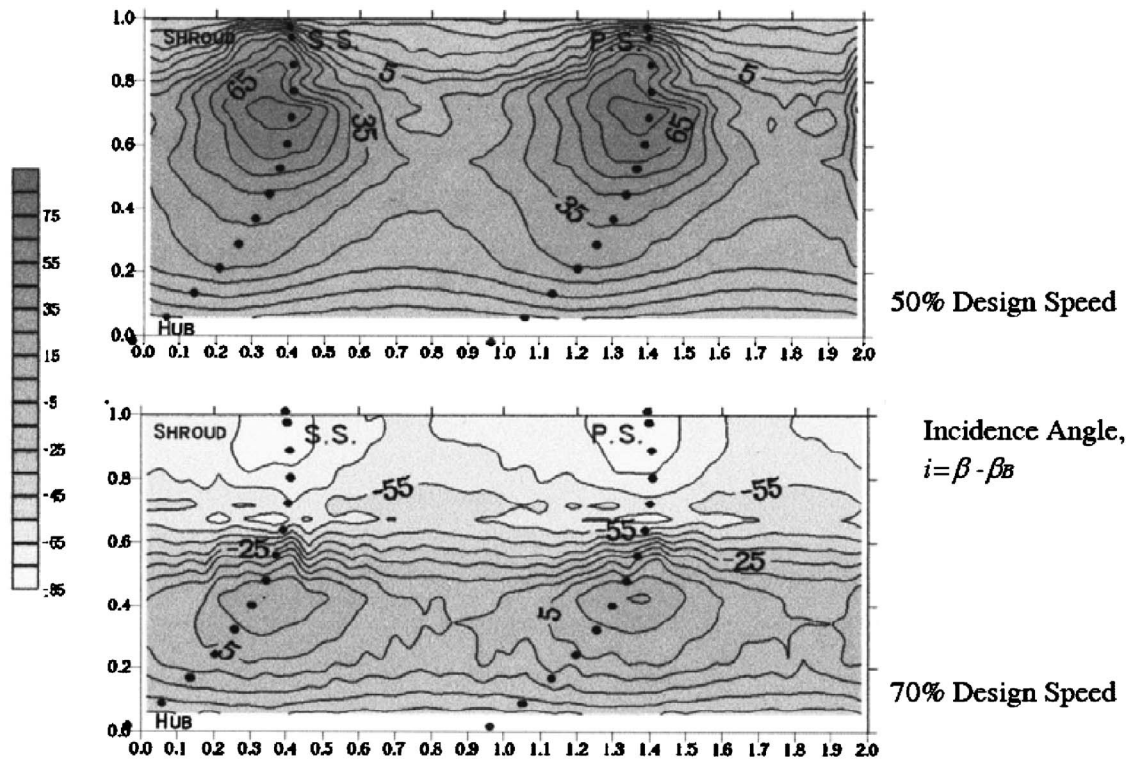


Fig. 14 Incidence angle contour at the mixed flow rotor leading edge measured with laser doppler velocimetry [29]

frequency cases (60 Hz and 80 Hz). This indicates a better choice of phase shifting method by Szymko et al. [22]. The technique used to measure the turbine actual power also affects the efficiency calculation during an unsteady cycle. Arcoumanis et al. [21] and Karamanis and Martinez-Botas [27] used a thermodynamic relation in a compressor coupled test to deduce the turbine power, while Szymko et al. [22] used a direct torque measurement with a high speed eddy-current dynamometer. The indirect thermodynamic deduction might be another factor contributing to the higher uncertainty in the work of Arcoumanis et al. [21] and Karamanis and Martinez-Botas [27].

It is a common practice to compare the unsteady performance to a quasisteady rotor analysis that assumes no dynamics in the system. In a quasisteady method, the turbine performance at an instance in an unsteady cycle is assumed to be similar to the equivalent pressure ratio/velocity ratio condition in its steady-state performance curve. Arcoumanis et al. [21] have shown comparisons between the unsteady and the quasisteady method. The unsteady results departed significantly from the quasisteady condition, hence questioning the credibility of using a quasisteady method in the design of a turbine. Szymko et al. [22] took this further by proposing an improved method of relating the turbine unsteady and quasisteady performances by means of an isentropic power averaging technique. They introduced the isentropic power as a weighting factor in the turbine efficiency and velocity ratio evaluation in an unsteady cycle; a better correlation was achieved with the quasisteady performance.

As a means to validate numerical methods and understand detailed flows, laser techniques have been used widely in radial turbines [28]. Similarly, Karamanis et al. [29] documented an extensive flow study in a mixed flow turbine using laser Doppler velocimetry (LDV) technique. They measured the blade inlet incidence angle (Fig. 14), which shows highly positive value at lower turbine speed, resulting in lower performance. The incidence angle eventually becomes negative as the turbine speed goes higher, showing performance improvement of the turbine.

Nevertheless, it was shown that the flow direction into the rotor is not optimized in most of the conditions, which indicates the need for a specially designed volute and nozzle ring for mixed flow turbines. Exploring both the performance and flow behavior in steady and unsteady conditions, Karamanis et al. [29] have shown good representation of a mixed flow turbine characteristic that is useful for the computer simulation validation. It will be shown in the coming section how these results were used to validate a complex unsteady simulation of a mixed flow turbine.

5 Computational Works on Mixed Flow Turbines

One of the earliest numerical work involving mixed flow turbines was documented by Steward [2], in which he analyzed the flow through a predesigned turbine. The initial method was actually presented by Hamerick et al. [1], who outlined the analysis for a mixed flow compressor. Steward [2] expanded the method to analyze the rotor's exit flow as well. A basic three-dimensional flow analysis showed the inefficiency of the turbine design process at that time, which used two-dimensional inlet and exit conditions. This is one of the earliest works on a three-dimensional flow analysis for turbine design that is widely used today. Steward [2] also outlined the extent of secondary flows in the mixed flow rotor, which was studied extensively by many researchers in the years later.

After Wallace [3] introduced the possibility of using a mixed flow turbine in automotive turbochargers, Baines et al. [10] documented a complete work on a mixed flow turbine from design to experimental evaluation. Computational method was adapted in the design process to predict flow characteristics and performance. Baines et al. [10] carried out a three-dimensional quasisteady flow analysis, where the unsteady conditions were treated as a summation of steady points, leading to a substantial decrease in the need of computational resources. They solved the flow equations in two two-dimensional surfaces, the meridional surface and the perpendicular blade-blade surface, to calculate the three-dimensional

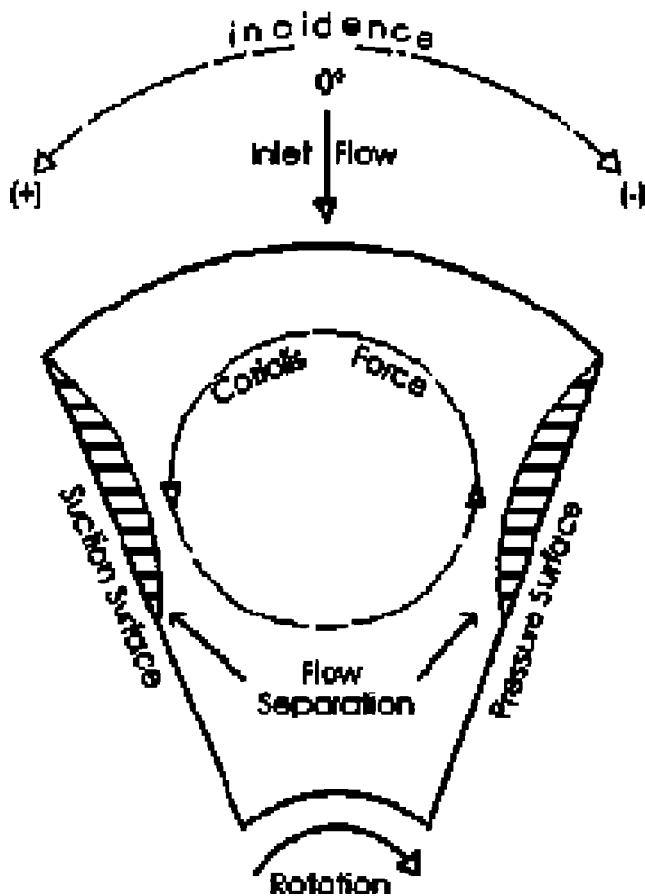


Fig. 15 Flow separation due to inlet flow condition and Coriolis force

flow components in a mixed flow rotor passage. The mixed flow rotor designed through this 3D flow analysis method yielded good correlation between the theoretical prediction and the experimental results (Fig. 10).

The last two decades have seen an increase of computational flow studies in mixed flow turbines. The computational effort progressed from a basic two- or three-dimensional analysis using the Euler code [12,30] to complex Navier–Stokes methods [20,31,32]. It had therefore been possible to predict flow features where it was rather difficult for experimental measurement. One such important feature is the occurrence of flow separation in the suction surface of the turbine rotor predicted by Okapuu [30], Abidat et al. [13], Kirtley et al. [31], and Kim and Civinskas [20]. The computational flow analysis has also predicted another important feature of a mixed flow turbine; the loading at the blade inlet has been found to be higher than the radial turbine [31], which correlates well with the experimental findings.

The pressure difference between the rotor surfaces and coupled with the reducing radius creates the Coriolis force in the rotor flow channel. As shown in Fig. 15, the Coriolis force induces flow rotation in the opposite direction to the rotor. Thus, high negative incidence creates a separation at the pressure surface, while zero or positive incidence moves the separation to the suction surface. Through computational prediction, the optimum inlet condition was found to be at lower negative region [30,12,20] with values between -20 deg and -40 deg. Similar values were also deduced through experiments by Kim and Civinskas [20] and, additionally, the incidence values were also found to vary with the turbine speed.

In most of the early computational flow analysis, a mixed flow rotor was considered to be stationary due to the complexity of

Blade Passage - 20% Chord

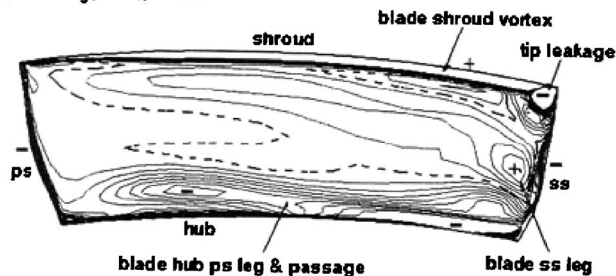


Fig. 16 Relative helicity in the mixed flow rotor blade passage at 20% chord [31]

generating and computing a moving mesh, which is also the case for radial rotor analysis. Even though it does not replicate the real condition, the results are considered accurate enough for an initial flow understanding. Kirtley et al. [31] documented an extensive numerical study in which an averaged passage Navier–Stokes method was used to analyze the transonic flow in a mixed flow rotor preceded by nozzle vanes. Kirtley et al. [31] took into consideration the blade row interaction in the analysis. The analysis was initiated from one blade row and the results were used to calculate the flow conditions in the next blade row. This was continued until the axisymmetric averages of each blade row flow were identical. Even though the analyses were not exactly modeling the rotor as rotating, the fact of calculating blade row effects from one to another was indeed a major improvement to the accuracy of the prediction. A mixed flow turbine was found to produce larger Coriolis force than an axial turbine due to its larger radial velocities.

Figure 16 shows the relative helicity plot in a mixed flow rotor blade passage as predicted by Kirtley et al. [31]. Based on the figure, the flow pattern of a mixed flow turbine was predicted to be closer to a radial than an axial turbine, mainly due to the accumulation of high loss flow in the shroud-suction side. Nevertheless, there is similarity with an axial turbine such as the formation of horseshoe-type vortex; the only drawback was the lack of validation against experimental data. Similar work has been reported by Kim and Civinskas [20] with experimental validation that showed some significant differences between a mixed flow and a radial turbine. The exit pressure and the flow angle measured in a mixed flow turbine agreed better with the prediction and showed discrepancies with the design intended which was based on a radial turbine. Thus, the flow predictions by Kim and Civinskas [20] and Kirtley et al. [31] are valuable for engineers and researchers working on improving the design of a mixed flow rotor.

Palfreyman and Martinez-Botas [8] simulated the internal flow field of a mixed flow turbine using a commercial CFD (computational fluid dynamics) code. The work was similar to that of Kirtley et al. [31] and Kim and Civinskas [20], but a more refined meshing of 393,872 cells was used and concentrated on a mixed flow turbine meant for automotive turbocharger application rather than a gas turbine. Figure 17 shows the streamwise vorticity comparison between a mixed flow and a radial turbine at 20% chord, as predicted by Palfreyman and Martinez-Botas [8]. They found that significant secondary flow is associated with the tip clearance. More detailed flow pattern shows that the interaction between the swept flow from the relative motion of the shroud wall and the tip clearance flow produces a highly disturbed flow field. This is in agreement with Kirtley et al. [31] and Kim and Civinskas [20] but with more detailed visualization. Furthermore, a significant difference between a mixed flow and a radial turbine was found to be the large vortex generated near the shroud in a radial turbine. This is due to the combined sharp turning of the streamline in the meridional direction and the motion of the shroud wall. Palfrey-

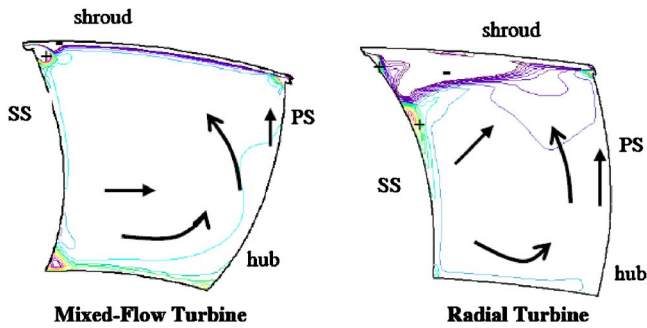


Fig. 17 Streamwise vorticity comparison between mixed flow and radial turbines at 20% chord [8]

man and Martinez-Botas [8] also found that a mixed flow rotor produces higher swirl component at the exit compared to a radial rotor, in agreement with the experimental observation by Chen et al. [19].

5.1 Unsteady-State Flow Computation. Most of the early computational studies on mixed flow turbines were based on steady flow; nevertheless, most researchers acknowledge the importance of understanding the unsteady flow when dealing with an automotive turbocharger application. From the 1990s and onward, some detailed investigations have been documented on the unsteady flow in a turbine. Chen et al. [33] modeled the flow in a volute and a mixed flow rotor using a modified one-dimensional unsteady code originally developed for a radial turbine by Chen and Winterbone [34]. The rotor was assumed to behave in a quasi-steady manner, which was adequate when considering the computational limitations at that time. Even though the prediction by Chen et al. [33] agrees well with the experiments, Abidat et al. [35] showed that better agreement can be achieved by using an analysis model with a four step Runge–Kutta scheme. Abidat et al. [35] suggested that the second order accuracy in time of the four step Runge–Kutta scheme improves the predictions compared to the method of characteristics used by Chen et al. [33], which is only of first order accurate. With the one-dimensional code and taking into consideration phase difference between the mass flow and the pressure, Abidat et al. [35] managed to numerically reproduce a hysteresis loop in the turbine performance as observed experimentally.

The turbine design procedure for an automotive turbocharger is still primarily confined to the steady-state consideration due to the huge computational and design time resources needed for a full unsteady analysis. Palfreyman and Martinez-Botas [32] docu-

mented a true three-dimensional full unsteady flow analysis in a mixed flow turbine, conducted with four mesh densities; 50,000, 200,000, 850,000, and 1,750,000 cells. The simulation code was validated against the experimental results with good agreement, as shown in Fig. 18. The simulation was carried out with a rotating rotor, thus capturing the true unsteady interaction between the stator exit and the rotor inlet. Palfreyman and Martinez-Botas [32] modeled a nozzleless volute, which is identical to the volute used in the experimental work. The pressure distribution in the volute has been captured with very good agreement to the experimental results.

Palfreyman and Martinez-Botas [32] found the predicted torque to be higher than the experimental value and claimed that the experimentally measured torque used for comparison is “damped” due to the inertia of the rotating assembly. Additionally, the blade torque and loading were found to fluctuate in accordance with the pulse frequency. This indicates the true effect of the pulsating flow on a turbine operation and the necessity to understand it thoroughly. The flow was observed to be poorly guided at the rotor inlet during high pressure ratio conditions, which agrees with the LDV measurement made by Karamanis et al. [29]. This shows that the nozzleless volute used in the analysis is not adequate in directing the flow into the mixed flow rotor, thus needing nozzle vanes. Overall, the work by Palfreyman and Martinez-Botas [32] has shown that a pulsating simulation is possible, providing the availability of computational and time resources.

6 Future of the Mixed Flow Turbine Research

Research into the use of a mixed flow turbine in automotive turbochargers started in the 1970s. Even though the benefits of a mixed flow turbine have been proven experimentally and computationally, it is still not widely used in engine turbochargers. This prompts for a study to identify the factors that hinder the industrial development of mixed flow turbines. Okapuu [30] addressed this issue in the gas turbine industry and justified the problem due to the high cost of developing a reliable rotor and the lack of funding from the gas turbine industry itself. Unlike gas turbines, a turbocharger is a subcomponent of an engine. Thus, it is a major concern of turbocharger and engine manufacturers to keep the cost as low as possible. Due to its matured technology, the cost of manufacturing a radial turbine is relatively cheap, thus, any attempt to replace it will involve cost that manufacturers will tend to avoid. Even though the cost for a new product development is inevitable, the overall cost of the turbocharger can be kept as close as the current condition with improved performance using a mixed flow turbine. This is because the design of a mixed flow

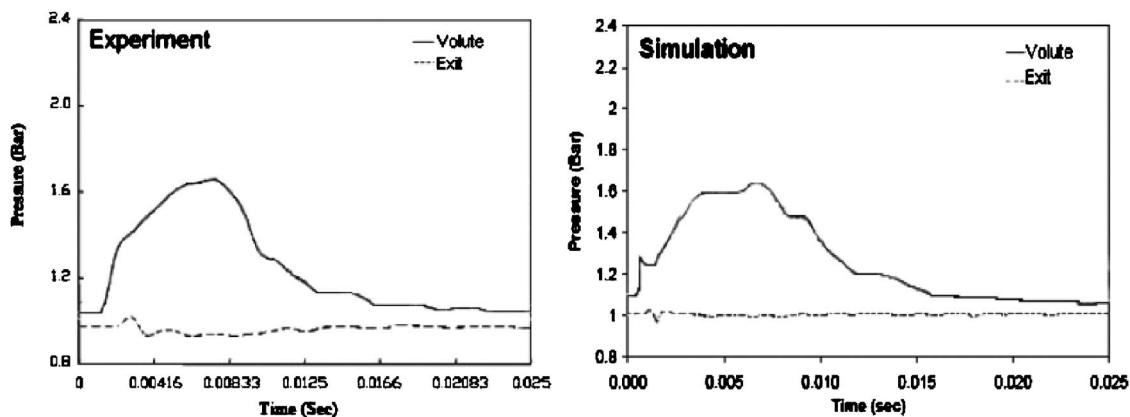


Fig. 18 Validation agreement between predicted and experimental unsteady pressure profiles in the volute [32]

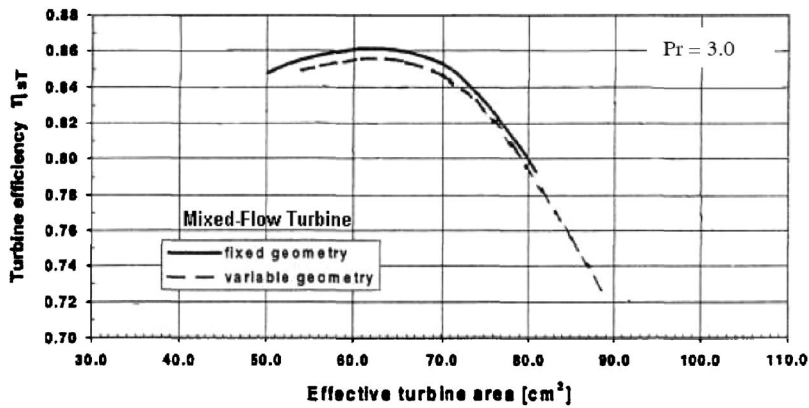


Fig. 19 Mixed flow turbine efficiency with fixed and variable geometry operations [36]

rotor closely resembles its radial counterpart and the manufacturing techniques involved in producing it will be almost similar or at least highly adaptable.

The last few decades have seen a dramatic advancement in the turbomachinery field due to the continuous research to push the technological boundary. Many new technologies have been introduced to improve the turbine performance, and eventually became standard features. One such technology is the variable geometry turbocharging (VGT), which was initially introduced in the early 1960s. The concept of VGT is based on the control of the turbine inlet area to regulate a turbocharger's boost. Two widely used methods of controlling the turbine inlet area are the pivoting nozzle vanes or the sliding wall. VGT has gone through many phases of development over the years with its performance and reliability improving gradually. Today, VGT has become a standard component in diesel engines used for heavy duty trucks, ships, off-road vehicles, and power generators. Since the inception of the idea, VGT has been based on radial turbines and it remains the case today. Considering the benefits of a mixed flow turbine, as discussed earlier, it would be profitable to use a mixed flow turbine in a VGT. One such rare research work was documented by Baets et al. [36], where VGT based on a mixed flow turbine was developed as part of a series of commercial turbochargers. Baets et al. [36] used a set of pivoting nozzle vanes as the variable part of the stator to control the turbine inlet area. The nozzle vanes used by Baets et al. [36] are of straight design, similar to those used in a radial turbine but the nozzle ring was arranged in a unique way to reduce the clearance leakage.

Figure 19 shows the efficiency curve obtained by Baets et al. [36] for a mixed flow turbine with fixed-geometry and variable geometry (VG) configurations. The efficiency in VG configuration is a little lower due to the sealing losses and the nozzle ring geometry losses. Nevertheless, in the VG configuration, Baets et al. [36] have demonstrated improvement in a diesel engine's part-load fuel consumption and exhaust smoke. With the increasing environmental concern, emission control of an engine is one of the key performance parameters especially for passenger cars and commercial vehicles. Thus, more research needs to be carried out to study the use of mixed flow turbines in VGTs in order to enhance its capability to assist emission control methods such as exhaust gas recirculation (EGR). Baets et al. [36] also showed good load response in a generator and gas engine regulation with the mixed flow turbine based VGT. Unfortunately, Baets et al. [36] did not present any comparison against a radial turbine VGT nor have they stressed the benefits of a mixed flow turbine, in particular. Thus, a definitive conclusion could not be made in terms of the practical benefit of a mixed flow turbine against a radial turbine in VG operation.

In a pivoting vane VGT system, the design of the nozzle vanes

is crucial for a good performance. Wallace and Pasha [9] indicated that the performance of a mixed flow turbine can be improved with an "ideal" nozzle vane ring, designed based on the nonradial inlet of a mixed flow rotor. Thus, straight nozzle vanes, which can be used satisfactorily in a radial turbine (Fig. 20(a)), are not optimal for a mixed flow turbine (Fig. 20(b)). The use of straight vanes in a mixed flow turbine will create an uneven interspace between the vane trailing edge and the rotor leading edge, which eventually will induce nonuniformity in the spanwise flow.

Nonuniform spanwise flow and its effects on a mixed flow turbine performance is an interesting phenomenon to investigate. Nevertheless, any possible improvement might result in a further complication in the process of the nozzle vane design, as spanwise shape of the nozzle vanes has to be designed specifically for a mixed flow rotor. Ideally, the best possible options of nozzle vane are shown in Fig. 21. Both the designs create an even matching with the leading edge of a mixed flow rotor, enabling better flow direction along the span of the rotor. In a fixed nozzle vane configuration, the design in Fig. 21(a) might be a better option as preferred by Kirtley et al. [31]. In a VG configuration, it is extremely difficult to build a reliable nozzle ring on an inclined surface for either pivoting or sliding operation; hence, the design in Fig. 21(b) is more practical. Even though the depiction in Fig. 21 is a common way of representing nozzle vanes, it does not portray a complete picture of a mixed flow turbine. The reason is that based on Fig. 6 and Eq. (2), by introducing a cone angle and maintaining the radial fiber, the leading edge of a mixed flow rotor is actually swept positively, hence the nonzero blade angle, which can be seen in Fig. 5. Thus, the design of the nozzle vane for a mixed flow turbine should take into consideration the three-

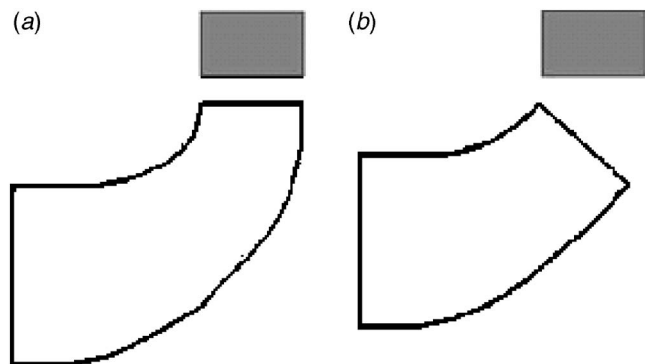


Fig. 20 Straight nozzle vane applied to (a) radial turbine and (b) mixed flow turbine

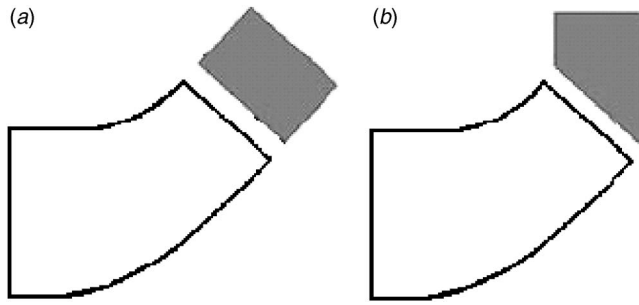


Fig. 21 Possible options of nozzle vane for mixed flow turbine: (a) vane with inclined hub/shroud surface and (b) vane with flat hub/shroud surface

dimensional variation at the leading edge. The benefits of a mixed flow turbine in VGT can be better realized with an optimal nozzle vane design. Such effort is undertaken in the authors' institution and the initial results are documented by Rajoo and Martinez-Botas [37].

The optimal turbine inlet geometry in commercial VGTs is precalibrated to follow a function based on the engine speed and load. The engine management system uses the function to regulate the turbine inlet area during its operation. Thus, at fixed engine speed and load, the turbine inlet geometry is fixed. However, the turbine is fed with an unsteady exhaust flow and the inlet condition changes continuously even at fixed engine speed and load. Because the turbine inlet geometry in a VGT is fixed over an exhaust pulse cycle, energy can only be effectively extracted in part of the cycle mainly at high pressure instances. Thus, there is still room for improvement in the operation of a VGT in order to cope better with the incoming exhaust flow. A new method of advance VGT operation called active control turbocharging (ACT) has been introduced [38]. The core of its operation is similar to a VGT but it enables the control of the turbine inlet geometry throughout the exhaust pulse.

The turbine inlet area is regulated to adapt to the incoming exhaust pressure pulses throughout the operation of the engine; the inlet area is increased gradually as the pressure of the exhaust pulse increases and vice-versa. Thus, optimal turbine geometry can be achieved at any position in the pulse, leading to a better energy extraction especially at the lower pressure instances in an exhaust pulse. Figure 22 shows the preliminary numerical analysis

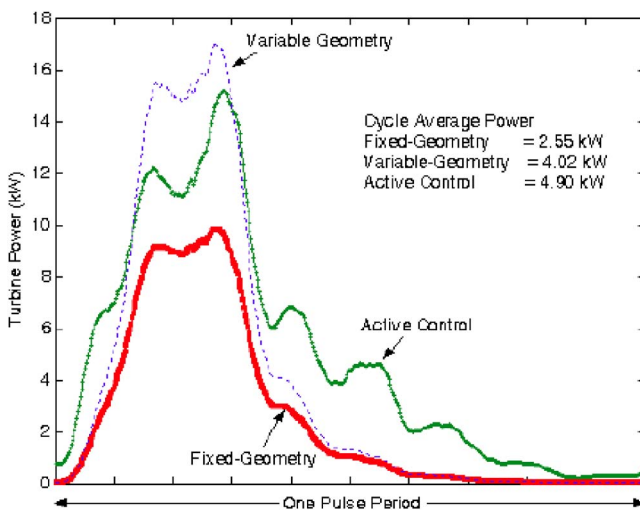


Fig. 22 Numerical calculation of turbine power over one pulse period with different operations

of the turbine power over one pulse cycle with a fixed geometry (nozzleless volute), a VG, and an active control operation. It can be noticed that the cycle averaged power during the active control operation is almost 22% more than the VG operation under ideal condition, even though the peak power reduced slightly. The authors believe that with an optimized control strategy, part of this benefit can be realized, which is currently investigated with a mixed flow turbine. The first phase of the investigation was documented by Pesiridis and Martinez-Botas [39,40].

Operating the turbine geometry to follow the exhaust pulse will require a mechanism capable of frequencies in the range of 20–100 Hz. This has been achieved satisfactorily for an experimental testing as reported by Pesiridis and Martinez-Botas [39,40], even though further improvement is needed. Nevertheless, a similar mechanism is not practical in an engine especially for road vehicles due to space constraint under the hood. Currently, the objective of this research is focused on the demonstration of the concept and its potential benefits. The next stage of the development will be the investigation of a reliable mechanism for the active operation of the turbine. ACT has the potential to improve the unsteady performance of a turbocharger in an internal combustion engine as it allows energy extraction in a wider range of the exhaust pulse. With its higher loading capacity, a mixed flow turbine will be an added advantage to the ACT operation.

7 Conclusions

This paper discussed the historical development of mixed flow turbines based on literature. A comprehensive compilation is presented as regards the research work involving mixed flow turbines for the past 50 years, with discussions categorized into three broad parts: experimental work, computational work, and future research directions.

The mixed flow concept was initially studied as an alternative to the axial design for gas turbines but later adapted to automotive turbocharger applications. The attractive benefits of a mixed flow turbine and its similarity to a radial design made it more suitable for turbocharger application, where the demand for better engine performance is ever increasing. Overall, a mixed flow turbine can be regarded as an intermediate design where it possesses the benefits of both the radial and an axial rotor. Some prominent experimental research is discussed in the paper where mixed flow turbines exhibit higher loading and swallowing capacity compared to its radial counterpart. Furthermore, an engine tested with a mixed flow turbine based turbocharger produced lower specific fuel consumption and higher response rate, mainly due to its lower inertia. Computational analysis is also discussed, where the flow pattern in a mixed flow rotor is shown to be more like a radial design but with higher exit swirl and lower separation in the rotor passage. Nevertheless, the formation of horseshoe-type vortex in a mixed flow rotor shows its similarity to an axial design as well.

The nonradial inlet of a mixed flow turbine creates a three-dimensional spanwise variation at its leading edge. This creates a nonuniform interspace match in the event of a mixed flow rotor coupled to a radial based nozzleed stator. Furthermore, experimental and computational evaluations have shown that the flow into a mixed flow rotor is not adequately guided in cases where the stator used is meant for a radial rotor. Thus, it would be profitable to investigate the possibility of designing a nozzleed stator meant for mixed flow turbines. This would be beneficial for the purpose of using a mixed flow rotor in VG turbines, where the current research and possible improvement are discussed in the paper with the aim of improving energy extraction from the engine exhaust gas.

Since the inception of the idea, mixed flow turbines have gone through many stages of improvement and proven to be suitable as a replacement for radial turbines. However, the very low cost to performance criteria of a radial turbine impose a big challenge on producing a mixed flow turbine with better overall performance. The authors believe that the higher swallowing capacity and load-

ing coefficient of a mixed flow turbine are a key to improve the unsteady performance of a turbocharger. The steady-state performance of a turbocharger can be considered to be at its maturity but it is not the case for the unsteady conditions. There is still need for more studies to be carried out in order to fully understand a turbocharger turbine's behavior under pulsating flow and eventually to improve it, where a mixed flow turbine can be useful.

The discussion of this paper is aimed at providing readers with an overview and literature references of the most prominent research works involving mixed flow turbines in the past 50 years. In the authors' opinion, this would benefit the new and current researchers in the turbomachinery field, especially in the engine turbocharging sector.

Acknowledgment

The authors would like to thank the Engineering and Physical Sciences Research Council (EPSRC) and University Technology Malaysia for the financial support.

Nomenclature

| | |
|-----------|---|
| U | = rotor velocity (m/s) |
| P | = pressure (Pa) |
| ss | = suction side |
| C_{is} | = isentropic velocity (m/s) |
| ps | = pressure side |
| T | = temperature (K) |
| cp | = specific heat (kJ/kg K) |
| r | = radial direction |
| z | = axial direction |
| γ | = specific heat ratio |
| η | = efficiency |
| θ | = radial angle (cylindrical coordinate) |
| λ | = cone angle (deg) |
| ϕ | = camber angle (deg) |
| β | = relative flow angle (deg) |
| ψ | = turbine loading |

Subscripts

| | |
|---------|-------------------|
| TS/ts/s | = total-static |
| 2 | = rotor inlet |
| T/t | = turbine |
| B | = blade |
| 0 | = total condition |

References

- [1] Hamerick, J. T., Ginsburg, A., and Osborn, W. M., 1950, "Method of Analysis for Compressible Flow Through Mixed-Flow Centrifugal Impellers of Arbitrary Design," NACA Report No. TN 2165.
- [2] Stewart, W. L., 1951, "Analytical Investigation of Flow Through High-Speed Mixed-Flow Turbine," NACA Report No. RM E51H06.
- [3] Wallace, F. J., 1971, "A Systematic Approach to the Design of Radial Inflow and Mixed Flow Turbines," NACA Report No. CP 1180.
- [4] Watson, N., and Janota, M. S., 1982, *Turbocharging the Internal Combustion Engine*, Macmillan, London.
- [5] Whitfield, A., and Baines, N. C., 1990, *Design of Radial Turbomachines*, Longman, England.
- [6] Japikse, D., and Baines, N. C., 1994, *Introduction to Turbomachinery*, Concepts ETI, Oxford University Press, Oxford, England.
- [7] Rodgers, C., 1990, "Review of Mixed Flow and Radial Turbine Options," AIAA Paper No. 90-2414.
- [8] Palfreyman, D., and Martinez-Botas, R. F., 2002, "Numerical Study of the Internal Flow Field Characteristics in Mixed Flow Turbines," ASME Paper No. GT-2002-30372.
- [9] Wallace, F. J., and Pasha, S. G. A., 1972, "Design, Construction and Testing of a Mixed Flow Gas Turbine," *The Second International JSME Symposium on Fluid Machinery and Fluids*, Tokyo, Japan, pp. 213-224.
- [10] Baines, N. C., Wallace, F. J., and Whitfield, A., 1979, "Computer Aided Design of Mixed-Flow Turbines for Turbochargers," ASME J. Turbomach., **101**, pp. 440-449.
- [11] Yamaguchi, H., Nishiyama, T., Horiai, K., and Kasuya, T., 1984, "High Performance Komatsu KTR150 Turbocharger," SAE Paper No. 840019.
- [12] Chou, C.-C., and Gibbs, C. A., 1989, "The Design and Testing of a Mixed-Flow Turbine for Turbochargers," SAE Paper No. 890644.
- [13] Abidat, M., Chen, H., Baines, N. C., and Firth, M. R., 1992, "Design of a Highly Loaded Mixed Flow Turbine," Proc. Inst. Mech. Eng., Part A, **206**, pp. 95-107.
- [14] Naguib, M., 1986, "Experience With the Modern RR 151 Turbocharger for High-Speed Diesel Engines," *IMEchE Turbocharging and Turbochargers Transactions*, Paper No. 99/86.
- [15] Minegashi, H., Matsushita, H., and Sakakida, M., 1995, "Development of a Small Mixed-Flow Turbine for Automotive Turbochargers," ASME Paper No. 95-GT-53.
- [16] Chen, H., and Baines, N. C., 1992, "Analytical Optimization Design of Radial and Mixed Flow Turbines," Proc. Inst. Mech. Eng., Part A, **206**, pp. 177-187.
- [17] Whitfield, A., 1990, "The Preliminary Design of Radial Inflow Turbines," ASME J. Turbomach., **112**, pp. 50-57.
- [18] Chen, H., Abidat, M., Baines, N. C., and Firth, M. R., 1992, "The Effect of Blade Loading in Radial and Mixed Flow Turbines," ASME Paper No. 92-GT-92.
- [19] Chen, H., Baines, N. C., and Abidat, M., 1997, "Exit Traverse Study of Mixed-Flow Turbines With Inlet Incidence Variation," Proc. Inst. Mech. Eng., Part A, **211**, pp. 461-475.
- [20] Kim, C. M., and Civinskas, K. C., 1994, "An Aerodynamic Analysis of a Mixed Flow Turbine," NASA Report No. TN-106674.
- [21] Arcoumanis, C., Hakeem, I., Khezzar, L., and Martinez-Botas, R. F., 1995, "Performance of a Mixed Flow Turbocharger Turbine Under Pulsating Flow Conditions," ASME Paper No. 95-GT-210.
- [22] Szymko, S., Martinez-Botas, R. F., and Pullen, K. R., 2005, "Experimental Evaluation of Turbocharger Turbine Performance Under Pulsating Flow Conditions," ASME Paper No. GT 2005-68878.
- [23] Dale, A., and Watson, N., 1986, "Vaneless Radial Turbocharger Turbine Performance," *Proceedings of IMechE International Conference on Turbochargers and Turbocharging*, Paper No. C110/86.
- [24] Winterbone, D. E., Nikpour, B., and Frost, H., 1991, "A Contribution to the Understanding of Turbochargers Turbine Performance in Pulsating Flow," *IMEchE Seminar*, Paper No. C433/011.
- [25] Baines, N. C., Hajilouy-Benisi, A., and Yeo, J. H., 1994, "The Pulse Flow Performance and Modelling of Radial Inflow Turbines," *IMEchE Conference on Turbocharging and Turbochargers*, Paper No. C484/006/94.
- [26] Baines, N. C., and Yeo, J. H., 1991, "Flow in a Radial Turbine under Equal and Partial Admission Conditions," *IMEchE Conference on Turbomachinery*, Paper No. C423/002.
- [27] Karamanis, N., and Martinez-Botas, R. F., 2002, "Mixed-Flow Turbines for Automotive Turbochargers: Steady and Unsteady Performance," Int. J. Engine Res., **3**(3), pp. 127-138.
- [28] Whitfield, A., and Noor, A. B., 1990, "Investigation of the Flow Characteristics of Radial Inflow Turbocharger Volutes," *Proceedings of IMechE International Conference on Turbochargers and Turbocharging*, pp. 23-38.
- [29] Karamanis, N., Martinez-Botas, R. F., and Su, C. C., 2001, "Mixed Flow Turbines: Inlet and Exit Flow Under Steady and Pulsating Conditions," ASME J. Turbomach., **123**, pp. 359-371.
- [30] Okapuu, U., 1987, "Design and Aerodynamic Performance of a Small Mixed-Flow Gas Generator Turbine," Report No. AGARD CP-421, pp. 16-1 and 16-11.
- [31] Kirtley, K. R., Beach, T. A., and Rogo, C., 1993, "Aeroloads and Secondary Flows in a Transonic Mixed-Flow Turbine Stage," ASME J. Turbomach., **115**, pp. 590-601.
- [32] Palfreyman, D., and Martinez-Botas, R. F., 2004, "The Pulsating Flow Field in a Mixed-Flow Turbocharger Turbine: An Experimental and Computational Study," *Proceedings of ASME Turbo Expo*, Paper No. GT-2004-53143.
- [33] Chen, H., Hakeem, I., and Martinez-Botas, R. F., 1996, "Modelling of a Turbocharger Turbine Under Pulsating Inlet Conditions," Proc. Inst. Mech. Eng., Part A, **210**, pp. 397-408.
- [34] Chen, H., and Winterbone, D. E., 1990, "A Method to Predict Performance of Vaneless Radial Turbine Under Steady and Unsteady Flow Conditions," *Proceedings of IMechE International Conference on Turbochargers and Turbocharging*, pp. 13-22.
- [35] Abidat, M., Hachemi, M., Hamidou, M. K., and Baines, N. C., 1998, "Prediction of the Steady and Non-Steady Flow Performance of a Highly Loaded Mixed Flow Turbine," Proc. Inst. Mech. Eng., Part A, **212**, pp. 173-184.
- [36] Baets, J., Bernard, O., Gamp, T., and Zehnder, M., 1998, "Design and Performance of ABB Turbocharger TPS57 with Variable Turbine Geometry," *International Conference on Turbocharging and Turbochargers*, Paper No. C554/017/98.
- [37] Rajoo, S., and Martinez-Botas, R. F., 2006, "Experimental Study on the Performance of a Variable Geometry Mixed Flow Turbine for Automotive Turbocharger," *IMEchE. Eighth International Conference on Turbocharging and Turbochargers*, London.
- [38] Pesiridis, A., Szymko, S., Rajoo, S., and Martinez-Botas, R. F., 2004, "Development of Active Flow Control in a Turbocharger Turbine for Emission Reduction," *IMEchE Internal Combustion Engine Performance and Emissions Conference*, London.
- [39] Pesiridis, A., and Martinez-Botas, R., 2005, "Experimental Evaluation of Active Flow Control Mixed-Flow Turbine for Automotive Turbocharger Application," *Proceedings of ASME Turbo Expo 2005*, Reno-Tahoe, NV, Paper No. GT 2005-68830.
- [40] Pesiridis, A., and Martinez-Botas, R., 2006, "Active Control Turbocharger for Automotive Application: An Experimental Evaluation," *IMEchE. Eighth International Conference on Turbocharging and Turbochargers*, London.

**Erratum: “Curtis Stage Nozzle/Rotor Aerodynamic Interaction
and the Effect on Stage Performance”
[Journal of Turbomachinery, 2007, 129(3), pp. 551–562]**

Stephen Rashid, Matthew Tremmel, John Waggott, and Randall Moll

In the published version, John Waggott’s affiliation was improperly listed. The proper affiliation is displayed below.

John Waggott
Independent Consultant
1933 Riverview Dr.,
Wellsville, NY 14895